ENABLING ELECTRONIC OPEN-GATE JFET (OG-JFET) FOUNDRY PROCESS: DESIGN, IMPLEMENTATION, SIMULATION AND CHARACTERIZATION

ABBAS PANAHI

A DISSERTATION SUBMITTED TO THE FACULTY

OF GRADUATE STUDIES IN PARTIAL

FULFILLMENT OF THE REQUIREMENTS FOR

THE DEGREE OF DOCTOR OF PHILOSOPHY

GRADUATE PROGRAM IN ELECTRICAL ENGINEERING AND COMPUTER SCIENCE

YORK UNIVERSITY

TORONTO, ONTARIO

AUGUST 2024

©ABBAS PANAHI, 2024

Abstract

Field-effect transistors (FETs) have emerged as a transformative platform in biosensing, effectively bridging the gap between electronics and biology by measuring the intrinsic charge of bioparticles. The development of FET-based sensing techniques can be traced back to the 1970s with the advent of the ion-sensitive FET (ISFET). This innovation stemmed from Bergveld's pioneering work on metal-oxide semiconductor-based FETs, which were modified to create ISFETs. The core innovation behind ISFETs and BioFETs was the realization that replacing the metal gate of a MOSFET-like structure with an ion-sensitive membrane could transform the device into a robust biosensor with biomolecular sensing capabilities. This modification, involving the replacement of the top gate with a solution gate, enables a sensing modality where the potential of the interface between the solution and the sensing layer (typically dielectrics) can be measured. These solid-state devices leverage the modulation of charge carriers at the semiconductor-electrolyte interface, facilitating label-free detection of biological and chemical analytes. FET biosensors offer numerous advantages, including intrinsic molecular charge sensing, real-time monitoring, high sensitivity, size scalability (ranging from a few nanometers to tens of micrometers), and compatibility with standard integrated circuit (IC) technologies such as complementary metal-oxide semiconductor (CMOS). Over the past three decades, researchers have harnessed the inherent charge sensitivity of FET sensors to detect a wide range of analytes, including ions, proteins, DNA, and other biomolecules. These sensors can selectively capture target analytes by functionalizing the FET's gate surface with specific receptors, such as antibodies or aptamers. This capability has positioned FET biosensors as crucial tools in medical diagnostics, environmental monitoring, and drug development, driving innovation and expanding the frontiers of these fields.

The widespread demand for FET sensors across diverse sensing domains underscores the critical role of standard foundry-based fabrication methodologies. Efforts to refine FET sensor fabrication processes for enhanced reliability, scalability, and reproducibility are crucial for mass production and widespread adoption. Standard foundry-based fabrication techniques ensure uniformity and consistency in device performance, enabling seamless integration into diverse sensing platforms across industries. Most standard FET sensors (or ion-sensitive FETs) have been realized by CMOS platforms, which allow these sensors to be manufactured in an almost flawless foundry process that creates ICs in our cell phones. Various CMOS-based ISFET configurations were made and

used for different biosensing applications. Later, graphene and carbonaceous materials were used as novel high-performance FET biosensors. However, the real breakthrough came with the efforts to standardize graphene FETs through foundry fabrication, pioneered by companies such as Cardea Bio and Graphena. This strategic initiative has not just made graphene FETs more accessible but has democratized access to them, previously hindered by prohibitive costs. This development fosters accessibility for researchers and industrial stakeholders, opening new avenues for research and innovation. By leveraging standard foundry-based fabrication approaches, FET sensors are poised to meet the escalating demand for reliable, high-performance sensing solutions. This advancement could catalyze innovation across various fields, spanning healthcare, environmental monitoring, agriculture, and beyond.

The recent introduction of the open-gate junction field-effect transistor (OG-JFET) by CMC Microsystem represents a significant advancement in silicon-foundry-based FET sensor technology standardization. The OG-JFET foundry enables the mass production of chips with diverse designs on a silicon wafer, allowing for customized configurations tailored to specific application requirements. The structural innovation of the OG-JFET, achieved by removing the top gate of a p-type JFET sensor and introducing a soft material, indicates a new era of charge-sensing capabilities within a JFET electronic structure. Understanding the intricate physics of the charge sensing mechanism and its integration with microfluidics has been pivotal in unlocking the full potential of the OG-JFET. As the technology is still in its early stages of development and scale-up, user-friendly CAD tools and dedicated portable characterization systems have emerged as a cornerstone for successful adoption and integration in academic and industrial research settings. This system enhances performance and facilitates seamless integration into diverse research environments.

This thesis is dedicated to tackling the challenges inherent in comprehending the charge-sensing physics of OG-JFET sensors and exploring the design and simulation of these sensors to discern the impacts of various design parameters. At the heart of this research lies developing a portable characterization system and electro-fluidics packaging schemes to streamline testing and characterization processes. A key objective of this endeavor is to standardize these processes, thereby overcoming the barrier posed by the high cost and limited accessibility of conventional characterization equipment such as probe stations and semiconductor analyzers. By providing

researchers with accessible and cost-effective alternatives, this research seeks to democratize access to this FET sensor foundry technology, thus fostering innovation and discovery in chemical and biological sensing. These concerted efforts aim to accelerate the adoption and advancement of FET sensor technology, paving the way for transformative breakthroughs in scientific inquiry and technological applications.

Dedication

To my family.

Acknowledgment

The completion of this dissertation stands as a testament to the support extended to me by numerous individuals and institutions, without whom this achievement would not have been possible. I express my profound appreciation to all who have contributed to this endeavor. First and foremost, I extend my heartfelt gratitude to my supervisor, Professor Ebrahim Ghafar-Zadeh, whose invaluable guidance, insightful comments, and encouragement have been instrumental in shaping my Ph.D. research journey. His expertise in electrical engineering, biomedical engineering, and microfluidics and his support have profoundly influenced my academic and personal growth.

I am also grateful to my co-supervisor, Professor Sebastian Magierowski, for his support and valuable mentorship for my research development. His mentorship has been invaluable, and I am sincerely thankful for his guidance and encouragement throughout this journey. I sincerely appreciate my esteemed committee members, Professor Gerd Grau and Professor Afshin Rezaei, for their invaluable insights, constructive feedback, and guidance during my annual committee meetings and the comprehensive exam. Additionally, I am deeply grateful to Professor Ali Asgari and Professor Amine Miled for graciously agreeing to serve as the internal and external referees for my oral examination. I want to express my sincere gratitude to Professor Amirali Amirsoleimani for graciously agreeing to serve on my defense committee.

I extend my heartfelt gratitude to my colleagues and friends, whose constant support has strengthened me throughout my Ph.D. journey. I want to express my special thanks to Dr. Hamed Osouli Tabrizi and Mr. Giancarlo Ayala-Charca for their invaluable contributions to the design and fabrication of the readout system. Additionally, I am grateful to Mr. Morteza Ghafar-Zadeh for his assistance with biology and chip packaging. I sincerely thank Dr. Paria Naderi for her patience and support in guiding me through the learning process of using the probe station and semiconductor analyzer when I started my work at York University. Furthermore, I would like to express my gratitude to Dr. Firouz Abbasian for his assistance with DNA synthesis and for leading a crucial part of the experiments for DNA mass measurement. Lastly, I would like to acknowledge and appreciate the invaluable help and mentorship provided by Dr. Saghi Forouhi throughout my project. Her guidance and collaboration on CMOS sensor projects have been instrumental in

extending my knowledge of CMOS capacitive sensors and CMOS-based ISFET electronics and circuitry.

I express my sincere gratitude to York University and Mitacs for the financial support provided throughout my Ph.D. program and to the Department of Electrical Engineering and Computer Science for the numerous awards bestowed upon me during my PhD.

Finally, I thank my family for their unconditional love, unwavering support, and encouragement. Their belief in me has been my guiding light, and I am forever grateful for their presence in my life.

TABLE OF CONTENTS

Abstract ii
Dedication v
Acknowledgment vi
TABLE OF CONTENTS viii
List of Figures xiv
List of Tables xxv
Abbreviations xxvi
Chapter 1 1
1.1. Motivation 1
1.2. Research Gaps, Challenges, and Solutions 4
1.3. Organization of thesis 6
1.3.1. Chapter 1: Introduction 6
1.3.2. Chapter 2: A Literature Survey 6
1.3.3. Chapter 3: OG-JFET Sensing System 6
1.3.4. Chapter 4: Microfluidics Integration 7
1.3.5. Chapter 5: Performance Analysis of OG-JFET (Simulation and Experimental Study) 7
1.3.6. Chapter 6: OG-JFET Application in Emerging DNA Storage 7
1.3.7. Chapter 7: Molecular dynamics simulation of DNA adsorption on the OG-JFET sensor surface and related experiments 8
1.3.8. Chapter 8: Evaporation-based sensing mechanism enabled with high-surface area OG-JFET 8
1.3.9. Chapter 9: Conclusions and Recommendations for the Future Work 9
1.4. References 9
Chapter 2 Literature Survey 12
2.1. Abstract 12
2.2. Introduction 13

2.3. Sensing Mechanism and Different Structures of Chem/BioFETs 16
2.4. Chem/BioFETs Device Structures 22
2.4.2. Chem/BioFET based on Standard CMOS 26
2.4.4. Extended Gate Chem/BioFET 29
2.4.5. Double Gate Chem/BioFET 31
2.5. Chem/BioFET Structures Used for Infectious Disease Screening 33
2.6.1. Surface Materials 39
2.7. Readout Circuit and Systems 48
2.9. Amelioration of Some Non-idealities 66
2.10. References 68
Chapter 3 Open-Gate Junction Field-Effect Transistor: A New FET Sensing System 87
3.1. Paper 2: Open-Gate Junction Field Effect Transistor (OG-JFET) for Life Science Applications: Design, Implementation, and Characterization 88
3.1.1. Abstract 88
3.1.2. Introduction 89
3.1.3. Related works 90
3.2. Paper 3: Electronic Sensing Platform (ESP) Based on Open-Gate Junction Field-Effect Transistor (OG-JFET) for Life Science Applications: Design, Modeling and Experimental Results 114
3.2.1. Abstract 115
3.2.2. Introduction 115
3.2.3. OG-JFET Mechanism of Working 118
3.2.4. Methods and Experiments 122
3.2.5. Numerical Simulation of OG-JFET 124
3.2.6. Results 130
3.2.7. Discussion 143
3.2.8. Conclusions 145
3.2.9. References 146
Chapter 4 Microfluidics Integration with Open-Gate Junction Field-Effect Transistor 151
4.1. Abstract 152

4.2. Introduction 152
4.3. Electronic Sensor 156
4.3.1. Open-gate junction field-effect transistor and microfluidics 156
4.3.2. Mathematical modeling 157
4.4. Microfluidics and electrical packaging 160
4.4.1. Electrical packaging 161
4.4.2. Microfluidic packaging 162
4.5. Results 164
4.5.1. Sensor response in dry condition 166
4.5.2. Solution tests in the microfluidic channel 167
4.5.3. Mathematical Modeling Results 169
4.5.4. Microfluidic Simulations 171
4.6. Discussion 173
4.7. Conclusion 174
4.8. References 176
Chapter 5 Parametric Desing of Open-Gate JFET 182
5.1. Abstract 183
5.2. Introduction 183
5.3. Materials and Methods 186
5.3.1. Single Channel Open-Gate Junction Field-Effect Transistor Sensor Fabrication 186
5.3.2. Sensor Characterization 187
5.3.3. COMSOL Simulation 189
5.4. Results 189
5.4.1. Effect of P-Channel Length (L_O) 195
5.4.2. The Effect of P-Channel Thickness (TP) 195
5.4.3. The Effect of N-Channel Thickness (TN) 196
5.4.4. The Effect of N-Channel and P-Channel Doping 198
5.4.5. Simulation of Charge Sensitivity of OG-JFET for Biosensing 200

5.4.6. Simulation Assumptions and Comparison with Experiment 202
5.5. Discussion 203
5.6. Conclusion 206
5.7. References 207
Chapter 6 Application 1: Open-Gate JFET for Emerging DNA Storage 212
6.1. Abstract 213
6.2. Introduction 213
6.3. Background 215
6.4. Proposed Sensing Mechanism 217
6.4.1. OG-JFET Working Principle 217
6.4.2. Design of OG-JFET Sensor 218
6.4.3. Fabrication 220
6.4.4. DNA Preparation 221
6.5. Modeling and Simulation 221
6.6. Measurements 223
6.7. Results 223
6.7.1. Sensor transfer characteristics 223
6.7.2. Sensor Response to Dry DNA 225
.6.7.3 Simulation results 228
6.8. Conclusion 232
6.9. References 233
Chapter 7 Application 2: Interdigital Open-Gate JFET (ID-OGJFET) for DNA Adsorption Monitoring 236
7.1. Abstract 237
7.2. Introduction 237
7.3. Related Works 239
7.4. Proposed Method and Materials 242
7.4.1. DNA Adsorption on ID-OGJFET and Sensing Principles 243
7.4.2. Molecular Dynamics (MD) Simulation 244

7.4.3. Proposed Sensing Platform 247
7.4.4. DNA Strand Sequence Preparations 247
7.5. Results 248
7.5.1. Computational Analysis of dsDNA in Extreme Dehydration on SiO_2: A MD Simulation 248
7.5.2. Fabrication of Chip and Measurement Setup 253
7.5.3. Transfer Characteristics of ID-OGJFET Sensor 253
7.5.4. DNA Adsorption Experimental Results 255
7.6. Discussion 257
7.7. Conclusion 258
7.8. References 259
Chapter 8 Evaporation-based Chemical Sensing Mechanism with Interdigital Open-Gate JFET (ID-OGJFET) 263
8.1. Abstract 264
8.2. Introduction 264
8.3. Related Works 266
8.4. Portable Electrochemical Sensing Platform 267
8.4.1. Proposed Thermo-FET Sensing Mechanism 267
8.4.2. Embedded Interface System 268
8.4.3. Hardware interface system 268
8.4.4. ID-OGJFET Sensor Fabrication 271
8.4.5. Simulation of ID-OGJFET Sensor 271
8.5. Results 272
8.5.1. ID-OGJFET Transfer Characteristics 272
8.5.2. Simulation Results 273
8.5.3. Droplet Evaporation Measurements with ID-OGJFET 275
8.5.4. FET-Enabled Evaporation-based Chemical Content Measurement 278
8.6. Conclusion 279
8.7. Appendix 280
8.7.1. Simulation 280

8.8. References 281
Chapter 9 Contributions, Future Work, and Conclusion 284
9.1. Summary of Contributions 284
9.2. Future works 286
9.2.1. Specific detection of a target DNA in solution 286
9.2.2. Chip design and fabrication for specific analyte detection 287
9.2.3. Device topologies 288
9.2.4. Microfluidics integration 288
9.3. Conclusions 289
9.4. Reference 289
Appendices 290
A1. Conference paper 1 290
A2. Conference paper 2 299
A3. Conference paper 3 308
B1. Collaboration Conference Paper 1 310
B2. Collaboration Conference Paper 2 310
B3. Collaboration Conference Paper 1 310

LIST OF FIGURES

Figure 2-1. (a) The standard structure of a bio field-effect transistor (Bio-FET); (b) the corresponding potential diagram showing the effect of electrolyte on the potential of interfaces. The potential at the oxide layer and solution interface arises and then decreases gradually to the solution potential. Adding the sample would manipulate this potential curve, influencing the charge transport inside the silicon channel. Three main capacitances are involved in the system: the oxide, channel depletion capacitance, and the solution double layer (CDL). 18
Figure 2-2. Showing how atomistic molecular dynamics simulation scales have been used to estimate the charge density on the surface of the oxide layer (here SiO_2): (a) Showing the silicon in atomic representation, which clearly shows the atomistic distribution of water and ions in the vicinity of surface silicon, which create a surface potential decaying into stable value in near zero in diffusion layer. The double layer has been shown, and its effect creates a specific potential on the surface based on the ionic strength of the solution. Molecular dynamics can be used to estimate this potential in very complex solutions containing biomolecules; (b) showing a 3D sketch of an FET device; (c) potential and ions layers on the interface of electrolyte and substrate in the sensor. 21
Figure 2-3. All structures of metal-oxide-semiconductor (MOS)-based ion-sensitive field-effect transistors (ISFETs) platforms that have been used for Chem/BioFET applications: (a) Representation of Oxide-electrolyte gate Chem/BioFETs, which include a reference in a solution on top of the oxide layer; (b) showing the floating gate structure by which the solution area has been separated from the conduction channel by an internal connection from the oxide layer on top of the channel to the solution and sensing membrane; (c) a demonstration of the integration of a floating gate with control gate, which helps to have more accurate control over the gate operation; (d) shows extended gate structure that allows us to have a more extensive sensing area for biosensing purposes. Moreover, an extended gate creates enough room for further integration with the microfluidic system, which in most cases was not applicable to add them to small ISFETs; € oxide-electrolyte gate Chem/BioFET with the back gate, which used the back gate to manipulate the working point of the sensor by changing the depletion effects in the conductive channel. 23
Figure 2-4. The general form of electrolyte and back gated structures of FETs, which have been used for the sensing elements in Chem/BioFET: This nanomaterial-based structure has been widely used for cell, DNA, enzymatic reaction, and chemical sensing; (a) sensor structure; (b) the most frequent nanomaterials used as sensing element and main conductive channel. 25
Figure 2-5. The stimulation and the response of the FET sensor from a cell on top of an oxide-semiconductor. (a) Sensor structure for culturing cells on the oxide layer on top of the conductive channel; (b) the stimuli and the sensor response simultaneously, which shows the successful loading and recording of a pulse onto/from the cell using the ISFET sensor. The FET response is “current,” and the stimulus is voltage. 26

Figure 2-6. The standard complementary metal-oxide-semiconductor (CMOS) ISFET is used to rapidly detect E. coli bacteria using an unchanged CMOS structure coated with a potassium-sensitive membrane. 27
Figure 2-7. The standard CMOS ISFET for cellular monitoring applications. 27
Figure 2-8. The floating gate structure and a real chip designed by Barbaro et al. for Label-free DNA analysis. This sensor contains 80 biosensors that are placed in 2 channels. A microfluidic system has also been bonded on this chip to provide access to the sensing areas for test solutions and reagents. 29
Figure 2-9. An extended gate sensor developed by Kaisti et al. shows a handheld system for biochemical analysis that utilizes a transistor and a specifically designed gate to transfer the detection unit to the sensing FET. 30
Figure 2-10. Extended gate Chem/BioFET structure in which the gold gate was deposited on SiO2 and Si substrate. The extended gate was connected to the fluidic channel through a liquid cell on top of the sensor. 31
Figure 2-11. The double gate structure Chem/BioFET was designed based on the structure. The SiO_2 is placed at the back of the channel (ZnO), and the electrolyte solution is placed on top of the sensing layer and the conductive channel. 32
Figure 2-12. A dual-gate ISFET sensor structure was developed in a standard 0.18 µm SOI-CMOS process. The back gate was created through a backside process to make a double-gate structure. The sensor is completely working based on the CMOS readout. 33
Figure 2-13. FET structure is used to detect RNA. In the figure, Au 1 and Au 2 demonstrate the source and drain pads, respectively. The gate potential has been applied through the Ag/AgCl as RE, and in this picture, the Vb is the bias voltage of the source-drain. 34
Figure 2-14. The sensor proposed by Lee et al. to detect the RNA of H5N1 AIV-based on hybridization detection on the surface of the gold electrode: (a) Showing the working electrode and reference electrode arrangement, which are dedicated for probing and reference reaction; (b) a brief schematic of circuit and the way it has been connected to the reference and working electrodes. 34
Figure 2-15. A CMOS-based Chem/BioFET structure using an underlap-FET biosensor: The cross-sectional of a water droplet is shown as the solution on top of the sensor. This sensor has been used to show the effect of wettability on the sensor characteristics and sensitivity..... 35
Figure 2-16. The silicon nanowire (SiNW) schematic integrated with the PDMS microfluidic channel is designed to direct the flow of the sample of interest toward the solution. An Ag/AgCl electrode is integrated by placing its tip in the inlet of the microfluidic channel. 36
Figure 2-17. The carbon nanotubes (CNT) sensor works based on a back-gate biasing, and the sample is introduced by an electro-aerodynamic separator without using wet samples..... 37
Figure 2-18. Illustration of the avian influenza virus (AIV) sensor configuration, combining double-gate and extended-gate configuration. 37
Figure 2-19. The configuration of ITONWs-FET genosensor. (a) Si/SiO2/Au/ITONWs device; (b) the FESEM images of indium tin oxide (ITO) samples. 39
Figure 2-20. The illustration of the FET-based aptasensor for detecting AIV in chicken serum. The surface of the gold electrode was modified with specific DNA aptamers to identify the

virus's surface protein. The interaction between the probe and the target resulted in the structural change of the aptamers, which was recorded as the surface potential. 40
Figure 2-21. The illustration of the reduced graphene oxide (rGO)-FET immunosensor for Ebola Virus recognition and Surface modification and the conductance changes that occur upon antigen attachment to the antibody. 41
Figure 2-22. (a) Electrical identification of the viral particles using a tailor-made single-walled carbon nanotube (SWCNT)-FET immunosensor; (b) AFM image of the SWCNT channel region. 43
Table 2-1.Recently proposed FET biosensors for detecting various infectious agents. 47
Table 2-2. Different readout circuits for Chem/BioFET sensors. 51
Figure 2-23. (a) Direct Wheatstone bridge; (b) the circuit used to characterize ISFET drift in the feedback mode. 54
Figure 2-24. (a) A basic diagram of a source/drain follower readout circuit; (b) an ISFET amplifier proposed by Bergveld et al. 55
Figure 2-25. (a) Schematic of a column of 16 pixels in the n × n-array sensor chip; (b) a standard ISFET pixel readout; (c) a dual-pixel schematic including a CMOS image sensor and a source follower. 57
Figure 2-26. (a) HCell with the translinear operation; (b) a log-domain filter with an ISFET used at its input; (c) a current-mode readout with current feedback; (d) schematic of a system including three configurations: (I) Current-mode configuration in a 64 × 200 array, (II) current-mode PG pixel architecture in a 64 × 200 array, (III) voltage-mode pixel structure in a 64 × 128 array. 58
Figure 2-27. Ratiometric measurement: (a) ISFET-based translinear divider; (b) a translinear circuit proposed by Kalofonou et al. 59
Figure 2-28. Three configurations of ISFET inverters: (a) p-type and n-type ISFET sharing the same membrane; (b) p-type ISFET with membrane and n-type MOSFET; (c) n-type ISFET with membrane and p-type MOSFET. 61
Figure 2-29. (a) An active pixel sensor (APS) based pH-to-time converter; (b) a readout circuit comprising a pH-to-time-to-voltage conversion (pH-TVC) amplification circuit and 10-bit voltage digital converter. 62
Figure 2-30. ISFET and REFET for array structure; (c) ISFET/REFET voltage-clamped configuration; (d) a chemical Gilbert cell; (e) a ΣΔ ISFET readout circuit using differential measurement. 64
Figure 3-1- 1. The mechanism of operation of OG-JFET in interaction with electrolytes and ions. The pH means the concentration of H+ ions in the solution, and with the increment in H+ concentration, the more negative potential will be created on the surface of the sensor. This will create more current in the p-type channel, resulting from hole current in the p-type channel (p-type JFET). 92
Figure 3-1- 2. The OG-JFET standard fabrication process. (a) Substrate wafer (Silicon <100>, 100 mm diameter, - 420 +/- 25 µm thick, Resistivity 0.006 to 0.02 Ohm-cm); (b) Alignment marker definition (first mask); (c) PECVD SiO_2 deposition; (d) SiO_2 etching to Si layer. (second mask); (e) Front and back-side ion implantation; (f) implantation annealing; (g) front and back side metallization and annealing; (h) PECVD Si_3N_4 deposition (passivation layer); (i) Pad and

channel opening. (b) Optical Microscopy image of the designed sensor based on the standard OG-JFET technology. The sensor has a common source pad, which serves seven OG-JFET in the chip. Channels have the same thickness, length, and width, which are 1.6 μm, 1000 μm, and 100 μm, respectively. (b) Optical microscopy image of the fabricated sensor; (c) the whole chip with pads, source, and drains. 93
Figure 3-1- 3. Demonstration of OG-JFET fluidic fixture. (a) demonstrates the tube connections to the inlet and outlet of the microfluidic channel and the BNC connectors on the PCB, which are responsible for connecting the sensor to the semiconductor analyzer. The fixture enables a continuous microfluidic system. A closeup of the fluidic system has been shown in (b). The microfluidic channel runs between two sets of spring-loaded connectors on both sides, connecting the PCB wirings to the sensor pads. The back gate has been connected through a wire (blue) from the back of the sensor to the PCB. (c) Demonstration of CAD design of microfluidic channel for transporting fluid on top of the sensor. (d) The fabricated sensor was placed on top of the OG-JFET. The glass slide is then glued on the surface of the four-pillared structure and PCB, as shown in (b). 94
Figure 3-1- 4. The circuit for sensor characterization was designed using a semiconductor analyzer (Keithley 4200 A-SCS). 96
Figure 3-1- 5. The size and parameters used in the COMSOL Multiphysics simulation software. (a): demonstrates the essential parameters required for simulating the OG-JFET sensor; (b) presents the meshing structure produced in COMSOL with a structured mesh in the p-type channel and unstructured mesh in the n-type layer. The back gate was also modeled with an ohmic contact according to the fabricated process. 97
Figure 3-1- 6. Experimental result of Ids-Vds curve of OG-JFET for different gate-source voltage changes from 0 to 1 with 0.1 V step. Positive biased voltage has been applied to the back gate and negative biased to drain while the source is maintained at a zero bias. 98
Figure 3-1- 7. Experimental result of Ids-Vgs curve of OG-JFET for different drain-source voltage ranges from 0 to -4.5 V with -0.5 V stepwise. 98
Figure 3-1- 8. COMSOL simulation result of p-type conduction channel OG-JFET drain-source current versus drain-source voltage in different gate-source voltages. The simulation perfectly shows the linear region and also the saturation region of the OG-JFET operation. 100
Figure 3-1- 9. COMSOL simulation results of OG-JFET Ids-Vgs curves. The simulation predicts the experiment trend very well. 100
Figure 3-1- 10. Simulation results of the hole concentration (log) in the different gate and drain biases in p-type and n-type layers. The effect of gate-source voltage depletion on the carriers in the p-channel is demonstrated. As is expected from the conventional JFET, the channel gets narrower very close to the drain. Higher Vds at this point would push the channel to pinch off and start saturation with a constant current..... 101
Figure 3-1- 11. The Ids-Vgs curves for different pH solutions ranged from 4 to 9. The reference current was 0.5 mA to compare the back-gate threshold voltages. Each pH test has been repeated ten times to make sure the curves are consistent and there is no change. In the stabilized condition, the curves are recorded. 102
Figure 3-1- 12. Experimental results of pH sensitivity of OG-JFET in the reference current of 0.5 mA. The sensor demonstrates a 52.12 mV/pH sensitivity at this reference current. The sensitivity

is concluded by fitting a linear line to the reference voltage versus pH values. The sensitivity was measured by obtaining the voltage in a contact current in Ids-Vgs curve for each pH values [31]. 103
Figure 3-1- 13. Comparing the response of all drains to pH variations at reference current of Ids = 0.5 mA. (a): D4, (b): D5, (c): D6, (d): D7, (e): D1, (f): D2, (g): D3. For drain nominations, see Fig. 3-1-2..... 104
Figure 3-1- 14. Representation of pH sensitivity for different reference currents. The selected reference current is: (a) 0.3 mA; (b) 0.35 mA; (c) 0.40 mA; (d) 0.45 mA; (e) 0.50 mA; (f) 0.55 mA..... 105
Figure 3-1- 15. Showing another OG-JFET operation mode for sensing H+ ion concentrations in the buffer solution. The change in Ids versus the pH values as the Vgs change from 0.1 V to 1.0 V in a constant Vds voltage. 106
Figure 3-1- 16. Current enhancement sensitivity for different pH values. pH=4 is the reference for current sensitivity analysis. 106
Figure 3-1- 17. Hysteresis analysis of OG-JFET in a cycle of pH:7→10→7→4→7. The sensor response was recorded every two minutes. For this analysis, the threshold voltage was defined as the back-gate voltage for a constant reference current. The voltage change due to the different pH effects was recorded..... 107
Figure 3-1- 18. Drift analysis of OG-JFET in a constant Vds and Vgs with only reading output current in a constant pH=7.0..... 107
Figure 3-1- 19. Sensitivity comparison of OG-JFET with literature. 108
Figure 3-2- 1. Schematic of OG-FET sensor showing the main material composition of the sensor. The sensing layer of OG-JFET is the p-type silicon between two electrodes of the source and drain. The open-gate area is covered with the native oxide layer, usually appearing when silicon is exposed to air. 119
Figure 3-2- 2. Microscopic images of the designed sensor. (a) The image was taken from the prob-station camera, showing the designed sensor with channels and the common source. (b) Close-up image under the optical microscope. 121
Figure 3-2- 3. Schematic of OG-FET sensor showing the main material composition of the sensor. (a) Substrate wafer (silicon <100>, 100 mm diameter, -420 +/− 25 µm thick, resistivity 0.006 to 0.02 Ohm-cm). (b) Alignment marker definition (first mask). (c) PECVD SiO2 deposition. (d) SiO_2 etching to Si layer (second mask). (e) Front- and back-side ion implantation. (f) Implantation annealing. (g) Front- and back-side metallization and annealing. (h) PECVD Si_3N_4 deposition (passivation layer). (i) Pad and channel opening. 121
Figure 3-2- 4. The experiments were set up using a probstation and the semiconductor analyzer. (a) The probstation was connected to the semiconductors through SMU cables. The droplet containing the analyte of interest was pipetted on the sensor. The droplet volume was 2 µL. (b) Different experiments were developed to characterize sensor capability toward surface charge variation detection. 123
Figure 3-2- 5. Schematic of OG-FET sensor showing the main material composition of the sensor. tn >> tp and tp >> n++ in terms of thickness. The blue color is the SiO_2/Si_3N_4 layer shown in the fabrication process (see Figure 3-2-3) used for passivation. 125
Table 3-2-1. Design parameters are used in the simulation and fabrication of OG-JFET. 125

Figure 3-2- 6. The current-voltage curves of the OG-JFET sensor for two bias conditions, forward and reverse. (a) Ids-Vgs of forwarding bias. (b) Ids-Vgs of reverse bias condition. (c) Ids-Vds curve for reverse bias condition (steps: 0.2 V)..... 131
Figure 3-2- 7. Transfer characteristics of OG-JFET sensor derived from COMSOL simulations. (a) Reverse-bias Ids-Vgs. (b) Reversed-bias Ids-Vds..... 132
Figure 3-2- 8. Drain-source voltage graphs for different pH values for OG-JFET at Vg = 0. (**a**) Ids-Vds curve for different pH values. (**b**) The current sensitivity for different values of Vds. 133
Figure 3-2- 9. Drain-source voltage graphs for different pH values for OG-JFET. (**a**) Ids-Vgs curve for different pH solutions from pH = 4 to pH = 9. (**b**) The voltage sensitivity relative to the back gate reference voltage..... 135
Figure 3-2- 10. The estimated native oxide of OG-JFET surface charge is equivalent to pH.... 136
Figure 3-2- 11. COMSOL simulation results of the pH variations effect on the sensor results. 137
Figure 3-2- 12. Sensor response to single-strand DNA concentration. (**a**) Ids-Vgs curve for different concentrations of ssDNA (370 ng/uL, 301 ng/uL, 270 ng/uL, 180 ng/uL, 101 ng/uL). (**b**) Voltage sensitivity results of OG-JFET response to ssDNA concentration at different reference currents of (1) 0.45 mA, (2) 0.50 mA, (3) 0.55 mA, (4) 0.60 mA, and (5) 0.65 mA. 138
Figure 3-2- 13. The result of the human exhalation test on the OG-JFET..... 140
Figure 3-2- 14. The sensor responds to different concentrations of cell solutions in comparison to bare conditions..... 142
Figure 3-2- 15. Analysis results of three repeats of testing current variations in different concentrations of neutrophils..... 142
Figure 3-2- 16. Nonidealities in neutrophil measurement: (**a**) non-uniformity of the cell distribution in the sample and (**b**) non-uniformity of cells cast on the surface of the sensor. 143
Figure 4-1. Schematic of OG-JFET structure and the microfluidic chamber. 156
Figure 4-2. The simplified model of OG-JFET for mathematical modeling of drain-source current 158
Figure 4-3. The electrical packaging technique. A spring-loaded connector was used to connect the sensor pads to a switch. The switch is connected to the BNC connector..... 161
Figure 4-4. The experiment setup was used to test the OG-JFET sensor. (a): shows the CAD design of the fixture used for connecting the sensor to the semiconductor analyzer. (b): the fabricated test setup, consisting of PCB (BNC, switch), 3D printed support, and microfluidic with its tubing. The back gate is contacted from the back of the sensor to top on the PCB, where it's connected to a BNC connector to the semiconductor analyzer. (c): shows the spring-loaded connectors used to connect the OG-JFET pads to the PCB. On the PCB, there is a switch that enables the user to select the specific channel on the OG-JFET sensor. 163
Figure 4-5. The processes led to the fabrication of a microfluidic channel on top of the sensor. (a): the PDMS replica molding process taken to create the 3D microfluidic with two 2D PDMS; (1) first the 3D printed mold was washed, (2) filling the mold with a 10:1 ratio of pre-prepared PDMS (after filling the mold, the PDMS and mold were put in the vacuum chamber for 20 mins for degassing), (3) after degassing, the PDMS and mold were put in the oven and baked for 5 min at 100 C, (4) the PDMS was peeled off from the mold, (5) at this point a channel is put on a PDMS sheet which has already been prepared with another mold, (6) bonding the PDMS and chip. (b): the used channel molds. (c) showing the peeled-off microfluidic structure. (d): the

PDMS sheet shown in step 5. (e) testing the fluidic connectors with water. (f) showing the adhesion of the PDMS channel on the glass. 163
Figure 4-6. Boding process of the microfluidic channel on the chip. (a): A copper conductive tape was utilized to create the back-gate connection on the glass slide. (b): the sensor is put on the sensor. (c): after heating the microfluidic, it was aligned with the chip under a microscope. (d) filling the gap underneath the microfluidic with UV-curable glue and applying UV light to make the structure strongly bonded. 164
Figure 4-7. The experiment setup was used to test the OG-JFET sensor. (a): shows the CAD design of the fixture that connects the sensor to the semiconductor analyzer. (b): the fabricated test setup, consisting of PCB (BNC, switch), 3D printed support, and microfluidic with its tubing. The back gate is contacted from the back of the sensor to the top of the PCB, where it's connected to a BNC connector to the semiconductor analyzer. (c): shows the spring-loaded connectors used to connect the OG-JFET pads to the PCB. On the PCB, a switch enables the user to select the specific channel on the OG-JFET sensor. 165
Figure 4-8. The Ids-Vds and Ids-Vgs curves of OG-JFET. (a): Ids vs drain-source voltage. (b): Ids vs back-gate voltage 165
Figure 4-9. Change of conductance of OG-JFET with back-gate 166
Figure 4-10. The transconductance of OG-JFET calculated for different values of back 167
Figure 4-11. Preliminary test results of sensor with DI water and 0.9% NaCl solution injected in microfluidic channel. 168
Figure 4-12. The effect of gain on the current sensitivity for different values of surface charges due to pH variations. Sv is the voltage sensitivity of the sensor with a unit of mV/pH 168
Figure 4-13. Mathematical results of the Ids-Vds curves for different Vgs values from 0 to 1 with 0.1 steps. The model can predict the sensor's response in low values of drain-source voltages before saturation. The back-gate voltage also is limited to the Vpo for good accuracy. 169
Figure 4-14. Mathematical modeling result of Ids-Vgs response for Vds values of 2 V and 5 V. 170
Figure 4-15. Mathematical modeling results of surface charge effects on the OG-JFET sensing area. The increment in pH results in more negative surface charge. 170
Figure 4-16. Flow velocity contour in the microfluidic channel for 260 mg/s inlet mass water flow 171
Figure 4-17. Velocity contours for different inlet mass flow rate values in the microfluidic channel. 172
Figure 4-18. The change in shear rate for different values of inlet mass flow rate condition along the centerline of the chamber 173
Figure 5-1. Optical image of single channel OG-JFET and schematics of device and sensing principle. (a): Left: sensor characterization under the optical microscope when placing the probe station needles on the sensing pads. Right: the structure of OG-JFET and the design parameters in a 3D sensor schematic showing the opened-gate area and the encapsulations with SiO_2-Si_3N_4 stacked layers. (b): the sensing mechanism for the sensor in solution and the relation between charge as input and Ids as output. 187

Figure 5-2. Experimental results. (a): The Ids-Vgs curve used for the derivation of gm-Ids (Lo = 5 μm) (b): the experimental results of the gm of the sensor for different back-gate voltages (Lo = 5μm). 190
Figure 5-3. The experimental results of the OG-JFET device efficiency (η). (a): for various Vds. (b): for various Lo values 191
Table 5-1. Comparison of Transconductance of the OG-JFET with literature 192
Figure 5-4. The numerical results of the gm and η of the device with Lo = 5 μm. (a): gm versus Vgs voltage. (b): η versus Vgs voltage. (c): the gm versus Vds for different Vgs. (d): The η (V-1) for different values of Vds. 193
Figure 5-5. The length (Lo) enhancement effect on the g_m and η (V^{-1}). (a): g_m vs p-channel length. (b): η (V^{-1}) vs p-channel length (μm). (c): A broader view of the η-Lo diagram is shown for Lo = 5 μm. 194
Figure 5-6. Numerical results of the effect of T_P (μm) on the sensors g_m and η (a) and (b). Numerical results of the effect of T_N (μm) on the sensor g_m and η (c) and (d). 196
Figure 5-7. Simulation results of the effect of impurity doping (boron and phosphorus) in p-type and n-type channels on the g_m and η performance factors. (a): effect of impurity concentration in p-channel on the g_m. (b): the effect of p-channel impurity doping level on η (The x-axis should be multiplied by 10^{15}). (c): effect of impurity concentration in N-channel on g_m. (d): the effect of impurity concentration in N-channel on the η (The x-axis should be multiplied by 10^{18}) 197
Figure 5-8. Experimental and numerical results of the OG-JFET in forward bias mode when a negative voltage is applied to the back-gate and a positive voltage to drain. (a): The experimental results of Ids-Vds curves for forward bias operation mode of OG-JFET. (b): The experimental results of Ids-Vgs curves for a forward-biased sensor for different Vds values. Current density comparison of two modes of operation of OG-JFET sensor. (c): When the p-n junction is open (forward bias), the current flows from the back side to the drain. (d): shows the reverse bias in which the current only flows inside the p-type channel (in c and d the passivation of metals is not displayed) 199
Figure 5-9. Numerical results of the response of OG-JFET to an equivalent charge sheet model of biomolecular attachment on the open-gate area. (a): COMSOL simulation result of the surface charge variation effects on the drain-source current for positive and negative charges. Comparison of the COMSOL semiconductor simulation with experiment values for g_m at (b): Vds = 1 V and Vds = 2 V and (c): Vds = 3 V and Vds = 4 V. (d): the electrical potential for surface charge values of Q = $+1\times10^{-4}$ C/m^2 and Q = -1×10^{-4} C/m^2. (e): the contour is for the hole doping concertation in the p-type and n-type channel when Lo is 10 μm, representing the place of the A-A line on which the electrical potential in (d) is calculated. 201
Figure 5-10. The experimental setup was used to characterize the sensor's electronic transfer characteristics to calculate transconductance (gm) and device efficiency. 205
Figure 6-1. Schematic of OG-FET sensor showing the main material composition of the sensor. The sensing layer of OG-JFET is the p-type silicon between two electrodes of the source and drain. The open-gate area is covered with the native oxide layer that usually appears when silicon is exposed to air. 215
Table 6-1. Recent biosensors based on field-effect transistor 216

Figure 6-2. Schematic of the fabricated OG-JFET sensor used for testing the dry DNA. The sensing area is shown as the drain/source arrangements. The design consists of seven drains with one common source. Drain 1 has been used in this report to measure the mass DNA concentration. 218
Figure 6-3. Microfabrication process for building OG-JFET sensor. (a) Substrate wafer (Silicon <100>, 100 mm diameter, - 420 +/- 25 µm thick, Resistivity 0.006 to 0.02 Ohm-cm); (b) Alignment marker definition (first mask); (c) PECVD SiO_2 deposition; (d) SiO_2 etching to Si layer. (second mask); (e) Front and back-side ion implantation; (f) implantation annealing; (g) front and back side metallization and annealing; (h) PECVD Si_3N_4 deposition (passivation layer); (i) Pad and channel opening. 219
Figure 6-4. The sensor surface was clean and non-chemically treated before testing with DNA samples. 220
Figure 6-5. Schematic of OG-FET sensor showing the main material composition of sensor. .. 222
Figure 6-6. Ids-Vgs and Ids-Vds curves of OG-JFET with no sample. 224
Figure 6-7. OG-JFET sensor response to different concentrations of DNA solvated in ultra-pure water. The droplet of DNA in ultrapure water has been put on top of the sensing area. The curves result from the sensor response to the dried DNA in the solution. 225
Figure 6-8. The effect of the washing process on the sensor response. 226
Figure 6-9. Sensitivity analysis of OG-JFET to dry DNA. Sensor response to different DNA concentrations in dry mode. 226
Figure 6-10. COMSOL simulation result of modeled DNA charge on the OG-JFET sensor which shows an almost linear dependency between current and the DNA concentration. 228
Figure 6-11. The electrical potential along the centerline (shown in figure inset). Cons: Concentration. 229
Figure 6-12. The current sensitivity obtained from COMSOL simulation at Vds = 5 V and Vg = 0 230
Figure 7-1. The sensing mechanism of OG-JFET for detection of charge distributed on native SiO_2 as the outer layer of OG-JFET due to evaporation of solution and accumulation of DNA charge. Top left: The enhancement of the hole concentration in the channel due to the attachment of DNA. Bottom left: The hole is transported in the channel when no adsorption occurs. 238
Figure 7-2. The simulation box (water and ions not shown) used in the MD simulation (a): the dimension of SiO_2 slab. (b): the length of dsDNA. (c): the initial distance between few atoms of dsDNA and surface atoms of SiO_2. 245
Table 7-1. The information on the synthesized DNA used in the experiments. 248
Figure 7-4. Result of MD simulation of DNA adsorption on silica in dehydrated mode. (a): ds-DNA induced surface potential of SiO_2 in solution mode with 14nm water box. (b): the snapshot of DNA in solution mode. (c): the DNA-induced surface potential of SiO_2 in extreme conditions of dehydration (low water molecules). (d): a snapshot of DNA wholly laid on the SiO_2 surface. (e): denaturation of dsDNA in dry mode (extreme dehydration). (f): DNA in a box with 2 nm water. (g): DNA in a box with 7 nm water. (h): DNA in a water box with 14 nm water 249
Figure 7-5. Three distances were measured on the adsorbed DNA on the surface of SiO2 when water molecules are diminished due to the evaporation to a thin layer of 10 nm × 10 nm × 1nm (x, y, and z). Due to evaporation, it appears that dsDNA denatures on the surface and no longer

holds helical structure in extremely low water density. (a): comparison of three distance values for DNA in 1nm and 14 nm water box. (b): the DNA in a 1nm water box. (c): The DNA in a 14nm water box..... 250
Figure 7-6. The surface potential of SiO_2 was measured with MD. (a) The averaged surface potential is based on the color scale bar for each system with a specific water volume (from 1nm thickness to 14 nm), and k is the arbitrary constant multiplied by the number of water atoms for each water thickness. Surface potential contours and related contours for (b): 1 nm, (c): 2 nm, (d): 7 nm, and (e): 14 nm water box thickness with x and y dimensions of 10 nm × 10 nm..... 251
Figure 7-7. The radial distribution function analysis of dsDNA on SiO_2 in (a): 14 nm water box, (b): 1nm water box. The g(r) results of water around dsDNA are shown for (c): dsDNA in 14 nm water box, (d): dsDNA in 1 nm water box. 252
Figure 7-8. The I-V curve characteristics of ID-OGJFET sensor. (a): the Ids-Vds curve. (b): the Ids-Vgs curve. 254
Figure 7-9. The experimental results of the sensor's response to the adsorption of the dsDNA on the sensor. (a): drain-source current versus the back gate for the different concentrations of dsDNA dehydrated on the sensor. (b): the Ids current versus dsDNA concentrations at Vgs = 0 and Vds = -5 256
Figure 8-1. The FET sensor configuration is used to show the droplet evaporation. (a) 3D schematic of sensor holding a droplet. The droplet spreads across the sensing region and establishes chemical bonding with the sensor's surface. The droplet in the actual experiment is shown in (b). As the sensor is interdigital, it ensures the sensing of all the areas of droplets in the sensing region. The cross-sectional structure of the sensor and the sensing mechanism is shown schematically in (c). 267
Figure 8-2. (a) The electronic readout system comprises a central block diagram of DAC, ADC, IC shunt, and DC power supply. (b): fabricated devices, (i) a photograph of a packaged readout system (i) that is connected to a computer, (ii) a photograph of a packaged electro-fluidic device, (iii) a fabricated PCB and circuit, and (iv) structure of ii consisting of (1) support layer, (2) fluidic layer, (3) probing, ID-OGJFET and small PCB for electro fluidic structure; and (c): image of GUI for setting the readout system. 270
Figure 8-4. (a): gm-Vgs curve. (b): gm-Vds curve at Vgs = 0. (c): Ids-Vds curves. (d): Ids-Vgs curves of ID-OGJFET 273
Figure 8-5. (a): COMSOL simulation result of Ids-Vds curve of an ID-OGJFET with a channel length of 100 um. (b): Ids-Vgs curves. 274
Figure 8-6. (a): the relationship between Ids and T (K). (b): Ids-Vds when Vgs is increasing for three different T (K) values 275
Figure 8-7. Shows the amperometric mode of ID-OGFET used to track the evaporation of a droplet until complete evaporation. The sensor is reverse biased, and the Vds is kept constant at—2 V when the Vgs = 0 and Vs = 0 V. As the droplet evaporates, optical microscopy records it during evaporation. 277
Figure 8-8. The ToE versus alcohol concentration was measured in water using ID-OGJFET. (a): ToE versus concentrations of ethanol in water. (b): ToE versus concentrations of methanol in water 279
Figure A1- 1. The structure of the open gate junction field affects the transistor sensor. 292

Figure A1- 2. The standard fabrication process of OG-JFET. 293
Table A1- 1. Design parameters values for OG-JFET 294
Figure A1- 3. OG-JFET design parameters that can be controlled in fabrication. 294
Figure A1- 4. The fabricated sensor consists of seven channels and one common source. (a) layout design, (b) the fabricated sensor 295
Figure A1- 5. The test setup used for pH tests on-chip. (a) connection of the syringe pump and the microfluidic channel; (b) the circuit schematic; (c) a closeup of the chip, microfluidic, 3D printed structure, and spring-loaded connectors. 296
Figure A1- 6. Ids-Vds curve of OG-JFET for reversed bias condition. (a) COMSOL result; (b) experiment results 296
Figure A1- 7. OG-JFET response to different pH values. Inset: OG-JFET sensitivity at reference current of 0.5 mA and Vds = 5 V. 297
Figure A2- 1. The structure of the OG-JFET sensor in comparison to other structures. (a): OG-JFET, (b): back gate structure, (c): Modified CMOS structure, (d): CMOS extended gate 301
Figure A2- 2. The microscopic image of the fabricated sensor 302
Figure A2- 3. The probstation and semiconductor analyzer are used to characterize the sensor.304
Figure A2- 4. The Ids-Vds curves of the sensor when the back gate voltage is increasing..... 304
Figure A2- 5. COMSOL simulation result showing Ids-Vds of OG-JFET when back gate voltage is increasing 305
Figure A2- 6. Simulation and experimental results of dried ssDNA tests on the sensor for different concentrations (ug/nL). (a): COMSOL simulation, (b): experimental result..... 305

LIST OF TABLES

Table 2-1.Recently proposed FET biosensors for detecting various infectious agents. 47
Table 2-2. Different readout circuits for Chem/BioFET sensors. 51
Table 3-2-1. Design parameters are used in the simulation and fabrication of OG-JFET. 125
Table 5-1. Comparison of Transconductance of the OG-JFET with literature 192
Table 6-1. Recent biosensors based on field-effect transistor..... 216
Table 7-1. The information on the synthesized DNA used in the experiments. 248
Table A1- 1: Design parameters values for OG-JFET……..…….294

Abbreviations

FET	Field-Effect Transistor
IC	Integrated Circuit
MEMS	Micro-Electro-Mechanical Systems
NEMS	Nano-Electro-Mechanical Systems
PoC	Point of Care
CRSIPR	Clustered Regularly Interspaced Short Palindromic Repeats
DNA	Deoxyribonucleic Acid
CMOS	Complementary Metal Oxide Semiconductor
JFET	Junction Field-Effect Transistor
OG-JFET	Open-Gate Junction Field-Effect Transistor
PCB	Printed Circuit Board
SMU	Source Measuring Unite
MD	Molecular Dynamics
FEM	Finite Element Method
LoD	Limit of Detection
COVID-19	Coronavirus disease 2019
BioFET	Biological Field-Effect Transistor
PCR	Polymerase Chain Reaction
HIV	Human immunodeficiency
ELISA	Enzyme-Linked Immunosorbent Assay
ISFET	Ion-Sensitive Fiel-Effect Transistor
MOSFET	Metal-Oxide-Semiconductor Field-Effect Transistor
PBS	Phosphate-Buffered Saline
pH	Potential of Hydrogen

DL	Double Layer
IHL	Inner Helmholtz
OHL	Outer Helmholtz
CNT	Carbon Nanotubes
MOS	Metal Oxide Semiconductor
GFET	Graphene Field-Effect Transistor
NW-FET	Nanowire Field-Effect Transistor
MOF	Metal-Organic Framework
PfGDH	Plasmodium falciparum glutamate dehydrogenase
RE	Reference Electrode
CνMOS	Chemoreceptive neuron MOS
BHV-1	Bovine Herpes Virus-1
SOI	Silicon-Oxide-Insulator
SNR	signal-to-noise ratio
SiNW	Silicon Nanowire
HCV	Hepatitis C Virus
PNA	Peptide Nucleic Acid
SWCNT	Single-Wall Carbon Nanotube
AIV	Avian Influenza Virus
RNA	Ribonucleic Acid
PDMS	Polydimethylsiloxane
RCA	Rolling Circle Amplification
EVD	Ebola Virus Disease
rGO	reduced Graphene Oxide
ITO	Indium Tin Oxide
HBV	Hepatitis B Virus
BRE	Bio-Recognition Elements
ssDNA	Single-strand Deoxyribonucleic Acid

GNR	Graphene Nanoribbon
TMD	Transition Metal Dichalcogenides
FGF	Fibroblast Growth Factor
PMO	Phosphorodiamidate Morpholino Oligos
CP	Conducting Polymers
CPNT	Carboxylated Polypyrrole Nanotubes
PBASE	Pyrene Butanoic Acid Succinimidyl Ester
APTES	3-Aminopropyl Triethoxysilane
LAMP	Loop-Mediated Isothermal Amplification
PNA	Peptide Nucleic Acid
PVC	Polyvinyl Chloride
CMP-NANA	Cytidine-50-onophospho-N-acetylneuraminic acid
STV	Streptavidin
HBV	Hepatitis B Virus
EDC	N-ethyl-N′-Dimethylaminopropyl Carbodiimide
NHS	N-Hydroxysuccinimide
MPTMS	3-mercaptopropyltrimethoxysilane
Biotin-HPDP	N-(6-(biotinamido)hexyl)-3’-(2’-pyridyldithio)-propionamide
DTT	Dithiothreitol
VM	Voltage Mode
CM	Current Mode
VS	Velocity Saturation
PG	Programmable Gate
PA	Pixel Array
AB	Analog Blocks
DB	Digital Block
pH-TVC	pH-to-Time-to-Voltage Converter

pH-TC	pH-to-time Converter
IDR	Input Dynamic Range
SFE	Single Front End
CVCC	Constant-Voltage Constant-Current
CC	Current Conveyor
SPT	Standard Pixel Topology
APS	Active Pixel Sensor
AER	Address Event Representation
MM	Magnetic Manipulation
S/H	Sample and Hold
RO	Ring Oscillator
Hcell	Hydrogen cell
ADC	Analog to Digital Converter
PWM	Pulse-Width Modulation
SOC	System-n-Chip
DG-FET	Double-Gate Field-Effect Transistor
TG-FET	Triple-Gate Field-Effect Transistor
PECVD	Plasma-Enhanced Chemical Vapor Deposition
RPM	Revolutions Per Minute.
HCL	Hydrochloric Acid
DNAc	DNA Concentration
IPA	Isopropyl Alcohol
DWFP	Direct-Write Microfluidic Fabrication Process
CAD	Computer Aided Desing
UV	Ultraviolet
VLSI	Very Large System Integration
SRH	Shockley-Read-Hall
SiC	Silicon Carbide

GaN	Gallium Nitride
InAs	Indium Arsenide
SEME	Simulation-Experiment Mismatch Error
DMF	Digital-Microfluidic
BFPA	2,6-bis(4-formylphenyl)- Anthracene
SRE	Solution Reference Electrode
SG	Solution Gate
NLR	Non-Linear Response
LDM	Low Dimension Materials
OFET	Organic Field-Effect Transistor
ID-OGJFET	Interdigital Open-Gate Junction Field-Effect Transistor
ODD	Optical Disc Drive
MD	Molecular Dynamics
RI	Radioisotope
XPS	X-ray photoelectron spectroscopy
AFM	Atomic Force Microscopy
OWLS	Optical Waveguide Lightmode Spectroscopy
QCM	Quartz Crystal Microbalance
SPR	Surface Plasmon Resonance
NAMD	Nanoscale Molecular Dynamics
VMD	Visual Molecular Dynamics
GUI	Graphical User Interface

Chapter 1

INTRODUCTION

1.1. Motivation

Adopting standard foundry processes is crucial in high-volume semiconductor-based biochip fabrication and integration with biomedical sensing devices, especially FET sensors, which are promising in biomedical applications [1]. In FET sensors, standard foundries, such as those used in IC semiconductor manufacturing, offer high precision, reproducibility, and scalability, which are critical for producing consistent quality and performance in FET-based sensing chips [2]. This standardization is essential as producing FET sensors through in-house laboratories (often in universities) usually leads to variations in device performance metrics, complicating the consistency of biological sensing results in batch testing [3], [4]. Leveraging standard foundries provides significant advantages in addressing these challenges. These processes, refined through decades of semiconductor industry advancements, enable precise control over the microfabrication of ICs, MEMS, and NEMS devices, ensuring the reliable production of complex miniaturized (nm to μm) structures [5], [6]. Standardizing these processes allows for the seamless integration of electronic and biological assays on a single chip, enhancing the functionality and versatility of electronic chips for biosensing applications [7]. This integration is crucial for advancing the development of reliable, high-performance biomedical sensors, paving the way for innovative medical diagnostics and health monitoring applications [8], [9].

Standard foundry processes encompass other technological merits, providing numerous advantages in FET-based biochip development for point-of-care (PoC) purposes [10]. Fabricating the sensing element directly on the circuit chip enables the integration of multiple functions, such as sensing, signal processing, and data transmission, all onto a single, compact chip [11]. This integration reduces the sensor's overall size and power consumption, making it ideal for portable and implantable medical devices [12], [13]. Additionally, these foundries can produce high-density arrays of sensors, as exemplified by products like the Ion Torrent company, which allow for the simultaneous monitoring of numerous biological interactions with high sensitivity and specificity

using CMOS-based ISFET sensors [14]. The provided technology has enabled the production of millions of sensing pixels on a single chip, which can be integrated with microfluidics to enhance functionality [15]. The established infrastructure and economies of scale associated with standard semiconductor manufacturing also contribute to cost-effective production, making advanced biochip technologies more accessible for widespread research and clinical applications. This accessibility is crucial for the proliferation of innovative diagnostic tools and therapeutic monitoring systems, ultimately advancing the field of biomedical sensing and improving patient care.

Several companies, particularly university spin-offs, leverage standard foundry processes to develop and produce FET-based sensors. For instance, Cardea Bio integrates graphene-based biological FETs into their biochips, utilizing standard graphene semiconductor foundry processes to ensure precision and scalability [16]. Their biochips are designed for various applications, including real-time molecular diagnostics, the CRISPR chip, and hall-effect measurement [17]. The established manufacturing techniques have enabled Cardea Bio to produce a high-quality, reliable standard graphene sensing platform for numerous purposes, demonstrating the significant advantages of leveraging these advanced processes in producing cutting-edge biosensing technology [18], [19].

Another example is DNAe, which specializes in semiconductor-based genomic analysis using silicon ISFET sensors based on CMOS technology [20], [21]. DNAe employs standard foundry processes to create next-generation sequencing devices incorporating silicon FETs, realized with CMOS technology [22], [23]. The DNAe’s devices offer rapid, point-of-care diagnostic capabilities by integrating electronic and biological components on a single chip. DNAe's use of standard semiconductor fabrication techniques ensure the production of cost-effective, high-performance sequencing tools, exemplifying the benefits of leveraging established foundry processes in advancing genomic analysis technologies for personalized medicine [24], [25].

The most recent example is Graphenea, which manufactures standard nanoscale graphene FET chips. Graphenea focuses on producing high-quality graphene materials and devices, including graphene FETs (gFETs) [26]. By leveraging standard foundry processes, Graphenea ensures its graphene-based biosensors' consistent quality and reproducibility [27]. These gFET-based biosensors find applications in diverse fields, ranging from healthcare diagnostics to

environmental monitoring, showcasing the versatility and scalability of biochips produced through standardized manufacturing techniques [28], [29]. This approach highlights the potential of standard foundry graphene FET technology in creating reliable, high-performance biosensors for various advanced applications.

1.1.1. Emergence of a new silicon FET foundry based on JFET electronics

The open-gate junction field-effect transistor (OG-JFET) has been introduced by CMC Microsystem as a potential electronic biological/chemical sensing platform capable of interfacing soft materials with a semiconductor sensor [30]. The OG-JFET foundry enables mass production of OG-JFET chips with versatile designs on a single silicon wafer, offering tailored configurations to meet specific application demands. Although initially intended for chemical and biosensing purposes or multipurpose applications, there were uncertainties regarding its utilization for these purposes. Understanding the intricate physics governing the charge sensing mechanism, integrating it seamlessly with microfluidics for sample delivery, and characterizing the sensor with a portable readout system has been crucial in unlocking the full potential of the OG-JFET. However, despite these advancements, the technology was still in its early stages of development and scale-up compared to well-established CMOS foundry-based FET sensors available today. In this context, we initiated a project to comprehend the physics behind the sensing mechanism of OG-JFET for solution charge sensing, utilizing numerical models to understand the device's working principle under different biasing conditions and developing a low-cost characterization readout system for sensor analysis and easier fluidic handling. This portable system enhances testing performance and facilitates seamless integration into various research environments, paving the way for further exploration and innovation.

Therefore, we conducted experiments and employed different instruments to characterize the sensor, understand the charge sensing mechanism, and interface the sensor with biological molecules like DNA, cells like oral neutrophils, and chemicals like alcohol and ions. Through numerical simulations, we provided a new application platform for parametric analysis of the sensor, offering insights for design comparison in the COMSOL simulation environment. A multiphysics simulation study was conducted to understand the sensor's charge-sensing response to ions and its interaction with DNA. It demonstrated the sensor's charge sensing mechanism and its integration potential with fluidics and packaging to hold a solution sample on the sensing site.

The results of these efforts could serve as a starting point for future users of this standard technology to understand better the sensing mechanism, design strategies for fluidic integration, and electrical readout design for developing a portable characterization system.

1.2. Research Gaps, Challenges, and Solutions

The OG-JFET sensor is a back-gated FET sensor designed with an opened top to facilitate the introduction of sample solutions onto the sensor's semiconductor channel. Typically supplied in diced chip form, the sensor requires electronic characterization before solution testing. However, this process presents numerous hands-on challenges, particularly in the connection of the sensor to a semiconductor analyzer for reliable characterization and the delivery of solution samples onto the sensor. Traditionally, utilizing a probe station for characterization offers limited space in the chuck area, making it cumbersome to handle the sensor, disconnect it, and reconnect it to probe the sensor pads. This compromises the reliability of characterization and complicates the delivery of solution samples. Consequently, a pressing need arose to engineer instrumentation and solutions to circumvent the limitations imposed by the probe station system. Furthermore, integrating a microfluidics chip with the sensor while maintaining connectivity to the semiconductor analyzer posed additional challenges. Given the necessity for sensor integration and fluidics packaging, standardized design strategies for layout design became imperative to accommodate fluidics handling—a consideration not previously addressed or provided by technology providers. Therefore, innovative engineering solutions were sought to streamline the process, enhance reliability, and ensure seamless connectivity between the sensor and semiconductor analyzer, thereby overcoming the inherent challenges associated with sensor characterization and solution delivery.

We devised two innovative solutions for implementing OG-JFET, leveraging 3D printing techniques and microfluidics to address the challenges. In the first design, we developed a new continuous microfluidics scheme integrated with a control PCB and probing system to establish connectivity between the sensor and the semiconductor analyzer via dedicated SMUs (Source Measure Units). This solution entailed utilizing a two-layer microfluidic configuration, enabling the creation of a three-dimensional microfluidic structure from two distinct 2D microfluidic layers. Notably, this integration scheme is not limited to OG-JFET sensors but can also be adapted to characterize any FET sensor using a semiconductor analyzer. In our second design, we engineered

a compact electro-fluidics packaging scheme tailored to connect the sensor to a semiconductor analyzer, such as Kiteley, or a portable readout system. This smaller packaging solution offers enhanced versatility, allowing for flexible integration with various analytical platforms while maintaining the reliability and efficiency required for accurate sensor characterization.

Furthermore, providing researchers with an estimation of the sensor output response for specific bias conditions and geometric values is paramount in the layout design process. Recognizing this need and challenge, we developed a user-friendly COMSOL simulation App to facilitate fast and efficient simulations of OG-JFET. This simulation tool lets researchers quickly assess the sensor's behavior, considering specific material properties and geometries. The COMSOL simulation App serves as a valuable resource for comprehending the semiconductor physics of OG-JFET sensors and the intricate multiphysics involved in their charge-sensing capabilities. We have demonstrated how this simulation platform offers insights into the sensor's response to ions, water solutions, and DNA molecules, even under extreme dehydration conditions. Additionally, to deepen our understanding of DNA sensing in such extreme states, we utilized molecular dynamics (MD) simulation techniques to unveil the charge and potential changes occurring on the silica layer atop the sensor. Through these simulation efforts, researchers gain invaluable insights into the sensor's behavior and interaction with various analytes, paving the way for enhanced sensor design and optimization.

Another significant challenge in the characterization and biosensing applications of OG-JFET is the absence of a dedicated characterization system capable of assessing the sensor while maintaining a stable fluidic package mounted on it. This limitation impedes the comprehensive analysis of the sensor. Compared to conventional methods involving probe stations and semiconductor analyzers, it restricts researchers from diverse backgrounds to a low-cost sensing platform. To address this challenge, we have developed a low-cost portable readout system specifically designed to characterize the sensor's I-V curves. This versatile system can characterize OG-JFET sensors and be utilized for various FET sensors. By offering a cost-effective alternative to traditional characterization setups, our portable readout system empowers researchers to conduct comprehensive sensory analysis with greater accessibility and affordability.

1.3. Organization of thesis

This section overviews this thesis's structure, consisting of eight journal papers published or submitted. Each paper addresses one of the challenges mentioned in the last subsection.

1.3.1. Chapter 1: Introduction

This chapter presents research motivation, challenges, solutions, scientific and technological gaps, research goals, and objectives. The discussion encompasses three levels of contribution: design and implementation strategies, simulation and modeling, and readout system and chip packaging.

1.3.2. Chapter 2: A Literature Survey

This chapter reviews recent research on FET sensors, including the physics of operation, FET sensor's structure, functionalization strategies, and readout circuit design strategies for FET biosensors. This chapter has already been published as "Abbas Panahi, Deniz Sadighbayan, Saghi Forouhi, and Ebrahim Ghafar-Zadeh, Recent Advances of Field-Effect Transistor Technology for Infectious Diseases, Biosensors 2021, 11, 103. The role of Abbas Panahi was writing the initial draft, performing the comments, and finalizing and submitting the paper.

1.3.3. Chapter 3: OG-JFET Sensing System

Part 1: This chapter presents the design, implementation, and characterization of a multi-channel OG-JFET sensor aimed at comprehending its response to varying pH of solution representing the ion sensitivity of the device. This chapter was published as " Abbas Panahi, Hamed Osouli Tabrizi, Priyadarshini Mangannavar, Oleg Chebotarev, Andrew Fung, Ebrahim Ghafar-Zadeh, "Open-Gate Junction Field Effect Transistor (OG-JFET) for Life Science Applications: Design, Implementation, and Characterization," IEEE Sensor Journal, Volume: 21, Issue: 23, 01 December 2021. Abbas Panahi's contribution to this paper was the chip design, fluidics fixture design, simulation, device characterization, dry and wet experiments, and writing the original paper draft and submission.

Part 2: This chapter presents multiphysics simulations and characterizations of a multichannel sensor, examining its response to DNA molecules (voltage-bio charge relationship), human exhaled breath, and oral cells (oral neutrophil cells). These investigations serve to elucidate its charge-sensing mechanism further. This chapter has been published as: Abbas Panahi, Deniz Sadighbayan, and Ebrahim Ghafar-Zadeh. 2021. "Electronic Sensing Platform (ESP) Based on Open-Gate Junction Field-Effect Transistor (OG-JFET) for Life Science Applications: Design,

Modeling and Experimental Results.", Sensors 21, no. 22: 7491. https://doi.org/10.3390/s2122749. Abbas Panahi's contributions included chip design, implementation, characterization, multiphysics simulation, experiments related to pH and DNA, human exhalation on the chip, writing the initial draft, and paper submission.

1.3.4. Chapter 4: Microfluidics Integration

This chapter elucidates integrating a microfluidics device with OG-JFET, providing a comprehensive overview of the fabrication process and implementation. Additionally, a mathematical modeling approach has been developed and introduced to delve into the charge-sensing mechanism of OG-JFET. Furthermore, a finite-element method (FEM) simulation is presented to gain insights into fluid transport within the fabricated microfluidics chip. This chapter has already been published as Panahi, A.; Ghafar-Zadeh, E. "A Hybrid Microfluidic Electronic Sensing Platform for Life Science Applications." Micromachines 2022, 13, 425. Abbas Panahi's contributions included sensor chip design, microfluidics chip design, simulation and fabrication, sensing system implementation and characterization, mathematical modeling of the device and charge sensing model, writing the original draft, and paper submission.

1.3.5. Chapter 5: Performance Analysis of OG-JFET (Simulation and Experimental Study)

This chapter delves into the performance analysis of OG-JFET and conducts a design parameter study to elucidate the impact of various geometrical and material parameters on the sensor response. Two key performance metrics, transconductance, and device efficiency, are thoroughly examined. The chapter presents an in-depth discussion on the effects of different design parameters on these metrics, providing valuable insights into optimizing sensor performance. This chapter is based on the following paper submitted to the IEEE Access journal. Contributions of Abbas Panahi were chip characterization, simulation of OG-JFET chip, parametric design, data analysis, preparing the initial draft of the paper, and submission of the paper.

Paper: Abbas Panahi, Ebrahim Ghafar-Zadeh, "Performance Analysis of Open-Gate Junction FET: A New Foundry-based Silicon Transistor for Biochemical Sensing Applications"

1.3.6. Chapter 6: OG-JFET Application in Emerging DNA Storage

This chapter introduces OG-JFET as a novel FET sensor for emerging DNA storage applications. It demonstrates how OG-JFET structure enables DNA measurement, fulfilling the initial

requirements of DNA storage applications for the first time. Additionally, a simple finite element method (FEM) simulation model is provided in the paper to gain further insight into the response of the OG-JFET. This chapter has already been published in the Journal of IEEE Transactions on Instrumentations and Measurements as: Abbas Panahi, Morteza Ghafar-Zadeh, Anthony Scime, Sebastian Magierowski; Ghafar-Zadeh, E. "Novel Field-Effect Transistor Sensor for DNA Storage Monitoring". IEEE Trans. Instrum. Meas. 2022, 71, 1–11. Abbas Panahi's contributions included chip design, chip preparation, and characterization, performing DNA experiments on the chip and the COMSOL model for the OG-JFET chip for DNA sensing, initial draft writing, and paper submission.

1.3.7. Chapter 7: Molecular dynamics simulation of DNA adsorption on the OG-JFET sensor surface and related experiments

This chapter presents a molecular dynamic simulation analysis of DNA adsorption on interdigital OG-JFET, shedding light on the structure and state of DNA during extreme dehydration phases characterized by low water molecule density. The simulations demonstrate that DNA, in its highly dehydrated state, absorbs onto the surface, altering the surface potential of SiO_2. This surface potential alteration correlates with sensor current changes and subsequent detection. Experimental validation on ID-OGJFET is conducted using the portable characterization system, which aligns with the simulation concept and further corroborates the findings.

This chapter is based on a paper submitted to Sensors and Actuators A: Physical. Abbas Panahi's contributions include chip design, chip characterization, conducting DNA tests on the chip, and performing molecular dynamics simulations of DNA interactions with the sensor's surface.

1.3.8. Chapter 8: Evaporation-based sensing mechanism enabled with high-surface area OG-JFET

This chapter introduces a novel sensing system based on the evaporation of a sessile droplet on the ID-OGJFET to analyze the droplet's polar solution content, such as ethanol and methanol. The discussion delves into how the structure of OG-JFET and the innovative design of interdigital OG-JFET enable a unique sensing mechanism on a FET structure. This mechanism relies on the evaporation of a droplet, allowing for the tracking of evaporation and correlation of the droplet's content to the time of evaporation using a FET sensor. This chapter is based on a paper submitted to the Journal of IEEE Transactions on Instrumentations and Measurements. Abbas Panahi's

contributions were chip design, chip characterization, simulation, performing all experiments, and writing the initial paper draft and submission.

1.3.9. Chapter 9: Conclusions and Recommendations for the Future Work

This chapter summarizes the conclusions and discussions from the preceding chapters of this thesis, along with recommendations for future research. It encapsulates the essential findings and dialogues, providing a cohesive overview of the study's outcomes. Subsequently, it outlines suggestions for future investigations, guiding potential avenues for further exploration and advancement.

1.4. References

[1] S. Carrara et al., 'Fully Integrated Biochip Platforms for Advanced Healthcare', Sensors 2012, Vol. 12, Pages 11013-11060, vol. 12, no. 8, pp. 11013–11060, Aug. 2012, doi: 10.3390/S120811013.

[2] 'Nanoscale Field Effect Transistors: Emerging Applications - Google Books'. Accessed: Jun. 12, 2024. [Online]. Available: https://books.google.ca/books?hl=en&lr=&id=O7brEAAAQBAJ&oi=fnd&pg=PP1&dq=In+FET+sensors,+standard+foundries,+such+as+those+used+in+IC+semiconductor+manufacturing,+offer+high+precision,+reproducibility,+and+scalability,+which+are+critical+for+producing+consistent+quality+and+performance+in+FET-based+sensing+chips.+&ots=krAAjYoke4&sig=-3fMj6lV1F78B2UdNhFo_sFJyCo&redir_esc=y#v=onepage&q&f=false

[3] H. H. Radamson et al., 'The challenges of advanced CMOS process from 2D to 3D', Applied Sciences (Switzerland), vol. 7, no. 10, Oct. 2017, doi: 10.3390/APP7101047.

[4] H. H. Radamson et al., 'State of the Art and Future Perspectives in Advanced CMOS Technology', Nanomaterials 2020, Vol. 10, Page 1555, vol. 10, no. 8, p. 1555, Aug. 2020, doi: 10.3390/NANO10081555.

[5] M. Hochberg and T. Baehr-Jones, 'Towards fabless silicon photonics', Nat Photonics, vol. 4, no. 8, pp. 492–494, Aug. 2010, doi: 10.1038/NPHOTON.2010.172.

[6] A. E. J. Lim et al., 'Path to Silicon Photonics Commercialization: The Foundry Model Discussion', Topics in Applied Physics, vol. 122, pp. 191–215, Jan. 2016, doi: 10.1007/978-3-642-10503-6_6.

[7] V. Iyer, D. A. Issadore, and F. Aflatouni, 'The next generation of hybrid microfluidic/integrated circuit chips: recent and upcoming advances in high-speed, high-throughput, and multifunctional lab-on-IC systems', Lab Chip, vol. 23, no. 11, pp. 2553–2576, May 2023, doi: 10.1039/D2LC01163H.

[8] M. Katari, G. Krishnamoorthy, M. K. Articleinfo, and J. Jeyaraman, 'Novel Materials and Processes for Miniaturization in Semiconductor Packaging', Journal of Artificial Intelligence General science (JAIGS) ISSN:3006-4023, vol. 2, no. 1, pp. 251–271, Jan. 2024, doi: 10.60087/JAIGS.V2I1.112.

[9] T. E. Lee, H. J. Kim, and T. S. Yu, 'Semiconductor Manufacturing Automation', Springer Handbooks, vol. Part F674, pp. 841–863, 2023, doi: 10.1007/978-3-030-96729-1_38.

[10] S. Y. Li et al., 'Proof of Concept for Sustainable Manufacturing of Neural Electrode Array for In Vivo Recording', Biosensors 2023, Vol. 13, Page 280, vol. 13, no. 2, p. 280, Feb. 2023, doi: 10.3390/BIOS13020280.

[11] S. Carrara, ‘Bio/CMOS Interfaces for Capacitance Sensing’, Bio/CMOS Interfaces and Co-Design, pp. 405–429, 2024, doi: 10.1007/978-3-031-31832-0_13.

[12] E. Ghafar-Zadeh, S. Forouhi, and T. Azadmousavi, ‘CMOS-based sensors and actuators for life science applications’, CMOS-Based Sensors and Actuators for Life Science Applications, pp. 1–548, Jan. 2024, doi: 10.1049/PBCS079E.

[13] E. Ghafar-Zadeh and S. Forouhi, ‘Emerging CMOS Capacitive Sensors for Biomedical Applications: A multidisciplinary approach’, Emerging CMOS Capacitive Sensors for Biomedical Applications: A multidisciplinary approach, pp. 1–229, Jan. 2021, doi: 10.1049/PBCS063E.

[14] C. Tlili et al., ‘Next-Generation DNA Sequencing: Ion Torrent Sequencers Versus Nanopore Technology’, Handbook of Biochips, pp. 1–16, 2021, doi: 10.1007/978-1-4614-6623-9_56-1.

[15] ‘Personal DNA Sequencing Machine One Step Closer | IBTimes’. Accessed: Jun. 12, 2024. [Online]. Available: https://www.ibtimes.com/personal-dna-sequencing-machine-one-step-closer-301169

[16] B. R. Goldsmith et al., ‘Digital Biosensing by Foundry-Fabricated Graphene Sensors’, Scientific Reports 2019 9:1, vol. 9, no. 1, pp. 1–10, Jan. 2019, doi: 10.1038/s41598-019-38700-w.

[17] R. Hajian et al., ‘Detection of unamplified target genes via CRISPR–Cas9 immobilized on a graphene field-effect transistor’, Nature Biomedical Engineering 2019 3:6, vol. 3, no. 6, pp. 427–437, Mar. 2019, doi: 10.1038/s41551-019-0371-x.

[18] ‘Paragraf acquires Cardea Bio to extend graphene electronics industry leadership’. Accessed: Jun. 12, 2024. [Online]. Available: https://www.cardeabio.com/news/paragraf

[19] ‘Cardea - home’. Accessed: Jun. 12, 2024. [Online]. Available: https://www.cardeabio.com/

[20] ‘Ability of Semiconductor DNA Sequencing to Transform Healthcare and Save Lives Recognised by the 2014 Faraday Medal to Professor Chris Toumazou | Business Wire’. Accessed: Jun. 12, 2024. [Online]. Available: https://www.businesswire.com/news/home/20141002005262/en/Ability-Semiconductor-DNA-Sequencing-Transform-Healthcare-Save

[21] ‘Technology | DNAe’. Accessed: Jun. 12, 2024. [Online]. Available: https://www.dnae.com/technology/

[22] S. Reed and Y. Liu, ‘Chemical sensing device’, Oct. 2018.

[23] G. Alexandrou et al., ‘Detection of Multiple Breast Cancer ESR1 Mutations on an ISFET Based Lab-on-Chip Platform’, IEEE Trans Biomed Circuits Syst, vol. 15, no. 3, pp. 380–389, Jun. 2021, doi: 10.1109/TBCAS.2021.3094464.

[24] X. Liu, C. H. Chen, M. Karvela, and C. Toumazou, ‘A DNA-Based Intelligent Expert System for Personalised Skin-Health Recommendations’, IEEE J Biomed Health Inform, vol. 24, no. 11, pp. 3276–3284, Nov. 2020, doi: 10.1109/JBHI.2020.2978667.

[25] C. H. Chen, M. Karvela, M. Sohbati, T. Shinawatra, and C. Toumazou, ‘PERSON - Personalized Expert Recommendation System for Optimized Nutrition’, IEEE Trans Biomed Circuits Syst, vol. 12, no. 1, pp. 151–160, Feb. 2018, doi: 10.1109/TBCAS.2017.2760504.

[26] ‘Dedicated Graphene Foundry – Graphenea’. Accessed: Jun. 12, 2024. [Online]. Available: https://www.graphenea.com/

[27] M. Soikkeli et al., ‘Wafer-Scale Graphene Field-Effect Transistor Biosensor Arrays with Monolithic CMOS Readout’, ACS Appl Electron Mater, vol. 5, no. 9, pp. 4925–4932, Sep. 2023, doi: 10.1021/ACSAELM.3C00706/ASSET/IMAGES/LARGE/EL3C00706_0006.JPEG.

[28] L. Xu et al., ‘Detection of Glial Fibrillary Acidic Protein in Patient Plasma Using On-Chip Graphene Field-Effect Biosensors, in Comparison with ELISA and Single-Molecule Array’, ACS Sens, vol. 7, no. 1, pp. 253–262, Jan. 2022, doi: 10.1021/ACSSENSORS.1C02232/ASSET/IMAGES/LARGE/SE1C02232_0005.JPEG.

[29] K. J. Tielrooij et al., ‘Electrical control of optical emitter relaxation pathways enabled by graphene’, Nature Physics 2014 11:3, vol. 11, no. 3, pp. 281–287, Jan. 2015, doi: 10.1038/nphys3204.

[30] ‘Electronic Sensor Platform (ESP) – CMC Microsystems’. Accessed: Jun. 12, 2024. [Online]. Available: https://www.cmc.ca/electronic-sensor-platform-esp/

Chapter 2 Literature Survey

Paper 1: Recent Advances of Field-Effect Transistor Technology for Infectious Diseases

Authors: Abbas Panahi, Deniz Sadighbayan, Saghi Forouhi, Ebrahim Ghafar-Zadeh,

Journal: Biosensors, 2021, 11, 103

Abbas Panahi's Contributions: Prepared the initial draft and wrote the whole manuscript except parts 2.5 and 2.6. He also submitted, edited, and revised the paper throughout publication.

This chapter, a significant component of the thesis, comprehensively reviews the related literature and has been published as a review paper[1]. The content of this review paper has been incorporated verbatim into this chapter.

2.1. Abstract

Field-effect transistor (FET) biosensors have been intensively researched for label-free biomolecule sensing in different disease detection applications. High sensitivity, incredible miniaturization capability, promising low minimum limit of detection (LoD) at the molecular level, integration with complementary metal oxide semiconductor (CMOS) technology, and finally, label-free operation were among the predominant motives for highlighting these sensors in the biosensor community. Although FET sensors target various diseases for detection, infectious diseases are still the most demanding sector that needs higher precision in detection and integration to realize the diagnosis at the point of care (PoC). The COVID-19 pandemic, nevertheless, was an example of the escalated situation in terms of the worldwide desperate need for fast, specific, and reliable home test PoC devices for the timely screening of vast numbers of people to restrict the

[1] Panahi, A.; Sadighbayan, D.; Forouhi, S.; Ghafar-Zadeh, E. Recent Advances of Field-Effect Transistor Technology for Infectious Diseases. Biosensors 2021, 11, 103. https://doi.org/10.3390/bios11040103

disease from further spread. This need spawned a wave of innovative approaches for early detection of COVID-19 antibodies in human swabs or blood, amongst which the FET biosensing gained much more attention due to their extraordinary LoD down to femtomolar (fM) with the comparatively faster response time. As the FET sensors are promising novel PoC devices with application in early diagnosis of various diseases, especially infectious diseases, in this research, we have reviewed the recent progress on developing FET sensors for contagious diseases diagnosis accompanied by a thorough discussion on the structure of Chem/BioFET sensors and the readout circuitry for output signal processing. This approach would help engineers and biologists gain enough knowledge to initiate their design for accelerated innovations in response to the need for more efficient management of infectious diseases like COVID-19.

2.2. Introduction

The recent decade has witnessed significant advancements in detecting and treating diseases, improving human health globally. However, the COVID-19 pandemic revealed that we are not well-prepared for early diagnosis and management of infectious diseases to control their spread [1]. Many hurdles exist in efficiently managing contagious diseases during emergencies like the COVID-19 pandemic. The most significant problems with current medical procedures for controlling infectious diseases are drug resistance, the evolution of pathogens, and the emergence of new genetically developed agents that might spread faster than previous viruses. An example of this was observed during the COVID-19 pandemic when a newly evolved version of the virus appeared in England and Africa, spreading significantly faster than the previous version [2, 3]. As we see, fast and accurate diagnosis and timely treatment could considerably curb the further spread of the virus. Well-established laboratory-based techniques are currently used to screen and test for infectious diseases, including microscopies, culturing techniques, immunoassays, and PCR (Polymerase Chain Reaction) methods [4, 5]. Although these methods have been effective in fighting many infectious diseases such as sepsis, tuberculosis, HIV, hepatitis, and malaria, during high-demand periods like pandemics, they have shown limitations in meeting the expectations for fast and highly accurate screening of the population. Microscopy must address the required high accuracy; immunoassays (e.g., enzyme-linked immunosorbent assay (ELISA)) are labor-intensive and poorly designed for multiplexing purposes. Furthermore, despite being accurate at the molecular level, PCR methods involve tedious sample preparation and experiment setup processes.

Apart from the equipment challenges and current state of the art, sampling and sending them to standard machines in specialized laboratories have been recognized as additional barriers to controlling the spread of diseases. These processes have increased human interactions at times when effective social distancing measures are crucial. This inefficient process has complicated the timely screening of the population, resulting in fewer daily tests than needed, leaving many people unscreened. Consequently, this leads to more infected cases and the further spread of the disease. This problem is exacerbated in countries with limited access to standard equipment and advanced laboratories, causing the spread of disease and hampering regular international connections.

Nevertheless, the recent decade was a booming time for the emergence of a wave of biosensing innovations toward the realization of early and timely detection of diseases through miniaturized devices with the anticipation of affordable-to-all handheld point-of-care (PoC) devices [5–7]. To better envisage the steps taken during this era of personalized medicine research and development, the glucose test is an excellent example of how to grasp fruitful endeavors. Glucose at-home tests are based on a potentiometric sensor and have been reported in different configurations [8]. These sensors have enabled the successful controlling and monitoring of diabetes disease, which was not possible with the standard medical treatments and regular doctor visits. Another alumnus of this school is the home pregnancy test, based on a lateral flow detection method that has significantly affected the biomedical sector [9]. Down the road, the fast development of microfabrication methods helped to fabricate a wide range of nano/micro microelectromechanical systems (NEMS/MEMS)-based sensors including microfluidic chips, potentiometric biosensors based on various nanomaterials (e.g., ion-sensitive field-effect transistors (ISFETs), complementary metal-oxide-semiconductor (CMOS)-based biosensors and other miniaturized microdevices dedicated to biosensing applications [10,11]).

Due to the superior sensing characteristics of field-effect transistors (FETs), they have attracted massive attention in the biosensing research community with the motivation to create disposable, low-cost, miniaturized PoC devices based on FET sensors for home diagnostic purposes. The superior technological features of these sensors have massive potential for miniaturization, parallelization, ultra-low response times, and seamless capability to be integrated with CMOS technology [12–14]. Historically, ISFETs were first introduced in the early 1970s by a subtle variation in the metal-oxide-semiconductor FETs (MOSFETs), which removed the metal layer on

top of the oxide layer [15]. Initially, it was conceived that by eliminating the metal gate on top of the oxide layer in MOSFET, space would be dedicated to an electrolyte solution as the fluidic gate in which a reference electrode (RE) can manipulate the surface potential of the oxide layer by changing the voltage.

Moving toward chemically/biologically gated ionic sensitive FETs (Chem/BioFET) has brought many advantages not observed in other potentiometric techniques. The central reasons for Chem/BioFET's popularity are their significant miniaturization, straightforward operational mechanism, integration with CMOS, and competitive final cost. Since the invention of ISFET in 1976, different ISFET structures have been introduced for various bio-analytes in solution, resulting in a range of Chem/BioFET configurations [16]. Generally, the electrolyte gate is standard in all Chem/BioFET structures, containing the analytes of interest for detection in an ionic solution (NaCl, KCl, PBS, etc.) buffer. The presence of the analyte is detected by the concentration or activity of the target molecule or by probing the presence/quantity of biomolecules in the sensing channel. The induced charge on the sensor changes the surface potential, causing a detectable electron current in the conductive channel of the FET sensor. After the physical sensing of chemical activities on the surface, signal processing schemes are conducted on the output voltage/current in the circuit. The signal is then remotely sent to a mobile device for a medical doctor's online and distant patient health screening [17].

Considering the enormous potential of Chem/BioFETs in rapid detection with a limit of detection (LoD) down to fM, their incredible sensitivity compared to other biosensors, and their lower cost (when integrated with CMOS technology), it becomes evident that these sensors can be considered a potential platform for manufacturing point-of-care (PoC) devices. These PoC devices could be designed to address the need for rapid at-home tests, especially during future pandemics like COVID-19 [18]. Label-free detection of infectious diseases can be achieved by immobilizing antibodies, nucleic acids, aptamers, enzymes, microorganisms, or artificial biomaterials on the sensing channels [19]. The immobilization of these bio-species helps detect specific disease biomarkers in solution in a label-free manner when a chemical reaction occurs or the target molecule approaches the surface. Furthermore, ISFETs can be used for screening infectious agents and their genomes by detecting the ions released by DNA polymerase [20, 21] or the bacterial cells

infected by bacteriophages [22], as well as measuring pH variations due to cellular metabolism and proliferation [23].

In this review, we have studied recent Chem/BioFET sensors dedicated to analyzing infectious diseases, the physics of operation, and the readout circuits. Section 2[1], describes the sensing mechanism in Chem/BioFET sensors. The third section[2], overviews the approaches for sensing surface modification and functionalizing Chem/BioFETs to detect infectious diseases. Some readout circuits are reviewed in the fourth section[3], potentially helpful in measuring the output parameters of Chem/BioFETs. This section focuses on CMOS-based circuits, which can pave the way for on-chip measurements and the development of affordable handheld PoC devices. This review has been prepared to convey information on all aspects of Chem/BioFET, which could help engineers and biologists accelerate their innovation in detecting infectious diseases.

2.3. Sensing Mechanism and Different Structures of Chem/BioFETs

The principal physics behind almost all kinds of Chem/BioFET operation is the capability of these sensors to sense the charge effects on the surface through the induced electric field due to the existence of target molecules in the solution. When an electrolyte solution meets a solid surface (like silicon dioxide or any other oxides), a capacitive double layer (DL) is created, which consists of different layers such as a stern layer, inner Helmholtz (IHL), and outer Helmholtz (OHL) [24] (see Figure 2-1 and Figure 2-2 for better understanding). These layers encompass different concentrations of ions concerning the vertical distance from the surface. This layered distribution of charges creates several ion layers that can then be modeled as capacitors on top of the surface of the oxide (dielectric). Many attempts have been made to understand the interwoven effects of these layers and their contribution to the overall oxide-surface potential [25]. The accumulated charge in the vicinity of the oxide surface (due to the creation of the electric double layer) changes the oxide electric field, which eventually contributes to changing the potential at the outer surface of the sensing conductive channel. Subsequently, the generated potential alters the space charge

[1] Section 2.3
[2] Section 2.4
[3] Section 2.5

distribution inside the conductive channel, leading to source-drain current variations inside the FET conduction channel.

Unraveling the exact physical phenomena taking place at the semiconductor-oxide-electrolyte is of imperative importance when it comes to fabricating BioFET sensors more efficiently. Furthermore, this understanding becomes more critical when we scale down to the nano BioFET structures, where the ions and molecular interactions dominate the electron conduction in the channel. This in-depth study would enable us to decipher and control unexpected and intrinsic interfacial noises. Significant advancements have been made on this matter, which has considerably assisted the multi-scale design of ISFETs and the discovery of novel BioFET sensing materials. As the fabrication of these FETs progressed well, the development of theories to explain the physical phenomena emerged parallel to explaining noises and some fabrication challenges [26, 27]. The type of ISFETs on which a layer of the ion-sensitive membrane interacted with solution has been theorized perfectly. However, the direct interaction of electrolytes with the oxide layer was developed at a different pace [28].

As shown in Figure 2-1, due to the interaction of ions and the oxide layer, the double-layer capacitance will be created in the proximity of the oxide. The oxide layer capacitance, a built-in characteristic of this layer, will appear on top of the channel. Due to the depletion effect of the adsorbed charges on the surface, the channel will create another capacitor that modulates the surface charge density and the electron/hole transport in the channel. Charge effects on the surface of the oxide layer would result in the source-drain current, which can be mathematically expressed as follows (we encourage readers to study an in-depth analysis in [28]):

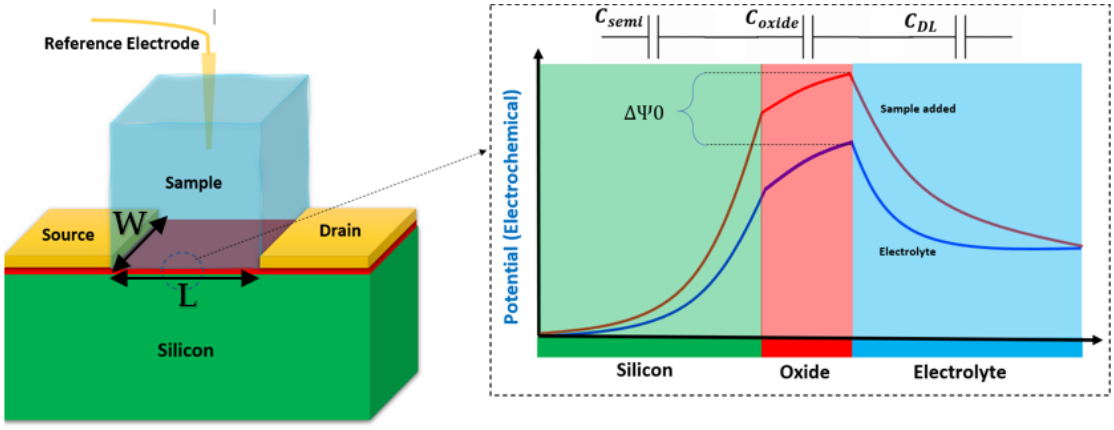
$$I_{\mathrm{D}} = \mu C_{\mathrm{ox}} \frac{W}{L} \left\{ \left[V_{\mathrm{GS}} - V_{\mathrm{t(ISFET)}} \right] V_{\mathrm{DS}} - \frac{1}{2} {V_{\mathrm{DS}}}^2 \right\}, \qquad (2\text{-}1)$$

Equation (2-1) shows the current in the channel when the sensor is exposed to an electrolyte with varying potential and works in the linear operational region ($V_{DS} < V_{GS} - V_{t\,(ISFET)}$). In this equation, the parameters are as follows: μ stands for average mobility in the channel; W and L are the width and the length of the gate, respectively; V_{DS} and V_{GS} are the drain-source voltage and the gate-

source voltage, respectively; C_{ox} identifies the capacitance of the gate oxide. $V_{t\ (ISFET)}$ is the threshold voltage of the ISFET, which can be expressed as follows:

$$V_{t(ISFET)} = E_{ref} - \Psi_0 + \chi^{sol} - \frac{\phi_{Si}}{q} - \frac{Q_{ox}+Q_{ss}}{C_{ox}} - \frac{Q_B}{C_{ox}} + 2\phi_f, \qquad (2\text{-}2)$$

Where E_{ref} identifies the potential of the reference electrode; Ψ_0 is the insulator-electrolyte potential; χ_{sol} stands for the surface dipole potential of the solution; ϕ_{Si} is silicon electron work function; q denotes the elementary charge; Q_{ox}, Q_{ss} and Q_B are the charges in the oxide, charges in surface states and interface states and the depletion charge, respectively; and ϕ_f is the potential difference between the Fermi levels of doped and intrinsic silicon.



(a) (b)

Figure 2-1. (a) The standard structure of a bio field-effect transistor (Bio-FET); (b) the corresponding potential diagram showing the effect of electrolyte on the potential of interfaces. The potential at the oxide layer and solution interface arises and then decreases gradually to the solution potential. Adding the sample would manipulate this potential curve, influencing the charge transport inside the silicon channel. Three main capacitances are involved in the system: the oxide, channel depletion capacitance, and the solution double layer (CDL).

All the parameters in Equations (2-1) and (2-2) are constant values except Ψ_0, which shows the effect of surface potential on the oxide layer and affects $V_{t\ (BioFET)}$. This will be changed by the ionic solution and biomolecular content of the solution, which directly influences the current in the channel. Through mathematical modeling and using site-bonding theory (please read [29] and [30] for detailed information), the potential of the surface could be related to the pH of the bulk solution. The corresponding equations for more insight are as follows:

$$\frac{\partial \Psi_0}{\partial pH_s} = \frac{\partial \Psi_0}{\partial \sigma_0}\frac{\partial \sigma_0}{\partial pH_s} = \frac{-q\beta_{int}}{C_{dif}}, \quad (2\text{-}3)$$

$$\frac{\partial \Psi_0}{\partial pH_s} = -2.3\,\frac{KT}{q}\,\alpha, with\ \alpha = \frac{1}{\left(\frac{2.3kTC_{dif}}{q^2\beta_{int}}\right)+1} \quad (2\text{-}4)$$

where α shows a dimensionless sensitivity parameter. The value of α varies between 0 and 1, depending heavily on the intrinsic buffer capacity and the differential capacitance. K is the Boltzmann constant, and T is the absolute temperature. Furthermore, σ_0 stands for the surface charge (charge on oxide surface and, generally, the interface between surface and electrolyte), β_{int} is the ionic capacity, and C_{dif} denotes the differential capacitance. The surface potential will be changed when a slight variation occurs in the electrolyte ion concentration that could result from either a chemical reaction in a biological sample or simply the existence of charged molecules in the solution. Generally, adding a specific concentration of an analyte varies the pH of the solution, which can be correlated to the potential of the surface through Equation (2-4). This potential affects the source-drain current in the conduction channel. So, the threshold voltage of an ISFET is [31]:

$$V_{\mathrm{t(ISFET)}} = V_{\mathrm{t(MOS)}} + (\gamma + 2.3\alpha V_{\mathrm{th}} pH), \quad (2\text{-}5)$$

Where γ is a pH-independent grouping of chemical potentials, Vth=kT/q denotes thermal voltage, and Vt (MOS) is the threshold voltage of a conventional MOSFET. Different operational regions of the ISFETs can be used for sensing, including (1) Triode (or linear region), (2) strong inversion (or saturation), (3) weak inversion (or subthreshold), and (4) velocity saturation. As aforementioned, Equation (1) describes the drain current in the triode region. The drain current of a saturated ISFET ($V_{DS} > V_{GS} - V_{t\ (ISFET)}$) is obtained by:

$$I_{\mathrm{D}} = \mu C_{\mathrm{ox}} \frac{W}{L}\left\{\left[V_{\mathrm{GS}} - V_{\mathrm{t(ISFET)}}\right]^2 (1 + \lambda V_{ds})\right\} \quad (2\text{-}6)$$

Where λ is the channel length modulation factor, if ID and V_{DS} are held constant, V_{GS} will adjust to compensate for changes in $V_{t\ (ISFET)}$.

By assuming a zero bulk-source voltage and $V_{DS} > 4V_{th}$, the operation of an ISFET in a weak inversion region can be described by [31]:

$$I_{\mathrm{D}} = I_0 \frac{W}{L} exp\left(\frac{V_{\mathrm{GS}} - V_{\mathrm{t(ISFET)}}}{nV_{\mathrm{th}}}\right), \quad (2\text{-}7)$$

I_0 is a positive constant current, and n is the subthreshold slope parameter.

In the velocity saturation region, the operation of the device can be expressed by [32]:

$$I_{\mathrm{D}} = v_{\mathrm{sat}} C_{\mathrm{ox}} W\left(V_{\mathrm{GS}} - V_{\mathrm{t(ISFET)}} - V_{\mathrm{D,sat}}\right), \quad (2\text{-}8)$$

where v_{sat} and $V_{\mathrm{D,sat}}$, respectively, stand for the saturated carrier velocity and the point when the drain current saturates.

These principles apply to semiconductor-oxide-electrolyte Chem/BioFETs regardless of their geometries and channel-gate arrangements. However, they may not be directly applicable to certain Chem/BioFETs that rely on the sensing properties of nanomaterials such as graphene or carbon nanotubes (CNTs). This discrepancy arises because ion complexation on these surfaces may not agree with the site-bonding theory used in describing common dielectrics in the fabrication of ISFETs. Mathematical modeling of molecular interactions at the surface (oxide or nitride) becomes complex, making it impossible to predict surface potential, as the site-bonding theory provides. Nonetheless, in terms of modeling interactions in complex BioFET surface systems, atomistic molecular dynamics simulation has recently been employed to analyze ion complexation on the surface and measure surface potential on the channel [33–35]. State-of-the-art molecular analysis has empowered researchers to gain insight into molecular interactions at the channel surface and estimate double-layer capacitance considering the interaction of nanomaterials, oxide, ionic solution, and proteins on the surface, which is not practically possible with current models. Figure 2-2 (a–c) illustrates the surface potential in a complex system containing ionic solutions.

Despite advancements in surface potential calculation modeling methods, uncertainties persist in predicting the exact potential on the oxide surface when different biomolecules are present that do not impact pH or ion concentration variations. While the pH sensing mechanism relies on detecting [H+] concentration, surface modification allows for the sensing of other ions in the solution, introducing alternative detection mechanisms solely based on variations in specific ion concentrations (e.g., [Na+] or [K+]) independent of [H+] [36]. These chemical FETs can be achieved by immobilizing a sensing layer permeable only to one or multiple ions in the solution.

Understanding the sensor response's dependence on specific ion concentrations (aside from [H+]) enables the design of a wide range of ChemFETs capable of detecting the presence of biomolecules or chemicals that do not alter pH but affect the concentration of other ions. Enzymatic reactions offer another detection mechanism whereby the analyte of interest can be detected by immobilizing the surface with a specific enzyme that reacts only with the targeted protein in the solution.

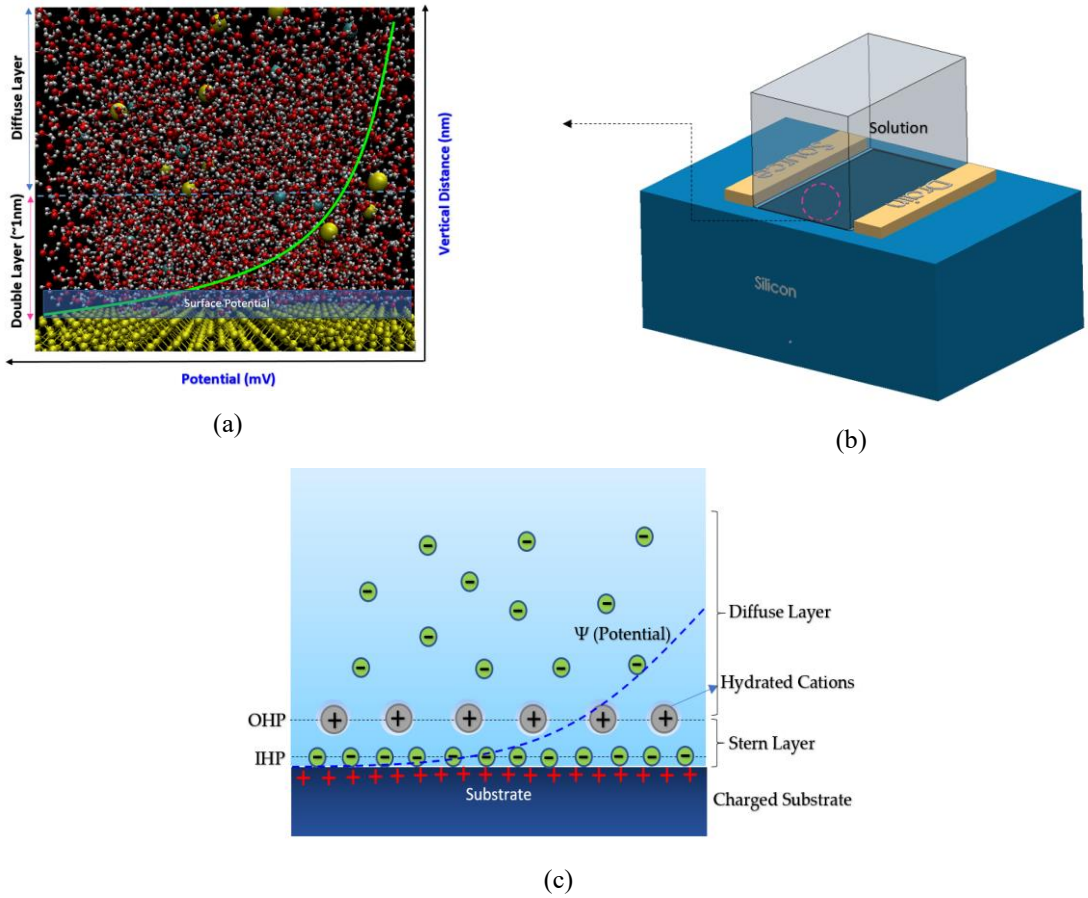


Figure 2-2. Showing how atomistic molecular dynamics simulation scales have been used to estimate the charge density on the surface of the oxide layer (here SiO_2): (a) Showing the silicon in atomic representation, which clearly shows the atomistic distribution of water and ions in the vicinity of surface silicon, which create a surface potential decaying into stable value in near zero in diffusion layer. The double layer has been shown, and its effect creates a specific potential on the surface based on the ionic strength of the solution. Molecular dynamics can be used to estimate this potential in very complex solutions containing biomolecules; (b) showing a 3D sketch of an FET device; (c) potential and ions layers on the interface of electrolyte and substrate in the sensor.

Enzymatic retractions contribute to the creation of acidic molecules, which could directly affect the pH of a solution that can be detected by the BioFET sensor [37]. In recent years, oligonucleotides have been introduced and gained growing popularity in the scientific community due to their contribution to directly detecting biomolecules in BioFET. The direct detection

mechanism includes the functionalization of oligonucleotides on the sensor's surface, which helps to screen the macromolecules in the Debye length on the surface since they are much smaller than proteins (target molecules) [38]. Generally, the mechanism of detection in BioFET embraces pH variation, reaction-origin detection (e.g., enzymatic or redox), direct sensing of a molecule based on Debye length screening, and indirect methods such as oligonucleotides functionalization of surface to detect the DNA on the surface. Many in-depth studies are still required to unravel the complex surface phenomena at the interface of electrolytes, oxides, and biomolecules.

2.4. Chem/BioFETs Device Structures

BioFET sensors refer to all family of FETs dedicated to measuring charge-induced field effects in different settings of bio-interfaces such as Gene-FETs (DNA-based FETs), Enzyme-FETs (Enzyme reaction detectors) and Cell-FETs (FETs with biological cells as their gate). While the biological targets in these sensors are different, the mechanism of their operation is based on ISFET's operation. The invention of ISFETs goes back to 1972 when Piet Bergveld introduced the technology and tested it for pH measurements of NaCl solution. From Piet's ISFET invention in 1972 forward (about 50 years of research), many geometries of ISFET sensors have been developed that generally can be categorized into six main groups based on their gate operation. These structures are conventional oxide-electrolyte structures (only the metal of MOS is removed, and an oxide layer is deposited), unmodified CMOS technology, floating gates, extended gates, double gate structures, and top-gated structures, which can be modified with different nanostructures and reinforced with materials (See Figure 2-3). These structures, specifically or in combination with other forms, have been recognized as the basis for further development of other biological FET sensors such as graphene-FETs (GFETs), CNT-FETs, nanowire FETs (NW-FETs), or other novel sensing materials such as MoS2 and Metal-Organic Frameworks (MOFs) [39–43] (See Figure 2-4).

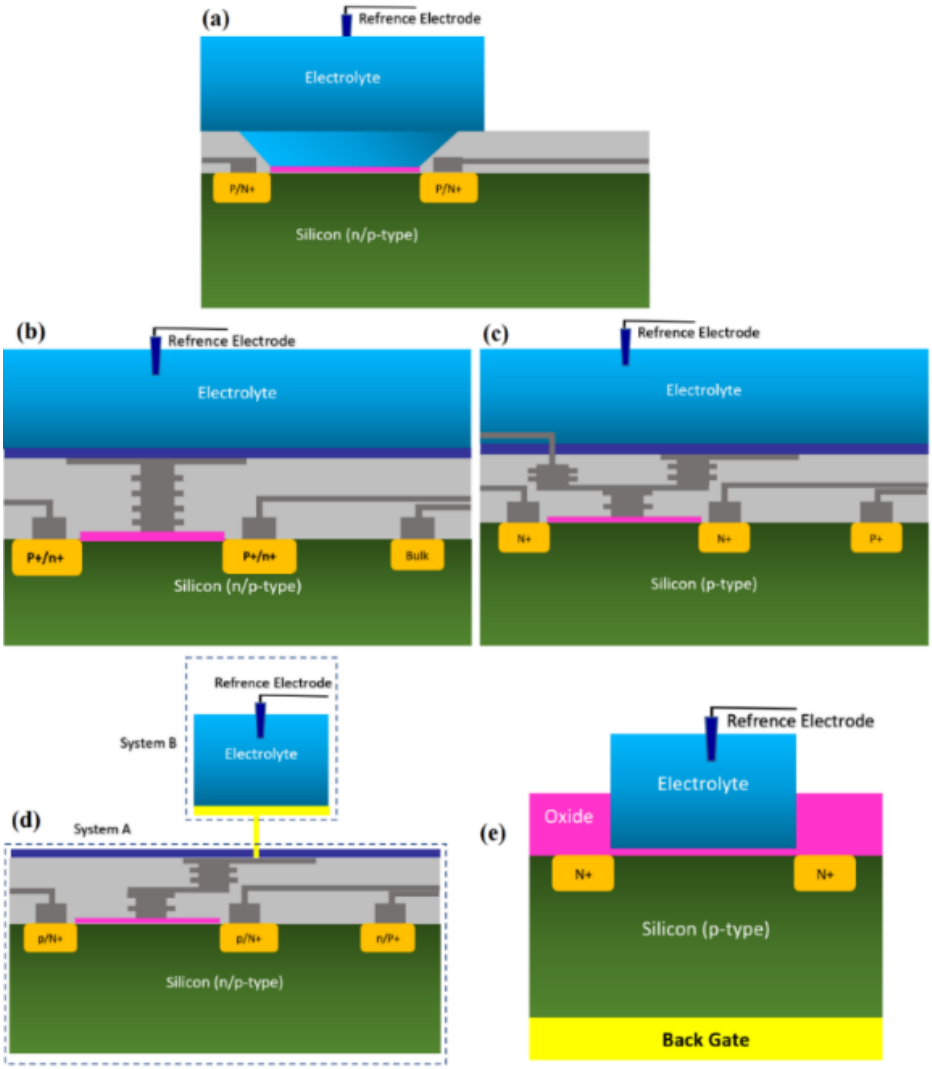
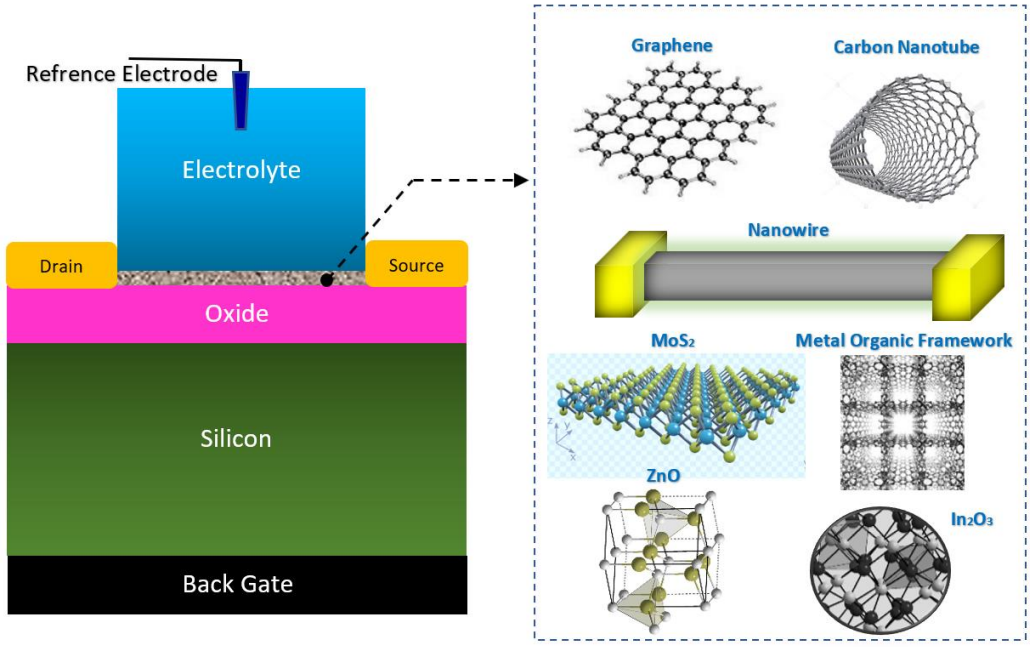


Figure 2-3. All structures of metal-oxide-semiconductor (MOS)-based ion-sensitive field-effect transistors (ISFETs) platforms that have been used for Chem/BioFET applications: (a) Representation of Oxide-electrolyte gate Chem/BioFETs, which include a reference in a solution on top of the oxide layer; (b) showing the floating gate structure by which the solution area has been separated from the conduction channel by an internal connection from the oxide layer on top of the channel to the solution and sensing membrane; (c) a demonstration of the integration of a floating gate with control gate, which helps to have more accurate control over the gate operation; (d) shows extended gate structure that allows us to have a more extensive sensing area for biosensing purposes. Moreover, an extended gate creates enough room for further integration with the microfluidic system, which in most cases was not applicable to add them to small ISFETs; € oxide-electrolyte gate Chem/BioFET with the back gate, which used the back gate to manipulate the working point of the sensor by changing the depletion effects in the conductive channel.

2.4.1. Oxide-Electrolyte Gate Chem/BioFETs

According to Figure 2-3 (a), the Chem/BioFET structures in this category closely resemble the early ISFET designs, which have been extensively applied in literature for pH and biological analysis since their inception [44]. In these structures, the metal gate on the MOS sensors is removed, and an oxide layer such as SiO_2, Al_2O_3, or Ta_2O_5 is deposited on the exposed gate area atop the conductive channel. While adding a nitride layer is optional, it is often deposited for specific applications. Although various arrangements of this sensing platform exist, the primary difference lies in the type of sensing mechanism (as depicted in Figure 2-3), with the conductive channel being the silicon itself, without using additional materials to enhance sensing capabilities. For these sensors (refer to Figure 2-3), SiO_2 and Si_3N_4 have typically been employed as the oxide and nitrite layers, respectively, serving as the dielectric. Si_3N_4 is usually deposited on SiO_2 to regulate the desired dielectric value in the sensor. While the deposition of these oxides is well-established, concerns have been raised regarding their suitability for ion sensing due to the abundance of charge-trapping sites created by oxide sites on the outer surface, which may contribute to unwanted parasitic responses from the sensor [45]. For instance, the FET developed in [40] exhibited a response to different concentrations of PfGDH protein spiked in buffer and serum, with corresponding calibration of source-drain current versus gate voltage for various Plasmodium falciparum glutamate dehydrogenase concentrations. The sensor's response varied from 0.5 µA to 0.8 µA in Vgs = 0.88 V as the concentration changed from 100 fM to 10nM. Initially used for detecting Na+ and H+ ions activity for monitoring extracellular ion pulses measured with a guinea pig taenia coli [46], this structure has also been utilized to evaluate bacterial deposition under conditions commonly employed for telemetric monitoring of changes in human dental plaque pH [47]. Furthermore, in an early attempt for neuronal recording, a neuron was mounted on a thin insulating layer of gate oxide on n-type Si in an electrolyte, like the configuration shown in Figure 2-5 (a), where a positive bias voltage was applied to the silicon to induce an accumulation of movable, positive defect electrons near the surface (strong inversion).



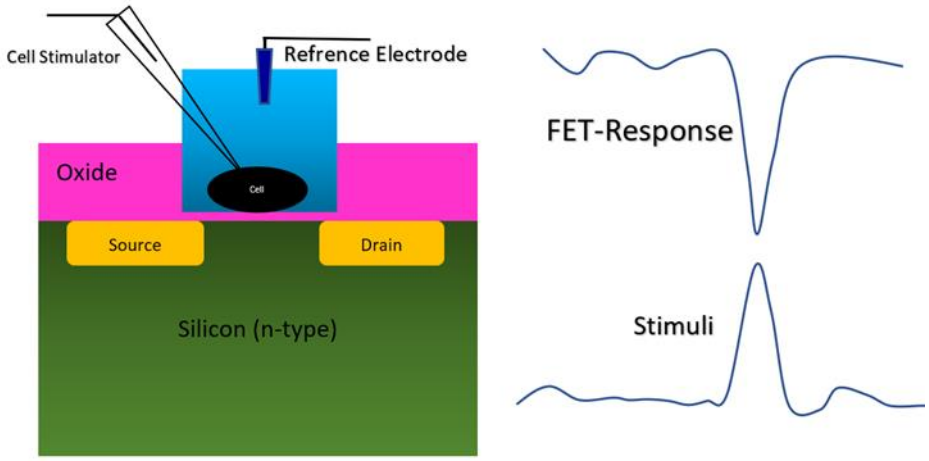
(a) (b)

Figure 2-4. The general form of electrolyte and back gated structures of FETs, which have been used for the sensing elements in Chem/BioFET: This nanomaterial-based structure has been widely used for cell, DNA, enzymatic reaction, and chemical sensing; (a) sensor structure; (b) the most frequent nanomaterials used as sensing element and main conductive channel.

As depicted in Figure 2-5 (b), when neurons undergo a positive voltage shift during voltage stimulation, the surface potential of silicon in the conduction channel region increases, resulting in a reduced current in the channel (as indicated by the curve showing the current response). The oxide-electrolyte gate structure accurately recorded the stimulation and recording of neuron cells. This configuration has found applications in various physicochemical settings, including the immunodetection of anaerobic bacteria using Clostridium thermocellum cells [48], adhesion analysis of single neuron cells on oxidized silicon [49], analysis of hybridization of synthetic homo-oligomer DNA sequences [50], electrogenic cell monitoring [51], monitoring cellular metabolism [52], and tracking excitable neurons in the rat brain [53] and cardiac muscle [54]. Furthermore, it has been employed in sensor and fluidic packaging for cellular monitoring [55] and analysis of cell proton transport mechanisms [56].

This structure has been beneficial for cellular activity analysis, focusing on local pH measurement near the surface [57,58] and adhesion analysis of cells on the substrate by measuring the pH of cells distant from their culture area [59]. In recent years, an ISFET sensor with an oxide-electrolyte structure has been employed for cell analysis and pH measurements. For example, a SiO_2-Ta_2O_5

oxide-gated ISFET was utilized for live-cell monitoring by measuring pH variations around cells on the gate [60,61]. In another application, a Si_3N_4/Ta_2O_5 oxide-gated ISFET was employed to study the self-assembly of photosynthetic proteins [62].



(a) (b)

Figure 2-5. The stimulation and the response of the FET sensor from a cell on top of an oxide-semiconductor. (a) Sensor structure for culturing cells on the oxide layer on top of the conductive channel; (b) the stimuli and the sensor response simultaneously, which shows the successful loading and recording of a pulse onto/from the cell using the ISFET sensor. The FET response is "current," and the stimulus is voltage.

2.4.2. Chem/BioFET based on Standard CMOS

Utilizing well-matured CMOS technology as the primary platform for developing ISFETs represented a significant advancement in creating standardized ISFET sensors for biological applications [22, 63]. For instance, in terms of transfer characteristics, the fabricated circuit exhibited a linear dynamic range of 2.5 V, enabling each ISFET to function as a pH sensor within the array [58]. These ISFETs possessed a threshold voltage of −1.5 V and a sensitivity of 46 mV/pH [58]. Employing unaltered CMOS structures (refer to Figure 2-3 (b)) for ISFET sensors offers several advantages that render this structure competitive compared to other Chem/BioFET configurations. Adapting CMOS technology ensures that Chem/BioFET-based sensors are highly scalable and low-powered, two critical attributes for handheld PoC devices. As illustrated in Figure 2-6, this sensor is manufactured by connecting the elongated gate of a transistor to the solution, effectively isolating the solution from the sensor area. The gates, connected through buried metal connectors within the oxide layer of CMOS, are linked to layers of Si_3N_4, SiO_2, etc., which serve

as the surface for ion complexation for H+ sensing [22]. Milgrw et al. [63] employed a 16 × 16 array of these sensors for direct extracellular imaging, exemplifying the application of the unaltered CMOS sensor. The structure of this sensor is depicted in Figure 2-7.

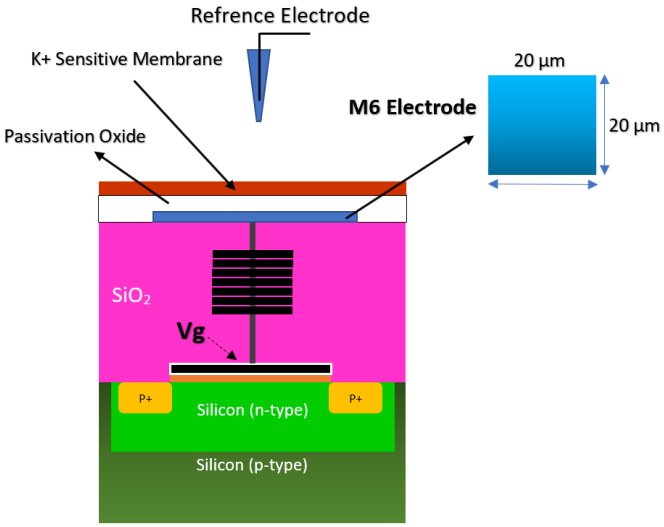


Figure 2-6. The standard complementary metal-oxide-semiconductor (CMOS) ISFET is used to rapidly detect E. coli bacteria using an unchanged CMOS structure coated with a potassium-sensitive membrane.

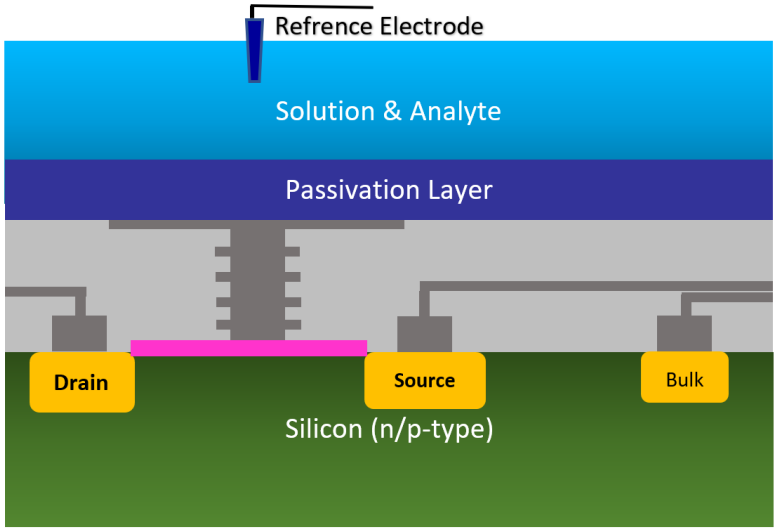


Figure 2-7. The standard CMOS ISFET for cellular monitoring applications.

In alignment with this trajectory, novel CMOS-based innovations emerged for chemical sensing. For instance, a needle-like ISFET sensor was devised to explore minuscule spaces in biological and chemical samples, boasting a sensitivity of 45 mV/pH [64]. Additionally, Georgiou and Toumazou modified a commercial 0.25 um CMOS technology into a standard ISFET for pH measurement [65]. Sohbati et al. conducted dimensional and shape analyses to consider all crucial geometrical parameters influencing the operation of ISFET-based standard CMOS technology [66]. A common characteristic among ISFETs based on CMOS technology is the utilization of SiO_2 and Si_3N_4, or a combination of both, which introduces additional capacitance above the silicon channel, impacting ISFET sensitivity (and inducing parasitic errors). However, covering all parts of the sensor with this thick oxide/nitride layer presents a drawback, resulting in undesired capacitance that affects the sensor's threshold voltage. This occurs as ion complexation/trapping sites on the oxide/nitrite surface influence the electron current in silicon during subsequent attempts [65,66]. This technology found successful real-world applications, particularly in pH measurements, including nucleic acid amplification detection [67] and next-generation genome sequencing [68].

2.4.3. Floating Gate Chem/BioFET

Commonly, a floating electrode is used to protect the oxide sensing region on top of the channel and provide better control over the sensitivity of the device in different operation settings, which is a preferred condition when it comes to having uniform modulation of the sensor. Figure 2-8 shows that the floating gate-based Chem/BioFET structure includes two gates, one for exposure to biological samples and another for controlling the gate. This gate structure has been used successfully to investigate DNA charges on the oxide surface, as depicted in Figure 2-8.

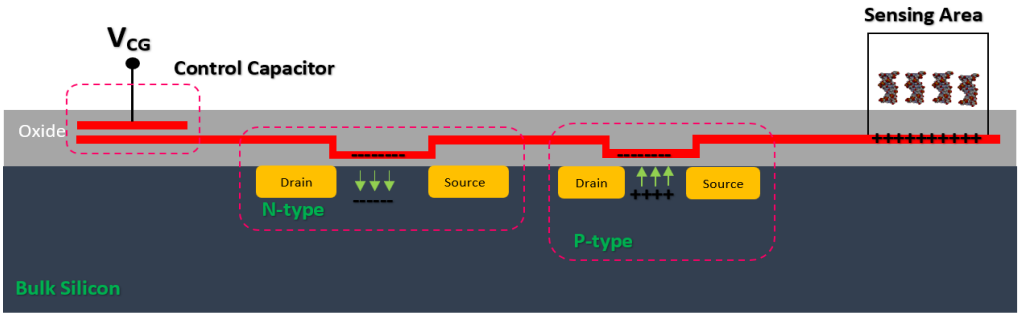


Figure 2-8. The floating gate structure and a real chip designed by Barbaro et al. for Label-free DNA analysis. This sensor contains 80 biosensors that are placed in 2 channels. A microfluidic system has also been bonded on this chip to provide access to the sensing areas for test solutions and reagents.

The sensor illustrated in Figure 2-8 operates without an RE as the floating gate was used for modulation and control of the gate on oxide in which the threshold voltage varied between −0.8 to 0.8 Volts in different stages of DNA sensing procedures [69]. The floating gate structure has been used in another Chem/BioFET sensor for oxide functionalization of conductive organic electronics [70]. In [70], the sensor was also tested without an RE, as the tests were performed in dry conditions. In an exciting job, the floating gate structure was also successfully tested for the realization of programmable ISFETs and used for DNA analysis [71,72]. In terms of investigating neuron interactions, a floating gate structure was used as a sensing platform by Cohen et al. [73]. They designed a floating gate structure that provides a wide gate area for monitoring the chemical reactions, which makes it a suitable sensor for integration with microfluidic [73]. Chemoreceptive neuron MOS (CvMOS) transistors have been used for electrochemical recordings of exocytosis from populations of the mast and chromaffin cells [74]. This sensor arrangement using a floating gate structure (coexistence of control gate, sensing gate, and floating gates together) allows the simultaneous control of the electrolyte and ions quiescent point to be independently controlled. The sensor is also CMOS-compatible and physically isolates the transistor channel from the electrolyte for stable long-term recordings [74].

2.4.4. Extended Gate Chem/BioFET

Integrating FET sensors with a microfluidic platform for directing the solution and biomaterials toward the sensor is a big challenge in biosensor integration. However, a promising approach for alleviating this issue is to extend the gate of the FET sensor compact area to meet biological matters [75,76]. This structure helps to have a much simpler fabrication process, as the sensing area can be fabricated according to the design demand of the fluidic section. Regular FET biosensor

designs, as discussed in previous sections (oxide-electrode gate and floating gates), come with some challenges primarily associated with the inevitable surface chemistry of ion complexations and the following ion trapping phenomena, which leads to the development of noise in the output signal [75]. Extended gate Chem/BioFETs have been designed to improve these deficiencies, which have been investigated in the literature with different applications for pH measurement of ion solutions and other bio-interfaces [16]. Compared with ISFETs, extended gate FETs have shown much better stability regarding chemical, thermal, and incident light disturbances in parallel with greater sensitivity [16, 77]. Figure 2-9 demonstrates an example of an extended gate FET sensor used as a platform for biochemical analysis [76].

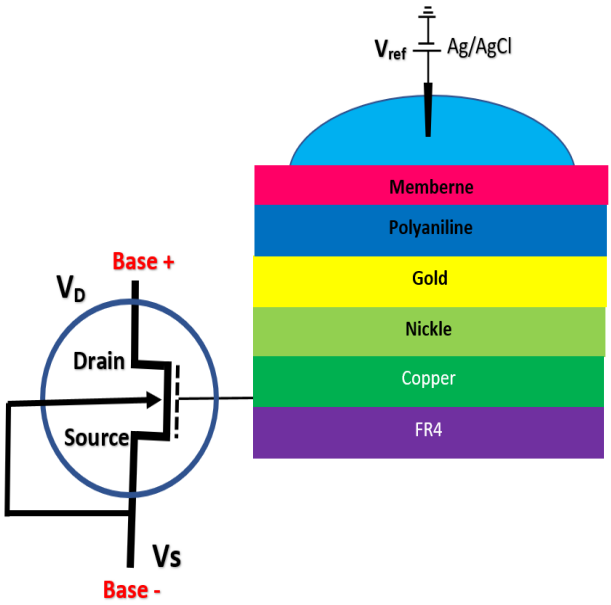


Figure 2-9. An extended gate sensor developed by Kaisti et al. shows a handheld system for biochemical analysis that utilizes a transistor and a specifically designed gate to transfer the detection unit to the sensing FET.

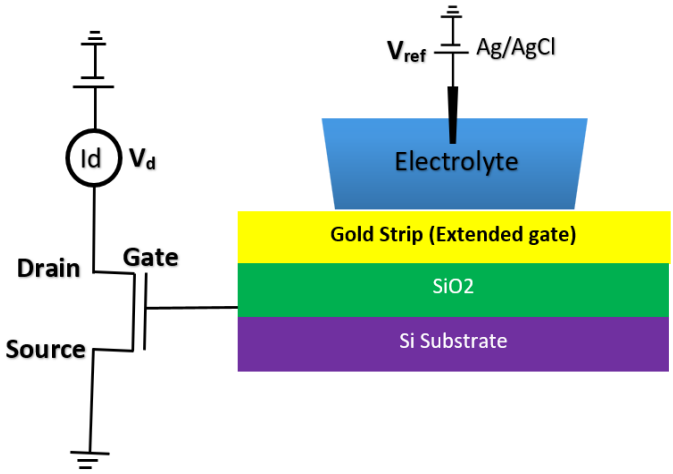


Figure 2-10. Extended gate Chem/BioFET structure in which the gold gate was deposited on SiO2 and Si substrate. The extended gate was connected to the fluidic channel through a liquid cell on top of the sensor.

Due to the specific characteristics of extended gate FET for biosensing applications, many are designed for various detection applications such as pH, urea, glucose, calcium ion, DNA, and immunosensors, which have been registered. A complete review of these sensors is done in other work by Pullano et al. [75]. An extended gate sensor was used for direct potentiometric serological diagnosis toward the detection of the Bovine Herpes Virus-1 (BHV-1) pathogen by Tarasov et al. [77]. Their design is shown in Figure 2-10, which demonstrates an extended gate connected to the gate of a MOSFET. In their experiment, concentrations of p53wt changed from 50 pM to 10 nM, which resulted in Ids jumps ranging from about -5.0×10^{-8} A up to about -5.0×10^{-7} A.

2.4.5. Double Gate Chem/BioFET

Double gate sensors have the same structures as before regarding the drain/source and channel operation mechanism. These sensors mainly operate under an RE, while another gate at the back of the sensor helps to manipulate the sensors' operation point. Due to this further operation control using the back gate, they were intended to go beyond the Nernstian limit, which defines the ISFETs sensitivity limit [78–80]. Spijkman et al., in a fascinating piece of research work, introduced a new configuration of ISFETs using a double gate concept in which they could push the Nernstian limit to about 2.25 V/pH using a self-assembly polymer as the solution interface gate on top of ZnO channel with a back gate that contributes to the creation of bottom capacitance [79,80] (Figure 2-11 shows the double gate sensor).

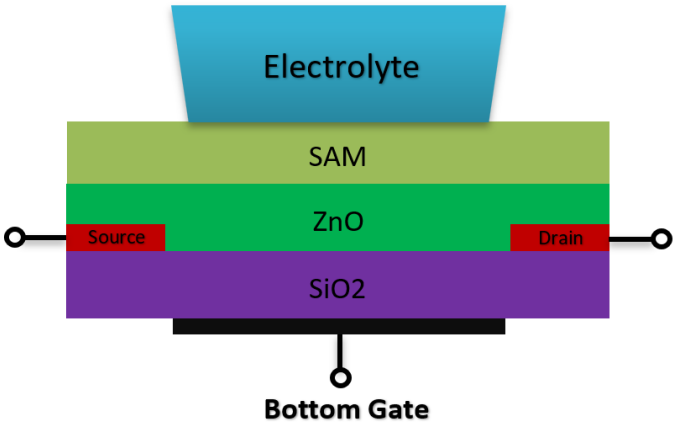


Figure 2-11. The double gate structure Chem/BioFET was designed based on the structure. The SiO_2 is placed at the back of the channel (ZnO), and the electrolyte solution is placed on top of the sensing layer and the conductive channel.

Huang et al. introduced the double gate structure as an effective method to enhance the performance of standard CMOS-based ISFETs. Their study presented a dual-gate ISFET sensor structure, depicted in Figure 2-12, developed using a standard 0.18 µm SOI-CMOS process and an additional backside process [81]. By employing a poly gate (PG) as the second gate in the double-gated CMOS standard ISFET structure (as shown in Figure 2-12), they achieved significant improvements in ISFET characteristics. These enhancements included a 155-fold increase in signal-to-noise ratio (SNR), a 53-fold decrease in drift rates, a 3.7-fold reduction in hysteresis, and a 7.5-fold increase in sensitivity [82]. The back gate structure has been widely utilized in FET structures where nanomaterials, as illustrated in Figure 2-3 (b), were deposited on the oxide and served as the primary conductive channel. Notable examples include CNT-based FETs, graphene-FETs, silicon nanowire (SiNW)-FETs, MoS_2 FETs, MOF FETs, ZnO FETs, and various other nanomaterials that leveraged the double gate configuration with a solution gate and a back gate for sensing applications.

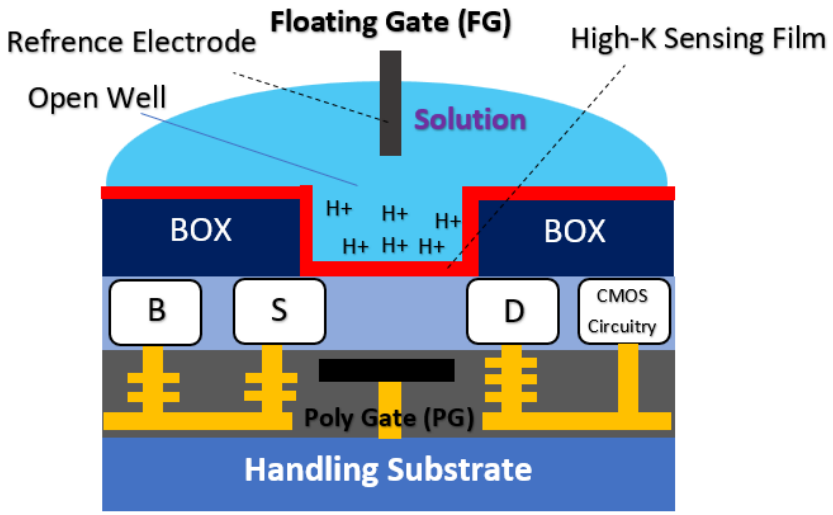


Figure 2-12. A dual-gate ISFET sensor structure was developed in a standard 0.18 µm SOI-CMOS process. The back gate was created through a backside process to make a double-gate structure. The sensor is completely working based on the CMOS readout.

2.5. Chem/BioFET Structures Used for Infectious Disease Screening

As previous discussions have shown, various structures of ISFETs have been employed in Chem/BioFET biosensing systems. These sensors have also been frequently used for the detection of infectious diseases. Almost all the Chem/BioFETs used for infectious diseases have been based on the electrolyte gate on the main channel. However, there were a few examples of other structures as well.

For detection of a sequence of Hepatitis C Virus (HCV) at deficient concentrations down to the pM range, a Peptide Nucleic Acid (PNA) CNT-based FET structure sensor was used in which the sensor was working based on the Ag/AgCl solution gate in the electrolyte [87]. The structure of the fabricated sensor is shown in Figure 2-13, which consists of metallic SWNTs that would lower the sensitivity of the devices for sensing applications. In this work, to minimize the effect of contact residence between single-wall CNTs (SWCNTs) and the metal layer, the contact areas were passivated with microlithograpically patterned Al2O3 (50 nm) or self-assembled dodecanethiol (DDT) monolayers [87].

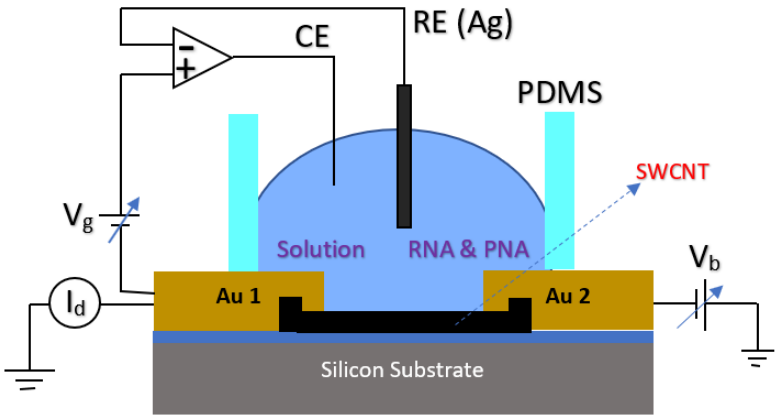


Figure 2-13. FET structure is used to detect RNA. In the figure, Au 1 and Au 2 demonstrate the source and drain pads, respectively. The gate potential has been applied through the Ag/AgCl as RE, and in this picture, the Vb is the bias voltage of the source-drain.

Lee et al. [88] developed an extended gate Chem/BioFET structure (see Figure 2-14) manufactured based on the 0.35 µm CMOS process, which was integrated with working electrodes, an RE, and readout circuits into one package. A detectable range of 88.3 dB and an LoD of 36 µV were reported for this sensor, which led to a successful Chem/BioFET for the detection of oligonucleotide sequences derived from the H5N1 avian influenza virus (AIV).

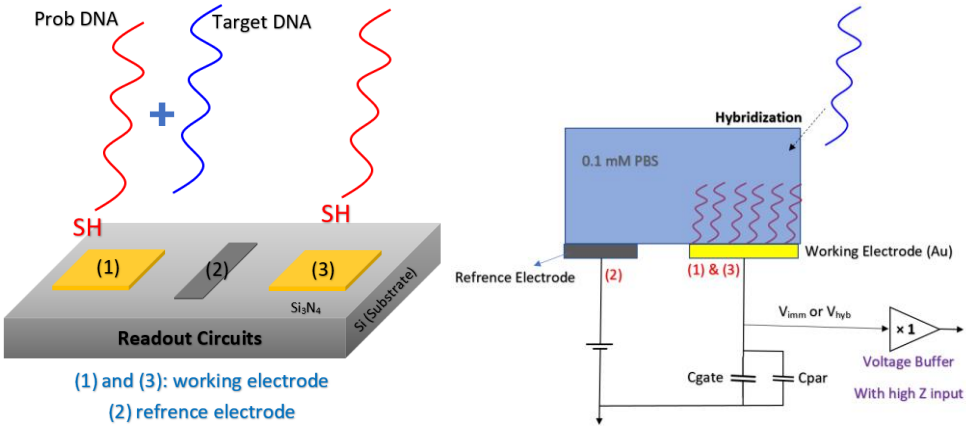


Figure 2-14. The sensor proposed by Lee et al. to detect the RNA of H5N1 AIV-based on hybridization detection on the surface of the gold electrode: (a) Showing the working electrode and reference electrode arrangement, which are dedicated for probing and reference reaction; (b) a brief schematic of circuit and the way it has been connected to the reference and working electrodes.

The structure of this sensor is introduced in Figure 2-14 (a, b), which shows a conceptual view of the integration and working principle of the device. All the electrodes were built in the device area, which included working electrodes, an Au (numbers (1) and (3)) modified along with DNA strands, and an RE (Al, number (2)) that determined the potential of the analyte solution. The signal will

be processed in the CMOS circuitry after introducing the sample to the functionalized extended gate.

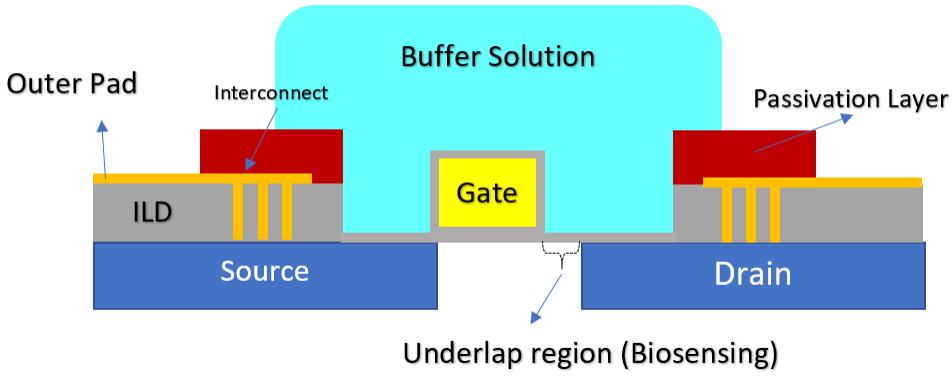


Figure 2-15. A CMOS-based Chem/BioFET structure using an underlap-FET biosensor: The cross-sectional of a water droplet is shown as the solution on top of the sensor. This sensor has been used to show the effect of wettability on the sensor characteristics and sensitivity

Another CMOS-based Chem/BioFET platform is shown in Figure 2-15, which utilizes a gated area on the main channel. At the same time, the solution is introduced onto the sensor through an underlap region [89]. In the sensor shown in Figure 2-15, to examine the effect of hydrophilicity and hydrophobicity on the response of the sensor, a thin film of CYTOPTM and silicon nitride has been used as the hydrophobic and hydrophilic passivation layers, respectively. The sensor was finally tested for surface antigen detection and its specific AIV antibody. This work introduced a method for enhancing the sensitivity of CMOS-based Chem/BioFET sensors to detect better.

Figure 2-2 shows that many sensors have employed nanomaterials as the sensing element, considered conductive channels. Almost all sorts of these sensors are working based on the back-gate structure. Therefore, double-gated Chem/BioFETs consider one of the gates as a RE in the electrolyte solution. One of these structures employing both the back gate and a solution gate was implemented on the SiNW-based sensor to detect H5N2 AIV in a very dilute solution [90]. To facilitate the integration of the RE with the SiNW, it was positioned inside the solution where the fluid was directed inside, as shown in Figure 2-16.

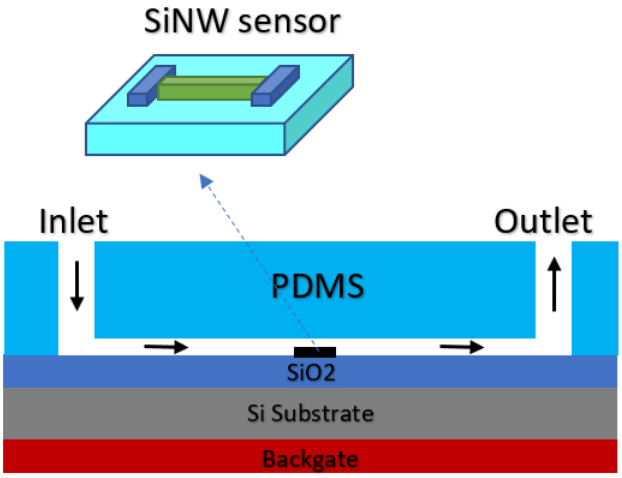


Figure 2-16. The silicon nanowire (SiNW) schematic integrated with the PDMS microfluidic channel is designed to direct the flow of the sample of interest toward the solution. An Ag/AgCl electrode is integrated by placing its tip in the inlet of the microfluidic channel.

The ultrasensitive detection of H5N2 AIV was demonstrated using a reusable SiNW FET, which was made possible by the reversible surface functionalization on the SiNW via a disulphide linker. They reported a successful reversible surface functionalization, which was then examined by electrical and microfluorescence methods. This innovation enabled them to detect very dilute H5N2 AIV at 10−12–10−17 M [90].

As a back-gated structure for SiNW sensors, based on a CMOS fabrication process, a label-free and specific DNA detector was devised in which, by applying rolling circle amplification (RCA) on SiNW-FET, they could get higher sensitivity and better performance. The back gated structure was also used to directly detect airborne viruses without using any solution and wet fluidic section [91]. According to this method, the virus–antibody-connected particles are delivered to the FET during detection, and the regular pre-treatment and antibody binding step on the FET channel is not required. In this method, they have eliminated the washing process for the virus–antibody binding [91]. On top of the sensor area, a layer of CNT was coated, which was used to detect virus deposition from the electro-aerodynamics separator (see Figure 2-17).

In another study, integrating a double gate and extended gate was studied to introduce a new sensor structure (see Figure 2-18). A so-called ‘disposable well gate’ was connected to the top gate of a

channel, which was used to detect AIV [92]. This research reports a FET-based AIV sensor capable of detecting nucleoproteins within 30 min, down to a LoD of 103 EID50 mL^{-1} from a live animal swab sample [92].

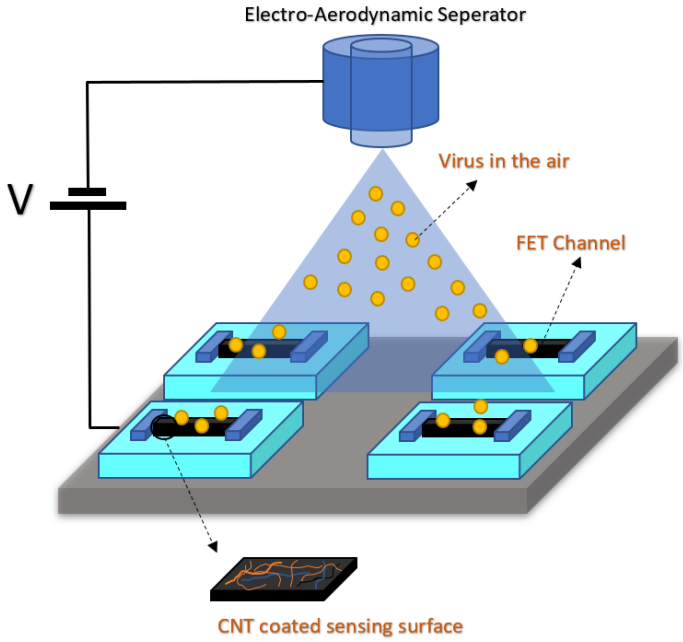


Figure 2-17. The carbon nanotubes (CNT) sensor works based on a back-gate biasing, and the sample is introduced by an electro-aerodynamic separator without using wet samples.

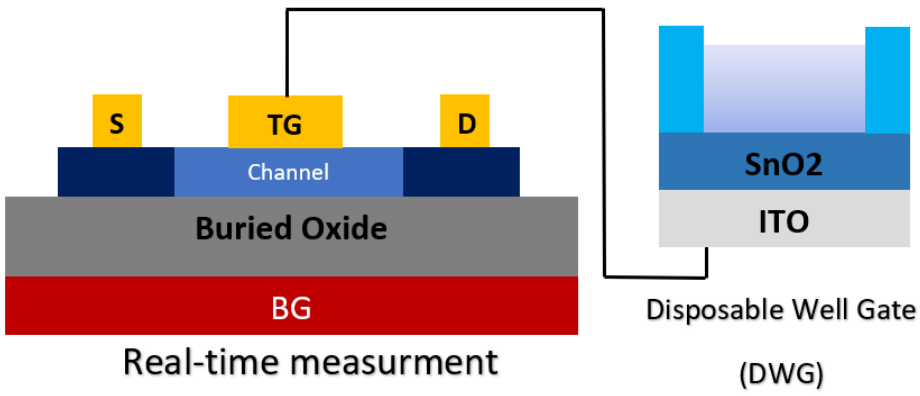


Figure 2-18. Illustration of the avian influenza virus (AIV) sensor configuration, combining double-gate and extended-gate configuration.

The back gate structure in another Chem/BioFET was used for Ebola virus disease (EVD) detection [93]. A reduced graphene oxide (rGO) FET, controlled by a back gate, was used for real-time detection of the Ebola virus antigen [93]. The same gating structure was used for developing

an indium tin oxide (ITO) NW-based FET for DNA biosensing, which was used for the detection of hepatitis B virus (HBV) based on ITONWs [94].

Based on our review, relatively few papers have utilized standard FET sensors fabricated using CMOS technology to detect infectious diseases. Instead, many of these sensors have been produced using laboratory microfabrication techniques. Many Chem/BioFET infectious disease detector structures have been top-gated in gating structure, typically featuring a solution gate with a reference electrode (RE). In the subsequent chapter, we delve into the biological interface of Chem/BioFETs, mainly focusing on their application in screening for infectious diseases.

2.6. Surface Modification and Functionalization of Chem/BioFETs

The operation of FET biosensors depends on the bioreactions that occur on their surface [95]. Their efficiency and preciseness are contingent on the selectivity and availability of the bio-recognition elements (BREs). Therefore, proper surface functionalization is imperative for optimizing the BRE immobilization, enhancing the sensitivity, preventing unwanted reactions, and minimizing the noise [96]. Additionally, the type of material used to cover the sensor's surface increases its biocompatibility, and surface chemistry plays a crucial role in improving the sensor's performance [97]. As mentioned in the previous section, a wide range of substrates is utilized for this purpose, including gold, nanowires (NWs), CNT, graphene, glycan, etc. [98]. Using nanomaterials with extraordinary characteristics such as small size, high chemical and mechanical stability, considerable electrical conductivity, nontoxicity, and high surface-to-volume ratio offers an optimum sensing area for operating an accurate detection [99]. One-dimensional nanostructures significantly improve the sensor's performance and increase the LoD to attomolar levels [100]. These structures enable label-free electrical detection of biospecies in a sensitive and precise manner [101]. Table 1 compares some of the FET biosensors reported recently for detecting various infectious agents, especially viruses. After introducing materials that cover the sensors' surface in Section 3.1[1], different types of BREs will be reviewed in Section 3.2[2].

[1] Section 2.6.1
[2] Section 2.6.2

2.6.1. Surface Materials

2.6.1.1. Nanowires

NW-FETs are one of the most used categories of Chem/BioFETs [117]. In these systems, the channel and gate of a standard Chem/BioFET are functionalized with NWs and BREs [118]. Despite their different configuration, they operate through the same procedure. NWs can be fabricated through bottom-up (chemical etching, vapor-liquid-solid, and oxide-assisted growth) or top-down approaches from semiconductor materials [119]. SiNWs are commonly preferred alternatives because of their facile fabrication and modification process [120]. Their surface should be functionalized with specific BREs to be sensitive to the target viruses. This can be done through physical adsorption and chemical cross-linking [121].

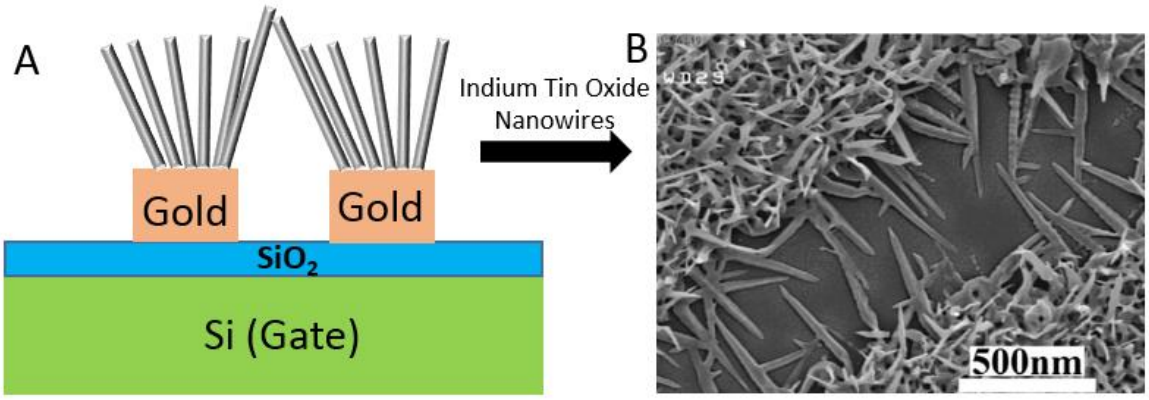


Figure 2-19. The configuration of ITONWs-FET genosensor. (a) Si/SiO2/Au/ITONWs device; (b) the FESEM images of indium tin oxide (ITO) samples.

After exposing the functionalized surface to the sample, an electric field is induced onto the NWs and changes their conductivity due to the interaction between the charged target and receptors [122]. Several types of biological interactions, such as antibody-antigen, protein-ligand, and oligonucleotide hybridization, can be inspected on the surface of NW-FET biosensors [123]. Recently, several studies have focused on developing novel biosensing platforms for detecting viruses. For example, a recent study was conducted to detect the influenza virus (IV) using a SiNW-FET-based biosensor fabricated through CMOS technology. This system could spot down to 1 fM of the target protein [102]. Figure 2-19 illustrates that another FET nanosensor was designed to detect HBV based on ITONWs, significantly facilitating surface functionalization and hybridization. After coating the nanowires with gold, they were modified with single-stranded

DNA (ssDNA). This arrangement successfully identified 1 fM of the viral genome in 37 s and differentiated the target from other oligonucleotides [94].

2.6.1.2. Gold

Au-modified surfaces represent a popular approach for surface functionalization of FET-based sensing systems since they provide a stable platform for immobilizing the BREs, boosting the electron shuttle rate, and upgrading the device performance [95,124]. Furthermore, the high biocompatibility of these surfaces preserves the functionality of the BREs and optimizes their efficiency in interacting with target biomolecules [125]. More importantly, the wide available area provided by gold nanoparticles enables the immobilization of many receptors and accordingly augments detection sensitivity [126]. Several recent studies have employed this strategy to design biosensors for detecting viral particles.

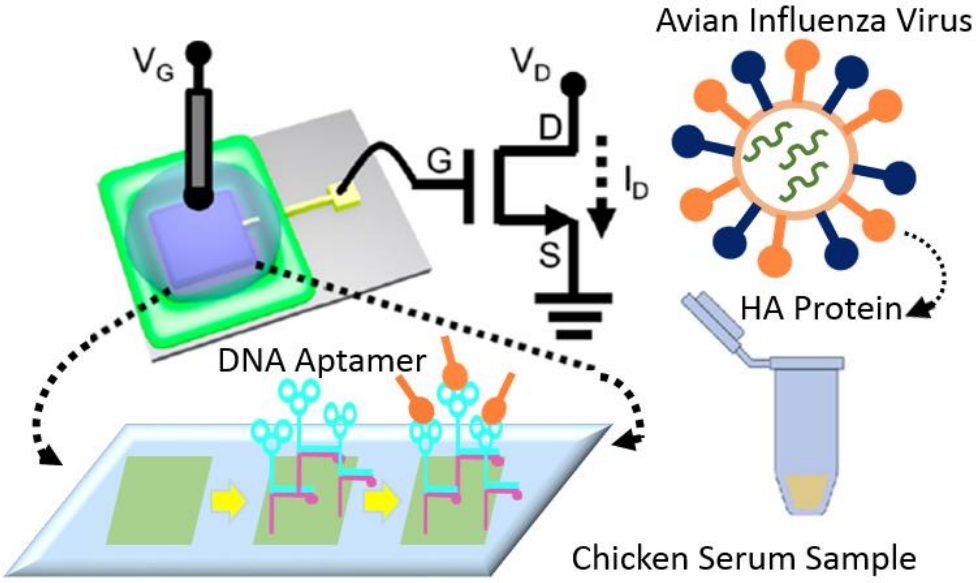


Figure 2-20. The illustration of the FET-based aptasensor for detecting AIV in chicken serum. The surface of the gold electrode was modified with specific DNA aptamers to identify the virus's surface protein. The interaction between the probe and the target resulted in the structural change of the aptamers, which was recorded as the surface potential.

For instance, using aptamer-modified gold microelectrodes, a reusable FET-based device was fabricated to identify AIV (see Figure 2-20). The hemagglutinin (HA)-specific aptamers' interaction with the target biomolecules alters the surface potential, which is recorded as a signal. The LoD was reported at 5.9 pM, which shows the preciseness of the detection in chicken serum. This portable platform's easy and cheap fabrication process makes it an ideal approach for PoC diagnosis of viral particles in biological samples [104]. In another study, an immune-FET was

designed to detect the capsid protein of HIV. A monolayer of gold covered the gate of the device to provide a biocompatible area for immobilizing target-specific antibodies. The ultra-sensitive recognition power of this strategy (LoD = 30×10^{-21} M) enables reliable, economical, and portable detection of single molecules [105] (see Table 2-1).

2.6.1.3. Graphene

Graphene is the other widespread material for surface coating in biosensor designs [127]. It has several different forms, such as graphene oxide (GO), rGO, and graphene nanoribbon (GNR), which have been extensively used in the structure of sensing devices because of their chemical, mechanical, and electronic attributions [128, 129]. This biologically friendly carbon-based material provides a wide area with numerous anchor spots for functionalizing the surface with diverse nanoparticles, polymers, or any other signal amplifier before immobilizing the BREs. Additionally, it has exceptional electrical conductivity, high capacitance, low contact resistance, and tunable ambipolar field-effect behaviors. Since it increases the electron transfer rate, the response time of the biosensor decreases significantly [130, 131]. Besides, its cost-effectiveness, easy fabrication, and biocompatibility make it one of the most preferred materials for coating the surface of virus-specific FET-based bioassays. As an instance, Jin et al. proposed a FET-based immunosensing device for the detection of the Ebola virus. Figure 2-21 shows that rGO functionalized the sensor's surface before immobilizing antibodies. The L_OD was reported to be 2.4 pg·mL^{-1} of the target glycoprotein in spiked serum samples [93].

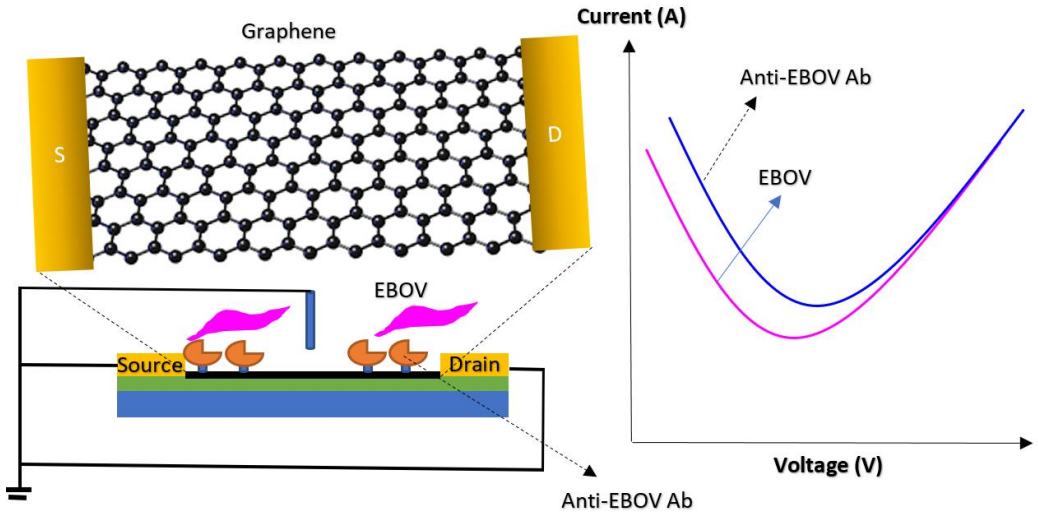


Figure 2-21. The illustration of the reduced graphene oxide (rGO)-FET immunosensor for Ebola Virus recognition and Surface modification and the conductance changes that occur upon antigen attachment to the antibody.

In another study, a GFET system was reported for detecting IV and studying the antiviral medications' effect on it. Sialic acid was used as a probe to recognize the HA on the virus's surface. Besides, the repressive effect of "zanamivir" on this interaction was investigated. This work represented the compatibility of these platforms for quantifying biological reactions in biosensing and drug development applications [113]. Aspermair and colleagues constructed a FET aptasensor to identify human papillomavirus (HPV). The sensor's surface was characterized by rGO, pyrene, and RNA aptamers to spot viral proteins in saliva samples. They successfully detected as low as 1.75 nM of the target molecules, indicating the device's competency in real-time detection of viral infections [109].

2.6.1.4. Carbon Nanotubes

The CNTs have been the focus of attention from researchers' viewpoint due to their superior conductivity and exceptional configuration [132, 133]. These hollow carbon-based arrangements might have one (SWCNT) or more walls (multi-walled CNT) consisting of hexagonal frames of carbon [134]. In other words, they are rolled graphene sheets capped at both ends. Owing to their systematic and well-organized structure, they display high mechanical stamina, which makes them an ideal choice for biosensing applications [135, 136]. In addition, CNTs deliver a broad surface area for immobilizing many BREs [137]. Thus, they are commonly employed in detecting virus-related biomarkers in biological samples. For instance, a FET-based assay was developed to recognize tiny amounts of HCV by employing SWCNT. PNA was used as the probe, and 0.5 pM of the target particles was detected [87]. In a different research work, a simple-to-use FET biosensor was projected to quantify aerosolized viruses (see Figure 2-22). The core strategy of this approach was the higher number of charge carriers and larger sizes of the antibody-antigen complexes compared to unbound antibodies or viruses. This fact led to these big particles' deposition on a specific substrate region. If this area overlaps with the SWCNT-modified channel of the transistor, a change will occur in the recorded current that signifies the existence of the virus [91].

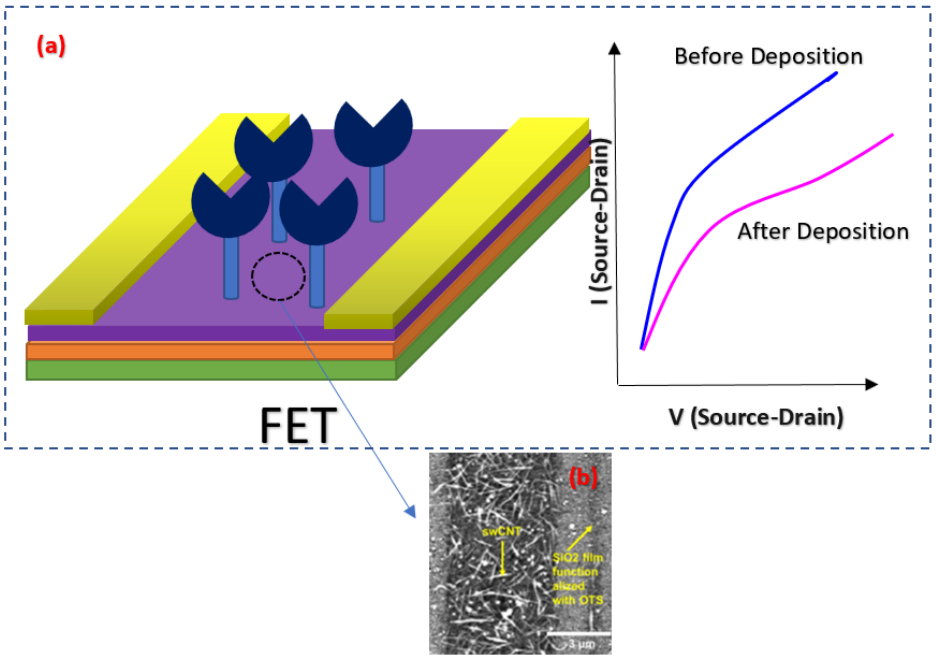


Figure 2-22. (a) Electrical identification of the viral particles using a tailor-made single-walled carbon nanotube (SWCNT)-FET immunosensor; (b) AFM image of the SWCNT channel region.

2.6.1.5. Transition Metal Dichalcogenides (TMDs)

The other category of surface functionalization materials is the TMDs [138]. They are single-layer semiconductors comprising two chalcogen atoms and a group IV, V, or VI transition metal component [139]. These single-layer hexagonal structures contain a direct bandgap, making them suitable candidates for electronic applications [140]. One of the most popular two-dimensional TMDs—Molybdenum disulfide (MoS_2)—has attracted attention in biomedical fields attributable to its superior electronic, chemical, and mechanical characteristics [141]. This graphene-like arrangement has a width equal to a single cell, which results in its ultra-sensitive performance when used in biosensing platforms. They can be easily integrated into biosensors since they do not have any loose bonds in their structure [142]. They are broadly employed today, especially in Chem/BioFETs [143]. For example, an accurate MoS_2-FET genosensor was established for detecting Down syndrome. They modified MoS_2 with gold nanoparticles to facilitate DNA immobilization. The device presented an ultra-sensitive performance by detecting down to 100 aM of the target DNA sequences [144]. Another easy-to-use and precise system was designed using a MoS_2-functionalized FET immunosensor to identify Fibroblast growth factor 21 (FGF21)—a fatty liver disease (NAFLD) detection biomarker. After introducing the sample containing the target

analyte and, accordingly, the production of Ab-Ag complexes, the detection occurred, and a LoD of 10 fg.mL^{-1} was recorded. This device demonstrated satisfactory selectivity even in complex serum samples [145]. A DNA biosensor based on a MoS_2-based FET was introduced, and it employed phosphorodiamidate morpholino oligos (PMO)-DNA hybridization as its detection strategy. Negatively charged MoS_2 was drop-casted on the positive-charge-baring sensing area and attached via electrostatic interactions. Next, the immobilization of PMOs took place, which enabled ultra-sensitive detection. This device's low LoD (6 fM) showed this structure's outstanding capability in biosensing applications [146]. The use of TMDs in Chem/BioFETs is exemplified in these successful studies and many others [147–150], which confirms their high performance in detecting tiny biomolecules in complex human biofluids.

2.6.1.6. Conducting polymers (CP)

CPs are one of the other appropriate choices for covering the surface of Chem/BioFETs since they are lightweight, cost-effective, highly scalable, easy to fabricate, and have adjustable properties [151]. These functional materials have exceptional electrochemical characteristics, high electrical conductivity, and mechanical stamina and thus are suitable for use in biosensors as transducers [152]. Controlling their configuration and using dopants in the structure of CPs can further improve their performance by providing a large surface-to-volume ratio and boosting electrocatalytic behavior [153]. They can be utilized as NWs or nanotubes on the sensing region of biosensors to enhance their sensitivity [154]. Modulating the CP surface for optimized biomolecule linkages makes their use in sensing platforms feasible [155]. For example, a recent study reported the development of a conducting polymer nanotubes-functionalized FET aptasensor for dopamine (DA) recognition. Tailor-made aptamers were immobilized on the surface of carboxylated polypyrrole nanotubes (CPNTs), detecting as low as 100 pM of the DA. Controlling the diameter of CPNTs was an important feature that the authors considered while constructing this device. It was reported that the tiny structures demonstrated higher sensitivity and specificity than the wider ones since they delivered a sizeable available area [156].

2.6.1.7. Different Types of Bio-Recognition Elements (BREs)

For Chem/BioFETs to precisely detect antigens, antibodies, nucleic acids, etc., their surface should be functionalized with tailored BREs. They operate based on the affinity between the antigen-antibody or DNA hybridization. Immobilizing specific BREs in their optimum arrangement enables the production of complementary complexes, which in turn change the conductance of the channel region. Generally, Chem/BioFETs can be categorized into three main groups: Immuno-, geno, and apta-sensors. Antibodies against the viral/bacteria-related antigens, complementary DNA/RNA probes against the genomic material of the pathogen, and tailor-made aptamers can be immobilized on the surface of modified FET devices to make them capable of capturing the desired target biomolecules.

2.6.1.8. Antibody or Antigen

Antibody/antigen-immobilized FET-based biosensors, so-called immunosensors, are one of the most preferred systems for identifying either pathogen-specific antigens or produced antibodies in the host body in response to the pathogen attack. For example, the most recent research for identifying SARS-CoV-2 utilized a FET-based biosensor decorated with ultra-selective antibodies to capture viral spike proteins. It could recognize an analyte as low as 100 fg/ml in a clinical transport medium [157]. A portable immunosensor was developed for sensing HIV-1. This single-molecule detection was carried out using an electrolyte-gated FET modified with antibodies against the capsid protein of HIV-1 p24 [105]. In another study, a GFET was designed using 1-pyrene butanoic acid succinimidyl ester (PBASE) as the linker to immobilize specific antibodies for detecting whole viruses. This strategy was successful enough to spot down to 47.8 aM of the target biomolecules [111]. The efficiency of these investigations and many others [89,91–93,103,106–108,110,115] acknowledges the capability of FET-based immunosensors in detecting infectious diseases.

2.6.1.9. Nucleic Acid

Nucleic acid-based sensing systems or genosensors are the next widespread category of FET biosensors. The matching DNA or RNA of the virus, bacteria, or any other pathogen is immobilized on the sensing area of the FET. A signal is recorded to indicate the detection if the target DNA/RNA is present in the sample. For instance, a pioneering DNA biosensor was fabricated employing a SiNW-FET for HBV recognition. The probes were stabilized on the surface of (3-Aminopropyl)

triethoxysilane (APTES)-functionalized nanowires. Due to the rolling circle amplification strategy, a long strand of DNA was produced after introducing the targets. Therefore, an amplified electronic signal was recorded to detect 1 fM of the target DNAs [90]. Another genosensing platform was proposed by Lee et al. They immobilized oligonucleotides on the surface of gold electrodes to detect the attachment of avian influenza virus sequences and achieved a LoD of 100 pM, as seen in Table 1 [88]. In another effort, DNA was immobilized on CMOS-based ISFETs as BREs to detect Plasmodium falciparum. This work employed an adapted version of loop-mediated isothermal amplification (LAMP), called pH-LAMP, which enables ISFETs to detect pH variations during nucleic acid amplification. This CMOS-based device presented an outstanding performance, which shows its potential for being used as a PoC test for malaria [116].

2.6.1.10. Aptamer

Aptamers are the other group of selective BREs, which have been used in several studies related to FET biosensors. They are popular for ultra-sensitive sensing, particularly when incorporated with nanoparticles. As an example, an aptasensor was established for detecting HPV employing an rGO-FET. The pyrene molecules acted as linkers for successfully immobilizing RNA aptamers on the sensor's surface. This real-time detection could sense down to 1.75 nM of HPV-16 E7 [109]. Another aptamer-functionalized Chem/BioFET was constructed to identify Plasmodium falciparum glutamate dehydrogenase in serum specimens. A specific aptamer was designed to capture the target pathogen precisely. A LoD of 48.6 pM was recorded, demonstrating that this device can detect malaria even in asymptomatic patients [45].

2.6.1.11. Others

Other types of BREs have been used for functionalizing Chem/BioFETs, such as PNAs, sialoglycans, sialoglycopeptides, or even bacteriophages. For instance, an on-chip bacteria sensing system was reported, which used bacteriophages as receptors for spotting a particular strain of E.coli. A CMOS-based ISFET measured the potassium ions released inside the bacterial cells due to phage infection with polyvinyl chloride (PVC)-based potassium-sensitive membrane. This sensor could detect as low as 48.6 pM of the target biomolecules below 30 min [22] (Table 1). PNAs are another novel type of BRE used in a study to recognize HCV. This SWNT-FET-based device could conduct a pM level detection [158]. Sialoglycans are also desirable BREs that can be used in designing novel pathogen biosensors. They can mimic the natural host-cell surface and enhance the performance of the biosensor.

Table 2-1.Recently proposed FET biosensors for detecting various infectious agents.

Application	Target	BRE	Linker	Surface	Detection Range	LoD	Sample	Ref.
IV diagnosis	GST-tagged-HA	CMP-NANA	APTES GA	SiNW	-	1 fM	Buffer	[102]
AIV diagnosis	Whole virus	Ab	MPTMS DTT biotin-HPDP	SiNW	-	10^{-17} M	Buffer	[103]
HBV diagnosis	HBV	ssDNA	Au	ITONWs	1 fM–10 μM	1fM	Buffer	[94]
HBV diagnosis	DNA	DNA	APTES EDC/NHS	SiNW		1 fM	Buffer	[90]
AIV diagnosis	oligonucleotide	ssDNA	Thiol chain mercaptohexanol	Al/Au	0.1–100 nM	100 pM	Buffer	[88]
AIV diagnosis	HA protein	DNA Aptamer	-	Au microelectrode	10 pM–10 nM	5.9 pM	Chicken serum	[104]
HIV-1 diagnosis	capsid protein	Ab	EDC/NHS	Au	-	30×10^{-21} M	Serum	[105]
HBV diagnosis	Whole virus	Ab	GA	GNR	0.05–0.055 fM	0.05 fM	Buffer	[106]
Rotavirus diagnosis	Whole virus	Ab	PSE	MrGO	10–10^5 pfu/mL	102 pfu	Buffer	[107]
Rotavirus diagnosis	Whole virus	Ab	pyrene-NHS	rGO	101–106 particle/ml	1 nm	Buffer	[108]
HPV diagnosis	E7 protein	RNA aptamer	EDC/NHS pyrene	rGO	30–1000 nM	1.75 nM	saliva	[109]
EVD diagnosis	glycoprotein	Ab	GA	rGO	-	1 $ng.ml^{-1}$	Buffer, human serum, and plasma	[110]
EVD diagnosis	glycoprotein	Ab	PASE	rGO	2.4×10^{-12}–1.2×10^{-7} $g \cdot mL^{-1}$	2.4 $pg \cdot mL^{-1}$	Spiked serum	[93]
VSV, MLV, HIV diagnosis	Whole virus	Ab	PASE	PET/PS /Graphene	47.8 aM–10.55 nM	47.8 aM	Buffer	[111]
Detection of HIV-1 viremia	RNA	?	-	SiO_2/ Si_3N_4	> 1000 $copies.mL^{-1}$	10 copies per reaction	Plasma samples	[21]
IV diagnosis	Whole virus	Sialoglycan	-	Graphene	-	2.56 HAU	Saliva	[112]
IV diagnosis	HA	SGP	PBASE	Graphene	-	200 nM	Buffer	[113]
COVID-19 diagnosis	S protein and whole virus	Ab	PBASE	Si/ SiO_2/Graphene	1.6×10^1–1.6×10^4 pfu/ml	2.42×10^2 $copies.mL^{-1}$	Clinical samples	[18]
HCV diagnosis	RNA	PNA	-	SWCNT	-	0.5 pM	buffer	[87]
virus detection	aerosolized bacteriophage MS2 and IV (H1N1)	Ab	-	OTS SAM SWCNT	-		Buffer	[91]
AIV diagnosis	Whole virus	sialic-acid-containing glycans	APTES LCEE	sialyllactose	$10^{0.5}$–$10^{8.5}$ TCID50/mL	$10^{0.5}$ $TCID50.mL^{-1}$	nasal mucus	[114]
AIV diagnosis	nucleoprotein	Ab	APTES EDC/NHS	SnO_2	10^2–10^5 EID50/mL	10^3 EID_{50} mL^{-1}	cloacal swab	[92]
Zika virus diagnosis	Whole virus	Ab	-	AlGaN/GaN/dispposable cover glass	0.1–100 $ng.ml^{-1}$	0.1 $ng.mL^{-1}$	Buffer	[115]
AIV diagnosis	AIa	Ab	SBP	CYTOPTM and Si_3N_4	10 $fg.ml^{-1}$–100 $pg.ml^{-1}$	1.9 fM 0.19 pM	Buffer	[89]
Plasmodium falciparum diagnosis	Nucleotide	DNA	-	SiO_2/ Si_3N_4	-	1 copy per reaction	Buffer	[116]
Plasmodium falciparum diagnosis	*Pf*GDH	Aptamer	MCH	IDμE	100 fM–10 nM		Serum	[45]
E.Coli diagnosis	K^+	Bacteriophage	-	PVC-based potassium-sensitive membrane	-	48.6 pM	Buffer	[22]

Ab: Antibody, GST: glutathione S-transferase, HA: Hemagglutinin, CMP-NANA: Cytidine-50-monophospho-N-acetylneuraminic acid, APTES: (3-Aminopropyl) triethoxysilane, GA: Glutaraldehyde, STV: streptavidin, AIV: Avian influenza virus, AIa: Avian influenza antigen, SBP: Silica binding protein, ssDNA: Single-stranded DNA, HBV: Hepatitis B virus, ITONWs: Indium tin oxide nanowire, EDC: N-ethyl-N′-dimethylaminopropyl carbodiimide, NHS: N-hydroxysuccinimide, MPTMS: 3-mercaptopropyltrimethoxysilane, Biotin-HPDP: N-(6-(biotinamido)hexyl)-3'-(2'-pyridyldithio)-propionamide, DTT: Dithiothreitol, HPV: Human papillomavirus, GNR: Graphene nanogrid, EVD: Ebola virus disease, HCV: Hepatitis C Virus, PNA: Peptide Nucleic Acid, LCEE: L-cysteine ethyl ester, PASE: 1-Pyrenebutanoic acid succinimidyl ester, PS: Polystyrene, VSV: Vesicular stomatitis Indiana, MLV: Murine leukemia virus, HIV: Human immunodeficiency virus, MrGO: Micropatterned reduced graphene oxide, PSE: 1-pyrenebutyric acid N-hydroxysuccinimide ester, SGP: Sialoglycopeptide, OTS SAM: Octadecyltri-chlorosilane self-assembled monolayer, PfGDH: Plasmodium falciparum glutamate dehydrogenase, MCH: Mercapto 1 hexanol, IDμE: Inter-digitated gold microelectrodes, PVC: Polyvinyl chloride.

For example, Ono and colleagues developed an influenza GFET-biosensing platform using sialic acid to coat the sensing region's surface. Owing to the affinity of the virus's HA molecules to this glycoprotein, the HA-sialic acid complexes are generated. Besides, neuraminidase (NA) interacts with these complexes, which results in the detection of the virus [113].

2.7. Readout Circuit and Systems

After preparation of the Chem/BioFET structure and modification and functionalization of the sensing surface according to the desired application, the parameters of Chem/BioFETs should be controlled and measured using electrical devices, which might be laboratory equipment like a potentiostat and a semiconductor parameter analyzer [87, 89, 91, 94] or integrated circuits [20, 22, 23, 88, 116]. This section gives an overview of readout techniques. Herein, the focus is on the CMOS-based integrated circuits, which can pave the way for developing affordable handheld PoC devices. If the Chem/BioFETs are adapted to CMOS technology, it would be possible to miniature them with the circuits of the required signal amplifiers, filters, multiplexers, and analog-to-digital converters (ADCs) on a single chip. CMOS technology offers the advantages of small size, lightweight, low cost, fast response, high spatiotemporal resolution, low power consumption, good noise immunity, and a high level of integration.

Table 2-2 compares various readout circuits reported for Chem/BioFET sensors, especially CMOS-based ones. In 1999, Bausells et al. [159] focused on the fabrication of ISFETs in an unmodified CMOS process (standard CMOS process following the exact steps for MOSFET fabrication) and showed that it is possible to integrate sensing and electronic functions. They designed an integrated ISFET amplifier circuit using standard CMOS process cells. Since many efforts have been made to fabricate ISFETs in CMOS technology, most of the circuits reported in Table 2 take advantage of ISFETs. Although many of them are used for pH measurement using ISFETs, they are potentially helpful in reading the output parameters of Chem/BioFETs. Furthermore, as seen in Tables 2-1 and 2-2, ISFETs [20, 22, 23, 88, 116] are also beneficial for detecting infectious agents. For instance, Rothberg et al. [20] presented a scalable CMOS-based ISFET sensor architecture for DNA sequencing of bacterial genomes, including V. fischeri, E. coli, and R. palustris, by measuring the pH variations during DNA sequencing. In other efforts,

Malpartida-Cardenas et al. [116] and Lee et al. [88] reported CMOS-based ISFETs for diagnosing P. falciparum and H5N1 AIV through DNA sensing, respectively.

As seen in Table 2-2, Chem/BioFETs can be biased in different operation regions, which provide various types of readout circuits with other features. Therefore, the measurement principles of these operation regions must be examined before introducing the readout circuits.

As mentioned, among various Chem/BioFETs, the equations of ISFETs have been theorized excellently and briefly reviewed in Section 2[1]. The output current of ISFET in the linear region was expressed by Equation (2-1), where the threshold voltage follows Equation (2-5). However, Since the gate of ISFET is in contact with electrolyte with no metal in its vicinity, internal source and drain resistances (Rs and Rd) are formed based on the actual geometry of the device in such a way that the actual drain-source voltage and the gate-source voltage of the ISFET are equal to VDS, ISFET = VDS − (Rs + Rd) ID and VGS, ISFET = VGS − Rs×ID and, consequently, the sensitivity is declined [160]. A technological approach to solve this problem is shortening the length of the source and drain diffusions, which implies new technologies. However, using electronic readout circuits insensitive to series resistances is much easier. By biasing an ISFET at a constant ID with a constant VDS, VGS will adjust to compensate for a change in threshold voltage due to a pH variation [160].

Linear operation mode is one of the operational regions that can be used in current-mode circuits. If the ISFET is biased in the triode region with a low VDS, the output current mentioned by equation (2-1) can be approximated by [32]:

$$I_{\mathrm{D}} = \mu C_{\mathrm{ox}} \frac{W}{L} \left[\left(V_{\mathrm{GS}} - V_{\mathrm{t(ISFET)}} \right) V_{\mathrm{DS}} \right], \tag{2-9}$$

$$\frac{dI_{\mathrm{D}}}{dpH} = g_{\mathrm{m}}(pH) = -2.3\alpha\mu C_{\mathrm{ox}} \frac{W}{L} V_{\mathrm{th}} V_{\mathrm{DS}}, \tag{2-10}$$

The gain requirements determine the width of the channel (W) biased in the triode region, but at the expense of the occupied area and array density. Moreover, the length of the transistor (L) should

[1] Section 2.3

be long enough to reduce the second-order sources of non-linearity (like mobility degradation) and short-channel effects.

The principle of measuring the threshold voltage of ISFET in the saturation region is like triode ISFET. Furthermore, low-voltage, low-power circuits are reported for the ISFETs operating in weak inversion as a translinear element. Velocity saturation as a short-channel effect can also be used as a linear mode of operation for current-mode readout circuits. Considering $V_{\mathrm{t\,(ISFET)}}$ follows Equation (5), the sensitivity of I_{D} to pH is linear [32]:

$$\frac{dI_{\mathrm{D}}}{dpH} = g_{\mathrm{m}}(pH) = -2.3\alpha V_{\mathrm{th}} v_{\mathrm{sat}} C_{\mathrm{ox}} W, \qquad (2\text{-}11)$$

Comparing Equation (2-10) with Equation (2-11), it can be deduced that, in contrast to the triode region, the operation of the transistor in velocity saturation is insensitive to mobility (μ), VDS, and length (L) mismatches, mainly when the minimum length is used. The transistor in velocity saturation naturally needs to be a short-channel device, and a small width is preferred to limit the biasing current [32]. The following subsections outline different circuits reported for measuring the outputs of Chem/BioFET.

2.7.1. Non-differential Measurements

Many Chem/BioFET readout circuits involve non-differential measurement topology, which can have various configurations as described in the following subsections.

2.7.1.1. Variable Voltage Reference in Feedback Mode

One technique is controlling the variations of ID in a feedback loop and automatically adjusting the potential of the RE, and thus of the liquid, concerning the source and drain potentials. So, any change in Vt will be compensated by the variation of Vgs via the reference voltage of RE, VRef. For instance, an automatically balanced bridge circuit [161] like Figure 2-23 (a) can compensate for a change in Vt by changing Vgs via the RE (see Table 2-2). However, this technique forces the liquid sample to a particular potential while the liquid may not be grounded. Moreover, the asymmetrical impedance of the source and drain makes the system sensitive to static electricity and electric fields [160].

Table 2-2. Different readout circuits for Chem/BioFET sensors.

CMOS Tech.	Array #	Diff.	Operational region of FET	Configuration	Output signal	Resolution	Sensitivity	IDR	Sensing area (μm²)	Pixel/ active area (μm²)	Total area (mm²)	Power (mW)	Ref.
1.6 μm	1	No	Sat.	Wheatstone-bridge, variable V_{Ref}	V	-	58 mV/pH	-	-	-	4 × 4	-	[161]
-	1	No	Tr.	CVCC	V	-	-	-	-	-	-	-	[160]
0.35 μm	1.5 M 7.2 M 13 M	-	-	CVCC	-	-	-	-	-	-	10.6 × 10.9 17.5 × 17.5 17.5 × 17.5	-	[20] *
1.0 μm	1	No	-	CVCC, Feedback	V	-	47 mV/pH	pH: 2.5 to 9.2	-	-	-	-	[159]
2.5 μm	-	No	Tr.	CVCC	V	-	58 mV/pH	pH: 3 to 11	-	-	< 0.25	10	[162]
0.18 μm	6	No	Tr.	CVCC	V	-	-	-	-	-	1.5 × 0.6	-	[22] *
0.35 μm	64 × 64	No	-	CVCC, SPT	V	-	20 mV/pH	pH: 4 to 10	-	10.2 × 10.2	0.7158 × 0.7158	-	[163]
0.35 μm	64 × 64	No	Tr.	CVCC, APS	D	-	−9.23 mV/pH	-	-	96	0.56	-	[116] *
5 μm	10 × 10	No	-	CVCC, APS	V	-	−229 mV/pH	pH: 4 to 9.1	2000 × 2000 (total)	200 × 200	5.1 × 5.1	-	[164]
2 μm	1024 × 1024	No	-	CVCC, Charge transfer APS	V	-	29.8 mV/pH	pH: 2 to 10	-	23.55 × 23.55	14.8 × 14.8	-	[165]
0.35 μm	3 × 11	No	Sub.	CVCC, integrate-and-fire topology, AER	D	-	−7.73 dB/pH	pH: 1 to 14	57.5 × 57.5	80 × 100	-	(EP: 157 nW)	[166]
0.35 μm	8 × 4	No	-	CVCC, Feedback to the gate	V	60.3 mpH	42.1 mV/pH	pH: 1 to 14	-	60 × 70	2 × 2.5	SFE: 4.841 × 10^{-4}	[167]
0.35 μm	1	No	Sat.	CVCC, Feedback, PG	V	-	200 mV/pH	-	30 × 100	-	0.6 × 0.5	-	[168]
0.18 μm	8 × 8	No	Sub.	CVCC, Current feedback	F	-	37 mV/pH	pH: 4 to 10	-	-	2.6	0.076	[169]
0.35 μm	1	No	-	CVCC, VCO	F	-	78 kHz/pH	pH: 0 to 7	-	-	0.045	0.12	[170]

CMOS Tech.	Array #	Diff.	Operational region of FET	Configuration	Output signal	Resolution	Sensitivity	IDR	Sensing area (μm²)	Pixel/ active area (μm²)	Total area (mm²)	Power (mW)	Ref.
0.35 μm	64 × 128 64 × 200 64 × 200	No	Tr. VS VS	CVCC, APS CM CM, PG	D	-	−9.23 mV/pH −1.033 μA/pH −0.717 μA/pH	-	9.3 × 10.3 6.5 × 7.775 6.5 × 7.775	-	2×4	-	[171]
-	1	No	Sub.	CM, Current feedback	V	-	−49.4 mV/pH	pH: 4 to 9	-	-	-	-	[172]
0.35 μm	3 × 3	No	Sub	CM, PG, RO	F	0.008 pH	6 to 8 kHz/pH	pH: 5 to 7	55 × 65	64 × 54	0.1089	6×10^{-3}	[173]
0.35 μm	128 × 128	No	Tr.	CM, CC, Auto-zeroing, S/H	D	0.24 pH (@1000 fps) 0.45 pH (@3000 fps)	50 LSBs/pH	pH: 4 to 10	-	18 × 12.5	2.6 × 2.2	376	[174]
0.35 μm	8 × 8	No	Sub.	VM , PG, Optic., MM	D		57 mV/pH	pH: 4 to 10	-	-	-	-	[175]
0.18 μm	64 × 64	No	-	pH-TC , Optic.	D	-	−26.2 mV/pH (G = 1) −103.8 mV/pH (G = 4)	pH ~ 1 to 14	Chem.: 22.3 Opt.: 20.1	10 × 10	2.5 × 5	105.6	[176] *
65 nm	512 × 128	No	Sub.	pH-TVC	D	0.01 pH	123.8 mV/pH	pH: 2.5 to 11.5	15	4.4. × 4.4	512 × 128	PA: 80.6, AB: 108.4, DB: 6.5	[23] *
0.18 μm	8 × 8	No	Sub.	pH-TC, APS, PWM	T	33 mpH	6.1 μs/pH	-	-	16.5 × 16.25	6.7	8.3	[177]
0.18 μm	3 × 3	No	-	pH-TC	D	0.028 pH	27 ns/pH	-	10 × 10	-	0.036	0.23	[178]
0.35 μm	1	No	Sub.	ISFET logic	V	0.5 pH	3700 mV/pH	pH: 3.7 to 10.95	95 × 200	-	-	-	[179]
0.35 μm	8 × 8	No	Sat.	ISFET logic	V	0.5 pH	50 mV/pH	pH: 1 to 14	-	-	-	-	[180]
0.35 μm	4 pairs	Yes	Sat.	CVCC, PG, Feedback to the gate	D	-	100 mV/pH	pH: 5 to 9	30 × 100	120 × 120	0.65 × 0.5	-	[181]
0.35 μm	2 × 2	Yes	Tr.	ISFET/REFET diff., CVCC	D	-	40 mV/pH	-	11.6 × 11.6	-	1.4 × 2.6	15	[182]

CMOS Tech.	Array #	Diff.	Operational region of FET	Configuration	Output signal	Resolution	Sensitivity	IDR	Sensing area (μm²)	Pixel/ active area (μm²)	Total area (mm²)	Power (mW)	Ref.
0.35 μm	16 × 16	Yes	Tr.	ISFET/REFET diff., CVCC	D	-	46 mV/pH	pH: 3.28 to 7.22	11.6 × 11.6	12.8 ×12.8	-	60	[63]
0.6 μm	1	Yes	Sat.	ISFET/REFET diff., CVCC	V	-	400 mV/pH	6 pH	-	-	18.225	2.1	[183]
(CMOS)	1	Yes	-	ISFET/REFET diff.	V	0.01 pH	−40 to −43 mV/pH	pH: 4 to 9	-	1650 × 2600	4.9 × 3.9	-	[184]
2.5 μm	1	Yes.	Tr.	ISFET/REFET diff., CVCC	C	0.15 pH	−0.3875 μA/pH	pH: 3 to 11	-	-	-	-	[185]
0.35 μm	1	Yes	Tr.	ISFET/ISFET diff., CM	D	0.1 pH	800 mV/pH	pH: 5 to 9	-	-	-	-	[186]
0.35 μm	1	Yes	Sub.	Diff, Gilbert gain cell, CM, Translinear	C	-	45 mV/pH	pH: 5 to 9	34 × 100	-	2.5 × 2.81	1.65×10^{-4}	[187]
0.35 μm	1	Yes	-	Diff, direct charge accumulation	D	36 μV	-	88.3 dB	71 × 71	1000 × 1640	4 × 5	-	[88] *

* The papers reported for the detection of infectious agents, VM: Voltage-mode, CM: Current-mode, VS: Velocity saturation, PG: Programmable gate, Tr.: Triode, Sat.: Saturation, PA: Pixel array, AB: Analog blocks, DB: Digital blocks, pH-TVC: pH-to-time-to-voltage converter, pH-TC: pH-to-time converter, Sub.: Subthreshold, IDR: Input dynamic range, F: Frequency, SFE: Single front end., CVCC: Constant-voltage constant-current, CC: Current conveyor, SPT: Standard pixel topology, APS: Active pixel sensor, AER: Address event representation, V: Voltage, D: Digital, C: Current, T: Time, EP: Each pixel, Opt.: Optical sensor, Chem.: Chemical, RO: Ring oscillator, S/H: Sample and hold, MM: Magnetic manipulation, G: Gain.

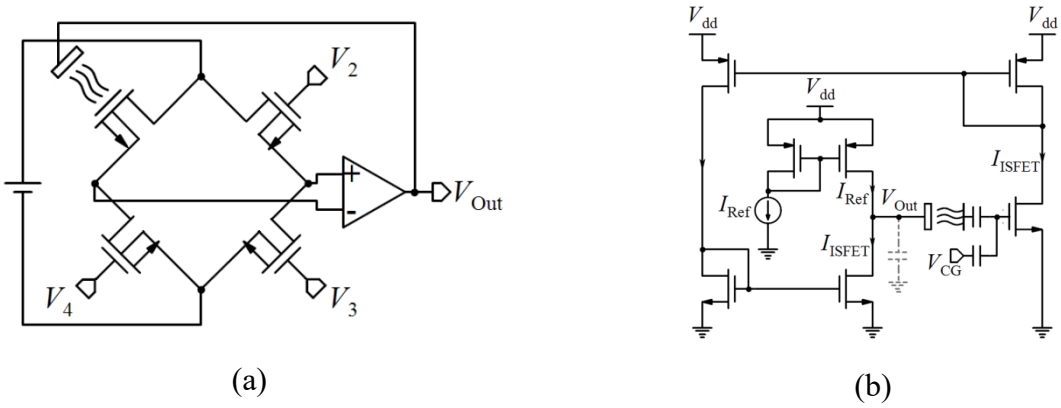


Figure 2-23. (a) Direct Wheatstone bridge; (b) the circuit used to characterize ISFET drift in the feedback mode.

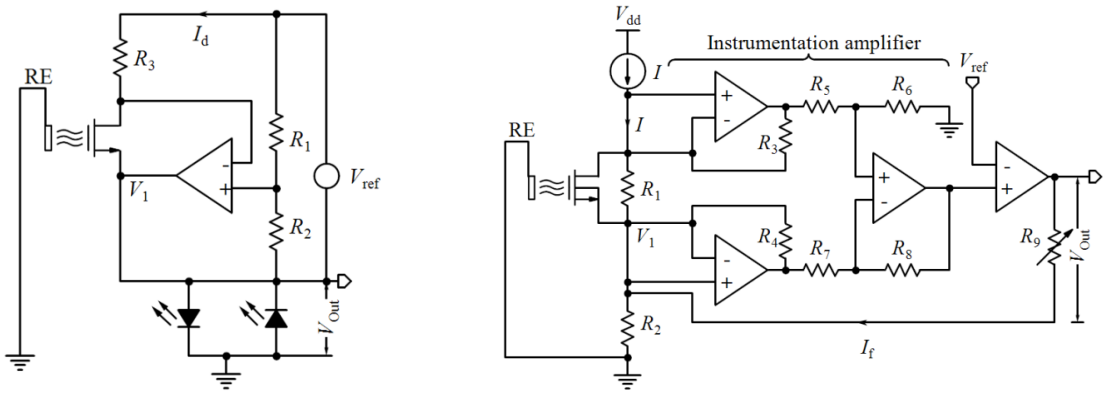
Furthermore, this approach is unsuitable for measuring multiple ISFETs with one RE [188]. Figure 2-23 (b) shows a programmable gate (PG)-ISFET readout circuit proposed by Georgiou et al. [189] in which the current of ISFET is compared and set with a reference current, IRef, in a feedback loop, and VOut is adjusted by the effective gate-source voltage of the ISFET. In another effort, Jamasb et al. [190] reported another circuit in which the voltage reference is set in a feedback loop.

Since this biasing is not constant, an array structure with this configuration will require a distinct RE for each pixel, leading to a complex setup. So, this technique is not a popular configuration [191].

2.7.1.2. Constant-Voltage Constant-Current (CVCC)

The CVCC configuration is the most popular one for the readout circuits of Chem/BioFET sensors. Chem/BioFET, current, and drain voltage is constant, and the source voltage varies according to pH. This technique, proposed by Bergveld [160], is an automatic adjustment of the source and drain potentials concerning a constant liquid potential, which can accidentally be the ground potential in practice. So, the best way is to ground the liquid utilizing a grounded reference. A source/drain follower circuit can provide these conditions and is the most convenient approach to detect the variations of ISFET threshold voltage [160]. CVCC configuration is immune to capacitive scaling of the pH signal at the floating gate of the ISFET. Moreover, the arrays designed based on this technique are compact and only need a switch and an ISFET for each pixel [191]. Figure 2-24 shows a simple source/drain follower version using unsaturated ISFET [188]. The operational amplifier provides equal input voltages, so $V_{R1} = V_{R3}$ and $V_{R2} = V_{ds}$, which are constant (V_{R1} and V_{R2} are parts of continuous V_{ref}). As a result, $I_d = V_{R3}/R_3$ is also steady. Thus, V_{gs}

automatically adapt the source potential concerning the ground to compensate for the variation of ISFET threshold voltage, V_t, and the output voltage accurately reproduces the changes in the oxide surface potential. The diodes at the output, which are practically light-emitting diodes (LEDs), provide a limitation of V_{Out}, and thus, the source voltage concerns ground and lights up when the system is out of range.



(a) (b)

Figure 2-24. (a) A basic diagram of a source/drain follower readout circuit; (b) an ISFET amplifier proposed by Bergveld et al.

Figure 2-24 (b) shows another source/drain follower that uses the instrumentation amplifier concept and unsaturated ISFET [160]. The inputs of the instrumentation amplifier are connected to a fixed voltage, IR1, and its output voltage is inversely proportional to the channel resistance of the ISFET. An operational amplifier amplifies the difference between the output voltage of the instrumentation amplifier and Vref, an adjustable reference voltage. The output of this amplifier injects a feedback current, If, into R2 and provides a constant Id and a constant Vds = IR1 by controlling the source voltage (VR2) and drain voltage (VR1 + R2). It is measured via the adjustable resistor R9. The source and drain potential regarding ground follow a change in the effective input voltage V1, the amplified version of which is available across R9 and is equal to VOut = (R9/R2) V1. The reference voltage, which should be independent of temperature, is adjusted so that If = 0 when the ISFET is placed in a neutral buffer (pH = 7). A circuitry (not shown in Figure 2-24 (b)) was also added for temperature measurement and compensation of temperature drift in Vgs(T) for constant Id.

As reported by Hammond et al. [192], two source measure units (SMU1 and SMU2) on a parameter analyzer along with a feedback loop composed of a fixed resistor and two operational amplifiers can provide the bias condition of saturated ISFET, and the RE can be biased at a suitable voltage by another SMU (SMU3). Nikkoo et al. [22] integrated a similar source/drain follower and potassium-sensitive FET using CMOS technology to detect E. coli bacteria rapidly.

In another effort, Ravezzi et al. [162] used a structure employing cascade current mirrors with output impedance to provide the ISFET drain current with low dependence on its Vds. Three operational amplifiers were adapted to the structure, two of which biased the ISFET at the triode region, and the last one operated in the follower configuration to de-couple the output terminal from the biasing circuit.

The infinite input impedance of a source/drain follower prevents the circuit from loading the system during measurement. However, op-amps increase area occupation and power consumption. To decrease the power consumption and area occupation of array structures with many pixels that employ op-amps, the readout circuit can be shared between pixels in the same row or column [63, 182, 183, 193, 194]. Figure 2-25 (a) illustrates a single column of n half-cells in an n × n array. Mulgrew et al. [63] used this architecture and reported a CMOS sensor chip including a 16 × 16-pixel array of ISFETs for direct extracellular imaging.

Rothberg et al. [194] improved FET pixel and array designs to achieve high accuracy and measurement sensitivity, small pixel sizes, and dense arrays. This group proposes different pixel designs based on both p-channel and n-channel ISFETs. The same group [20] fabricated a chip with 1.5 M, 7.2M, and 13M ISFETs (see Table 2-2). It was used to simultaneously detect independent DNA sequencing of three bacterial genomes (V. fischeri, E. coli, and R. palustris).

Some other techniques are also based on the CVCC method, but the circuit's output node is connected to the ISFET floating gate through a capacitor or switch. For instance, Hu et al. [167] designed a circuit using feedback and a low leakage switching scheme. They overcame the problems of transconductance reduction due to capacitive division and DC offset due to trapped charge. Chan et al. [169] also used an averaging array based on a global negative current feedback technique to regulate the undefined threshold voltages of ISFETs.

Some array structures [163, 195] are designed based on a standard pixel readout like Figure 2-25 (b), which is like CVCC and consists of an ISFET and two switches. In another effort, as Table 2-2 mentioned, Malpartida-Cardenas et al. [116] used a 64 × 64 array whose pixels were implemented as a source follower configuration and converted pH to voltage. They employed this sensor for plasmodium falciparum malaria diagnosis and artemisinin-resistance detection.

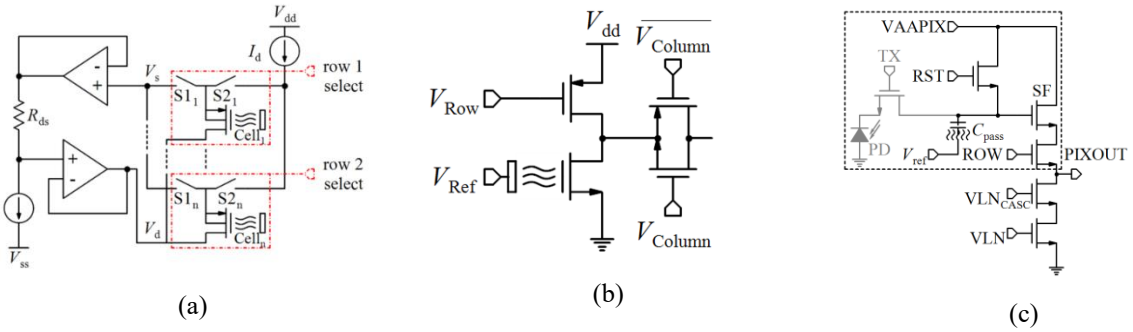


Figure 2-25. (a) Schematic of a column of 16 pixels in the n × n-array sensor chip; (b) a standard ISFET pixel readout; (c) a dual-pixel schematic including a CMOS image sensor and a source follower.

Several papers integrated active pixel sensors (APS) using ISFETs by employing the ISFETs as the standard buffer [175, 176] or the replacement of the photodiode by the ISFET [164, 165] (by using a charge transfer technique). Huang et al. [176] proposed a dual-mode sensor by integrating a CMOS image sensor with the ISFET as the standard buffer to achieve accurate pH detection towards DNA sequencing. The dual-mode pixel is depicted in Figure 2-25 (c). The circuit shown in gray is added to an ISFET pixel to provide optical sensing and pH measurement. The poly-gate of ISFET (SF) is connected to the top metal and Si_3N_4 passivation layer (as the ion-sensitive membrane of ISFET). They also employed correlated double sampling to mitigate pixel-to-pixel non-uniformity like threshold voltage mismatch.

2.7.1.3. Current-mode Readout Circuits

Researchers have also noticed current-mode readout techniques [31, 32, 172, 196, 197]. In this approach, the output current of an ISFET is measured, which can take advantage of current-mode techniques and is compatible with weak inversion operation, as well as linear and velocity saturation regions [191].

The weak inversion region provides drain currents in the order of nano-ampers and below that are suitable for designing low-power circuits. In addition, the area has the highest transconductance to current ratio and the maximum intrinsic voltage gain [31]. Low V_{ds} required for saturation,

minimum gate capacitance, and low gate voltage in this region are the other advantages of weak inversion [65]. Moreover, the exponential relationship of V_{gs}-I_d allows for using bipolar circuit techniques like log-domain filters and translinear circuits for ISFET applications, leading to novel biochemical systems. For example, Figure 2-26 (a) illustrates a hydrogen cell (Hcell) based on a translinear operation reported by Shepherd et al. [31, 198] whose output current is directly proportional to hydrogen ion [H^+] concentration. By setting I_{b1}=I_{b2} and considering K_{chem} = $exp(-\gamma/nV_{th})$ and Equation (2-7), it can be proved that [31]:

$$I_{Out} = I_{b1} exp\left(\frac{-2V_{ref}}{nV_{th}}\right) K_{chem}^2 [H^+], \qquad (2\text{-}12)$$

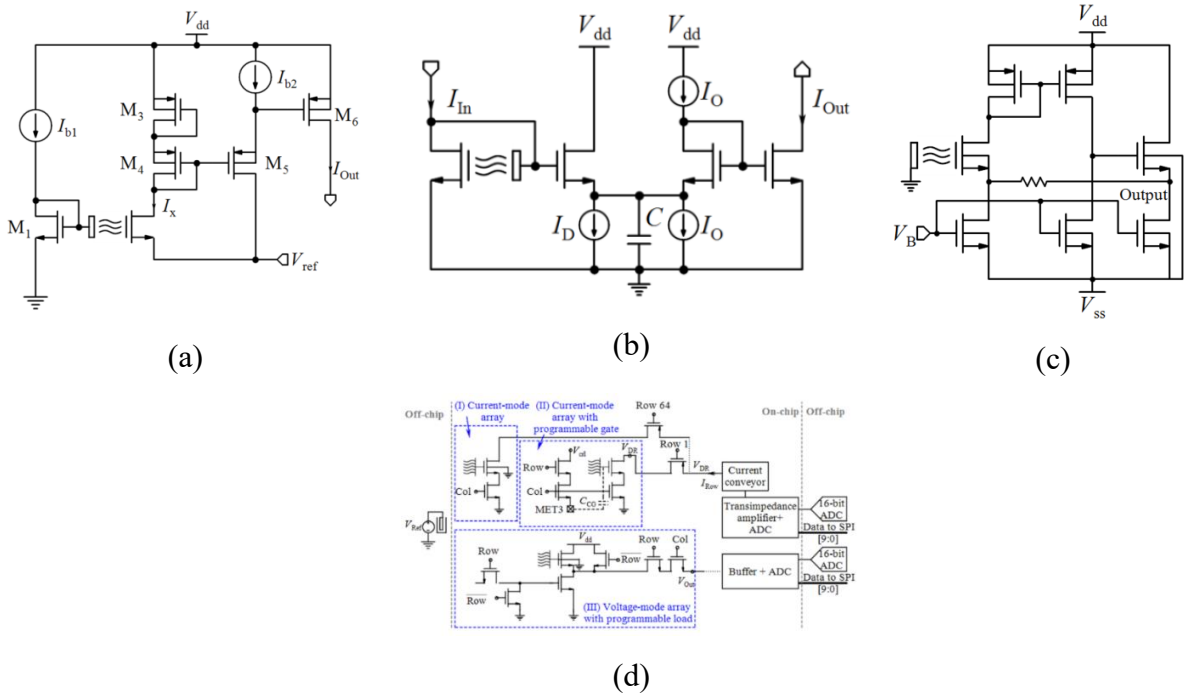


Figure 2-26. (a) HCell with the translinear operation; (b) a log-domain filter with an ISFET used at its input; (c) a current-mode readout with current feedback; (d) schematic of a system including three configurations: (I) Current-mode configuration in a 64 × 200 array, (II) current-mode PG pixel architecture in a 64 × 200 array, (III) voltage-mode pixel structure in a 64 × 128 array.

Georgiou et al. [197] presented a log domain chemical filter utilizing an ISFET biased in weak inversion as another technique. Figure 2-26 (b) shows a log-domain filter with an ISFET used at its input. The filter parameters like gain and cut-off frequency can depend on the analyte's ion concentration.

An array configuration was used by Miscourides et al. [32] in which direct controlling of the Vds of each device gets access to an individual pixel. Each drain row is connected to a generic current conveyor (CC), which leads the voltage of that row to be constant at VDR and guarantees the generation of an output current depending only on Vgs during the readout of each pixel. A 128 × 128 current-mode ISFET array with in-pixel calibration is proposed by Zeng et al. [174], which takes advantage of a CC, auto zeroing technique, and sample and hold (see Table 2-2). In another effort, Pookaiyaudom et al. [199] embedded a CC type 2 (CCII+) with two ISFETs as its input transistors.

A configuration was used by Miscourides et al. [32] in which the ISFETs were biased in the velocity saturation region and included a pixel switch to turn on only one pixel at any time. The higher drain current in the velocity saturation region in comparison to the triode region would make it unsustainable to simultaneously output the currents of all column pixels (see Equations (10) and (11)). To compensate for the offset, the same group [200] extended their current-mode array to include a PG inside each pixel. As a continuation of these works, this group compares these two configurations with a voltage-mode source-follower configuration. Figure 2-26 (d) shows the schematic of a system including a current-mode configuration in a 64 × 200 array, current-mode PG pixel architecture in a 64 × 200 array, voltage-mode pixel structure in a 64 × 128 array, current conveyor, trans-impedance amplifier, buffer, two on-chip and two off-chip ADC. The two current-mode configurations showed better linearity and smaller size than the voltage-mode circuit, and they concluded that the current-mode approach provides the best overall performance [171].

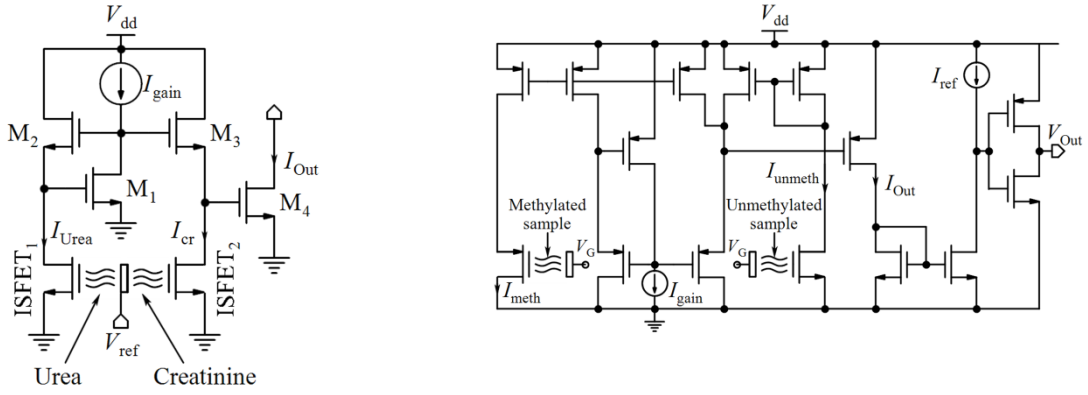


Figure 2-27. Ratiometric measurement: (a) ISFET-based translinear divider; (b) a translinear circuit proposed by Kalofonou et al.

Georgiou et al. [166] used an integrate-and-fire topology with address event representation (AER) to encode the pH-sensitive current in frequency. Despite its low power consumption (157 nW at pH=7), the signal processing using specific ADCs in the spike domain makes this technique complex. The same group [173] used a similar current-mode pixel architecture, an averaging mirror for robust measurement, and a ring oscillator for converting the current to frequency.

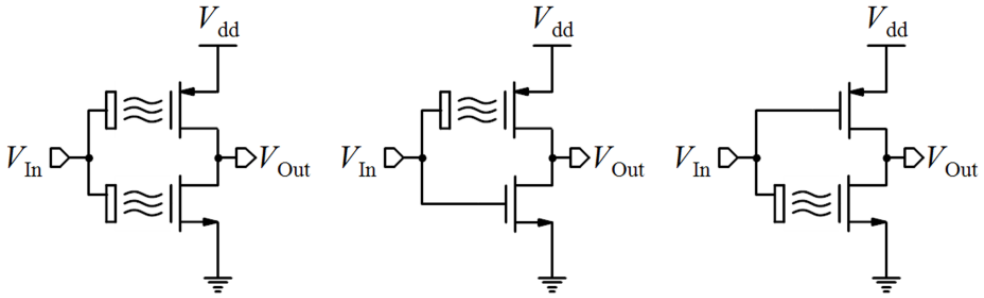
In some current-mode circuits, current feedback is used for stable DC operation [172, 201, 202]. For example, Figure 2-26 (c) shows a current-mode readout with global feedback proposed by Premanode et al. [172].

Juffali et al. [203] proposed another circuit based on translinear operation employing a division circuit and two ISFETs that can directly measure the ratio of urea to creatinine (an essential marker for detecting pre-renal failure). Figure 2-27 (a) illustrates the ISFET-based translinear divider. In another effort, Kalofonou et al. [204] proposed a ratiometric approach to DNA methylation using ISFET in a translinear circuit (as depicted in Figure 2-27 (b)). This sensor can determine the level of aberrancy of methylation between unmethylated and highly methylated genes and identify early signs of human neoplasias through blood circulation.

2.7.1.4. ISFET logic

In 2009, Wong et al. [205] proposed discrete ISFET logic for detecting chemical reaction thresholds. This logic is helpful for applications like detecting a specific gene in a DNA sequence where there is no need to measure the exact pH value. For example, the switching threshold of an inverter can give a yes/no answer based on the pH variations. Other components like a switch [179,206], Schmitt trigger [207], or a NAND gate [40] can also be used as comparators.

Figure 2-28 (a-c) illustrates three configurations of an ISFET inverter with only one n-type, p-type ISFET, or pair of both. For example, Al-Ahdal et al. [179, 206] used a complimentary pair of p-type and n-type ISFETs sharing the same ion-sensitive membrane, as shown in Figure 2-28 (a), and formed an ISFET-based chemical switch. Nabovati et al. [180] placed these switches in each pixel of an 8 × 8 array, achieving a wide pH range from 1 to 14 and a sensitivity of 50 mV/pH (see Table 2-2).



(a) (b) (c)

Figure 2-28. Three configurations of ISFET inverters: (a) p-type and n-type ISFET sharing the same membrane; (b) p-type ISFET with membrane and n-type MOSFET; (c) n-type ISFET with membrane and p-type MOSFET.

2.7.1.5. pH-to-Time Conversion

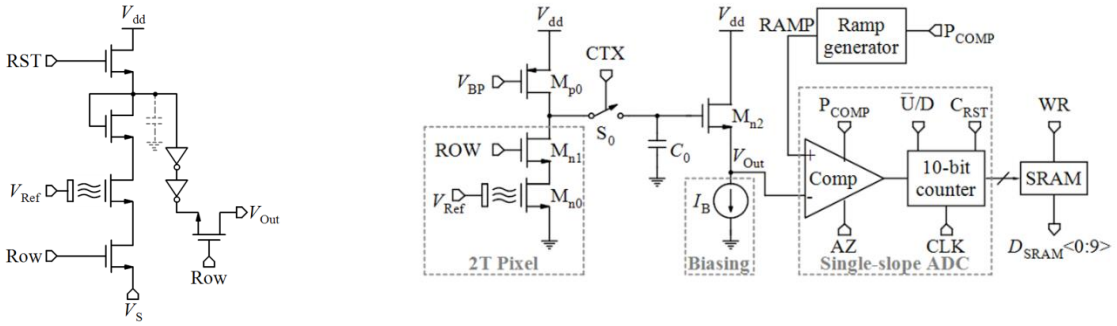
As mentioned above, the inverter with complementary ISFETs [208,209] can be the core of a compact pH-to-time converter capacitively coupled to a triangular wave whose switching point and, consequently, its output pulse width is modulated with pH. Pulse-width modulation (PWM)--based topologies are suitable structures that allow in-pixel quantization and thus improve the SNR [191]. Wang et al. [178] proposed an ISFET pH-to-time sensor integrated with an exemplary on-chip time-to-digital converter (TDC) as the ADC with a thermometer-to-binary coder and a delay line. In another effort, Moser et al. [177,210] reported a pH-to-time converter based on APS, as depicted in Figure 2-29 (a). This circuit modulates pH to pulse width using a periodic reset scheme and discharging a capacitor through the ISFET.

Jiang et al. [23, 211] proposed a subthreshold pH-to-time-to-voltage conversion (pH-TVC) readout structure using pixel-level calibration and digital double sampling. As a result, the sensor can mitigate non-ideal effects, like passivation attenuation, parasitic capacitance, and trapped charge. As demonstrated in Figure 2-29 (b), Mn_0 and Mn_1 are an ISFET and a row-selected transistor, and the other parts are shared by pixels in each column. Mp0 and S0 (including complementary NMOS and PMOS transistor pair) are pre-charge and transfer switches, respectively. C_0, the source follower Mn_2, and current source I0 are, in turn, used as an integrator, buffers, and biasing circuits. A ramp generator, a single-slope ADC, and an SRAM group are also utilized along with the pH-TVC readout circuit—any change in pH results in a shift in the V_{Out}.

It can be proved that ΔVOut is obtained by:

$$\Delta V_{\mathrm{Out}} = \left(\frac{\Delta t}{C_0}\right).G_{\mathrm{m}}.A.\Delta V_{\mathrm{chem}}, \qquad (2\text{-}13)$$

Gm, Δt, ΔVchem, and A stand for the ISFET transistor transconductance, the charge integration time, pH-related potential change, and the attenuation factor, respectively. The amplification factor, (Δt/C0) Gm, compensates for the passivation sensitivity attenuation effect. This group [23] used this sensor for E. coli detection and achieved the sensitivity and resolution of 118.7 mV/pH and 0.01 pH, respectively (see Table 2-2).



(a) (b)

Figure 2-29. (a) An active pixel sensor (APS) based pH-to-time converter; (b) a readout circuit comprising a pH-to-time-to-voltage conversion (pH-TVC) amplification circuit and 10-bit voltage digital converter.

2.8. Differential Measurements

Several differential architectures have been developed that measure the difference of the output signals of two ISFETs with the same REs. Differential techniques offer the advantages of temperature and long-term drift compensation and eliminating common-mode noise. Moreover, these techniques can solve the problems of the unstable electrolyte-RE potential and the instability caused by the membrane layers of the ISFETs.

The lack of a solid-state RE is one of the issues in solid-state chemical potentiometric sensors because they must be combined with a liquid filled RE with a limited stable lifetime. Thus, in practice, a small sensor probe and a rather large RE are used together, restricting the possibility of measuring small sample volumes. For this reason, many research efforts have been dedicated to a

differential measurement between an ISFET and an identical reference FET (REFET), which has a very low (ideally zero) sensitivity to the ion concentration under measurement. In this case, a metal wire can ground the sample solution [188]. So, a wholly integrated ISFET-based sensor can be implemented by a differential structure composed of an ISFET and a REFET biased by a common counter-electrode as a pseudo-reference electrode (PRE) (Figure 2-30 (a)) [188]. In this arrangement, the conventional RE is replaced by a PRE made of a noble metal, such as gold and platinum, to define the potential of the electrolyte without the need for any external RE. Covering the gate oxide of an ISFET within an additional ion-insensitive membrane like a polymer [212, 213] or chemical modification of the original gate oxide surface sites [214] are the most popular techniques to create a low-sensitive REFET. For practical reasons, bulk and source connections are usually short-circuited [213]. However, in their seminal works, Bergveld et al. [46] used bulk feedback to control the depletion charge in the bulk. Moreover, drift and different electrical properties of REFET and ISFET are some of the issues of this technique [193, 215, 216]. The DC bias of REFET and ISFET should be the same so that they behave electrically and identically. Chudy et al. [217] proposed using a modified ISFET with additional membranes (CHEMFET), of which the outer membrane comprises a buffer component for the ion measurement. In a differential CHEMFET/REFET system, the electrically identical REFET with the same membrane does not contain such a buffer.

In 1989, Wong and White [184] proposed a CMOS-integrated op-amp for pH measurement with an ISFET input and a feedback loop to a MOSFET. Then, they differentially amplified the outputs of two ISFET operational amplifiers with a PRE. In this primary implementation, a special coating on the gate of ISFETs was used to achieve different sensitivities. An ISFET submerged in a buffer solution of known pH was a reference device. One of these ISFET-op-amps was composed of an ISFET with a Ta_2O_5/SiO_2 gate, and the other one included a $SiOxNy/Si_3N_4/SiO_2$-gate ISFET with a sensitivity of 58–59 mV/pH and 18–20 mV/pH, respectively. The device could provide 40–43 mV/pH sensitivity and cancel common temperature effects and drift in both ISFETs (see Table 2-2).

Chodavarapu et al. [218] proposed another differential architecture for pH measurement, including a gold PRE and a pair of ISFET operational transconductance amplifiers (IOTAs), each composed of an ISFET as its input. The ISFETs used in both IOTAs are identical, but different sizes of the p-

MOSFET loads used in IOTAs cause variations in the sensitivity of these two IOTAs (50 mV/pH and 30 mV/pH). They could achieve a sensitivity of 40–45 mV/pH.

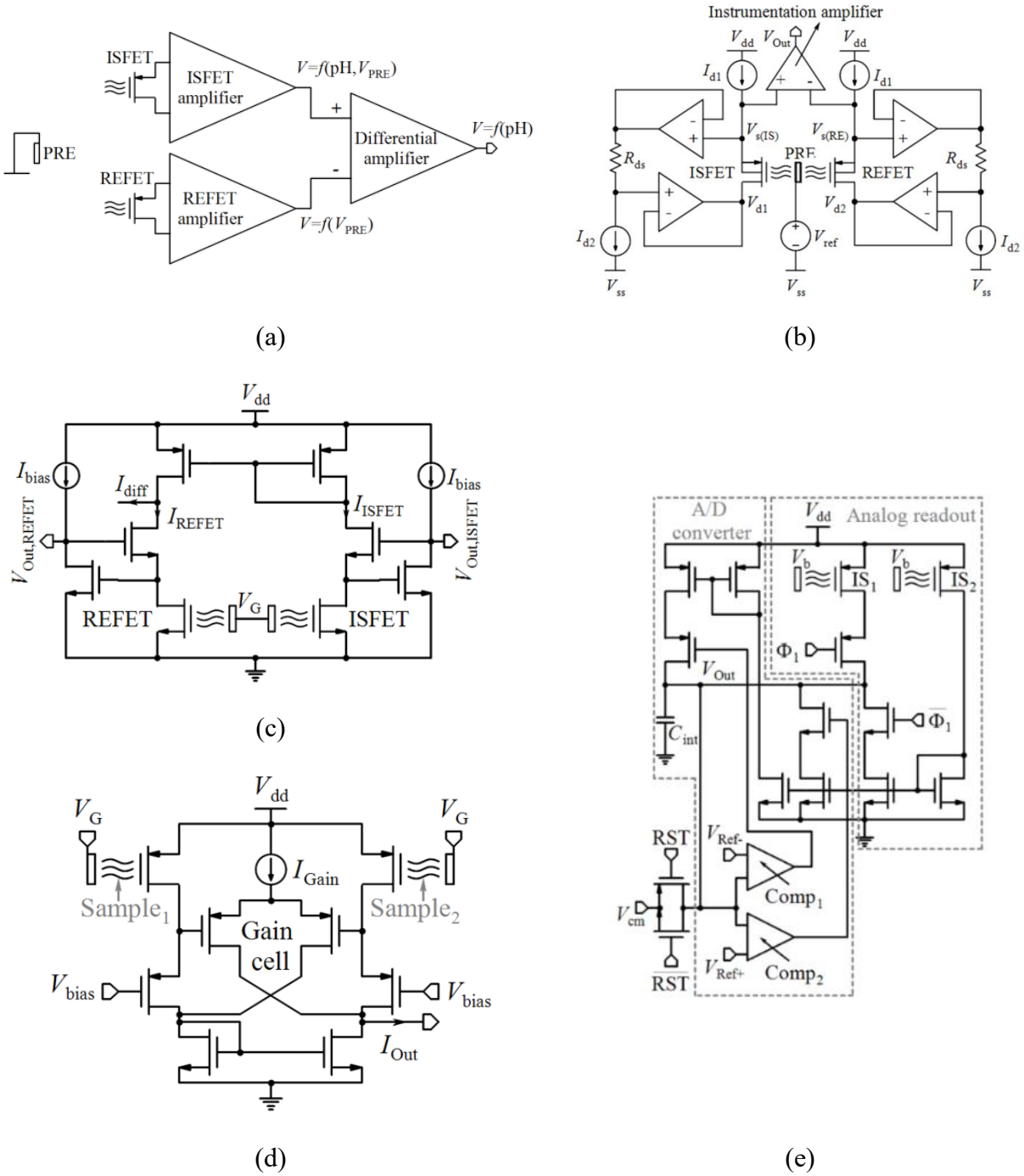


Figure 2-30. ISFET and REFET for array structure; (c) ISFET/REFET voltage-clamped configuration; (d) a chemical Gilbert cell; (e) a ΣΔ ISFET readout circuit using differential measurement.

Hammond et al. [193] reported a system-on-chip (SOC) digital pH meter containing on-chip programmable voltage references and multiplexers controlled by a specially designed 8-bit microcontroller for use in a wireless diagnostic capsule. They achieved a sensitivity of 37 bits/pH within an operating range of 7 pH units. Figure 2-30 (b) shows the analog part of this differential ISFET/REFET pH-measurement circuit with a standard PRE that includes two source-drain-follower configurations for the ISFET and REFET whose outputs are given to an instrumentation amplifier. In another effort, Palan et al. [185] presented a similar differential structure comprising two sources/drain follower circuits and a voltage-to-current converter (V/I). ISFET1 and ISFET2 were composed of Si_3N_4 and SiO_2 ion-sensitive layers with 52–58 mV/pH sensitivity and 24–36 mV/pH, respectively, and implemented in a 2.5 μm CMOS technology. The simulation showed that this interface circuit could provide a precision of ±0.15 pH (see Table 2-2).

An example of a pseudo-differential ISFET-REFET topology is the voltage-clamped circuit shown in Figure 2-30 (c) [219], which can provide a fixed electrical bias and operate in either weak or strong inversion. In another effort, Sohbati et al. [220] implemented an ISFET/REFET sensing front-end as part of an input differential pair. The same group [221] also proposed a pH-to-digital converter using two current comparator-based circuits, including ISFET and REFET, in each of which the output node is connected to the floating gate of FET. In another work, Liu et al. [181] proposed a differential topology based on the CVCC principle controlled with feedback to the floating gate of ISFET.

A ΣΔ ISFET readout circuit using differential current-mode measurement is also reported by Nabovati et al. [186], depicted in Figure 2-30 (e). The ISFETs depicted in Figure 2-30 (e) operate in the linear region, and the circuit works in three phases: (1) Reset, (2) evaluation, and (3) sampling. During the reset phase, activated by RST and $(RST)^{-}$, the value of C_{int} capacitor is set to the common-mode voltage, Vcm. During the evaluation phase, the clock Φ_1 is activated, and the ISFET current charges the Cint. Combining Equations (1) and (5), we can deduce that the ISFET current in this region is proportional to the pH value. The current differential scheme increases sensitivity. The second ISFET (IS2) is a reference with a pH value of 7. In the sampling phase, the circuit is connected to the output for sampling. A charge-to-digital converter converts the output voltage to digital.

Figure 2-30 (d) demonstrates a chemical Gilbert cell as another technique. The differential pair includes two ISFETs considered a chemical translinear circuit [187]. This circuit is appropriate for applications that require differential monitoring in small volumes and several chambers, like studying more than one gene in DNA detection.

Lee et al. [88] proposed a CMOS device that directly measures the electrostatic induction of molecular charges in the working electrode with improved SNR and without any conversion loss. As seen in Figure 2-14, both working electrodes are connected to a voltage buffer circuit with high input impedance (due to employing a transistor with an isolated gate), and their voltages are within the operating range of the buffer circuit. The buffer transfers the induced charges in working electrodes to a fully differential switched-capacitor integrator, followed by an ADC to accumulate and digitize the signal.

2.9. Amelioration of Some Non-idealities

Trapped charges, noise, and temperature sensitivity are non-idealities in ISFET measurements. This sub-section reviews some solutions to these problems.

2.9.1. Trapped Charges

The accumulation of trapped charge on the gate and passivation layer is a non-ideality that occurs during the fabrication of floating gate ISFETs in the standard CMOS process and causes a significant, unpredictable change in the threshold voltage of ISFET. UV radiation and bulk substrate biasing are the most convenient methods for removing excess charge. The UV radiation can reach the inner polysilicon through a small aperture formed on top of the ISFET and excites the trapped charge that charges into the bulk region. This technique does not need additional circuitry and can be employed to match the electrical characteristics of ISFET pixels in an array structure. A single RE can bias the entire array by eliminating the mismatch between pixels threshold voltage [222].

Another technique is hot-electron injection, which can be adapted for threshold voltage programming. The operating point of an ISFET can be calibrated by adding an electron to the floating gate and raising the threshold voltage [223]. However, this technique cannot decline the threshold voltage. Thus, Al-Ahdal et al. [224] propose electron tunneling to eliminate electrons from the floating gate of the ISFET.

Georgiou et al. [225] reported another approach to programming the floating gate of the ISFET: using a capacitively coupled floating gate. This allows tuning the operating point to maintain its tenability and keep the device operating within a tolerable gate voltage range. Yan et al. [168] also used two extra programmable nodes driven by a feedback configuration. Another technique is using a switch for additional connections to the floating gate of the ISFET in a feedback loop [167].

2.9.2. Noise

The noise performance of the ISFETs is another non-ideality that can directly affect the sensor accuracy and resolution. The dominant low-frequency noise is 1/f noise. The measured noise characteristics in [226] showed that the Si/SiO_2 interface dominates the noise behavior, and the interface between the gate insulator and the solution does not contribute to measurable noise. To reduce the noise, the ISFETs based on p-MOSFET can be used rather than n-MOSFET because it is well established that the noise of p-MOSFET is lower by nearly two orders of magnitude [227]. However, n-type ISFETs have higher mobility and better drift performance.

2.9.3. Temperature Sensitivity

Another factor affecting the performance of the ISFET is temperature sensitivity. Circuit compensation techniques can alleviate temperature variations.

Wong et al. [184] proposed using an operational amplifier's differential configuration to match the ISFET sensor with a MOSFET and eliminate the temperature sensitivity. The two devices' Equal electrical biases are required to have similar temperature characteristics, which might be difficult to acquire by a differential pair comprising an ISFET and a MOSFET on the same chip [160] because of the differences in Vt, leading to different bias conditions.

In another technique [228], the ISFET temperature coefficient, which depends on the operating point, is canceled out by choosing a proper bias condition and empirical determination of a thermal operating point. Simultaneous detection and use of the parameters of the measuring device that cause the temperature drift is an unusual approach in conventional electronics. Bergveld et al. [160] used the feedback system of Figure 2-24 (b). They injected a sinusoidal signal by employing a transformer connected between the bulk and the source of the ISFET to adjust a certain bias condition and produce sensitivity independent of $\beta = \mu Cox\ (W/L)$ and internal source and drain

resistances. Sohbati et al. [221] used a periodic gate reset to set the DC operating point of the ISFET accurately.

Chin et al. [229] utilized a p-n diode as a temperature sensor whose negative temperature coefficient can cancel out the positive temperature coefficient of the ISFET by employing a summing circuit. Chung et al. [230] proposed another technique using a threshold voltage extractor circuit to compensate for the ISFET thermal characteristic.

2.10. References

[1] Mahase, E. Covid-19: *What Have We Learnt about the New Variant in the UK?* British Medical Journal Publishing Group: London, UK, 2020.

[2] Al-Jighefee, H.T.; Yassine, H.M.; Nasrallah, G.K. Evaluation of Antibody Response in Symptomatic and Asymptomatic COVID-19 Patients and Diagnostic Assessment of New IgM/IgG ELISA Kits. *Pathogens* 2021, *10*, 161.

[3] Haliga, R.E.; Sorodoc, V.; Lionte, C.; Petris, O.R.; Bologa, C.; Coman, A.E.; Vata, L.G.; Puha, G.; Dumitrescu, G.; Sirbu, O. Acute Clinical Syndromes and Suspicion of SARS-CoV-2 Infection: The Experience of a Single Romanian Center in the Early Pandemic Period. *Medicina* 2021, *57*, 121.

[4] Oyewole, A.O.; Barrass, L.; Robertson, E.G.; Woltmann, J.; O'Keefe, H.; Sarpal, H.; Dangova, K.; Richmond, C.; Craig, D. COVID-19 Impact on Diagnostic Innovations: Emerging Trends and Implications. *Diagnostics* 2021, *11*, 182.

[5] Salas Rojas, M.; Silva Garcia, R.; Bini, E.; Pérez de la Cruz, V.; León Contreras, J.C.; Hernández Pando, R.; Bastida Gonzalez, F.; Davila-Gonzalez, E.; Orozco Morales, M.; Gamboa Domínguez, A. Quinacrine, an Antimalarial Drug with Strong Activity Inhibiting SARS-CoV-2 Viral Replication In Vitro. *Viruses* 2021, *13*, 121.

[6] Eftekhari, A.; Alipour, M.; Chodari, L.; Maleki Dizaj, S.; Ardalan, M.; Samiei, M.; Sharifi, S.; Zununi Vahed, S.; Huseynova, I.; Khalilov, R.; et al. A Comprehensive Review of Detection Methods for SARS-CoV-2. *Microorganisms* 2021, *9*, 232.

[7] Adeel, M.; Rahman, M.M.; Caligiuri, I.; Canzonieri, V.; Rizzolio, F.; Daniele, S. Recent advances of electrochemical and optical enzyme-free glucose sensors operating at physiological conditions. *Biosens. Bioelectron.* 2020*, 165,* 112331.

[8] Liu, J.; Geng, Z.; Fan, Z.; Liu, J.; Chen, H. Point-of-care testing based on smartphone: The current state-of-the-art (2017–2018). *Biosens. Bioelectron.* 2019, *132*, 17–37.

[9] Naresh, V.; Lee, N. A Review on Biosensors and Recent Development of Nanostructured Materials-Enabled Biosensors. *Sensors* 2021, *21*, 1109.

[10] Dzik, S. COVID-19 convalescent plasma: Now is the time for better science. *Transfus. Med. Rev.* 2020, *34*, 141–144.

[11] Ho, W.-J.; Chen, J.-S.; Ker, M.-D.; Wu, T.-K.; Wu, C.-Y.; Yang, Y.-S.; Li, Y.-K.; Yuan, C.-J. Fabrication of a miniature CMOS-based optical biosensor. *Biosens. Bioelectron.* 2007, *22*, 3008–3013.

[12] Forouhi, S.; Dehghani, R.; Ghafar-Zadeh, E. CMOS Based Capacitive Sensors for Life Science Applications: A Review. *Sens. Actuators A Phys.* 2019, *297*, 111531–111526.

[13] Mehrotra, P. Biosensors and their applications–A review. *J. Oral Biol. Craniofacial Res.* 2016, *6*, 153–159.

[14] Bergveld, P. Development of an ion-sensitive solid-state device for neurophysiological measurements. *IEEE Trans. Biomed. Eng.* 1970, 70-71.

[15] Kaisti, M. Detection principles of biological and chemical FET sensors. *Biosens. Bioelectron.* 2017, *98*, 437–448.

[16] Xu, D.; Huang, X.; Guo, J.; Ma, X. Automatic smartphone-based microfluidic biosensor system at the point of care. *Biosens. Bioelectron.* 2018, *110*, 78–88.

[17] Seo, G.; Lee, G.; Kim, M.J.; Baek, S.-H.; Choi, M.; Ku, K.B.; Lee, C.-S.; Jun, S.; Park, D.; Kim, H.G. Rapid detection of COVID-19 causative virus (SARS-CoV-2) in human nasopharyngeal swab specimens using field-effect transistor-based biosensor. *Acs Nano* 2020, *14*, 5135–5142.

[18] Chen, Y.; Qian, C.; Liu, C.; Shen, H.; Wang, Z.; Ping, J.; Wu, J.; Chen, H. Nucleic acid amplification free biosensors for pathogen detection. *Biosens. Bioelectron.* 2020, *153*, 112049.

[19] Rothberg, J.M.; Hinz, W.; Rearick, T.M.; Schultz, J.; Mileski, W.; Davey, M.; Leamon, J.H.; Johnson, K.; Milgrew, M.J.; Edwards, M. An integrated semiconductor device enabling non-optical genome sequencing. *Nature* 2011, *475*, 348–352.

[20] Gurrala, R.; Lang, Z.; Shepherd, L.; Davidson, D.; Harrison, E.; McClure, M.; Kaye, S.; Toumazou, C.; Cooke, G. Novel pH sensing semiconductor for point-of-care detection of HIV-1 viremia. *Sci. Rep.* 2016, *6*, 1–6.

[21] Nikkhoo, N.; Gulak, P.G.; Maxwell, K. Rapid detection of E. coli bacteria using potassium-sensitive FETs in CMOS. *Ieee Trans. Biomed. Circuits Syst.* 2013, *7*, 621–630.

[22] Jiang, Y.; Liu, X.; Dang, T.C.; Huang, X.; Feng, H.; Zhang, Q.; Yu, H. A High-Sensitivity Potentiometric 65-nm CMOS ISFET Sensor for Rapid E. coli Screening. *Ieee Trans. Biomed. Circuits Syst.* 2018, *12*, 402–415.

[23] Lim, J.; Whitcomb, J.; Boyd, J.; Varghese, J. Transient finite element analysis of electric double layer using Nernst–Planck–Poisson equations with a modified Stern layer. *J. Colloid Interface Sci.* 2007, *305*, 159–174.

[24] Nagy, T.; Henderson, D.; Boda, D. Simulation of an electrical double layer model with a low dielectric layer between the electrode and the electrolyte. *J. Phys. Chem. B* 2011, *115*, 11409–11419.

[25] Meixner, L.; Koch, S. Simulation of ISFET operation based on the site-binding model. *Sens. Actuators B Chem.* 1992, *6*, 315–318.

[26] Fernandes, P.G.; Stiegler, H.J.; Zhao, M.; Cantley, K.D.; Obradovic, B.; Chapman, R.A.; Wen, H.-C.; Mahmud, G.; Vogel, E.M. SPICE macromodel of silicon-on-insulator-field-effect-transistor-based biological sensors. *Sens. Actuators B Chem.* 2012, *161*, 163–170.

[27] Van Hal, R.; Eijkel, J.; Bergveld, P. A novel description of ISFET sensitivity with the buffer capacity and double-layer capacitance as key parameters. *Sens. Actuators B Chem.* 1995, *24*, 201–205.

[28] Yates, D.E.; Levine, S.; Healy, T.W. Site-binding model of the electrical double layer at the oxide/water interface. *J. Chem. Soc. Faraday Trans. 1: Phys. Chem. Condens. Phases* 1974, *70*, 1807–1818.

[29] Bourg, I.C.; Sposito, G. Molecular dynamics simulations of the electrical double layer on smectite surfaces contacting concentrated mixed electrolyte (NaCl–CaCl2) solutions. *J. Colloid Interface Sci.* 2011, *360*, 701–715.

[30] Shepherd, L.; Toumazou, C. Weak inversion ISFETs for ultra-low power biochemical sensing and real-time analysis. *Sens. Actuators B Chem.* 2005, *107*, 468–473.

[31] Miscourides, N.; Georgiou, P. Linear current-mode ISFET arrays. In Proceedings of the 2016 IEEE International Symposium on Circuits and Systems (ISCAS), Montreal, QC, Canada, 22–25 May 2016; pp. 2827-2830.

[32] Ben-Yaakov, D.; Andelman, D.; Podgornik, R.; Harries, D. Ion-specific hydration effects: Extending the Poisson-Boltzmann theory. *Curr. Opin. Colloid Interface Sci.* 2011, *16*, 542–550.

[33] Ozcelik, H.G.; Sozen, Y.; Sahin, H.; Barisik, M. Parametrizing nonbonded interactions between silica and water from first principles. *Appl. Surf. Sci.* 2020, *504*, 144359.

[34] Jiang, G.; Cheng, C.; Li, D.; Liu, J.Z. Molecular dynamics simulations of the electric double layer capacitance of graphene electrodes in mono-valent aqueous electrolytes. *Nano Res.* 2016, *9*, 174–186.

[35] Fakih, I.; Durnan, O.; Mahvash, F.; Napal, I.; Centeno, A.; Zurutuza, A.; Yargeau, V.; Szkopek, T. Selective ion sensing with high resolution large area graphene field effect transistor arrays. *Nat. Commun.* 2020, *11*, 1–12.

[36] Molinnus, D.; Beging, S.; Lowis, C.; Schöning, M.J. Towards a multi-enzyme capacitive field-effect biosensor by comparative study of drop-coating and nano-spotting technique. *Sensors* 2020, *20*, 4924.

[37] Poghossian, A.; Schöning, M.J. Label-Free Sensing of Biomolecules with Field-Effect Devices for Clinical Applications. *Electroanalysis* 2014, *26*, 1197–1213.

[38] Su, S.; Sun, Q.; Gu, X.; Xu, Y.; Shen, J.; Zhu, D.; Chao, J.; Fan, C.; Wang, L. Two-dimensional nanomaterials for biosensing applications. *TrAC Trends Anal. Chem.* 2019, *119*, 115610.

[39] Sengupta, J.; Hussain, C.M. Graphene-based field-effect transistor biosensors for the rapid detection and analysis of viruses: A perspective in view of COVID-19. *Carbon Trends* 2020, *2*, 100011.

[40] Pilehvar, S.; De Wael, K. Recent advances in electrochemical biosensors based on fullerene-C60 nano-structured platforms. *Biosensors* 2015, *5*, 712–735.

[41] Wang, B.; Luo, Y.; Gao, L.; Liu, B.; Duan, G. High-performance field-effect transistor glucose biosensors based on bimetallic Ni/Cu metal-organic frameworks. *Biosens. Bioelectron.* 2021, *171*, 112736.

[42] Campbell, M.G.; Dincă, M. Metal–organic frameworks as active materials in electronic sensor devices. *Sensors* 2017, *17*, 1108.

[43] Syu, Y.-C.; Hsu, W.-E.; Lin, C.-T. Field-effect transistor biosensing: Devices and clinical applications. *ECS J. Solid State Sci. Technol.* 2018, *7*, Q3196.

[44] Singh, N.K.; Thungon, P.D.; Estrela, P.; Goswami, P. Development of an aptamer-based field effect transistor biosensor for quantitative detection of Plasmodium falciparum glutamate dehydrogenase in serum samples. *Biosens. Bioelectron.* 2019, *123*, 30–35, doi:10.1016/j.bios.2018.09.085.

[45] Bergveld, P. Development, operation, and application of the ion-sensitive field-effect transistor as a tool for electrophysiology. *IEEE Trans. Biomed. Eng.* 1972, 342-351.

[46] Chida, R.; Igarashi, K.; Kamiyama, K.; Hoshino, E.; Esashi, M. Characterization of human dental plaque formed on hydrogen-ion-sensitive field-effect transistor electrodes. *J. Dent. Res.* 1986, *65*, 448–451.

[47] Akimenko, V.; Khomutov, S.; Obraztsova, A.Y.; Vishnivetskii, S.; Chuvilskaya, N.; Laurinavichus, K.; Reshetilov, A. A rapid method for detection of Clostridium thermocellum by field-effect transistor-based immunodetection. *J. Microbiol. Methods* 1996, *24*, 203–209.

[48] Weis, R.; Müller, B.; Fromherz, P. Neuron adhesion on a silicon chip probed by an array of field-effect transistors. *Phys. Rev. Lett.* 1996, *76*, 327.

[49] Souteyrand, E.; Cloarec, J.; Martin, J.; Wilson, C.; Lawrence, I.; Mikkelsen, S.; Lawrence, M. Direct detection of the hybridization of synthetic homo-oligomer DNA sequences by field effect. *J. Phys. Chem. B* 1997, *101*, 2980–2985.

[50] Sprössler, C.; Richter, D.; Denyer, M.; Offenhäusser, A. Long-term recording system based on field-effect transistor arrays for monitoring electrogenic cells in culture. *Biosens. Bioelectron.* 1998, *13*, 613–618.

[51] Brischwein, M.; Baumann, W.; Ehret, R.; Schwinde, A.; Kraus, M.; Wolf, B. Mikrosensorische Systeme in der zellbiologischen Grundlagenforschung und der medizinischen Diagnostik. *Naturwissenschaften* 1996, *83*, 193–200.

[52] Wolf, B.; Brischwein, M.; Baumann, W.; Ehret, R.; Kraus, M. Monitoring of cellular signalling and metabolism with modular sensor-technique: The PhysioControl-Microsystem (PCM®). *Biosens. Bioelectron.* 1998, *13*, 501–509.

[53] Vassanelli, S.; Fromherz, P. Transistor records of excitable neurons from rat brain. *Appl. Phys. A* 1998, *66*, 459–463.

[54] Sprössler, C.; Denyer, M.; Britland, S.; Knoll, W.; Offenhäusser, A. Electrical recordings from rat cardiac muscle cells using field-effect transistors. *Phys. Rev. E* 1999, *60*, 2171.

[55] Baumann, W.; Lehmann, M.; Schwinde, A.; Ehret, R.; Brischwein, M.; Wolf, B. Microelectronic sensor system for microphysiological application on living cells. *Sens. Actuators B Chem.* 1999, *55*, 77–89.

[56] Eversmann, B.; Jenkner, M.; Hofmann, F.; Paulus, C.; Brederlow, R.; Holzapfl, B.; Fromherz, P.; Merz, M.; Brenner, M.; Schreiter, M. A 128×128 CMOS biosensor array for extracellular recording of neural activity. *IEEE J. Solid-State Circuits* 2003, *38*, 2306–2317.

[57] Lambacher, A.; Jenkner, M.; Merz, M.; Eversmann, B.; Kaul, R.; Hofmann, F.; Thewes, R.; Fromherz, P. Electrical imaging of neuronal activity by multi-transistor-array (MTA) recording at 7.8 μm resolution. *Appl. Phys. A* 2004, *79*, 1607–1611.

[58] Lehmann, M.; Baumann, W. New insights into the nanometer-scaled cell-surface interspace by cell-sensor measurements. *Exp. Cell Res.* 2005, *305*, 374–382.

[59] Sakata, T.; Sugimoto, H.; Saito, A. Live monitoring of microenvironmental pH based on extracellular acidosis around cancer cells with cell-coupled gate ion-sensitive field-effect transistor. *Anal. Chem.* 2018, *90*, 12731–12736.

[60] Sakata, T. Biologically coupled gate field-effect transistors meet in vitro diagnostics. *ACS Omega* 2019, *4*, 11852–11862.

[61] Takshi, A.; Yaghoubi, H.; Wang, J.; Jun, D.; Beatty, J.T. Electrochemical Field-Effect Transistor Utilization to Study the Coupling Success Rate of Photosynthetic Protein Complexes to Cytochrome c. *Biosensors* 2017, *7*, 16.

[62] Milgrew, M.; Riehle, M.; Cumming, D. A large transistor-based sensor array chip for direct extracellular imaging. *Sens. Actuators B: Chem.* 2005, *111*, 347–353.

[63] Errachid, A.; Zine, N.; Samitier, J.; Bausells, J. FET-Based Chemical Sensor Systems Fabricated with Standard Technologies. *Electroanal. Int. J. Devoted Fundam. Pract. Asp. Electroanal.* 2004, *16*, 1843–1851.

[64] Georgiou, P.; Toumazou, C. ISFET characteristics in CMOS and their application to weak inversion operation. *Sens. Actuators B Chem.* 2009, *143*, 211–217.

[65] Sohbati, M.; Toumazou, C. Dimension and shape effects on the ISFET performance. *IEEE Sens. J.* 2014, *15*, 1670–1679.

[66] Barbaro, M.; Caboni, A.; Loi, D.; Lai, S.; Homsy, A.; Van Der Wal, P.; De Rooij, N. Label-free, direct DNA detection by means of a standard CMOS electronic chip. *Sens. Actuators B Chem.* 2012, *171*, 148–154.

[67] Park, M.-H.; Han, D.; Chand, R.; Lee, D.-H.; Kim, Y.-S. Mechanism of label-free DNA detection using the floating electrode on pentacene thin film transistor. *J. Phys. Chem. C* 2016, *120*, 4854–4859.

[68] Barbaro, M.; Bonfiglio, A.; Raffo, L.; Alessandrini, A.; Facci, P.; BarakBarak, I. A CMOS, fully integrated sensor for electronic detection of DNA hybridization. *IEEE Electron Device Lett.* 2006, *27*, 595–597.

[69] Zhang, Q.; Majumdar, H.S.; Kaisti, M.; Prabhu, A.; Ivaska, A.; Österbacka, R.; Rahman, A.; Levon, K. Surface functionalization of ion-sensitive floating-gate field-effect transistors with organic electronics. *IEEE Trans. Electron Devices* 2015, *62*, 1291–1298.

[70] Jayant, K.; Auluck, K.; Funke, M.; Anwar, S.; Phelps, J.B.; Gordon, P.H.; Rajwade, S.R.; Kan, E.C. Programmable ion-sensitive transistor interfaces. I. Electrochemical gating. *Phys. Rev. E* 2013, *88*, 012801.

[71] Jayant, K.; Auluck, K.; Rodriguez, S.; Cao, Y.; Kan, E.C. Programmable ion-sensitive transistor interfaces. III. Design considerations, signal generation, and sensitivity enhancement. *Phys. Rev. E* 2014, *89*, 052817.

[72] Cohen, A.; Spira, M.E.; Yitshaik, S.; Borghs, G.; Shwartzglass, O.; Shappir, J. Depletion type floating gate p-channel MOS transistor for recording action potentials generated by cultured neurons. *Biosens. Bioelectron.* 2004, *19*, 1703–1709.

[73] Jayant, K.; Singhai, A.; Cao, Y.; Phelps, J.B.; Lindau, M.; Holowka, D.A.; Baird, B.A.; Kan, E.C. Non-Faradaic Electrochemical Detection of Exocytosis from Mast and Chromaffin Cells Using Floating-Gate MOS Transistors. *Sci. Rep.* 2015, *5*, 1–15.

[74] Pullano, S.A.; Critello, C.D.; Mahbub, I.; Tasneem, N.T.; Shamsir, S.; Islam, S.K.; Greco, M.; Fiorillo, A.S. EGFET-based sensors for bioanalytical applications: A review. *Sensors* 2018, *18*, 4042.

[75] Tarasov, A.; Gray, D.W.; Tsai, M.-Y.; Shields, N.; Montrose, A.; Creedon, N.; Lovera, P.; O'Riordan, A.; Mooney, M.H.; Vogel, E.M. A potentiometric biosensor for rapid on-site disease diagnostics. *Biosens. Bioelectron.* 2016, *79*, 669–678.

[76] Baldacchini, C.; Montanarella, A.F.; Francioso, L.; Signore, M.A.; Cannistraro, S.; Bizzarri, A.R. A Reliable BioFET Immunosensor for Detection of p53 Tumour Suppressor in Physiological-Like Environment. *Sensors* 2020, *20*, 6364.

[77] Jang, H.-J.; Cho, W.-J. Performance enhancement of capacitive-coupling dual-gate ion-sensitive field-effect transistor in ultra-thin-body. *Sci. Rep.* 2014, *4*, 1–8.

[78] Spijkman, M.J.; Myny, K.; Smits, E.C.; Heremans, P.; Blom, P.W.; De Leeuw, D.M. Dual-gate thin-film transistors, integrated circuits and sensors. *Adv. Mater.* 2011, *23*, 3231–3242.

[79] Spijkman, M.; Smits, E.; Cillessen, J.; Biscarini, F.; Blom, P.; De Leeuw, D. Beyond the Nernst-limit with dual-gate ZnO ion-sensitive field-effect transistors. *Appl. Phys. Lett.* 2011, *98*, 043502.

[80] Huang, Y.-J.; Lin, C.-C.; Huang, J.-C.; Hsieh, C.-H.; Wen, C.-H.; Chen, T.-T.; Jeng, L.-S.; Yang, C.-K.; Yang, J.-H.; Tsui, F. High performance dual-gate ISFET with non-ideal effect reduction schemes in a SOI-CMOS bioelectrical SoC. In Proceedings of the 2015 IEEE International Electron Devices Meeting (IEDM), Washington, DC, USA, 7–9 December 2015.

[81] Novodchuk, I.; Bajcsy, M.; Yavuz, M. Graphene-Based Field Effect Transistor Biosensors for Breast Cancer Detection: A Review on Biosensing Strategies. *Carbon* 2020, doi:10.1016/j.carbon.2020.10.048.

[82] Yang, N.; Chen, X.; Ren, T.; Zhang, P.; Yang, D. Carbon nanotube-*based* biosensors. *Sens. Actuators B Chem.* 2015, *207*, 690–715.

[83] Shen, M.-Y.; Li, B.-R.; Li, Y.-K. Silicon nanowire field-effect-transistor based biosensors: From sensitive to ultra-sensitive. *Biosens. Bioelectron.* 2014, *60*, 101–111.

[84] Gan, X.; Zhao, H.; Quan, X. Two-dimensional MoS2: A promising building block for biosensors. *Biosens. Bioelectron.* 2017, *89*, 56–71.

[85] Ahmad, R.; Ahn, M.-S.; Hahn, Y.-B. ZnO nanorods array based field-effect transistor biosensor for phosphate detection. *J. Colloid Interface Sci.* 2017, *498*, 292–297.

[86] Hagen, J.A.; Kim, S.N.; Bayraktaroglu, B.; Leedy, K.; Chávez, J.L.; Kelley-Loughnane, N.; Naik, R.R.; Stone, M.O. Biofunctionalized Zinc Oxide Field Effect Transistors for Selective Sensing of Riboflavin with Current Modulation. *Sensors* 2011, *11*, 6645-6655.

[87] Lee, K.H.; Lee, J.O.; Choi, S.; Yoon, J.B.; Cho, G.H. A CMOS label-free DNA sensor using electrostatic induction of molecular charges. *Biosens. Bioelectron.* 2012, *31*, 343–348, doi:10.1016/j.bios.2011.10.042.

[88] Kim, J.Y.; Choi, K.; Moon, D.I.; Ahn, J.H.; Park, T.J.; Lee, S.Y.; Choi, Y.K. Surface engineering for enhancement of sensitivity in an underlap-FET biosensor by control of wettability. *Biosens. Bioelectron.* 2013, *41*, 867–870, doi:10.1016/j.bios.2012.08.036.

[89] Gao, A.; Zou, N.; Dai, P.; Lu, N.; Li, T.; Wang, Y.; Zhao, J.; Mao, H. Signal-to-noise ratio enhancement of silicon nanowires biosensor with rolling circle amplification. *Nano Lett.* 2013, *13*, 4123–4130, doi:10.1021/nl401628y.

[90] Park, K.-T.; Cho, D.-G.; Park, J.-W.; Hong, S.; Hwang, J. Detection of airborne viruses using electro-aerodynamic deposition and a field-effect transistor. *Sci. Rep.* 2015, *5*, doi:10.1038/srep17462.

[91] Park, S.; Choi, J.; Jeun, M.; Kim, Y.; Yuk, S.S.; Kim, S.K.; Song, C.S.; Lee, S.; Lee, K.H. Detection of Avian Influenza Virus from Cloacal Swabs Using a Disposable Well Gate FET Sensor. *Adv. Healthc. Mater.* 2017, *6*, doi:10.1002/adhm.201700371.

[92] Jin, X.; Zhang, H.; Li, Y.-T.; Xiao, M.-M.; Zhang, Z.-L.; Pang, D.-W.; Wong, G.; Zhang, Z.-Y.; Zhang, G.-J. A field effect transistor modified with reduced graphene oxide for immunodetection of Ebola virus. *Microchim. Acta* 2019, *186*, doi:10.1007/s00604-019-3256-5.

[93] Shariati, M. The field effect transistor DNA biosensor based on ITO nanowires in label-free hepatitis B virus detecting compatible with CMOS technology. *Biosens. Bioelectron.* 2018, *105*, 58–64, doi:10.1016/j.bios.2018.01.022.

[94] Vu, C.A.; Chen, W.Y. Field-Effect Transistor Biosensors for Biomedical Applications: Recent Advances and Future Prospects. *Sensors* 2019, *19*, 4214, doi:10.3390/s19194214.

[95] Dai, X.; Vo, R.; Hsu, H.H.; Deng, P.; Zhang, Y.; Jiang, X. Modularized Field-Effect Transistor Biosensors. *Nano Lett.* 2019, *19*, 6658–6664, doi:10.1021/acs.nanolett.9b02939.

[96] Rajan, N.K.; Brower, K.; Duan, X.; Reed, M.A. Limit of detection of field effect transistor biosensors: Effects of surface modification and size dependence. *Appl. Phys. Lett.* 2014, *104*, 084106, doi:10.1063/1.4867025.

[97] Yüce, M.; Kurt, H. How to make nanobiosensors: Surface modification and characterisation of nanomaterials for biosensing applications. *RSC Adv.* 2017, *7*, 49386–49403, doi:10.1039/c7ra10479k.

[98] Noah, N.M.; Ndangili, P.M. Current Trends of Nanobiosensors for Point-of-Care Diagnostics. *J. Anal. Methods Chem.* 2019, *2019*, 2179718, doi:10.1155/2019/2179718.

[99] Chartuprayoon, N.; Zhang, M.; Bosze, W.; Choa, Y.H.; Myung, N.V. One-dimensional nanostructures based bio-detection. *Biosens. Bioelectron.* 2015, *63*, 432–443, doi:10.1016/j.bios.2014.07.043.

[100] Hou, S.; Zhang, A.; Su, M. Nanomaterials for Biosensing Applications. *Nanomaterials* 2016, *6*, 58, doi:10.3390/nano6040058.

[101] Uhm, M.; Lee, J.M.; Lee, J.; Lee, J.H.; Choi, S.; Park, B.G.; Kim, D.M.; Choi, S.J.; Mo, H.S.; Jeong, Y.J.; et al. Ultrasensitive Electrical Detection of Hemagglutinin for Point-of-Care Detection of Influenza Virus Based on a CMP-NANA Probe and Top-Down Processed Silicon Nanowire Field-Effect Transistors. *Sensors* 2019, *19*, 4502, doi:10.3390/s19204502.

[102] Chiang, P.L.; Chou, T.C.; Wu, T.H.; Li, C.C.; Liao, C.D.; Lin, J.Y.; Tsai, M.H.; Tsai, C.C.; Sun, C.J.; Wang, C.H.; et al. Nanowire transistor-based ultrasensitive virus detection with reversible surface functionalization. *Chem. Asian J.* 2012, *7*, 2073–2079, doi:10.1002/asia.201200222.

[103] Kwon, J.; Lee, Y.; Lee, T.; Ahn, J.H. Aptamer-Based Field-Effect Transistor for Detection of Avian Influenza Virus in Chicken Serum. *Anal. Chem.* 2020, *92*, 5524–5531, doi:10.1021/acs.analchem.0c00348.

[104] Macchia, E.; Sarcina, L.; Picca, R.A.; Manoli, K.; Di Franco, C.; Scamarcio, G.; Torsi, L. Ultra-low HIV-1 p24 detection limits with a bioelectronic sensor. *Anal. Bioanal. Chem.* 2020, *412*, 811–818, doi:10.1007/s00216-019-02319-7.

[105] Basu, J.; RoyChaudhuri, C. Graphene Nanogrids FET Immunosensor: Signal to Noise Ratio Enhancement. *Sensors* 2016, *16*, 1481, doi:10.3390/s16101481.

[106] Liu, F.; Kim, Y.H.; Cheon, D.S.; Seo, T.S. Micropatterned reduced graphene oxide based field-effect transistor for real-time virus detection. *Sens. Actuators B Chem.* 2013, *186*, 252–257, doi:10.1016/j.snb.2013.05.097.

[107] Pant, M.; Kharkwal, H.; Singh, K.P.; Joshi, H.C. Detection of Rota Virus with the Help of Nanomaterial Based Field Effect Transistor (BIO-FET). *Biosens. J.* 2017, *06*, doi:10.4172/2090-4967.1000149.

[108] Aspermair, P.; Mishyn, V.; Bintinger, J.; Happy, H.; Bagga, K.; Subramanian, P.; Knoll, W.; Boukherroub, R.; Szunerits, S. Reduced graphene oxide-based field effect transistors for the detection of E7 protein of human papillomavirus in saliva. *Anal. Bioanal. Chem.* 2020, 10.1007/s00216-020-02879-z, doi:10.1007/s00216-020-02879-z.

[109] Chen, Y.; Ren, R.; Pu, H.; Guo, X.; Chang, J.; Zhou, G.; Mao, S.; Kron, M.; Chen, J. Field-Effect Transistor Biosensor for Rapid Detection of Ebola Antigen. *Sci. Rep.* 2017, *7*, doi:10.1038/s41598-017-11387-7.

[110] Kim, J.W.; Kim, S.; Jang, Y.H.; Lim, K.I.; Lee, W.H. Attomolar detection of virus by liquid coplanar-gate graphene transistor on plastic. *Nanotechnology* 2019, *30*, 345502, doi:10.1088/1361-6528/ab0f52.

[111] Ono, T.; Kawata, T.; Kanai, Y.; Ohno, Y.; Maehashi, K.; Inoue, K.; Watanabe, Y.; Nakakita, S.; Suzuki, Y.; Kawahara, T.; et al. High-Sensitive and Selective Detection of Human-Infectious Influenza Virus Using Biomimetic Graphene Field-Effect Transistor. In Proceedings of the 2018 76th Device Research Conference (DRC), Santa Barbara, CA, USA, 24–27 June 2018, doi:10.1109/drc.2018.8442255.

[112] Ono, T.; Kamada, K.; Hayashi, R.; Piacenti, A.R.; Gabbutt, C.; Sriwilaijaroen, N.; Hiramatsu, H.; Kanai, Y.; Inoue, K.; Nakakita, S.; et al. Lab-on-a-graphene-FET detection of key molecular events underpinning influenza virus infection and effect of antiviral drugs. *bioRxiv* 2020, doi:10.1101/2020.03.18.996884.

[113] Hideshima, S.; Hayashi, H.; Hinou, H.; Nambuya, S.; Kuroiwa, S.; Nakanishi, T.; Momma, T.; Nishimura, S.I.; Sakoda, Y.; Osaka, T. Glycan-immobilized dual-channel field effect transistor biosensor for the rapid identification of pandemic influenza viral particles. *Sci. Rep.* 2019, *9*, 11616, doi:10.1038/s41598-019-48076-6.

[114] Yang, J.; Carey, P.; Ren, F.; Mastro, M.A.; Beers, K.; Pearton, S.J.; Kravchenko, I.I. Zika virus detection using antibody-immobilized disposable cover glass and AlGaN/GaN high electron mobility transistors. *Appl. Phys. Lett.* 2018, *113*, 032101, doi:10.1063/1.5029902.

[115] Malpartida-Cardenas, K.; Miscourides, N.; Rodriguez-Manzano, J.; Yu, L.-S.; Moser, N.; Baum, J.; Georgiou, P. Quantitative and rapid Plasmodium falciparum malaria diagnosis and artemisinin-resistance detection using a CMOS Lab-on-Chip platform. *Biosens. Bioelectron.* 2019, *145*, 111678.

[116] Zhang, A.; Zheng, G.; Lieber, C.M. *Nanowire Field-Effect Transistor Sensors*; Springer: Cham, Switzerland, 2016; doi:10.1007/978-3-319-41981-7_10.

[117] Ambhorkar, P.; Wang, Z.; Ko, H.; Lee, S.; Koo, K.I.; Kim, K.; Cho, D.D. Nanowire-Based Biosensors: From Growth to Applications. *Micromachines*2018, *9*, 679, doi:10.3390/mi9120679.

[118] Meyyappan, M.; Lee, J.-S. Nanowire BioFETs: An Overview. *Nanowire Field Effect Transistors Princ. Appl.* 2014, doi:10.1007/978-1-4614-8124-9_9.

[119] Namdari, P.; Daraee, H.; Eatemadi, A. Recent Advances in Silicon Nanowire Biosensors: Synthesis Methods, Properties, and Applications. *Nanoscale Res. Lett.* 2016, *11*, 406, doi:10.1186/s11671-016-1618-z.

[120] Zheng, G.; Lieber, C.M. Nanowire biosensors for label-free, real-time, ultrasensitive protein detection. *Methods Mol. Biol.* 2011, *790*, 223–237, doi:10.1007/978-1-61779-319-6_18.

[121] Wu, J.Y.; Lin, C.H.; Feng, M.H.; Chen, C.H.; Su, P.C.; Yang, P.W.; Zheng, J.M.; Fu, C.W.; Yang, Y.S. Preparation of Silicon Nanowire Field-effect Transistor for Chemical and Biosensing Applications. *J. Vis. Exp.* 2016, 10.3791/53660, doi:10.3791/53660.

[122] He, B.; Morrow, T.J.; Keating, C.D. Nanowire sensors for multiplexed detection of biomolecules. *Curr. Opin. Chem. Biol.* 2008, *12*, 522–528, doi:10.1016/j.cbpa.2008.08.027.

[123] Bhattarai, J.K.; Neupane, D.; Nepal, B.; Mikhaylov, V.; Demchenko, A.V.; Stine, K.J. Preparation, Modification, Characterization, and Biosensing Application of Nanoporous Gold Using Electrochemical Techniques. *Nanomaterials* 2018, *8*, 171, doi:10.3390/nano8030171.

[124] Jiang, P.; Wang, Y.; Zhao, L.; Ji, C.; Chen, D.; Nie, L. Applications of Gold Nanoparticles in Non-Optical Biosensors. *Nanomaterials* 2018, *8*, 977, doi:10.3390/nano8120977.

[125] Lan, S.; Veiseh, M.; Zhang, M. Surface modification of silicon and gold-patterned silicon surfaces for improved biocompatibility and cell patterning selectivity. *Biosens. Bioelectron.* 2005, *20*, 1697–1708, doi:10.1016/j.bios.2004.06.025.

[126] Forsyth, R.; Devadoss, A.; Guy, O.J. Graphene Field Effect Transistors for Biomedical Applications: Current Status and Future Prospects. *Diagnostics* 2017, *7*, 45, doi:10.3390/diagnostics7030045.

[127] Banerjee, A.N. Graphene and its derivatives as biomedical materials: Future prospects and challenges. *Interface Focus* 2018, *8*, 20170056, doi:10.1098/rsfs.2017.0056.

[128] Sturala, J.; Luxa, J.; Pumera, M.; Sofer, Z. Chemistry of Graphene Derivatives: Synthesis, Applications, and Perspectives. *Chemistry* 2018, *24*, 5992–6006, doi:10.1002/chem.201704192.

[129] Bai, Y.; Xu, T.; Zhang, X. Graphene-Based Biosensors for Detection of Biomarkers. *Micromachines* 2020, *11*, 60, doi:10.3390/mi11010060.

[130] Szunerits, S.; Boukherroub, R. Graphene-based biosensors. *Interface Focus* 2018, *8*, 20160132, doi:10.1098/rsfs.2016.0132.

[131] Wang, X.-N.; Hu, P.-A. Carbon nanomaterials: Controlled growth and field-effect transistor biosensors. *Front. Mater. Sci.* 2012, *6*, 26–46, doi:10.1007/s11706-012-0160-x.

[132] Giordano, C.; Filatrella, G.; Sarno, M.; Di Bartolomeo, A. Multi-walled carbon nanotube films for the measurement of the alcoholic concentration. *Micro Nano Lett.* 2019, *14*, 304–308, doi:10.1049/mnl.2018.5412.

[133] Tilmaciu, C.M.; Morris, M.C. Carbon nanotube biosensors. *Front. Chem.* 2015, *3*, 59, doi:10.3389/fchem.2015.00059.

[134] Simon, J.; Flahaut, E.; Golzio, M. Overview of Carbon Nanotubes for Biomedical Applications. *Materials* 2019, *12*, 624, doi:10.3390/ma12040624.

[135] Eatemadi, A.; Daraee, H.; Karimkhanloo, H.; Kouhi, M.; Zarghami, N.; Akbarzadeh, A.; Abasi, M.; Hanifehpour, Y.; Joo, S.W. Carbon nanotubes: Properties, synthesis, purification, and medical applications. *Nanoscale Res. Lett.* 2014, *9*, 393, doi:10.1186/1556-276X-9-393.

[136] Camilli, L.; Passacantando, M. Advances on Sensors Based on Carbon Nanotubes. *Chemosensors* 2018, *6*, 62, doi:10.3390/chemosensors6040062.

[137] Sedki, M.; Chen, Y.; Mulchandani, A. Non-Carbon 2D Materials-Based Field-Effect Transistor Biosensors: Recent Advances, Challenges, and Future Perspectives. *Sensors* 2020, *20*, 4811, doi:10.3390/s20174811.

[138] Manzeli, S.; Ovchinnikov, D.; Pasquier, D.; Yazyev, O.V.; Kis, A. 2D transition metal dichalcogenides. *Nat. Rev. Mater.* 2017, *2*, doi:10.1038/natrevmats.2017.33.

[139] Zhou, X.; Sun, H.; Bai, X. Two-Dimensional Transition Metal Dichalcogenides: Synthesis, Biomedical Applications and Biosafety Evaluation. *Front. Bioeng. Biotechnol.* 2020, *8*, 236, doi:10.3389/fbioe.2020.00236.

[140] Pumera, M.; Loo, A.H. Layered transition-metal dichalcogenides (MoS2 and WS2) for sensing and biosensing. *Trac Trends Anal. Chem.* 2014, *61*, 49–53, doi:10.1016/j.trac.2014.05.009.

[141] Singh, A.K.; Kumar, P.; Late, D.J.; Kumar, A.; Patel, S.; Singh, J. 2D layered transition metal dichalcogenides (MoS2): Synthesis, applications and theoretical aspects. *Appl. Mater. Today* 2018, *13*, 242–270, doi:10.1016/j.apmt.2018.09.003.

[142] Hu, Y.; Huang, Y.; Tan, C.; Zhang, X.; Lu, Q.; Sindoro, M.; Huang, X.; Huang, W.; Wang, L.; Zhang, H. Two-dimensional transition metal dichalcogenide nanomaterials for biosensing applications. *Mater. Chem. Front.* 2017, *1*, 24–36, doi:10.1039/c6qm00195e.

[143] Liu, J.; Chen, X.; Wang, Q.; Xiao, M.; Zhong, D.; Sun, W.; Zhang, G.; Zhang, Z. Ultrasensitive monolayer MoS2 field-effect transistor based DNA sensors for screening of down syndrome. *Nano Lett.* 2019, *19*, 1437–1444.

[144] Gong, X.; Liu, Y.; Xiang, H.; Liu, H.; Liu, Z.; Zhao, X.; Li, J.; Li, H.; Hong, G.; Hu, T.S.; et al. Membraneless reproducible MoS2 field-effect transistor biosensor for high sensitive and selective detection of FGF21. *Sci. China Mater.* 2019, *62*, 1479–1487, doi:10.1007/s40843-019-9444-y.

[145] Mei, J.; Li, Y.T.; Zhang, H.; Xiao, M.M.; Ning, Y.; Zhang, Z.Y.; Zhang, G.J. Molybdenum disulfide field-effect transistor biosensor for ultrasensitive detection of DNA by employing morpholino as probe. *Biosens. Bioelectron.* 2018, *110*, 71–77, doi:10.1016/j.bios.2018.03.043.

[146] Lee, J.; Dak, P.; Lee, Y.; Park, H.; Choi, W.; Alam, M.A.; Kim, S. Two-dimensional Layered MoS2 Biosensors Enable Highly Sensitive Detection of Biomolecules. *Sci. Rep.* 2014, *4*, doi:10.1038/srep07352.

[147] Nam, H.; Oh, B.-R.; Chen, M.; Wi, S.; Li, D.; Kurabayashi, K.; Liang, X. Fabrication and comparison of MoS2 and WSe2 field-effect transistor biosensors. *J. Vac. Sci. Technol. BNanotechnol. Microelectron. Mater. Process. Meas. Phenom.* 2015, *33*, 06FG01, doi:10.1116/1.4930040.

[148] Sarkar, D.; Liu, W.; Xie, X.; Anselmo, A.C.; Mitragotri, S.; Banerjee, K. MoS(2) field-effect transistor for next-generation label-free biosensors. *ACS Nano* 2014, *8*, 3992–4003, doi:10.1021/nn5009148.

[149] Wang, H.; Zhao, P.; Zeng, X.; Young, C.D.; Hu, W. High-stability pH sensing with a few-layer MoS2 field-effect transistor. *Nanotechnology* 2019, *30*, 375203, doi:10.1088/1361-6528/ab277b.

[150] Borole, D.D.; Kapadi, U.R.; Mahulikar, P.P.; Hundiwale, D.G. Conducting polymers: An emerging field of biosensors. *Des. Monomers Polym.* 2012, *9*, 1–11, doi:10.1163/156855506775526205.

[151] Gerard, M. Application of conducting polymers to biosensors. *Biosens. Bioelectron.* 2002, *17*, 345–359, doi:10.1016/s0956-5663(01)00312-8.

[152] Arshak, K.; Velusamy, V.; Korostynska, O.; Oliwa-Stasiak, K.; Adley, C. Conducting Polymers and Their Applications to Biosensors: Emphasizing on Foodborne Pathogen Detection. *IEEE Sens. J.* 2009, *9*, 1942–1951, doi:10.1109/jsen.2009.2032052.

[153] Hangarter, C.M.; Bangar, M.; Mulchandani, A.; Myung, N.V. Conducting polymer nanowires for chemiresistive and FET-based bio/chemical sensors. *J. Mater. Chem.* 2010, *20*, 3131, doi:10.1039/b915717d.

[154] Park, C.S.; Lee, C.; Kwon, O.S. Conducting Polymer Based Nanobiosensors. *Polymers* 2016, *8*, 249, doi:10.3390/polym8070249.

[155] Park, S.J.; Lee, J.; Seo, S.E.; Kim, K.H.; Park, C.S.; Lee, S.H.; Ban, H.S.; Lee, B.D.; Song, H.S.; Kim, J.; et al. High-Performance Conducting Polymer Nanotube-based Liquid-Ion Gated Field-Effect Transistor Aptasensor for Dopamine Exocytosis. *Sci. Rep.* 2020, *10*, 3772, doi:10.1038/s41598-020-60715-x.

[156] Su, P.-C.; Chen, B.-H.; Lee, Y.-C.; Yang, Y.-S. Silicon Nanowire Field-Effect Transistor as Biosensing Platforms for Post-Translational Modification. *Biosensors* 2020, *10*, 213

[157] Dastagir, T.; Forzani, E.S.; Zhang, R.; Amlani, I.; Nagahara, L.A.; Tsui, R.; Tao, N. Electrical detection of hepatitis C virus RNA on single wall carbon nanotube-field effect transistors. *Analyst* 2007, *132*, 738–740, doi:10.1039/b707025j.

[158] Bausells, J.; Carrabina, J.; Errachid, A.; Merlos, A. Ion-sensitive field-effect transistors fabricated in a commercial CMOS technology. *Sens. Actuators B Chem.* 1999, *57*, 56–62.

[159] Bergveld, P. The operation of an ISFET as an electronic device. *Sens. Actuators* 1981, *1*, 17–29.

[160] Morgenshtein, A.; Sudakov-Boreysha, L.; Dinnar, U.; Jakobson, C.G.; Nemirovsky, Y. Wheatstone-Bridge readout interface for ISFET/REFET applications. *Sens. Actuators B Chem.* 2004, *98*, 18–27.

[161] Ravezzi, L.; Conci, P. ISFET sensor coupled with CMOS read-out circuit microsystem. *Electron. Lett.* 1998, *34*, 2234–2235.

[162] Nemeth, B.; Piechocinski, M.S.; Cumming, D.R. High-resolution real-time ion-camera system using a CMOS-based chemical sensor array for proton imaging. *Sens. Actuators B Chem.* 2012, *171*, 747–752.

[163] Hizawa, T.; Sawada, K.; Takao, H.; Ishida, M. Fabrication of a two-dimensional pH image sensor using a charge transfer technique. *Sens. Actuators B Chem.* 2006, *117*, 509–515.

[164] Futagawa, M.; Otake, R.; Dasai, F.; Ishida, M.; Sawada, K. Realization of 1 million pixel charge transfer type ion image sensor with 12 μm pixel pitch. In Proceedings of the 2015 Transducers-2015 18th International Conference on Solid-State Sensors, Actuators and Microsystems (TRANSDUCERS), Anchorage, AK, USA, 21–25 June 2015; pp. 236–239.

[165] Georgiou, P.; Toumazou, C. An adaptive ISFET chemical imager chip. In Proceedings of the 2008 IEEE International Symposium on Circuits and Systems, Seattle, WA, USA, 18–21 May 2008; pp. 2078–2081.

[166] Hu, Y.; Georgiou, P. A robust ISFET pH-measuring front-end for chemical reaction monitoring. *IEEE Trans. Biomed. Circuits Syst.* 2014, *8*, 177–185.

[167] Yan, L.; Georgiou, P.; Constandinou, T.G.; Garner, D.; Toumazou, C. An auto-offset-removal circuit for chemical sensing based on the PG-ISFET. In Proceedings of the 2009 IEEE International Symposium on Circuits and Systems, Taipei, Taiwan, 24–27 May 2009; pp. 1165–1168.

[168] Chan, W.P.; Premanode, B.; Toumazou, C. An integrated ISFETs instrumentation system in standard CMOS technology. *IEEE J. Solid-State Circuits* 2010, *45*, 1923–1934.

[169] Croce, R.A.; Vaddiraju, S.; Legassey, A.; Zhu, K.; Islam, S.K.; Papadimitrakopoulos, F.; Jain, F.C. A highly miniaturized low-power CMOS-based pH monitoring platform. *IEEE Sens. J.* 2014, *15*, 895–901.

[170] Miscourides, N.; Georgiou, P. ISFET arrays in CMOS: A head-to-head comparison between voltage and current mode. *IEEE Sens. J.* 2018, *19*, 1224–1238.

[171] Premanode, B.; Silawan, N.; Chan, W.P.; Toumazou, C. A composite ISFET readout circuit employing current feedback. *Sens. Actuators B Chem.* 2007, *127*, 486–490.

[172] Douthwaite, M.; Koutsos, E.; Yates, D.C.; Mitcheson, P.D.; Georgiou, P. A thermally powered ISFET array for on-body pH measurement. *IEEE Trans. Biomed. Circuits Syst.* 2017, *11*, 1324–1334.

[173] Zeng, J.; Kuang, L.; Miscourides, N.; Georgiou, P. A 128× 128 current-mode ultra-high frame rate ISFET array with in-pixel calibration for real-time ion imaging. *IEEE Trans. Biomed. Circuits Syst.* 2020, *14*, 359–372.

[174] Goh, Z.D.C.; Georgiou, P.; Constandinou, T.G.; Prodromakis, T.; Toumazou, C. Live demonstration: A CMOS-based lab-on-chip array for combined magnetic manipulation and opto-chemical sensing. In Proceedings of the 2011 IEEE International Symposium of Circuits and Systems (ISCAS), Rio de Janeiro, Brazi, 15–18 May 2011; pp. 1997–2001.

[175] Huang, X.; Yu, H.; Liu, X.; Jiang, Y.; Yan, M.; Wu, D. A dual-mode large-arrayed CMOS ISFET sensor for accurate and high-throughput pH sensing in biomedical diagnosis. *IEEE Trans. Biomed. Eng.* 2015, *62*, 2224–2233.

[176] Moser, N.; Lande, T.S.; Georgiou, P. A robust ISFET array with in-pixel quantisation and automatic offset calibration. In Proceedings of the 2016 IEEE Biomedical Circuits and Systems Conference (BioCAS), Shanghai, China, 17–19 October 2016; pp. 50–53.

[177] Wang, K.; Liu, Y.; Toumazou, C.; Georgiou, P. A TDC based ISFET readout for large-scale chemical sensing systems. In Proceedings of the 2012 IEEE Biomedical Circuits and Systems Conference (BioCAS), Hsinchu, Taiwan, 28–30 November 2012; pp. 176–179.

[178] Al-Ahdal, A.; Toumazou, C. High gain ISFET based νMOS chemical inverter. *Sens. Actuators B Chem.* 2012, *171*, 110–117.

[179] Nabovati, G.; Ghafar-Zadeh, E.; Sawan, M. A 64 pixel ISFET-based biosensor for extracellular pH gradient monitoring. In Proceedings of the 2015 IEEE International Symposium on Circuits and Systems (ISCAS), Lisbon, Portugal, 24–27 May 2015; pp. 1762–1765.

[180] Liu, Y.; Toumazou, C. An ISFET based sensing array with sensor offset compensation and pH sensitivity enhancement. In Proceedings of the Proceedings of 2010 IEEE International Symposium on Circuits and Systems, Paris, France, 30 May–2 June 2010; pp. 2283–2286.

[181] Milgrew, M.; Hammond, P.; Cumming, D. The development of scalable sensor arrays using standard CMOS technology. *Sens. Actuators B Chem.* 2004, *103*, 37–42.

[182] Hammond, P.A.; Ali, D.; Cumming, D.R. Design of a single-chip pH sensor using a conventional 0.6 μm CMOS process. *IEEE Sens. J.* 2004, *4*, 706–712.

[183] Wong, H.-S.; White, M.H. A CMOS-integrated'ISFET-operational amplifier'chemical sensor employing differential sensing. *IEEE Trans. Electron Devices* 1989, *36*, 479–487.

[184] Palan, B.; Santos, F.; Karam, J.; Courtois, B.; Husak, M. New ISFET sensor interface circuit for biomedical applications. *Sens. Actuators B Chem.* 1999, *57*, 63–68.

[185] Nabovati, G.; Ghafarzadeh, E.; Awwad, F.; Sawan, M. A sigma delta ISFET readout circuit for Lab-on-Chip applications. In Proceedings of the New Circuits and Systems Conference (NEWCAS), Paris, France, 16–19 June 2013; pp. 1–4.

[186] Kalofonou, M.; Toumazou, C. A Low Power Sub-μW Chemical Gilbert Cell for ISFET Differential Reaction Monitoring. *IEEE Trans. Biomed. Circuits Syst.* 2013, *8*, 565–574.

[187] Bergveld, P. Thirty years of ISFETOLOGY: What happened in the past 30 years and what may happen in the next 30 years. *Sens. Actuators B Chem.* 2003, *88*, 1–20.

[188] Georgiou, P.; Toumazou, C. An adaptive CMOS-based PG-ISFET for pH sensing. In Proceedings of the 2009 IEEE International Symposium on Circuits and Systems, Taipei, Taiwan, 24–27 May 2009; pp. 557–560.

[189] Jamasb, S. An analytical technique for counteracting drift in ion-selective field effect transistors (ISFETs). *IEEE Sens. J.* 2004, *4*, 795–801.

[190] Moser, N.; Lande, T.S.; Toumazou, C.; Georgiou, P. ISFETs in CMOS and emergent trends in instrumentation: A review. *IEEE Sens. J.* 2016, *16*, 6496–6514.

[191] Hammond, P.; Cumming, D. Performance and system-on-chip integration of an unmodified CMOS ISFET. *Sens. Actuators B Chem.* 2005, *111*, 254–258.

[192] Hammond, P.A.; Ali, D.; Cumming, D.R. A system-on-chip digital pH meter for use in a wireless diagnostic capsule. *IEEE Trans. Biomed. Eng.* 2005, *52*, 687–694.

[193] Rothberg, J.M.; Hinz, W.; Johnson, K.L.; Bustillo, J. Methods and Apparatus for Measuring Analytes Using Large Scale FET Arrays. Google Patents: 2011, GB2461127B.

[194] Hu, Y.; Georgiou, P. 3-T ISFET front-end utilising parasitic device capacitance. *Electron. Lett.* 2014, *50*, 1507–1509.

[195] Uzzal, M.M.; Zarkesh-Ha, P.; Edwards, J.S.; Coelho, E.; Rawat, P. A highly sensitive ISFET using pH-to-current conversion for real-time DNA sequencing. In Proceedings of the 2014 27th IEEE International System-on-Chip Conference (SOCC), Las Vegas, NV, USA, 2–5 September 2014; pp. 410–414.

[196] Georgiou, P.; Toumazou, C. Chemical log-domain filter. *Electron. Lett.* 2009, *45*, 391–392.

[197] Shepherd, L.M.; Toumazou, C. A biochemical translinear principle with weak inversion ISFETs. *IEEE Trans. Circuits Syst. I: Regul. Pap.* 2005, *52*, 2614–2619.

[198] Pookaiyaudom, P.; Toumazou, C.; Lidgey, F. The chemical current-conveyor: A new microchip biosensor. In Proceedings of the 2008 IEEE International Symposium on Circuits and Systems, Seattle, WA, USA, 18–21 May 2008; pp. 3166–3169.

[199] Miscourides, N.; Georgiou, P. A linear programmable-gate ISFET array operating in velocity saturation. In Proceedings of the 2016 IEEE Biomedical Circuits and Systems Conference (BioCAS), Shanghai, China, 17–19 October 2016; pp. 292–295.

[200] Premanode, B.; Chan, W.; Toumazou, C. Ultra-low power precision ISFET readout using global current feedback. *Electron. Lett.* 2006, *42*, 1264–1265.

[201] Chan, W.; Premanode, B.; Toumazou, C. 64 pH-ISFET averaging array employing global negative current feedback. *Electron. Lett.* 2009, *45*, 536–537.

[202] Juffali, W.; Georgiou, P.; Toumazou, C. ISFET based Urea: Creatinine translinear sensor. *Electron. Lett.* 2010, *46*, 746–748.

[203] Kalofonou, M.; Georgiou, P.; Ou, C.-P.; Toumazou, C. An ISFET based translinear sensor for DNA methylation detection. *Sens. Actuators B Chem.* 2012, *161*, 156–162.

[204] Wong, W.; Shepherd, L.; Georgiou, P.; Toumazou, C. Towards ISFET based DNA logic for rapid nucleic acid detection. In Proceedings of the SENSORS, Christchurch, New Zealand, 25–28 October 200; pp. 1451–1454.

[205] Al-Ahdal, A.; Toumazou, C. ISFET-based chemical switch. *IEEE Sens. J.* 2011, *12*, 1140–1146.

[206] AlAhdal, A.; Toumazou, C. ISFET-based chemical Schmitt trigger. *Electron. Lett.* 2012, *48*, 549–551.

[207] Liu, Y.; Al-Ahdal, A.; Georgiou, P.; Toumazou, C. Minimal readout scheme for ISFET sensing arrays based on pulse width modulation. *Electron. Lett.* 2012, *48*, 548–549.

[208] Do, A.T.; Minkyu, J.; Yeo, K.S. Improved inverter-based read-out scheme for low-power ISFET sensing array. *Electron. Lett.* 2013, *49*, 1517–1518.

[209] Moser, N.; Lande, T.S.; Georgiou, P. A novel pH-to-time ISFET pixel architecture with offset compensation. In Proceedings of the 2015 IEEE International Symposium on Circuits and Systems (ISCAS), Lisbon, Portugal, 24–27 May 2015; pp. 481–484.

[210] Jiang, Y.; Coquet, P.; Yu, H. Fast food safety screening with CMOS high-sensitivity large-arrayed ISFET sensor. In Proceedings of the 2017 IEEE Biomedical Circuits and Systems Conference (BioCAS), Turin, Italy, 19–21 October 2017; pp. 1–4.

[211] Nakajima, H.; Esashi, M.; Matsuo, T. The cation concentration response of polymer gate ISFET. *J. Electrochem. Soc.* 1982, *129*, 141.

[212] Matsuo, T.; Nakajima, H. Characteristics of reference electrodes using a polymer gate ISFET. *Sens. Actuators* 1984, *5*, 293–305.

[213] Chovelon, J.; Fombon, J.; Clechet, P.; Jaffrezic-Renault, N.; Martelet, C.; Nyamsi, A.; Cros, Y. Sensitization of dielectric surfaces by chemical grafting: Application to pH ISFETs and REFETs. *Sens. Actuators B Chem.* 1992, *8*, 221–225.

[214] Errachid, A.; Bausells, J.; Jaffrezic-Renault, N. A simple REFET for pH detection in differential mode. *Sens. Actuators B Chem.* 1999, *60*, 43–48.

[215] Bergveld, P.; Van Den Berg, A.; Van Der Wal, P.; Skowronska-Ptasinska, M.; Sudhölter, E.; Reinhoudt, D. How electrical and chemical requirements for REFETs may coincide. *Sens. Actuators* 1989, *18*, 309–327.

[216] Chudy, M.; Wróblewski, W.; Brzózka, Z. Towards REFET. *Sens. Actuators B Chem.* 1999, *57*, 47–50.

[217] Chodavarapu, V.; Titus, A.; Cartwright, A. Differential read-out architecture for CMOS ISFET microsystems. *Electron. Lett.* 2005, *41*, 698–699.

[218] Shepherd, L.; Georgiou, P.; Toumazou, C. A novel voltage-clamped CMOS ISFET sensor interface. In Proceedings of the 2007 IEEE International Symposium on Circuits and Systems, New Orleans, LA, USA, 27–30 May 2007; pp. 3331–3334.

[219] Sohbati, M.; Georgiou, P.; Toumazou, C. REFET replication for ISFET-based SNP detection arrays. In Proceedings of the 2013 IEEE International Symposium on Circuits and Systems (ISCAS), Beijing, China, 19–23 May 2013; pp. 185–188.

[220] Sohbati, M.; Toumazou, C. A temperature insensitive continuous time ΔpH to digital converter. In Proceedings of the 2014 IEEE International Symposium on Circuits and Systems (ISCAS), Melbourne, VIC, Australia, 1–5 June 2014; pp. 37–40.

[221] Milgrew, M.J.; Cumming, D.R. Matching the transconductance characteristics of CMOS ISFET arrays by removing trapped charge. *IEEE Trans. Electron Devices* 2008, *55*, 1074–1079.

[222] Georgiou, P.; Toumazou, C. ISFET threshold voltage programming in CMOS using hot-electron injection. *Electron. Lett.* 2009, *45*, 1112–1113.

[223] Al-Ahdal, A.; Toumazou, C. ISFET threshold voltage programming in CMOS using electron tunnelling. *Electron. Lett.* 2011, *47*, 1398–1399.

[224] Georgiou, P.; Toumazou, C. CMOS-based programmable gate ISFET. *Electron. Lett.* 2008, *44*, 1289–1291.

[225] Jakobson, C.; Feinsod, M.; Nemirovsky, Y. Low frequency noise and drift in ion sensitive field effect transistors. *Sens. Actuators B Chem.* 2000, *68*, 134–139.

[226] Jakobson, C.; Nemirovsky, Y. 1/f noise in ion sensitive field effect transistors from subthreshold to saturation. *Ieee Trans. Electron Devices* 1999, *46*, 259–261.

[227] Aw, C.-Y.; Cheung, P.W. A pH-ISFET sensor with on-chip temperature sensing. In Proceedings of the Annual International Conference of the IEEE Engineering in Medicine and Biology Society, New Orleans, LA, USA, 4–7 November 1988; pp. 772–773.

[228] Chin, Y.-L.; Chou, J.-C.; Sun, T.-P.; Chung, W.-Y.; Hsiung, S.-K. A novel pH sensitive ISFET with on chip temperature sensing using CMOS standard process. *Sens. Actuators B Chem.* 2001, *76*, 582–593.

[229] Chung, W.-Y.; Lin, Y.-T.; Pijanowska, D.G.; Yang, C.-H.; Wang, M.-C.; Krzyskow, A.; Torbicz, W. New ISFET interface circuit design with temperature compensation. *Microelectron. J.* 2006, *37*, 1105–1114.

Chapter 3 Open-Gate Junction Field-Effect Transistor: A New FET Sensing System[1,2]

The last chapter's review of FET sensor structures provided ample information about the FET chemical and biological sensors from all aspects, which further shed light on the novelty of the open-gate junction field-effect transistor (OG-JFET) as a new charge-sensitive planar FET structure not previously utilized for biomolecular or ion-sensing applications. The sensor's structure resembles a p-type JFET electronic device with the top n-type layer removed, resulting in a sizeable open-gate area that serves as a sensing site for introducing a solution or charged liquid on top. While most silicon-based FET sensors are based on the CMOS foundry process, the open-gate JFET represents the first silicon structure in the form of JFET devices interfacing with liquid or charged solutions.

This thesis chapter outlines the steps to characterize the OG-JFET and interface it with a probe station and semiconductor analyzer to test its response to charged solutions. It also explores how the sensor responds to charge variations in liquids in the open-gate area.

The results of these investigations are published in IEEE Sensors Journal and Sensors[1, 2], covering the first and second parts of this chapter, respectively.

[1] The first part (section 3.1) of this chapter is based on the published paper: Abbas Panahi, Hamed Osouli Tabrizi, Priyadarshini Mangannavar, Oleg Chebotarev, Andrew Fung, Ebrahim Ghafar-Zadeh, “Open-Gate Junction Field Effect Transistor (OG-JFET) for Life Science Applications: Design, Implementation, and Characterization”. IEEE Sensors Journal, 2021

[2] This chapter's second part (section 3.2) is based on the published paper: Panahi, Abbas, Deniz Sadighbayan, and Ebrahim Ghafar-Zadeh. 2021. "Electronic Sensing Platform (ESP) Based on Open-Gate Junction Field-Effect Transistor (OG-JFET) for Life Science Applications: Design, Modeling and Experimental Results" Sensors 21, no. 22: 7491. https://doi.org/10.3390/s21227491

3.1. Paper 2: Open-Gate Junction Field Effect Transistor (OG-JFET) for Life Science Applications: Design, Implementation, and Characterization

Authors: Abbas Panahi, Hamed Osouli Tabrizi, Priyadarshini Mangannavar, Oleg Chebotarev, Andrew Fung, Ebrahim Ghafar-Zadeh

Journal: IEEE Sensors

Abbas Panahi's contributions include chip design and characterizations, fixture design (fixture 3D CAD and fabrication) and implementations, fluidics fabrication (3D CAD and fabrication) and integrations, and semiconductor device simulations.

3.1.1. Abstract

This article introduces a new foundry-based ion-sensitive field-effect transistor named open-gate junction field-effect transistor (OG-JFET), intended for chemical and biological sensing applications. OG-JFET can be realized by removing the n-type gate in a p-type JFET to open the space for electrolyte gating. The new configuration enables the application of a bias voltage via a back-gate that results in more efficient channel current control. Accordingly, based on a standard foundry process, a 1.6 µm thick p-type conductive layer has been epitaxially grown on a 450 µm thick n-type silicon layer. The design promotes a large sensing area, including seven p-type conduction channels with dimensions of 1000 µm × 100 µm (W × L) and a depth of 1.6 µm. All the transfer characteristics required for biosensing/ion sensing of OG-JFET have been derived. Furthermore, we have conducted a COMSOL Multiphysics simulation on OG-JFET to verify the operation of the sensor, which helps to comprehend the sensor's functionality in different biasing conditions. The COMSOL semiconductor simulation results were consistent with experimental results, making the simulations a reliable reference for optimizing and customizing the chip for specific applications. OG-JFET showed a sensitivity of 55.29 mV/pH, a hysteresis of 16 mV, and a drift of 3 µA/hours, in the order of standard ISFET sensors in the literature. For the first time, this paper's simulation and experimental results put forward the OG-JFET as a new foundry-process-based, mass-producible ion-sensitive FET sensor for chemical and biological applications.

3.1.2. Introduction

A tremendous effort has been made to develop field-effect transistor (FET) sensors during the last decades for chemical and biological sensing applications [1], [2]. Owing to their unparalleled potential for miniaturization, high sensitivity, fast response time, low sample volume requirement, and tremendous capability in integration with complementary metal-oxide semiconductors (CMOS), FET-based chemical/biosensors have received significant attention in the biosensing community [3]. Biological field-effect transistors (BioFET) have been used for different applications, such as gene detection [4], cell analysis [5], enzyme reaction-based biosensors [6], and other biomolecular detection [7], which have been proven to improve the biosensing characteristics significantly.

Recently, a graphene BioFET was reported as a promising sensor for early detection of COVID-19 spike protein in human samples [8]. This success has drawn more attention to developing FET-based biosensors for early diagnosis [9]. The superior characteristics of FET sensors in biological sample sensing have led to their recognition as a potential sensing element for point-of-care devices, which are expected to impact the personalized medicine area significantly [10]. Many papers have reported FET-based sensors showing time-consuming and bulky tasks through in-house microfabrication clean rooms. However, there is a need for fabless microfabrication of FET sensors, which affects the accuracy of processing and packaging for higher production yield. A lengthy manufacturing process prevents the rapid production of FET-based sensing platforms during urgent situations such as the COVID-19 pandemic, which hampers the mass production of FET sensors as a potential point-of-care diagnostic device. This paper addresses this challenge by introducing a new foundry process to fabricate FET-based sensors. Herein, we focus on designing, modeling, fabricating, and characterizing the proposed sensor using chemical solutions with various pH values.

The organization of this paper is as follows. Section II[1] introduces the work related to OG-JFET. Section III[2] presents the proposed sensing methodology, the sensor's fabrication, simulation, design, and chemical preparation procedures. Section IV[3] discusses the results and presents the

[1] Section 3.1.3
[2] Section 3.1.4
[3] Section 3.1.5

experimental and simulation results. Section V[1] expresses the concluding remarks and summarizes different aspects of the OG-JFET proposed in this paper.

3.1.3. Related works

Hitherto, various FET structures have been introduced with different conduction channel topologies and gate arrangements for chemical and biological sensing purposes. In one of the most well-known topologies, ISFETs, the most significant step was exploiting the powerful features of unmodified CMOS technology as the basis for developing ISFETs [11], [12]. Considering low power consumption, these sensors revealed robust and improved sensing characteristics with outstanding scalability. Based on the same principle of fabrication, other structures such as floating gate, [13], floating control gate, [13], [14], extended gate, [15], [16], have also been manufactured following the unmodified CMOS ISFETs fabrication pattern. In almost all these structures, the metal gate was either removed from or extended to the top layer of the chip. Following the deposition of the passivation layer, the constructed interface can detect the ions in the solution [10]. Nevertheless, extending the metal layer throughout the sensor over the via-pads typically creates parasitic capacitive noises, which are difficult to remove from the signal [10]. Furthermore, the trapped charges in the passivation layer can offset the threshold voltage [17], [18].

Besides the abovementioned limitations, most of the developed ISFET sensors need a bulky reference electrode (e.g., Ag/AgCl) in the solution. This has impeded further development of these sensors and prevented large-scale integration with compact BioFET-based point-of-care devices [19]. Their further development for integration with the microfluidic chip was also hindered due to huge drift and noises associated with the stability of miniaturized electrodes in solution [20]. For such drawbacks, the operation of ISFETs based on a back gate or double gate structure has been of interest in many research works. Also, it was reported that double-gate FET (DG-FET) structures attribute substantial increments in the sensor response characteristics due to inherent amplification in the signal, which has made them more attractive to the FET community [21], [22]. More specifically, the DG-ISFET implemented on CMOS has been proven to have substantially higher pH sensitivity, and it was recognized that using double-gate structures would exceedingly improve the signal-to-noise ratio and significantly reduce the hysteresis [23]. Recently, the sensitivity of DGFET ion-sensitive structures has been shown to push the Nernst limit dramatically

[1] Section 3.1.6

by taking advantage of DG-ISFET, which works in dual amplification [24]– [26]. More complex fabrication procedures have been reported in which triple-gate FET (TGFET) showed the operation of the sensor without the need for a bulky reference electrode in the electrolyte solution [27]. Nevertheless, for perfect integration of ISFETs with lab-on-chip devices for biosensing purposes, reference electrodes are preferred to be replaced by a back gate. Thus, for the ideal integration of BioFET into the lab-on-chip devices, new FET structures, free from bulky reference electrodes, are highly demanded.

In this work, for the first time, we employ a back-gated JFET structure (already exists) for chemical sensing applications named OG-JFET, which can be considered a new platform for chemical/biological sensing applications with enough sensitivity compared to other available ISFETs. The new configuration avoids bulky reference electrodes by introducing a back-gated vertical p-n junction configuration with a p-type conductive channel. The sensor works based on the JFET structure (p-type JFET) with an open gate for introducing the sample. Another gate is placed on the back of a p-n junction that can be used for sensing without needing an electrode in solution (e.g., Ag/AgCl). The chemical sensing was tested by studying the sensor's sensitivity to different [H+] concentrations in the buffer solution (PBS). The OG-JFET can be considered a p-type channel JFET, with an n-type gate where the other gate has been removed to open the space for introducing chemical/biological samples. Previously, the same technology was used for photovoltage field-effect transistor applications, which showed a novel structure for pushing the infrared detection limits in silicon [28] by taking the superior advantage of JFET in signal amplification and back-gated structure. A porous silicon junction field-effect transistor (PSJFET) was another similar structure to JFET, used for NO_2 detection applications [29]. Another reported structure based on the JFET was the cSi-Au-JFET sensor, which used the JFET structure for NO_2 detection [30]. The current OG-JFET structure based on the introduced fabrication process that CMC Microsystem in Canada offers has not yet been reported for chemical sensing applications. In this work, we seek the pH sensing performance of OG-JFET as a new ISFET structure, which is the basis for further developments of this sensor platform for other biological sensing applications.

3.1.4. Proposed Method and Materials

3.1.4.1. OG-JFET Sensing Mechanism

The fabricated open gate JFET consists of a 1.6 µm thick silicon p-type channel that is placed on top of an n-type silicon layer with a thickness of 450 µm which holds a gate on the backside of the n-channel for biasing the p-type channel (See Fig. 3-1-1 and Fig. 3-1-2).

The distinction from the standard JFET structure is that the top gate and corresponding n-type layer have been removed to open the space for introducing the fluidic samples and biomaterials on top of the sensor. When the solution meets the silicon layer (here p-type channel) in the opened area (according to site-bonding theory) due to the interaction of SiO_2 (here native oxides) sites on the surface (Si-OH) with ions and water molecules, a charge layer will be created on the sensor surface that is correlated with the hydrogen concentration in the solution through site-bonding relation (for detail information, please refer to [31], [32]). In the current work, the pH test has been carried out to show sensor function towards pH variations. Different pH means different concentrations of hydrogen ions (pH=log([H+])), which affects the surface potential on top of the silicon (p-type) channel in the open-gate area. More [H+] concentration in the solution grounds a higher negative charge on the channel, which causes a higher source-drain current.

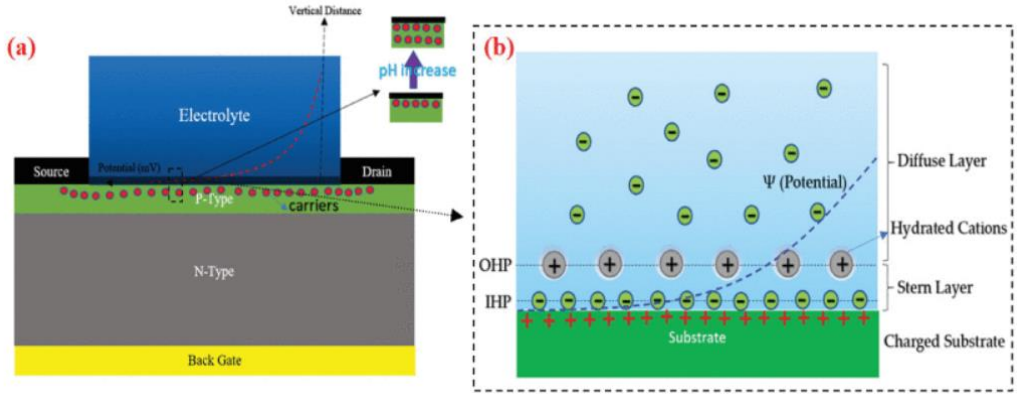


Figure 3-1- 1. The mechanism of operation of OG-JFET in interaction with electrolytes and ions. The pH means the concentration of H+ ions in the solution, and with the increment in H+ concentration, the more negative potential will be created on the surface of the sensor. This will create more current in the p-type channel, resulting from hole current in the p-type channel (p-type JFET).

As the sensor comes with a back gate, the operation point of the sensor can be changed. Furthermore, one can implement the sensor without the need for a reference electrode (e.g., Ag/AgCl) in the electrolyte solution since the back gate can be used as the reference voltage for sensitivity analysis and also in the constant voltage mode to read the decade changes in output drain-source current. Fig. 3-1-1-b shows the OG-JFET opened gate area's interface when it interacts with the electrolyte. First, a very thin atomic layer of negatively charged ions attaches on

the positive surface, which gives rise to the Inner Helmholtz Layer (IHL) and, as a result, the Outer Helmholtz Layer (OHL). The H+ variations in the diffuse layer would contribute to the surface potential in different pH values (See Fig. 3-1-1). The surface potential is maximum on the oxide surface on top of the p-channel.

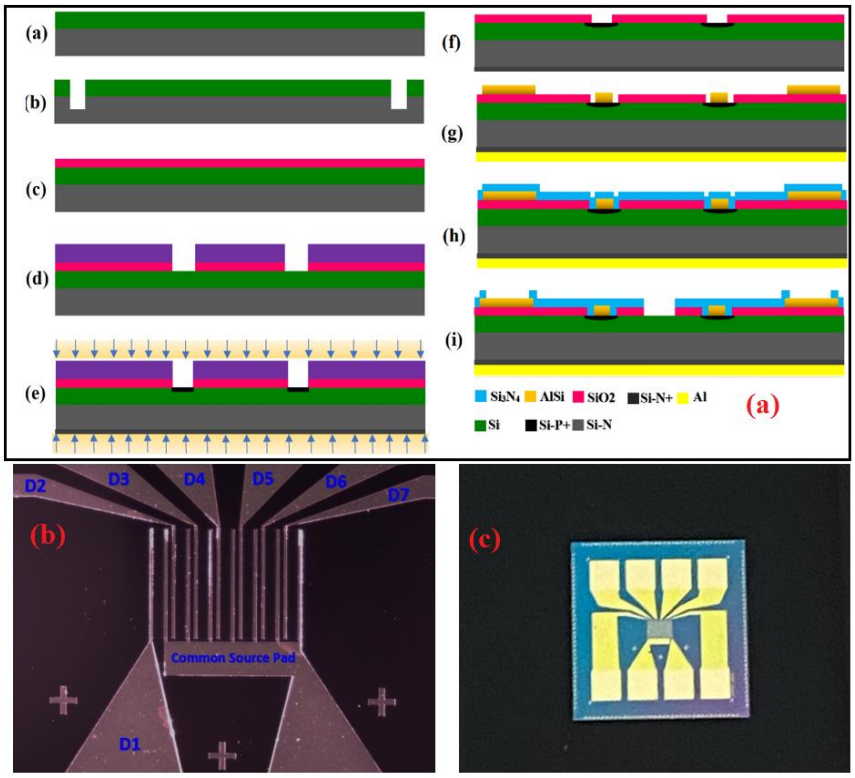


Figure 3-1- 2. The OG-JFET standard fabrication process. (a) Substrate wafer (Silicon <100>, 100 mm diameter, -420 +/- 25 µm thick, Resistivity 0.006 to 0.02 Ohm-cm); (b) Alignment marker definition (first mask); (c) PECVD SiO_2 deposition; (d) SiO_2 etching to Si layer. (second mask); (e) Front and back-side ion implantation; (f) implantation annealing; (g) front and back side metallization and annealing; (h) PECVD Si_3N_4 deposition (passivation layer); (i) Pad and channel opening. (b) Optical Microscopy image of the designed sensor based on the standard OG-JFET technology. The sensor has a common source pad, which serves seven OG-JFET in the chip. Channels have the same thickness, length, and width, which are 1.6 µm, 1000 µm, and 100 µm, respectively. (b) Optical microscopy image of the fabricated sensor; (c) the whole chip with pads, source, and drains.

3.1.4.2. OG-JFET Desing

Before fabrication, parallel OG-JFET channels with a common source and seven drains were designed using L-Edit software. The schematic of the fabricated sensor is demonstrated in Fig. 3-1-2. Each sensor on the die has a channel with a width and length of 100 µm and 1000 µm, respectively. All channels have a depth of 1.6 µm. There is a distance between the surface and drain edge, with the opened channel covered with a stacked layer of SiO_2/Si_3N_4. The covered space here in our design is 10 µm. The distance between two separate OG-JFET channels is 40 µm. Eight

pads with an area of 1700 µm × 1700 µm were designed with a pitch of 200 µm while we managed to maintain a 200 µm distance from both end sides of the chip. Only one of the pads is assigned to operate as the common source, and the rest are all independent drains for seven OG-JFET sensors. As shown in Fig. 3-1-2, a perfect area has remained for the fluidic chamber and microfluidics integration. Our design enables better control over the sensing area for biological and chemical sensing applications. It allows a multiplexing structure to screen all the biomaterials in the sensing area.

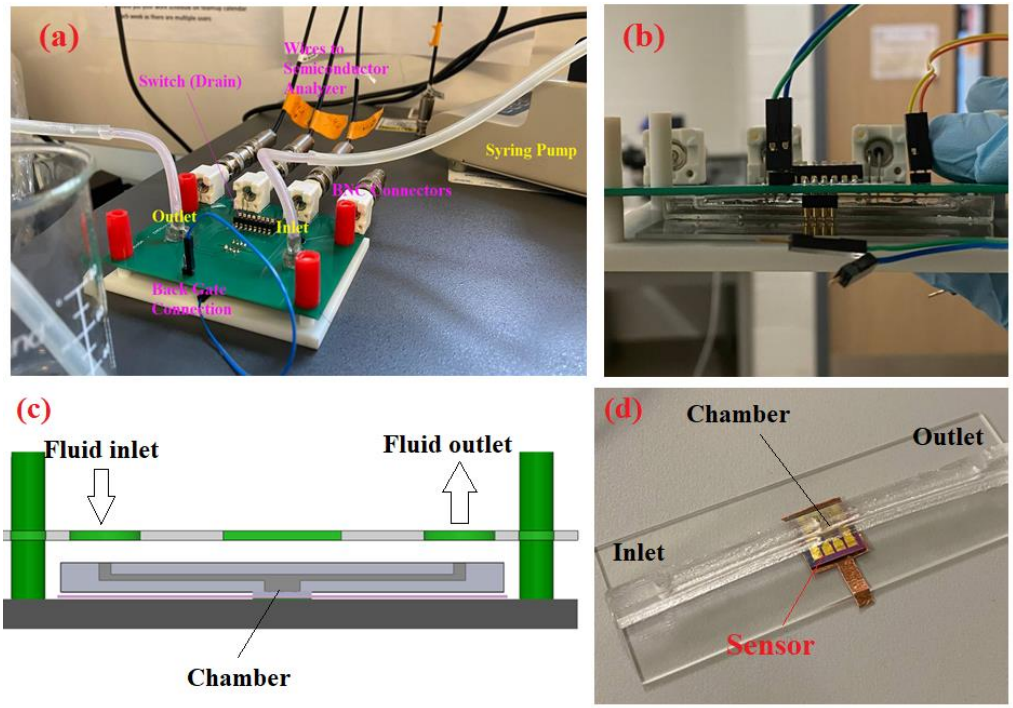


Figure 3-1- 3. Demonstration of OG-JFET fluidic fixture. (a) demonstrates the tube connections to the inlet and outlet of the microfluidic channel and the BNC connectors on the PCB, which are responsible for connecting the sensor to the semiconductor analyzer. The fixture enables a continuous microfluidic system. A closeup of the fluidic system has been shown in (b). The microfluidic channel runs between two sets of spring-loaded connectors on both sides, connecting the PCB wirings to the sensor pads. The back gate has been connected through a wire (blue) from the back of the sensor to the PCB. (c) Demonstration of CAD design of microfluidic channel for transporting fluid on top of the sensor. (d) The fabricated sensor was placed on top of the OG-JFET. The glass slide is then glued on the surface of the four-pillared structure and PCB, as shown in (b).

3.1.4.3. pH solution and wet tests on OG-JFET

The OG-JFET sensor has been integrated with a low-complexity microfluidic chamber on top of the sensor, which seals the sensor, prevents the pads from being in direct contact with the solution, and allows the solution to be held on the sensing surface. PBS was used as the buffer, and HCL

and NaOH solutions were prepared as the titration agents for preparing different PBS with specific pH ranging from 4 to 9. To do so, PBS was prepared, and its pH was measured with a standard commercially available pH meter (Hanna HI98103). The PBS pH was measured at 7.4 in all our experiments. To reach pH values lower than 7, an HCL solution was added meticulously (micro litter step), and the pH was recorded using a standard pH meter. Similarly, NaOH solution was used to titrate PBS to reach a pH higher than 7. We designed a fixture to hold the sensor and chamber together and a PCB to connect the sensor to a semiconductor analyzer (Keithley 4200A-SCS Parameter Analyzer). All transfer characteristics of the sensor were measured using a semiconductor analyzer device. Then, the same structure was used for pH tests on the chip.

3.1.4.4. Fixture for sensor and fluidics

A fixture has been designed and fabricated to transport the wet samples on the chip, which includes a fluidic channel with an inlet and outlet to facilitate the sensing process, which enables better continuous measurements. The fixture encompasses a Printed Circuit Board (PCB) on four pillars that direct the spring-loaded connectors onto the sensor pads, which have already been bonded onto the glass slides. The glass slide is glued to the 3D printed structure, as shown in Fig. 3-1-3 (d). The fluidic channel was fabricated using the standard replica molding method with PDMS. Fig. 3-1-3 (c)-(d) shows a schematic of the microfluidic channel. We have used four PCB BNC connectors to connect the sensor to the semiconductor analyzer device. Also, two holes were on the PCB for the fluidic inlet and outlet to the channel on the sensor.

3.1.4.5. Measurements

All the measurements were conducted using a semiconductor analyzer device (Keithley 4200A-SCS Parameter Analyzer) connected to the sensor through BNC connectors on the PCB board (See Fig. 3-1-3). The switch on the PCB was used to connect different drains (see Fig. 3-1-4) of OG-JFETs to the BNC and semiconductor analyzer. All the tests were done by biasing the sensor in reversed bias mode by applying a negative voltage to the drains and a positive voltage to the back gate. Then, the source was grounded (set in a semiconductor analyzer), and the Ids-Vgs and Ids-Vds curves were obtained for different transfer characteristics. The back-gate voltage was increased stepwise for Ids-Vds curves, and the drain-source voltage was swept linearly. All the measurements were conducted at room temperature and undercover in a dark chamber. Figure 3-

1-4 demonstrates the circuit schematics using a semiconductor analyzer to characterize the sensor. To connect the semiconductor analyzer to the sensor, the 4200 Medium Power SMU was used.

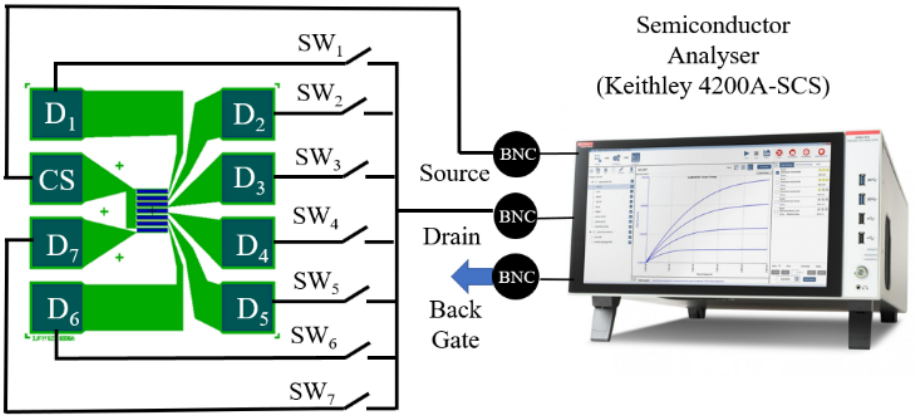


Figure 3-1- 4. The circuit for sensor characterization was designed using a semiconductor analyzer (Keithley 4200 A-SCS).

3.1.4.6. Simulation and modeling of OG-JFET using COMSOL

A multi-physics finite element simulation was performed on the OG-JFET to extract its electronic transfer characteristics. With this regard, COMSOL Multiphysics 5.5 software was used to model the semiconductor device. Finite Element Method (FEM) simulation has been used frequently in the semiconductor industry since it helps to evaluate the sensor response before fabrication which is essential in MEMS/NEMS sensors development due to the enormous cost of sensor fabrications. Accordingly, a 2D sensor model was designed in COMSOL with the specified size and dimensions, as demonstrated in Fig. 3-1-2. As is shown in Fig. 3-1-2, the sensor consists of parallel OG-JFET channels with one common source pad. The same geometry with experiment size (See Fig. 3-1-2) was modeled in COMSOL, and the semiconductor module was used to solve the corresponding equations in the specific geometry of OG-JFET. To do so, Maxwell's equations, Boltzmann transport theory, and Neumann boundary conditions were solved numerically in a meshed domain with the specific boundary conditions in COMSOL software. The meshing was required to define the nodes for numerical calculations, as demonstrated in Fig. 5. To analyze the p-n junction depletion due more precisely to the back-gate voltage sweep, a structured mesh was implemented for the p-type channel, and an unstructured mesh was considered for the p-type layer, as it revealed better computation convergence. The sensor's source, drain, and back gate contacts were modeled as "Ohmic Contacts" in COMSOL. All faces around the sensor except the opened gate area were

modeled as “insulated.” Doping levels in the semiconductor channels were considered as $N_A = 5 \times 10^{15}$ /cm^3 for the p-type channel and $N_D = 1 \times 10^{18}$ /cm^3 for the n-type channel.

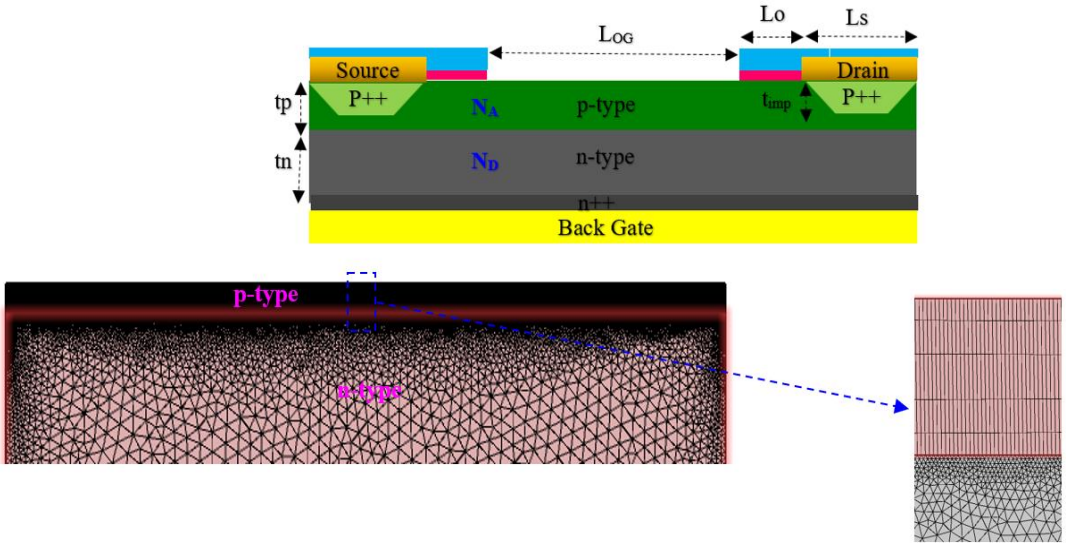


Figure 3-1- 5. The size and parameters used in the COMSOL Multiphysics simulation software. (a): demonstrates the essential parameters required for simulating the OG-JFET sensor; (b) presents the meshing structure produced in COMSOL with a structured mesh in the p-type channel and unstructured mesh in the n-type layer. The back gate was also modeled with an ohmic contact according to the fabricated process.

In Figure 3-1-4, L_{OG} (opened gate length), L_O (overlap length), and L_S (source/drain length) are 100, 10, and 20 µm, respectively. P-channel thickness (tp) was set to 1.6 µm, and the n-type channel (tn) was 450 µm according to the dimensions in fabrication. In the COMSOL semiconductor environment, a p++ doping level (~2×10^{16}/cm^3) for implantation of source and drain was considered for better accuracy of the numerical results. Doping levels for p-type (NA) and n-type layers (N_D) were 5×10^{15}/cm^3 and 1×10^{18}/cm^3, respectively. It was essential to model the effect of electrolyte solution-induced surface potential on the SiO_2 surface in the opened gate area, affecting the majority/minority carrier in the semiconductor channel. The simulation for both fermi-dirac and Maxwell-Boltzmann approximations of carrier statistics was performed, but insignificant differences were witnessed.

3.1.5. Results and Discussions

3.1.5.1. Sensor Transfer Characteristics Experimental Results

The OG-JFET transfer characteristics were derived by a semiconductor analyzer connected to the sensor through a PCB (See Fig 3-1-3 and Fig 3-1-4), sweeping the drain-source voltage from 0 to -10 volts, and positive gate voltage was changed stepwise from 0 to 1 V with 0.1 V steps. To

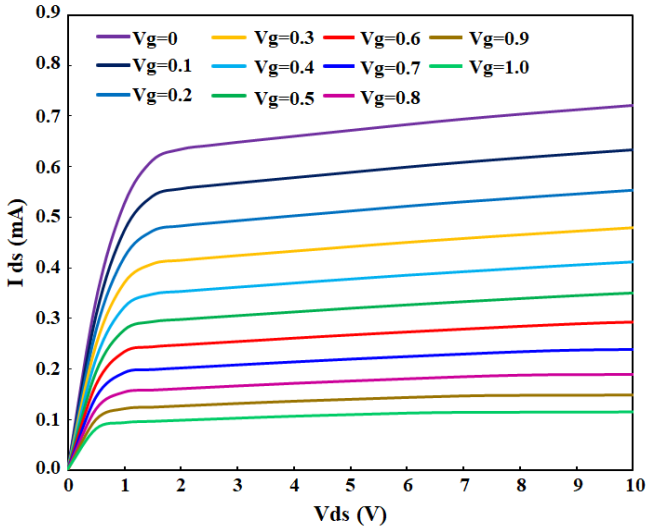


Figure 3-1- 6. Experimental result of Ids-Vds curve of OG-JFET for different gate-source voltage changes from 0 to 1 with 0.1 V step. Positive biased voltage has been applied to the back gate and negative biased to drain while the source is maintained at a zero bias.

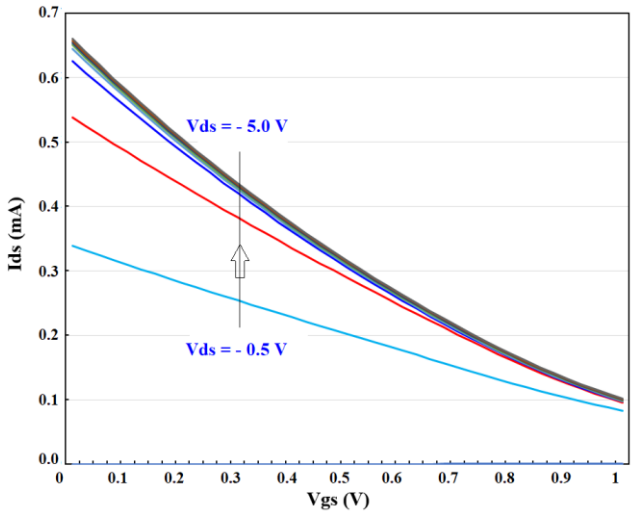


Figure 3-1- 7. Experimental result of Ids-Vgs curve of OG-JFET for different drain-source voltage ranges from 0 to -4.5 V with -0.5 V stepwise.

Operate the sensor in a reversed biased mode and ensure the p-n junction diode is not forwarded, a negative voltage is set for the drain, and a positive voltage is assigned to the gate. At the same time, the source was maintained at a zero-bias state as the reference point. As the results are shown in Fig. 3-1-6, the channel gets pinched off at around 1.3 V for Vgs = 0 (varied from 0.8 V to 1.5 V based on the Vg), and after that, the saturation regions begin; however, the Ids saturation regime is not entirely constant showing a minimal slop.

This means that in the saturation, we still have a very small conductance (dIds/dVds). This might be due to the sensor's long channel length and substantial width. As was expected, the higher voltage of the gate depletes the channel very fast, resulting from choosing a thin layer of p-type (1.6 μm) on a very thick n-type layer. The channel's conductance diminishes at substantial back gate voltage as the gradient of change of the current versus drain-source voltage becomes smaller compared to zero back gate voltage. Fig 3-1-6 only shows the Ids-Vds curve for a drain in the sensor.

All devices were tested in the dry mode, and the results showed consistent I-V curves. The Ids-Vds curves for all drains were obtained by sweeping the back gate after ensuring that all drains yielded the same results for all devices considered for further chemical test analysis. The same was done for Ids-Vgs at the same time as obtaining the Ids-Vds curves. Control over the channel conduction by a back-gate bias is essential in the sensor implementation for charge detection. For this reason, we have also analyzed the sensor Ids-Vgs (drain-source current versus gate-source voltage), demonstrated in Fig 3-1-7. To get the Ids-Vgs, the back gate voltage was swept from 0 to 1 V, and at the same time, the drain-source voltage was increased from 0 to 4.5 V (negative bias) to see the variations in the current due to the depletion effects of back-gate voltage. In a part of the Ids-Vgs curve, we can see an almost constant gain over the entire regime of 0-0.5 volts of gate-source voltage; however, for higher drain-source, it is not a perfect linear trend. In the pinched-off region, as we expected, the conduction change due to the shift in drain-source voltage is not the same voltage changes as in the linear section of the Ids-Vds curve; however, we can see the same gain for all values of the drain-source voltage range for all values of gate voltage.

3.1.5.2. OG-JFET Transfer Characteristics Simulation Results

A COMSOL Multiphysics simulation was performed to evaluate the OG-JFET transfer characteristics. The simulation methodology and the boundary conditions were discussed in

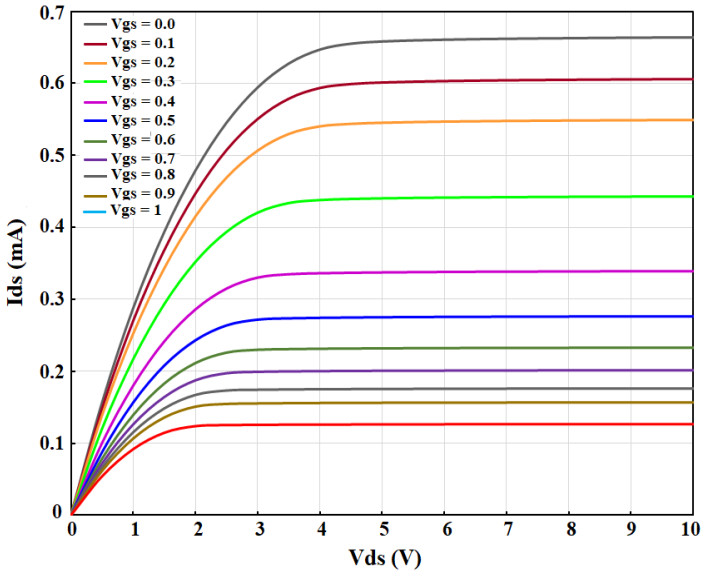


Figure 3-1- 8. COMSOL simulation result of p-type conduction channel OG-JFET drain-source current versus drain-source voltage in different gate-source voltages. The simulation perfectly shows the linear region and also the saturation region of the OG-JFET operation.

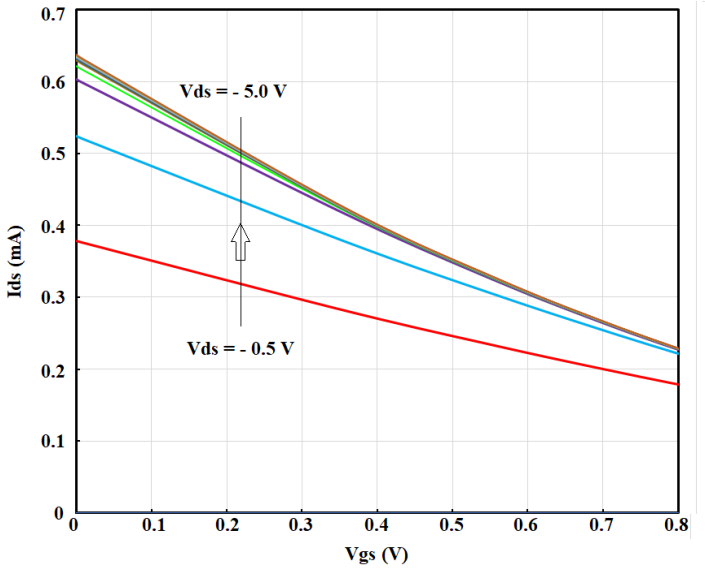


Figure 3-1- 9. COMSOL simulation results of OG-JFET Ids-Vgs curves. The simulation predicts the experiment trend very well.

previous sections (section G[1]). We have used the same voltage settings in the experiments in the COMSOL software to evaluate the results, and COMSOL is used as a reference to design more complicated conditions, which are impossible with mathematical modeling models of JFET. Since OG-JFET is based on a standard fabrication process, predicting the design output is very helpful in checking the desired output parameters and signals.

We mainly used COMSOL Multiphysics 5.0 because it could be further developed to enable multiphysics simulations on the OG-JFET for biosensor development, such as reaction and biological kinetics in fluid flow. COMSOL simulation can predict trends and output results, which

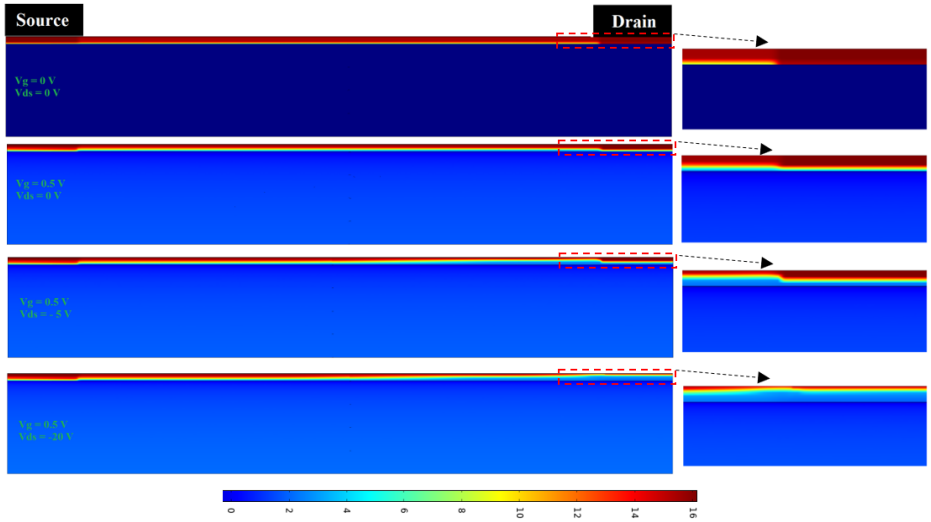


Figure 3-1- 10. Simulation results of the hole concentration (log) in the different gate and drain biases in p-type and n-type layers. The effect of gate-source voltage depletion on the carriers in the p-channel is demonstrated. As is expected from the conventional JFET, the channel gets narrower very close to the drain. Higher Vds at this point would push the channel to pinch off and start saturation with a constant current.

is very useful in the design and interpretation of data afterward. Nevertheless, due to the inherent limitations of numerical simulations, the perfect confirmation of the experiment is not possible with FEM methods, and we always see an error in the simulation. In the saturation region, an average of 11.58% error (for all Vg values in Vds = 10) can be considered the simulation error for the sensor's design before fabrication.

The Ids-Vds curves of OG-JFET have been derived by COMSOL simulation, presented in Fig. 3-1-8. As the curves demonstrate, the software predicts the saturation area and the linear section (subthreshold), which can be used for sensor parametric analysis and design before fabrication.

[1] Section 3.1.3.6

One can design the sensor layout and use COMSOL software to predict the sensor transfer characteristics to reach the desired design. Fig. 3-1-9 demonstrates the Ids-Vgs curve of the sensor for different values of drain-source voltages. A specific range error is inevitable for COMSOL simulations compared to experiments since there are many non-idealities in the wafer fabrication and during the sensor development process, as shown in Fig. 3-1-2. The doping levels, channel length, current leakages, perfect ohmic contact, and distribution of doping levels in the p-channel and the n-type channel are all conditions that are not linear in actual experiments and might cause non-linear responses.

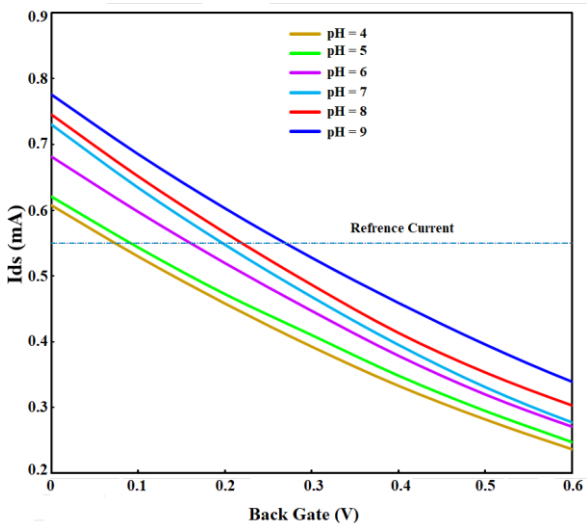


Figure 3-1- 11. The Ids-Vgs curves for different pH solutions ranged from 4 to 9. The reference current was 0.5 mA to compare the back-gate threshold voltages. Each pH test has been repeated ten times to make sure the curves are consistent and there is no change. In the stabilized condition, the curves are recorded.

According to Fig. 3-1-9, COMSOL predicts a linear Ids-Vgs curve for OG-JFET, almost like the pattern of experimental results shown in Fig. 3-1-6. The experimental result exhibits a curve-shaped current decrease with an increase in the back gate; however, the simulation predicts an almost linear dependence due to many fabrication-origin errors, such as length and doping distribution. Fig. 3-1-10 demonstrates the hole concentration in the OG-JFET p-type and n-type channels for different drain and back gate bias values. A narrow conduction channel near the drain position with a very narrow concentration was expected to be seen that permits a constant current in higher drain-source voltages. It seems there is a stepwise channel narrowing throughout the p-channel, and it is not a linear decay of potential, which was the assumption for previously used mathematical modeling of JFET [28]. By looking precisely at the hole concentration profile of the

p-type channel, we see that although the gate has pinched off the channel, there is still a very narrow space for the conduction of holes near the drain, which gets narrower in higher Vds (=20 V). Even though there are many sources of non-idealities in the OG-JFET system that affect the current and conductance of the p-type channel, the COMSOL Multiphysics software predicts the sensor transfer characteristics perfectly by showing the trends.

3.1.5.3. Chemical Experiment Results

OG-JFET sensor was tested under different pH solutions to analyze its sensitivity towards ion concentration changes in the PBS (here [H+] concentration). pH solutions were prepared according to the procedure explained before, and the solutions were injected into the sensor through a PDMS

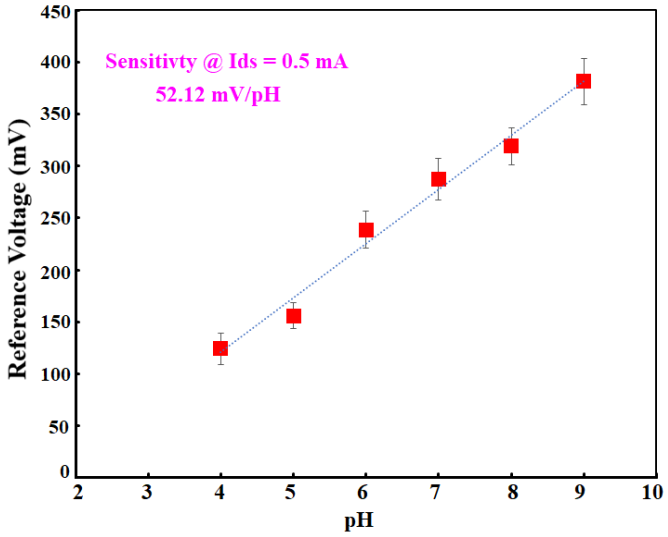


Figure 3-1- 12. Experimental results of pH sensitivity of OG-JFET in the reference current of 0.5 mA. The sensor demonstrates a 52.12 mV/pH sensitivity at this reference current. The sensitivity is concluded by fitting a linear line to the reference voltage versus pH values. The sensitivity was measured by obtaining the voltage in a contact current in Ids-Vgs curve for each pH values [31].

chamber on top of the sensor. In the measurement process, all care was taken not to mitigate the setup to avoid flow turbulences in the chamber.

These turbulences lead to streaming current, which affects the charge distribution on the surface of the native oxide layer on the channel and causes errors in response. Each experiment was repeated eight times to confirm the sensor's stable response. All experiments were performed at dark and room temperature (25 C). Fig. 3-1-11 demonstrates the Ids-Vgs curve for different pH values ranging from 4 to 9. As can be seen, in the range of 0 to 0.6 volts of gate bias, the Ids curves are shifted because of the H+ concentration increment in the buffer solution. The Ids-Vgs of OG-

JFET are almost linear in all back-gate voltage values, which helps to have a linear response from sensitivity analysis. When the back gate is considered the reference voltage, the sensor at the reference current of 0.5 mA and a 5 V drain-source voltage will result in a 55.29 mV/pH sensitivity in the range of < 59 mV/pH Nernst limit.

Fig. 3-1-12 shows the sensitivity curve for OG-JFET when operating at a constant drain-source voltage, and the reference current is maintained at 0.5 mA for pH variation analysis (measurement performed based on [26]). For determining the sensitivity, linear regression was used to determine the slope of curves and the data points' correlation coefficient (linearity). The sensitivity has also been determined for other drains on the chip, as shown in Fig. 3-1-13. The results show variations in the sensitivity for drains, which might be due to the crosstalk in the channels. Fig. 3-1-12 demonstrates the pH sensitivity for different reference currents, which is, according to Fig. 3-1-11, the Ids-Vgs response of the sensor for pH values between 4 and 9. As can be seen with the change of reference current from 0.3 mA to 0.5 mA, a range of sensitivities from 39.45 mV/pH to 55.29 mV/pH can be seen, which are in the Nernst limit range (under 59 mV/pH).

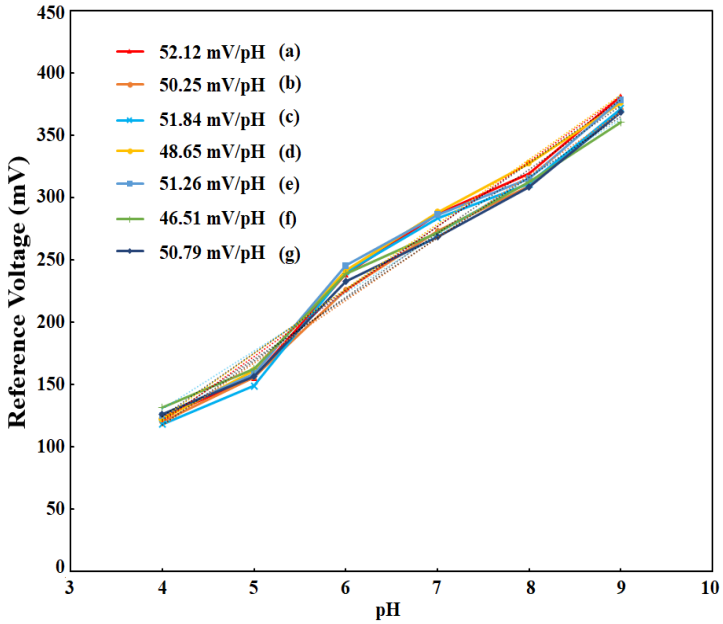


Figure 3-1- 13. Comparing the response of all drains to pH variations at reference current of Ids = 0.5 mA. (a): D4, (b): D5, (c): D6, (d): D7, (e): D1, (f): D2, (g): D3. For drain nominations, see Fig. 3-1-2.

According to the Ids-Vgs curves (See Fig. 3-1-11), which are used to estimate the sensor sensitivity to change in H+ concentration, the sensor response is almost linear. It shows a consistent result compared to other values for the sensitivity of the ISFETs when they have an oxide layer on top

of the channel. Being dependent on the reference current selection, the sensor will show different sensitivities toward the surface potential resulting from ions complexation/reaction on the open-gate area of OG-JFET. Fig. 3-1-14 demonstrates the effect of reference current on the sensor sensitivity. The constant-current scenario will result in the sensitivity in terms of mV/pH to be compared to the Nernst limit, which is 59 mV/pH. Another operational mode of the sensor is based on the constant voltage, which enables us to evaluate the current for different inputs. Here the input is the surface potentials resulted from the change of pH of solution on top of the conductive channel. As shown in Fig. 3-1-15, with the back-gate bias voltage, we can change the sensor's operation point. In higher back gate voltages, the sensor sensitivity (the slope of curves) is lower than for low gate voltage values.

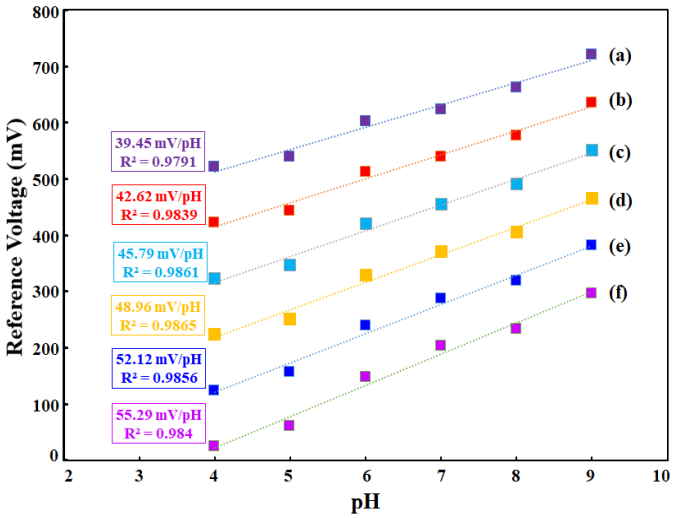


Figure 3-1- 14. Representation of pH sensitivity for different reference currents. The selected reference current is: (a) 0.3 mA; (b) 0.35 mA; (c) 0.40 mA; (d) 0.45 mA; (e) 0.50 mA; (f) 0.55 mA.

Sensor output current enhancement when increased pH is called current sensitivity, as shown in Fig. 3-1-16. Current sensitivity has been recently used for sensitivity analysis of other configurations of a new structure of ISFET [26]. Current sensitivity shows how the sensor responds to the change in input pH in the solution. According to Fig. 15, as Vg decreases, the sensitivity is enhanced from 0.0616 at Vg=1 to 0.1965 at Vg = 0.

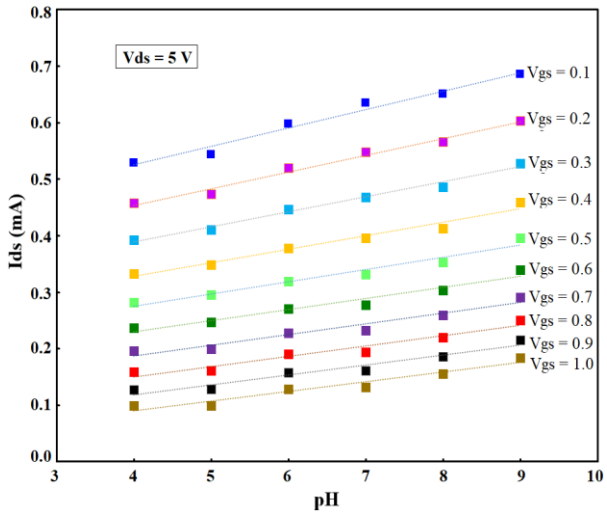


Figure 3-1- 15 shows another OG-JFET operation mode for sensing H+ ion concentrations in the buffer solution. The change in Ids versus the pH values as the Vgs changes from 0.1 V to 1.0 V in a constant Vds voltage.

Fig. 3-1-17 demonstrates the hysteresis analysis of OG-JFET for a pH input cycle of pH:7-10-7-4-7. The hysteresis phenomenon reflects the reliability of the sensors in cyclic operation in a certain period. The purpose of hysteresis analysis is to measure the sensor stability when the ion concentration

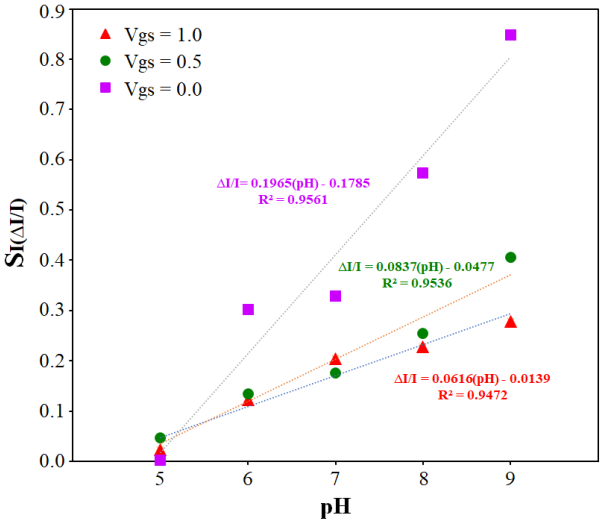


Figure 3-1- 16. Current enhancement sensitivity for different pH values. pH=4 is the reference for the current sensitivity analysis.

(here [H+]) changes over time and the sensor goes through a cycle from pH=7 and then operates in pH=10 (a basic solution).

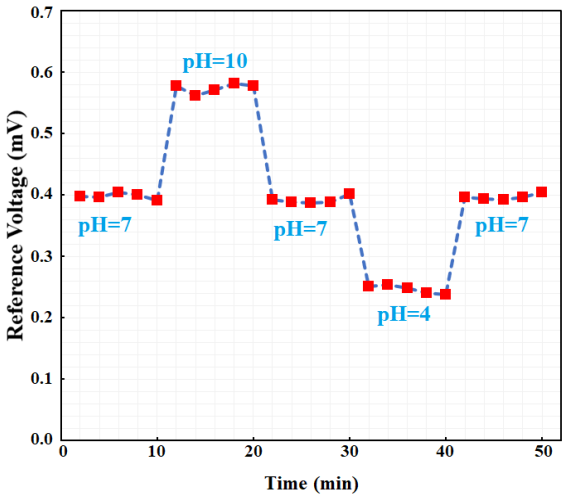


Figure 3-1- 17. Hysteresis analysis of OG-JFET in a cycle of pH:7→10→7→4→7. The sensor response was recorded every two minutes. For this analysis, the threshold voltage was defined as the back-gate voltage for a constant reference current. The voltage change due to the different pH effects was recorded.

Then it goes down to pH=4 (an acidic solution) followed by returning to the first solution with pH=7. In our analysis, the definition of hysteresis was the difference between the sensor response at the pH=7 in the third stage to the sensor response (threshold voltage) in the initial condition when the sensor was experiencing pH=7.

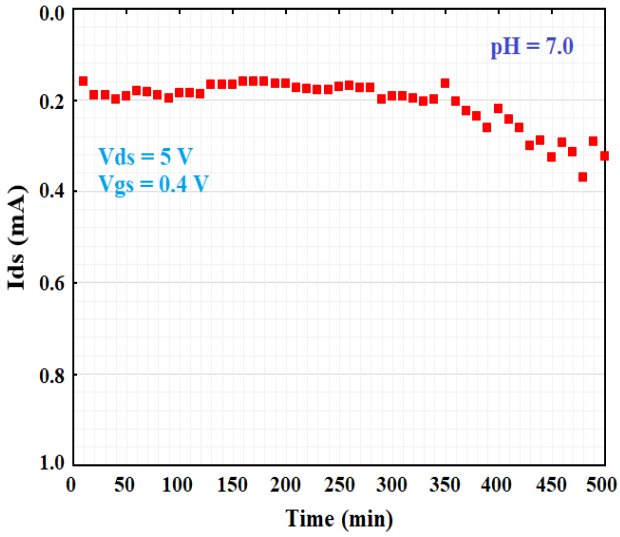


Figure 3-1- 18. Drift analysis of OG-JFET in a constant Vds and Vgs with only reading output current in a constant pH=7.0.

We measured the OG-JFET's hysteresis of 16 mV in the cycle of pH input described above, which is an average hysteresis value compared to the reported ISFETs. Based on the result shown in Fig. 3-1-17, the sensor is more stable in acidic solutions than in the alkaline state.

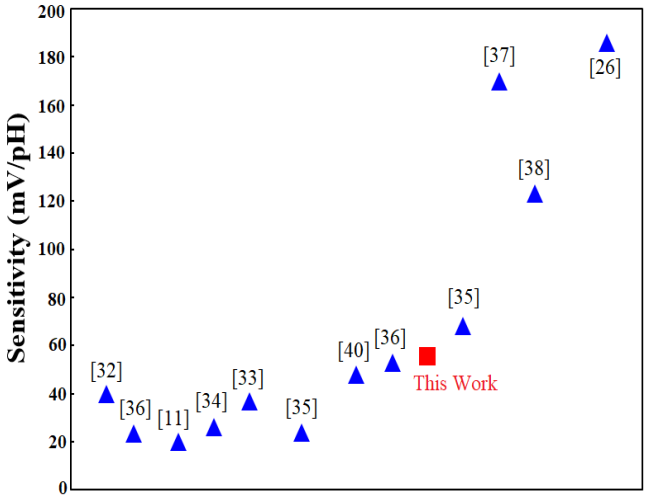


Figure 3-1- 19. Sensitivity comparison of OG-JFET with literature.

Another essential characteristic of ion-sensitive sensors is the change in the sensor output over a certain period called drift. The drift measures the degradation of the sensor oxide layer (dielectric or sensitive layer) over a long period of operation, which leads to ion trapping in oxide sites both in native oxides on the silicon and the oxide sites on the oxide layer on the channel. The drift explains how the sensitive layer on top of the channel is stable when a solution with a specific pH exists across the surface for a long time. Here, we have evaluated the sensor's output current at room temperature under constant Vds and continuous Vgs for a long time of 500 mins (=8.3 hours). The result is demonstrated in Fig. 3-1-16. As shown in Fig. 3-1-18, the sensor response is almost stable in almost 350 minutes of working; however, after that, we see a deviation from the stable pattern in a constant pH = 7. Based on a linear fit to this curve, we can estimate a ~ 3 µA/hour drift for the fabricated OG-JFET shown in Fig. 3-1-1.

The sensitivity of OG-JFET is improved compared to other silicon-based single-gate (mostly in solution) ISFETs (e.g., CMOS-based) as shown in Fig. 3-1-19, [11], [26], [39], [40], [31]–[38]. However, the OG-JFET sensitivity is lower than the double gate structures that generate sensitivity higher than the 59 mV/pH limit. The OG-JFET sensor has been operated with only a back gate to facilitate the integration with microfluidics. The existence of the back gate in OG-JFET alleviates

the cumbersome associated with bulky top gate (solution gate) integration for point-of-care device development.

Comparing the hysteresis of OG-JFET sensor (16 mV, see Fig. 3-1-17) and drift rate (3 μA/hours ~ 2 mV/hour, see Fig. 3-1-18) with other drift rates in literature (3.34 [40], 17.9 [41], 12.43 [42], 19.9 [43] mV/hours) and hysteresis (27 [40], 39.71 [41], 9.47 [42], 71.9 [43] mV) indicates good stability of native oxide layer produced with the proposed fabrication scheme.

3.1.6. Conclusion

This paper has introduced OG-JFET as a new ion-sensitive field-effect transistor based on the so-called junction field-effect transistor sensors for the first time. The sensor is based on a standard microfabrication process that allows scalable sensor production for further biosensor developments. The sensor was designed using L-Edit software and then submitted for fabrication. Our design includes seven conduction channels that allow for multiplexing. Nevertheless, in this work, we have used only one pad to evaluate the sensor characteristics toward pH variations in a solution. A fixture for the sensor was fabricated to have a PDMS-made chamber on top of the sensing area to have better control over the wet experiments and avoid the solution contact with pads. The sensor sensitivity toward pH variations was characterized, and a range of sensitivity for the sensor based on the constant current point was examined, which changed from 39.45 mV/pH to 55.29 mV/pH.

Furthermore, the sensor showed a hysteresis of 16 mV/pH and a drift of 3 μA/hours in our experiments. As was expected, the sensitivity of the designed sensor is in the range of the Nernst limit (<59 mV/pH). Experiments confirm that due to the existence of native SiO_2. However, the sensitivity is larger than the reported values for ISFETs with SiO_2 dielectric sensing layer (see Fig. 19). The device-to-device analysis (see Fig. 3-1-13.) shows that the sensitivity changes are not a constant value for all channels. This might be due to the crosstalk effects and dopant distribution, which should be investigated in more detail in future studies. As the back-gate structure is designed to modulate the sensing and provide the reference voltage for sensitivity analysis, experiments confirm that the sensor works without needing the bulky electrode (e.g., Ag/AgCl). In addition to the experimental investigations, a COMSOL Multiphysics simulation was also performed to

evaluate the sensor transfer characteristics, such as the Ids-Vds and Ids-Vgs curve, to ensure the experimental results from the actual die. Our simulations also enable a better understanding of the sensor structure and carrier transport in the main channel. As OG-JFET is based on a standard fabrication process, we also offer a simulation package in COMSOL, which enables the community to have a more efficient design for future applications. Also, to make the fabrication process more efficient in future works, the SU-8 layer passivation of the source and drain could be another viable method to reduce the number of fabrication steps. Moreover, further investigation is required to analyze the effectiveness of OG-JFET in response to biological prob immobilization on its sensing area to understand the noises associated with biomolecular interaction on the surface and the related background noises.

Based on our experimental results and simulation studies, we put forward the OG-JFET for the first time as a new ion-sensitive FET sensor for chemical and biological applications.

3.1.7. Acknowledgment

We would like to acknowledge CMC Microsystems for the provision of products and services that facilitated this research, including software design packages such as Mentor Tanner, COMSOL Multiphysics, fabrication services for the Electronic Sensor Platform at 3IT, and engineering support.

3.1.8. References

[1] R. J. E. Hueting, S. E. J. Vincent, J. G. Bomer, R. G. P. Sanders, and W. Olthuis, 'Ion-Sensitive Gated Bipolar Transistor', *IEEE Trans Electron Devices*, vol. 66, no. 10, pp. 4354–4360, 2019, doi: 10.1109/TED.2019.2933666.

[2] S. Sasa, M. Ozaki, K. Koike, M. Yano, and M. Inoue, 'High-performance ZnO/ZnMgO field-effect transistors using a hetero-metal-insulator-semiconductor structure', *Appl Phys Lett*, vol. 89, no. 5, 2006, doi: 10.1063/1.2261336.

[3] J. S. Moon *et al.*, 'Top-gated epitaxial graphene FETs on si-face sic wafers with a peak transconductance of 600 mS/mm', *IEEE Electron Device Letters*, vol. 31, no. 4, pp. 260–262, 2010, doi: 10.1109/LED.2010.2040132.

[4] H. Xu, Z. Zhang, H. Xu, Z. Wang, S. Wang, and L.-M. Peng, 'Top-Gated Graphene Field-Effect Transistors with High Normalized Dirac Point Voltage', *ACS Nano*, vol. 5, no. 6, pp. 5031–5037, 2011.

[5] Q. T. Do, K. Blekker, I. Regolin, W. Prost, and F. J. Tegude, 'High transconductance MISFET with a single InAs nanowire channel', *IEEE Electron Device Letters*, vol. 28, no. 8, pp. 682–684, 2007, doi: 10.1109/LED.2007.902082.

[6] Nidhi, S. Dasgupta, J. Lu, J. S. Speck, and U. K. Mishra, 'Self-aligned N-Polar GaN/InAlN MIS-HEMTs with record extrinsic transconductance of 1105 mS/mm', *IEEE Electron Device Letters*, vol. 33, no. 6, pp. 794–796, 2012, doi: 10.1109/LED.2012.2190965.

[7] Q. Cao, S. J. Han, G. S. Tulevski, Y. Zhu, D. D. Lu, and W. Haensch, 'Arrays of single-walled carbon nanotubes with full surface coverage for high-performance electronics', *Nat Nanotechnol*, vol. 8, no. 3, pp. 180–186, 2013, doi: 10.1038/nnano.2012.257.

[8] Y. Cui, Z. Zhong, D. Wang, W. U. Wang, and C. M. Lieber, 'High performance silicon nanowire field effect transistors', *Nano Lett*, vol. 3, no. 2, pp. 149–152, 2003, doi: 10.1021/nl025875l.

[9] H. Mousa and K. Teker, 'High-transconductance silicon carbide nanowire-based field-effect transistor (SiC-NWFET) for high-temperature applications', *Microelectronics International*, vol. 38, no. 2, pp. 78–83, 2021, doi: 10.1108/MI-05-2021-0043.

[10] T. Iwasaki *et al.*, 'High-temperature operation of diamond junction field-effect transistors with lateral p-n junctions', *IEEE Electron Device Letters*, vol. 34, no. 9, pp. 1175–1177, 2013, doi: 10.1109/LED.2013.2271377.

[11] D. Lembke and A. Kis, ' Correction to Breakdown of High-Performance Monolayer MoS 2 Transistors ', *ACS Nano*, vol. 7, no. 4, pp. 3730–3730, 2013, doi: 10.1021/nn400554k.

[12] Y. Liang, X. Liang, Z. Zhang, W. Li, X. Huo, and L. Peng, 'High mobility flexible graphene field-effect transistors and ambipolar radio-frequency circuits', *Nanoscale*, vol. 7, no. 25, pp. 10954–10962, 2015, doi: 10.1039/c5nr02292d.

[13] W. M. Zhou, F. Fang, Z. Y. Hou, L. J. Yan, and Y. F. Zhang, 'Field-effect transistor based on β-SiC nanowire', *IEEE Electron Device Letters*, vol. 27, no. 6, pp. 463–465, 2006, doi: 10.1109/LED.2006.874219.

[14] W. F. Yang, S. J. Lee, G. C. Liang, R. Eswar, Z. Q. Sun, and D. L. Kwong, 'Temperature dependence of carrier transport of a silicon nanowire schottky-barrier field-effect transistor', *IEEE Trans Nanotechnol*, vol. 7, no. 6, pp. 728–732, 2008, doi: 10.1109/TNANO.2008.2003353.

[15] J. Bausells, J. Carrabina, A. Errachid, and A. Merlos, 'Ion-sensitive field-effect transistors fabricated in a commercial CMOS technology', *Sens Actuators B Chem*, vol. 57, no. 1–3, pp. 56–62, 1999, doi: 10.1016/S0925-4005(99)00135-5.

[16] S. Meyburg, R. Stockmann, J. Moers, A. Offenhäusser, and S. Ingebrandt, 'Advanced CMOS process for floating gate field-effect transistors in bioelectronic applications', *Sens Actuators B Chem*, vol. 128, no. 1, pp. 208–217, 2007, doi: 10.1016/j.snb.2007.06.003.

[17] P. Beyazkilic, A. Saateh, M. Bayindir, and C. Elbuken, 'Evaporation-Induced Biomolecule Detection on Versatile Superhydrophilic Patterned Surfaces: Glucose and DNA Assay', *ACS Omega*, vol. 3, no. 10, pp. 13503–13509, Oct. 2018, doi: 10.1021/acsomega.8b00389.

[18] A. Ebrahimi *et al.*, 'Nanotextured superhydrophobic electrodes enable detection of attomolar-scale DNA concentration within a droplet by non-faradaic impedance spectroscopy', *Lab Chip*, vol. 13, no. 21, pp. 4248–4256, Nov. 2013, doi: 10.1039/c3lc50517k.

[19] M. Chopra, L. Li, H. Hu, M. A. Burns, and R. G. Larson, 'DNA molecular configurations in an evaporating droplet near a glass surface', *J Rheol (N Y N Y)*, vol. 47, no. 5, pp. 1111–1132, Sep. 2003, doi: 10.1122/1.1595097.

[20] X. L. Du, D. M. Duan, R. Cao, G. Jin, and J. Li, 'Enhancing DNA detection sensitivity through a two-step enrichment method with magnetic beads and droplet evaporation', *Anal Lett*, vol. 43, no. 9, pp. 1525–1533, Jun. 2010, doi: 10.1080/00032710903502140.

[21] L. P. Xu *et al.*, 'Ultratrace DNA Detection Based on the Condensing-Enrichment Effect of Superwettable Microchips', *Advanced Materials*, vol. 27, no. 43, pp. 6878–6884, Nov. 2015, doi: 10.1002/adma.201502982.

[22] K. Fukada, N. Kawamura, and S. Shiratori, 'Trace Material Capture by Controlled Liquid Droplets on a Superhydrophobic/Hydrophilic Surface', *Anal Chem*, vol. 89, no. 19, pp. 10391–10396, Oct. 2017, doi: 10.1021/acs.analchem.7b02369.

[23] B. Shi, Y. K. Shin, A. A. Hassanali, and S. J. Singer, 'DNA Binding to the Silica Surface', *Journal of Physical Chemistry B*, vol. 119, no. 34, pp. 11030–11040, Aug. 2015, doi: 10.1021/acs.jpcb.5b01983.

[24] S. Bag, S. Rauwolf, S. P. Schwaminger, W. Wenzel, and S. Berensmeier, 'DNA Binding to the Silica: Cooperative Adsorption in Action', *Langmuir*, vol. 37, no. 19, pp. 5902–5908, May 2021, doi: 10.1021/acs.langmuir.1c00381.

[25] B. M. Lowe, C. K. Skylaris, N. G. Green, Y. Shibuta, and T. Sakata, 'Molecular dynamics simulation of potentiometric sensor response: the effect of biomolecules, surface morphology and surface charge', *Nanoscale*, vol. 10, no. 18, pp. 8650–8666, May 2018, doi: 10.1039/C8NR00776D.

[26] B. M. Lowe, Y. Maekawa, Y. Shibuta, T. Sakata, C. K. Skylaris, and N. G. Green, 'Dynamic behaviour of the silica-water-bio electrical double layer in the presence of a divalent electrolyte', *Physical Chemistry Chemical Physics*, vol. 19, no. 4, pp. 2687–2701, 2017, doi: 10.1039/c6cp04101a.

[27] M. T. Hwang *et al.*, 'Ultrasensitive detection of nucleic acids using deformed graphene channel field effect biosensors', *Nat Commun*, vol. 11, no. 1, Dec. 2020, doi: 10.1038/s41467-020-15330-9.

[28] F. Liu *et al.*, 'Study on the adsorption orientation of DNA on two-dimensional MoS2 surface via molecular dynamics simulation: A vertical orientation phenomenon', *Chem Phys*, vol. 529, p. 110546, Jan. 2020, doi: 10.1016/J.CHEMPHYS.2019.110546.

[29] M. Morita, T. Ohmi, E. Hasegawa, M. Kawakami, and M. Ohwada, 'Growth of native oxide on a silicon surface', *J Appl Phys*, vol. 68, no. 3, pp. 1272–1281, 1990, doi: 10.1063/1.347181.

[30] P. Mercier and R. Savoie, 'Interaction of DNA with Silica Particles: A Vibrational Spectroscopic Study', *Biospectroscopy*, vol. 3, pp. 299–306, 1997, doi: 10.1002/(SICI)1520-6343(1997)3:4<299::AID-BSPY5>3.0.CO;2.

[31] K. D. Kwon, V. Vadillo-Rodriguez, B. E. Logan, and J. D. Kubicki, 'Interactions of biopolymers with silica surfaces: Force measurements and electronic structure calculation studies', *Geochim Cosmochim Acta*, vol. 70, no. 15, pp. 3803–3819, Aug. 2006, doi: 10.1016/j.gca.2006.05.016.

[32] P. Stoliar *et al.*, 'DNA adsorption measured with ultra-thin film organic field effect transistors', *Biosens Bioelectron*, vol. 24, no. 9, pp. 2935–2938, May 2009, doi: 10.1016/j.bios.2009.02.003.

[33] A. Panahi and E. Ghafar-Zadeh, 'A Hybrid Microfluidic Electronic Sensing Platform for Life Science Applications', *Micromachines (Basel)*, vol. 13, no. 3, 2022, doi: 10.3390/mi13030425.

[34] A. Panahi, H. O. Tabrizi, P. Mangannavar, O. Chebotarev, A. Fung, and E. Ghafar-Zadeh, 'Open-Gate Junction Field Effect Transistor (OG-JFET) for Life Science Applications: Design, Implementation and Characterization', *IEEE Sens J*, vol. XX, no. XX, 2021, doi: 10.1109/JSEN.2021.3121339.

[35] B. Smaani, N. Paras, S. B. Rahi, Y. S. Song, R. Yadav, and S. Tayal, 'Impact of the Self-Heating Effect on Nanosheet Field Effect Transistor Performance', *ECS Journal of Solid State Science and Technology*, vol. 12, no. 2, p. 021005, Feb. 2023, doi: 10.1149/2162-8777/ACB96B.

[36] B. M. Tenbroek, M. S. L. Lee, W. Redman-White, R. John T Bunyan, and M. J. Uren, 'Self-heating effects in SOI MOSFET's and their measurement by small signal conductance techniques', *IEEE Trans Electron Devices*, vol. 43, no. 12, pp. 2240–2248, 1996, doi: 10.1109/16.544417.

[37] X. Xu and L. Ma, ‘Analysis of the effects of evaporative cooling on the evaporation of liquid droplets using a combined field approach’, *Scientific Reports 2015 5:1*, vol. 5, no. 1, pp. 1–6, Feb. 2015, doi: 10.1038/srep08614.

[38] K. Zhang, L. Ma, X. Xu, J. Luo, and D. Guo, ‘Temperature distribution along the surface of evaporating droplets’, *Phys Rev E Stat Nonlin Soft Matter Phys*, vol. 89, no. 3, p. 032404, Mar. 2014, doi: 10.1103/PHYSREVE.89.032404/FIGURES/8/MEDIUM.

3.2. Paper 3: Electronic Sensing Platform (ESP) Based on Open-Gate Junction Field-Effect Transistor (OG-JFET) for Life Science Applications: Design, Modeling and Experimental Results[1]

Authors: Abbas Panahi, Deniz Sadighbayan and Ebrahim Ghafar-Zadeh

Journal: Sensors

Abbas Panahi's contributions include chip design, characterization, implementation, and performing DNA, pH, and exhalation tests and data analysis. Multiphysics FEM simulations. Writing the first draft and all parts except the experiments and related writings about neutrophil cell detection.

This section of Chapter 3 complements the previous chapter by characterizing the sensors with a more in-depth analysis of sensors with examples of charged liquids, such as oral cell (oral neutrophil) samples, single-strand DNA (ssDNA), human exhalation, and ions. Additionally, the physics of simulation is discussed in detail here, with a multiphysics simulation explaining the H+, OH- sensitivity of the OG-JFET.

In this chapter, the ion sensitivity of the OG-JFET is explored and simulated in detail. The ion sensitivity of the OG-JFET in its bare state is attributed to the presence of native SiO_2 on the sensing channel and Si_3N_4, another ion-sensitive material in the OG-JFET structure. These dielectrics on the sensing channel enable the sensing mechanism based on site-bonding theories. A detailed discussion on surface charge variations due to the presence of ions, ssDNA, human exhalation, and oral cells is provided in this chapter.

[1] This chapter is based on the published paper: Panahi, Abbas, Deniz Sadighbayan, and Ebrahim Ghafar-Zadeh. 2021. "Electronic Sensing Platform (ESP) Based on Open-Gate Junction Field-Effect Transistor (OG-JFET) for Life Science Applications: Design, Modeling and Experimental Results" Sensors 21, no. 22: 7491. https://doi.org/10.3390/s21227491

3.2.1. Abstract

This paper presents a new field-effect sensor called open-gate junction gate field-effect transistor (OG-JFET) for biosensing applications. The OG-JFET consists of a p-type channel on top of an n-type layer in which the p-type serves as the sensing conductive layer between two ohmic contacted sources and drain electrodes. The structure is novel based on a junction field-effect transistor with a subtle difference in that the top gate (n-type contact) has been removed to open the space for introducing the biomaterial and solution. The channel can be controlled through a back gate, enabling the sensor's operation without a bulky electrode inside the solution. In this research, to demonstrate the sensor's functionality for chemical and biosensing, we tested OG-JFET with varying pH solutions, cell adhesion (human oral neutrophils), human exhalation, and DNA molecules. Moreover, the sensor was simulated with COMSOL Multiphysics to gain insight into the sensor operation and its ion-sensitive capability. The complete simulation procedures and the physics of pH modeling are presented here, numerically solved in COMSOL Multiphysics software. The outcome of the current study puts forward OG-JFET as a new platform for biosensing applications.

3.2.2. Introduction

Field-effect transistor-based biosensors have received significant attention during the last decade due to their unique sensing characteristics, making them valuable sensing platforms for a range of applications such as diagnostics [1–8], gas sensors [9,10], food safety, and environmental monitoring [11]. The most appealing features of FET sensors are their low cost, label independence, and rapid bio-analyte detection. Label-free detection significantly reduces the sensor production cost and enables a more straightforward detection mechanism for developing point-of-care devices. FET-based biosensors have shown the fast and low-sample-input detection of various driven diseases, establishing a new avenue in biosensing research [12,13]. With a demonstrated low limit of detection (LoD), this extraordinary feature has motivated many researchers to develop FET sensors for integration with lab-on-a-chip devices to realize low-cost, hand-held personalized medical diagnostic devices. More importantly, FET-based sensors offer higher sensitivity and mass production capabilities (e.g., CMOS-based ISFETs) and are seamlessly miniaturized for high-throughput integration with lab-on-a-chip technologies. Furthermore, FET-based sensors enable sample charge detection, which allows for the obtaining of rich quantitative

biological data from biomolecules in solution, such as conformational changes, biomolecule structural variations, and monitoring extracellular potentials in a label-free fashion that is not easily accessible with other sensing mechanisms [2]. Based on these characteristics, FET biosensors have been considered promising candidates in the label-free biosensing area [14–20].

Thus far, various structures for FET sensors have been introduced that, along with many biological targets for detection, have established the foundation of many biological FET (BioFETs) sensors. Amongst different BioFETs, the silicon-based BioFETs have witnessed significant progress in CMOS technology. The unmodified CMOS technology, in particular, has leveraged silicon-based ISFETs to a commercial-grade [21,22]. Developing ISFETs based on CMOS technology enables significant improvement in scalability with low power consumption, which is extremely important for developing remote biosensing devices. As a result, different structural variants have emerged based on the CMOS fabrication technology, such as the extended gate, the floating gate, and the floating control gate. The ISFET was created by removing the metal gate on top of the conventional MOSFET to create an exposure to solution by making a solution oxide semiconductor structure [23]. Other forms of BioFETs include the incorporation of novel materials as the conductive channel (sensing element), such as graphene, carbon nanotubes, MoS_2, and metal-organic frameworks (MOF) [24], either in the back gate or solution gate mode [25]. While these materials have great potential for different biosensing applications, their scalable fabrication is still challenging.

Regarding integration with lab-on-a-chip for high-throughput fabrication, new BioFET sensor designs are needed to work without the bulky electrode due to the high demand for personalized medical devices for blood or other human fluid testing. Removing bulky reference electrodes enables easier integration with lab-on-a-chip devices since the reference electrode seriously hinders high-throughput packaging [26]. Many attempts have been made to miniaturize the bulky reference electrode (e.g., Ag/AgCl); nevertheless, the downscaling of the materials has caused more drift and unwanted noise issues along with the electrode's material instability [27]. A practical solution for BioFETs is to develop back-gated structures to use the stable gate as the reference voltage. Therefore, introducing new FET structures based on a back gate is highly desirable for biomedical applications of FET sensors [28,29].

In this paper, we introduce a novel back gate FET sensor called OG-JFET, showing the capability of the sensor operation without a reference electrode in the solution, which makes the sensor integration with lab-on-a-chip more straightforward. The current JFET-based back gate structure has not been introduced for biosensing applications thus far. Furthermore, the OG-JFET requires a very low voltage (<0.5 Volt) for the gate, which yields a low-power electronic platform for hand-held point-of-care devices. To better understand the device, we simulated the sensor with COMSOL Multiphysics and a detailed discussion on the biasing conditions. The OG-JFET can be considered a p-type channel JFET, with an n-type gate where the other gate has been removed to open the space for introducing chemical/biological samples. Contrary to the previous silicon-based structure that used bulk oxide as the back gate, OG-JFET controls the channel through a p–n junction in reverse bias. Previously, the same technology was used for photovoltage field-effect transistor applications, which showed a novel structure for pushing the infrared detection limits in silicon [30] by taking the superior advantage of JFET in signal amplification and back-gated design.

FET sensors have been used frequently for pH sensing applications as they provide miniaturized sensors with high sensitivity that can be integrated with lab-on-chip devices for point-of-care device development [2,31–33]. Here, we demonstrated the functionality of the OG-JFET for sensing the ion concentration variation in the solution with pH experiments. The sensor was tested with a phosphate buffer solution with different pH values, showing the sensor's capability to detect the H+ and OH concentrations in the base solution. The pH sensitivity of OG-JFET's response was also verified with a COMSOL simulation to prove its ion-sensitive capability. There are various emerging structures for pH sensing, such as extended gate [34] and Fin-FETs [35], as well as graphene-based FETs [36], which are promising new structures for enhancing the performance of BioFETs.

The DNA molecule is a critical biomolecule for all aspects of life science [37]. FET sensors have been recognized as sensitive charge detectors for analyzing DNA molecules, providing quantitative data on hybridization and structural conformations [38,39]. Many efforts have been made to use FET sensors for DNA detection [40–42]; however, DNA charge analysis has not been reported in dry conditions, which are very important for DNA-based data storage applications. We used ssDNA molecules in different concentrations as a negative charge model to demonstrate

sensor response to a known charged biomolecule, showing increased sensor drain-source current when biomolecules are loaded on a sensor. It was revealed that sensors can be used to monitor dried ssDNA, which can also be used in DNA sensors. The ssDNA in dry condition was tested to illustrate the possible sensor application in DNA-based data storage, which requires monitoring the mass DNA in a specific spot [43–45].

FET sensors have been widely used in cell analysis, showing great potential for cell analysis for different applications [46,47]. The sensor was tested with oral neutrophil cells in ultrapure water to demonstrate further the sensor's applicability in directly detecting bioparticles. The ultrapure water droplet containing oral neutrophil cells caused sedimentation of cells in the sensing area, leading to direct cell adhesion on the sensing gate. The existence of cells on the sensing site caused a local variation in the surface charge of the sensor, leading to a change in the source-drain current. In this regard, the sensor demonstrated potential applications in cell sensing and direct bioparticle detection. The negative charge of cells changes the sensor response in the same way as DNA molecules, leading to an increment in output current [48,49].

Knowing that FET sensors have been used for humidity tests [50,51], we tested the sensor in this study with direct human exhalation to show the effect of natural human breath on the response as the humidity model. Most human exhalation consists of water vapor rapidly evaporating when it meets solid surfaces. This sensor has tested the process, showing its usefulness for human exhalation analysis.

The device's functionality for sensing charge on the surface was verified with pH solution, DNA molecule, oral neutrophil cells, and human exhale condensation and evaporation. The models were used to show the operation of the sensor that put the sensor for any charge detection applications from biomolecules to human breath analysis.

3.2.3. OG-JFET Mechanism of Working

3.2.3.1. OG-JFET Sensing Principle

The OG-JFET sensor is fabricated using a VLSI microfabrication method, which realizes a vertical p–n junction in which the p-type layer is the sensing layer. On top of the p-type layer, two electrodes, the source and drain, are deposited, creating a conductive channel between two separate electrodes.

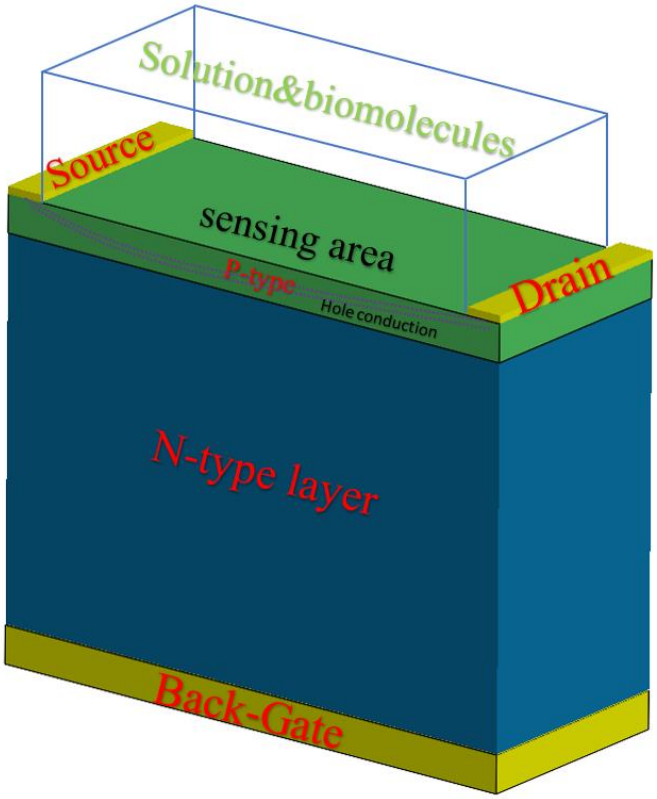


Figure 3-2- 1. Schematic of OG-FET sensor showing the main material composition of the sensor. The sensing layer of OG-JFET is the p-type silicon between two electrodes of the source and drain. The open-gate area is covered with the native oxide layer, usually appearing when silicon is exposed to air.

The p-type layer and electrodes are epitaxially grown on top of a thick n-type layer connected to a back gate on the other side of the chip. There are holes in the p-type layer as the primary charge carrier that flows from source to drain. The charge transport in the semiconductor sense induces electric field effects from the opened gate area (see Figure 3-2-1); consequently, the current in the channel changes when exposed to the biomaterial in the opened space. The sensor is like conventional JFETs, with the subtle difference that one of the top gates (here n-type) is removed. The sensor's electrical output curves are expected to be like JFETs, as this is proved in other variants of the JFET for different applications. A layer of p-type silicon (1.6 µm) is epitaxially grown on a 450 µm thick n-type silicon to form the OG-JFET main structure. The p-type layer is boron-doped with a density of $5 \times 10^{15}/cm^3$, and for the n-type, it is $1 \times 10^{18}/cm^3$ with doping of phosphor. A high-doped region is created on the backside of the sensor (on the back of the n-type layer), and then the back gate is formed through an ohmic contact. When a solution or a biometrical meets the silicon in the opened gate area, the charges induce an electric field that influences the

positively charged holes. The silicon is not covered with silicon dioxide, but it is a naturally formed oxide called native oxide that is very thin. The silicon dioxide is the first sensing layer of the sensor in contact with the substances and chemical solutions in the opened gate area. Through the Si-OH bonds and ion complexation on the surface of silicon dioxide, we can sense the chemical potential in the solution in the oxide layer that leads to changes in the conduction of holes.

3.2.3.2. Design and Fabrication of OG-JFET

The OG-JFET chip was fabricated through a standard microfabrication process offered by CMC Microsystem (Montreal, Canada). The layout design was performed in L-Edit software and then submitted for fabrication. The sensor was designed based on the common source principle, which enables a large pad to connect all sources. The drains were linked to their corresponding large pads. The channel size was 100 µm × 1000 µm (W × L) with a thickness of 1.6 µm. In this design, we had seven channels. The distance between the two channels (source to drain) was 40 µm. The width of the source and drain was 20 µm, and their length was 1000 µm. All sources were connected, and the drains were regulated with a switch implemented in the printed circuit board (PCB). The sensor was designed to position a total sensing area of 1000 × 1500 μm^2 at the center of the chip, as demonstrated in Figure 3-2-2. The pad area was 1700 × 1700 μm^2 with a pitch of 2 mm. The minimum surround for the sensors (the SiO_2/Si_3N_4 layer on both sides of the opened channel, see Figure 3-2-3 step (i)) was considered at 10 µm. The total sensing area exposed to the solution in the current design was 0.7 mm^2. The schematic of the geometry of the designed sensor is shown in Figure 3-2-2.

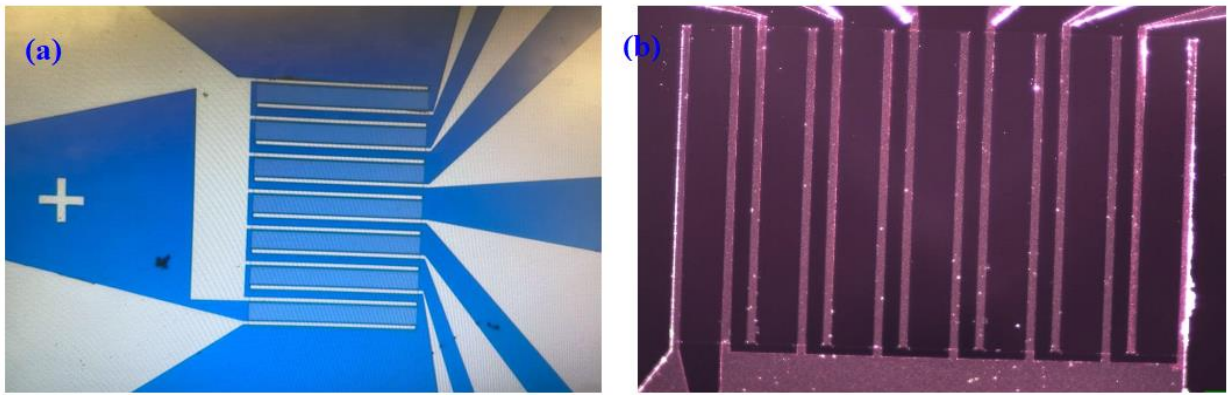


Figure 3-2- 2. Microscopic images of the designed sensor. (a) The image was taken from the prob-station camera, showing the designed sensor with channels and the common source. (b) Close-up image under the optical microscope.

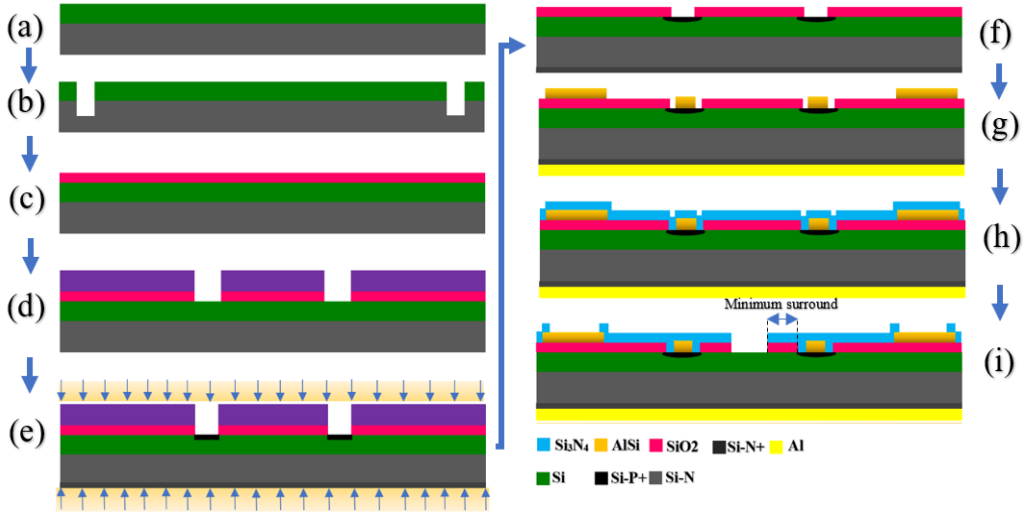


Figure 3-2- 3. Schematic of OG-FET sensor showing the main material composition of the sensor. (a) Substrate wafer (silicon <100>, 100 mm diameter, -420 +/− 25 µm thick, resistivity 0.006 to 0.02 Ohm-cm). (b) Alignment marker definition (first mask). (c) PECVD SiO2 deposition. (d) SiO_2 etching to Si layer (second mask). (e) Front- and back-side ion implantation. (f) Implantation annealing. (g) Front- and back-side metallization and annealing. (h) PECVD Si_3N_4 deposition (passivation layer). (i) Pad and channel opening.

3.2.3.3. Fabrication

The sensor fabrication was conducted through a standard microfabrication process, shown in Figure 3-2-3. The method included seven primary developing processes, as shown in Figure 3-2-3. First, a substrate wafer (silicon <100>, 100 mm diameter, -420 +/− 25 µm thick, resistivity 0.006 to 0.02 Ohm-cm) is prepared. Then, the first mask is applied to define the positions for the

alignment marker. Subsequently, the PECVD process is performed for SiO_2 deposition, followed by SiO_2 etching to the Si layer, which is the opened gate area (Figure 3-2-3). The next step is front- and back-side ion implantation, followed by implantation annealing. After this stage, the metallization process is initiated, including front and backside metallization and annealing. A thick layer of Si_3N_4 is deposited with PECVD to passivate the source and drain. The next step is to open the dielectric layers to prepare them for solution interaction with the silicon channel. The sensor layout was designed using L-Edit software. Then, the files were submitted for fabrication at Institut interdisciplinaire d'innovation technologique (3IT), Université de Sherbrooke.

3.2.4. Methods and Experiments

3.2.4.1. Measurement setup

The OG-JFET was tested with a probe station (MPI TS200-SE Probe Station) that connects the sensor to a semiconductor analyzer (Keithley 4200A-SCS Parameter Analyzer) device, as shown in Figure 3-2-4.

The probstation was connected to the sensor, as shown in Figure 3-2-4. The sensor was placed on a glass slide on the conductive copper tape to create a back gate connection. The back gate connection was soldered. To characterize the sensor, we swept the drain voltage between 0 and 10 with a negative voltage, and then the back gate was changed from 0 to 1 in steps of 0.1 V. The back gate voltage was positive to ensure the sensor operated in reverse bias conditions. However, the voltage range varied in different experiments based on the experiment's condition, but the same biasing scheme was preserved.

3.2.4.2. pH and DNA Sample Preparation

The sensor's functionality was verified with three samples: the PBS (phosphate buffer solution) with different pH, dried ssDNA, and oral neutrophil cells as the models for showing the sensor response to varying surface charges. The PBS was used as the solution, and different HCl and NaOH solutions were added to the PBS with a pH of 7.4 to create different pH solutions. The pH was measured with a pH meter. The DNA concentrations were prepared in ultrapure water solution. The solvated ssDNA molecules in ultrapure water were put on the sensor with pipetting (see Figure 3-2-4) and left to evaporate at room temperature. After evaporation of the droplet, the dried ssDNA concentration on the sensor's surface was tested.

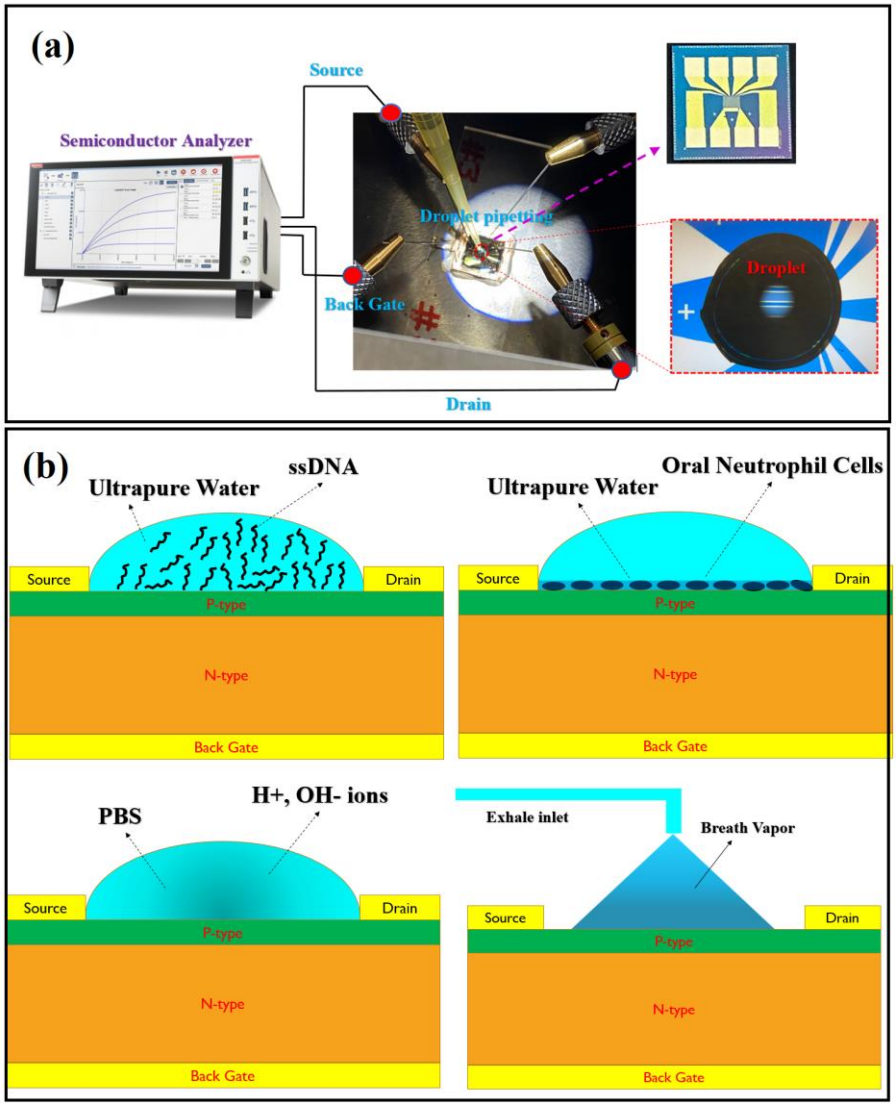


Figure 3-2- 4. The experiments were set up using a probstation and the semiconductor analyzer. (a) The probstation was connected to the semiconductors through SMU cables. The droplet containing the analyte of interest was pipetted on the sensor. The droplet volume was 2 µL. (b) Different experiments were developed to characterize sensor capability toward surface charge variation detection.

3.2.4.3. Oral Neutrophil Preparation

To prepare neutrophil samples, we advised participants to consume only water within 30 min before sample collection and to rinse their mouths with water for 30 s. Next, they were asked to wait for 2 minutes before their oral cavity was rinsed with 10 mL of saline, which was measured using the 15 mL falcon tube, and the sample was collected into the 50 mL falcon tube. After one wash, there was a 2 min wait time, and the same process was repeated five times. Then, the final sample was filtered with two different sizes of filters. It was distributed into two new 50 mL falcon tubes (25 mL in each, T1 and T2) via 40 µm filters that separated debris and cells more significant

than 40 μm. After this step, two 11 μm filters that mainly separate epithelial cells (with 20 mL syringes, 11 um white membranes) were prepared and tightened gently into the syringes. T1 and T2 were poured gently and periodically through the membranes. The process was repeated with four 15 mL falcon tubes of 1-time-filtered oral neutrophils through new syringes so that the PMNs were double-filtered. The tubes were centrifuged at 4 °C for 5 min with 2600 RPM, and the supernatant was discarded until 1 mL of the sample remained. Finally, all four samples were collected into one tube and centrifuged for 5 min at 2600 RPM and 4 °C in a microcentrifuge. To dilute the neutrophil sample, we used ultrapure water and four different concentrations were prepared such that 100% of the first, 75% of the second, 50% of the third, and 25% of the fourth solution consisted of cells. Then, each sample was cast on the sensor using a sampler.

3.2.4.4. DNA Sample Preparation

For DNA experiments, ssDNA (Sigma-Aldrich Company) was prepared with a 10.0 ± 1.0 mg ssDNA concentration in 1 mL in ultra-pure water (Sigma-Aldrich). The prepared solution was then diluted to obtain 101 ng/μL, 180 ng/μL, 270 ng/μL, 301 ng/μL, and 370 ng/μL concentrations of ssDNA. The prepared ssDNA was put on the sensor with pipetting, as shown in Figure 3-2-4.

3.2.5. Numerical Simulation of OG-JFET

The OG-JFET sensor was simulated using COMSOL Multiphysics software to obtain the transfer characteristic curves. The I-V curves and other physical information that COMSOL simulation provides enable us to understand the sensor operation better. The semiconductor module of COMSOL software was used for the finite element simulation study. To simulate the sensor, we created a 2-D model of the sensor in the model builder of COMSOL according to the size and dimensions shown in Figure 3-2-5, further explained in Table 3-2-1. There were many errors during all the development stages (see Figure 3-2-5). The errors in fabrication associated with developing the open-gate area and the wafer itself, as well as the doping-level estimations, were the primary sources of errors in the simulation. Therefore, the simulation helps estimate the fabrication errors to understand the noises associated with the possible fabrication errors.

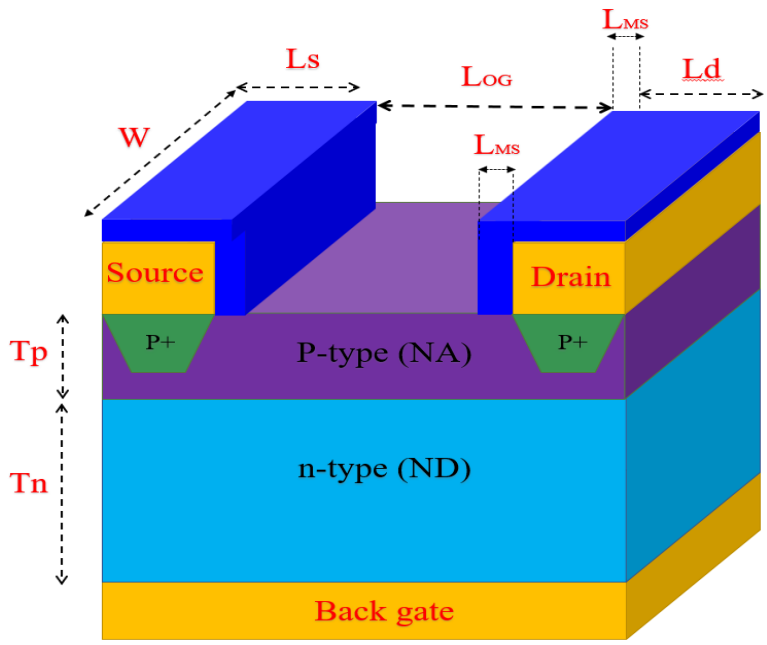


Figure 3-2- 5. Schematic of OG-FET sensor showing the main material composition of the sensor. tn >> tp and tp >> n++ in terms of thickness. The blue color is the SiO_2/Si_3N_4 layer shown in the fabrication process (see Figure 3-2-3) used for passivation.

Table 3-2-1. Design parameters are used in the simulation and fabrication of OG-JFET.

Design Parameters	Values
P-type length (L_{OG})	100 µm
P-type doping (N_A)	5×10^{15} /cm^3
P-type channel thickness (tp)	1.6 µm
Channel depth (3D, not shown)	1000 µm
N-type length	100 µm
N-type thickness (tn)	450 µm
N-type doping (N_D)	1×10^{18}/cm^3
Source/drain length (Ls, Ld) and width (W)	20 µm and 1000 µm
Source/drain implantation doping (P+)	2×10^{16}/cm^3
Source/drain minimum surround (L_{MS})	10 µm

The principal parameter values used in the simulation are presented in Table 3-2-1. However, these values were not perfectly met during the fabrication due to inherent fabrication errors. Moreover, the doping concentration and distributions in both n-type and p-type layers were not precisely preserved. The p-type layer was verified to have a resistivity of 3.0 Ohm.cm +/− 10% as an

epitaxial layer on the n-type layer as the substrate with a resistivity of 0.006 to 0.02 Ohm.cm. The n-type thickness was considered at approximately 450 μm in the simulations.

3.2.5.1. Semiconductor Simulation

The semiconductor module of COMSOL was used to simulate the OG-JFET sensor. It consists of interfaces and integrated models that can solve the non-linear equations of semiconductor devices. COMSOL software solves semiconductor equations because the energy bands are parabolic and have the same temperature for carriers and lattices. In this module, the proposed 2D geometry was meshed for numerical analysis. The following Equations (3-2-1)– (3-2-5) were solved numerically based on the applied boundary conditions in the semiconductor module of COMSOL software. Maxwell's equations, Boltzmann transport theory, and Neumann boundary conditions were employed to simulate the sensor. The basic equations used are:

$$\rho += q(p - n + N_d^{+} - N_a^{-}) \tag{3-2-1}$$

$$\nabla . J_n = -qUn \, , \nabla . J_p = -qUp \tag{3-2-2}$$

$$J_n = qn\mu_n \nabla E_c + \mu_n K_B T G \left(\frac{n}{N_c}\right) \nabla n + qnD_{n,th} \nabla \ln(T) \tag{3-2-3}$$

$$J_n = qn\mu_p \nabla E_v - \mu_p K_B T G \left(\frac{p}{N_v}\right) \nabla p - qpD_{p,th} \nabla \ln(T) \tag{3-2-4}$$

$$E_c = -(V + \chi_0) - \alpha \Delta E_g \, , E_v = -\left(V + \chi_0 + E_{g,0}\right) + (1 - \alpha)\Delta E_g \tag{3-2-5}$$

where ψ equals electrostatic potential, q indicates the elementary charge, and n and p are the electron and hole concentrations, respectively. N represents the fixed charge associated with ionized donors. In the above equations, q is the elementary charge; ε means the permittivity of the material; V is the electric potential; ND+ and NA- are ionized donor and acceptor concentrations, respectively; μn is electron mobility; μp is hole mobility; Jn is electron current density; Jp is hole current density; D is diffusion; Eg is bandgap energy; K_B is Boltzmann constant; T is temperature; and p and n are the hole and electron concentrations, respectively. Un and Up are the net electron

and hole recombination rates for all generation and recombination mechanisms. Fermi–Dirac statistics were also used to solve the probability of carriers' occupancy in existing energy levels when the system was in its thermal equilibrium. We also tested Maxwell–Boltzmann statistics, but the results were not satisfactory compared to Fermi–Dirac statistics. Both p-type and n-type channels were modeled as analytical doping with a Gaussian decay profile.

The Shockley–Read–Hall model for trap-assisted recombination was used to simulate the recombination process. The recombination process involves the trapping of an electron or hole in a defect in the material. Then, they are emitted into the valence or conduction band, reducing the number of available carriers. The energy involved in this process is released as heat.

3.2.5.2. Boundary Conditions and Meshing of Semiconductor Simulation

The boundary conditions were applied based on the OG-JFET physical structure, as presented in Figure 3-2-5. The sensors comprised three ohmic contacts in the source, drain, and back gate regions. The opened gate area and the minimum surrounds were modeled as insulated surfaces, meaning no flux in/out of this face. This face was opened to air conditions but was not considered for device simulation. The sensor included a p-n junction; thus, the continuity/heterojunction model was used at the junction interface, allowing continued quasi-fermi levels. All surrounding sides of the sensor were modeled as insulation, the same as the opened gate area. All the simulations were performed based on these assumptions of boundary conditions. The p-type channel was meshed with structured rectangular meshes, followed by the unstructured mesh for the n-type channel.

3.2.5.3. Simulation of Electrolyte Solution

The OG-JFET sensing surface is made of native oxide, which forms naturally when the silicon is exposed to the environment. When this sensing membrane is exposed to the electrolyte solution, the corresponding surface reactions (ion complexations and water molecules) create surface charges, a thin layer of charge amount that depends on the ionic strength and H+ concentration inside the solution (i.e., pH). The formed stacked layer of charges near the surface can potentially influence the surface charge density at the silicon channel in OG-JFET. Consequently, the change in pH can be modeled as interface charge variation at the opened-gate area (see Figure 3-2-5), translated as the gate's effective potential. The cascade effect of solution ions and surface charges

are frequently modeled as the source voltage depending on the pH of the solution, which can be mathematically demonstrated in Equation (6) [51–53].

$$\Psi_0 = -\log_e 10 \times \delta_w \times \frac{K_B T}{q} \times (pH - pH_{pzc}) \qquad (3\text{-}2\text{-}6)$$

In Equation (3-2-6), pH_{pzc} is the point of zero charges, q represents the charge of an electron, K_B is the Boltzman's constant, T is the temperature in Kelvin, and δ_w is $\frac{\beta}{\beta+1}$ where the β is the sensitivity parameter, i.e., $\beta = q^2 N_s \frac{\eta}{C_{eq} \times K_B T}$. In the sensitivity parameter, N_s is the surface site available of the sensing layer (here it is SiO_2) that is the property of a material (surface effect) when it is in contact with a solution [41]. For SiO_2, this N_s equals $5 \times 10^{12}/cm^2$ [53]. We can also define the η as $2 \times 10^{-(\frac{\Delta pK}{2})}$, in which the $\Delta pH = \Delta pK_b - \Delta pK_a$.

As the surface is SiO_2 (native oxide), according to the site-bonding theory, the electrolyte and oxide interaction complex can be represented as the following surface reactions. The sites for bonding oxide and the hydroxyl group can be considered S and OH in the presented responses [54]. The protonation ($Si\text{-}OH^{2+}$) and deprotonation (SO^-) species from S–OH occur due to the adsorption of ions by hydroxyl groups on the sensing layer (here, SiO_2). The following equations (3-2-7,3-2-8) describe the phenomena:

$$[S - OH_2^+] \rightleftharpoons [S - OH] + [H_s^+] \qquad (3\text{-}2\text{-}7)$$

$$[S - OH] \rightleftharpoons [S - O^-] + [H_s^+] \qquad (3\text{-}2\text{-}8)$$

On the surface of OG-JFET, when the medium is more acidic, the $[H_s^+]$ is greater; consequently, the neutral species S–OH groups will accept a proton to form acceptor type and form $SiOH^{+2}$, which leads to a positive charge effect on the outer surface of the native SiO_2 in OG-JFET, leading to an increase in the current. In the more basic solutions, the concentration of $[OH^-]$ increases to a level more than $[H^+]$, causing S–OH species to release proton and form the donor type $S - O^-$ that contributes to a more negative effect on the surface of the p-type silicon, leading to an increase in the current. For the state at which the interface charge density becomes zero, the pH is called zero charges (pH_{pzc}), which can be correlated with reaction constants in (3-2-7) and (3-2-8) with the following equations:

$$pH_{pzc} = \frac{pK_a + pK_b}{2} \quad (3\text{-}2\text{-}9)$$

$$pK_a = -\log_{10}(K_a) \quad \text{where } K_a = \frac{[S-OH] + [H_s{}^+]}{[S-OH_2{}^+]} \quad (3\text{-}2\text{-}10)$$

$$pK_b = -\log_{10}(K_b) \quad \text{where } K_b = \frac{[S-O^-] + [H_s{}^+]}{[S-OH]} \quad (3\text{-}2\text{-}11)$$

In Equations (9)–(11), K_a is the dissociation constant for acid, and K_b demonstrates the base dissociation constants. Here, we considered the $pH_{pzc} = 2$, and the pK_a and pH_b values used for pH determination on SiO_2 were 6 and −2, respectively [52–54]. Moreover, it is essential to calculate the hydrogen ion concentration at the interface of OG-JFET surface with solution (SiO_2), which is given in Equation (12) [55]:

$$[Hs^+] = 10^{-pH} \times e^{-(\frac{q\Psi_0}{KT})} \quad (3\text{-}2\text{-}12)$$

The variations in $[Hs^+]$ modulate the surface charge density, which is

$$\sigma_0 = q([S-OH_2{}^+] - [S-O^-]) \quad (3\text{-}2\text{-}13)$$

With some mathematical efforts, the following equation will result in the calculation of surface charge density:

$$\sigma_0 = qN_s\left(\frac{\frac{[Hs^+]}{Ka} - \frac{Kb}{[Hs^+]}}{\frac{[Hs^+]}{Ka} + \frac{Kb}{[Hs^+]} + 1}\right) \quad (3\text{-}2\text{-}14)$$

With the abovementioned formula, we can calculate the equivalent surface potential of each pH value, as was used in other works, and then use it as input in the COMSOL simulation.

3.2.6. Results

3.2.6.1. Sensor Functions in Dry Mode

The OG-JFET sensor has a vertical p-n junction that enables channel control through the back gate (see Figure 3-2-6). According to the structure, the sensor can be operated in two modes: reverse bias and forward bias. The reverse bias guarantees that the p–n junction is turned off; as a result, there is only a current inside the channel (p-type, see Figure 3-2-6). However, there is another mode of working for this sensor, the condition of forward bias, wherein the p–n junction is turned on if the voltage difference between the p-type and n-type junction is more than ≈0.67 V. If the voltage is higher than this value, the p–n junction is opened. The current directly flows from the back gate to the drain, which is more current than the reverse bias current. The transfer characteristics of the OG-JFET for both states of biases are shown in Figure 3-2-6.

According to Figure 3-2-6, the I–V curves for the forward bias condition demonstrate the operation of the sensor in elevated current when the p–n diode is turned on. The experiments are conducted at room temperature. According to the data, the p–n junction will be turned on at a voltage of 0.67 V for a p-type concentration of 5×10^{15} and n-type concentration of 1×10^{18}, meaning that when the Vd-Vg is equal to or higher than this value, the current will directly flow from the back gate to the drain. However, the reverse bias condition works with the current in the p-type channel, which is lower than the current in the forward bias condition. This is expected as a massive channel with an area of 10 × 10 mm and length of ≈450 μm is in front of the current from the back gate to the drain, in forward bias. The Ids-Vgs for the reverse condition are depicted in Figure 3-2-6. The graph shows a linear decay of the current versus the back-gate voltage, as shown in Figure 3-2-5. The back gate controls the space charge in the channel by which the current can be modulated. When the I-V curves were obtained from the fixture setup, the sensor was in dry condition, and there was no solution or other material. The sensor response was repeated multiple times to ensure consistency.

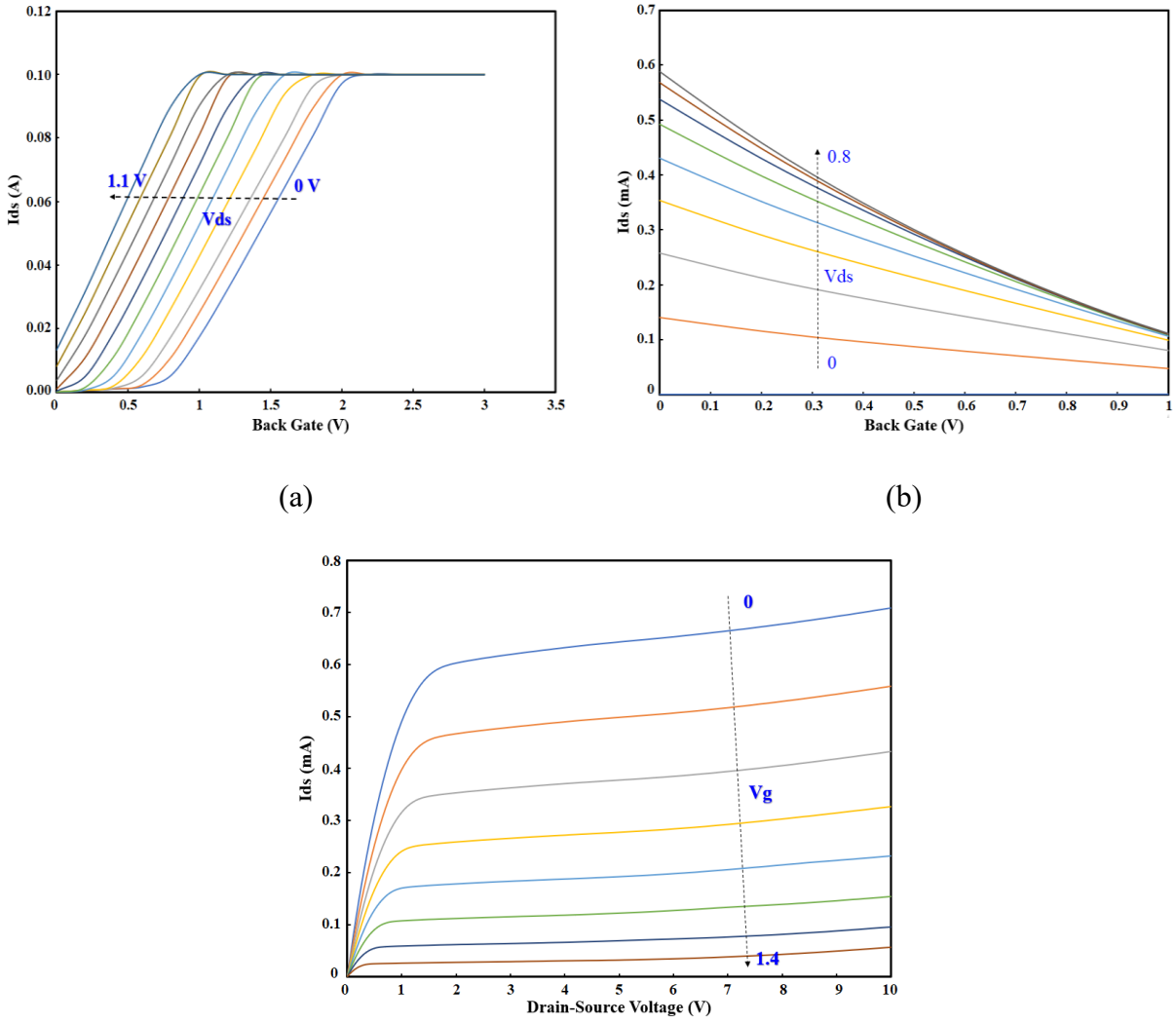
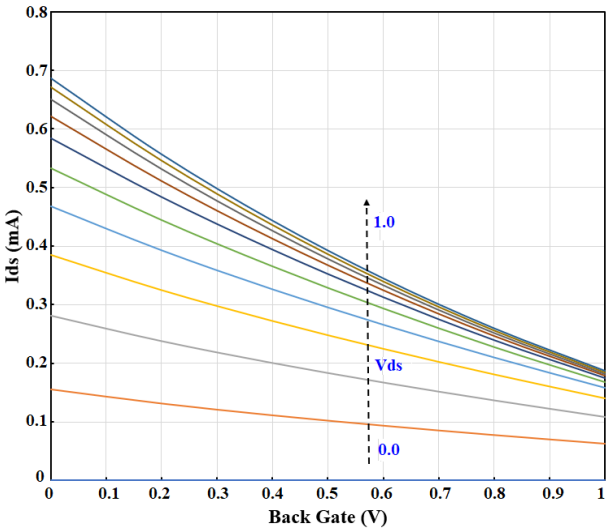


Figure 3-2- 6. The current-voltage curves of the OG-JFET sensor for two bias conditions, forward and reverse. (a) Ids-Vgs of forwarding bias. (b) Ids-Vgs of reverse bias condition. (c) Ids-Vds curve for reverse bias condition (steps: 0.2 V).

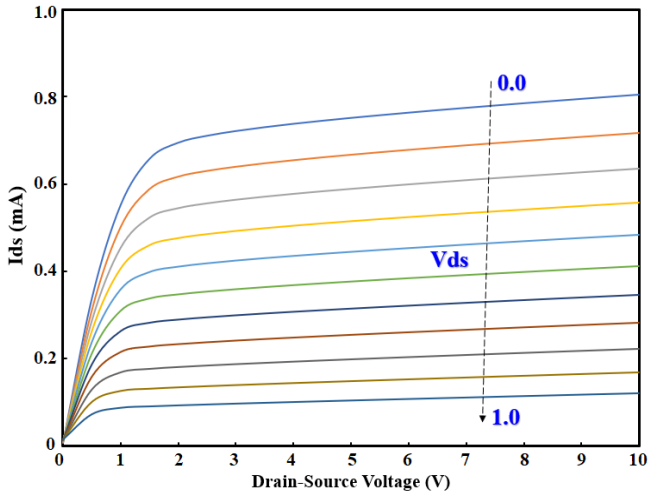
The tests were conducted in the fixture setup (the microfluid is attached). The sensor's stable function represents the sensor's good working condition, showing good alignments.

The structure is new; thus, the sensor's operation needs to be validated with simulation to gain insight into the physics of the sensor. The COMSOL Multiphysics software was used for the semiconductor analysis of OG-JFET. There are inherent non-idealities associated with the sensor fabrication during the standard fabrication procedures shown in Figure 3-2-3, leading to simulation errors. However, the user-friendly features of COMSOL software enable the sensor to perform multiphysics simulations to take care of all physical phenomena on the sensing surface, such as

molecular detection and solution simulation. The simulation results (see Figure 3-2-7) ideally represent the sensor response trend, which can be used to design the sensor for other geometries before fabrication.



(**a**)



(**b**)

Figure 3-2- 7. Transfer characteristics of OG-JFET sensor derived from COMSOL simulations. (a) Reverse-bias Ids-Vgs. (b) Reversed-bias Ids-Vds.

3.2.6.2. Sensor Response to Surface Charge Variations

The OG-JFET was tested in the probstation shown in Figure 3-2-4 to demonstrate its functionality in detecting surface charge. The sensor was connected to a semiconductor analyzer, and the liquid with a specific load of ssDNA, pH, and oral neutrophil was loaded on the sensor in a droplet form, as shown in Figure 3-2-4. The fluid was not in continuous mode as it changed the surface charge concentrations due to the motion of fluid in the sensing area; therefore, considerations were taken not to mitigate the droplet liquid condition in the sensing area that creates turbulences inside the charge layers on the sensor.

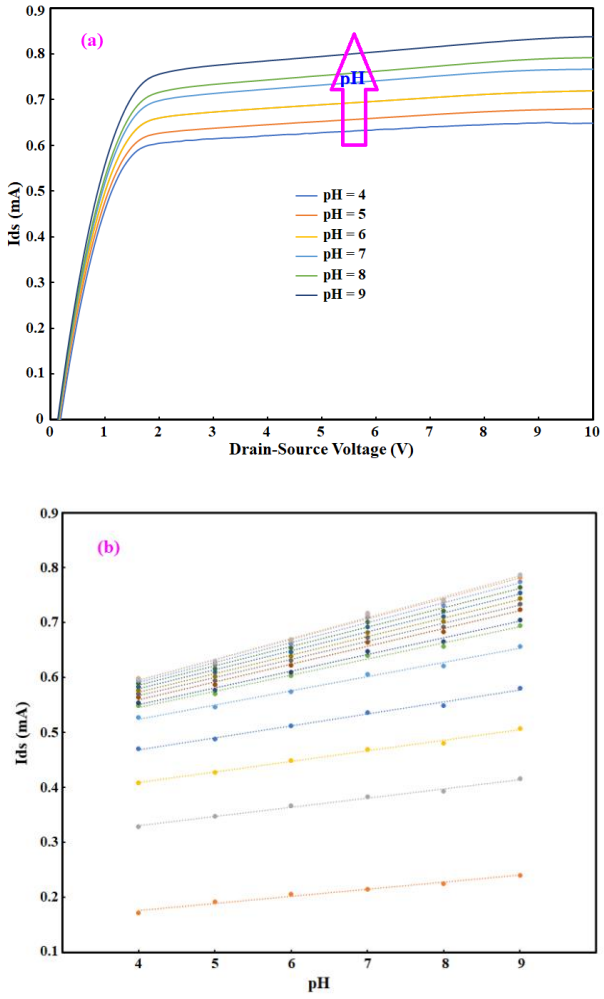


Figure 3-2- 8. Drain-source voltage graphs for different pH values for OG-JFET at Vg = 0. (**a**) Ids-Vds curve for different pH values. (**b**) The current sensitivity for different values of Vds.

To model the surface charge variations, we used phosphate buffer solution (PBS) as the primary fluid with the extra addition of HCL and NaOH to create different concentrations of ion charge in

the solution. With PBS titration, the solution samples were prepared and then loaded onto the sensor with a pipette. After testing a specific solution with a known pH, the sensor was rinsed with DI water to prepare it for the next pH solution. Before every try with the pH solution, the sensor response was measured to ensure it returned to the baseline condition. Figure 3-2-8 demonstrates the sensor response to the pH solution. We obtained the current-voltage curves from the same device to measure the baseline. Then, we determined the current difference to ensure a return to the same current in a specific back gate voltage.

Figure 3-2-8 demonstrates the sensor response when the concentration of hydrogen ions was changed in the microfluidic channel. The variations in the concentration of H+ and OH- were generated by producing different pH solutions. This is an excellent way to characterize the sensor functionality in response to the ion/species concentration in the solution. As Figure 3-2-8-a shows, the curves for all pH values were distinctively separated in the saturation region, which shows the effectiveness of OG-JFET in detecting the change in ion concentrations. The current sensitivity analysis was performed on the sensor, shown in Figure 3-2-8 (b). The current sensitivity was measured for different Vds values: 0.5 V, 0.8 V, 1.0 V, 1.5 V, 2.0 V, 3 V, 4 V, 5 V, 6 V, 7 V, 8 V, 9 V, and 10 V, as shown in Figure 3-2-7 from the lowest curve to the last one. The current sensitivity for these values of Vds changed from 2.0×10^{-5} A/pH at low Vds voltages to 4.0×10^{-5} A/pH in higher Vds in the saturation region. Figure 3-2-8 (b) shows that in the saturation region, the current sensitivity was almost the same and more significant than the ohmic region (linear part of Ids-Vds). This current sensitivity enhancement dependency on the Vds values should be considered when designing sensors for specific applications.

A back gate in the structure makes the sensing process more straightforward than when there is a reference electrode in the solution. We conducted pH tests to show the sensor's performance in the back-gate structure. The Ids-Vgs variations are plotted in Figure 3-2-9, demonstrating the effect of pH variations on the Ids-Vgs (drain-source current versus back gate voltage). As can be seen, the pH increment enhanced the current in the p-type channel. The sensor was biased in reverse mode, meaning there was no current in the p–n junction. The sensor showed a 51.26 mV/pH sensitivity, as shown in Figure 3-2-9. To obtain the voltage sensitivity of the device, we plotted the Ids-Vgs; then, the reference current was defined for voltage sensitivity analysis. As shown in Figure 3-2-9, the voltage required to be applied on the back gate to maintain a constant current of 0.5 mA in the

main p-type channel was defined as the reference voltage. By plotting that voltage versus the pH values, we were able to calculate the voltage sensitivity, which is the slope of the linear fit.

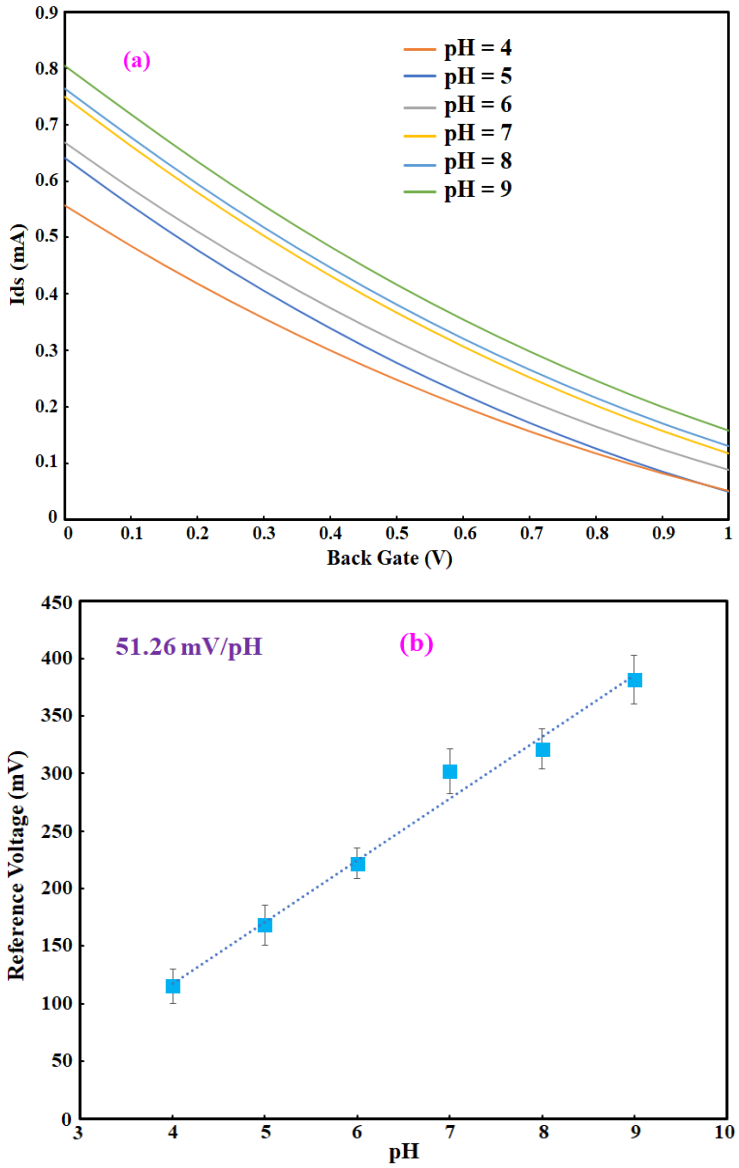


Figure 3-2- 9. Drain-source voltage graphs for different pH values for OG-JFET. (**a**) Ids-Vgs curve for different pH solutions from pH = 4 to pH = 9. (**b**) The voltage sensitivity relative to the back gate reference voltage.

The sensor (OG-JFET) showed a super-Nernstian pH sensitivity of 51.26 mV/pH, which is more than the limit of this value (<40 mV/pH) for SiO_2 sensing membrane in previous research works on ISFET [56]. Despite this range of pH sensitivity for ISFETs with SiO_2, a sensitivity of 47 mV/pH (close to our sensitivity) was reported for silicon nanowire-based ISFET with SiO_2 sensing membrane, which is an example of sensitivity more than the reported limit for SiO_2 (≈ 40 mV/pH) [57]. The linearity of the pH sensitivity is another vital point to note. The reported curves in the

literature are not entirely linear for SiO_2, but some cases have revealed linear responses, such as [57].

More discussion on the pH sensitivity is found in Section 6[1].

3.2.6.3. Simulation of Surface Charge Effects

To better understand the sensor response to pH change as a model of surface charge modulation, we conducted a simulation in which the pH effects on the sensor drain-source current were simulated. Based on modeling, the pH effect was assessed by measuring the effective surface charge due to the existence of ions and solution on the oxide surface. The pH equivalent surface charge was calculated and is shown in Figure 3-2-10.

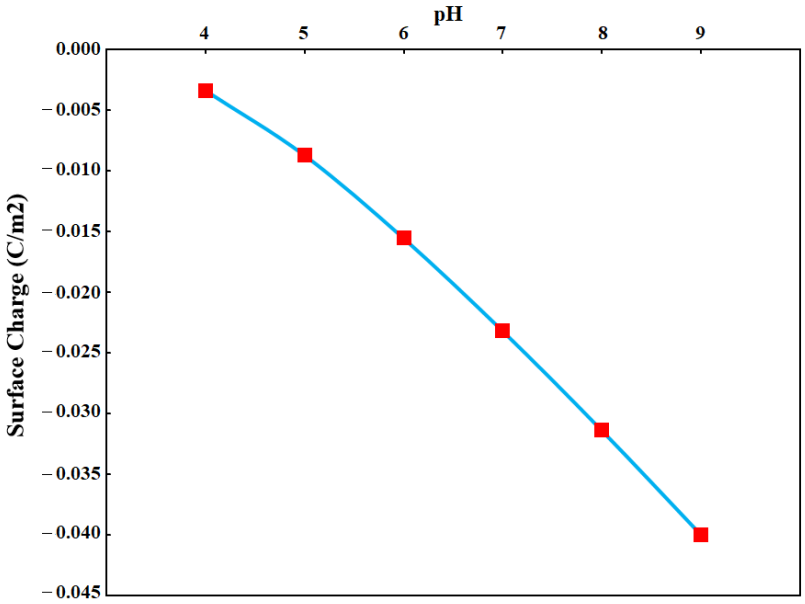


Figure 3-2- 10. The estimated native oxide of OG-JFET surface charge is equivalent to pH.

The surface charge equivalent to pH was calculated using site bonding modelling. The surface charges were then used in COMSOL to estimate the OG-JFET sensor's response to pH variations. The model allows us to gain insight into the physics of the OG-JFET sensor in response to surface charge variations.

Figure 3-2-11 demonstrates the effect of the pH variations on the OG-JFET. The COMSOL simulation yields the trend of pH variations that agree with the experiment. According to the experiment, the surface net charge will become more negative as the pH increases. As a result, the

[1] Section 3.2.7

hole conduction in p-type semiconductors will increase due to this effect. The graph was measured in a constant back gate (here, Vg = 0), showing the effectiveness of COMSOL software in estimating the OG-JFET response trend when different surface charges are applied. This implies that COMSOL can potentially be used for multiphysics problems and specific multiscale designs of biosensors. However, the COMSOL simulations come with approximately 11% error, mainly due to the non-idealities and errors in the fabrication process and the physical model of pH surface charge that we used to estimate the surface charge values on the oxide region. Another possible source of error might be the model's estimation of the oxide site density, which is different from the actual concentration in the experiment.

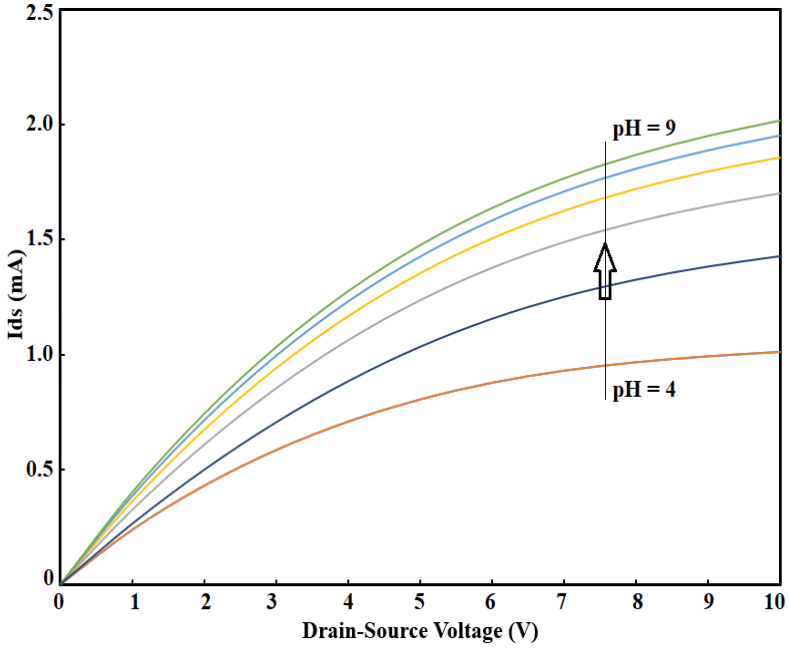
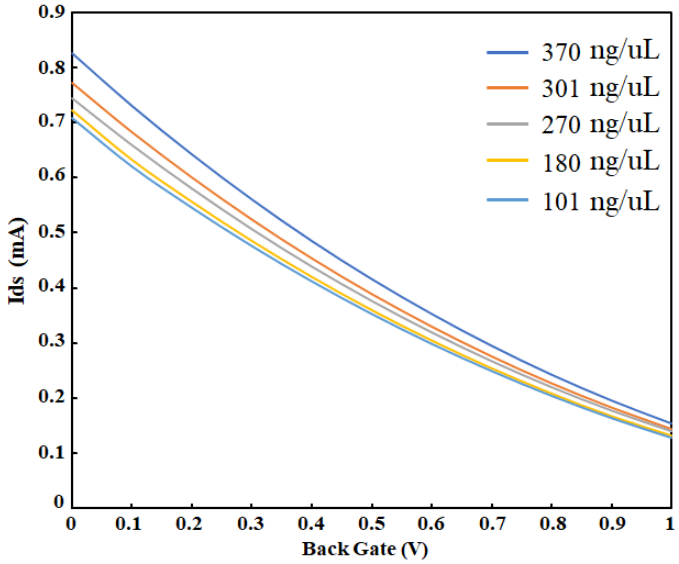


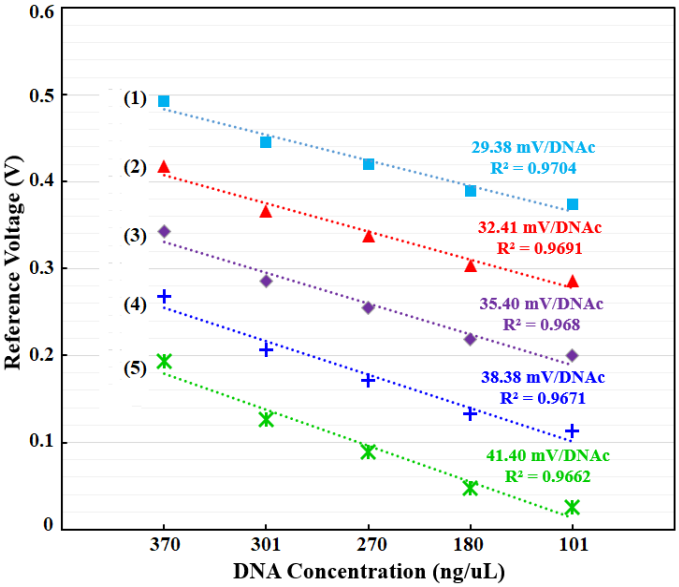
Figure 3-2- 11. COMSOL simulation results of the pH variations effect on the sensor results.

3.2.6.4. Sensor Response to DNA Concentration

Single-strand DNA (ssDNA) molecules were prepared with different concentrations in ultrapure water and tested on the OG-JFET to test sensor response to known charged biomolecules. A droplet of ssDNA solution in ultrapure water was placed on the sensing area, and the sensor drain-source current was monitored. The ssDNA molecules are negatively charged; due to the accumulation of negative charge on the p-type layer, the current was expected to increase in the same way that increasing pH affects the sensor.



(a)



(b)

Figure 3-2- 12. Sensor response to single-strand DNA concentration. (a) Ids-Vgs curve for different concentrations of ssDNA (370 ng/uL, 301 ng/uL, 270 ng/uL, 180 ng/uL, 101 ng/uL). (b) Voltage sensitivity results of OG-JFET response to ssDNA concentration at different reference currents of (1) 0.45 mA, (2) 0.50 mA, (3) 0.55 mA, (4) 0.60 mA, and (5) 0.65 mA.

Negative charge accumulation causes the attraction of holes in the channel, which leads to current enhancement. The Ids-Vgs diagram was recorded in each concentration of ssDNA in a constant Vds of 10 V, as demonstrated in Figure 3-2-12. The experiments were conducted ten times, and the graph shows the average response of the sensor in a constant Vds. The experiments were all performed at room temperature. As the ssDNA molecules were in ultrapure water, it was

guaranteed that no charge existed in the solution, and the sensor gate was only affected by the ssDNA molecules' charge.

Figure 3-2-12 (a) demonstrates the Ids-Vgs curves of OG-JFET when dried ssDNA was placed on the sensor. The droplet containing ssDNA was left to evaporate, and after evaporation, the sensor response was recorded. A 2 µL droplet was placed on top of the sensor, which covered all the sensing areas, as shown in Figure 3-2-4. The sensing area was 0.7 mm^2, large enough to accommodate the droplet. Therefore, all DNA molecules were expected to cover the sensing area after drying. As the sensor is sensitive to light, it was placed entirely in darkness in the probstation cage during the experiments. Figure 3-2-12 (b) demonstrates the voltage sensitivity curves of the sensor to ssDNA molecules. A sensitivity of 41.40 mV/DNAc[1] was determined based on the characterization. However, the sensitivity was analyzed for other drain current values, as shown in Figure 3-2-11. For drain-source currents of 0.45, 0.50, 0.55, 0.60, and 0.65 mA, the sensitivities were determined to be 29.38, 32.41, 35.40, 38.38, and 41.40 mV/DNAc. The DNAc is the concentration of the DNA unit, which here was ng/µL.

3.2.6.5. Direct Human Exhalation Test

We conducted the human exhalation test to test the effectiveness of OG-JFET in measuring surface wetness upon applying vapor. As shown in Figure 3-2-13, when the sensor sensed the exhalation's condensation due to the creation of tiny droplets of water due to the condensation of the vapor, the sensor surface charge changed suddenly. The change from 0.5 to 2.5 mA occurred in <3 s, which shows the significant sensitivity of the sensor towards the sudden surface charge variation.

[1] DNA Concentration: DNAc

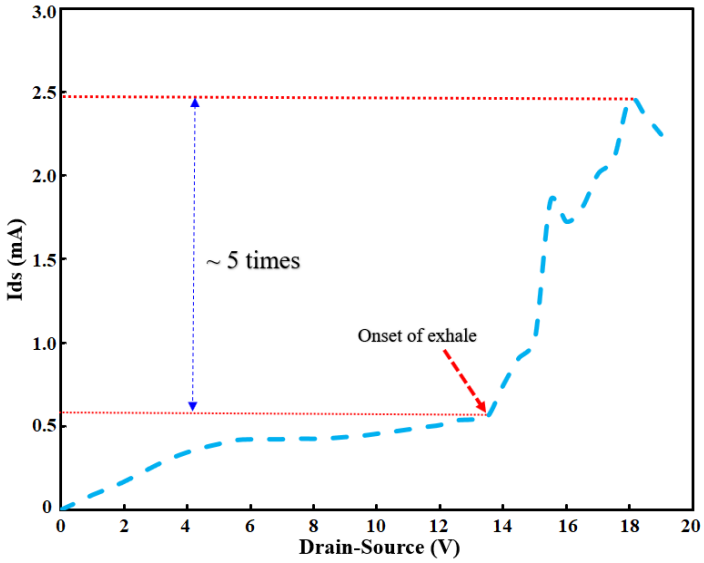


Figure 3-2- 13. The result of the human exhalation test on the OG-JFET.

A tube was used to direct the exhalation on the sensor, which caused the rapid change in the sensor signal (see Figure 3-2-4). This simple experiment was conducted to demonstrate the application of this sensor for charge analysis of human exhalation. The ≈ 5 times increase in drain-source current showed the charge effects on enhancing sensor response.

3.2.6.6. Sensor Response to Oral Neutrophils

After preparing the cell solutions using ultrapure water, we cast 2 µL of the samples on the sensing region with a sampler. The sensor's surface was subsequently washed with isopropanol alcohol (IPA) to eliminate the remnants from the previous test. This step is necessary to ensure the sensor returns to its initial condition before each test. For this purpose, 2 µL of IPA was cast on the sensing region of the sensor and sucked to remove the remnants. After repeating this process three times, we left the sensor to dry. Next, 2 µL of the second sample was cast on the sensor, and the current of the drain-source was recorded. Like the increase of pH and ssDNA concentration, negatively charged neutrophil cells resulted in the accumulation of holes in the channel, which caused an enhancement in the current. Figure 3-2-14 represents the sensor response to different concentrations of cell solutions. The curves for each concentration can be differentiated clearly from the others, which confirms the capability of OG-JFET in distinguishing different cell levels. The current sensitivity analysis was performed on the sensor for different Vds values: 1 V, 1.5 V, 2 V, 2.5 V, 3 V, 3.5 V, and 4 V. Cell tests were performed using the back gate of the sensor to examine its proficiency. The variations of Ids were recorded in different Vgs. As can be inferred

from Figure 3-2-14, the increase in the concentration enhanced the p-type channel's current. The experiments were all conducted at room temperature. As the cells were in ultrapure water, it was guaranteed that no charge existed in the solution, and the sensor gate was only affected by the neutrophil cells' charge.

To examine the repeatability of the device, we conducted the test three times. The result of the analysis can be seen in Figure 3-2-15. It demonstrates that increasing the concentration of the cells in the solution increases electric current. Almost all three trials followed this trend, which showed that the sensors were responsive, functional, and repeatable. However, its sensitivity could be further improved by decreasing the incidence of some inevitable situations. There were two possible reasons for the low preciseness of the device. The concentration of cells can vary due to the poor uniformity of the cell distribution in the sample. A high precipitation rate increases the probability of error while sampling and sets the stage for imprecise sample casting. Furthermore, the location of the cells in the sensing region is critical since it is impossible to visualize cells on the surface. Therefore, we cannot give an exact estimate of their final location (see Figure 3-2-16). They might be in a region that cannot be sensed, so the sensitivity decreases. It is noteworthy that neutrophil cells have a size of 9–15 μm, whereas the DNA molecules are between 2.2 and 2.6 nm. This fact results in the low charge density in neutrophils compared to DNA. This means many negatively charged cells are needed to accumulate holes in the sensor's sensing region and trigger a response.

The Debye length plays a vital role in charge detection in BioFET sensors. In the experiment of oral neutrophil cells, the cells were in ultrapure water with low ion concentration, causing a higher Debye length for detection of biomolecular charge due to the cells' surface charge. Furthermore, for the ssDNA molecules, sensing is based on the charge effects due to the binding of ssDNA with silicon oxide. The oxide charging mechanism is unlike the solution-based detection in BioFETs in which Debye length plays an important role. The charge of ssDNA in dry mode requires further theoretical and experimental analysis. For the PBS (1X) solution, the Debye length is expected to be between 0.7 and 2.2 nm in biological solution [58]. Here, as we had the native solution dioxide with PBS, we expected that such a range of Debye length would exist.

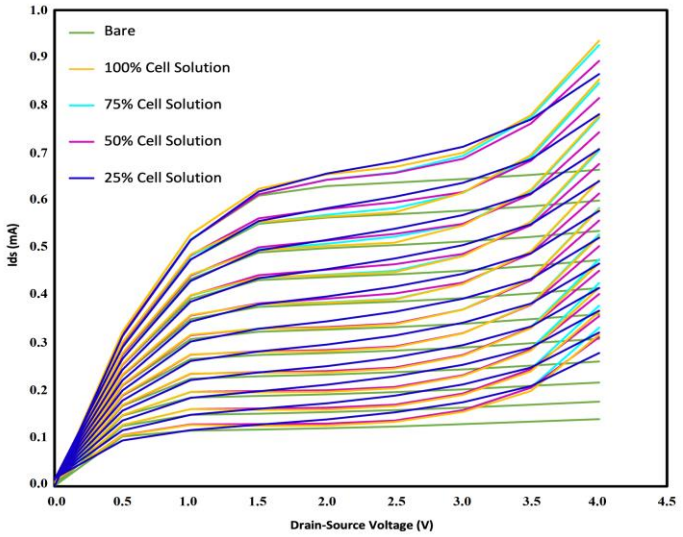


Figure 3-2- 14. The sensor responds to different concentrations of cell solutions in comparison to bare conditions.

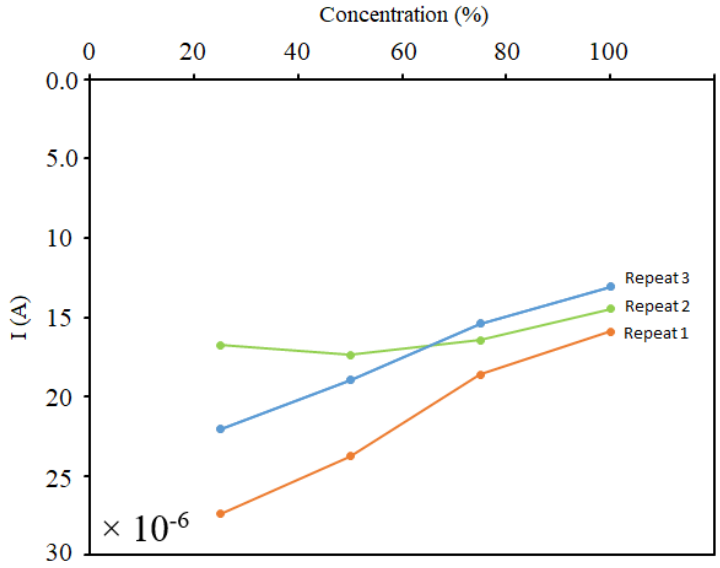


Figure 3-2- 15. Analysis results of three repeats of testing current variations in different concentrations of neutrophils.

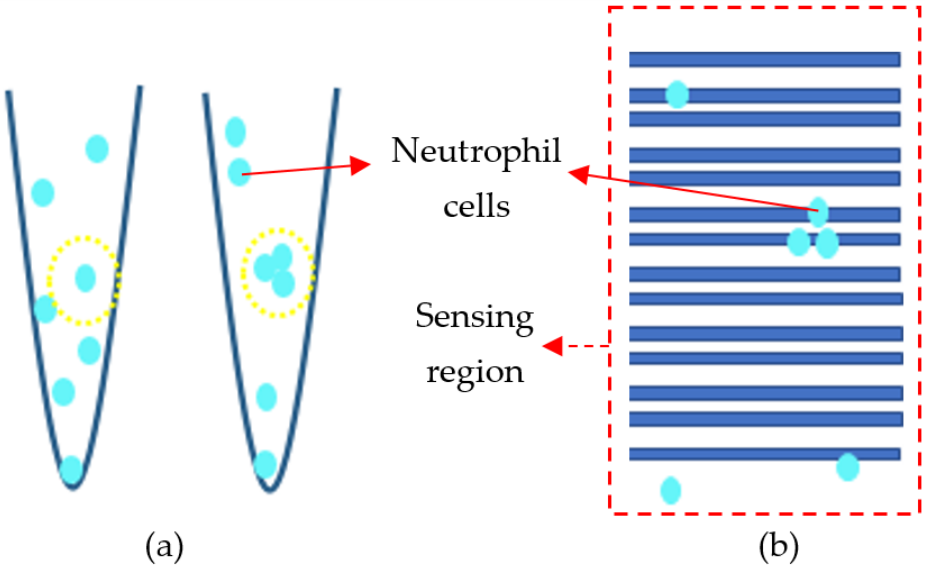


Figure 3-2- 16. Nonidealities in neutrophil measurement: (**a**) non-uniformity of the cell distribution in the sample and (**b**) non-uniformity of cells cast on the surface of the sensor.

3.2.7. Discussion

The OG-JFET sensor was fabricated and tested with pH solution, ssDNA molecules in dry mode, oral neutrophil cells, and exhalation moisture to demonstrate its capability to sense surface charge variations. In the pH experiments, it was interesting that the sensor indicated a high sensitivity (super-Nernstian region) of 51.26 mV/pH for the native silicon dioxide sensing layer in the open-gate sensing area. In previously reported works for silicon dioxide, the pH sensitivity was <40 mV/pH [59,60]. However, the sensitivity of SiO_2 was reported to be 47 mV/pH in [57], showing a close sensitivity to the OG-JFET pH sensitivity in this work. The native oxide naturally grows on silicon; however, the environmental condition affects its growth, thickness, and distribution over time. It has been proven that exposure of silicon to air causes native oxide formation with a thickness of ≈2 to ≈10 Å for silicon at room temperature [61]. The OG-JFET is exposed to air after fabrication and in the shipping process; therefore, based on the precise analysis of Morita et al. [61], it is expected to have a native oxide layer with a certain thickness in the opened-gate area (exposure of silicon to air) of OG-JFET. The study [61] offers a model for forming native oxide when silicon is exposed to air, suggesting the existence of oxide sites that set the stage for ion complexation and pH sensitivity [61]. However, the distribution of these available sites on the outermost oxide layer is not as uniform as a deposited layer of SiO_2 in other ISFETs, which might

have affected the sensor's sensitivity. Further studies are required for surface oxide site bond analysis of OG-JFET and its distribution throughout the sensing area for a better understanding of surface effects on the comparatively higher sensitivity of OG-JFET.

The sensor was tested with dried ssDNA molecules. Dry ssDNA mass monitoring is essential for developing next-generation DNA-based data storage platforms in digital microfluidics [45]. In this study, the ssDNA molecule solution was left to dry in the sensing area. The main mechanisms of ssDNA attachment on the surface of SiO_2 are the hydrophobic interaction and phosphate–silanol binding that occurs despite the negativity of ssDNA and the negative surface charge of SiO_2. The ssDNA concentrations were prepared in ultrapure water, cast on the sensor, and left to dry. In this condition, the ssDNA created the hydrophobic and silanol–phosphate binding, leading to the attachment of ssDNA on the OG-JFET open-gate area. The bonding led to an extra negative charge on the skinny oxide layer, increasing the current. While experiments showed the current enhancement due to the binding of ssDNA and native SiO_2, more in-depth theoretical experiments are required to understand the surface charge of oxides when dry DNA is placed on its surface and the resultant charge profile of DNA.

In another part of the study, oral neutrophil cells were cast on the sensor. The cell concentrations were prepared in ultrapure water, which ensured the existence of oral neutrophils in the sensor. Previous studies have demonstrated the negative overall charge densities on neutrophil cells [48,49]. Some research studies state that neutrophil cells have a negative surface charge. For example, Marco et al. [49] investigated the effect of changes in the composition of membrane phospholipids on the net cytoplasmic membrane surface charge. They successfully demonstrated that the combination of PS, PIP2, and PIP3 in the membrane resulted in a high negative charge at the plasma membrane of neutrophils. In another study, it was shown that the negative surface charge of the neutrophil cells decreased when incubated with degranulating stimuli. They also reported that the immature neutrophils produced in the bone marrow are negatively charged. However, this charge decreases by degranulation and cell maturation [59]. The interaction of the surface negatively charged membrane of these cells probably causes an increment in the negativity of the surface, contributing to the enhancement in the hole current in the p-type conductive layer of the sensor.

3.2.8. Conclusions

A new field-effect transistor biosensor is introduced in this work for life science applications from biomolecular to biological cell analysis. The advantage of OG-JFET is that it offers control of the channel conduction through a back gate, eliminating the need for a bulky reference electrode in the solution. Moreover, the sensor provides a wide sensing area on top of the sensing channel without an oxide layer, enabling a more accessible sample introduction and fluidic integration as bulky reference electrodes frequently used in the other in the solution make the integration significantly simpler for developing complex lab-on-a-chip designs as an integrated biosensing element. The sensor is operated at a low voltage (<0.5 V) of the back gate, a low-voltage device for developing remote biosensing applications. Furthermore, the mass production capability promises this technology for many biosensing applications for the biosensor community.

To demonstrate the sensor functionality in terms of response to the change in surface charge, we tested the sensor with pH solution, ssDNA molecules, oral cell neutrophils, and human exhalation vapor as a model for solution charge biomolecule, cell detection, and moisture detection, respectively. We calculated a sensitivity of 51.26 mV/pH, 41.4 mV/ssDNAc, and 0.15 mA/%-cell for ion solution, dried ssDNA, and oral neutrophil cell detection, respectively. Moreover, we have shown that the sensor was sensitive to the human exhalation-generated moisture with five times increment in the source-drain current upon exposure to the exhalation.

Furthermore, COMSOL simulation modeling was also provided for the multiphysics simulation of OG-JFET to ensure the sensor's sensing mechanism was working toward surface charge detection. The simulation model validated the correctness of experimental curves. The resultant surface charge of pH solutions was calculated and applied in the COMSOL Multiphysics simulation to estimate the trend of sensor response to the pH solution. The model showed an increment in the reaction of the p-type channel to an increment in pH. However, the introduction can be extended in future works to model more complex surface interactions for the multiscale simulation of OG-JFET.

Based on the successful experiments of OG-JFET with pH solution, oral neutrophils, and ssDNA biomolecules, we put forward this technology as a new mass-producible BioFET sensor for the biosensing community.

Author Contributions: Methodology, simulation, validation, investigation, writing—original draft preparation, A.P.[1]; conducting experiments, data analysis, writing—original draft preparation, writing Sections 3.3 and 5.6[2], D.S.[3]; conceptualization, methodology, writing—review and editing, supervision, project administration, funding acquisition, E.G.-Z.[4]; All authors have read and agreed to the published version of the manuscript.

Funding: This research received no external funding

Institutional Review Board Statement: This research received ethics review and approval by the Human Participants Review Sub-Committee of York University (Canada, Toronto, M3J1P3) and University's Ethics Review Board (No: STU 2020-146).

Informed Consent Statement: Informed consent was obtained from all subjects involved in the study.

Data Availability Statement:

Acknowledgments: We acknowledge the support of Mitacs and CMC microsystem for financial and technical assistance. We would also like to thank Morteza Ghafar-Zadeh for the DNA sample preparation related to Section 5.4[5].

Conflicts of Interest: The authors declare no conflict of interest.

3.2.9. References

[1] Vu, C.-A.; Chen, W.-Y. Field-Effect Transistor Biosensors for Biomedical Applications: Recent Advances and Future Prospects. Sensors 2019, 19, 4214. https://doi.org/10.3390/s19194214.

[2] Panahi, A.; Sadighbayan, D.; Forouhi, S.; Ghafar-Zadeh, E. Recent Advances of Field-Effect Transistor Technology for Infectious Diseases. Biosensors 2021, 11, 103. https://doi.org/10.3390/bios11040103.

[3] Cho, S.-K.; Cho, W.-J. Highly Sensitive and Transparent Urea-EnFET Based Point-of-Care Diagnostic Test Sensor with a Triple-Gate a-IGZO TFT. Sensors 2021, 21, 4748. https://doi.org/10.3390/s21144748.

[1] Abbas Panahi
[2] Sections 3.2.4.3 and 3.2.5.9 in this thesis format
[3] Deniz Sadighbayan
[4] Ebrahim Ghafar-Zadeh
[5] Section 3.2.4.4

[4] Cho, S.K.; Cho, W.J. Ultra-high sensitivity pH-sensors using silicon nanowire channel dual-gate field-effect transistors fabricated by electrospun polyvinylpyrrolidone nanofibers pattern template transfer. Sens. Actuators B Chem. 2021, 326, 128835.

[5] Garcia-Cordero, E.; Bellando, F.; Zhang, J.; Wildhaber, F.; Longo, J.; Guerin, H.; Ionescu, A.M. Three-dimensional integrated ultra-low-volume passive microfluidics with ion-sensitive field-effect transistors for multiparameter wearable sweat analyzers. ACS Nano 2018, 12, 12646–12656.

[6] Zhang, J.; Rupakula, M.; Bellando, F.; Garcia Cordero, E.; Longo, J.; Wildhaber, F.; Herment, G.; Guerin, H.; Ionescu, A.M. Sweat biomarker sensor incorporating picowatt, three-dimensional extended metal gate ion sensitive field effect transistors. ACS Sens. 2019, 4, 2039–2047.

[7] Ma, S.; Lee, Y.K.; Zhang, A.; Li, X. Label-free detection of Cordyceps sinensis using dual-gate nanoribbon-based ion-sensitive field-effect transistor biosensor. Sens. Actuators B Chem. 2018, 264, 344–352.

[8] Schuck, A.; Kim, H.E.; Jung, K.-M.; Hasenkamp, W.; Kim, Y.-S. Monitoring the hemostasis process through the electrical characteristics of a graphene-based field-effect transistor. Biosens. Bioelectron. 2020, 157, 112167.

[9] Lee, S.; Jin, J.; Baek, J.; Lee, J.; Chae, H. Readout Integrated Circuit for Small-Sized and Low-Power Gas Sensor Based on HEMT Device. Sensors 2021, 21, 5637. https://doi.org/10.3390/s21165637.

[10] Feng, P.; Shao, F.; Shi, Y.; Wan, Q. Gas Sensors Based on Semiconducting Nanowire Field-Effect Transistors. Sensors 2014, 14, 17406–17429. https://doi.org/10.3390/s140917406.

[11] Mougkogiannis, P.; Turner, M.; Persaud, K. Amine Detection Using Organic Field Effect Transistor Gas Sensors. Sensors 2021, 21, 13. https://doi.org/10.3390/s21010013.

[12] Mirsian, S.; Khodadadian, A.; Hedayati, M.; Manzour-Ol-Ajdad, A.; Kalantarinejad, R.; Heitzinger, C. A new method for selective functionalization of silicon nanowire sensors and Bayesian inversion for its parameters. Biosens. Bioelectron. 2019, 142, 111527.

[13] Ivanov, Y.; Pleshakova, T.; Malsagova, K.; Kurbatov, L.; Popov, V.; Glukhov, A.; Smirnov, A.; Enikeev, D.; Potoldykova, N.; Alekseev, B.; et al. Detection of Marker miRNAs, Associated with Prostate Cancer, in Plasma Using SOI-NW Biosensor in Direct and Inversion Modes. Sensors 2019, 19, 5248.

[14] Kim, H.E.; Schuck, A.; Lee, J.H.; Kim, Y.-S. Solution-gated graphene field effect transistor for TP53 DNA sensor with coplanar electrode array. Sens. Actuators B Chem. 2019, 291, 96–101.

[15] Yao, X.; Zhang, Y.; Jin, W.; Hu, Y.; Cui, Y. Carbon Nanotube Field-Effect Transistor-Based Chemical and Biological Sensors. Sensors 2021, 21, 995.

[16] Dorfman, K.D.; Adrahtas, D.Z.; Thomas, M.S.; Frisbie, C.D. Microfluidic opportunities in printed electrolyte-gated transistor biosensors. Biomicrofluidics 2020, 14, 011301.

[17] Neuper, F.; Chandresh, A.; Singaraju, S.A.; Aghassi-Hagmann, J.; Hahn, H.; Breitung, B. Tailoring threshold voltages of printed electrolyte-gated field-effect transistors by chromium doping of indium oxide channels. ACS Omega 2019, 4, 20579–20585.

[18] Huang, Q.; Lin, X.; Tong, L.; Tong, Q.-X. Graphene quantum dots/multiwalled carbon nanotubes composite-based electrochemical sensor for detecting dopamine release from living cells. ACS Sustain. Chem. Eng. 2020, 8, 1644–1650.

[19] Jin, B.; Lee, G.-Y.; Park, C.; Kim, D.; Choi, W.; Yoo, J.-W.; Pyun, J.-C.; Lee, J.-S. Electrical Characteristics and pH Response of a Parylene-H Sensing Membrane in a Si-Nanonet Ion-Sensitive Field-Effect Transistor. Sensors 2018, 18, 3892.

[20] Ambhorkar, P.; Wang, Z.; Ko, H.; Lee, S.; Koo, K.I.; Kim, K.; Cho, D.I.D. Nanowire-Based Biosensors: From Growth to Applications. Micromachines 2018, 9, 679.

[21] Rothberg, J.M.; Hinz, W.; Rearick, T.M.; Schultz, J.; Mileski, W.; Davey, M.; Leamon, J.H.; Johnson, K.; Milgrew, M.J.; Edwards, M.; et al. An integrated semiconductor device enabling non-optical genome sequencing. Nature 2011, 475, 348–352.

[22] Toumazou, C.; Shepherd, L.M.; Reed, S.C.; Chen, G.I.; Patel, A.; Garner, D.M.; Wang, C.-J.A.; Ou, C.-P.; Amin-Desai, K.; Athanasiou, P.; et al. Simultaneous DNA amplification and detection using a pH-sensing semiconductor system. Nat. Methods 2013, 10, 641–646.

[23] Sun, P.; Cong, Y.; Xu, M.; Si, H.; Zhao, D.; Wu, D. An ISFET Microarray Sensor System for Detecting the DNA Base Pairing. Micromachines 2021, 12, 731. https://doi.org/10.3390/mi12070731.

[24] Sung, D.; Koo, J. A review of BioFET's basic principles and materials for biomedical applications. Biomed. Eng. Lett. 2021, 11, 85–96. https://doi.org/10.1007/s13534-021-00187-8.

[25] Lowe, B.M.; Sun, K.; Zeimpekis, I.; Skylaris, C.K.; Green, N.G. Field-effect sensors—from pH sensing to biosensing: Sensitivity enhancement using streptavidin-biotin as a model system. Analyst 2017, 142, 4173–4200. https://doi.org/10.1039/c7an00455a.

[26] Zhao, D.; Zhang, J.; Zhang, J.; Xu, M.; Wu, D. A Platinum Reference Electrode for Ion-Sensitive Field-Effect Transistor. IEEE Sens. J. 2019, 19, 2003–2008.

[27] Guth, U.; Gerlach, F.; Decker, M.; Oelßner, W.; Vonau, W. Solid-state reference electrodes for potentiometric sensors. J. Solid State Electr 2009, 13, 27–39.

[28] Park, J.K.; Jang, H.J.; Park, J.T.; Cho, W.J. SOI dual-gate ISFET with variable oxide capacitance and channel thickness. Solid-State Electron. 2014, 97, 2–7.

[29] Duarte-Guevara, C.; Vikhram, V.S.; Burgess, M.; Reddy, B.,Jr.; Salm, E.; Liu, Y.; Rodriguez-Lopez, J.; Bashir, R. On-chip metal/polypyrrole quasi-reference electrodes for robust ISFET operation. Analyst 2015,140, 3630–3641.

[30] Adinolfi, V.; Sargent, E.H. Photovoltage field-effect transistors. Nature, 2017, 542, 324–327. https://doi.org/10.1038/nature21050.

[31] He, Y.; Wang, X.; Zhou, J.; Wang, T.; Ren, M.; Chen, G.; Pu, T.; Li, X.; Jia, M.; Bu, Y.; Ao, J. Enhanced pH Sensitivity of AlGaN/GaN Ion-Sensitive Field-Effect Transistor by Recess Process and Ammonium Hydroxide Treatment. IEEE Trans. Electron Devices 2021, 68, 1250–1254. https://doi.org/10.1109/TED.2021.3053496.

[32] Jeon, J.; Cho, W. Triple Gate Polycrystalline-Silicon-Based Ion-Sensitive Field-Effect Transistor for High-Performance Aqueous Chemical Application. IEEE Electron Device Lett. 2019, 40, 318–320. https://doi.org/10.1109/LED.2018.2890741.

[33] Li, Q.; Zhao, J.; Huang, Y.; Tang, W.; Peng, S.; Qiu, S.; Zhang, Q.; Guo, X. Integrated Low Voltage Ion Sensing Organic Field Effect Transistor System on Plastic. IEEE Electron Device Lett. 2018, 39, 591–594. https://doi.org/10.1109/LED.2018.2808192.

[34] Jeon, J.; Cho, W. Ultrasensitive Coplanar Dual-Gate ISFETs for Point-of-Care Biomedical Applications. ACS Omega 2020, 5, 12809–12815.

[35] Rollo, S.; Rani, D.; Olthuis, W.; Pascual García, C. High performance Fin-FET electrochemical sensor with high-k dielectric materials. Sens. Actuators B Chem. 2020, 303, 127215.

[36] Purwidyantri, A.; Domingues, T.; Borme, J.; Guerreiro, J.R.; Ipatov, A.; Abreu, C.M.; Martins, M.; Alpuim, P.; Prado, M. Influence of the Electrolyte Salt Concentration on DNA Detection with Graphene Transistors. Biosensors 2021, 11, 24.

[37] Davies, J.; Thomas, C.; Rizwan, M.; Gwenin, C. Development of Electrochemical DNA Biosensor for Equine Hindgut Acidosis Detection. Sensors 2021, 21, 2319. https://doi.org/10.3390/s21072319.

[38] Zhang, Y.; Jiang, W.; Feng, D.; Wang, C.; Xu, Y.; Shan, Y.; Wang, J.; Yin, Z.; Deng, H.; Mi, X.; Dai, N. Bio-Separated and Gate-Free 2D MoS2 Biosensor Array for Ultrasensitive Detection of BRCA1. Nanomaterials 2021, 11, 545.

[39] Schaffhauser, D.; Fine, M.; Tabata, M.; Goda, T.; Miyahara, Y. Measurement of Rapid Amiloride-Dependent pH Changes at the Cell Surface Using a Proton-Sensitive Field-Effect Transistor. Biosensors 2016, 6, 11. https://doi.org/10.3390/bios6020011.

[40] Napoli, C.; Lai, S.; Giannetti, A.; Tombelli, S.; Baldini, F.; Barbaro, M.; Bonfiglio, A. Electronic Detection of DNA Hybridization by Coupling Organic Field-Effect Transistor-Based Sensors and Hairpin-Shaped Probes. Sensors 2018, 18, 990.

[41] Diculescu, V.C.; Chiorcea-Paquim, A.M.; Oliveira-Brett, A.M. Applications of a DNA-electrochemical biosensor. TrAC Trends Anal. Chem. 2016, 79, 23–36.

[42] Barbaro, M.; Bonfiglio, A.; Raffo, L.; Alessandrini, A.; Facci, P.; Barák, I. A CMOS, fully integrated sensor for electronic detection of DNA hybridization. IEEE Electron Device Lett. 2006, 27, 595–597.

[43] Minhas-Khan, A.; Ghafar-Zadeh, M.; Shaffaf, T.; Forouhi, S.; Scime, A.; Magierowski, S.; Ghafar-Zadeh, E. UV-Vis Spectrophotometric Analysis of DNA Retrieval for DNA Storage Applications. Actuators 2021, 10, 246. https://doi.org/10.3390/act10100246.

[44] Matange, K.; Tuck, J.M.; Keung, A.J. DNA stability: A central design consideration for DNA data storage systems. Nat. Commun. 2021, 12, 1358.

[45] Newman, S.; Stephenson, A.P.; Willsey, M.; Nguyen, B.H.; Takahashi, C.N.; Strauss, K.; Ceze, L. High density DNA data storage library via dehydration with digital microfluidic retrieval. Nat. Commun. 2019, 10, 1706.

[46] Fromherz, P. Current-Induced Transistor Sensorics with Electrogenic Cells. Biosensors 2016, 6, 18. https://doi.org/10.3390/bios6020018.

[47] Matsumoto, A.; Miyahara, Y. Current and emerging challenges of field-effect transistor based bio-sensing. Nanoscale 2013, 5, 10702–10718.

[48] Gallin, J.I. Degranulating Stimuli Decrease the Negative Surface Charge and Increase the Adhesiveness of Human Neutrophils. J. Clin. Invest. 1980, 65, 298–306. https://doi.org/10.1172/JCI109672.

[49] Magalhaes, M.A.O.; Glogauer, M. Pivotal Advance: Phospholipids determine net membrane surface charge resulting in differential localization of active Rac1 and Rac2. J. Leukoc. Biol. 2010, 87, 545–555.

[50] Kuberský, P.; Altšmíd, J.; Hamáček, A.; Nešpůrek, S.; Zmeškal, O. An electrochemical NO2 sensor based on ionic liquid: Influence of the morphology of the polymer electrolyte on sensor sensitivity. Sensors 2015, 15, 28421–28434.

[51] Dwivedi, P.; Singh, R.; Chauhan, Y. S. Crossing the Nernst limit (59 mV/pH) of sensitivity through tunneling transistor-based biosensor. IEEE Sens. J. 2021, 21, 3233–3240.

[52] Singh, A.; Narang, R.; Saxena, M.; Gupta, M. Novel junctionless electrolyte-insulator-semiconductor field-effect transistor (JL EISFET) and its application as pH/biosensor. Microsyst. Technol. 2017, 23, 3149–3159. https://doi.org/10.1007/s00542-016-3013-1.

[53] Bhat, A.M.; Shafi, N.; Sahu, C.; Periasamy, C. AlGaN/GaN HEMT pH Sensor Simulation Model and Its Maximum Transconductance Considerations for Improved Sensitivity. IEEE Sens. J. 2021, 21, 19753–19761. https://doi.org/10.1109/JSEN.2021.3100475.

[54] Narang, R.; Saxena, M.; Gupta, M. Analytical model of pH sensing characteristics of junctionless silicon on insulator ISFET. IEEE Trans. Electron. Devices 2017, 64, 1742–1750.

[55] Van Hal, R.E.G.; Eijkel, J.C.T.; Bergveld, P. A general model to describe the electrostatic potential at electrolyte oxide interfaces. Adv. Colloid Interface Sci. 1996, 69, 31–62.

[56] Sinha, S.; Pal, T. A comprehensive review of FET-based pH sensors: Materials, fabrication technologies, and modeling. Electrochem. Sci. Adv. 2021, 2100147. https://doi.org/10.1002/elsa.202100147.

[57] Kim, S.; Rim, T.; Kim, K.; Lee, U.; Baek, E.; Lee, H.; Baek, C.-K.; Meyyappan, M.; Deenbd, M.J.; Lee, J.-S. Silicon nanowire ion sensitive field effect transistor with integrated Ag/AgCl electrode: PH sensing and noise characteristics. Analyst 2011, 136, 5012–5016. https://doi.org/10.1039/c1an15568g.

[58] Tadmor, R.; Hernández-Zapata, E.; Chen, N.; Pincus, P.; Israelachvili, J.N. Debye Length and Double-Layer Forces in Polyelectrolyte Solutions. Macromolecules 2002, 35, 2380–2388.

[59] Chan, W.P.; Premanode, B.; Toumazou, C. An integrated ISFETs instrumentation system in standard CMOS technology. IEEE J. Solid-State Circuits 2010, 45, 1923–1934. https://doi.org/10.1109/JSSC.2010.2053863.

[60] Jang, H.J.; Cho, W.J. Fabrication of high-performance fully depleted silicon-on-insulator based dual-gate ion-sensitive field effect transistor beyond the Nernstian limit. Appl. Phys. Lett 2012, 100, 073701. https://doi.org/10.1063/1.3685497.

[61] Morita, M.; Ohmi, T.; Hasegawa, E.; Kawakami, M.; Ohwada, M. Growth of native oxide on a silicon surface. J. Appl. Phys. 1990, 68, 1272–1281.

Chapter 4 Microfluidics Integration with Open-Gate Junction Field-Effect Transistor[1]

Paper 5: A Hybrid Microfluidic Electronic Sensing Platform for Life Science Applications

Authors: Abbas Panahi and Ebrahim Ghafar-Zadeh

Journal: Micromachines

Abbas Panahi's contributions include chip design and characterization, microfluidics design, fabrication, implementation, and fixture design and implementation. Performing experiments and data analysis. Mathematical modeling (device and charge sensing)

Microfluidics is crucial in developing point-of-care devices utilizing Field-Effect Transistor (FET) sensors. It facilitates the precise delivery of samples to the sensing site while avoiding interference with the pads connected to the circuit. The successful integration of microfluidics with sensors largely depends on the sensor's structure and geometry.

For instance, integrating a microfluidic channel with an OG-JFET is more feasible due to a back gate and a planar sensing site. This configuration allows for effective charge sensing without necessitating a solution gate. However, integrating microfluidics with an OG-JFET presents challenges, mainly due to the sensor's non-uniformity in edges when placed on a substrate, complicating its alignment and bonding with a planar microfluidic channel.

This chapter delves into the detailed processes of designing and fabricating a scalable microfluidics integration for OG-JFETs. The methodologies we discuss apply to OG-JFETs and can also be

[1] This chapter is based on the published paper: Panahi, A.; Ghafar-Zadeh, E. A Hybrid Microfluidic Electronic Sensing Platform for Life Science Applications. Micromachines 2022, 13, 425. https://doi.org/10.3390/mi13030425

customized for other FET sensors, ensuring versatility and adaptability in various point-of-care applications.

4.1. Abstract

This paper presents a novel hybrid microfluidic electronic sensing platform featuring an electronic sensor incorporated with a microfluidic structure for life science applications. This sensor with a large sensing area of 0.7 mm^2 is implemented through a foundry process called open-gate junction FET (OG-JFET). The proposed OG-JFET sensor with a back gate enables the charge by directly introducing the biological and chemical samples on the top of the device. This paper puts forward the design and implementation of a PDMS microfluidic structure integrated with an OG-JFET chip to direct the samples toward the sensing site. At the same time, the sensor's gain is controlled with a back gate electrical voltage. Herein, we demonstrate and discuss the functionality and applicability of the proposed sensing platform using a chemical solution with different pH values. Additionally, we introduce a mathematical model to describe the charge sensitivity of the OG-JFET sensor. Based on the results, the sensor's maximum value of transconductance gain is ~1 mA/V at Vgs = 0, which is decreased to ~0.42 mA/V at Vgs = 1, all in Vds = 5. Furthermore, the variation of the back-gate voltage from 1.0 V to 0.0 V increases the sensitivity from ~40 mV/pH to ~55 mV/pH. Per this paper's experimental and simulation results and discussions, the proposed hybrid microfluidic OG-JFET sensor is a reliable and high-precision measurement platform for various life science and industrial applications.

Keywords: field effect transistor (FET); biosensor; DNA sensor; oral neutrophil; ISFET; BioFET

4.2. Introduction

Electrochemical sensors are used in various applications such as the food industry, pharmaceuticals, oil and gas, environmental monitoring, and biomedical engineering [1-4]. These sensors promise faster and more sensitive techniques for detecting diseases and hazardous materials [5], [6]. A well-established member of electrochemical sensors, so-called ion-sensitive field-effect transistor (ISFET) sensors have been utilized in different applications for ion/charge detection in chemical solutions. The ISFETs range from carbonaceous FET sensors (e.g., graphene, carbon nanotubes) to 2D materials (e.g., MoS_2) [7–10]. Many efforts have been made to develop ISFETs based on technologically flawless silicon-based Complementary Metal-Oxide Semiconductors (CMOS) technology, resulting in different sensing structures and topologies [4]

offering high-yield productions. They have been successfully verified to detect diseases such as malaria, influenza, hepatitis B virus, COVID-19, and bacteria-based diseases [4], [11]. Immobilizing the surface of ISFETs with different biomolecules gives rise to biological FETs (BioFETs), which could be GEN-FET (DNA sensors), Cell-FET (for cell analysis), Enzyme-FET (for enzymatic reactions analysis), etc. [12–14]. Also, as the ISFETs are sensitive to ion concentration in liquids, they have been used directly for pH measurements [4].

The above-mentioned miniaturized sensors must be incorporated with microfluidics to direct the samples toward sensing sites and prevent the solution from reaching the rest of the platform. Microfluidics technology has been under intense research in the last decades, aiming to miniaturize bioprocesses and bioanalysis towards enabling lab-on-a-chip [15], [16]. Microfluidics and nanofluidics provide other advantages such as low reagent consumption, low cost, laminar flow operation, reduced exposure risk to toxic mate-rials, parallelization, portability, and excellent versatility in design and engineering [17], [18]. Microfluidics-integrated biosensors are used for parallel analysis of different biomarkers in human blood [19-24]. Also, the high-throughput integration of fluidics and biosensors has resulted in commercialized products such as Ion Torrent's genome machine and illumina's Miseq, in which integrated bio-sensing has enabled parallelized analysis [25-27].

Today, many papers have reported the integration of microfluidics with electronic sensors. Sensor-integrated microfluidic devices were reported for applications such as DNA hybridization [28], [29], polymerase chain reaction (PCR) on-chip [30], [31], virus detection [32], [33], cancer detection [34], [35], circulating tumor cells (CTC) analysis [36], [37], exosomes analysis [38], [39], nucleic acids analysis [40], [41], liquid biopsy-based assays for cancer detection [42]. CMOS-based sensors integration with microfluidic are put forward for cell analysis [43], [44], chemical sensing [45], optical biosensing [46], ultraprecise micro pumping [47], 2D nanomaterial detection [48], optofluidic biomedical devices [49]. For CMOS sensors integration with microfluidic, the direct-write microfluidic fabrication process (DWFP) was introduced as a comparatively new rapid technique for creating microfluidics atop an electronic chip [50]. The same DWFP method was used for chemical sensing [51]. More advanced techniques were implemented to integrate continuous microfluidic with capacitive CMOS sensor real-time cell analysis [45].

BioFET sensors have shown great potential in unique charge detection capabilities for many applications [4], [52]. They should be integrated with microfluidics for successful prospects in point-of-care devices by taking advantage of unique microfluidics features. Many attempts have been made to incorporate BioFETs with microfluidics so far. A graphene-FET integrated with microfluidic has been introduced for femtomolar detection of chlorpyrifos [53]. Digital microfluidics was combined with a FET sensor for bioanalysis in lab-on-a-chip [54]. In another work, to accelerate the process of biomarker detection, a silicon nanowire-based FET structure was integrated with microfluidics for parallelization of cardiac biomarker detection in human blood [55]. Graphene-FET was implemented in a planar microfluidic channel for ultra-sensitive flow velocity sensing application [56]. Microfluidics enabled continuous flow measurement from an extended-gate FET structure applicable for ion sensing [57]. Integrated BioFET with microfluidics was used for aerosol particle detection in air, promising such integration potentials for high-throughput air quality measurements [58]. A microfluidics-integrated CMOS sensor was used to detect metabolites in blood, and PDMS was used to create multiple channels in the sensor [59]. The same packaging method was utilized to develop a novel CMOS-microfluidics platform for prostate cancer detection in blood that promises a rapid and cost-effective bedside platform [60]. Elastomeric microfluidics was integrated with a semiconductor sensor using a novel integration method with negligible sensitivity to the strain from bending and flexures, promising a novel packaging for wearable sensors [61-62]. BioFETs also showed good sensing capabilities toward packaged graphene-based sensors [63]. A microfluidics-integrated floating gate FET sensor was developed, which put continuous microfluidics in place to detect proteins [64]. Organic FET sensors were also integrated with microfluidics, encompassing reference electrodes in the packaged sensor [65]. Microfluidics was integrated with polymeric organic FET for marine environmental detection with high stability [66].

Despite the successful experiments on integrated BioFETs with microfluidics at a laboratory scale, specific integration hindrances exist for FET-based lab-on-a-chip for high-throughput integration. As evident in the BioFETs structures, they need a reference electrode in solution for their operation, making microfluidic integration and packaging extremely difficult [67], [68]. One viable solution might be using the on-chip reference electrodes. Still, it is reported that on-chip microfabricated electrodes are not as stable as Ag/AgCl bulky electrodes frequently used in BioFETs experiments due to the inherent noise associated with downscaling of material [69]. An

engineering solution to avoid bulky reference electrodes is to design a back-gate structure to control the channel conduction in BioFETs and use it for sensor characterization. Removing the reference electrode on top and placing it on the back creates open space for running a microfluidic channel on the sensing area.

We introduce a simple 3D-printed microfluidic integration scheme for a new semiconductor biosensor called OG-JFET. The sensor is based on the open-gate junction field-effect transistor, which works based on a back-gate structure that enables sensor operation without a reference electrode in solution, such as bulky Ag/AgCl electrodes used in previous sensors. This capability led us to use a simple method to integrate a microfluidic channel on top of the sensor. The microfluidic has been developed with PolyJET 3D printing technology, which can deliver tiny samples to the sensing area. Due to its small fluidic size, previous sensors used advanced and complex microfabrication processes to create the microfluidic part. Nevertheless, the large sensing area provided by our sensor and the back-gate allowed us to use 3D printing for creating higher minimum feature sizes as large as 2000 μm in microfluidics. Two molds were used to create 3D microfluidics for making a chamber on top of the sensing area, which differed from previous planar microfluidics used for BioFET integration.

The PDMS fluidic cell fabrication process is introduced, which can be molded with PolyJET 3D printing. Furthermore, the sensor (OG-JFET) sensing mechanism is detailed with mathematical modeling and experimental evidence to show the device's functionality in delivering samples onto the sensor and performing charge detection in an aqueous solution. The sensor provides a back-gate, making integrating with microfluidic more straightforward. Furthermore, the sensor works at a low voltage (<0.2 V), which is essential in developing a low-power hand-held electronic platform for industrial applications.

The organization of this paper is as follows: part two[1] explains the electronics sensor (OG-JFET) mathematical modeling; Part three[2] introduces the electrical and fluidic packaging and sensor characterization; and part four[3] is dedicated to results and discussions, followed by the conclusion part.

[1] Section 4.3
[2] Section 4.4
[3] Section 4.5

4.3. Electronic Sensor

4.3.1. Open-gate junction field-effect transistor and microfluidics

The current sensing platform is like the well-established JFET with the subtle difference that the top gate of a JFET is removed to open the space for introducing a solution. Physically, the structure is based on a p-type JFET without the top n-type gate, as we have reported in our previous works [70], [71,72]. Therefore, the structure only has a back gate that can control the conduction channel. The sensor is provided through a standard microfabrication process, which further helps to establish this sensor as a mass-producible platform for industrial applications (for more information about fabrications, we invite the reader to read [70-72]). The platform includes a PDMS channel integrated with the OG-JFET sensor to deliver samples to the sensing area. A schematic of the integrated microfluidic sensor platform is presented in Figure 4-1.

As shown in Figure 4-1, the OG-JFET sensor has a back gate that is not inside the solution. This gate helps control the conduction in the channel and can be used as the same reference electrode for voltage—or current-based sensing characterization.

The sensor consists of a p-type channel epitaxially grown on a thick n-type layer with doping levels of 5×10^{15} /cm^3 and 1×10^{18} /cm^3, respectively. The p-type layer thickness is 1.6 µm ± 10% (resistivity of 3.0 Ohm-cm ± 10 %) on the n-type layer with a thickness of 450 µm with a resistivity of 0.006 to 0.02 Ohm-cm. A source and drain with a width of 20 µm are developed on the p-type channel covered with a thick stacked layer of SiO_2-Si_3N_4. The dielectric layers create an encapsulation layer for the drain and source metal layers to avoid contact with the solution.

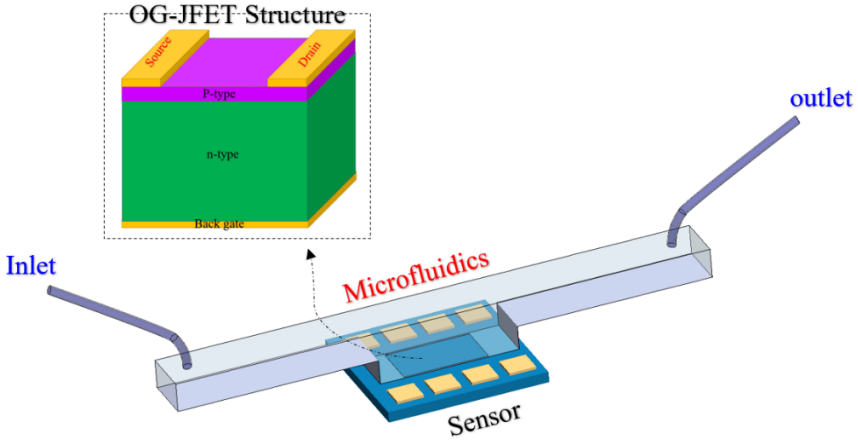


Figure 4-1. Schematic of OG-JFET structure and the microfluidic chamber.

When the p-type channel is exposed to air or natural moisture, it is expected to have a particular layer of native silicon dioxide on the silicon layer. The native silicon oxide grows naturally when the silicon is open to the air. It is experimentally validated that a layer with a thickness of up to 10 Å can be expected with an exposure of 80 days to solely air [73]. The silicon dioxide provides hydroxyl groups on top of the silicon layer in the opened gate area, which can participate in the chemical reactions with ions in the solution, leading to ion-complexation with SiO_2 surface bonds that create a stacked layer of ions on the surface of silicon [73]. The created ion layers generate a local electric field, which causes a detectable change in the hole conduction inside the p-type layer. The sensor is tested in reverse bias condition of p-n junction for biosensing.

4.3.2. Mathematical modeling

For a better understanding of sensor operation, mathematical modeling is introduced here, by which the sensing mechanism could be explained in much more detail. The OG-JFET structure can be imagined as half of a p-type JFET (n^+p JFET) structure in which the two n-type gates control the sensor. However, in OG-JFET, the top gate is solution charge effects. The n^+p JFET is usually called on the device, which means a voltage should be applied to the gate to close the channel; otherwise, the channel is open, and the hole current can be on even if Vg is zero. When a positive voltage is applied on the back gate, the space charge pushes the region to close where the current in the channel reaches zero. This condition is called *a pinched-off* state. The pinch-off voltage (Vp) for a n^+p JFET can be defined with the following equations:

$$V_p = V_{p0} - V_{bi} \qquad (4\text{-}1)$$

$$V_{bi} = V_t \ln\left(\frac{N_a N_d}{{n_i}^2}\right) \qquad (4\text{-}2)$$

$$V_{SD}(sat) = V_{p0} - (V_{bi} + V_{BG}) \qquad (4\text{-}3)$$

In equation (4-1) the V_{p0} is the inherent pinch-off voltage which depends on the structure and doping levels. The structure shown in Figure 4-1 can be simplified for mathematical modeling, as shown in Figure 4-2.

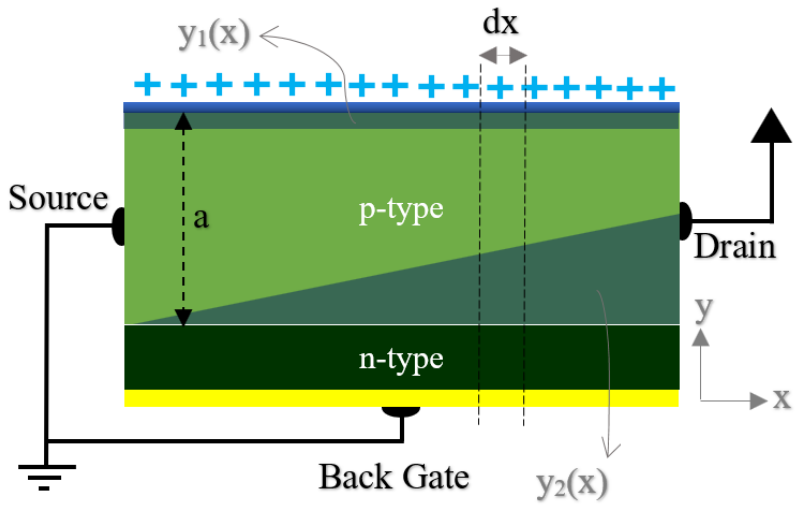


Figure 4-2. The simplified model of OG-JFET for mathematical modeling of drain-source current

The Vsd (sat) represents the drain-source voltage, which leads to a pinch-off condition at the drain region [65]. According to Figure 4-2, considering a differential element of the channel in the x-direction, we can develop the current-voltage relation starting from Ohm's law and extend the equations based on the space charge effects in the channel.

$$dR = \frac{\rho dx}{A(x)} \qquad (4\text{-}4)$$

$$\rho = \frac{1}{e\mu_n N_d} \qquad (4\text{-}5)$$

Equation (4-4) shows the Ohms law that can be applied to the device element shown in Figure 4-2. The A(x) is the surface perpendicular to the surface. Equation (4-2) shows the resistivity formula of the device where e is the elemental charge, μn is the mobility by the assumption of neglecting minor carrier charge. Based on Figure 4-2, the cross-sectional area is $A(x) = [a - y1(x) - y2(x)]W$ where W is the channel width along the z-direction (not shown here). With the assumption of A(x), equation (4-4) can be developed to reach (6):

$$I_{D1}dx = e\mu_n N_d W[a - x_1(y) - x_2(y)]dV(x) \qquad (4\text{-}6)$$

The depletion width for space charge due to the back gate is:

$$x_2(y) = \left[\frac{2\epsilon_s\left[V(x) - V_{bi} + V_{gs}\right]}{eN_d}\right]^{\frac{1}{2}} \quad (4\text{-}7)$$

The depletion because of the surface charge on the top gate can be modeled as follows:

$$x_1(y) = \frac{Q}{qN_A}t_{ox} \quad (4\text{-}8)$$

In equation (4-8), the Q is the surface charge because of the aqueous solution, t_{ox} is the thickness of the oxide layer, the N_A is the doping level in the semiconductor, and the q is the elemental charge. Due to the surface charge in the solution, a depletion of space charge in the p-type layer happens (see Figure 4-2); equation (4-8) models that layer. This layer is considered constant along the open-gate area surface, which generates a continual depletion of layer thickness in the semiconductor. Therefore, the output value of equation (4-8) is constant. By substituting equations (4-7) and (4-8) into equations (4-6) and integrating over the length of the open-gate area of OG-JFET, the relation for drain-source current (equation (4-11)) can be developed with the following boundary conditions (at 0 and L):

$$w_1{}^2 = \frac{2\varepsilon_s}{qN_A}\left(V_{bi} - V_{gs}\right) \qquad @\ Lc = 0 \quad (4\text{-}9)$$

$$w_2{}^2 = \frac{2\varepsilon_s}{qN_A}\left(V_{bi} - V_{gs} + V_{ds}\right) @\ Lc = L \quad (4\text{-}10)$$

The resultant drain-source current relation is (9):

$$I_D = \frac{q^2\mu N_A{}^2\tau^3 Z}{\varepsilon_s L}\left\{\frac{V_{DS}}{V_{po}} - \frac{2}{3}\left(\frac{[(V_{bi} - V_{GS} + V_{DS})]^{\frac{3}{2}}}{V_{po}} - \frac{[(V_{bi} - V_{GS})]^{\frac{3}{2}}}{V_{po}}\right)\right\} \quad (4\text{-}11)$$

Where $\tau = a - x_1(y)$, with $x_1(y)$, which demonstrates the depletion effect due to surface charge on the sensor. Equation (4-11) can be used to calculate gain (g_m), which is as follows:

$$g_m = \frac{\partial I_D}{\partial V_{gs}} \qquad (4\text{-}12)$$

It is noteworthy to mention that equation (4-11) is valid for the range of voltages $0 \leq |V_{gs}| \leq V_{po}, 0 \leq |V_{ds}| \leq V_{ds(sat)}$.

The sensor structure affects the response of the sensor to changes in the charges on the surface (opened gate area). The sensor's output is current and changes with the electric field generated due to the charge on the sensor. The back gate can be used to modulate the drain-source current. Therefore, the charge on top of the sensor can also be considered a second gate that modulates the channel space charge. As there is a correlation between back gate voltage and current ($\Delta I \sim \Delta V g$) therefore, the same can be applied to charge the sensor (($\Delta I \sim \Delta C$). The following relation can be used to correlate the sensor output to the change in surface charge and the gain, demonstrating the structure's effect.

$$\frac{dI}{dC} = \frac{dI}{dV_{gs}} \times \frac{dV_{gs}}{dC} \qquad (4\text{-}13)$$

In formula (4-9), the $\frac{dI}{dVgs}$ is the gain (gm) or transconductance based on the relation (4-12). Therefore, the general relation can be simplified to equation (4-10).

$$\frac{dI}{dC} = g_m \times \frac{dV_{bg}}{dC} \qquad (4\text{-}14)$$

In formulas (4-13) and (4-14), the C is the charge sensing on the sensing region.

4.4. Microfluidics and electrical packaging

To prepare the sensor for applying the chemical solution, a customized microfluidic was developed that includes a channel running on top of the sensor that encompasses a chamber on the sensing area (See Figure 4-3). Creating and integrating a microfluidic chip would be extremely difficult if the BioFET works based on a reference electrode (e.g., Ag/AgCl) inside the solution. However, the OG-JFET structure offers a back-gate, making microfluidic integration easier. Developing microfluidic helps to ensure that the sensor's pads are not in contact with the solution as this creates noises in the sensor response and could even damage the sensor.

4.4.1. Electrical packaging

A PCB used a spring-loaded connector to connect the sensor to the semiconductor analyzer (Keithley 4200A-SCS Parameter Analyzer). On the PCB, the spring-loaded connectors were connected to a switch. The switch is used to choose the drain of interest of the sensor. The PCB is 100 mm × 80 mm, covering a 3D printed structure. Four pillars on the 3D printed design were used to align the PCB with the sensors' pads. The pad area is 1.7 mm × 1.7 mm with a 2 mm pitch. The BNC connectors are placed on one side of the PCB. The PCB and the semiconductor analyzer are connected through SMU cables. Before fabricating the fixture, it was modeled using CAD software (Solid work) to ensure alignment. A closeup of the electrical packaging is shown in Figure 4-3.

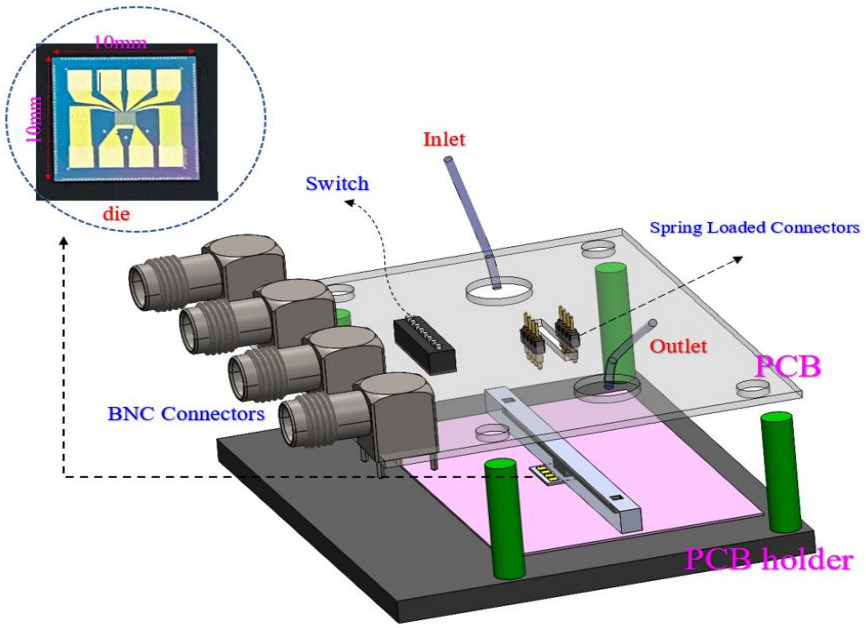


Figure 4-3. The electrical packaging technique. A spring-loaded connector was used to connect the sensor pads to a switch. The switch is connected to the BNC connector.

The die size is 10 mm × 10 mm, and the comparatively sizeable total sensing area is 1 mm × 2 mm, contributing 0.7 mm^2 of the whole die. The chip pad area is generously large, allowing the spring-loaded connector in the electrical packaging scheme.

4.4.2. Microfluidic packaging

The microfluidic channel was fabricated based on the PDMS replica molding method. The mold was 3D printed using the PolyJet method, then the PDMS was prepared with a 10:1 ratio and poured into the mold for curation. The size and dimensions for the designed microfluidic channel based on the sensor sensing area constraints are shown in Figure 4-4. To fabricate the microfluidic shown in Figure 4-4, two separate 2D microfluidics were fabricated. Two parts were then adhered with UV curable glue (MMOBIEL UV LOCA TP-N1000). The adhesion of a PDMS sheet and a microfluidic channel creates a 3D structure placed on top of the sensor.

The microfluidic channel was prepared according to the methods demonstrated in Figure 4-5. According to our customized microfluidic fabrication protocol, the molds are washed with an ethanol solution to ensure no debris is in the mold. To further improve the washing, the molds are put in the mixture of water and oil for 10 minutes at 50 C°. Afterward, the mold was washed to be prepared for PDMS injection. The PDMS was ready with a 10:1 ratio of the base polymer and curing agent, and then the polymer was blended with a stirrer for 10 minutes at each try. After pouring the PDMS into the mold, it was degassed in the vacuum chamber. The degassing was done for 20 minutes to remove all the bubbles.

The PDMS chip was placed inside the oven and baked for 5 mins at 100 C. This condition yields a flexible PDMS structure; therefore, it is in excellent condition to easily be peeled off from the thin mold. Other temperatures with a longer time (@ lower temperatures) result in a solid PDMS, making it hard to remove, and in most cases, it breaks near the inlet or outlet. At the same time, these processes were tried for another mold, creating a thin layer of PDMS (1 mm) to cover the channel (See Figure 4-5 (d)). After placing the channel on the PDMS sheet with UV curable glue, the bonding was strengthened by applying UV light on both sides with a hand-held UV lamp (UV 365nm light) for 5 minutes. This helped to make a strong bond between the PDMS and the PDMS. The mold that includes the channel geometry is placed on a uniform large PDMS sheet; therefore, the issue of the cumbersome bonding process of PDMS-PDMS is avoided. Subsequently, the whole microfluidic channel was cut out under the microscope to release the structure shown in Figure 4-5-f. After removing the structure, it was again heated and immediately put on the chip.

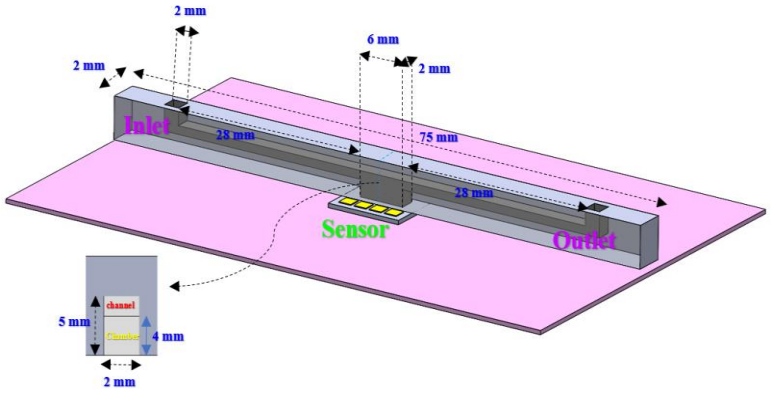


Figure 4-4. The experiment setup was used to test the OG-JFET sensor. (a): shows the CAD design of the fixture used for connecting the sensor to the semiconductor analyzer. (b): the fabricated test setup, consisting of PCB (BNC, switch), 3D printed support, and microfluidic with its tubing. The back gate is contacted from the back of the sensor to top on the PCB, where it's connected to a BNC connector to the semiconductor analyzer. (c): shows the spring-loaded connectors used to connect the OG-JFET pads to the PCB. On the PCB, there is a switch that enables the user to select the specific channel on the OG-JFET sensor.

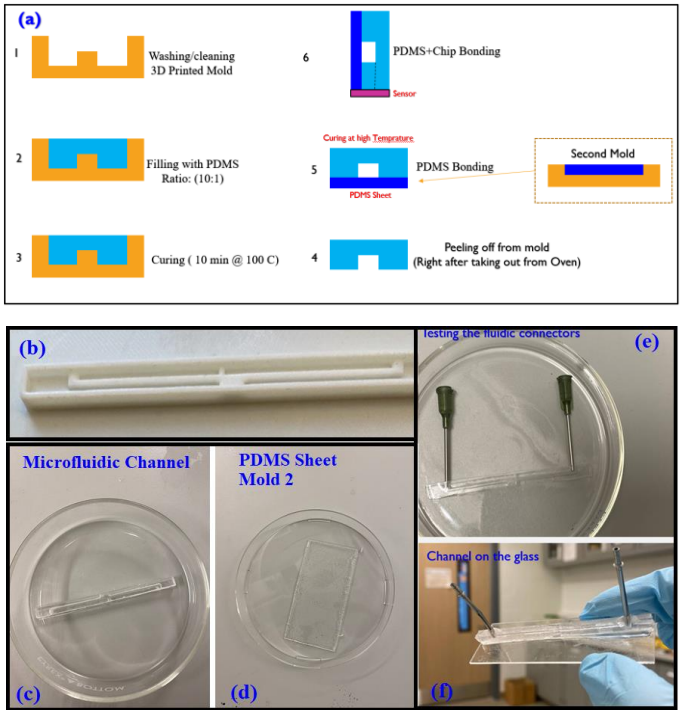


Figure 4-5. The processes led to the fabrication of a microfluidic channel on top of the sensor. (a): the PDMS replica molding process taken to create the 3D microfluidic with two 2D PDMS; (1) first the 3D printed mold was washed, (2) filling the mold with a 10:1 ratio of pre-prepared PDMS (after filling the mold, the PDMS and mold were put in the vacuum chamber for 20 mins for degassing), (3) after degassing, the PDMS and mold were put in the oven and baked for 5 min at 100 C, (4) the PDMS was peeled off from the mold, (5) at this point a channel is put on a PDMS sheet which has already been prepared with another mold, (6) bonding the PDMS and chip. (b): the used channel molds. (c) showing the peeled-off microfluidic structure. (d): the PDMS sheet shown in step 5. (e) testing the fluidic connectors with water. (f) showing the adhesion of the PDMS channel on the glass.

Figure 4-6 shows the steps for making a back-gate contact connection using conductive copper tape. The copper conductive tape was soldered to a wire connecting the wire to a pin header on the PCB as the back-gate connection. It is noteworthy that, as shown in Figure 4-6, the sensor comes with seven drains, and since they provide almost the same results (transfer characteristics), we arbitrarily used one of them.

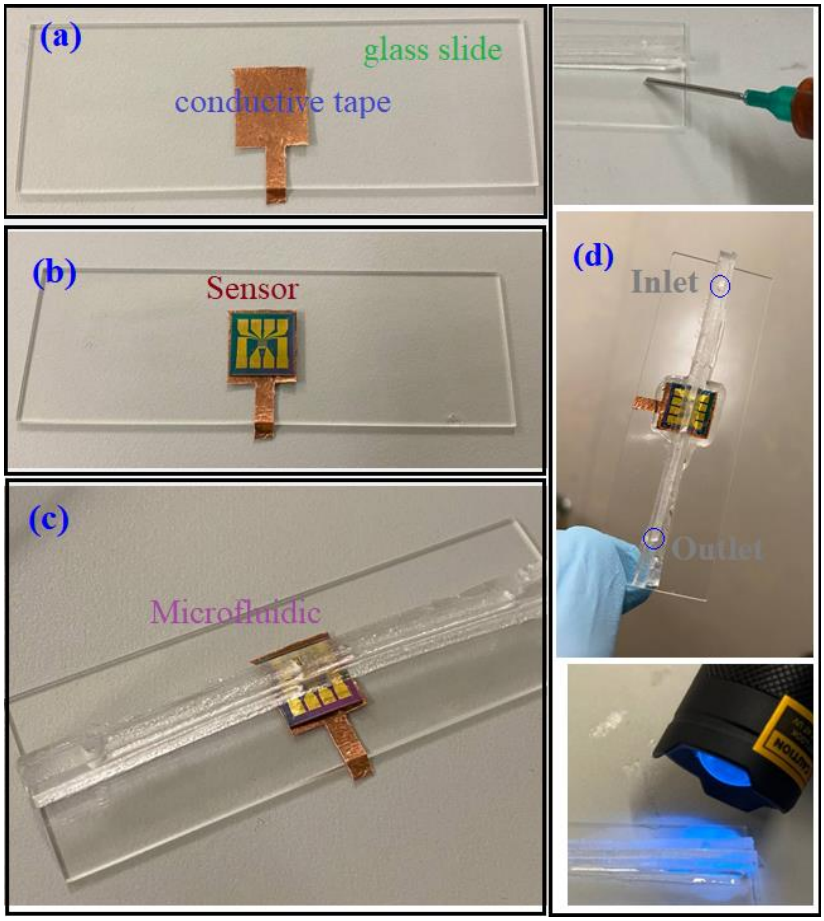


Figure 4-6. Boding process of the microfluidic channel on the chip. (a): A copper conductive tape was utilized to create the back-gate connection on the glass slide. (b): the sensor is put on the sensor. (c): after heating the microfluidic, it was aligned with the chip under a microscope. (d) filling the gap underneath the microfluidic with UV-curable glue and applying UV light to make the structure strongly bonded.

4.5. Results

The OG-JFET sensor has been fabricated with standard microfabrication technology (See S1 for more information). Here, the integration with a PDMS-based microfluidic is detailed. The sensor's back-gated structure allows running a microfluidic channel atop the sensor in the sensing region. This section's results are associated with the sensor transistor response in dry mode and when the

sensor is exposed to solution in the microfluidic channel. Furthermore, the results of mathematical modeling and fluidic simulations are explained here.

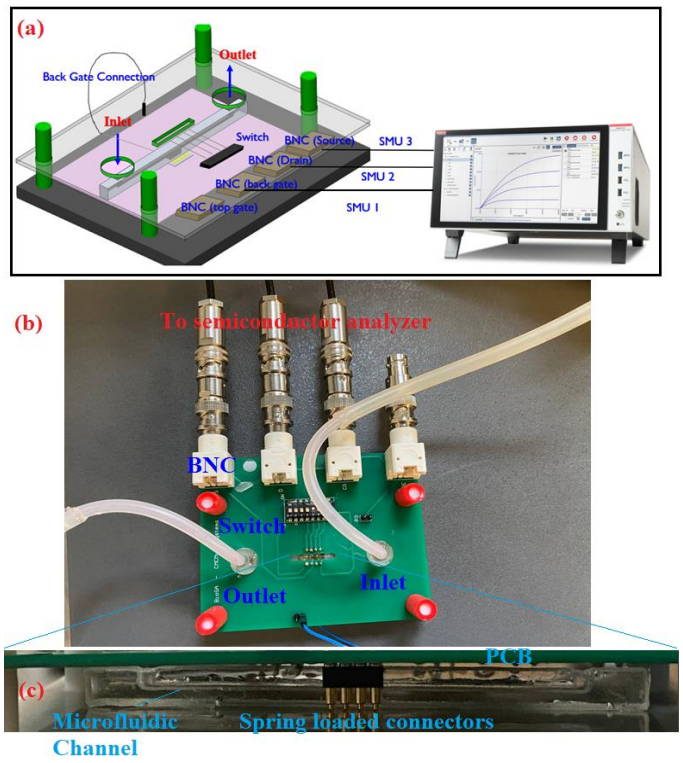


Figure 4-7. The experiment setup was used to test the OG-JFET sensor. (a): shows the CAD design of the fixture that connects the sensor to the semiconductor analyzer. (b): the fabricated test setup, consisting of PCB (BNC, switch), 3D printed support, and microfluidic with its tubing. The back gate is contacted from the back of the sensor to the top of the PCB, where it's connected to a BNC connector to the semiconductor analyzer. (c): shows the spring-loaded connectors used to connect the OG-JFET pads to the PCB. On the PCB, a switch enables the user to select the specific channel on the OG-JFET sensor.

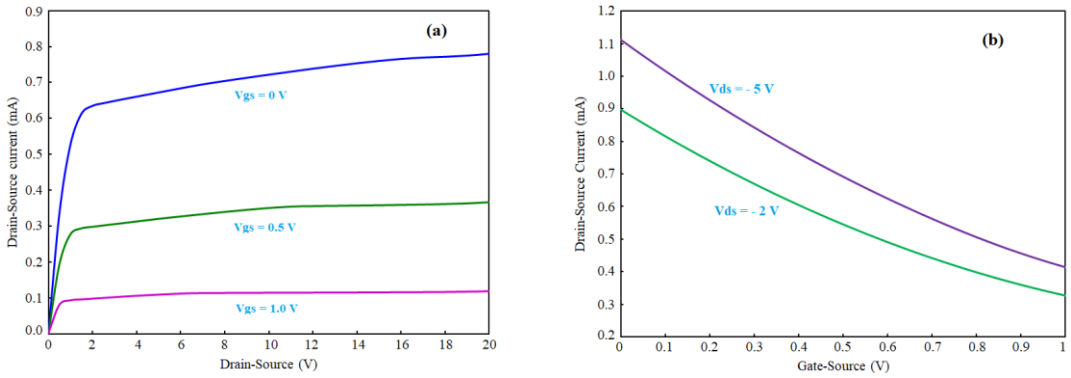


Figure 4-8. The Ids-Vds and Ids-Vgs curves of OG-JFET. (a): Ids vs drain-source voltage. (b): Ids vs back-gate voltage

4.5.1. Sensor response in dry condition

The sensor consists of a p-n junction, which can be imagined as a conventional JFET with an opened top gate. The top gate is devoted to sensing a solution or any biomaterials. The back gate can be used to control the channel's conduction. The p-n junction can be turned on or off based on the polarity of the voltages applied on the p-type and n-type layers. If a positive voltage is applied to the p-type and a negative to the n-type (see Figure 4-1), the sensor is forward-biased, which allows the p-n junction to be opened. The difference between drain and gate voltage is more than a specific threshold voltage.

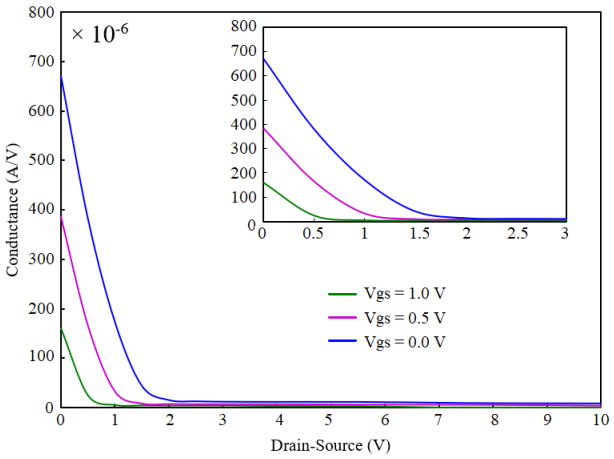


Figure 4-9. Change of conductance of OG-JFET with back-gate

The calculated turn-on voltage for this p-n junction here is ≈ 0.67 V. However, when the voltage difference between a drain and the back gate reaches this number, the p-n junction is opened, and a huge current will be directed from the back gate to the drain, which is not preferable for biosensing applications. For this reason, the sensor is suggested to be used in reverse-biased conditions as it allows the channel to be controlled with the back gate for more efficient sensing of the surface charge and solution chemical potential. After being integrated with microfluidics, the sensor was characterized when no solution was available. The Ids-Vds and Ids-Vgs of OG-JFET are demonstrated in Figure 4-8.

Figure 4-9 demonstrates the conductance of OG-JFET for different drain-source voltages when the gate-source is applied to the sensor. This curve clearly shows the effect of the back gate on the control of the channel conductance. Figure 4-9 shows that the conductance decreases when drain-source voltage is applied, narrowing the channel due to back-gate space charge modulation. The channel conductance approaches zero at higher back-gate voltages (=1 V).

The transconductance (gm) of the sensor is calculated based on the experimental results (see Figure 4-10). The gm is depicted versus the back gate, which shows the controllability of gain with the back gate. Also, the result demonstrates that the gm linearly decreases with increasing the back gate. The gain is calculated by taking the first derivative of the Ids-Vgs curve shown in Figure 4-8-b. The maximum gain of the sensor happens at the Vgs = 0. It is noteworthy that the Vds enhancement leads to higher gains. Based on this result, the gain estimates the current enhancement in equations (4-13) and (4-14).

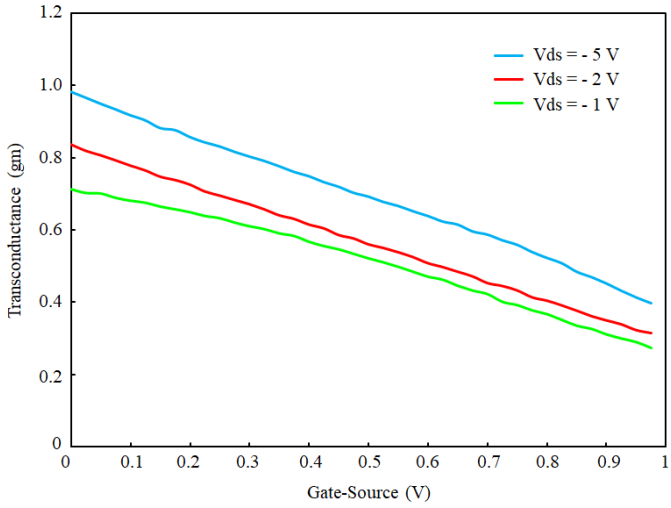


Figure 4-10. The transconductance of OG-JFET calculated for different values of back

4.5.2. Solution tests in the microfluidic channel

Simple wet tests are performed to demonstrate the fabricated microfluidics functionality and the sensor's integration. The sensor is tested with DI water and 0.9 % NaCl solution to show its response to a change in the concentration of ions in the solution. The concentration of ions in the NaCl solution is higher than in the DI water, and the sensor shows more current enhancement toward this change in solution (see Figure 4-11).

Also, a solution with a different pH was prepared and tested in the microfluidic channel to have precise control over the sensor's response to changes in the surface charge. The fluid was injected into the channel with a syringe pump and then stopped to have stationary fluid in the chamber. In our previous work, the change in Vgs with different pH levels was reported to be 39.45 mV/pH, 42.62 mV/pH, 45.79 mV/pH, 48.96 mV/pH, 52.12 mV/pH, and 55.29 mV/pH were determined

for different reference current measurement [62]. These values can be considered as $\frac{dV_{bg}}{dC}$ in relations

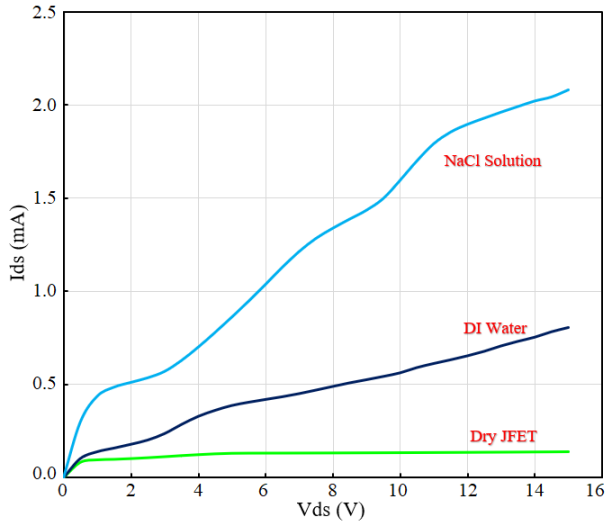


Figure 4-11. Preliminary test results of sensor with DI water and 0.9% NaCl solution injected in microfluidic channel.

(4-13) and (4-14). The surface charge can be correlated with the pH, [62], therefore, we can use pH in this formula. To calculate the above charge (=pH) sensitivities, back gate electrode of OG-JFET was used which demonstrates the effectiveness of this sensor topology for measuring surface charge variations without the need for bulky reference electrodes in solution.

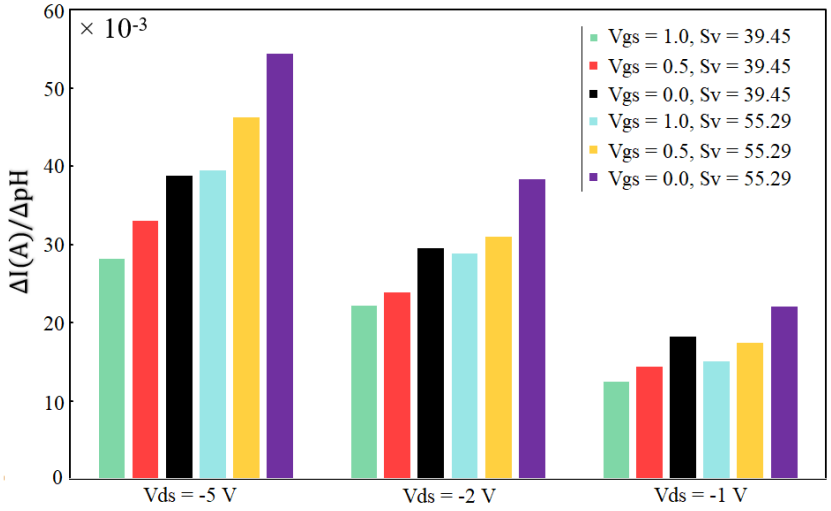


Figure 4-12. The effect of gain on the current sensitivity for different values of surface charges due to pH variations. Sv is the voltage sensitivity of the sensor with a unit of mV/pH

Furthermore, the back gate can be used to change the sensor's gain to change the current sensitivity. The gain was calculated based on the experimental results using the relations (4-13) and (4-14) and used in calculating the current sensitivity. Figure 4-12 shows the effect of back-gate on the sensing variation. The back-gate in OG-JFET is an advantage in the packaging. It allows easier integration of a microfluidic channel in continuous fluidic; furthermore, it enables changing the working point of the sensor and changing the current sensitivity to surface charge.

4.5.3. Mathematical Modeling Results

This paper presents the sensor's mathematical modeling to confirm its transfer characteristics. Mathematical modeling is developed to estimate the sensor's response to variations in surface charge. Therefore, the surface charge effect is approximated with a simple model that considers the space charge variation of the p-type channel. The simple model cannot be used for general surface potential modeling on the JFET.

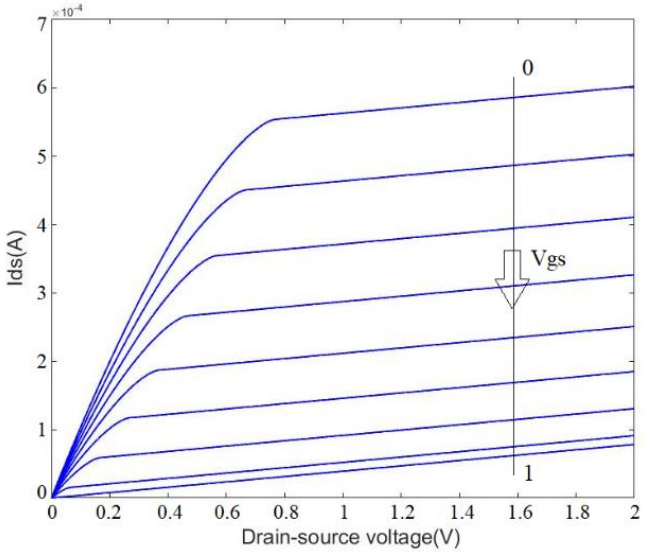


Figure 4-13. Mathematical results of the Ids-Vds curves for different Vgs values from 0 to 1 with 0.1 steps. The model can predict the sensor's response in low values of drain-source voltages before saturation. The back-gate voltage also is limited to the Vpo for good accuracy.

Equation (4-11) is solved for the gate-source voltage range of 0 to 1 for Vds values 2 V and 5 V (see Figures 4-13 and 4-14). Comparing the mathematical modeling results with the experiment indicates the model is not accurate for predicting the experiment trend for back gate voltages higher than 0.7 V. After this voltage, the sensor response remains constant, which is not according to the experiments. The mathematical modeling was discussed in previous work [74]; however, the model's limitations were not discussed for OG-JFET with showing transfer characteristics. Figure

4-13 demonstrates this point that the model is not helpful for high back gate voltage. Therefore, the model introduced in this work and also [74], can be used for the low back gate (preferably < 0.7) and drain-source voltages (preferably <0.6). Comparing the experimental result of sensor transfer characteristics (see Figure 4-8) with the model result (see Figure 4-13) indicates that the non-idealities in fabrication processes, such as non-uniformity of doping levels, uncertainties in controlling the channel length with implantation of source and drain might be responsible for the inconsistency between model and experiment.

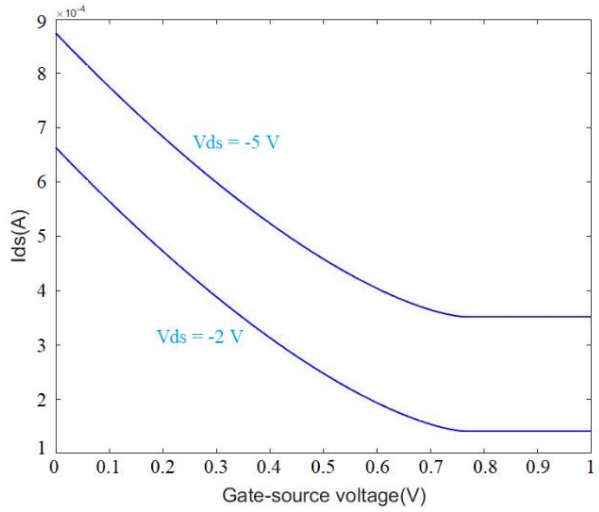


Figure 4-14. Mathematical modeling result of Ids-Vgs response for Vds values of 2 V and 5 V.

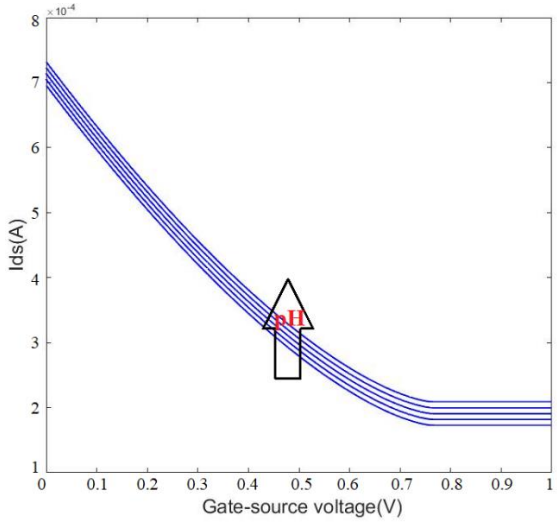


Figure 4-15. Mathematical modeling results of surface charge effects on the OG-JFET sensing area. The increment in pH results in more negative surface charge.

Figure 4-15 shows the modeling result of the surface charge effects on the sensor response. Experiments showed that the pH causes an increment in output current. Here, the surface charge modeling is inspired by the work done in [75] for NO_2 detection using a similar JFET structure. However, the charge density is determined using the simulation modeling of pH equivalent surface charge we introduced in our previous work [72], as with the experiment and multiphysics simulation, current mathematical models show that currents enhance with an increase in pH (Figure 4-15).

4.5.4. Microfluidic Simulations

The microfluidic is designed to deliver the sample onto the sensing region of OG-JFET. The fluidic transport inside the channel is analyzed with COMSOL Multiphysics software to gain insight into the fluid dynamics in the chamber atop the sensor and the channel. The analysis estimates the fluid velocity in the chamber for different mass flow rates, which is helpful for future designs.

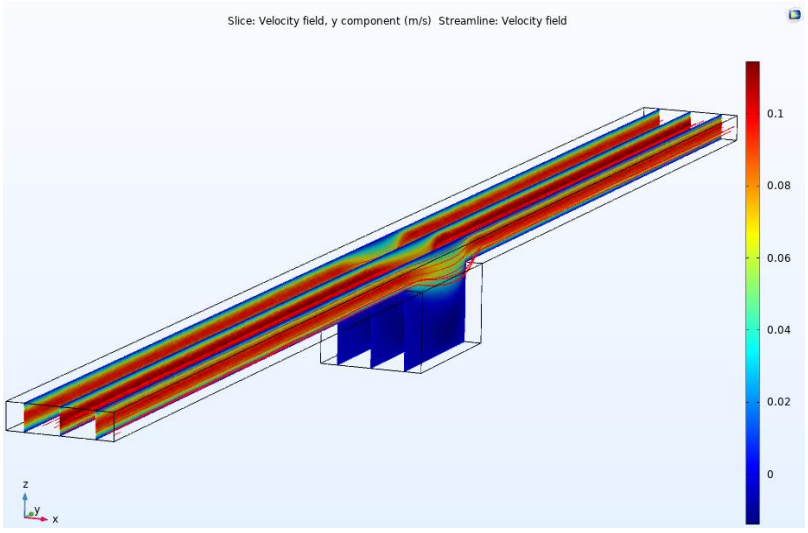


Figure 4-16. Flow velocity contour in the microfluidic channel for 260 mg/s inlet mass water flow

The velocity is higher in the middle of the channel and almost zero near the walls as the no-slip boundary condition is applied to the channel simulation. When the fluid approaches the chamber, suddenly, the flow velocity decreases, which leads to the partial transport of fluid into the chamber; therefore, a specific fraction of fluid will always be captured in the chamber in the microfluidic continuous operation mode. Considering the sample homogeneity in the base fluid, we can expect the same volume fraction of the analyte of interest in the channel.

The flow condition is demonstrated by observing the flow with velocity contours in the middle plane of the microfluidic channel. As can be seen in Figure 4-17, when the flow rate increases from a low value (10 mg/s) to a high value (> 350 mg/s), the flow starts to become unstable around 50 mg/s and continues to pass the chamber in the middle.

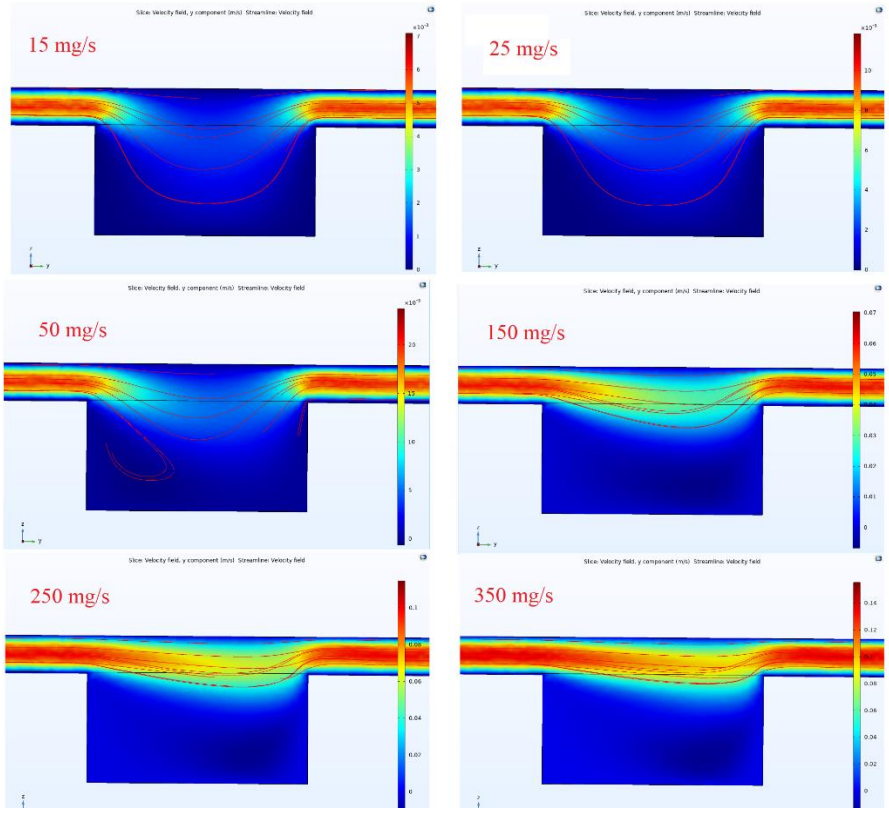


Figure 4-17. Velocity contours for different inlet mass flow rate values in the microfluidic channel.

At high flow velocities, the volume fraction of fluidic trapped in the chamber decreases as the flow gains high momentum to pass the chamber. For specific applications such as the cells under perfusion or analyte transportation on the sensing region (with this microfluidic topology), this analysis helps choose the best range of flow rate in the channel.

The flow shear rate distribution is calculated to demonstrate the effect of flow on the sensing region. Shear rate explains the impact of inlet flow on the flow shear stress in the sensing region, which is suitable for quantifying flow effects on the bottom of the chamber. In other words, the shear rate can be used to demonstrate the impact of change in inlet velocity on transport in the sensing region. Figure 4-18 shows the change in shear rate on the centerline of the bottom plane of the chamber where the sensor is placed in the middle.

According to the results shown in Figure 4-18, the flow is unstable for all ranges of inlet conditions. For instance, the flow around 50 mg/s yields wavy shear stress on the surface, indicating turbulence in the flow, which is not desirable for working a biosensor in continuous mode. Therefore, according to the simulation, we suggest a flow rate lower than 50 mg/s for the operation of this sensor in this microfluidic channel. However, we conducted experiments in stationary conditions to avoid stream currents in the flow that affect pH sensitivity when doing pH tests. The microfluidic analysis provides insights for using this sensor for biosensing applications, which need precise control of the injection of an analyte on the sensing region with this chamber-included microfluidics.

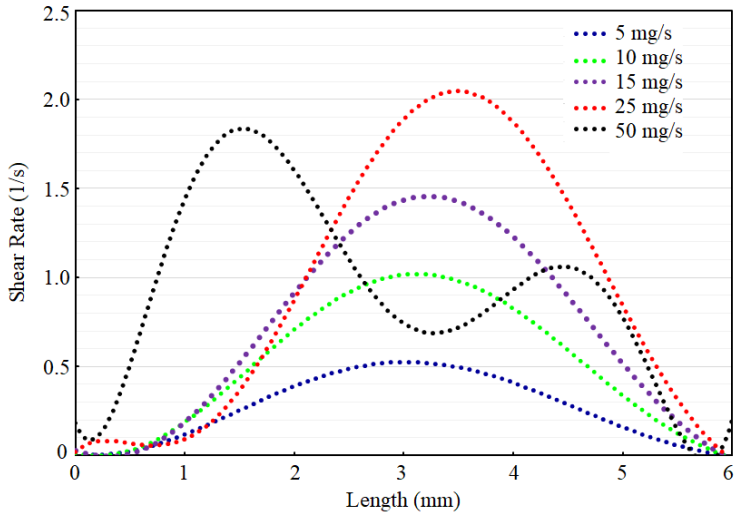


Figure 4-18. The change in shear rate for different values of inlet mass flow rate condition along the centerline of the chamber

4.6. Discussion

Using 3D-printed microfluidics, a simple method is introduced in the paper for integrating a miniaturized fluidics part with a FET sensor for life science applications. The methodology allows two planar microfluidics to be used to create a chamber on top of the sensor's sensing area. The introduced microfluidic system allows higher feature sizes, making the fabrication feasible with 3D printing. Furthermore, the bonding is made through UV-curable glue, which makes the integration much more accessible. Also, the design of microfluidics parts avoids the alignment issues primarily associated with small microfluidics that must be developed in the top area of the chip. The microfluidics is tested with simple fluids to show the functionality of the sensor and the operation of the introduced packaging methodology. It has been proved that using thin

microfluidics, as described in this paper, will be appropriate for the back-gate FET sensors that are becoming popular due to their enhanced sensing properties. This microfluidics can be used for those sensors to eradicate the need for bulky electrodes in the solution. The introduced packaging method for the FET sensor can be used to create a platform for rapid testing of solutions and avoid the cumbersome associated with testing the sensor inside the prob-station cage that has limited space and is risky due to the possible fluid leakages that are detrimental for the expensive machine electronics. Furthermore, it is discussed how 3D printing (PolyJet) can be recruited to rapidly build a testing fixture integrated with microfluidics for testing a solution and other bioassays on a FET sensor. Also, theoretically and experimentally, it is proved that the back-gate structure can be used to change the sensor's gain, which enables more sensitivity (e.g., pH sensitivity). Mathematical modeling is introduced for theoretical analysis, which helps predict the trends of the sensor's response and comparison with the sensor's function. However, more work should be done to improve the model, especially the charge modeling in the solution.

The FET sensor in this work has been proven to be charge-sensitive with a demonstration of simple liquids and pH solutions. Based on the successful utilization of FET sensors in different life science applications, we believe the charge sensing capability of the current platform could be extended to sensor other charged proteins and chemical reactions that lead to the enhancement of solution charge density. Nevertheless, this sensor could be unutilized with receptors for the specific analyte in the solution for other life science applications since the charge sensing capability of the sensor enables those sensing mechanisms.

4.7. Conclusion

This research explains the integration of OG-JFET sensors into 3D-printed PDMS-based microfluidics for biosensing applications. The microfluidics can be easily fabricated with 3D-printed molds. The sensor's large die size and sensing area (≈ 0.7 mm^2) provide a large size, allowing the use of high aspect ratios for molding. This makes PDMS fabrication easier without complex methods such as photolithography. The sensor has a back-gate structure that enables easier integration with a microfluidic channel without bulky reference electrode integration. Many efforts have been made to fabricate miniaturized reference electrodes on the sensing dies, making their stability and lifetime a severe matter of concern in integrated microfluidics biosensors. Nevertheless, we have shown in this paper how PolyJET 3D printing technology can be used to

fabricate PDMS microfluidic molds for a back-gated sensor. The sensor is successfully integrated and tested with a solution to demonstrate its functionality for solution charge sensing, which is the aim of every BioFET sensor.

For this reason, DI water and 0.9% NaCl solution were tested in a microfluidic channel to show the functionality of the integration. To be more precise in demonstrating the effectiveness of the back-gate and its importance in the integrated sensor, the current sensitivity of the sensor was analyzed, showing the sensor's effect on controlling the sensor's operation point. Furthermore, it is shown that the back gate can enhance the current sensitivity through its inherent amplification potential. In other words, back-gate significantly eases the integration by providing an open-gate area for running a microfluidic channel. It can be used to take advantage of the sensor structure to enhance the current sensitivity by changing the gain (gm). It is shown that the change of back-gate from 1 V to 0 V changes the gain from ~ 0.42 mA/V to ~ 1 mA/V in a constant Vds. It is shown that the sensing layer's physically controlled surface charge sensitivity (here, SiO_2) can be amplified by the sensor's gain to change the current sensitivity. It is shown that the change of the back gate from 1.0 to 0.0 can increase the sensitivity from ~ 40 mV/pH to ~ 55 mV/pH.

Author Contributions: AP[1] contributed in the "Conceptualization; Methodology; Experiments; Simulations; writing—original draft preparation" and EG[2] contributed in the "Conceptualization, writing—review and editing; supervision; funding acquisition ".

Funding: This work was supported in part by the Mitacs under Grant ITi1887

Data Availability Statement: Not applicable

Acknowledgments: We would like to acknowledge CMC Microsystems for providing products and services that facilitated this research, including software design packages such as Mentor Tanner, COMSOL Multiphysics, fabrication services for the Electronic Sensor Platform at 3IT, and engineering support. The first author also thanks Hamed Osouli Tabrizi for his help in designing the printed circuit board (PCB) used for the electrical packaging of the platform.

Conflicts of Interest: The authors declare no conflict of interest.

[1] Abbas Panahi
[2] Ebrahim Ghafar-Zadeh

4.8. References

[1] Hassanvand, Z.; Jalali, F.; Nazari, M.; Parnianchi, F.; Santoro, C. Carbon Nanodots in Electrochemical Sensors and Biosensors: A Review. *ChemElectroChem*, 2021, 8, 15–35, , doi: 10.1002/celc.202001229

[2] Mani, V. *et al.* Electrochemical sensors targeting salivary biomarkers: A comprehensive review. *TrAC - Trends Anal. Chem* **2021**, 135, 116164. doi: 10.1016/j.trac.2020.116164

[3] Huang, L.; Tian, S.; Zhao, W.; Liu, K.; Guo, J. Electrochemical vitamin sensors: A critical review. *Talanta* **2021**, 222, 121645. doi: 10.1016/j.talanta.2020.121645.

[4] Panahi, A.; Sadighbayan, D.; Forouhi, S.; Ghafar-Zadeh, E. Recent advances of field-effect transistor technology for infectious diseases. *Biosensors* **2021**,11, 4. doi: 10.3390/bios11040103.

[5] Sadighbayan, D.; Minhas-Khan, A.; Ghafar-Zadeh, E. Laser-Induced Graphene-Functionalized Field-Effect Transistor-Based Biosensing: A Potent Candidate for COVID-19 Detection. *IEEE Trans. Nanobioscience* 2021, 1–1. doi: 10.1109/tnb.2021.3119996.

[6] Forouhi, S.; Ghafar-Zadeh, E. Applications of cmos devices for the diagnosis and control of infectious diseases. *Micromachines* 2020, 11, 11. doi: 10.3390/mi11111003.

[7] Li, L.; Chakik, M.; Prakash, R. A review of corrosion in aircraft structures and graphene-based sensors for advanced corrosion monitoring. *Sensors* **2021** 21, 9. doi: 10.3390/s21092908.

[8] Hasan, N.; Kansakar, U.; Sherer, E.; DeCoster, M. A.; Radadia, A. D. Ion-Selective Membrane-Coated Graphene–Hexagonal Boron Nitride Heterostructures for Field-Effect Ion Sensing. *ACS Omega* **2021**, doi: 10.1021/acsomega.1c02222.

[9] Oh, H. G. *et al.* Two–dimensional disposable graphene sensor to detect na+ ions. *Nanomaterials* 2021, 11, 3, 1–12. doi: 10.3390/nano11030787.

[10] Munteanu, R. E.; Moreno, P. S.; Bramini, M.; Gáspár, S. 2D materials in electrochemical sensors for in vitro or in vivo use. *Anal. Bioanal. Chem.* **2020**, 701–725. doi: 10.1007/s00216-020-02831-1.

[11] Sadighbayan, D.; Hasanzadeh, M; Ghafar-Zadeh, E. Biosensing based on field-effect transistors (FET): Recent progress and challenges. *TrAC - Trends Anal. Chem.* **2020,** 133, 116067. doi: 10.1016/j.trac.2020.116067.

[12] Wei, J.; Zhao, Z.; Lan, K.; Wang, Z.; Qin, G.; Chen, R. Highly sensitive detection of multiple proteins from single cells by MoS2-FET biosensors. *Talanta* 2021, 236, 122839. doi: 10.1016/j.talanta.2021.122839.

[13] Chen, L.; Li, G.; Yang, A.; Wu, J.; Yan, F.; Ju, H. A DNA-functionalized graphene field-effect transistor for quantitation of vascular endothelial growth factor. *Sensors Actuators B Chem.* 2021, 130964, 351. doi: 10.1016/j.snb.2021.130964.

[14] Schuck, A.; Kim, H.E.; Moreira, J.K.; Lora, P.S.; Kim, Y.-S. A Graphene-Based Enzymatic Biosensor Using a Common-Gate Field-Effect Transistor for L-Lactic Acid Detection in Blood Plasma Samples. *Sensors* 2021, *21*, 1852. https://doi.org/10.3390/s21051852

[15] Alias, A. B.; Huang, H. Y.; Yao, D. J. A review on microfluidics: An aid to assisted reproductive technology. *Molecules* **2021**, 1–19,26. doi: 10.3390/molecules26144354.

[16] Kalyan, S. *et al.* Inertial microfluidics enabling clinical research. *Micromachines* 2021, 12, 1–43. doi: 10.3390/mi12030257.

[17] David, S.; Walt, R.; Stubbs, J.; Andersson-svahn, H.; Gilligan, M.; Wilson, E. Lab on a Chip Lab on a Chip," *Lab Chip*, pp. 1037–1043, 2014, doi: 10.1039/D1LC00869B.Volume.

[18] Hur, J.; Chung, A. J. Microfluidic and Nanofluidic Intracellular Delivery. *Adv. Sci.* 2021, 8, 15. doi: 10.1002/advs.202004595.

[19] Lee, J.; Nolan, M.; Lee, H. Feasibility Study of a Microfluidic Solenoid for Discrete Quantitation of Magnetized Cells. *IEEE Trans. Nanobioscience* **2019**, 18, 2, 240–243. doi: 10.1109/TNB.2019.2905506.

[20] Ochoa-Vazquez, G. *et al.* Microfluidics and Surface-Enhanced Raman Spectroscopy: A Perfect Match for New Analytical Tools. *IEEE Trans. Nanobioscience* **2019**, 18, 4, 558–566. doi: 10.1109/TNB.2019.2943078.

[21] Nitrite, I. Microfluidic Soil Nutrient Detection System. **2020** vol. 20, no. 8, pp. 4504–4511, 2020.

[22] Bhattacharjee, S.; Banerjee, A.; Ho, T. Y.; Chakrabarty, K.; Bhattacharya, B. B. Efficient generation of dilution gradients with digital microfluidic biochips. *IEEE Trans. Comput. Des. Integr. Circuits Syst* **2019**, 38, 5, 874–887. doi: 10.1109/TCAD.2018.2834413.

[23] Rewatkar, P.; Goel, S. Next-Generation 3D Printed Microfluidic Membraneless Enzymatic Biofuel Cell: Cost-Effective and Rapid Approach. *IEEE Trans. Electron Devices* 2019, 66, 8, 3628–3635. doi: 10.1109/TED.2019.2922424.

[24] Zengerle, R.; Koltay, P.; Ducrée, J. Microfluidics: An enabling technology for the life sciences. *Proc. 2004 Int. Symp. Micro-NanoMechatronics Hum. Sci. MHS2004; Fourth Symp. 'Micro-NanoMechatronics Information-Based Soc. 21st Century* 2004, 1–6. doi: 10.1109/mhs.2004.1421260.

[25] B. Zhang, Zhang; Penton, C. Ryan; Xue, C.; Wang, Q.; Zheng, T.; Tiedje, J. M. Evaluation of the ion torrent personal genome machine for gene-targeted studies using amplicons of the nitrogenase gene nifH. *Appl. Environ. Microbiol.* 2015, 81, 13, 4536–4545. doi: 10.1128/AEM.00111-15.

[26] Vogel, U.; Szczepanowski, R.; Claus, H.; Jünemann, S.; Prior, K.; Harmsen, D. Ion torrent personal genome machine sequencing for genomic typing of Neisseria meningitidis for rapid determination of multiple layers of typing information. *J. Clin. Microbiol.* **2012**, 50, 6, 1889–1894. doi: 10.1128/JCM.00038-12.

[27] Pereira, F. L.; Soares, S. C.; Dorella, F. A.; G. Leal, C. A.; Figueiredo, H. C. P. Evaluating the efficacy of the new Ion PGM Hi-Q Sequencing Kit applied to bacterial genomes. *Genomics*, 2016, 107, 5, 189–198. doi: 10.1016/j.ygeno.2016.03.004.

[28] Hajialyani, M.; Hosseinzadeh, L.; Wu, J. J. Microfluidics-Integrated Sensors toward Rapid Detection of Single Nucleotide Variations. *ACS Omega* **2021**, 6, 38, 24297–24303, doi: 10.1021/acsomega.1c02563.

[29] Dutta, G.; Rainbow, J.; Zupancic, U.; Papamatthaiou, S.; Estrela, P.; Moschou, D. Microfluidic devices for label-free DNA detection. *Chemosensors* 2018, 6, 4, doi: 10.3390/chemosensors6040043.

[30] Z. Li *et al.* Design and fabrication of portable continuous flow PCR microfluidic chip for DNA replication. *Biomed. Microdevices* **2020**, 22, 1. doi: 10.1007/s10544-019-0457-y

[31] Shen, K. M. *et al.* An integrated microfluidic system for rapid detection and multiple subtyping of influenza A viruses by using glycan-coated magnetic beads and RT-PCR. *Lab Chip* **2019**, 19, 7, 1277–1286. doi: 10.1039/c8lc01369a.

[32] Kim, Y. *et al.* Integrated microfluidic preconcentration and nucleic amplification system for detection of influenza a virus H1N1 in saliva. *Micromachines* 2020, 11, 2, 1–11, doi: 10.3390/mi11020203.

[33] Basiri, A. *et al.* Microfluidic devices for detection of RNA viruses. *Rev. Med. Virol.* **2021**, 31, 1, 1–11, doi: 10.1002/rmv.2154.

[34] Chung, Y. Da; Liu, T. H.; Liang, Y. L.; Lin, C. N.; Hsu, K. F.; Lee, G. Bin. An integrated microfluidic platform for detection of ovarian clear cell carcinoma mRNA biomarker FXYD2. *Lab Chip* **2021**, 21, 13, 2625–2632, 2021. doi: 10.1039/d1lc00177a.

[35] A. Fragoso *et al.* Integrated microfluidic platform for the electrochemical detection of breast cancer markers in patient serum samples. *Lab Chip* **2011**, 11, 4, 625–631. doi: 10.1039/c0lc00398k.

[36] Zhao, W. *et al.* Microsphere mediated exosome isolation and ultra-sensitive detection on a dielectrophoresis integrated microfluidic device. *Analyst* 2021, 146, 19, 5962–5972. doi: 10.1039/d1an01061a.

[37] Xu, M. *et al.* Design and clinical application of an integrated microfluidic device for circulating tumor cells isolation and single-cell analysis. *Micromachines* 2021, 12, 1, doi: 10.3390/mi12010049.

[38] Cho, H. Y.; Choi, J. H.; Lim, J.; Lee, S. N.; Choi, J. W. Microfluidic chip-based cancer diagnosis and prediction of relapse by detecting circulating tumor cells and circulating cancer stem cells. *Cancers (Basel)* **2021**, 13, 6, 1–17. doi: 10.3390/cancers13061385.

[39] Hassanpour Tamrin, S.; Sanati Nezhad, A.; Sen, A. Label-Free Isolation of Exosomes Using Microfluidic Technologies. ACS Nano 2021, 15, 11, 17047–17079. doi: 10.1021/acsnano.1c03469.

[40] Zhu, F. *et al.* Controllable design of a nano-bio aptasensing interface based on tetrahedral framework nucleic acids in an integrated microfluidic platform. *Biosens. Bioelectron.* 2020, 176, 112943. doi: 10.1016/j.bios.2020.112943.

[41] Ye, X.; Li, Y.; Wang, L.; Fang, X.; Kong, J. All-in-one microfluidic nucleic acid diagnosis system for multiplex detection of sexually transmitted pathogens directly from genitourinary secretions. *Talanta* 2020, 221, 121462. doi: 10.1016/j.talanta.2020.121462.

[42] Kumar, S. *et al.* Microfluidic-integrated biosensors: Prospects for point-of-care diagnostics. *Biotechnol. J.* 2013, 8, 11, 1267–1279, doi: 10.1002/biot.201200386.

[43] Huang, Y.; Mason, A. J. Lab-on-CMOS integration of microfluidics and electrochemical sensors. *Lab Chip*, 13, 19, 3929–3934, doi: 10.1039/c3lc50437a.

[44] Ettehad, H. M.; Wenger, C. Characterization and separation of live and dead yeast cells using cmos-based dep microfluidics," *Micromachines* 2021, 12, 3, 1–19. doi: 10.3390/mi12030270.

[45] Nabovati, G.; Ghafar-Zadeh, E.; Letourneau, A.; Sawan, M. Smart Cell Culture Monitoring and Drug Test Platform Using CMOS Capacitive Sensor Array. *IEEE Trans. Biomed. Eng.* 2019, 66, 4, 1094–1104. doi: 10.1109/TBME.2018.2866830.

[46] Dorst, B. Van *et al.* Integration of an optical CMOS sensor with a microfluidic channel allows a sensitive readout for biological assays in point-of-care tests. *Biosens. Bioelectron.* 2016, 78, 126–131. doi: 10.1016/j.bios.2015.11.027.

[47] Yen, P. W. *et al.* A Low-Power CMOS Microfluidic Pump Based on Travelling-Wave Electroosmosis for Diluted Serum Pumping. *Sci. Rep.* 2019, 9, 1, 1–8. doi: 10.1038/s41598-019-51464-7.

[48] Hogan, B. T. *et al.* Dynamic in-situ sensing of fluid-dispersed 2D materials integrated on microfluidic Si chip. *Sci. Rep. 2017*, 7, 1–7. doi: 10.1038/srep42120.

[49] Măriuţa, D. *et al.* Miniaturization of fluorescence sensing in optofluidic devices. *Microfluid. Nanofluidics* **2020**, 24, 9, 1–28. doi: 10.1007/s10404-020-02371-1.

[50] Ghafar-Zadeh, E.; Sawan, M.; Therriault, D. A microfluidic packaging technique for lab-on-chip applications. *IEEE Trans. Adv. Packag.* 2009, 32, 2, 410–416. doi: 10.1109/TADVP.2008.920655.

[51] Ghafar-Zadeh, E.; Sawan, M.; Therriault, D. A 0.18-μm CMOS capacitive sensor Lab-on-Chip. *Sensors Actuators, A Phys.* **2008**, vol. 141, 2, 454–462, 2008, doi: 10.1016/j.sna.2007.10.007.

[52] Leonardi, A. A.; Lo Faro M. J.; Irrera, A. Biosensing platforms based on silicon nanostructures: A critical review. *Anal. Chim. Acta*, vol. 1160, 2021, doi: 10.1016/j.aca.2021.338393.

[53] S. Islam *et al.*, "Microfluidic-based graphene field effect transistor for femtomolar detection of chlorpyrifos," *Sci. Rep.*, vol. 9, no. 1, pp. 1–7, 2019, doi: 10.1038/s41598-018-36746-w.

[54] Choi, K.; Kim, J. Y.; Ahn, J. H.; Choi, J. M.; Im, M.; Choi, Y. K. Integration of field effect transistor-based biosensors with a digital microfluidic device for a lab-on-a-chip application. *Lab Chip* **2012**, 12, 8, 1533–1539. doi: 10.1039/c2lc21203j.

[55] Sinha, A. *et al.* An integrated microfluidic system with field-effect-transistor sensor arrays for detecting multiple cardiovascular biomarkers from clinical samples. *Biosens. Bioelectron.* 2018, 129, 155–163, 2019. doi: 10.1016/j.bios.2019.01.001.

[56] He, R. X. *et al.* Solution-gated graphene field effect transistors integrated in microfluidic systems and used for flow velocity detection. *Nano Lett.* 2012, 12, 3, 1404–1409. doi: 10.1021/nl2040805.

[57] Lai, Y. H.; Lim, J. C.; Lee, Y. C.; Huang, J. J. Analysis of the biochemical reaction status by real-time monitoring molecular diffusion behaviors using a transistor biosensor integrated with a microfluidic channel. *ACS Omega* 2021, 6, 18, 11911–11917. doi: 10.1021/acsomega.1c00222.

[58] Shen, F. *et al.* Integrating silicon nanowire field effect transistor, microfluidics and air sampling techniques for real-time monitoring biological aerosols," *Environ. Sci. Technol.* 2011, 45, 17, 7473–7480. doi: 10.1021/es1043547.

[59] Annese, V.F.; Giagkoulovits, C.; Hu, C.; Al-Rawhani, M.A.; Grant, J.; Patil, S.B.; Cumming, D.R.S. Micromolar Metabolite Measurement in an Electronically Multiplexed Format. *IEEE Trans of Biomed Eng* **2022**, Early Access, DOI: 10.1109/TBME.2022.3147855.

[60] Annese, Valerio F. et al. A monolithic single-chip point-of-care platform for metabolomic prostate cancer detection. *Microsystems & Nanoengineering* **2021**, 7, 21, https://doi.org/10.1038/s41378-021-00243-4.

[61] Muluneh, Melaku; Issadore, David. A multi-scale PDMS fabrication strategy to bridge the size mismatch between integrated circuits and microfluidics. Lab Chip **2014**,14, 4552-4558. DOI: https://doi.org/10.1039/C4LC00869C

[62] Zhang, Bowei; Dong, Quan; Korman, Can E.; Li, Zhenyu; Zaghloul, Mona E. Flexible packaging of solid-state integrated circuit chips with elastomeric microfluidics. *Scientific Reports* **2013**, 3, 1098. DOI: 10.1038/srep01098

[63] Larisika, Melanie et al. Electronic Olfactory Sensor Based on A. mellifera Odorant-Binding Protein 14 on a Reduced Graphene Oxide Field-Effect Transistor. Angew.Chem **2015**,127,13443–1344, https://doi.org/10.1002/ange.201505712.

[64] White, Scott P; Sreevatsan, Srinand; Frisbie, C. Daniel; D. Dorfman, Kevin. Rapid, Selective, Label-Free Aptameric Capture and Detection of Ricin in Potable Liquids Using a Printed Floating Gate Transistor. *ACS Sens.* 2016, 1, 10, 1213–1216. https://doi.org/10.1021/acssensors.6b00481

[65] Berto, Marcello et al. Biorecognition in Organic Field Effect Transistors Biosensors: The Role of the Density of States of the Organic Semiconductor. *Anal. Chem.* **2016**, 88, 24, 12330–12338. https://doi.org/10.1021/acs.analchem.6b03522

[66] Knopfmacher, Oren; L. Hammock, Mallory; L. Appleton, Anthony; Schwartz, Gregor; Mei, Jianguo; Lei, Ting; Pei, Jian; Bao, Zhenan. Highly stable organic polymer field-effect transistor sensor for selective detection in the marine environment. *Nat Commun* **5,** 2954 (2014). https://doi.org/10.1038/ncomms3954

[67] Papamatthaiou, S.; Zupancic, U.; Kalha, C.; Regoutz, A.; Estrela, P.; Moschou, D. Ultra stable, inkjet-printed pseudo reference electrodes for lab-on-chip integrated electrochemical biosensors. *Sci. Rep.* **2020**, 10, 1, 1–10, 2020. doi: 10.1038/s41598-020-74340-1.

[68] Shinwari, M. Waleed; Zhitomirsky, D.; Deen, I. A.; Selvaganapathy, P. R.; Jamal Deen, M.; Landheer, D. Microfabricated reference electrodes and their biosensing applications. *Sensors* **2010**, 10, 3, 1679–1715. doi: 10.3390/s100301679.

[69] Zhou, J. *et al.* Fabrication of a microfluidic Ag/AgCl reference electrode and its application for portable and disposable electrochemical microchips. *Electrophoresis* **2010**, 31, 18, 3083–3089. doi: 10.1002/elps.201000113.

[70] Panahi, A.; Tabrizi, H. O.; Mangannavar, P.; Chebotarev, O.; Fung, A.; Ghafar-Zadeh, E. Open-Gate Junction Field Effect Transistor (OG-JFET) for Life Science Applications: Design, Implementation and Characterization. *IEEE Sens. J.* 2021, 21, 26503 - 26514 doi: 10.1109/JSEN.2021.3121339.

[71] Panahi, A.; Sadighbayan, D.; Ghafar-Zadeh, E. Electronic Sensing Platform (ESP) Based on Open-Gate Junction Field-Effect Transistor (OG-JFET) for Life Science Applications: Design, Modeling and Experimental Results. *Sensors* 2021, 21, 7491. https://doi.org/10.3390/s21227491

[72] Panahi, A.; O. Tabrizi H.; Mangannavar, P.; Chebotarev, O.; Fung, A.; Ghafar-Zadeh, E. A New Foundry-Based Open-Gate Junction Field-Effect Transistor (OG-JFET) as Electronic Sensing Platform (ESP) for Life Science Applications. *2021 IEEE Sensors* **2021**, 1-4, doi: 10.1109/SENSORS47087.2021.9639830.

[73] Morita, M.; Ohmi, T.; Hasegawa, E.; Kawakami, M.; Ohwada, M. Growth of native oxide on a silicon surface. *J. Appl. Phys. 1990*, 68, 3, 1272–1281. doi: 10.1063/1.347181.

[74] Adinolfi, V.; Sargent, E. H. Photovoltage field-effect transistors. *Nature* **2017**, 542, 7641, 324–327. doi: 10.1038/nature21050.

[75] Barillaro, G.; Lazzerini G. M.; Strambini, L. M. Modeling of porous silicon junction field effect transistor gas sensors: Insight into NO2 interaction. *Appl. Phys. 2010, Lett.*, 96,16. doi: 10.1063/1.3391620.

Chapter 5 Parametric Desing of Open-Gate JFET[1]

Paper 6: Performance Analysis of Open-Gate Junction FET: A New Foundry-based Silicon Transistor for Biochemical Sensing Applications

Journal: Submitted to IEEE Access (under review)

Authors: Abbas Panahi and Ebrahim Ghafar-Zadeh

Abbas Panahi's contribution: chip characterization, data analysis, simulation of device and data analysis, manuscript writing, submission, editing and revisions.

This chapter provides essential information on the critical design parameters affecting the performance of the OG-JFET sensor. We utilized COMSOL simulations to analyze the impact of both geometrical and material properties on the transconductance and efficiency of the OG-JFET. The study identifies and ranks the most and least influential parameters, offering valuable insights for future designers. Additionally, the charge-sensing mechanism of the OG-JFET is explored, with sensor responses calculated for a range of charges from positive to negative. This analysis provides a deeper understanding of the sensor's operational mechanism. Furthermore, the chapter discusses the OG-JFET's transconductance and its relation to charge sensing, demonstrating its competitive performance compared to existing FET biosensors. Overall, this chapter serves as a comprehensive guide for the parametric design of the OG-JFET.

[1] The content of this chapter is based on a submitted paper: A. Panahi, E. Ghafar-Zadeh, "Performance Analysis of Open-Gate Junction FET: A New Foundry-based Silicon Transistor for Biochemical Sensing Applications" submitted to the IEEE Access Journal and is under review.

5.1. Abstract

This paper investigates the performance and parametric design of a new foundry-based silicon field-effect transistor (FET) platform, the open-gate junction field-effect transistor (OG-JFET), intended for bio/chemical sensing applications. The fabrication process of the OG-JFET relies on a standard foundry process, requiring the establishment of parametric design rules to understand the effect of crucial sensor performance factors, including transconductance (g_m) and device efficiency ($\eta = g_m/I_{ds}$). The study examines the impact of various geometric parameters (e.g., channel length and thickness) and material-related parameters (such as boron and phosphorous impurity doping levels) on sensor performance. Simulations provide insights and guidelines for the efficient design and characterization of the OG-JFET, focusing on enhancing g_m and maximizing η for biosensing applications. Experimental measurements of the OG-JFET demonstrate a current range of ~ 200 µA/µm, a high g_m of approximately ~ 1700 µS (340 µS/µm), and η of ~ 4.5 V^{-1} (for a channel length of 5 µm), which are of importance for circuit design and biosensing application of OG-JFET. These results showcase the performance of this sensor compared to other silicon-based FET platforms for internal signal amplification in sensing applications of OG-JFET and as an electronic FET element. The findings of this paper offer valuable guidelines for the design of sensors based on OG-JFET technology, enabling gaining insights into the impact of sensor structure on sensing performance. Also, we have demonstrated how two performance parameters can be utilized to compare two different designs of OG-JFET, which is useful for future designers.

INDEX TERMS Field-Effect Transistor (FET), Semiconductor, Simulation, COMSOL, Biosensor

5.2. Introduction

Field-effect transistors (FETs) biosensors have attracted significant attention in the past decade due to their unique sensing characteristics, making them highly desirable for various applications, including diagnostics, gas sensing, food safety, and environmental monitoring [1], [2]. FET sensors offer several advantages, such as low cost, label-independent detection, and rapid analysis of biological analytes. Label-free detection significantly reduces the overall cost of sensor development [3], [4], [5]. These sensors have demonstrated exceptional capabilities in the fast and

sensitive detection of various diseases, exhibiting a competitive low limit of detection (LOD) in many applications [6], [7]. This remarkable feature has motivated researchers to integrate FET sensors into lab-on-a-chip devices, enabling the realization of low-cost, handheld, personalized medical diagnostic devices [6], [8], [9], [10], [11], [12], [13]. The portability of FET sensors has been identified as one of the most appealing features for developing point-of-care devices [14]. FET-based sensors provide higher sensitivity, are suitable for mass production (e.g., CMOS-based FETs), offer low cost, and can be easily miniaturized and integrated with microfluidics [15], [16].

Moreover, FET sensors can detect inherent molecular charges directly from neutral biomolecules and assess novel biological assays, including sensing chemical reactions. This capability allows for the digital analysis of physical interactions of biomolecules, such as protein conformational changes and spatial arrangements, which is not readily achievable with other sensing methods [17], [18]. Unlike other label-free sensing techniques, FET-based biosensors eliminate the need for bulky optical instruments and equipment. Due to the unique features of FET biosensors, there has been a strong focus on enhancing their sensing performance through the development of new structures or improvements in surface functionalization chemistry. Various FET sensor structures have been explored for biosensing applications, including metal-oxide-semiconductor FETs (MOSFETs) [19], FinFETs [20], [21], Graphene FETs (GFETs) [4], [22], Carbon Nanotube FETs (CNT FETs) [23], [4], and FETs based on 2D materials [24], [25]. These advancements pave the way for further improvements in FET biosensors and their integration into diverse applications in the biomedical field.

Among various FET structures explored in research, silicon-based FETs (Si-BioFETs) have gained significant attention due to their compatibility with standard CMOS technology, enabling low-cost and easy miniaturization [15]. The particular interest in CMOS-based technology is the fact that the technology is scalable and can be easily integrated and mass-produced [26]. Silicon nanowire based FinFETs have been employed for biosensing applications [20]. These nanowire FET sensors have been successfully integrated with microfluidics, showcasing their potential for high-throughput bioanalysis applications [27]. The mechanisms underlying the sensing capabilities of Si-BioFETs are discussed in a pioneering study by Matti Kaisti [28]. This study delves into using Si-BioFET technology for various applications in biomolecular and cellular analysis [28]. The

research highlights the potential of Si-BioFETs in advancing the field of biosensing and their suitability for diverse applications in the biomedical domain.

A novel addition to the FET sensor family is the emerging foundry-based open-gate junction field-effect transistor (OG-JFET), facilitated by CMC Microsystem as a Si-FET platform designed explicitly for multipurpose applications [29]. This innovative FET structure, also known as an electronic sensing platform (ESP), offers promising capabilities in the field of biosensing [30]. The OG-JFET has demonstrated exceptional performance as a photovoltage transistor, significantly enhancing light detection [31]. In our previous work, we investigated the potential of the OG-JFET as a charge-sensing platform and demonstrated its H+ sensitivity [29]. Our findings revealed that the open-gate area of the p-OGJFET structure can facilitate the sensing charge of biomolecules, including DNA or solution ions like H+ [32], [33]. This highlights the OG-JFET in facilitating OG-JFET versatility in the detection and analysis of the inherent charge of biomolecules (e.g., Oral cells and ssDNA) or ions (Na+, H+).

The OG-JFET, a novel FET sensing platform with the potential for large-scale production [33], needs a comprehensive examination of sensor performance influenced by various geometrical and material parameters. By considering the design guidelines provided by the manufacturer, we have conducted both experimental and theoretical investigations to identify the critical design factors that significantly impact the sensing performance. Utilizing COMSOL Multiphysics software, we have assessed the influence of these design characteristics on two crucial performance metrics: sensor transconductance (gm) and efficiency (gm/Ids). These metrics serve as valuable figures of merit for comparative analysis, enabling us to evaluate the overall performance of the OG-JFET platform.

Within this research paper, our findings indicate that the OG-JFET structure offers a significantly higher gm in comparison to other FET structures commonly utilized for biosensing applications, including GFET, CNT FET, silicon nanowire FET, and FinFET, among others. Additionally, we delve into the design guidelines that facilitate the achievement of specific gm values while considering η. The design principles outlined in this study can be a valuable resource for future users of this foundry Si-FET sensing technology.

5.3. Materials and Methods

5.3.1. Single Channel Open-Gate Junction Field-Effect Transistor Sensor Fabrication

The sensor structure comprises a vertical p-n junction, where a thin layer of p-type silicon (~ 1.6 μm) is uniformly formed on a thicker layer of n-type silicon (~ 450 μm) serving as the support layer. A thick Si_3N_4 layer is deposited on top of a SiO_2 layer to passivate the source and drain metals, as illustrated in Figure 5-1. A frontside metal contact is established using a 50 nm Cr layer followed by a 500 nm Au layer. A 50 nm Ti layer and a 500 nm Al layer are utilized for the back-side contact. Boron implantation is employed to define the source and drain wells, and subsequently, aluminum-silicon contacts are patterned using standard lithography and liftoff processes. A detailed fabrication process can be found in [32], which has a different layout design (a common source for multiplexing). The sensing layer in the current sensor structure is the p-type layer between two ohmic-contacted sources and a drain. The channel is exposed to the environment to enable the introduction of biological samples to the sensor. The p-n junction can be biased in forward or reverse mode, with the reverse bias being more suitable due to improved controllability of charge sensing in the channel and lower power consumption at higher voltages. Figure 5-1 (a) shows a schematic representation of the sensor, where the source and drain electrodes are encapsulated with SiO_2 and Si_3N_4. The Lo (see Figure 5-1) defines the active available sensing channel length, and Lsur, the oxide-covered portion of the channel, corresponds to the minimum surround. The structure consists of geometrical and material components, which can be controlled during manufacturing to achieve application-specific designs and targeted performance. The gm and η are crucial figure-of-merit parameters for comparing design parameters.

The sensor was developed using a standard microfabrication process based on a Very Large System Integration (VLSI), resulting in back-gated p-OG-JFET, as shown in Figure 5-1. The design layout is performed in L-Edit software for fabrication. The design encompasses two Cr/Au pads demonstrating drain and source electrodes. The different lengths of channels ranging from 5 μm to 150 μm with p-channel thickness of ~ 1.6 μm and n-channel of ~ 450 μm same for all have been fabricated. The uniform thin p-type channel extends across the entire chip area.

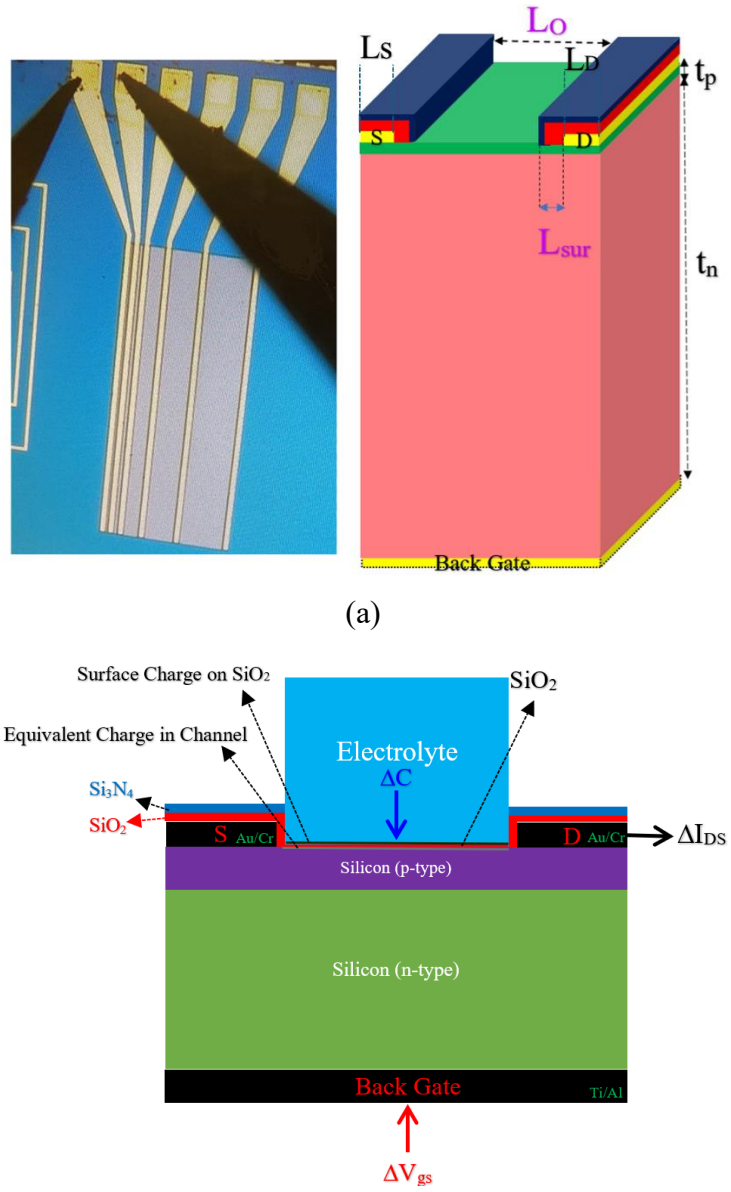


Figure 5-1. Optical image of single channel OG-JFET and schematics of device and sensing principle. (a): Left: sensor characterization under the optical microscope when placing the probe station needles on the sensing pads. Right: the structure of OG-JFET and the design parameters in a 3D sensor schematic showing the opened-gate area and the encapsulations with SiO_2-Si_3N_4 stacked layers. (b): the sensing mechanism for the sensor in solution and the relation between charge as input and Ids as output.

5.3.2. Sensor Characterization

The OG-JFET device is subjected to characterization using a probe station (MPI TS200-SE Probe Station) and a semiconductor analyzer (Keithley 4200A-SCS Parameter Analyzer). The measurement involved recording the drain-source current as a function of the back gate and drain-

source voltage. By applying a step voltage to the back gate, Ids-Vgs curves were obtained, and the drain voltage was swept from 0 to -10 V for OG-JFET devices on the chip.

Experimental measurements determined the sensor gm and η for various channel lengths. These values (gm, η) were calculated using specific formulas derived from the data obtained through experimental measurements and simulations.

$$g_m = \frac{\partial I_{ds}}{\partial V_{gs}} \tag{5-1}$$

$$\eta = \frac{g_m}{I_{ds}} \tag{5-2}$$

When a FET sensing channel is in touch with liquid, the outermost oxide layer on the channel interacts with the solution. It creates a charge layer, producing a double-layer capacitance [34]. This layer is mirrored in conductive channels that influence (through the created electric field) the space charge (electron/hole) inside the channel [28]. This charge on the channel can be considered an input amplified with a specific factor toward the enhancement of current sensitivity [35], [36], [37]. This enhancement factor is the sensor's gm.

$$\frac{\Delta I_D}{\Delta Q} = \frac{\Delta I_D}{\Delta V_{gs}} \times \frac{\Delta V_{gs}}{\Delta Q} \rightarrow \frac{\Delta I_D}{\Delta Q} = g_m \times \frac{\Delta V_{gs}}{\Delta Q} \tag{5-3}$$

ΔI_D is the change in the current, ΔQ is the change in the surface charge on oxide, and ΔVgs is the resultant change in back-gate reference voltage. Based on equation (5-3), higher gm contributes to higher current sensitivity, which can be used for real-time analysis of charge variation in the solution. Considering the rationale stated above, improving the gm is essential for developing new FET devices for biosensing. Another critical parameter that should be considered in designing a FET-based biosensor is η. The higher η, the higher the performance of the FET sensor for biological sample detection would be. The current sensitivity of the sensor can be correlated to the η through the following relation. [38]:

$$\frac{\Delta I_D}{I_0} = \frac{g_m}{I_0} \times \Delta V_{gs} = \eta \times \Delta V_{gs} \tag{5-4}$$

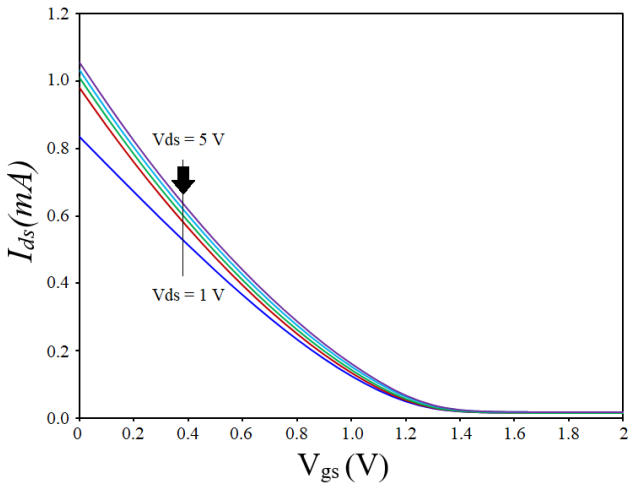
5.3.3. COMSOL Simulation

The sensor is modeled using COMSOL Multiphysics software, which provides a versatile design platform for Multiphysics simulations for different applications [39], [40], [41]. A complete parametric design based on the size and dimensions specified in the OG-JFET design rule can be modeled with the COMSOL simulation application. Important OG-JFET parameters are channel length, channel thickness, and doping levels in the p-type and n-type layers that can be modified to acquire the desired functionality of the sensor in the layout design process. If we consider a single channel of OG-JFET, the sensing performance of that channel would depend on the parameters defined in Figure 5-1 (a). Figure 5-1 (a) shows the design parameters affecting the sensor response based on the design rules provided by the manufacturer (CMC Microsystem). The LS, LD, LO, and Lsur variables can be directly controlled in the layout design. Other parameters defined in Figure 5-1 (a) are related to the material properties. The simulation is performed in the Semiconductor Module of COMSOL Multiphysics 5.5 software to predict the sensor electrical response (e.g., I-V curves) in different bias conditions. All geometrical aspects can be controlled by parameters defined in the global function section. The silicon has been selected for both p-type and n-type sections. The doping levels are controlled and set in the semiconductor section with analytical doping models 1 and 2. For the p-n junction of the p-type and n-type layers, the Continuity/heterojunction model is applied. The Shockley-Read-Hall (SRH) trapping model is used for the whole area of the chip (both n-type and p-type layers). The Ohmic contact model is set according to the fabrication process for all metal contacts. Except for source/drain and back gate contacts, all other faces in the simulation are considered insulated boundaries, meaning there is no electron/hole flux through these boundaries. The simulation has limitations in the exact prediction of the real-world I-V curves due to various non-idealities in the fabrication, experimentation, and the semiconductor model itself; therefore, we have calibrated the simulation with experimental results for one device and used it for prediction on other designs. We have used the back-gate voltage and the out-of-plane thickness as the calibration parameters.

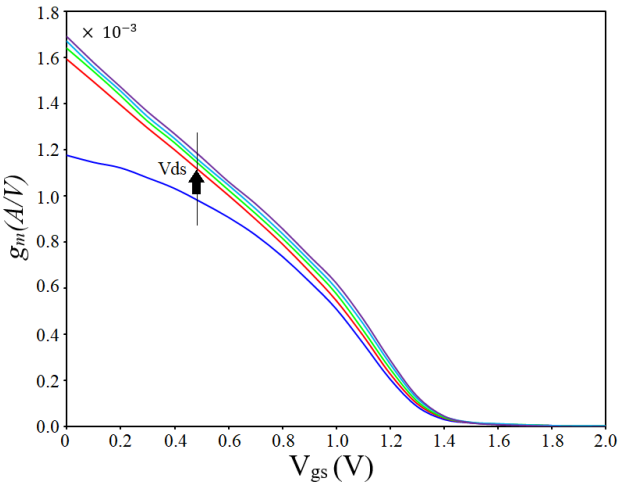
5.4. Results

The transfer characteristics of the sensor were acquired with a probe station and utilized for determining the transconductance (gm) and device efficiency (η) to compare different designs. Since the sensor operates in reverse bias mode, special attention was given to the p-type channel. The gm parameter plays a crucial role in this JFET-based sensor as it could directly affect the

charge sensitivity of the device, enabling inherent amplification of ionic charges or biomolecular charges [35], [36], [37] (see Figure 5-1 (b), illustration of the relation of charge input and sensor output). The η is another important figure of merit in designing FET-based biosensors, as it quantifies the gm achieved per unit of energy consumption in the device directly related to Ids [42].



(a)

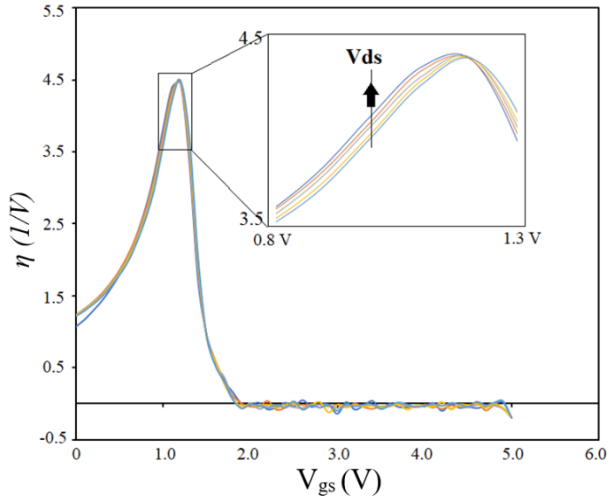


(b)

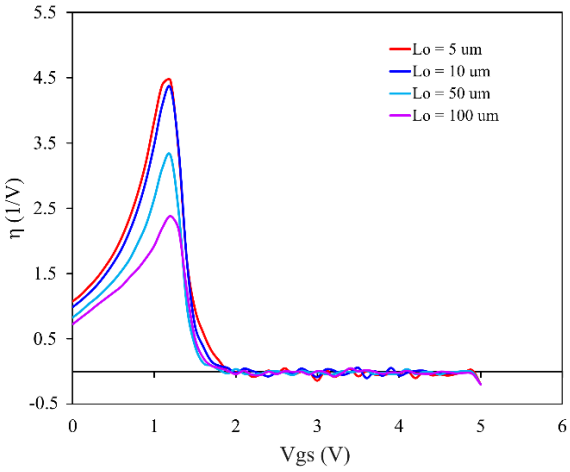
Figure 5-2. Experimental results. (a): The Ids-Vgs curve used for the derivation of gm-Ids (Lo = 5 µm) (b): the experimental results of the gm of the sensor for different back-gate voltages (Lo = 5µm).

The fabrication of OG-JFET devices with different aspect ratios (L/W) was performed, as depicted in Figure 5-1 (a), on the left side, showing probes on the source and drain. These devices were then subjected to experimental characterization to calculate the gm and η. A negative voltage was applied to the drain, while a positive voltage was applied to the back gate, allowing the sensor to

operate in reverse bias mode. Using equations (1) and (2), the gm and η were calculated based on the recorded experimental data. Figure 5-2 (b) presents the gm profiles for an OG-JFET with a 5 μm channel length, a p-type impurity concentration of approximately ~ 4.5×10^{15} /cm^3, a p-type channel thickness of ~ 1.6 μm, and an n-type support layer thickness of roughly ~ 450 μm with a concentration of ~ 1×10^{18} /cm^3. The experimental results demonstrate that the gm is maximized when the open channel has a zero back-gate voltage. The dependence of gm to back-gate voltage gives a unique advantage to OG-JFET to control the sensing performance such as gm and η.



(a)



(b)

Figure 5-3. The experimental results of the OG-JFET device efficiency (η). (a): for various Vds. (b): for various Lo values

Table 5-1. Comparison of Transconductance of the OG-JFET with literature

FET Type	W (µm)	L (µm)	$\|V_{gs}\|$	g_m (µS)	Standard Foundry	Sensing Area μm^2	Ref.
ZnO	50	1	5.1	1400	No	50	43
Graphene (solid-state)	2.7	0.31	~1.2	1863	No	0.83	44,45
n-InAs NW	0.05	2	0.56	97.5	No	0.1	46
GaN/InAlN	NR	0.06	1.75	NR	No	NR	47
CNT	10	1.5	1	50	No	15	48
Silicon NW	0.01	0.8-2	2-4	2	No	0.008-0.02	49
4H-SiC	26	NR	<1	800	No	NR	50
Diamond	0.5	0.5	4	34.6	No	0.25	51
MoS_2	0.5	2	4	34	No	1	52
Graphene (solution gate)	~10	~10	0.5	~1200	No	100	53
SiNW	0.005	0.5	0.05	0.8	No	0.0025	54
SiNW	10	0.02	0.1	0.2	No	0.2	55
CMOS Planar ISFET	2.5	NA	6.4	< 40	YES	250-500	56
CMOS Planar ISFET	2	NA	< 1	< 1100	YES	225	57
Open-Gate JFET	5	1000	0	1700	YES	~5000	This Work

In the case of a p-OGJFET, the channel conduction decreases due to the space charge induced by a positive back-gate voltage, which develops depletion. This channel narrowing leads to a pinch-off effect after reaching a threshold gate voltage, known as the pinch-off voltage. Increasing the drain-source voltage (Vds) increases gm (Figure 5-2 (b)). The analysis of device η reveals a peak for the OG-JFET, indicating the highest efficiency point, as shown in Figure 5-3 (a and b). This peak occurs at a back-gate voltage (Vgs) of approximately ~ 1.2 V. While the analysis of gm suggests the highest gm at Vgs = 0 V, the study of η indicates that the device performs better at Vgs ≈ 1.2 V. Therefore, there is a tradeoff between achieving the highest gm and minimizing energy consumption. As shown in Figure 5-3 (b), the sensor gm decreases rapidly when higher back-gate voltages (> 1 V) are applied. This region coincides with the point where η starts to drop. Therefore, for biosensing applications, it is recommended to operate the sensor within the linear part of the gm diagram, which corresponds to back-gate voltages below 1 V. This voltage range ensures that there is no sharp decrease in efficiency and gm when there are fluctuations in the back-gate voltage. The η decreases from 4.39 V-1 to 2.38 V-1 as the channel length increases from 5 µm to 100 µm. The maximum gm occurs when Vgs = 0 V. For the OG-JFET with an open-gate channel length (Lo) of 5 µm, the gm ranges from approximately 1200 µS to 1700 µS as the drain-source voltage (Vds) increases from 1 V to 5 V as presented in Figure 5-3 (b).

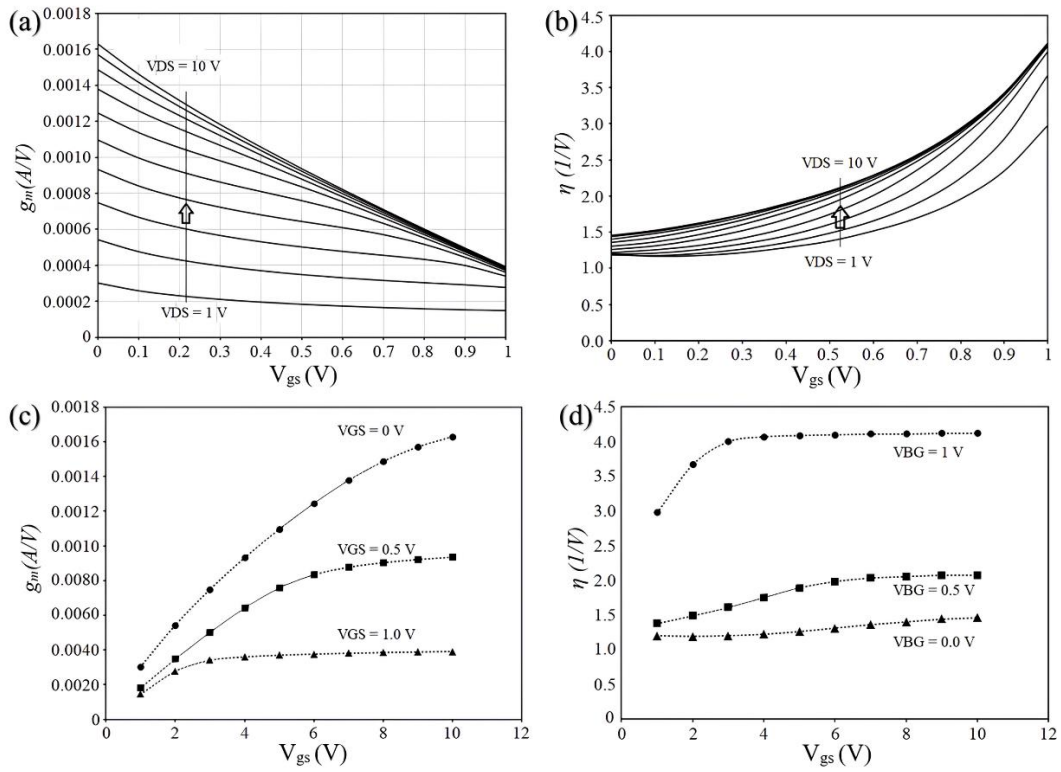


Figure 5-4. The numerical results of the gm and η of the device with Lo = 5 µm. (a): gm versus Vgs voltage. (b): η versus Vgs voltage. (c): the gm versus Vds for different Vgs. (d): The η (V-1) for different values of Vds.

FET sensor g_m plays a crucial role in the performance of FET-based biosensors [1]. Experimental analysis of the OG- JFET g_m demonstrates that this sensor exhibits a highly competitive g_m compared to other reported FET sensors. To provide a comprehensive comparison, we evaluated the OG-JFET g_m alongside various available FETs, as presented in Table 5-1. Our analysis focuses solely on solid-state FET sensors. Among the different structures considered, the OG-JFET exhibits a g_m of approximately 1700 µS, surpassing the performance of planar CMOS ISFETs and silicon-based nanowire biosensors. Specifically, the OG-JFET device gm/W is 850 times higher than silicon nanowire FETs, 34 times higher than carbon nanotubes, and 1.2 times higher than ZnO-based FETs. As the g_m depends on the structural geometry, we have normalized the gm of the OG-JFET concerning the channel length. The resulting score for the OG-JFET is 340 for a channel length of 5 µm, which exceeds the values of many FET sensors listed in Table 1, including ZnO, graphene (solution electrolyte), silicon nanowires, carbon nanotubes, planar silicon, and ZnO nanowires [2], [3], [4], [5], [6], [7], [8], [9], [10], [11], [12], [13], [14], [15], [16].

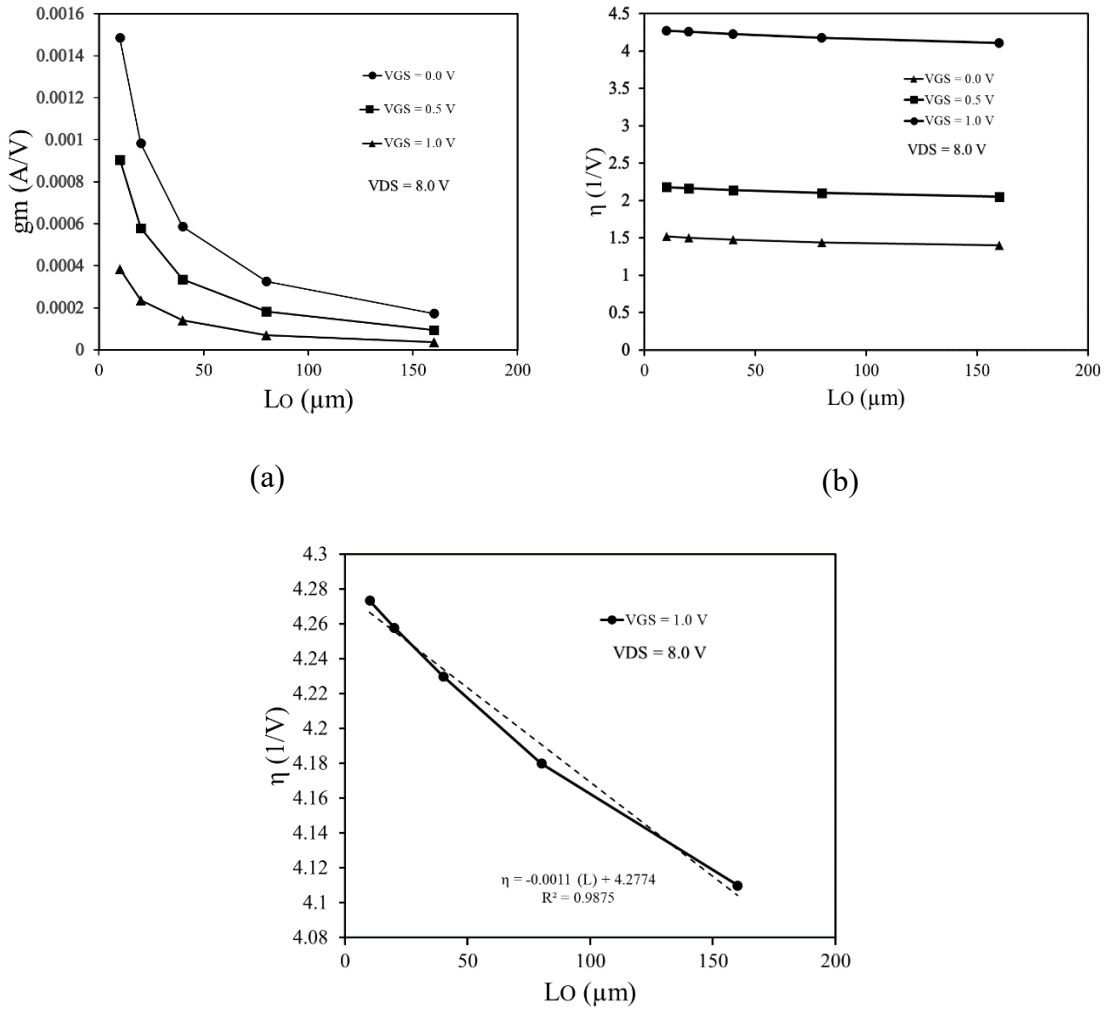


Figure 5-5. The length (Lo) enhancement effect on the g_m and η (V^{-1}). (a): g_m vs p-channel length. (b): η (V^{-1}) vs p-channel length (µm). (c): A broader view of the η-Lo diagram is shown for Lo = 5 µm.

The g_m of a transistor-based sensor represents its ability to change the output current in response to variations in the gate voltage. The gm can be mathematically defined as $g_m=(dI_{ds})/(dV_{gs})$, where I_{ds} is the drain-source current, and Vgs is the back-gate voltage. In the case of the OG-JFET, which features a back gate, this analysis quantifies the control that the gate has over the conduction of the channel. In addition to g_m, another critical parameter for evaluating a transistor is η, which indicates the amount of g_m achieved per unit of energy loss (dissipated energy in the device). While higher g_m is crucial for device performance in charge sensing and other applications, efficiency should also be considered to assess the device's overall effectiveness. Simulation is performed to estimate the device η, taking into account the following conditions: Lo = ~ 5 µm (open gate length),

T_P = ~ 1.6 µm (p-type channel thickness), T_N = ~ 20 µm (n-type support layer thickness), N_P-type = ~ $4.5 \times 10^{15}/cm^3$ (p-type impurity doping level), N_N-type = ~ 1×10^{18} (n-type impurity doping level), and L_{SD} = ~ 20 µm (source-drain length). The g_m and η values are plotted based on these parameters to analyze the device performance. According to Figure 5-4, the simulation results for g_m exhibit a similar trend to the experimental. However, at lower values of V_{gs} (gate-source voltage), the simulation tends to overpredict the experimental results. At higher V_{gs} values, the simulation and experimental data align more closely. The simulation results also exhibit a similar trend to the experimental for η considering the calibration on V_{gs} and out-of-plane thickness.

5.4.1. Effect of P-Channel Length (L_O)

The length of the p-channel is a crucial parameter in OG-JFET design. Its effect on the gm and device η is evaluated in Figure 5-5. Increasing the channel length results in a decrease in both gm and η. For Vgs = 0 and Vds = 8.0, the sensitivity of η to length dη/dL is calculated to be 0.0011 V-1 of η per 1 µm increment in the channel length. Simulation results indicate different sensitivity values for the short-channel and long-channel ranges. Consequently, the sensitivity of gm and η is calculated for two sets of channel lengths. The short-channel OG-JFET exhibits a higher variation in gm and η with a decade change in channel length. For example, at Vgs = 1.0 V, the (dgm)/dL values for the short channel and long channel are 8×10^{-6} A/V/µm and 7.7×10^{-6} A/V/µm, respectively. A similar trend is observed for η at Vgs = 1.0 V in the short-channel and long-channel regimes. The values of dη/dL for short-channel and long-channel are 0.0015 and 0.00061 V-1/µm, respectively.

5.4.2. The Effect of P-Channel Thickness (TP)

The T_P is another design parameter that needs to be investigated for the OG-JFET performance. The Ids-Vgs curves of the sensor were obtained, then the g_m and η were calculated according to the equations (1) and (2). For a constant V_{ds}, the variation of g_m and η are calculated versus T_P, as demonstrated in Figure 5-6 (a) and (b). According to the numerical results shown in Figure 5-6, the g_m is more sensitive to the change of thickness in the 1.4-1.6 µm range than in the 1.6-1.8 µm. At V_{gs} = 1.0 V, the g_m is 2.721×10^{-3} A/V/µm and 2.081×10^{-3} A/V/µm for 1.4-1.6 µm and 1.6-1.8 µm range respectively. The device performance in terms of η has also been investigated. At V = 1.0 V, the η sensitivity to every 1 µm change in the thickness of the channel is 36.9 V^{-1}/µm and

9.50 V^{-1}/µm for 1.4-1.6 µm and 1.6-1.8 µm range respectively. The sensitivity analysis shows the importance of accuracy in the fabrication process and the possible effects on the sensor performance. To better understand this effect, if we consider a design value of 1.6 µm for the channel thickness for operation in V_{gs} = 0 V and V_{ds} = 8.0 V, the 10% error/inaccuracy in the fabrication process results in a maximum of 5.68% inaccuracy in the g_m.

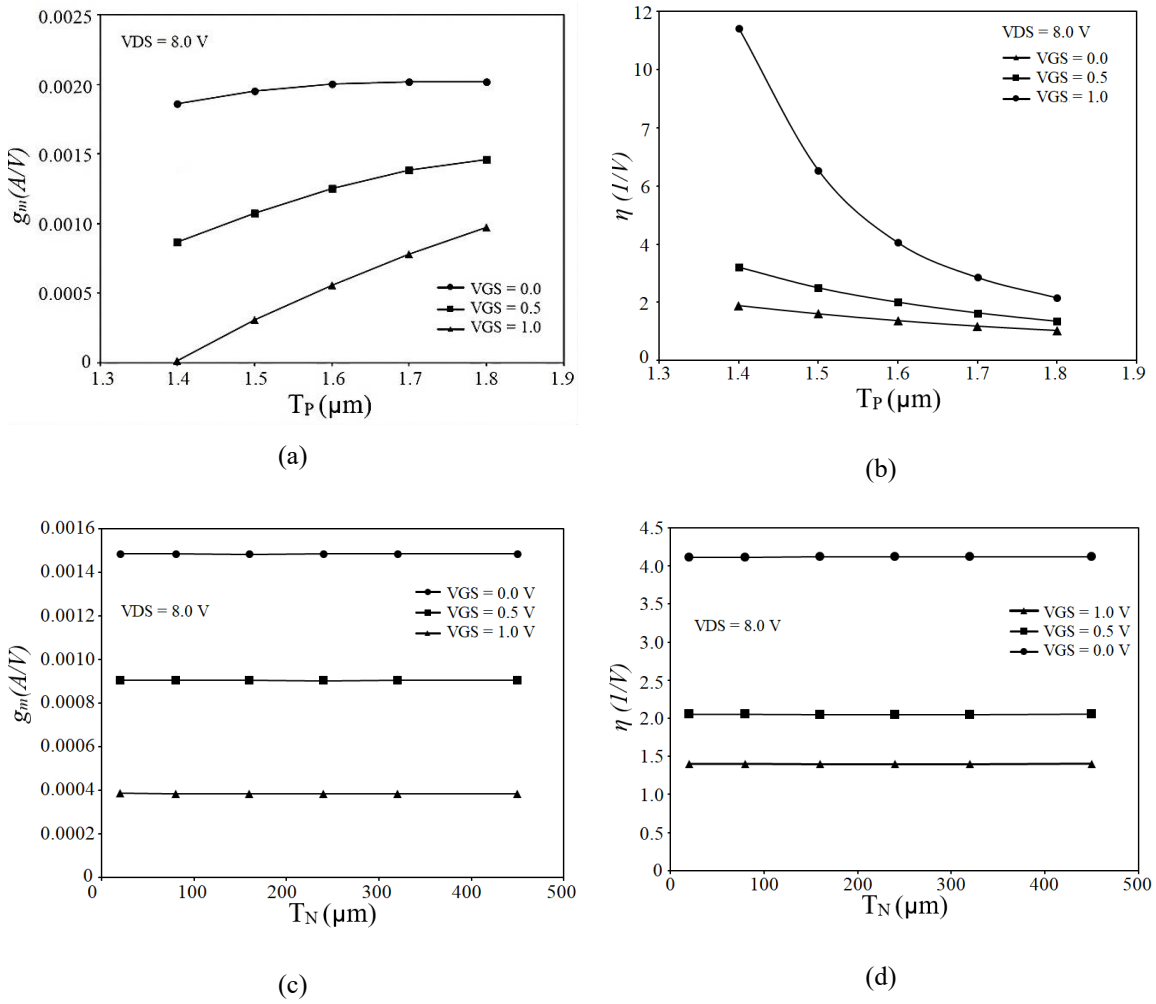


Figure 5-6. Numerical results of the effect of T_P (µm) on the sensors g_m and η (a) and (b). Numerical results of the effect of T_N (µm) on the sensor g_m and η (c) and (d).

5.4.3. The Effect of N-Channel Thickness (TN)

In another attempt, the T_N was investigated to analyze its impact on the gm and η. As the numerical simulation shown in Figure 5-6 (c) and (d), the n-type support layer thickness change does not significantly alter the sensor targeted performance (g_m, η). This minimal dependency is because

the sensor works in reverse bias mode (positive voltage on n-type and negative voltage on p-type in the vertical p-n junction of OG-JFET, and the depletion is controlled through the p-n junction. In this mode (reverse bias), the n-type layer is almost ineffective in the space charge modulation of the p-type channel since the p-n junction spatial charge occurs in a few micrometers near the channel. The rest of this thick layer is ineffective for sensor performance. However, as the sensor is fabricated with a p-n wafer, the support layer no longer needs to be processed to reduce its thickness, and the sensor can be operated in this form.

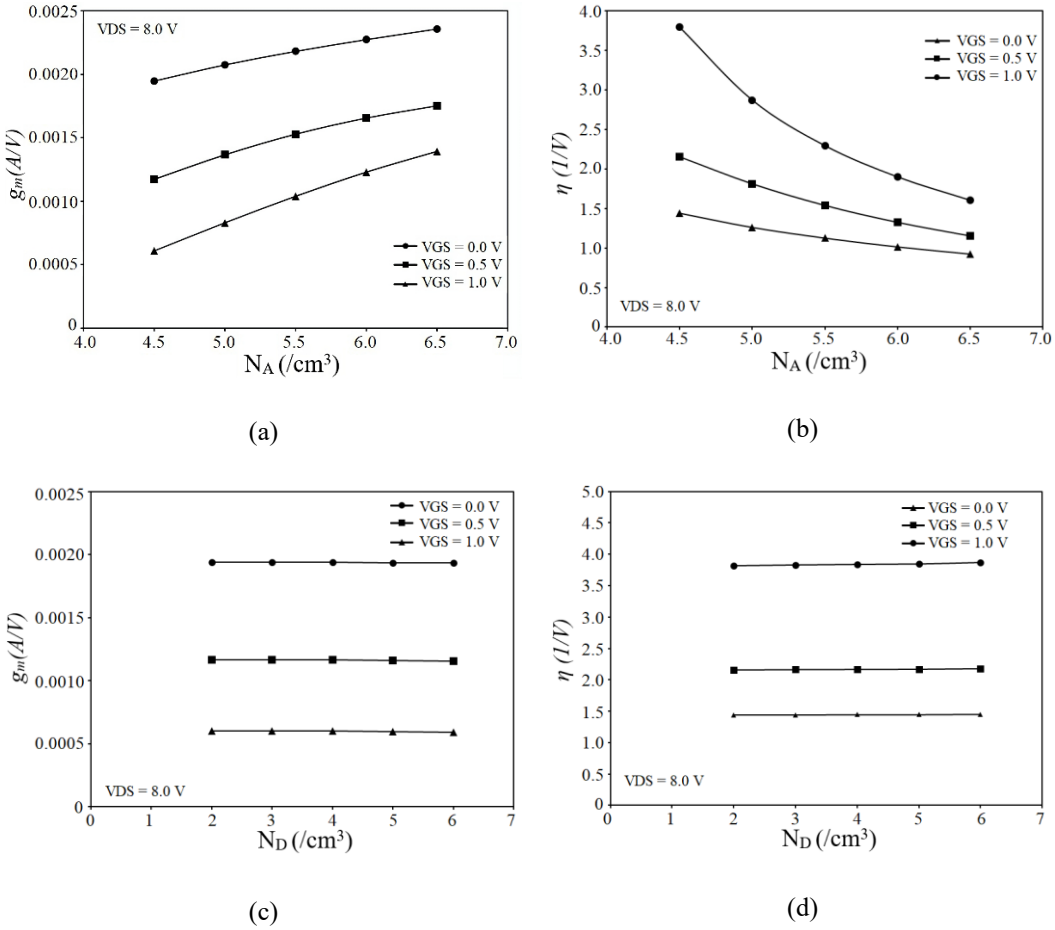


Figure 5-7. Simulation results of the effect of impurity doping (boron and phosphorus) in p-type and n-type channels on the g_m and η performance factors. (a): effect of impurity concentration in p-channel on the g_m. (b): the effect of p-channel impurity doping level on η (The x-axis should be multiplied by 10^{15}). (c): effect of impurity concentration in N-channel on g_m. (d): the effect of impurity concentration in N-channel on the η (The x-axis should be multiplied by 10^{18})

Nevertheless, reducing this thick layer does not significantly affect the p-type channel conduction; therefore, it could be omitted from the design if the thickness of the sensor is not a desired parameter for a specific application. Figures 5-6 (c) and (d) demonstrate the gm and η of OG-JFET in the reverse bias mode of the device. With an increment of the TN from 20 μm to 450 μm, the gm and η showed slight variation in this wide range. The gm and η for three different Vgs are plotted to analyze this effect further, showing the minimal impact on the sensor performance.

5.4.4. The Effect of N-Channel and P-Channel Doping

As described above and considering Figure 5-1, the N_A and N_D level is another design parameter that affects the sensor functionality since the doping in silicon affects the conductivity and, as a result, influences the gm and η. The p-channel plays a vital role in biosensing as this layer is exposed to solution; as a result, its conductivity and material properties in terms of the doping level are imperative to be investigated, as shown in Figures 5-7 (a) and (b). The NA range has been considered between 4.5×10^{15} /cm^3 to 6.5×10^{15} /cm^3 with a 0.5×10^{15} /cm^3 increment.

Simulation results showed that enhancing the N_A increases the gm in all Vgs biases (0, 0.5, and 1 V) from ~ 2000 μS to ~ 2400 μS in the Vgs = 0 as the higher gm. The simulation showed that the enhancement in the p-type impurity leads to a reduction in the η. The results of the gm and η simulation versus the variation of N_A and N_D are shown in Figure 5-7 (a) to (e). It is shown that changing the N_D has no significant effect on the sensor gm and η. For the doping change from 2×10^{18} /cm^3 to 6×10^{18} /cm^3 there is almost no change in the gm and η. This is an essential insight from simulation as it shows how the electronic performance of OG-JFET can be manipulated with impurity doping in the channels (N_A and N_D).

As the sensor structure shows (see Figure 5-1 (a, b)), the OG-JFET consists of a vertical p-n junction. The p-n junction is between two electrodes, the source/drain pad and the back-gate electrode. The drain has been realized on the p-type channel with implantation doping of the p-channel (~ 1.6-2 × 1015, B11+, 25 KeV), and the back-side implantation is done with P31+ and dose of 5 × 1015 /cm3. If the vertical p-n junction is forward-biased, we apply a positive voltage to the drain and a negative voltage to the back gate.

The Ids-Vgs for the forward bias of the sensor are shown in Figure 5-8 (a) and (b). In the forward bias, the p-n junction will be open after a specific threshold voltage, which opens a direct current from the back gate to the drain, orders of magnitudes more than the regular current from the drain

when the sensor is operating in reverse bias. The chip size is 10 mm × 10 mm; therefore, there is a p-n junction with an area of 100 mm^2 and a drain size of 5 µm × 1000 µm, which leads to a considerable current directly from the back-gate to drain. Also, using COMSOL simulation, we have shown the two working principles of OG-JFET in reverse and forward bias mode of the p-n junction, as shown in Figures 5-8 (c) and (d). According to the COMSOL simulation shown in Figure 5-8 (c and d), when the p-n junction is opened, the current will also be conducted between the source and gate, comparable to the current between the drain and back gate. In the same voltage difference as shown in Figure 5-8 (c, d), we have performed a joule heating simulation to understand the thermal generation close to the drain, which is in the order of ~ 10^{16} W/cm^3 and ~ 10^{11} W/cm^3 (see Figure 5-8 (e) and (f)) for forward and reverse bias respectively. The research indicates that the reverse bias would be more energy efficient for sensing applications, considering the power consumption and the local heat generation.

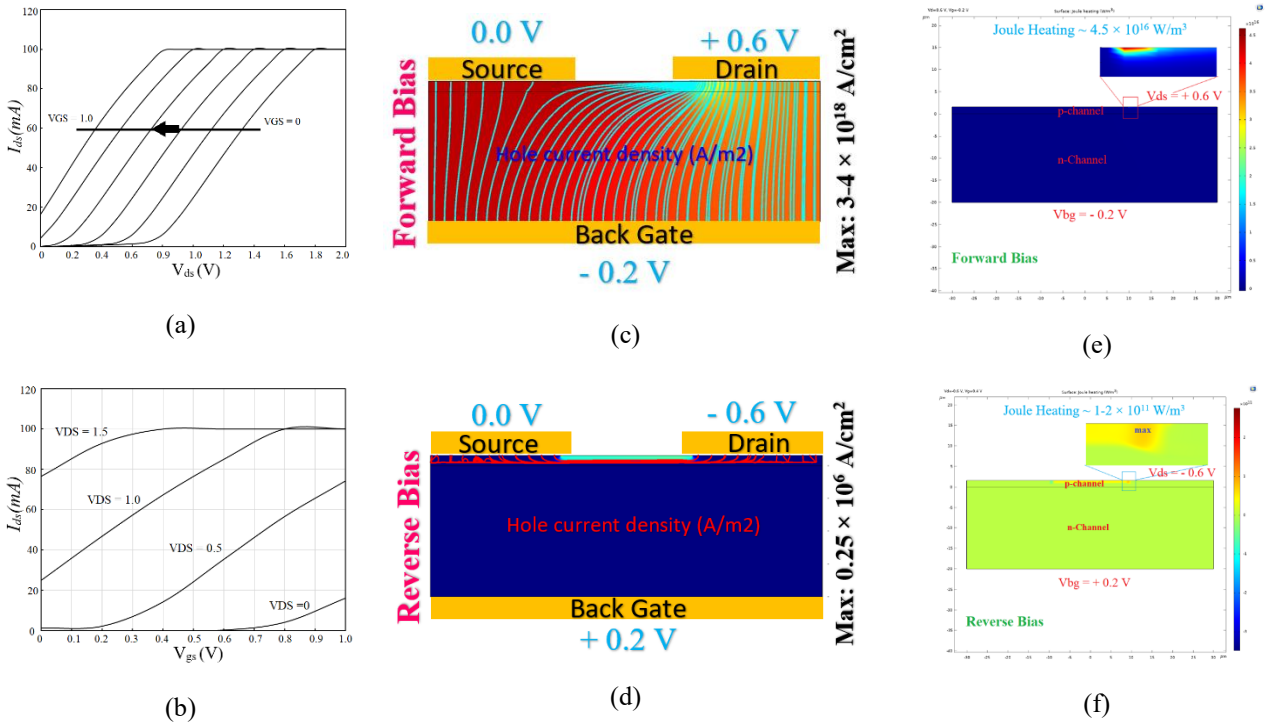
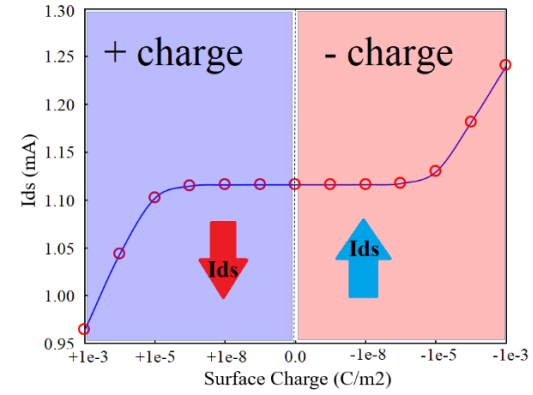


Figure 5-8. Experimental and numerical results of the OG-JFET in forward bias mode when a negative voltage is applied to the back-gate and a positive voltage to drain. (a): The experimental results of Ids-Vds curves for forward bias operation mode of OG-JFET. (b): The experimental results of Ids-Vgs curves for a forward-biased sensor for different Vds values. Current density comparison of two modes of operation of OG-JFET sensor. (c): When the p-n junction is open (forward bias), the current flows from the back side to the drain. (d): shows the reverse bias in which the current only flows inside the p-type channel (in c and d the passivation of metals is not displayed)

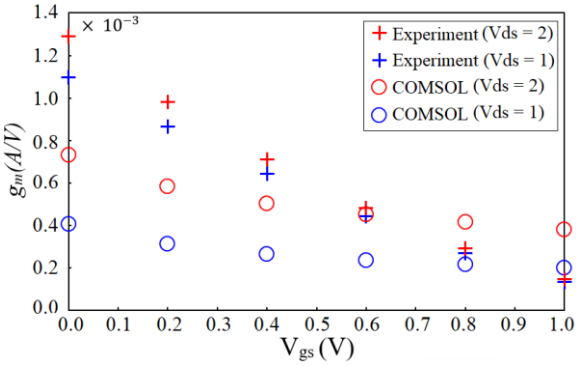
5.4.5. Simulation of Charge Sensitivity of OG-JFET for Biosensing

In this section, we explore the influence of charge in the opened gate area on hole conduction in the OG-JFET channel. A thin layer of native oxide on the silicon surface, formed due to exposure to ambient moisture over time, affects the conduction behavior. In ion-sensitive FET (ISFET) sensors, the oxide layer is usually functionalized with a bioreceptor to enable specific detection of target biomolecules in a solution. Various methods have been employed to functionalize the surface of the dielectric layer (SiO_2 or Si_3N_4). One common approach is saline chemistry, where the oxide surface is functionalized with a silane agent such as 3-aminopropyltriethoxysilane (APTES). The APTES introduces a primary amine terminal group, which can react with aldehyde, carboxylic acid, and epoxy groups in proteins and other biomolecules. Other methods for oxide functionalization include β-cyclodextrin (β-CD) and poly-l-lysine [27]. These functionalized layers immobilize proteins or other biomolecules that bind to the target analyte through intermolecular interactions. The functionalization of the oxide surface with chemical binders alters the surface potential (or surface charge density), which further changes with the attachment of a bioreceptor protein. After immobilization, the silicon channel senses the new surface potential, recording the binding of biomolecules on the sensor. Depending on the Debye length and ionic strength of the solution, the sensor can detect a fraction of the surface charge of the target molecules [25]. This charge is mirrored in the channel, leading to the manipulation of hole transport and, consequently, variations in Ids. Since the target biomolecules may exhibit negative and positive charges during attachment to the biorecognition element, a charge sensitivity analysis of the OG-JFET is performed.

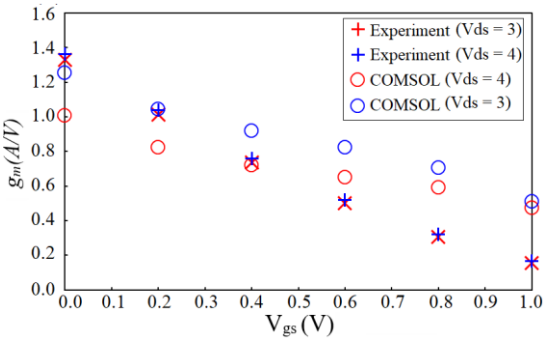
A uniform charge sheet model is used to consider the effects of biological charges on the open-gate area (as shown in Figure 5-1 (a), denoted as Lo). The charge varies from -1×10^{-3} C.m^{-2} to $+1 \times 10^{3}$ C.m^{-2} to demonstrate the sensor sensitivity to positive and negative charge variations. Figure 5-9 (a) demonstrates the COMSOL simulation results of the sensor response to charge on the sensing area. The charge layer is considered positive and negative, reducing and enhancing the drain-source current. Interestingly, the pattern of Ids changes to surface charge variations is almost symmetric for the sensor positive and negative charge accumulations. However, the charge sensitivity (Ids/ΔQ) for the high charge density of -1×10^{-3} to -1×10^{-5} and $+1\times10^{-3}$ to $+1\times10^{-5}$ are ~ 70 μA. (C.m^{-2})$^{-1}$ and ~ 60 μA. (C.m^{-2})$^{-1}$, respectively, showing more sensitivity to positive charge variations. This insight is useful in understanding the charge fingerprint of biomolecules on OG-



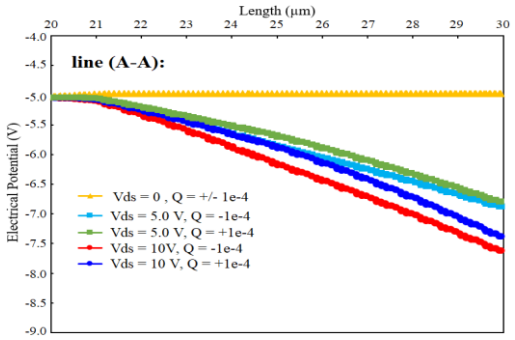
(a)



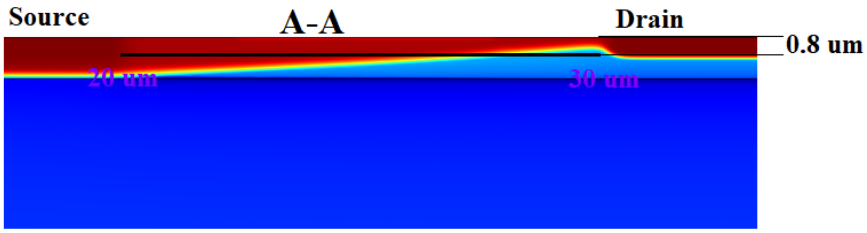
(b)



(c)



(d)



(e)

Figure 5-9. Numerical results of the response of OG-JFET to an equivalent charge sheet model of biomolecular attachment on the open-gate area. (a): COMSOL simulation result of the surface charge variation effects on the drain-source current for positive and negative charges. Comparison of the COMSOL semiconductor simulation with experiment values for g_m at (b): Vds = 1 V and Vds = 2 V and (c): Vds = 3 V and Vds = 4 V. (d): the electrical potential for surface charge values of Q = $+1\times10^{-4}$ C/m^2 and Q = -1×10^{-4} C/m^2. (e): the contour is for the hole doping concertation in the p-type and n-type channel when Lo is 10 μm, representing the place of the A-A line on which the electrical potential in (d) is calculated.

JFET. To further understand the charge sensing mechanism of OG-JFET, we have calculated the electrical potential of the p-type channel 0.8 μm under the outermost silicon layer in the open-gate area for charge densities of $+1\times10^{-4}$ C.m^{-2} and -1×10^{-4} C.m^{-2}. Figure 5-9 (d, e) demonstrates the

electrical potential in line A-A. As can be seen, the effect of charge density variation on the open-gate area is evident for two values of surface charge.

5.4.6. Simulation Assumptions and Comparison with Experiment

We have used COMSOL software to simulate the sensor. Since 2D modeling is performed in a discretized finite-element domain with simplified models, the simulation-experiment mismatch error (SEME) analysis is necessary compared to the experiment. The comparison with the investigation is presented in this section. To compare the simulation and experimentation, we have calculated the gm for a sensor with Lo = 5 μm. Figures 5-9 (b) and (c) compare gm-Vgs for two sets of Vds values. We have different SEME values at different Vgs values; however, at the middle of the spectrum ($0 < Vgs < 1$), the SEMEs are minimum, making it a reliable region for the design, especially for higher Vds values. There are various reasons for the SEME. The impurity doping concentration in the channels (in fabrication) is not the same as the profile that COMSOL assumes, affecting the channel conductivity. During the channel development, the implantation and the dose of impurities are not controlled as the values used in the simplified simulation model. As the sensor is not isolated from the rest of the p-type channel throughout the die, there might be current leakage, which is impossible for the current COMSOL model to predict, considering the isolation boundary condition we applied. However, we have considered an isolation boundary condition for those parts. To reduce the errors and compensate for the unknown experimental erroneous parameters, we have used an effective voltage (as fitting parameters) for the back-gate, which follows the experiment as $Vgs\ (effective) = A \times Vgs\ (experiment) + B$ that is driven with Ids-Vgs curves comparison of simulation and the Ids-Vgs of the investigation.

This correction is applied to the experimentally related portion of the back-gate voltage in the COMSOL (Veq) ohmic contact model that depends on the interface at the metal-semiconductor in the back-gate metallization in the real device. The values used in the current simulation are A= 6.2 and B = 0.092 (fitting parameters). It appears that correction on the back gate significantly impacts the channel conduction. Defining experimentally driven constants in the modeling (fitting parameters) is a method that has been used in literature for more accurate predictions of sensor output [58], [59] (using a gate voltage [60]). COMSOL has been used to simulate FET-based biosensors, which showed SEME compared to experimental data, mainly due to the nonidealities

in the experimentation and fabrication [58]. However, more complex calibration is required to fully capture the experimentation in all bias conditions, which opens avenues for future work.

The simulation utilized semiconductor device equations with parabolic energy bands to model charge carriers' energy as a function of momentum, valid near band edges. It assumed thermal equilibrium, equating charge carriers' temperature with the semiconductor lattice. A 2D mesh discretized the OG-JFET sensor's geometry for numerical analysis, solving Maxwell's equations, Boltzmann transport theory, and Neumann boundary conditions numerically [61]. Maxwell's equations govern electric and magnetic field propagation, while Boltzmann's transport theory calculates charge carrier movement. Neumann boundary conditions ensure no electric flux crosses boundaries. The SRH model was included to simulate trap-assisted recombination, affecting current flow [61]. The OG-JFET structure was modeled with three ohmic contacts at the source, drain, back gate, and an insulated gate area. The Veq in the Ohmic contact model of COMSOL, which includes many material-dependent variables [61], was used as one of the calibration parameters. This might be associated with a non-ideal shared back gate metallization on a large area on the back side of the OG-JFET die. The p-n junction was represented using the continuity/heterojunction model, ensuring smooth quasi-Fermi level transitions. Meshing involved structured meshes for the p-type channel and unstructured meshes for the n-type channel, aiding complex geometry accommodation.

5.5. Discussion

This paper explains the performance of OG-JFET as a low-voltage (< 0.5 V), high gm (~ 1700 μS), and gm/Ids of ~ 4.5-5 V^{-1} through experimental analysis. Low voltage operation is essential in biosensing while producing high gm for inherent signal amplification upon receiving signal input from a biological phenomenon on top of the sensor. So far, other silicon-based platforms, such as silicon nanowires and silicon nanoribbons, have been introduced, showing perfect sensing properties for biosensing. However, the complex fabrication process for realizing this sensor does not make them potential volunteers for PoC applications.

Furthermore, as the silicon dioxide is removed from the open-gate area of JFET, there is a lower ion-trapped noise, which leads to higher stability, drift = 3 μA/hours [29], and hysteresis ~ 16 mV, which are competitive amongst the other oxide-deposited gates such as silicon nanowire-based ISFETs [62]. The OG-JFET offers a comprehensive and easily accessible sensing area, making it

desirable for biosensing. The sensor has an optimum operation point in terms of efficiency (~ 1.2 V) while showing the maximum g_m at zero voltage as it is a normally ON transistor and can be pinched off with a back-gate. Therefore, there is a tradeoff between efficiency and the gm for this sensor as it demonstrates higher gm at lower voltages (< 0.1 V). The gm and η are device-dependent parameters that can be used as figures of merits for design. Here, we have shown how the geometrical parameters affect the sensor response, giving future designers insights into this standard multi-user technology. This paper reveals the low dependency of sensor performance on the n-type silicon support layer thickness and doping level. However, it is shown that the most critical parameters that significantly affect sensor operation are the p-channel length, thickness, and doping levels.

Hence, following this guideline, the designer may consider the impact of N-channel thickness and doping level negligible (with variations on the order of ~10 nA when changed from 5 μm to 450 μm). This suggests that during OG-JFET manufacturing, less emphasis can be placed on the thickness and doping of the n-channel if it conflicts with reducing the sensor's overall cost. However, it is essential to consider such variations for highly sensitive applications such as DNA hybridization. Furthermore, we have identified a new voltage parameter, the maximum efficiency voltage, which can serve as a valuable figure of merit for comparing different OG-JFET designs. This voltage peak indicates the optimal operating point. Additionally, it is observed that larger sensing areas contribute to both a decrease in gm and η; therefore, keeping the Lo (length of the open-gate area) as low as possible to achieve higher charge sensitivity is recommended.

To ascertain the electronic properties of the device, such as gain, device efficiency, and other parameters, one must obtain the device’s transfer characteristics. For this purpose, we utilized a probe station and a semiconductor analyzer, as depicted in Figure 5-10. The device was centrally positioned on the semiconductor chuck, and probes were connected to the source and drain pads. To establish a connection with the back gate of the sensor for measurement, we employed the chuck’s surface, placing a probe upon it to complete the circuit. The probe station chuck ensures a constant temperature and humidity when testing the device inside the shielded environment of the probe station, as shown in Figure 5-10. An optical microscopy is used to see the device inside the probe station’s chuck, as shown in Fig. 5-10. It also creates a dark area, preventing the light from entering. The experimental setup is provided, as shown in Figure 5-10.

In this study, we have explored the performance and parametric design of the open-gate junction field-effect transistor (OG-JFET) imperative for design of bio/chemical sensing applications using this technology. While our findings lay a foundation for the OG-JFET's charge sensing capabilities and performance-oriented design, we acknowledge the importance of further investigations into environmental controls (e.g., temperature, humidity, light), long-term stability in biological samples (. e.g., drift and hysteresis when exposed to biomolecules), and sensitivity to biological samples. These factors are critical for the practical application of biosensors and represent important directions for future research. Additionally, the scalability and integration of the OG-JFET into larger systems (such as microfluidics microfabrication processes and CMOS technology), its cost-effectiveness, and its specificity and cross-sensitivity to various biomolecules are essential considerations for ensuring the technology's applicability and utility in PoC real-world scenarios. The integration of OG-JFET with CMOS will significantly reduce the overall cost of the sensor and impact its utilization in next-generation PoC devices [63], [64]. An in-depth cost analysis is required to predict such an integrated device [1], [65].

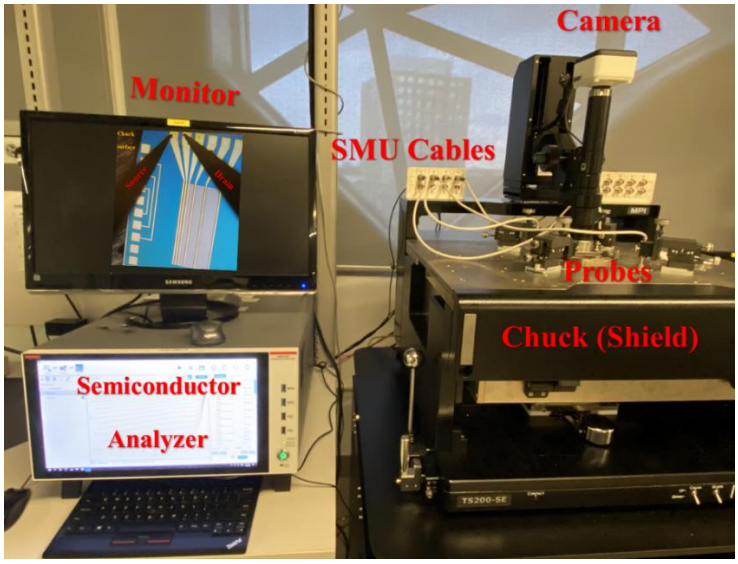


Figure 5-10. The experimental setup was used to characterize the sensor's electronic transfer characteristics to calculate transconductance (gm) and device efficiency.

Moreover, the reproducibility and consistency of the fabrication process and the device's performance across multiple batches are paramount for the advancement of the OG-JFET technology [63], [64]. This needs to be performed for devices after fabrication, and the yield of fabrication run must be calculated by evaluating a known performance metric. Our initial study provides a foundational understanding of the OG-JFET's performance characteristics and charge

sensitivity through a parametric design strategy. Yet, a comprehensive exploration of these factors is necessary with experimentation with biomolecules and surface modification chemistries applied to other silicon-based FET biosensors [66]. While here the charge sensing capability of the sensor is simulated, future works will aim to validate the OG-JFET's potential as a promising platform for bio/chemical sensing applications using biomolecular assays such as antigen-antibody, DNA, RNA, and cells, addressing the broader considerations that will enable its widespread adoption in the field. The existence of dielectric like SiO_2 and Si_3N_4 in the structure of the sensing area promises different surface chemistry applied to another FET-based biosensor to adapt DNA proteins and cells; the sensing area promises different surface chemistry applied to another FET-based biosensor to adapt it for DNA, proteins, cell, and enzyme sensing.

5.6. Conclusion

This paper discusses OG-JFET as a high transconductance and low voltage transistor dedicated to bio/chemical sensing, promising a new foundry-based silicon biosensing platform. Here, we have experimentally probed OG-JFETs with 5 µm, 10 µm, 50 µm, and 100 µm to derive their g_m and η. A high transconductance of ~ 1700 µS and η of ~ 4.5 V^{-1} can be achieved at $V_{gs} = 0$ and ~ V_{gs} = 1.2 V, respectively, outperforming many existing FET sensors for biosensing and other applications. We have developed a parametric design approach for OG-JFET, a promising mass-producible platform that CMC Microsystem offers. The simulation outcomes predict the transfer characteristics of OG-JFET and its performance. Simulation has been used to explain the charge sensitivity of OG-JFET, which further describes how the sensor responds to positive and negative charges due to biomolecules in the Lo region. Two OG-JFET operation modes are discussed using simulation and experiments, and the reverse bias mode is considered the best mode for biosensing. Furthermore, this paper presents design strategies and models for predicting g_m and η, which are essential performance metrics for OG-JFET. These design strategies and models can serve as valuable references for future designs of this standard technology.

ACKNOWLEDGMENT

The authors thank CMC Microsystems for providing services that facilitated this research.

5.7. References

[1] C. Dai, Y. Liu, and D. Wei, 'Two-Dimensional Field-Effect Transistor Sensors: The Road toward Commercialization', Chem Rev, 2021, doi: 10.1021/acs.chemrev.1c00924.

[2] Y.-C. Syu, W.-E. Hsu, and C.-T. Lin, 'Review—Field-Effect Transistor Biosensing: Devices and Clinical Applications', ECS Journal of Solid State Science and Technology, vol. 7, no. 7, pp. Q3196–Q3207, 2018, doi: 10.1149/2.0291807jss.

[3] M. G. Abdallah, R. Khan, C. Garcia, Y. T. Kim, and S. M. Iqbal, 'Ion-Sensitive Field-Effect Transistors with Micropillared Gates for Measuring Cell Ion Exchange at Molecular Levels', IEEE Access, vol. 6, pp. 72675–72682, 2018, doi: 10.1109/ACCESS.2018.2874274.

[4] S. S. Alabsi, A. Y. Ahmed, J. O. Dennis, M. H. M. Khir, and A. S. Algamili, 'A Review of Carbon Nanotubes Field Effect-Based Biosensors', IEEE Access, vol. 8, pp. 69509–69521, 2020, doi: 10.1109/ACCESS.2020.2987204.

[5] S. Sheibani, A. M. Ionescu, and P. Norouzi, 'Extended gate field effect transistor based sensor for detection of trace amounts of anti-depressant drug', IEEE Access, vol. 8, pp. 198010–198020, 2020, doi: 10.1109/ACCESS.2020.3034691.

[6] L. Chao et al., 'Recent advances in field effect transistor biosensor technology for cancer detection: A mini review', J Phys D Appl Phys, vol. 55, no. 15, 2022, doi: 10.1088/1361-6463/ac3f5a.

[7] L. Mu, Y. Chang, S. D. Sawtelle, M. Wipf, X. Duan, and M. A. Reed, 'Silicon nanowire field-effect transistors - A versatile class of potentiometric nanobiosensors', IEEE Access, vol. 3, pp. 287–302, 2015, doi: 10.1109/ACCESS.2015.2422842.

[8] M. Monfared Dehbali, M. Farahmandpour, S. Hamedi, and Z. Kordrostami, 'Development of a portable smart Glucometer with two electrode bio-electronic test strip patch based on Cu/Au/rGO/PEDOT:PSS', Sci Rep, vol. 13, no. 1, pp. 1–13, 2023, doi: 10.1038/s41598-023-36612-4.

[9] K. A. Muratore et al., 'Alanine aminotransferase assay biosensor platform using silicon nanowire field effect transistors', Communications Engineering, vol. 2, no. 1, 2023, doi: 10.1038/s44172-023-00057-4.

[10] S. Papamatthaiou, P. Estrela, and D. Moschou, 'Printable graphene BioFETs for DNA quantification in Lab-on-PCB microsystems', Sci Rep, vol. 11, no. 1, pp. 1–9, 2021, doi: 10.1038/s41598-021-89367-1.

[11] D. Kwong Hong Tsang et al., 'Chemically Functionalised Graphene FET Biosensor for the Label-free Sensing of Exosomes', Sci Rep, vol. 9, no. 1, pp. 2–11, 2019, doi: 10.1038/s41598-019-50412-9.

[12] B. R. Goldsmith et al., 'Digital Biosensing by Foundry-Fabricated Graphene Sensors', Sci Rep, vol. 9, no. 1, Dec. 2019, doi: 10.1038/s41598-019-38700-w.

[13] M. Kumari, N. K. Singh, and M. Sahoo, 'A detailed investigation of dielectric-modulated dual-gate TMD FET based label-free biosensor via analytical modelling', Sci Rep, vol. 12, no. 1, pp. 1–17, 2022, doi: 10.1038/s41598-022-24677-6.

[14] D. Sadighbayan and E. Ghafar-Zadeh, 'Portable Sensing Devices for Detection of COVID-19: A Review', IEEE Sens J, vol. 21, no. 9, pp. 10219–10230, May 2021, doi: 10.1109/JSEN.2021.3059970.

[15] A. Panahi, D. Sadighbayan, S. Forouhi, and E. Ghafar-Zadeh, 'Recent advances of field-effect transistor technology for infectious diseases', Biosensors (Basel), vol. 11, no. 4, 2021, doi: 10.3390/bios11040103.

[16] A. Poghossian and M. J. Schöning, 'Recent progress in silicon-based biologically sensitive field-effect devices', Curr Opin Electrochem, vol. 29, p. 100811, 2021, doi: 10.1016/j.coelec.2021.100811.

[17] D. C. Li, P. H. Yang, and M. S. C. Lu, ‘CMOS open-gate ion-sensitive field-effect transistors for ultrasensitive dopamine detection’, IEEE Trans Electron Devices, vol. 57, no. 10, pp. 2761–2767, 2010, doi: 10.1109/TED.2010.2063330.

[18] D. J. Baek, S. J. Choi, J. H. Ahn, J. Y. Kim, and Y. K. Choi, ‘Addressable nanowire field-effect-transistor biosensors with local backgates’, IEEE Trans Electron Devices, vol. 59, no. 9, pp. 2507–2511, 2012, doi: 10.1109/TED.2012.2201484.

[19] J. Lee et al., ‘A Highly Responsive Silicon Nanowire/Amplifier MOSFET Hybrid Biosensor’, Sci Rep, vol. 5, pp. 1–6, 2015, doi: 10.1038/srep12286.

[20] S. Rollo, Di. Rani, R. Leturcq, W. Olthuis, and C. Pascual García, ‘High Aspect Ratio Fin-Ion Sensitive Field Effect Transistor: Compromises toward Better Electrochemical Biosensing’, Nano Lett, vol. 19, no. 5, pp. 2879–2887, 2019, doi: 10.1021/acs.nanolett.8b04988.

[21] M. Gupta et al., ‘Size Independent pH Sensitivity for Ion Sensitive FinFETs Down to 10 nm Width’, IEEE Sens J, vol. 19, no. 16, pp. 6578–6586, 2019, doi: 10.1109/JSEN.2019.2912503.

[22] A. Medina-Rull et al., ‘A Graphene Field-Effect Transistor Based Analogue Phase Shifter for High-Frequency Applications’, IEEE Access, vol. 8, pp. 209055–209063, 2020, doi: 10.1109/ACCESS.2020.3038153.

[23] S. M. Monavari, F. Marsusi, N. Memarian, and M. Qasemnazhand, ‘Carbon nanotubes and nanobelts as potential materials for biosensor’, Sci Rep, vol. 13, no. 1, pp. 1–10, 2023, doi: 10.1038/s41598-023-29862-9.

[24] B. M. Lowe, K. Sun, I. Zeimpekis, C. K. Skylaris, and N. G. Green, ‘Field-effect sensors-from pH sensing to biosensing: Sensitivity enhancement using streptavidin-biotin as a model system’, Analyst, vol. 142, no. 22, pp. 4173–4200, 2017, doi: 10.1039/c7an00455a.

[25] A. Matsumoto and Y. Miyahara, ‘Current and emerging challenges of field effect transistor based bio-sensing’, Nanoscale, vol. 5, no. 22, pp. 10702–10718, 2013, doi: 10.1039/c3nr02703a.

[26] N. Moser, T. S. Lande, C. Toumazou, and P. Georgiou, ‘ISFETs in CMOS and Emergent Trends in Instrumentation: A Review’, IEEE Sens J, vol. 16, no. 17, pp. 6496–6514, 2016, doi: 10.1109/JSEN.2016.2585920.

[27] L. Mu, Y. Chang, S. D. Sawtelle, M. Wipf, X. Duan, and M. A. Reed, ‘Silicon nanowire field-effect transistors - A versatile class of potentiometric nanobiosensors’, IEEE Access, vol. 3, pp. 287–302, 2015, doi: 10.1109/ACCESS.2015.2422842.

[28] M. Kaisti, ‘Detection principles of biological and chemical FET sensors’, Biosensors and Bioelectronics, vol. 98. Elsevier Ltd, pp. 437–448, Dec. 15, 2017. doi: 10.1016/j.bios.2017.07.010.

[29] A. Panahi, H. O. Tabrizi, P. Mangannavar, O. Chebotarev, A. Fung, and E. Ghafar-Zadeh, ‘Open-Gate Junction Field Effect Transistor (OG-JFET) for Life Science Applications: Design, Implementation, and Characterization’, IEEE Sens J, vol. 21, no. 23, pp. 26503–26514, 2021, doi: 10.1109/JSEN.2021.3121339.

[30] J. F. Transistor, O. Life, A. Design, and E. Results, ‘Electronic Sensing Platform (ESP) Based on Open-Gate’, 2021.

[31] V. Adinolfi and E. H. Sargent, ‘Photovoltage field-effect transistors’, Nature, vol. 542, no. 7641, pp. 324–327, 2017, doi: 10.1038/nature21050.

[32] A. Panahi and E. Ghafar-Zadeh, ‘A Hybrid Microfluidic Electronic Sensing Platform for Life Science Applications’, Micromachines (Basel), vol. 13, no. 3, 2022, doi: 10.3390/mi13030425.

[33] A. Panahi, H. O. Tabrizi, P. Mangannavar, O. Chebotarev, A. Fung, and E. Ghafar-Zadeh, ‘A New Foundry-Based Open-Gate Junction Field-Effect Transistor (OG-JFET) as Electronic Sensing Platform (ESP) for Life Science

Applications', Proceedings of IEEE Sensors, vol. 2021-Octob, pp. 22–25, 2021, doi: 10.1109/SENSORS47087.2021.9639830.

[34] B. G. Sonmez, O. Ertop, and S. Mutlu, 'Modelling and Realization of a Water-Gated Field Effect Transistor (WG-FET) Using 16-nm-Thick Mono-Si Film', Sci Rep, vol. 7, no. 1, pp. 27–29, 2017, doi: 10.1038/s41598-017-12439-8.

[35] D. Khodagholy et al., 'High transconductance organic electrochemical transistors', Nature Communications 2013 4:1, vol. 4, no. 1, pp. 1–6, Jul. 2013, doi: 10.1038/ncomms3133.

[36] K. Shoorideh and C. O. Chui, 'On the origin of enhanced sensitivity in nanoscale FET-based biosensors', Proc Natl Acad Sci U S A, vol. 111, no. 14, pp. 5111–5116, Apr. 2014, doi: 10.1073/PNAS.1315485111/SUPPL_FILE/PNAS.201315485SI.PDF.

[37] W. Tang et al., 'Solution processed low power organic field-effect transistor bio-chemical sensor of high transconductance efficiency', npj Flexible Electronics 2022 6:1, vol. 6, no. 1, pp. 1–8, Mar. 2022, doi: 10.1038/s41528-022-00149-9.

[38] I. A. Pindoo, S. K. Sinha, and S. Chander, 'Performance analysis of heterojunction tunnel FET device with variable Temperature', Appl Phys A Mater Sci Process, vol. 127, no. 10, pp. 1–10, 2021, doi: 10.1007/s00339-021-04891-1.

[39] H. Hatefi Ardakani, A. Mehrdadian, and K. Forooraghi, 'Analysis of Graphene-Based Microstrip Structures', IEEE Access, vol. 5, pp. 20887–20897, Sep. 2017, doi: 10.1109/ACCESS.2017.2757453.

[40] Y. Yan, T. Qu, and F. Grilli, 'Numerical modeling of AC loss in HTS coated conductors and roebel cable using T-A formulation and comparison with H formulation', IEEE Access, vol. 9, pp. 49649–49659, 2021, doi: 10.1109/ACCESS.2021.3067037.

[41] R. B. Y. Syah, A. Veisi, Z. A. Hasibuan, M. A. Al-Fayoumi, M. S. Daoud, and E. Eftekhari-Zadeh, 'A Novel Smart Optimized Capacitance-Based Sensor for Annular Two-Phase Flow Metering With High Sensitivity', IEEE Access, vol. 11, pp. 60709–60716, 2023, doi: 10.1109/ACCESS.2023.3281754.

[42] R. J. E. Hueting, S. E. J. Vincent, J. G. Bomer, R. G. P. Sanders, and W. Olthuis, 'Ion-Sensitive Gated Bipolar Transistor', IEEE Trans Electron Devices, vol. 66, no. 10, pp. 4354–4360, 2019, doi: 10.1109/TED.2019.2933666.

[43] S. Sasa, M. Ozaki, K. Koike, M. Yano, and M. Inoue, 'High-performance ZnO/ZnMgO field-effect transistors using a hetero-metal-insulator-semiconductor structure', Appl Phys Lett, vol. 89, no. 5, 2006, doi: 10.1063/1.2261336.

[44] J. S. Moon et al., 'Top-gated epitaxial graphene FETs on si-face sic wafers with a peak transconductance of 600 mS/mm', IEEE Electron Device Letters, vol. 31, no. 4, pp. 260–262, 2010, doi: 10.1109/LED.2010.2040132.

[45] H. Xu, Z. Zhang, H. Xu, Z. Wang, S. Wang, and L.-M. Peng, 'Top-Gated Graphene Field-Effect Transistors with High Normalized Dirac Point Voltage', ACS Nano, vol. 5, no. 6, pp. 5031–5037, 2011.

[46] Q. T. Do, K. Blekker, I. Regolin, W. Prost, and F. J. Tegude, 'High transconductance MISFET with a single InAs nanowire channel', IEEE Electron Device Letters, vol. 28, no. 8, pp. 682–684, 2007, doi: 10.1109/LED.2007.902082.

[47] Nidhi, S. Dasgupta, J. Lu, J. S. Speck, and U. K. Mishra, 'Self-aligned N-Polar GaN/InAlN MIS-HEMTs with record extrinsic transconductance of 1105 mS/mm', IEEE Electron Device Letters, vol. 33, no. 6, pp. 794–796, 2012, doi: 10.1109/LED.2012.2190965.

[48] Q. Cao, S. J. Han, G. S. Tulevski, Y. Zhu, D. D. Lu, and W. Haensch, 'Arrays of single-walled carbon nanotubes with full surface coverage for high-performance electronics', Nat Nanotechnol, vol. 8, no. 3, pp. 180–186, 2013, doi: 10.1038/nnano.2012.257.

[49] Y. Cui, Z. Zhong, D. Wang, W. U. Wang, and C. M. Lieber, ‘High performance silicon nanowire field effect transistors’, Nano Lett, vol. 3, no. 2, pp. 149–152, 2003, doi: 10.1021/nl025875l.

[50] H. Mousa and K. Teker, ‘High-transconductance silicon carbide nanowire-based field-effect transistor (SiC-NWFET) for high-temperature applications’, Microelectronics International, vol. 38, no. 2, pp. 78–83, 2021, doi: 10.1108/MI-05-2021-0043.

[51] T. Iwasaki et al., ‘High-temperature operation of diamond junction field-effect transistors with lateral p-n junctions’, IEEE Electron Device Letters, vol. 34, no. 9, pp. 1175–1177, 2013, doi: 10.1109/LED.2013.2271377.

[52] D. Lembke and A. Kis, ‘ Correction to Breakdown of High-Performance Monolayer MoS 2 Transistors ’, ACS Nano, vol. 7, no. 4, pp. 3730–3730, 2013, doi: 10.1021/nn400554k.

[53] Y. Liang, X. Liang, Z. Zhang, W. Li, X. Huo, and L. Peng, ‘High mobility flexible graphene field-effect transistors and ambipolar radio-frequency circuits’, Nanoscale, vol. 7, no. 25, pp. 10954–10962, 2015, doi: 10.1039/c5nr02292d.

[54] W. M. Zhou, F. Fang, Z. Y. Hou, L. J. Yan, and Y. F. Zhang, ‘Field-effect transistor based on β-SiC nanowire’, IEEE Electron Device Letters, vol. 27, no. 6, pp. 463–465, 2006, doi: 10.1109/LED.2006.874219.

[55] W. F. Yang, S. J. Lee, G. C. Liang, R. Eswar, Z. Q. Sun, and D. L. Kwong, ‘Temperature dependence of carrier transport of a silicon nanowire schottky-barrier field-effect transistor’, IEEE Trans Nanotechnol, vol. 7, no. 6, pp. 728–732, 2008, doi: 10.1109/TNANO.2008.2003353.

[56] J. Bausells, J. Carrabina, A. Errachid, and A. Merlos, ‘Ion-sensitive field-effect transistors fabricated in a commercial CMOS technology’, Sens Actuators B Chem, vol. 57, no. 1–3, pp. 56–62, 1999, doi: 10.1016/S0925-4005(99)00135-5.

[57] S. Meyburg, R. Stockmann, J. Moers, A. Offenhäusser, and S. Ingebrandt, ‘Advanced CMOS process for floating gate field-effect transistors in bioelectronic applications’, Sens Actuators B Chem, vol. 128, no. 1, pp. 208–217, 2007, doi: 10.1016/j.snb.2007.06.003.

[58] M. Ba, A. K. Diallo, E. H. B. Ly, J. Launay, and P. Temple-Boyer, ‘Numerical Modeling of Glucose Biosensor with pH-Based Electrochemical Field-Effect Transistor Device’, IEEE Trans Electron Devices, vol. 67, no. 4, pp. 1787–1792, 2020, doi: 10.1109/TED.2020.2975739.

[59] G. Barillaro, G. M. Lazzerini, and L. M. Strambini, ‘Modeling of porous silicon junction field effect transistor gas sensors: Insight into NO2 interaction’, Appl Phys Lett, vol. 96, no. 16, 2010, doi: 10.1063/1.3391620.

[60] A. Ghomi and M. Shalchian, ‘Design-Oriented Physical Model of Ion-Sensitive Field Effect Transistor for pH Sensing’, IEEE Sens J, vol. 23, no. 3, pp. 2354–2363, Feb. 2023, doi: 10.1109/JSEN.2022.3230849.

[61] ‘Model Semiconductor Devices with the Semiconductor Module’. Accessed: May 05, 2024. [Online]. Available: https://www.comsol.com/semiconductor-module

[62] S. Cao et al., ‘ISFET-based sensors for (bio)chemical applications: A review’, Electrochemical Science Advances, no. November 2021, pp. 1–25, 2022, doi: 10.1002/elsa.202100207.

[63] M. Soikkeli et al., ‘Wafer-Scale Graphene Field-Effect Transistor Biosensor Arrays with Monolithic CMOS Readout’, ACS Appl Electron Mater, vol. 5, no. 9, pp. 4925–4932, Sep. 2023, doi: 10.1021/ACSAELM.3C00706/ASSET/IMAGES/LARGE/EL3C00706_0006.JPEG.

[64] B. R. Goldsmith et al., ‘Digital Biosensing by Foundry-Fabricated Graphene Sensors’, Scientific Reports 2019 9:1, vol. 9, no. 1, pp. 1–10, Jan. 2019, doi: 10.1038/s41598-019-38700-w.

[65] N. Zhou and L. Ma, ‘Smart bioelectronics and biomedical devices’, Biodes Manuf, vol. 5, no. 1, pp. 1–5, Jan. 2022, doi: 10.1007/S42242-021-00179-8/FIGURES/1.

[66] M. Kaisti, ‘Detection principles of biological and chemical FET sensors’, Biosens Bioelectron, vol. 98, pp. 437–448, Dec. 2017, doi: 10.1016/J.BIOS.2017.07.010.

Chapter 6 Application 1: Open-Gate JFET for Emerging DNA Storage[1]

Paper 6: Novel Field-Effect Transistor Sensor for DNA Storage Monitoring

Authors: Abbas Panahi, Morteza Ghafar-Zadeh, Anthony Scime, Sebastian Magierowski, Ebrahim Ghafar-Zadeh

Journal: IEEE Transactions on Instrumentations and Measurements

Abbas Panahi's contributions: chip design, characterization, and implementation; performing DNA tests on the chip and data analysis, FEM simulations; writing the initial draft, submission, and revisions.

This chapter discusses how the OG-JFET's structural advantages position this technology as a promising candidate for DNA data storage applications, particularly when integrated with novel on-chip DNA storage devices as the sensing element. We demonstrated how the open gate on top and a back gate can be utilized for DNA detection on the chip. Additionally, we explore the potential of the OG-JFET as a sensing element in integrated DNA chips, emphasizing its suitability for these advanced applications.

[1] The content of this chapter is wholly based on a published paper: Panahi, A.; Ghafar-Zadeh, M.; Scime, A.; Magierowski, S.; Ghafar-Zadeh, E. Novel Field-Effect Transistor Sensor for DNA Storage Monitoring. IEEE Trans. Instrum. Meas. 2022, 71, 1–11.

6.1. Abstract

This paper presents a novel open gate junction field effect transistor (OG-JFET) based sensor that can be used for various life science applications, including Deoxyribonucleic Acid (DNA) storage monitoring. We put forward the design, modeling, implementation, and characterization of the OG-JFET sensor using a foundry process through CMC Microsystems. We also demonstrate and discuss the functionality and applicability of the proposed sensor for monitoring DNA samples that are suitable for DNA storage applications. Synthetic storage has emerged as an intriguing data storage solution with high density and long-term preservation potential. Most common modalities include converting digital data into synthesized nucleotides, physically storing DNA materials, and reading out data via sequencing and other computational processes. Among these, this paper tackles the challenge of physical storage monitoring of DNA materials by developing a sensor for measurement of DNA samples in dry conditions. The proposed sensor reveals a linear sensor response towards DNA concentration in ultra-pure water. Across a 0.7 mm^2 sensing area, a DNA mass concentration from approximately 100 ng/uL to 400 ng/uL has been detected using the OG-JFET, demonstrating a sensitivity of 30 μA/(ng/uL). These performance quantities imply a promising role for OG-JFETs in emerging biotechnology applications, including DNA storage monitoring.

Index Terms— Field Effect Transistor (FET), biosensor, DNA sensor, DNA storage, ISFET, BioFET

6.2. Introduction

With the rapid growth of the amount of digital data, a huge global demand has emerged for data storage that has motivated cutting-edge research for new technologies for super high-capacity memories. According to studies by the International Data Corporation, worldwide data storage will grow to 175 zettabytes by 2025 [1]. At least for long-term storage needs, available technologies such as magnetic hard disk drives and solid-state drives will not be able to meet the need and provide enough storage capacities to store the data produced worldwide soon. Moreover, the data being stored in these media are sometimes subject to being unrecoverable in the long term due to obsolescence and corruption [2]. Additionally, the current data storage devices have short life spans lower than seven years [3]. Therefore, there is a growing interest in developing alternative storage media.

Novel strategies such as quantum-dot-encoded silica nanospheres [4], wavelength-encoded laser particles [5], color-barcoded magnetic microparticles [6], and DNA [6], [7], have recently been proposed for encoding and storing data in new storage media at the molecular or atomic level. Among these new storage media, DNA has emerged as a promising material due to its immense storage density and its longevity.

DNA can be used to store a significant amount of data in an astonishingly small footprint 215 petabytes in a gram, [8], for thousands of years. The superiority of DNA for storing digital data has recently attracted the attention of major tech companies, such as Amazon, Google, Facebook, Apple, and Microsoft, which are now investing in this approach. As an example, the global software giant Microsoft is developing a proto-commercial DNA-based storage device with the intended size of a commercial Xerox copier for pilot exploitation in one of its data centers [9]. The workflow of the DNA storage system includes: i) encoding the binary digital file to the sequence of four DNA bases of adenine (A), guanine (G), cytosine (C) and thymine (T), ii) synthesis of the related information DNA (iDNA); and iii) organizing and storing the products using a reliable physical storage system with the capability of random access to the desired sequences [9]. In order to read the information, the stored DNA oligonucleotides are read using a sequencer and this is followed by decoding to obtain the initial binary codes. The synthesis and sequencing processes act similarly to writing, and the abovementioned challenge is a digital-microfluidic (DMF) platform reported by Newman et al. on tasks in conventional digital data memories [10]. Many challenges have limited the applicability of DNA storage systems [11]. These challenges include costly synthesis and sequencing steps, long turn-around time, high rate of errors and absence of efficient storage systems for long-term preservation and storage of DNA. One of the notable solutions to address the abovementioned challenge is a digital-microfluidic (DMF) platform reported by Newman et al [12]. As described in the Adhikari

et al., [13], a micropipette is used to drop iDNA on DMF. The dehydration of the DNA resulted in the deposition of iDNA on the specific spot in the DMF system. Another droplet of ultrapure water can be introduced using a micropipette to hydrate the same DNA sample. Improper physical storage of the DNA may result in its loss, as well as increased risk of contamination in the storage device, the outcome of both consequences is the loss of information [14]. It is certainly an imperative need in any DNA-based storage system to develop sensors that integrate with the

storage and digital microfluidic parts to sense the DNA mass continuously both in the process of storing and retrieval.

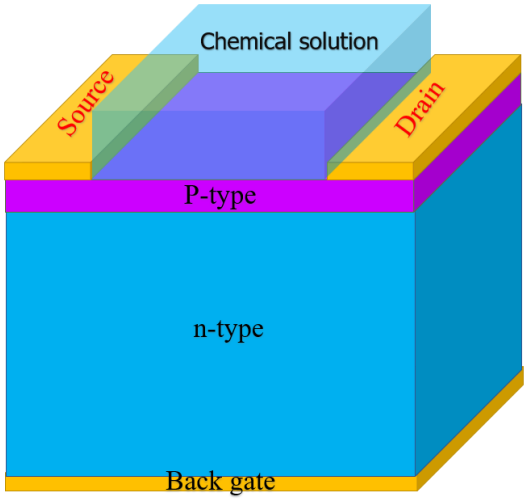


Figure 6-1. Schematic of OG-FET sensor showing the main material composition of the sensor. The sensing layer of OG-JFET is the p-type silicon between two electrodes of the source and drain. The open-gate area is covered with the native oxide layer that usually appears when silicon is exposed to air.

6.3. Background

There has been concentrated research on biochemical sensors that are important elements for a wide range of applications from disease diagnostics to environmental monitoring [15], [16]–[18], [18]–[20]. Amongst the diverse set of chemical sensors described in the literature, field-effect transistors (FET) have received significant interest due to their unique sensing capabilities such as high sensitivity, label-free detection mechanism, cost-effective (e.g., Complementary Metal Oxide Semiconductor (CMOS) based ion-sensitive field-effect transistors (ISFETs)) and seamless integration capabilities with lab-on-a-chip devices that promise their application in next-generation handheld personalized medicine devices [21], [22]. The integration capability of these sensors enables smart measurement integrated systems empowering efficient fluidic implementation for remote sensing and hand-held devices [23], [24]. Biological FET (BioFET) sensors are made through modification of ISFET sensors with biorecognition elements which gives rise to different biosensing mechanisms and associated measurement technique [25], [26]. In the last decade, one of the most researched BioFETs are Gene-FETs (DNA detection-based FETs), in which DNA molecules are used as biorecognition elements for the detection of specific genes based on the charge fingerprint of the DNA molecules.

Table 6-1. Recent biosensors based on field-effect transistor

Sensor type	**Channel material**	**Control Gate**	**Application**	**Advantage**	**Disadvantage**
Au-SiO2-Semi (MOS), [27]	Poly-silicon	SG, Ag/AgCl	Cardiac Troponin-I (cTnI)	Gold sensing substrate	NLR
Ti/Au-SiO2-Semi (MOS), [28]	p-type silicon	EG, Ag/AgCl	pH Sensing	Metal sensing layer, easier functionalization	Need for SRE
LDM, [29]	molybdenum disulfide/graphene	SG (Ag/AgCl)	DNA HD	High sensitivity and small size	MP, repeatability, stability
LDM, [30]	Ni/Cu-MOFs	SG (Ag/AgCl)	glucose sensing	High sensitivity, good stability	MP, Need for SRE
OFET, [31]	BFPA	BG	Liver Cancer Diagnosis	Low cost, fast response time	MP, stability
SiNW FET, [32]	N+ poly silicon	Side Gate	Immunosensor kit	High sensitivity	Need for SRE
SiNW FET, [33]	p-type silicon	DG	Cancer tumor markers detection	Minimizing Debye length effect	High voltage
SiNW FET, [34]	n-type In2O3	SG (Ag/AgCl)	DNA HD	High sensitivity	Need for SRE
LDM, [35]	Graphene	SG (Ag/ACl)	DNA HD	Linear response, High Sensitivity	Need for bulky SRE
LDM, [36]	Carbon Nanotube	SG (Ag/ACl)	Disease biomarkers	High sensitivity, stable, scalable	Need for bulky SRE
CMOS-based FET, [37]	p-type Silicon	SG (Ag/ACl)	DNA HD	Scalable, CMOS-based, stability	Need for bulky SRE, high noise
JFET (This work)	p-type silicon	BG	Dried-DNA detection	Scalable, linearity, stability	No need for RE, LR

* MOS: Metal Oxide Semiconductor; BFPA: 2,6-bis(4-formylphenyl)- anthracene; SiNW: Silicon nanowire; SRE: solution reference electrode; SG: solution gate; DG: double-gate; JFET: junction field-effect transistor; MP: mass production; Semi: Semiconductor; BG: Back-gate; HD: hybridization detection; NLR: non-linear response; LR: linear response; LDM: Low Dimension Materials; OFET: Organic FET.

Mostly, the DNA detection with FET-based sensors was conducted for DNA hybridization and sequencing purposes. Although much progress has been made, dry DNA detection for its mass density analysis has not been reported with FET sensors. Nevertheless, in this paper, we address this challenge by monitoring various concentrations of negatively charged single-stranded DNAs (ssDNAs) deposited on the surface of an FET chip using the dehydration method previously reported [12],[13]. The motivation for such analysis comes from the requirement in DNA storage devices for DNA mass monitoring over time in a specific spot. This is to assure the existence of uncontaminated DNA at a specific storage location or, during the retrieval process, guarantee the complete removal of DNA from the storage location to access the stored data. Table 1 compares the most recent FET biosensors dedicated to detecting biomolecules. While there are various FET sensors in the literature, Table 1 provides an example of each category for a better comparison of OG-JFET with the previous works [27]–[37]. Almost all the works dedicated to DNA sensing have detected DNA hybridization; however, to the best of our knowledge, the current work, for the first time, uses a FET sensor for dried-DNA sensing.

In this paper, we are introducing a new FET technology which is based on the junction field effect transistor (JFET) sensing mechanism for the application of DNA mass measurement. The sensor works based on a back-gate structure with a comparatively direct large sensing area (without the need for gate extension). This is done to avoid using bulky reference electrodes in a solution containing DNA, as this would affect the integration of the sensor with DNA storage digital microfluidic devices. Relying on a back-gate structure opens the top area for integration with microfluidic channels for both droplets and continues microfluidic integrations; however, (see Table 1) many FET biosensors use bulky reference electrodes, which is a big challenge in the integration process. Such integration is an essential element for high throughput DNA storage devices with integrated sensing elements to analyze the DNA mass throughout the storage processes [12].

For the first time, dried DNA was detected with a field-effect transistor with high sensitivity that is applicable in DNA mass monitoring for DNA storage applications. The back-gate structure makes monitoring biomaterials in dry mode possible, which can be extended to other sensing applications for biomolecules in dry mode or as a gas sensor.

The sensor can be operated at a very low back-gate voltage (<0.5 V), demonstrating its potential as a sensing element for hand-held point-of-care diagnostic devices. Furthermore, the sensor response to ssDNA concentration is linear, which is very important in the circuit modeling and design for this sensor integration with the digital microfluidic DNA-storage platform [12]The sensor is modeled with COMSOL Multiphysics, which predicts the same experiment pattern, validating the sensing mechanism for dried ssDNA concentration.

6.4. Proposed Sensing Mechanism

6.4.1. OG-JFET Working Principle

The OG-JFET sensor consists of a vertical p-n junction in which a very thin (sensing) layer of p-type silicon (1.6 μm) is grown on top of a very thick (450 μm) layer of n-type silicon. A metal back gate is deposited on a highly doped (> $10^{19}/cm^3$) silicon on the back side of the wafer that altogether brings a JFET sensor with a sensitive p-type layer (demonstrated in Fig. 6-1). Compared with a standard JFET structure, the OG-JFET is a new variant with the subtle difference that the traditional n-type top gate on top is absent. Hence, the OG-JFET presents an opening for a solution or introduction of biological material to serve as the gate material. The total area of the

experimental chip used in this report is around 10×10 mm^2, in which a total sensing area of approximately 0.7 mm2 is developed. This design characteristic of OG-JFET would allow more room for an enormous gate on top, which is a distinct advantage of OG-JFET structure compared to other FET structures. When a solution or any charged group of molecules (in this work, ssDNA molecules) is brought in contact with the p-type layer in the sensing area (here single-strand DNA molecules), the charged outer layer of native oxide (SiO_2) will interact with the biomolecules. Consequently, this interaction creates a charge-induced electrical field in the double-layer capacitance that affects the conductance of electrons/holes in the p-type layer. In our experiments with ssDNA, the DNA molecules create a thin layer of negative charge on top of the sensor due to ssDNA molecules having a total negative charge.

6.4.2. Design of OG-JFET Sensor

The OG-JFET sensor fabrication is based on a new standard mass-producible microfabrication process offered by CMC Microsystems (Montreal, Canada). The design consists of seven open-gate channels with dimensions of 100 µm × 1000 µm (W×L). There is a pitch of 40 µm for channels with the common source to extend the sensing gate.

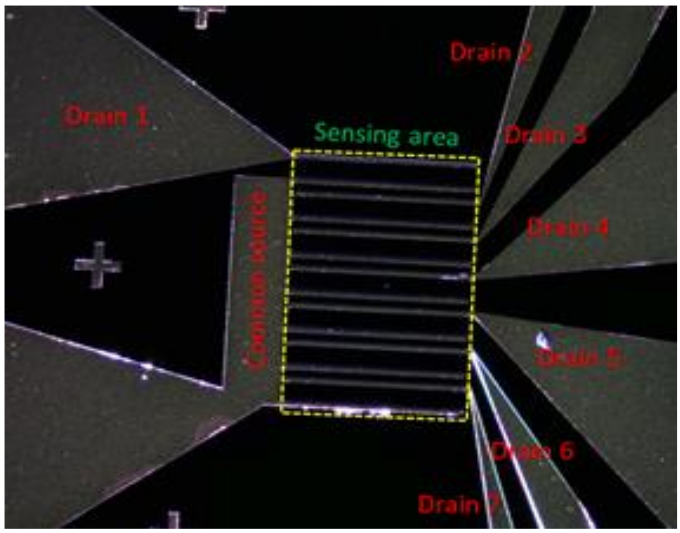


Figure 6-2. Schematic of the fabricated OG-JFET sensor used for testing the dry DNA. The sensing area is shown as the drain/source arrangements. The design consists of seven drains with one common source. Drain 1 has been used in this report to measure the mass DNA concentration.

Source and drains with a width of 20 µm are considered for each channel. All the sources are connected to a common pad as the common source. Therefore, the sensor works based on a common source and seven drains. The drains are not connected; only one has been used in this

experiment. All channels have a 1.6 µm depth underneath (the thickness of the p-type layer). The p-type layer is grown on a 450 µm n-type layer, which forms a p-n junction. Drains and source are connected to pads with area of 1700 µm × 1700 µm that were designed with a pitch of 200 µm while a 200 µm distance from both end sides of the chip is set for the design. The minimum surround for the opened gate is considered 10 µm, which is the stacked layer of Si_3N_4/SiO_2 on the silicon (p-type). The total sensing area is 0.7 mm^2, large enough to accommodate all the DNA samples in the 2 µL droplet.

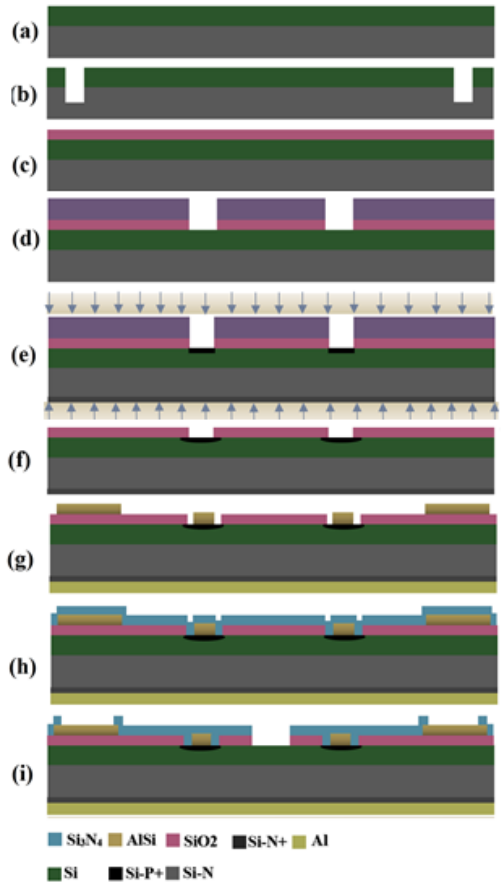


Figure 6-3. Microfabrication process for building OG-JFET sensor. (a) Substrate wafer (Silicon <100>, 100 mm diameter, - 420 +/- 25 µm thick, Resistivity 0.006 to 0.02 Ohm-cm); (b) Alignment marker definition (first mask); (c) PECVD SiO_2 deposition; (d) SiO_2 etching to Si layer. (second mask); (e) Front and back-side ion implantation; (f) implantation annealing; (g) front and back side metallization and annealing; (h) PECVD Si_3N_4 deposition (passivation layer); (i) Pad and channel opening.

6.4.3. Fabrication

The main OG-JFET sensor fabrication steps are shown in Fig. 6-3. According to this process, a 1.6 um thick p-type silicon layer has been epitaxially grown on a 450 µm n-type layer with the conduction doping of 1×10^{18} cm^{-3} and 5×10^{15} cm^{-3} respectively (Semiconductor Wafer Inc.) using standard very large scale of integration (VLSI) processes at Institut interdisciplinaire d'innovation technologique (3IT) at Université de Sherbrooke. To create pad contacts on the epitaxial channel, ion implantation is performed, followed by the lithographic patterning of aluminum as a routing. The pads are passivated by a 500-nm layer of Si_3N_4. The layout of the sensor was firstly designed in L-Edit software, and then the files were submitted for fabrication at Institut interdisciplinaire d'innovation technologique (3IT), Université de Sherbrooke, through the Electronic Sensor Platform technology offered by CMC Microsystems.

The fabrication process begins with alignment marker patterning on a silicon wafer with an orientation of <100> and 100 mm diameter, which has approximately 420 µm +/- 25 µm thickness with a resistivity of 0.006 to 0.02 Ohm-cm (see Fig. 6-3). This step is followed by PECVD deposition of 200 nm +/- 25 of SiO_2 on the sensor top silicon later. After the deposition of SiO_2, a layer of photoresist was deposited, followed by an etching process to open the space for implantation, which is required for metallization and for making silicon ready for drain and source contact. Before metallization was continued, back and front annealing was conducted, which promotes consolidated metallization. Afterward, all the front area was encapsulated using 500-nm thick Si_3N_4. The final stage of fabrication opened the gate area and contact pads, as shown in Fig. 6-3. For future integration of the microfluidic chip, some metal plus signs is created on the sensor shown in Figure 6-2.

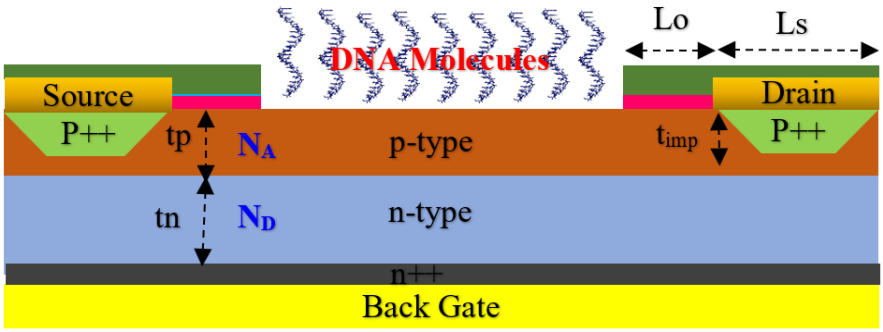


Figure 6-4. The sensor surface was clean and non-chemically treated before testing with DNA samples.

6.4.4. DNA Preparation

In this work, ssDNA (Sigma-Aldrich Company) at a concentration of 10.0 ± 1.0 mg DNA in 1 mL of ultra-pure water (Sigma-Aldrich) was used. This ssDNA solution was diluted to obtain concentrations of 101 ng/µL,180 ng/µL, 270 ng/µL, 301 ng/µL and 370 ng/µL.

6.5. Modeling and Simulation

A multiphysics simulation was performed using COMSOL Multiphysics software to validate the sensor response in experiments. The semiconductor device was simulated using the Semiconductor Module of COMSOL based on the Finite Element Method (FEM). DNA molecules on top of the open-gate area would create a negative charge accumulation (in dry conditions), which affects the positive charges of hole transport inside the p-type channel. For this purpose, a 2D model of the OG-JFET has been simulated with specific boundary conditions applied on the outer faces of the sensor. The simulated sensor consists of seven conductive channels with the dimensions provided in Section 2[1]. In the simulations, the common source pad is considered, and the fabricated chip is modeled with the same geometry (as shown in Fig. 6-2).

The FEM method was used in a meshed domain to solve Maxwell's equations, Boltzmann transport theory, and Neumann boundary conditions with the defined boundary conditions. To solve the equations, meshing was required to determine the place of required nodes for calculation. The meshing was performed to have minimum and maximum sizes of 0.01 µm and 0.1 µm, respectively. The p-type layer includes a structured mesh, and the n-type layer has an unstructured mesh for better convergence. An "ohmic contact" was used to model the drain, source, and back-gate contacts. The remaining faces are all "insulated," meaning there is no charge transfer into /out of these faces.

Fig. 6-4 shows the physical cross-section of OG-JFET, simulated with the parameters. The exact charge density for the DNA molecules in the open gate area is unknown. For this reason, an estimation of the molecule charge has been used in the simulation to approximate the tendency to draw negative inversion charges on top of the sensing channel and verify the sensor response's correctness. DNA molecules are solved in ultra-pure water; therefore, the only surface contribution

[1] Section 6.7.3

is from the DNA and water molecules. DNA molecules can align themselves with SiO_2 surfaces in different shapes; however, for simulation and understanding the sensor response trend to the existence of DNA, we have assumed that DNA molecules are aligned vertically and cover the sensing area equally. The DNA molecules have a negative charge on their surface, which arises mainly from the negative charge of phosphate on the Adenine (A), Thiamine (T), Guanine (G), and Cytosine (C) subunits of the DNA. The basis for our charge calculation assumption considers the DNA negative charge (e) per base spacing of about 0.34 nm and the reported DNA surface packing density (number/cm^2) of about $10^{12}/cm^2$ [38]. Taking this value for packing density and the total sensing area of OG-JFET, the charge accumulation calculated for DNA in our simulation would be 0.001086 C/m2. The value used here is based on the packing density assumption [38], which enables us to have an estimation of the negative charge of DNA when it is put on the surface. Also, we have assumed that only one single negative charge of DNA participates in the charging effect; therefore, the calculated charge value is based on that assumption. Understanding the exact pattern of DNA distribution on the surface of the p-type channel is very difficult. Therefore, we have applied the abovementioned assumptions to evaluate the effect of the negative charge on the response of the OG-JFET sensor. The modeling helps us to grasp the sensor incremental trend in response to DNA concentration. Adding more DNA to ultrapure water seems to increase the density of the negative charge on the sensor, resulting in a linear curve of Ids-DNA.

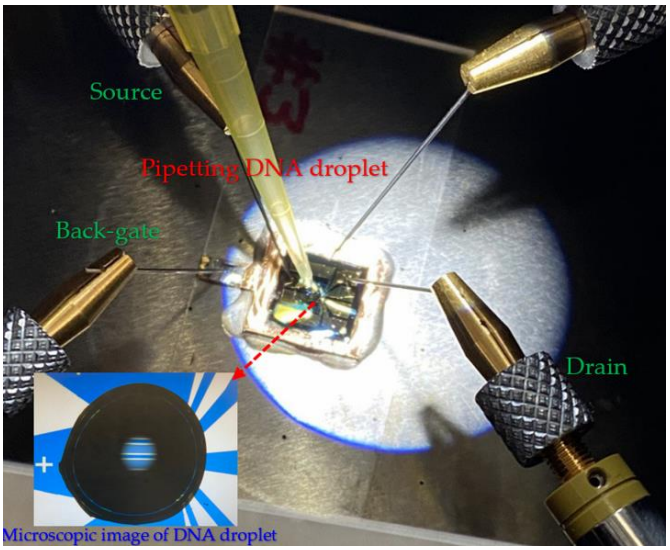


Figure 6-5. Schematic of OG-FET sensor showing the main material composition of sensor.

6.6. Measurements

All the measurements were conducted using a Semiconductor analyzer device (Keithley 4200A-SCS Parameter Analyzer) connected to a probe station frequently used for semiconductor characterization and measurements [39]–[41]. As shown in Fig. 6-5, the sensor is connected to the semiconductor analyzer through 3 needles, which connect the source, drain, and back gate of the sensor to the analyzer input cables. The measurements were done by biasing the sensor in reversed mode (positive voltage to n-type and negative to p-type). As the measurement system shows, the device has been tested in a prob station (TS200-SE, MPI Corporation) cage with complete darkness to avoid the photo-current noises because of light on the conduction in the channel. The transfer characteristics of the sensor recorded were Ids-Vds and Ids-Vgs curves, which are essential for sensor sensitivity analysis in the post-processing stage. To acquire a sensor response, the back gate was increased stepwise, and a sweep voltage was assigned to the drain voltage. The DNA samples were put on top of the sensor's sensing area by adding a 2 µL droplet with a pipette, as shown in Fig. 6-5.

6.7. Results

6.7.1. Sensor transfer characteristics

The sensor has been characterized to obtain its I-V curves, which include the Ids-Vds and Ids-Vgs curves. The I-V curves will assess the sensor sensitivity towards the DNA mass concentration in dry mode. To obtain the transfer characteristics of the sensor, a positive voltage was applied to the back gate by increasing from 0 to 2 volts stepwise by 0.2 volts. Also, a negative voltage was applied to the drain with a sweep of 0-10 volts. The applied voltage operated the sensor in reverse-biased mode, which assures that the p-n junction was off during the experiments. By doing so, we make sure that there is no current from the back gate and that only the electrons flow from the source to drain in the p-type channel. The Ids-Vds and Ids-Vgs curves of the OG-JFET in the dry condition are shown in Fig. 6-6, which exhibits that OG-JFET current decreases when the back gate applies positive voltage and manipulates the space charge in the main channel. The channel is almost blocked for Vgs of 1.4 V, and the maximum drain-source current for OG-JFET is around 0.65 mA for this design in reverse bias mode.

Fig. 6-6 shows the general I-V curve of OG-JFET in which a pinch off voltage of around 1.75 V can be considered for the highest current in Vgs = 0 V. The current in the designed sensor does not

saturate, as we can see a slope in the Ids-Vds curve, which confirms that we still have carrier conduction from source to drain. The channel conduction decreases very fast as the voltage changes from 0 to 1 V as the current in the channel is close to zero at high back gate voltages (e.g. 1 V). The sensor has been tested over a wide voltage range (0 to 10 V).

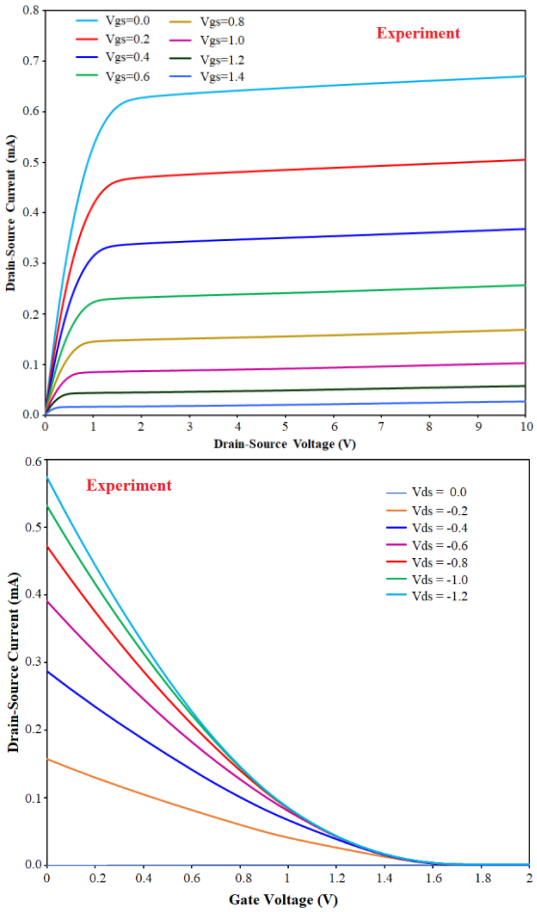


Figure 6-6. Ids-Vgs and Ids-Vds curves of OG-JFET with no sample.

The Ids-Vgs curves show the change in the conduction of charge carriers in the channel and its sensitivity to the back-gate voltage. Previously it was discussed that the back gate is used for assessing the sensitivity analysis which generally the change in the threshold voltage is being used as the figure-of-merit for design optimization or sensitivity analysis in biosensing applications. The Ids-Vgs curves show that at around 1.8 V the current is blocked, and the space charge has pushed the channel to get pinched off.

6.7.2. Sensor Response to Dry DNA

After preparing the DNA solutions in ultra-pure water, the samples were put on top of the sensing area of the OG-JFET, as shown in Fig. 6-5. A 2 µL droplet of DNA solution was added atop the OG-JFET via pipette and then allowed to evaporate at room temperature for 10 minutes. The results of this vaporization are a layer of air-dried DNA molecules covering the sensing area. The sensing area is approximately 0.7 mm^2, which is a substantially large space for accommodating the 2 µL droplet of DNA. The DNA creates a negative charge, increasing the current when more DNA concentration is placed. Fig. 6-7 shows the sensor Ids-Vds curve towards different concentrations of DNA.

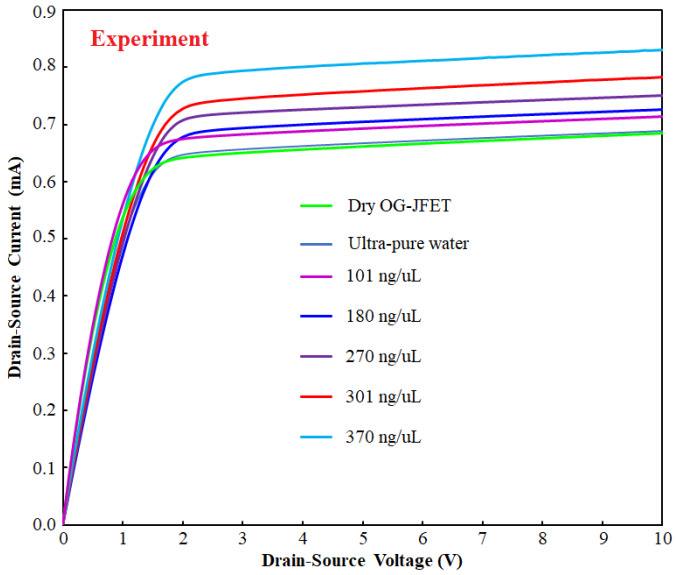


Figure 6-7. OG-JFET sensor response to different concentrations of DNA solvated in ultra-pure water. The droplet of DNA in ultrapure water has been put on top of the sensing area. The curves result from the sensor response to the dried DNA in the solution.

Fig. 6-8 demonstrates the output current of the OG-JFET sensor when it is exposed to varying concentrations of dried DNA on its surface. First, the dry sensor is tested, and then an ultrapure water (PW) droplet is added. Then, the surface is allowed to be dried completely before other DNA concentrations are measured on the sensor. The concentrations were 101 ng/uL, 180 ng/uL, 270 ng/uL, 301 ng/uL, and 370 gn/uL in ultrapure water. As shown, an almost linear response to DNA concentration in dry mode. The sensor output current changed from 0.714 mA to 0.821 mA when the DNA concentration changed from 101 ng/uL to 370 ng/uL. The sensor sensitivity to the DNA has been calculated to be 30 µA/(ng/µL) of ssDNA. This sensitivity is produced with a linear fit

to the linear part of the DNA concentrations. The sensor current changes with the DNA concentration according to the following formula:

$$I\ (A) = 30\ \times 10^{-6}(C_{DNA}) + 0.0007 \qquad (1)$$

$$R^2=0.9903$$

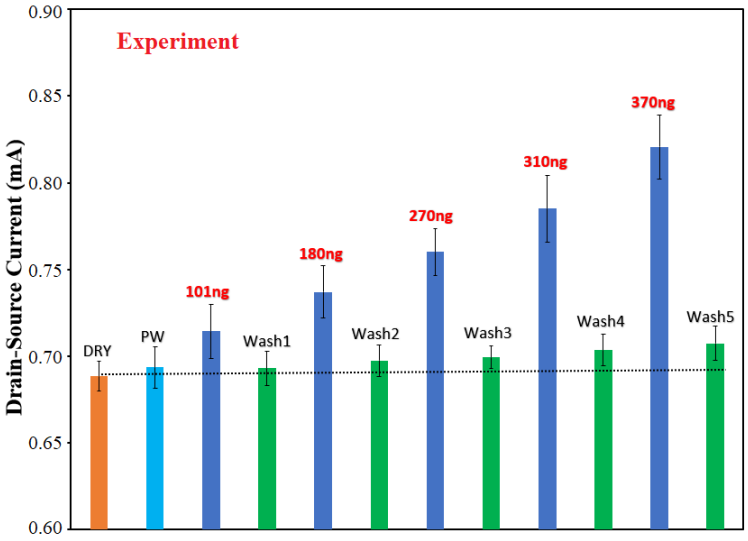


Figure 6-8. The effect of the washing process on the sensor response.

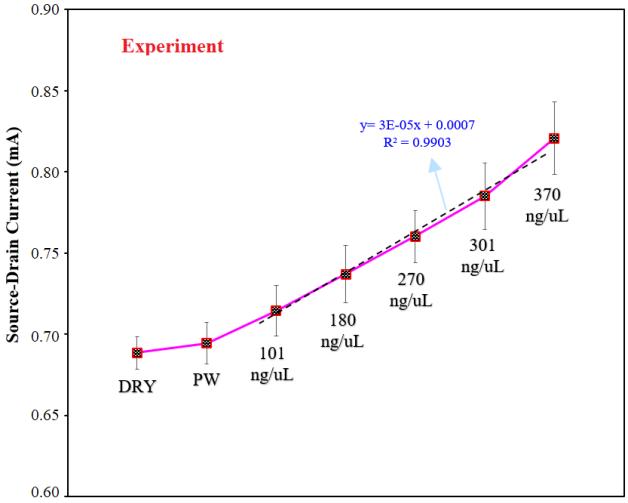


Figure 6-9. Sensitivity analysis of OG-JFET to dry DNA. Sensor response to different DNA concentrations in dry mode.

In formula (1), the C_{DNA} unit is ng/uL. Equation (1) is essentially the OG-JFET sensor's response to the dried DNA concentration. The data shown in Fig. 6-8 Is driven from the Ids-Vds curves of OG-JFET in different DNA concentrations in dry mode. After 10 minutes, the Ids-Vds curves were collected, and the output current was recorded at Vds = 10 V and Vgs = 0. Fig. 6-8 demonstrates that the OG-JFET can be used for monitoring the mass of ssDNA in a specific location in the integrated DNA storage devices. Although the integration of OG-JFET has not been performed, the results show that the sensor provides a sensitivity of 30 μA/(ng/μL) for monitoring the DNA mass storage. Each point in Fig. 6-8 is the result of the average of 5 independent experiments. The error bars are calculated based on the minimum average deviation. DNA molecules could arrange themselves in various ways, which affects the response of the sensor. The surface of the sensing layer is native silicon oxide, which affects the distribution of DNA molecules in the proximity of surface bonds. For this reason, the sensor was tested several times to obtain an average measure for each concentration.

Another important experiment for showing the usefulness of the sensor to be used for DNA storage applications is to demonstrate the effectiveness of the DNA retrieval process. Because it is needed to store the DNA in a known location and leave it for future needs to retrieve the stored data. To access the information, it is required to sequence the stored DNA, therefore it is needed to solve the dried DNA in a droplet and move it to the sequencer location. This process needs a droplet to remove the DNAs from the surface first and then move it to a new position. To show if the retrieval process is effective and the sensor response, after testing, it was washed with ultrapure water 10 times, and a subsequent DNA concentration was tested. The effectiveness of the retrieval process is shown in Fig. 6-9. After each washing by pipetting ultrapure water, the sensor response was recorded to determine if we can manage the retrieval process by only monitoring the sensor response when the DNA exists on the sensor. The washing was done with ultra-pure water and rapid pipetting of that on the sensing area (Fig. 6-5). The results shown in Fig. 6-9 are the average of 10 times of washing with a pipette. After finalizing this process, the next concentration is used, and the process is continued. From the molecular perspective, using OG-JFET helps to characterize the storage surfaces on which the DNA molecules are stored (here, SiO_2), which makes the retrieval process more efficient. It also provides a quantitative method to find the best condition for DNA storage and more efficient retrieval.

6.7.3. Simulation results

The sensor response to DNA can be modeled with an accumulation of negative charge on top of the sensor. To prove the sensor's response and ensure its response towards the charged DNA molecules, a COMSOL Multiphysics simulation has been conducted on the sensor with the dimensions and sizes used in fabrication. Simulation helps to characterize the sensor response and validate the correctness of experiments. As the simulation demonstrates, the sensor response to increasing negative charge is assumed to be due to the DNA molecules that resemble the effect of negative charge on the p-type silicon channel.

Fig. 6-10 shows the simulation results of the effect of the DNA-modeled equivalent charge on the response of OG-JFET. As we can see, the drain-source current increases as the negative charge on top of the sensor increases. The sensor response is almost linear to DNA concentration, which the experimental results verified. COMSOL simulations demonstrated the sensor response trend and helped to evaluate and design the OG-JFET more efficiently for DNA storage applications. For a better understanding of the effect of the negative charge on the sensor operation, the electrical potential has been analyzed in the middle of the opened gate along a vertical line, as shown in Fig. 6-11. The attachment of DNA molecules creates a negative charge accumulation on the channel, which increases the electrical potential in a constant bias state of Vgs and Vds. The current sensitivity has been calculated for simulation results, as shown in Fig. 6-12. Based on this calculation, a current sensitivity of 36.8 µA/(ng/uL) of DNA concentration has been calculated.

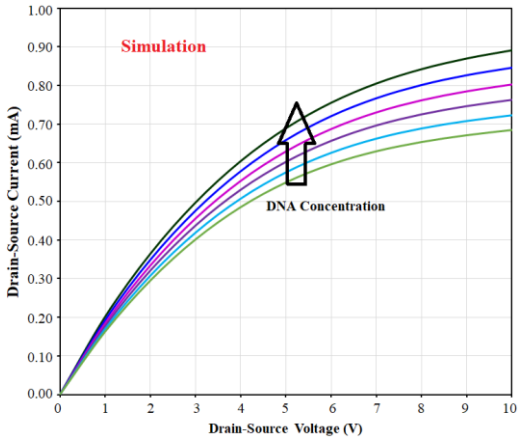


Figure 6-10. COMSOL simulation result of modeled DNA charge on the OG-JFET sensor which shows an almost linear dependency between current and the DNA concentration.

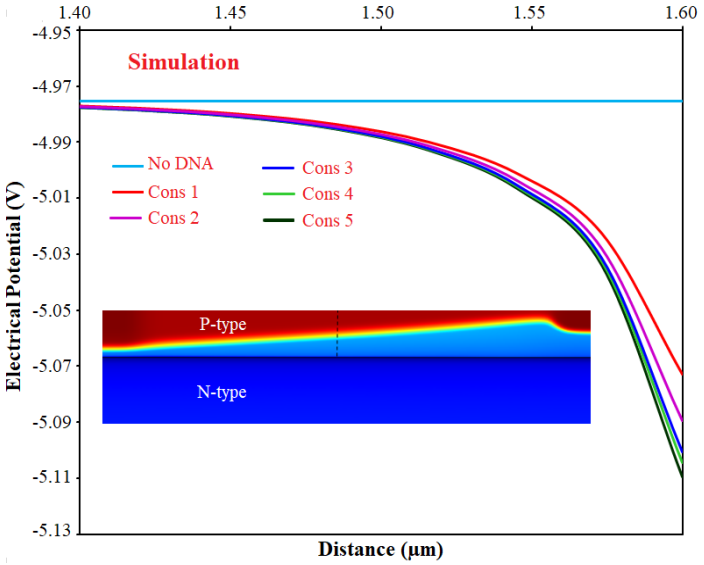


Figure 6-11. The electrical potential along the centerline (shown in figure inset). Cons: Concentration.

There is a growing interest in exploiting the unique advantage of DNA biomolecules as new organic platforms for storing data. While platforms for manipulating and storing DNA have developed and are widely discussed in the digital microfluidic area, the need for DNA mass assessment as an inevitable integrated part of storage spaces is impacting the successful realization of this technology. This paper introduces a new FET sensor called an open-gate junction field effect transistor (OG-JFET). The sensor operation is based on a back-gate structure by which the carrier transport in the p-type channel can be regulated. Relying on a back-gate structure of JFET, a vast space on top of the sensor for DNA sample placement would be offered, which is desirable for DNA storage applications and further integration with digital microfluidic devices. Furthermore, chip fabrication is based on a standard fab-less microfabrication process, which increases the chance of high production and standard integration with CMOS technology such as readout circuitry. The described OG-JFET sensor was fabricated based on proven VLSI fabrication methods and was characterized by its main transfer characteristics: Ids-Vds and Ids-Vgs curves. The sensor offers a 0.7 mm^2 total sensing area with seven active sensing channels. The channels sensing surface are covered with native silicon oxide, which forms naturally due to silicon environmental exposure.

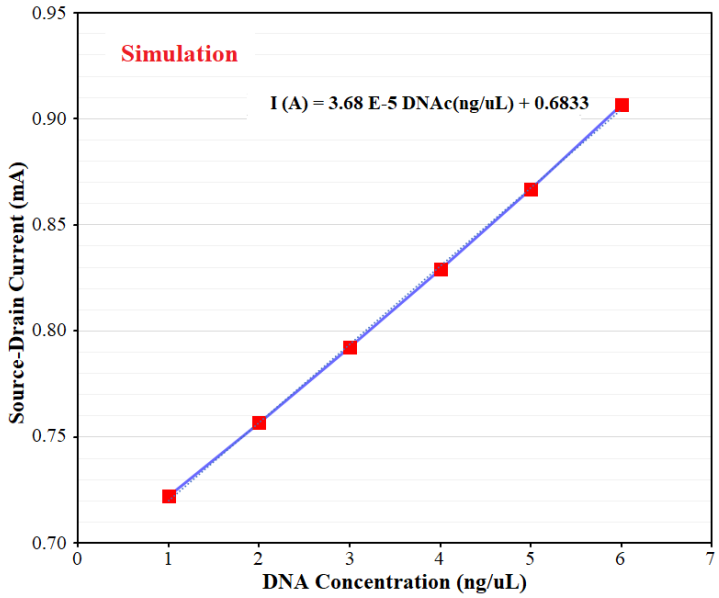


Figure 6-12. The current sensitivity obtained from COMSOL simulation at Vds = 5 V and Vg = 0.

We have measured a sensitivity of 30 µA/(ng/µL) for OG-JFET toward dry DNA (solvated in ultra-pure water). The sensor response to DNA concentration was proved linear, and the linear fit to the Ids-DNA(Cons) diagram resulted in the sensitivity mentioned. The retrieval process is an integral part of a DNA storage device, and its efficiency impacts data storage significantly. We have demonstrated that washing with ultrapure water affects DNA retrieval in the sensor's current condition. Also, the current sensitivity has been determined for comparison with the experiment, as shown in Fig. 6-12. Based on the simulation result, the current sensitivity is 36.8 µA/(ng/uL) of DNA concentration. The current sensitivity is higher than the experiment, possibly due to non-idealities associated with the device and experiments besides the simulation errors. More importantly, this paper shows the importance of monitoring the retrieval process by comparing the sensor output current with a baseline and using the sensitivity curve for DNA mass monitoring. The sensor does not need a bulky reference electrode to check the availability of DNA, yet it works with an opened gate on top. The DNA molecules might interact with the surface differently, and their arrangement affects the sensor response; therefore, surface DNA affinity enhancement is a vital future study for this technology to increase retrieval efficiency.

Dried-DNA storage sensing with a FET sensor is a novel concept proposed by the current study. However, storing DNA on digital microfluidic has been discussed recently by S. Newman et al. [12], which demonstrates moving DNA in droplets and drying it in different storage locations. In the introduced technology, it is necessary to monitor the dried DNA in a specific spot on the chip

before and after retrieval. Our work is one step forward for using FET biosensor in sensing DNA in dry mode for the DNA storing applications. To the best of the authors' knowledge, no research reports dried-DNA sensing with a biosensor. However, various research studies have reported DNA hybridization sensing with FET sensors, all of which are in solution mode [30], [33], [35], [36], [38].

The current sensor structure can be exposed to biomaterials in the open-gate area to make biological/solution gates for sensing charges. The present experiment shows that the sensor is sensitive to biomolecule (here ssDNA) upon placement on the conductive channel. Grounding the observations in this study, this sensor is expected to operate in other charge-based biosensing applications like other biologically field-effect transistors [42]–[44]. The immobilization of a bioreceptor would change the sensing layer of OG-JFET (here is native SiO_2) to a layer of biorecognition elements sensitive to a specific analyte. The immobilization of the bioreceptor would change the sensor's baseline. The sensor's exposure to a solution containing the analyte of interest can chemically react with the bioreceptor. This would change the new baseline since the sensor is sensitive to charge variation in the opened-gate area. However, like other BioFETs, the limit of detection and sensitivity might differ, which opens the avenue for this charge-sensitive sensor for further meticulous characterization of different biomolecules. Well-established chemical methods for functionalizing SiO_2 and other oxides for protein sensing can be conducted on OG-JFET as the sensor provides a native oxide layer or a certain thickness of oxide on top. The current work establishes the charge sensitivity of the sensor with experiments and simulations, putting forward this standard technology for further biosensing applications.

In this work, a known ssDNA concertation was used. However, the effect of impurities on the sensor response is also essential to address. If other biomolecular and charge impurities are present in the prepared sample, the surface charge density on top of the sensor will be altered. Upon the presence of a new protein in the prepared sample, after drying, new biomolecules could distribute differently on the available oxide sites and establish different charge arrangements based on the chemistry of the reaction in the environment. Such variation will change the current in the silicon channel near the changed bio-layer. Simulation (Fig. 6-10 and Fig. 6-12) shows that the sensor undergoes a current enhancement when it is exposed to a negative charge; therefore, depending on the negativity or positivity of the top layer due to the existence of biomolecules, the current might

be decreased or increased. Nevertheless, future works must address these effects to estimate their impact on sensor response.

For other biological samples (e.g., blood serum), the sensor needs to be further studied regarding selective recognition of an analyte, which was impossible to perform in the current study. Our end application required us to perform a dried test on ssDNA to evaluate its appropriateness for next-generation DNA-based data storage applications.

6.8. Conclusion

The open-gate junction field effect transistor (OG-JFET) has been introduced as a new platform for DNA storage applications. The sensor has been characterized, and its electronic transfer characteristics have been derived. The sensor works based on a p-type sensing layer on top of an n-type thick support layer, which can be biased in reverse mode to ensure the vertical p-n junction is turned off. The sensor characterized for DNA storage application as the sensing element, the DNA solvated in ultra-pure water was put on top of the sensing layer, which is a process normally conducted in digital microfluidic chips designed for DNA storage. The sensor comes with a 0.7 mm2 sensing area, which easily accommodates a 2 μL pipette-driven DNA droplet (solvated in ultrapure water). The characterization curve, the most critical curve for DNA storage applications, shows a 30 μA/(ng/μL) sensitivity to ssDNA in dry mode. Also, a COMSOL Multiphysics simulation was performed to validate the experiment and to simulate the sensor in response to negative charge accumulation due to DNA molecules. The simulations showed that increased DNA concentration would increase the sensor current. The sensor response was linear, which is essential for OG-JFET integration with digital microfluidic DNA storage systems. The sensor showed a response of $I\ (A)=30 \times (10)^{-6}\ (C_{DNA})+0.0007$ to DNA concentration.

Based on the results and analysis, this paper presents the OG-JFET sensor for DNA storage monitoring applications for the first time.

Acknowledgment

We would like to acknowledge CMC Microsystems for providing products and services that facilitated this research, including software design packages such as Mentor Tanner and COMSOL Multiphysics, fabrication services for the Electronic Sensor Platform at 3IT, and engineering support.

6.9. References

[1] Patrizio, Andy, “No Title,” Network World, 2018. [Online]. Available: https://www.networkworld.com/article/3325397/idc-expect-175-zettabytes-of-data-worldwide-by-2025.html.

[2] F. D. S. Lima, F. L. F. Pereira, L. G. M. Leite, J. P. P. Gomes, and J. C. MacHado, “Remaining Useful Life Estimation of Hard Disk Drives based on Deep Neural Networks,” Proc. Int. Jt. Conf. Neural Networks, vol. 2018-July, 2018, doi: 10.1109/IJCNN.2018.8489120.

[3] W. A. Bhat, “Bridging data-capacity gap in big data storage,” Futur. Gener. Comput. Syst., vol. 87, no. 2018, pp. 538–548, 2018, doi: 10.1016/j.future.2017.12.066.

[4] P. P. Pillai, S. Reisewitz, H. Schroeder, and C. M. Niemeyer, “Quantum-dot-encoded silica nanospheres for nucleic acid hybridization,” Small, vol. 6, no. 19, pp. 2130–2134, 2010, doi: 10.1002/smll.201000949.

[5] N. Martino et al., “Wavelength-encoded laser particles for massively multiplexed cell tagging,” Nat. Photonics, vol. 13, no. 10, pp. 720–727, 2019, doi: 10.1038/s41566-019-0489-0.

[6] Y. Hao, Q. Li, C. Fan, and F. Wang, “Data Storage Based on DNA,” Small Struct., vol. 2, no. 2, p. 2000046, 2021, doi: 10.1002/sstr.202000046.

[7] K. Matange, J. M. Tuck, and A. J. Keung, “DNA stability: a central design consideration for DNA data storage systems,” Nat. Commun., vol. 12, no. 1, p. 1358, 2021, doi: 10.1038/s41467-021-21587-5.

[8] Antonio Regalado, “No Title,” MIT Technol. Rev.

[9] C. K. Lim, S. Nirantar, W. S. Yew, and C. L. Poh, “Novel Modalities in DNA Data Storage,” Trends Biotechnol., pp. 1–14, 2021, doi: 10.1016/j.tibtech.2020.12.008.

[10] M. Hao, J. Qiao, and H. Qi, “Current and emerging methods for the synthesis of single-stranded DNA,” Genes (Basel)., vol. 11, no. 2, 2020, doi: 10.3390/genes11020116.

[11] Z. Ezziane, “DNA computing: Applications and challenges,” Nanotechnology, vol. 17, no. 2, 2006, doi: 10.1088/0957-4484/17/2/R01.

[12] S. Newman et al., “High density DNA data storage library via dehydration with digital microfluidic retrieval,” Nat. Commun., vol. 10, no. 1, pp. 1–6, 2019, doi: 10.1038/s41467-019-09517-y.

[13] P. R. Adhikari, N. T. Tasneem, R. C. Reid, and I. Mahbub, “Electrode and electrolyte configurations for low frequency motion energy harvesting based on reverse electrowetting,” Sci. Rep., vol. 11, no. 1, pp. 1–13, 2021, doi: 10.1038/s41598-021-84414-3.

[14] P. Y. De Silva and G. U. Ganegoda, “New Trends of Digital Data Storage in DNA,” Biomed Res. Int., vol. 2016, 2016, doi: 10.1155/2016/8072463.

[15] A. Panahi, D. Sadighbayan, S. Forouhi, and E. Ghafar-Zadeh, “Recent advances of field-effect transistor technology for infectious diseases,” Biosensors, vol. 11, no. 4, 2021, doi: 10.3390/bios11040103.

[16] N. Cennamo et al., “Green LSPR Sensors Based on Thin Bacterial Cellulose Waveguides for Disposable Biosensor Implementation,” IEEE Trans. Instrum. Meas., vol. 70, 2021, doi: 10.1109/TIM.2021.3070612.

[17] F. Marvi and K. Jafari, “A Measurement Platform for Label-Free Detection of Biomolecules Based on a Novel Optical BioMEMS Sensor,” IEEE Trans. Instrum. Meas., vol. 70, 2021, doi: 10.1109/TIM.2021.3052001.

[18] P. Y. Kuo, Z. X. Dong, and Y. Y. Chen, “The Stability Analysis of Potentiometric Urea Biosensor under Microfluidic System and Remote Measurement,” IEEE Trans. Instrum. Meas., vol. 70, 2021, doi: 10.1109/TIM.2021.3075036.

[19] Q. Wang, J. Y. Jing, and B. T. Wang, “Highly Sensitive SPR Biosensor Based on Graphene Oxide and Staphylococcal Protein A Co-Modified TFBG for Human IgG Detection,” IEEE Trans. Instrum. Meas., vol. 68, no. 9, pp. 3350–3357, 2018, doi: 10.1109/TIM.2018.2875961.

[20] Y. H. Nien et al., “Investigation of flexible arrayed lactate biosensor based on copper doped zinc oxide films modified by iron–platinum nanoparticles,” Polymers (Basel)., vol. 13, no. 13, 2021, doi: 10.3390/polym13132062.

[21] S. Forouhi, R. Dehghani, and E. Ghafar-Zadeh, “CMOS based capacitive sensors for life science applications: A review,” Sensors Actuators, A Phys., vol. 297, p. 111531, 2019, doi: 10.1016/j.sna.2019.111531.

[22] M. Kaisti, “Detection principles of biological and chemical FET sensors,” Biosens. Bioelectron., vol. 98, no. April, pp. 437–448, 2017, doi: 10.1016/j.bios.2017.07.010.

[23] M. Mar, B. Sullam, and E. Blom, “An architecture for a configurable mixed-signal device,” IEEE J. Solid-State Circuits, vol. 38, no. 3, pp. 565–568, 2003, doi: 10.1109/JSSC.2002.808298.

[24] S. Hazarika, R. Choudhury, B. Montazer, S. Medhi, M. P. Goswami, and U. Sarma, “Detection of Citrus Tristeza Virus in Mandarin Orange Using a Custom-Developed Electronic Nose System,” IEEE Trans. Instrum. Meas., vol. 69, no. 11, pp. 9010–9018, 2020, doi: 10.1109/TIM.2020.2997064.

[25] H. Hafdallah, A. Ouslimani, R. Adde, G. Vernet, and P. Crozat, “Feasibility of picosecond electrical sampling using GaAs FET,” IEEE Trans. Instrum. Meas., vol. 49, no. 1, pp. 172–177, 2000, doi: 10.1109/19.836330.

[26] C. G. Siontorou, F. A. Batzias, and V. Tsakiri, “A knowledge-based approach to online fault diagnosis of FET biosensors,” IEEE Trans. Instrum. Meas., vol. 59, no. 9, pp. 2345–2364, 2010, doi: 10.1109/TIM.2009.2036464.

[27] R. Prajesh et al., “Polysilicon Field Effect Transistor Biosensor for the Detection of Cardiac Troponin-I (cTnI),” J. Electrochem. Soc., vol. 168, no. 2, p. 027501, 2021, doi: 10.1149/1945-7111/abdde6.

[28] H. L. Kang et al., “Verification of Operating Principle of Nano Field-effect Transistor Biosensor with an Extended Gate Electrode,” Biochip J., vol. 14, no. 4, pp. 381–389, 2020, doi: 10.1007/s13206-020-4410-1.

[29] C. F. Chang and M. S. C. Lu, “CMOS Ion Sensitive Field Effect Transistors for Highly Sensitive Detection of DNA Hybridization,” IEEE Sens. J., vol. 20, no. 16, pp. 8930–8937, 2020, doi: 10.1109/JSEN.2020.2986461.

[30] S. Chen, Y. Sun, Y. Xia, K. Lv, B. Man, and C. Yang, “Donor effect dominated molybdenum disulfide/graphene nanostructure-based field-effect transistor for ultrasensitive DNA detection,” Biosens. Bioelectron., vol. 156, no. February, pp. 1–7, 2020, doi: 10.1016/j.bios.2020.112128.

[31] B. Wang, Y. Luo, L. Gao, B. Liu, and G. Duan, “High-performance field-effect transistor glucose biosensors based on bimetallic Ni/Cu metal-organic frameworks,” Biosens. Bioelectron., vol. 171, no. October 2020, p. 112736, 2021, doi: 10.1016/j.bios.2020.112736.

[32] C. Sun et al., “Ultrasensitive and Reliable Organic Field-Effect Transistor-Based Biosensors in Early Liver Cancer Diagnosis,” Anal. Chem., vol. 93, no. 15, pp. 6188–6194, 2021, doi: 10.1021/acs.analchem.1c00372.

[33] C. A. Vu, W. P. Hu, Y. S. Yang, H. W. H. Chan, and W. Y. Chen, “Signal Enhancement of Silicon Nanowire Field-Effect Transistor Immunosensors by RNA Aptamer,” ACS Omega, vol. 4, no. 12, pp. 14765–14771, 2019, doi: 10.1021/acsomega.9b01264.

[34] H. Chen et al., “A new biosensor detection system to overcome the debye screening effect: Dialysis-silicon nanowire field effect transistor,” Int. J. Nanomedicine, vol. 14, pp. 2985–2993, 2019, doi: 10.2147/IJN.S198734.

[35] K. M. Cheung et al., “Detecting DNA and RNA and Differentiating Single-Nucleotide Variations via Field-Effect Transistors,” Nano Lett., vol. 20, no. 8, pp. 5982–5990, 2020, doi: 10.1021/acs.nanolett.0c01971.

[36] M. Tian et al., “Highly-sensitive graphene field effect transistor biosensor using PNA and DNA probes for RNA detection,” Appl. Surf. Sci., vol. 527, no. June, 2020, doi: 10.1016/j.apsusc.2020.146839.

[37] Y. Liang et al., “Wafer-Scale Uniform Carbon Nanotube Transistors for Ultrasensitive and Label-Free Detection of Disease Biomarkers,” ACS Nano, vol. 14, no. 7, pp. 8866–8874, 2020, doi: 10.1021/acsnano.0c03523.

[38] Y. Nishio, S. Uno, and K. Nakazato, “Three-dimensional simulation of DNA sensing by ion-sensitive field-effect transistor: Optimization of DNA position and orientation,” Jpn. J. Appl. Phys., vol. 52, no. 4 PART 2, 2013, doi: 10.7567/JJAP.52.04CL01.

[39] R. Sakamaki and M. Horibe, “Realization of Accurate On-Wafer Measurement Using Precision Probing Technique at Millimeter-Wave Frequency,” IEEE Trans. Instrum. Meas., vol. 67, no. 8, pp. 1940–1945, 2018, doi: 10.1109/TIM.2018.2806058.

[40] C. Ciofi, F. Crupi, C. Pace, and G. Scandurra, “Micro-prober for wafer-level low-noise measurements in MOS devices,” IEEE Trans. Instrum. Meas., vol. 52, no. 5, pp. 1533–1536, 2003, doi: 10.1109/TIM.2003.817913.

[41] L. R. Chaar and A. D. van Rheenen, “Low-Frequency Noise Measurements on Semiconductor Devices Using a Probe Station,” IEEE Trans. Instrum. Meas., vol. 43, no. 4, pp. 658–660, 1994, doi: 10.1109/19.310184.

[42] Y. H. Lai, J. C. Lim, Y. C. Lee, and J. J. Huang, “Analysis of the biochemical reaction status by real-time monitoring molecular diffusion behaviors using a transistor biosensor integrated with a microfluidic channel,” ACS Omega, vol. 6, no. 18, pp. 11911–11917, 2021, doi: 10.1021/acsomega.1c00222.

[43] H. W. Lu et al., “The promise of graphene-based transistors for democratizing multiomics studies,” Biosens. Bioelectron., vol. 195, no. May 2021, p. 113605, 2022, doi: 10.1016/j.bios.2021.113605.

[44] R. Hajian et al., “Detection of unamplified target genes via CRISPR–Cas9 immobilized on a graphene field-effect transistor,” Nat. Biomed. Eng., vol. 3, no. 6, pp. 427–437, 2019, doi: 10.1038/s41551-019-0371-x.

Chapter 7 Application 2: Interdigital Open-Gate JFET (ID-OGJFET) for DNA Adsorption Monitoring[1]

Paper 7: DNA Adsorption Monitoring with Interdigital Open-Gate Junction Field Effect Transistor for DNA Storage Applications: MD Modeling, Design, and Experimental Results

Authors: Abbas Panahi, Firouz Abbasian, Giancarlo Ayala-Charca, Hamed Osouli Tabrizi, Morteza Ghafar-Zadeh, Sebastian Magierowski, and Ebrahim Ghafar-Zadeh

Journal: Submitted to Sensors and Actuators A: Physical (under review)

Abbas Panahi's contribution: chip design and characterization, DNA tests and data analysis, molecular dynamics simulations and data analysis, literature review and writing the manuscript, editing and submission.

[1] The content of this chapter is based on a submitted paper.

Abbas Panahi, Firouz Abbasian, Giancarlo Ayala-Charca, Hamed Osouli Tabrizi, Morteza Ghafar-Zadeh, Sebastian Magierowski, and Ebrahim Ghafar-Zadeh. "DNA Adsorption Monitoring with Interdigital Open-Gate Junction Field Effect Transistor for DNA Storage Applications: MD Modeling, Design, and Experimental Results"

7.1. Abstract

This paper introduces a pioneering sensing platform designed to explore the intricate interaction between DNA molecules and silicon dioxide (SiO_2) coated on a field effect transistor (FET), bearing profound implications for a spectrum of life science applications, particularly DNA storage. In-silico molecular Dynamic (MD) simulations are employed to gain insights into the effects of DNA on the FET surface's potential under extreme conditions of dehydration of double-stranded DNA (dsDNA), verifying its capacity to generate surface charge when dehydrated due to the evaporation of droplets. The platform is comprised of a backgated interdigital open gate junction FET (ID-OGJFET) fabricated through an innovative electronic sensing platform foundry and accompanied by an electronic interface system incorporated with a fluidic sample holder that reads the surface charge data induced by negatively charged nucleotides in dsDNA and single-stranded DNA (ssDNA). This novel ID-OGJFET sensor coated with native SiO_2 enables a direct-on-channel sensing area of >16 mm^2 without top gate extension for the target application, working at low back gate voltage (<0.4 V) for adsorption analysis in the dry mode. Our study involves the design, synthesis, and introduction of DNA sequences onto the chip surface at various concentrations. In this paper, we present and discuss experimental results that align with MD simulations, elucidating the impact of DNA's intrinsic charge on the chip's surface under extreme dehydration conditions. These findings pave the way for the development of DNA monitoring techniques, particularly in the physical storage of DNA.

Index Terms—DNA adsorption, DNA Storage, Open-Gate Junction Filed Effect Transistor (OG-JFET), Molecular Dynamic Simulation

7.2. Introduction

The exponential growth in digital data has led to an unprecedented global demand for storage technologies capable of handling super high-capacity memories. Internet data center (IDC) projections indicate a potential surge to 175 zettabytes in worldwide data storage by 2025 [1]. Current technologies such as magnetic hard disk drives, optical disc drives (ODDs), and solid-state drives need to be revised to cope with this immense data influx [1], [2]. DNA's inherent potential as a digital data storage medium has gained significant attention from major tech companies and researchers due to its exciting potential to store vast amounts of data for millennia [3]. This involves encoding binary digital files into sequences of four DNA bases and synthesizing

the data into DNA strands for physical storage. Subsequently, the stored data can be retrieved, sequenced, and decoded back into its original digital format. Numerous studies have addressed the challenges associated with these processes, including the physical movement and storage of DNA mass, often incorporating digital microfluidics [4].

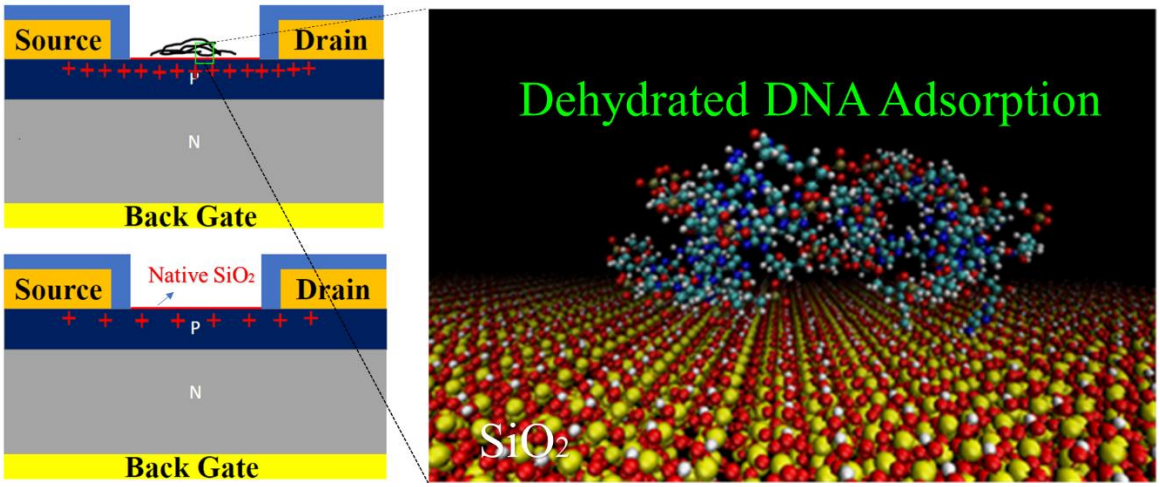


Figure 7-1. The sensing mechanism of OG-JFET for detection of charge distributed on native SiO_2 as the outer layer of OG-JFET due to evaporation of solution and accumulation of DNA charge. Top left: The enhancement of the hole concentration in the channel due to the attachment of DNA. Bottom left: The hole is transported in the channel when no adsorption occurs.

The storage of DNA on surfaces like silica is heavily studied [5], [6], prompting questions about DNA adsorption and the feasibility of monitoring DNA-based stores kept in dehydrated mode [4]. Our recent work has highlighted the advantages of FETs in DNA storage, explicitly using an OG-JFET [7]. By developing a novel portable experimental measurement setup, this study aims to expand on previous work by employing MD simulations. These simulation insights are compared with experimental results to understand further the sensor response to DNA adsorption on the OG-JFET sensor. This marks the first step toward DNA storage monitoring. Our goal is to advance the understanding of optimal solutions for DNA adsorption on the OG-JFET sensor and, by extension, the practical potential for monitoring DNA during storage.

In this paper, the subsequent section details the related works and challenges of DNA adsorption analysis in the extreme dehydration state of a droplet using field-effect sensors and other apparatus for the DNA analysis phase of the droplet. The methods and materials employed in our study are elaborated in section III. This section encompasses several key components, including the proposed DNA adsorption monitoring mechanism, MD simulation for understanding the sensing

mechanism utilizing the OG-JFET, the design and implementation of the OG-JFET sensor and reader, and the DNA design and synthesis process. Following this section, the subsequent segments IV and V delve into the presentation and discussion of results.

7.3. Related Works

This section presents recent advances in state-of-the-art research related to DNA adsorption, particularly on SiO_2. Additionally, we discuss the effect of evaporation on DNA adsorption, as outlined in the literature, to elucidate the specific challenges, especially for DNA storage applications. We reviewed the apparatus and sensing mechanisms dedicated to DNA adsorption studies. We stated their limitations regarding the need for DNA-based data storage, particularly when dehydrating a droplet containing DNA molecules.

7.3.1. State-of-the-Art DNA Adsorption on Surface Analysis

The investigation of biomolecular interactions, especially the adsorption of biomolecules onto surfaces, constitutes a significant area of scholarly inquiry aimed at advancing biophysical understanding and fostering the development of innovative biosensors. A variety of methodologies have been deployed in this endeavor. These methodologies encompass spectrophotometry [8], fluorescent labeling [9], radioisotope (RI) labeling [10], attenuated total reflectance-infrared spectroscopy [11], X-ray photoelectron spectroscopy (XPS) [12], atomic force microscopy (AFM), [13], ellipsometry [14], optical waveguide lightmode spectroscopy (OWLS) [15], nanopore sensing devices [16], surface plasmon resonance (SPR) [17], quartz crystal microbalance (QCM) [18].

SPR and QCM sensors excel in this group, offering susceptible, quantitative, real-time, label-free, and noninvasive detection of adsorbed proteins [19]. The SPR gauges dry mass changes in adsorbed proteins by assessing shifts in the dielectric constant at the interface. At the same time, QCM monitors variations in the electromechanical response of a shear oscillating piezoelectric sensor, reflecting total mass changes due to biomolecule adsorption coupled with water molecules in the system. Even though these techniques, when combined [19], offer valuable insights into the kinetics of mass adsorption and conformational changes of surface-attached biomolecules, they suffer from inherent technological challenges in scalability and integration. These challenges include their bulky nature, high cost, and difficulty adapting them for various applications such as DNA-based storage monitoring and point-of-care diagnostics [20], [21] that require more compact

portable footprints. Due to these challenges, new technologies such as charge-sensitive field-effect transistors (FET) have been introduced to address the need for finely studying the adsorption of biomolecules such as protein and DNA on both non-specific and specific surfaces (e.g., bare SiO2 or APTES functionalized SiO_2). For instance, the utilization of FET sensors, particularly potentiometric sensors, has been recognized as a reliable tool for label-free and susceptible detection of proteins and other biological materials in a sample solution [22], [23], [24]. These sensors have been utilized for DNA hybridization analysis [25], DNA sequencing [26], and other biomolecules that have all been successfully detected using FET-based sensors. The main physical principle behind existing devices for applications using FET seeing methods involves these components' potential to quantify the target DNA's charge when absorbed onto the surface or attached to the target probe molecule.

For DNA detection with FET potentiometric sensors working with off-chip reference electrode, targeting DNA inherent charge of ssDNA and dsDNA (hybridized). This requires a solution containing DNA attached to a probe, creating a biological gate that potentially modulates the voltage threshold of the FET sensor [27], [28]. However, this approach poses challenges when seeking to analyze the dehydration of DNA samples over time, especially for charge-induced analysis of DNA adsorption on surfaces in a dehydrated state—a crucial aspect in DNA mass monitoring for DNA-based data storage. While P. Stoliar et al. [29] demonstrated the use of an OFET for dried DNA sensing, the suitability of this device's pentacene surface for DNA storage is not common, and issues related to washability pose significant challenges. On the other hand, DNA adsorption on SiO2 is more aligned with the requirements for DNA storage applications. Also, in certain areas of life science applications, it's important to monitor DNA adsorption and purification processes on silica surfaces. Our research addresses these challenges by developing an interdigital back-gate OG-JFET that can be utilized to study DNA adsorption in extreme dehydration mode.

7.3.2. Evaporation-Induced Protein/DNA Adsorption

Upon droplet evaporation, substances undergo enrichment, increasing molecular interaction frequencies, boosting reaction rates, and enhancing detection signals, while signals may be too low in low-concentration samples. Literature reports showcase DNA, RNA, proteins, and bacteria detection in stationary droplets, leveraging the high sensitivity of evaporation-induced enrichment [17]. Aida Ebrahimi et al., [18], reported a nanotextured device for evaporation-based DNA-

containing bio droplets, achieving a low detection limit and distinguishing ssDNA and dsDNA [18]. Manish Chopra et al., [19], investigated DNA attachment on glass surfaces and APTES-covered glass during droplet evaporation, revealing DNA attachment on both, with APTES-covered glass being more favorable. Their study, employing Brownian dynamics simulation, validated DNA adsorption findings [19]. Xing-Li Du et al., [20] used droplet evaporation with magnetic nanoparticles for enhanced DNA detection on glass, yielding a linear response with higher hybridization occurrences [20]. Pinar Beyazkilic et al. [17] applied microdroplet evaporation to enrich glucose and DNA concentrations on a surface, demonstrating increased detection signals [17]. Li-Ping Xu et al. leveraged condensing-enrichment during sample droplet evaporation, achieving significant improvements in DNA detection but with increased detection time and reliance on optical fluorescence [21]. Kenta Fukada et al. [22] explored condensing enrichment for detecting trace materials in droplets, achieving this on a superhydrophobic surface with hydrophilic collection areas. Tingting Wu and team developed the RSMB biochip for quantitative miRNA141 detection, using hydrothermally synthesized TiO_2 nanowires on FTO as a reusable substrate [22]. Yanxia Chen et al. introduced an AIE-based superwettable microchip, demonstrating excellent reproducibility, sensitivity, and specificity in detecting miR-141 with a low detection limit of 1 pM [21].

While significant progress has been achieved in droplet evaporation-based sensing, there is a notable gap in comprehending the charge analysis of DNA adsorption on a surface in extreme dehydration mode where almost most of the droplet volume is evaporated (> 95% V), especially on SiO_2 as the gate of a charge sensitive FET. This study aims to provide insights into the molecular biophysics of DNA molecule dehydration compared with experimental results with a new sensing platform, which holds immense relevance in applications related to DNA data storage and DNA microarray technology. This paper provides insight into the possibilities of using open-gate, direct-on-channel, high-surface-area FETs for DNA storage and adsorption analysis.

7.3.3. Using MD in Adsorption Studies for Sensing

MD simulation has proven instrumental in unraveling the intricate physics of DNA-surface interfaces, yielding valuable information about the adsorption mechanism applicable in sensing applications. An analysis of the adsorption mechanism of ssDNA on silica through MD simulations

has offered insights into the role of water molecules and hydrophobic forces. These simulations shed light on creating non-chemical bonding between DNA and silica binding sites (e.g., Si-OH) [23]. The study employs MD simulations to elucidate large-scale experimental phenomena by exploring the energy landscape in DNA-Silica interactions. The discussion in the study delves into the different attachment forces observed in dsDNA and ssDNA, emphasizing their dynamics and flexibility near the surface. Comprehending the intricate physical phenomena involving cations (e.g., Na^{+}, Mg^{2+}) bridging DNA to silica is challenging through experimentation alone, but MD simulations provide detailed insights with significant implications in DNA biotechnology [24]. In another study, MD was utilized to unravel the complex interactions between DNA and silica, contributing to better control potentiometric sensors for DNA detection [25]. Experimental understanding of these complex interactions is challenging, and MD simulations offer valuable information for improved control of the response in potentiometric sensors. Additionally, MD modeling was employed to investigate the surface potential change due to the presence of DNA on silica, providing insights into the operation of FET-based DNA sensors when different ions are involved [25], [26].

MD simulations were employed to comprehend the enhanced capability of a crumpled graphene surface for DNA detection compared to a uniform graphene surface [27]. These simulations also contributed to the study of DNA adsorption on MoS_2, a novel and complex material with applications in biosensing [28]While MD simulations have provided insights into the dynamics of DNA in solution on surfaces, the specific scenario of DNA adsorption on a surface like silica in a highly dehydrated state has not been explored in the literature. This research aims to address this gap, presenting related experimental results obtained from a silicon-based charge-sensitive sensor known as OG-JFET.

7.4. Proposed Method and Materials

In this section, we detail the OG-JFET sensing mechanism for dehydrated DNA. Accompanied by an MD simulation campaign, we describe details of the proposed sensing platform, including a microfluidics packaging and portable system. The last part of this section deals with DNA sample preparation used in experiments on the chip.

7.4.1. DNA Adsorption on ID-OGJFET and Sensing Principles

When a water droplet containing DNA is placed on the top gate of an OGJFET sensor surface – an ultra-thin layer of native silicon dioxide, [29] The interaction between DNA and this naturally occurring oxide surface in a non-specific adsorption mode would be the solution's primary source of DNA detection. Bobo Shi et al. have studied the interaction of DNA and the SiO2 surface. [23]. According to their theoretical study, despite both SiO_2 and DNA being negatively charged, two central binding mechanisms exist: i) attractive interactions between DNA phosphate and oxide surface silanol groups, and ii) hydrophobic bonding between DNA bases and the silica hydrophobic region [23]. The study reveals that, in solution, ssDNA forms stronger non-chemical bonding with SiO_2 compared to dsDNA. This is attributed to the ssDNA's greater flexibility, maximized binding interactions, and free unpaired bases for hydrophobic attachment to silica. Conversely, dsDNA must break hydrogen bonds with base partners to expose free bases. Finally, the net linear charge of dsDNA is more than ssDNA, which contributes to this difference [23].

There are numerous reports on the bonding of DNA with SiO_2, both with and without the existence of chaotropic salts (e.g., NaCl) as the salt bridge, another adsorption mechanism in solution for DNA on silica [24]. Phosphate-silanol and hydrophobic interactions appear to be the principal mechanisms for binding DNA to silica. These short-range attractions can be sufficiently strong to overcome the electrostatic repulsion between negatively charged DNA and a negatively charged silica surface. In a theoretical study, B. M. Lowe et al. confirmed the surface charge and potential change of SiO_2 when DNA is bonded to silanol bonding sites on SiO_2 [25]. Through experimental analysis, DNA binding to silica nanoparticles in a salt-free solution was detected by observing a subtle alteration in the intensity and frequency of a Raman spectral band associated with the DNA phosphate group [30]. In exploring the nature of interactions between DNA and silica, Kwon et al. [31] conducted atomic force microscope measurements, employing a silica particle as the AFM probe and a surface coated with phosphorylated dextran. DNA binding on SiO_2 could add a negative surface charge on the inherently negatively charged SiO_2, as confirmed in both solution [38] and dry mode [32]. The negative charge carried by DNA on its phosphate groups is significant, as it enables detection using a charge-sensitive sensor like OG-JFET for DNA mass quantification. In [32], the authors detected the negative charge of dehydrated DNA using a p-type organic FET [32]. Therefore, based on the evidence in the literature, it is reasonable to argue that the accumulation and adsorption of DNA on ultra-thin SiO_2, in both solution and dehydrated modes,

enhance the hole current in the p-type channel of OG-JFET, as illustrated in Fig. 7-1. The accumulation of DNA's negative charge on the channel enhances the conduction of positively charged holes and leads to current enhancement in the hole current in the p-type semiconductor channel [32].

The direct-on-channel deposition of DNA enabled by our proposed OG-JFET with an open top gate allows current measurement between the source and drain. This facilitates the assessment of DNA charge resulting from its bonding on SiO_2. As discussed in [32], through a back-gate structure and monitoring the change in the potential (back gate voltage) upon adsorption of DNA, they could correlate the adsorption sites with the enhancement in charge carrier accumulated in the semiconductor channel. Through AFM analysis, DNA bundles were imaged on the surface of pentacene, which allowed the determination of their thickness and the DNA number density [32]. However, the lack of washability of DNA from the OFET's pentacene surface is a significant challenge for DNA storage application and reusability [32]Alternatively, our OG-JFET structure's reliance on a back gate has enabled us to study the dehydration of DNA droplets on a washable surface of SiO_2, which is impossible in other ISFET structures heavily reliant on a bulky solution gate.

7.4.2. Molecular Dynamics (MD) Simulation

To further understand the sensing principle of ID-OGJFET when exposed to dehydrated DNA absorbed on its surface and to understand the experimental observations better, we have performed an in-silico analysis using MD simulation. The MD was conducted to describe the potential changes on SiO2 (representing the native silica on ID-OGJFET) and to possibly explain the physics of DNA when extremely dehydrated on SiO_2.

The system model is shown in Fig. 7-2. We performed a classical MD simulation using the NAMD 2.9 software package [45]. Our results were analyzed in Visual MD (VMD) software [46]. The simulation box consists of water, an ionic solution, and a DNA molecule of a random sequence with 17 base pairs on a SiO_2 surface. To perform the MD simulation, a unit cell of amorphous silicon is prepared with dimensions of 10 nm × 10 nm × 1 nm as width, length, and thickness, respectively (see Fig. 7-2). The 1-nm thickness estimate is based on the experimental work of Morita et al. which provided estimated thicknesses of native SiO_2 [42]. The crystalline silica slab model was prepared using the CHARMM GUI [47]. The resultant SiO2 volume is 130164.8 A3.

The degree of ionization is 13.3%. The surface concentration of Si-OH is set to 4.9 OH/nm2. The degree of ionization in the DNA dehydration simulation represents an equivalent pH of 7 based on the CHARMM GUI recommendations.

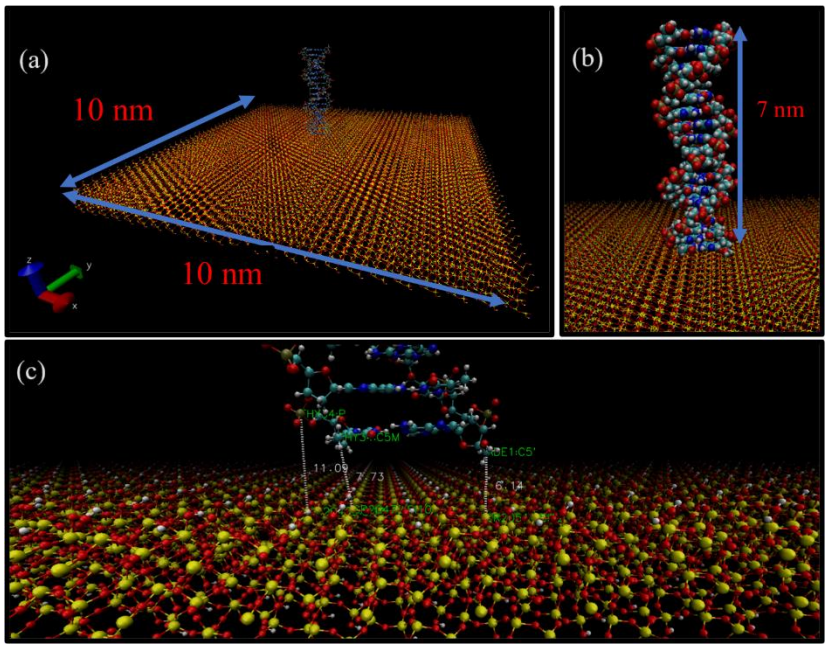


Figure 7-2. The simulation box (water and ions not shown) used in the MD simulation (a): the dimension of SiO_2 slab. (b): the length of dsDNA. (c): the initial distance between few atoms of dsDNA and surface atoms of SiO_2.

A solvent box was created within 1 Å from the surface to prepare the simulation environment. A TIP3P solvent box was generated for different simulation systems with thicknesses of 140 Å, 70 Å, 40 Å, 20 Å, and 10 Å with x-y dimensions of 100 × 100 A^2 that covers the silica unit cell produced in the previous stage. The VMD software was used to ionize the system where needed. For the silica model, the ionization was performed with CHARMM GUI, which places Na+ ions to balance the negative charge of silica. The system is initially solved by placing a water box on SiO2 using the 'solvate' plugin to perform the water and ion solvation. To put the ions in the solvate box, the 'autoionize' plugin is used to achieve a concentration of 150 mM NaCl, and a specific number of ions (Na+ and Cl-) were added and distributed randomly in the system. To ensure the water molecules are charging and that an electrostatic effect is not affecting the SiO_2 slab from underneath, a vacuum layer is considered on top of the water box with a thickness of 100 Å.

The required force fields such as CHARMM 36, [48], and INTERFACE, [49], were used in addressing the MD of a system of SiO_2, water-ions, and the dsDNA. In our study, we used a cutoff

radius of 1.2 nm. A pairlist distance of 14 with a margin of 3 was applied in simulations. To maintain a temperature of 300 K, a Berendsen thermostat with a time step of 0.1 ps was employed.

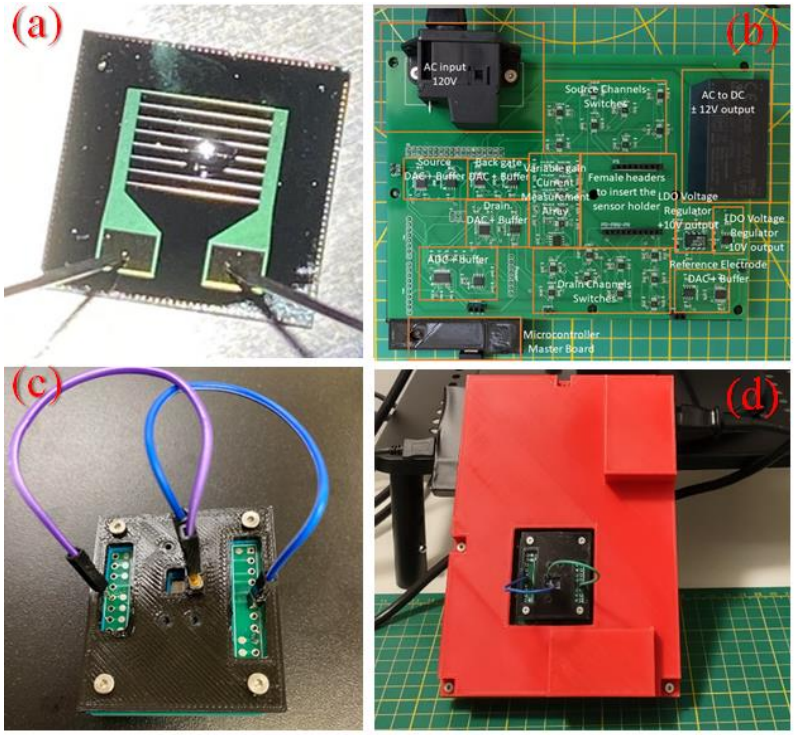


Figure 7-3. The chip, readout system, and microfluidic packaging, (a) the fabricated chip and the positioning of droplets on the chip. (b): the readout system and components. (c): the electro-fluidics packaging connecting the device to the readout PCB in (b). (d): 3D printed packaging of the PCB and the placement of electro-fluidics packaging

Before each run, the system was energy-minimized using the steepest descent algorithm. First, it was minimized for 500 steps at T = 0 K, and then, over 500 steps, its temperature was gradually elevated to 295 K for better equilibration. Afterward, it was equilibrated for 2 ns before the 20 ns MD production run. Also, selecting a minimized distance of 0.5 nm for the DNA to approach the SiO_2 surface further helped reduce the simulation time.

All the simulations were performed in NPT and NVT ensembles depending on the process at 300 K and pressure of 1 atm. To apply the temperature and pressure in the different methods of simulation, an Andersen thermostat was used during equilibration, and Langevin dynamics were used during production runs. Specifically, in the NPT ensemble, the pressure was maintained using a modified Nose´-Hoover barostat with Langevin dynamics to control fluctuations. Electrostatic interactions were evaluated up to a maximum distance of 12 Å, while the Particle Mesh Ewald method with a grid spacing of 50 × 50 × 100 Å was employed for distances beyond this threshold.

Integration was performed utilizing a modified Verlet algorithm with 1 fs time-steps, and bonded forces were calculated at each time step. Our simulations adopt parallelepiped simulation boxes featuring periodic boundary conditions. They carefully select a box size to ensure a separation of at least 10 nm between the DNA and their periodic images in the Z direction. This approach effectively prevents DNA from interacting with its periodic images through van der Waals (vdW)/electrostatic potentials that might affect the surface potential. The evaporation of water in which the water molecule physically diffuses into the medium was implicitly modeled by arbitrarily reducing the water box size from 14 nm to 1 nm.

7.4.3. Proposed Sensing Platform

The goal of our study was to understand DNA adsorption in extreme modes of dehydration and the further application of this as a portable storage space for data stored on DNA. Therefore, we have developed a portable system alongside an electro-fluidics packaging compartment. Portable ID-OGJFET sensing platform allows fast acquisition of the transfer characteristics of the OG-JFET when a known concentration of DNA is dehydrated on its surface for DNA storage monitoring. The system enables the physical storage of DNA on a sensor and provides a mobile storage device while monitoring the existence of DNA on the surface. The sensing platform includes a multichannel board and electro-fluidic fixture with 3D printed microfluidics that enables an opening on top while connecting the device to the board through a spring-loaded connector. The microfluidic layers are connected to a small PCB, which connects the spring-loaded connectors to a readout circuit board. The sensor is a novel interdigital design on the OG-JFET platform, which reduces the number of pads to two and enhances the surface size to 16.52 mm^2, as presented in Fig. 7-3. The proposed sensing platform is shown in Fig. 7-3.

7.4.4. DNA Strand Sequence Preparations

Two complementary 24-nucleotides DNA oligo fragments were synthesized and used in this experiment (Table 7-1). The original concentrations were serially diluted into four samples (49 ng/µL, 98 ng/µL, 197 ng/µL, and 393 ng/µL). Considering the addition of 2 µL of the serially diluted samples on the sensors, the final sample mass is 98 ng, 197 ng, 393 ng, and 786 ng). The samples were prepared in RNs/DNs free water and then were dehydrated on the sensor for further experiments.

Table 7-1. The information on the synthesized DNA used in the experiments.

Name	DNA Fragment	Length
F-Forward	5'-CAGTAGTTGCATCACCAGAAGTTG-3'	24
F-Reverse	5'-CAACTTCTGGTGATGCAACTACTG-3'	24

7.5. Results

7.5.1. Computational Analysis of dsDNA in Extreme Dehydration on SiO_2: A MD Simulation

A classical MD simulation was performed using NAMD 2.9 software and analyzed with VMD 1.9.3 to explore the adsorption of DNA on the SiO_2 surface. The objective of the MD study was to understand how DNA attaches to the sensor surface when it is extremely dehydrated, the water having been reduced due to evaporation. Water evaporation is not physically modeled due to limitations in MD simulation time for capturing evaporation physics time scale. Therefore, we reduced the number of water molecules in the initial water box from 14 nm, 7 nm, 2 nm, and 1 nm thickness to reach equilibrium before the MD production runs to model the evaporation implicitly. Snapshots and results of dsDNA configurations predicted in the MD simulation are presented in Fig. 7-4. In the solution mode, dsDNA stays in a stable helical structure and exhibits stable interaction with SiO_2 at the beginning of the simulation. However, it starts to move near the SiO_2 surface due to complex intermolecular interactions and interactions with SiO_2 and the aqueous solution. It appears that dsDNA does not remain firmly connected to SiO_2 but begins to fluctuate and move within the solution over a specific distance primarily due to thermal fluctuations in the molecular size space and resultant Brownian motions. However, when the water concentration is reduced due to evaporation, the dsDNA has limited space to move into the solution and comes closer to the SiO_2.

The MD simulation study confirms the adsorption of the dsDNA on SiO_2 in extreme dehydration conditions, as presented in Fig. 7-4 (d). According to the results, as water molecule density reduces, dsDNA undergoes distinct behaviors that are not easily determined with experiments alone. The dsDNA is forced to approach the SiO_2 surface as the water layer becomes thinner. Due to denaturation in the structure of DNA caused by lower water and ions in its surroundings and

interactions with SiO_2 surface, it covers a larger surface area, increasing the site bonding of phosphate groups on the surface. As a result, the accumulation of negative charges increases.

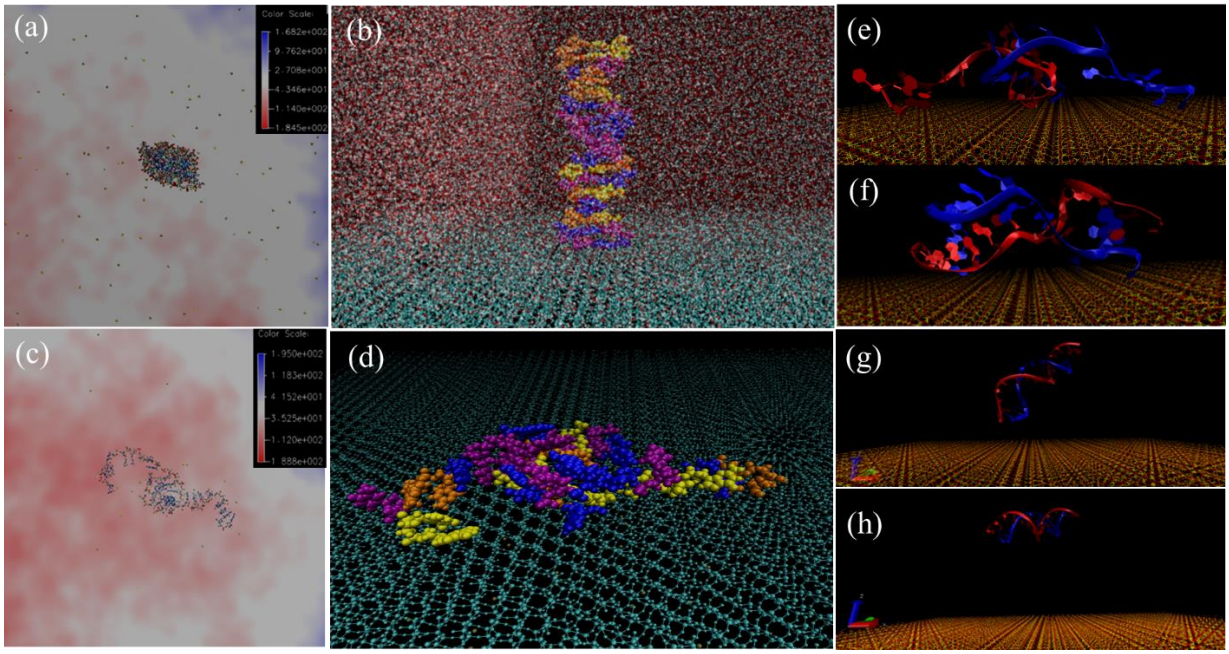
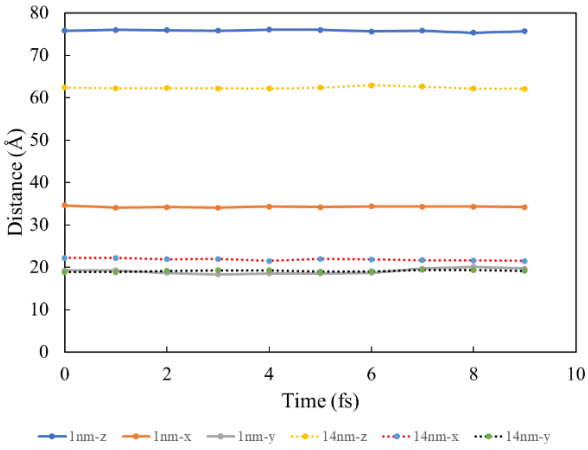
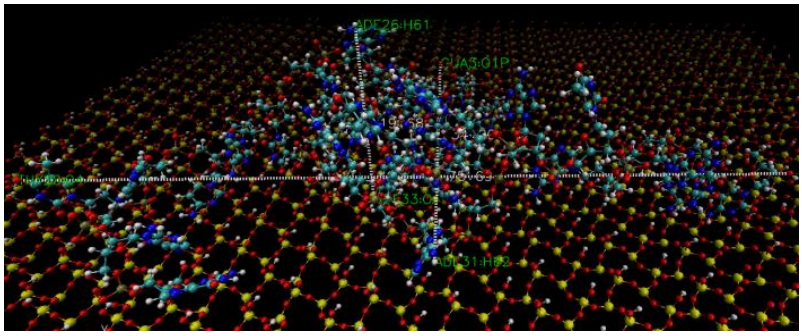


Figure 7-4. Result of MD simulation of DNA adsorption on silica in dehydrated mode. (a): ds-DNA induced surface potential of SiO_2 in solution mode with 14nm water box. (b): the snapshot of DNA in solution mode. (c): the DNA-induced surface potential of SiO_2 in extreme conditions of dehydration (low water molecules). (d): a snapshot of DNA wholly laid on the SiO_2 surface. (e): denaturation of dsDNA in dry mode (extreme dehydration). (f): DNA in a box with 2 nm water. (g): DNA in a box with 7 nm water. (h): DNA in a water box with 14 nm water

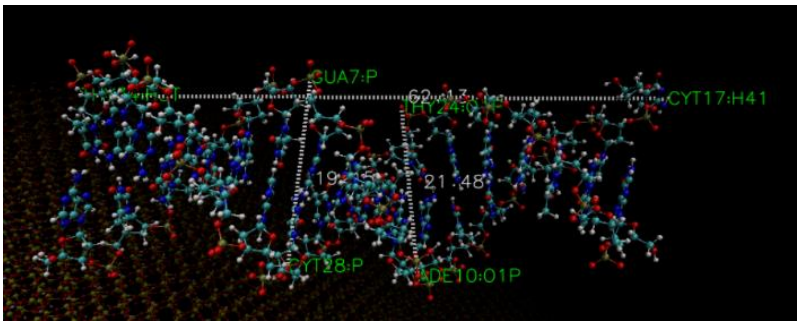
The denaturation of dsDNA when attached to SiO_2 under extreme dehydration conditions is illustrated in Fig. 7-5 (b) and compared with the state in which dsDNA is floating in a 14 nm water box (Fig. 7-4 (h)). Three distances measured on the dsDNA in Fig. 7-5 (b) and plotted in Fig. 7-5 (a) show a non-helical structure. However, in helical DNA, the sizes along x and y are ~ 2nm, as presented in Fig. 7-5 (c), which is nearly uniform along the DNA. However, Fig. 7-5 (b) demonstrates the denaturation of dsDNA and complete strand disruption, resulting in a more spread-out configuration on the SiO_2 surface, leading to the spread of negative charge of the phosphate groups carrying negative charge on the surface. This accumulation of negative charge changes the surface potential, as presented in Fig. 7-4 (c). In each simulation of DNA in water boxes from 14 nm to 1 nm, we measured the surface electrical potential, showing an increase in the surface potential as the DNA approached the surface due to a reduction in the water solvation and screening effect.



(a)



(b)



(c)

Figure 7-5. Three distances were measured on the adsorbed DNA on the surface of SiO2 when water molecules are diminished due to the evaporation to a thin layer of 10 nm × 10 nm × 1nm (x, y, and z). Due to evaporation, it appears that dsDNA denatures on the surface and no longer holds helical structure in extremely low water density. (a): comparison of three distance values for DNA in 1nm and 14 nm water box. (b): the DNA in a 1nm water box. (c): The DNA in a 14nm water box.

Fig. 7-6 demonstrates the results of surface electrical potential when the number of water molecules in the system is reduced due to evaporation. The simulation results show the average

surface electrical potential based on the scale bar generated in VMD's PME Electrostatic plugin, for a surface plane on the SiO_2. As the results demonstrate, the surface potential (in mV) increases as the dsDNA approaches the surface and spreads on the surface to adapt itself to the extremely thin (1 nm) water layer on the surface.

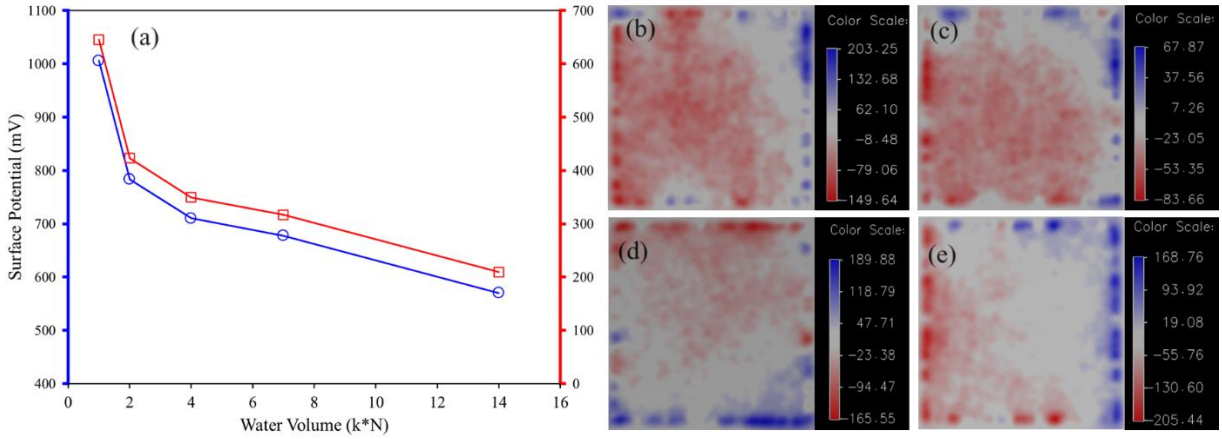


Figure 7-6. The surface potential of SiO_2 was measured with MD. (a) The averaged surface potential is based on the color scale bar for each system with a specific water volume (from 1nm thickness to 14 nm), and k is the arbitrary constant multiplied by the number of water atoms for each water thickness. Surface potential contours and related contours for (b): 1 nm, (c): 2 nm, (d): 7 nm, and (e): 14 nm water box thickness with x and y dimensions of 10 nm × 10 nm.

The results are presented in Fig. 7-6. The surface potential is measured by averaging the surface potential contours derived from VMD and the related scale bar, as shown in Fig. 7-6 (a). We also subtracted the surface potential from the liquid bulk potential, as shown in the diagram with a red line. The potential increases from ≈ 570.1 mV (≈ 209.54 mV, red line) when DNA is in solution and floating in the water to ≈ 1006.03 mV (645.47 mV, red line) when the dsDNA is in an extreme condition of dehydration (see Fig. 7-4- d). To better understand the DNA adsorption on silica in extremely low water density due to evaporation on SiO_2, we have calculated the g(r) function for dsDNA on SiO_2 in both 14 nm and 1 nm water box as presented in Fig. 7-7 (b) and (a), respectively. As the g(r) (radial distribution function) analysis shows, when dsDNA is in the last phase of evaporation with an extremely low density of water, it exhibits a rigid structure. The g(r) function presents a sharp and high peak, starting at 1.8-1.9 Å from the SiO_2 surface, according to Fig. 7-7 (b). This indicates that dehydrated DNA resembles a solid phase more than a liquid phase, as shown by the spread of g(r) values and the smooth rise and fall with radial distances.

Based on Fig. 7-7 (a), it appears that when DNA is in a liquid state, the probability of finding its atoms around SiO_2 starts to increase after approximately 4 nm, a value subject to change based on

the DNA dynamics around the surface and ionic strength of the system. However, in the same situation, a system with insufficient water molecules due to evaporation increases the radial distribution function (g(r)) for DNA-SiO_2, leading to a higher probability of sensing DNA's inherent charge in the vicinity of SiO_2. We further analyzed the distinct evaporation effect on dsDNA by understanding the water structure around dsDNA. The g(r) for DNA-Water was calculated for both systems with 14 nm water and 1 nm water, as presented in Fig. 7-7 (c) and Fig. 7-7 (d), respectively. The results show a distinct difference between the two systems. The system with low water density exhibits sharp peaks in < 10 Å.

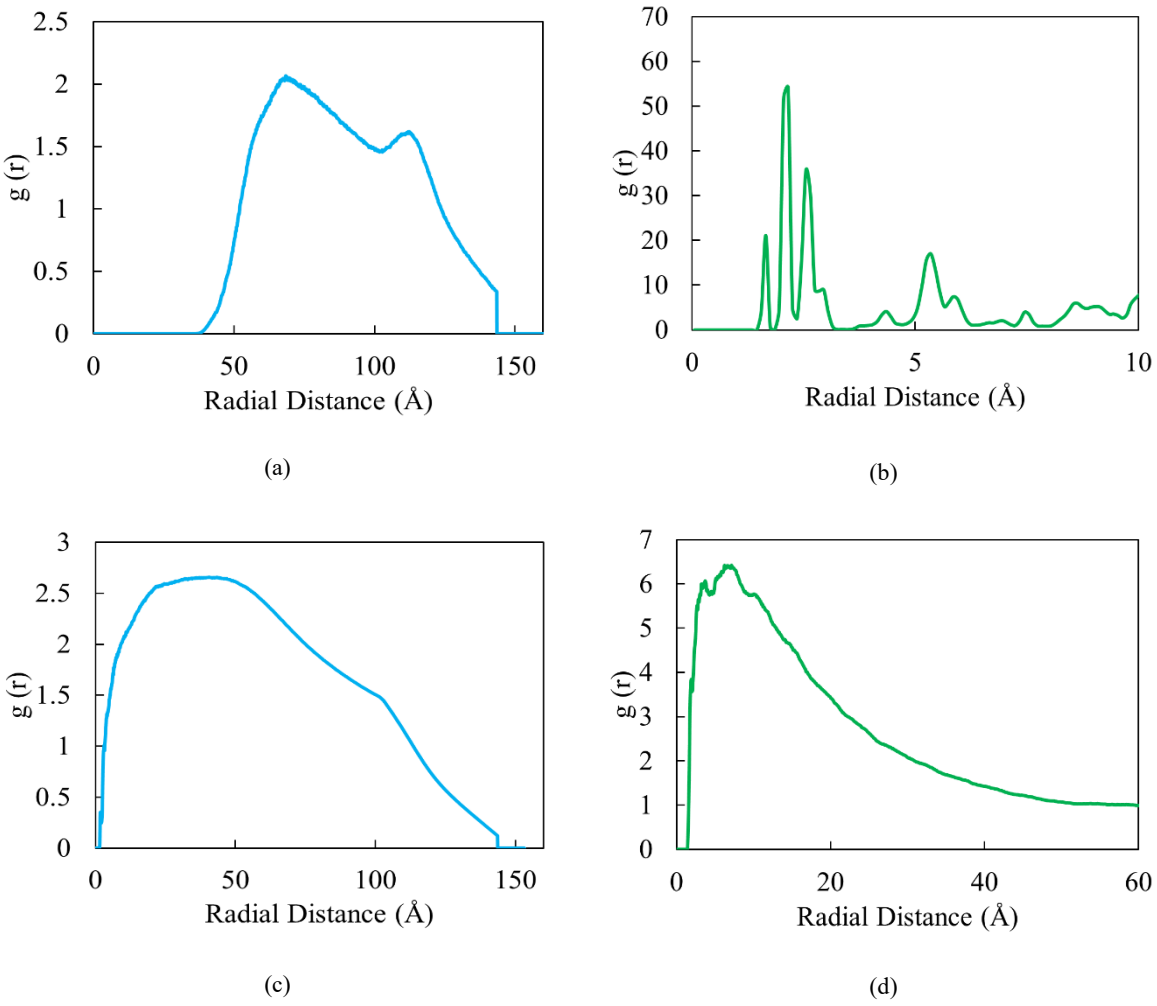


Figure 7-7. The radial distribution function analysis of dsDNA on SiO_2 in (a): 14 nm water box, (b): 1nm water box. The g(r) results of water around dsDNA are shown for (c): dsDNA in 14 nm water box, (d): dsDNA in 1 nm water box.

However, the g(r) is lower for the system with high water density, occurring at 44.3 Å. This can significantly affect the sensing of dsDNA charge by keeping the DNA attached to the surface and

creating a higher potential change on the surface. The g(r) illustrates that when DNA is dehydrated, the accumulation of negative charge resembles a 3D nanoparticle structure on the surface, approximately covering an area of ~ 7.5nm × 3.5 nm (~ 26.25 × 10^{-6} μm^2) with a total negative charge determined by the number of phosphate atoms multiplied by -1q (see Fig. 7-5). The MD simulation is also aligned with the AFM results of Manish Chopra et al, [32], that showed DNA molecules tend to spread over the surface in an evaporating droplet.

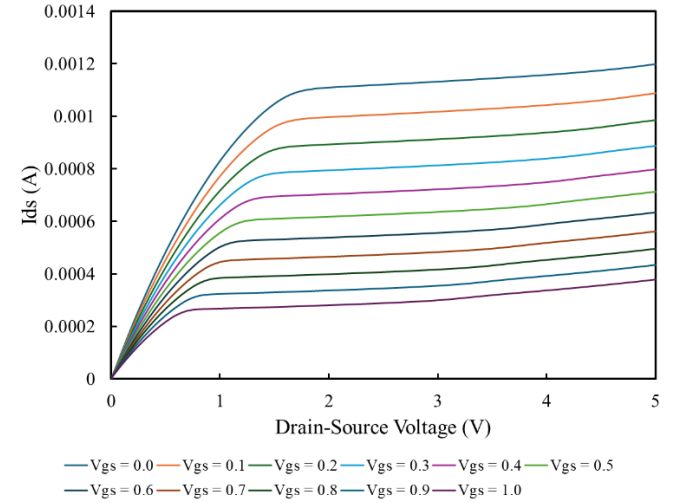
7.5.2. Fabrication of Chip and Measurement Setup

The proposed OG-JFET sensing chip was fabricated using a novel Electronic Sensing Platform foundry process supported by CMC Microsystems. As depicted in Fig. 7-3, the chip includes an interdigitated (ID) structure with a set of fingers constituting the drain and source of FETs, all connected to a common back gate. In this study, we developed two printed circuit boards (PCBs). The first PCB was designed to host the sensing chip and incorporated 3D printed layers to facilitate droplet deposition on the chip's surface, as illustrated in Fig. 7-3 (b). The second PCB features a custom-made microcontroller-based electronic system, which generates DC voltages (V_{DS} and V_{GS}) and reads the current (Id) from the interdigitated OG-JFET device. For communication with the computer and recording characterization parameters, an Arduino Duo Board was utilized in conjunction with a custom-made electronic board (refer to Fig. 7-3). The recorded data, including V_{DS} and V_{GS} ranges and related current curves, were sent to the computer for display. A graphical user interface (GUI) was developed using Qt5 software, offering a user-friendly environment. The custom-made electronic board incorporates Analog Digital Converter (ADC) and Digital Analog Converter (DAC) chips, enabling the microcontroller to supply DC voltages (V_{DS}, V_{GS}) to the OG-JFET chip and read the current from a shunt chip. A 3D printed design (Fig. 7-3 (d)) was also developed to create the required package. The fabricated chip, electronic reader system, electro-fluidic 3D structure (Fig. 7-3 (c)), and GUI were successfully tested and utilized to characterize DNA adsorption, as detailed in the following subsection.

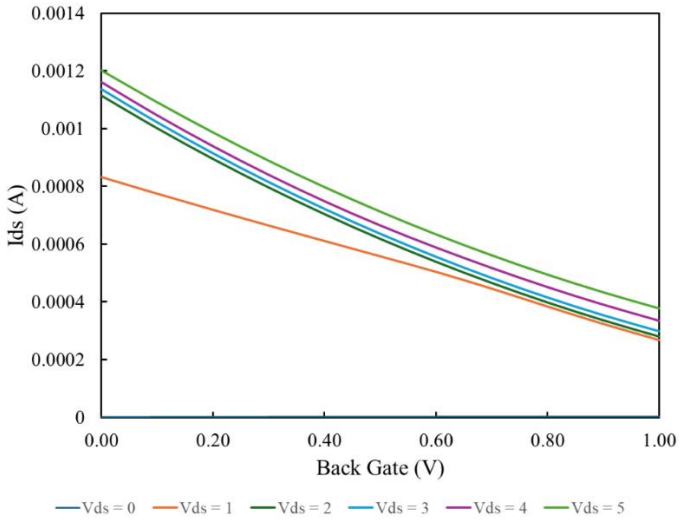
7.5.3. Transfer Characteristics of ID-OGJFET Sensor

The sensor has been characterized in reverse biased mode by applying a negative voltage to the ID-OGJFET's drain terminal and a positive voltage to its back gate (for demonstration, the positive sign is used in Fig. 7-8 for Vds and Ids). The I-V relationship for both Ids-Vds (drain-source current vs. voltage) and Ids-Vgs (drain-source current vs. back-gate voltage) is acquired at these

settings. As Fig. 7-8. demonstrates, the ID-OGJFET sensor demonstrates a p-type JFET behavior. As shown, by applying a positive voltage to the back gate, the channel can be controlled to reduce the absolute value of current between the source and drain by reducing the space charge distribution in the channel. The sensor's design is based on an interdigital configuration that enables parallel JFETs in the channels between each two fingers. Still, the accumulative current can be recorded with two pads, as shown in Fig. 7-3.



(a)



(b)

Figure 7-8. The I-V curve characteristics of ID-OGJFET sensor. (a): the Ids-Vds curve. (b): the Ids-Vgs curve.

7.5.4. DNA Adsorption Experimental Results

The adsorption of DNA in dehydration mode, following the evaporation of water, was examined on the ID-OGJFET. DNA droplets with concentrations of 49 ng/µL, 98 ng/µL, 197 ng/µL, and 393 ng/µL were prepared as outlined above. A 2 µL droplet containing DNA was drop-cast onto the center of the ID-OGJFET, and the system was allowed to undergo a complete evaporation. Subsequently, the drain-source current was recorded. Following the initial measurement, the sensor underwent a washing procedure. It was rinsed with ultra-pure water two times by applying a reciprocating droplet from the tip of a pipette. Subsequently, the spot was washed twice with an IPA (Isopropanol Alcohol) solution using the same procedure. The sensor was then dried with a blow dryer and left to rest for 5 minutes before introducing the following sample onto the sensor. The Ids-Vgs curve recorded for each dehydrated concentration is presented in Fig. 9, and the Ids current for a sample at the Vgs = 0 and Vds = -5 is presented in Fig. 7-9 (b). The experimental results demonstrate an increase in the current, which is the amount of hole transport inside the ID-OGJFET p-type channel.

The increase in hole current is attributed to the electrostatic interaction between the negative charge of the DNA sites adsorbed on the native silicon dioxide surface of the sensor, leading to the accumulation of holes within the channel. The MD simulations have indicated that DNA on the SiO_2 alters the electrostatic surface potential near the SiO_2, influencing the current of holes within the p-type channel. The work of P. Stoliar et al. explored the monitoring of DNA adsorption sites on a surface using a p-type organic FET [32]. Through a rough estimation of DNA as a cylinder with a specific diameter and length, they correlated the adsorption site (ns) to the back gate voltage of their transistor, employing the Ids-Vgs standard characteristics of the device. The results showed that DNA adsorption sites can accumulate several acceptor states in the channel. In the case of the ID-OGJFET, since the sensor has a native SiO_2 on its channel, the MD simulation results suggest enhanced electrostatic interactions that can potentially influence the positively charged hole current. The MD simulation provides ample information about the possible topological surface when DNA is adsorbed on SiO_2 due to evaporation. As discussed in Fig. 7-5, the coverage of DNA on the surface increases at the final stages of evaporation, which is related to the lower number of water molecules around the DNA; at this stage, the DNA can have a roughness of 2nm – 3 nm (Fig. 7-5 – a). This estimate from simulation agrees with the results of [32]surface changing from 1 nm to 2 nm using AFM to enhance the concentration. Therefore, one aspect of the current

enhancement in the ID-OGJFET could be due to the enhancement in DNA binding sites in dehydration mode with an increase in the concentration.

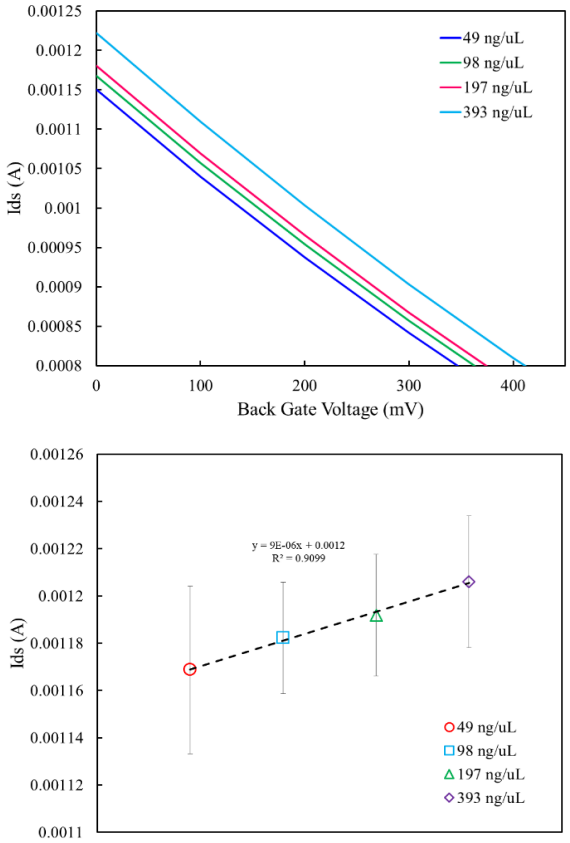


Figure 7-9. The experimental results of the sensor's response to the adsorption of the dsDNA on the sensor. (a): drain-source current versus the back gate for the different concentrations of dsDNA dehydrated on the sensor. (b): the Ids current versus dsDNA concentrations at Vgs = 0 and Vds = -5

The ID-OGJFET, with its wide sensing surface area, has been used to understand the adsorption of dsDNA at concentrations of 49 ng/µL, 98 ng/µL, 197 ng/µL, and 393 ng/µL. The design of the ID-OGJFET, leveraged by the interdigital fingers, creates many elemental OG-JFETs that enable sensing the adsorbed DNA. The sensor's output current was measured, revealing an increase in hole current as more dsDNA is absorbed on the sensor.

The sensor demonstrated effective washability for each sample, showcasing its cleaning capabilities compared to the organic FET introduced in [26] on a p-type channel. The ID-OGJFET sensor operated at low back gate voltages (< 0.4 V), a considerable improvement over their work, which required 0 < Vgs < 15 V for DNA sensing.

Moreover, the ID-OGJFET sensor's wide detection range is well-suited for DNA data storage, where a substantial amount of dehydrated DNA can be stored and monitored on the expansive 16.52 mm^2 sensing area, enabling the storage of a significant volume of data [1], [3]. With only a small portion of the sensing site dedicated, we achieved sensing approximately 20 times more DNA mass than reported in the literature [26]. This research not only contributes to the understanding of DNA adsorption analysis with a silicon-based FET sensor, both experimentally and through in-silico molecular modeling, but it also paves the way for advanced research in FET-based biological sensors and the biophysics of dehydrated DNA on surfaces, dedicated to advancing DNA data storage.

7.6. Discussion

The measurement of DNA adsorption on silica is significant in biotechnology, including DNA purification [47], [48], and diagnostics [20], [27], especially in the context of emerging DNA-based data storage technologies [4]. The physical storage of human-made information in DNA and monitoring its presence on surfaces have become crucial for fully integrated DNA-based data storage and sequencing technologies. The dehydration of DNA droplets in digital microfluidics has been discussed in [4], where a digital microfluidic system was utilized to deliver a DNA droplet to a spot, dehydrate it, and then access it for sequencing and data retrieval. It has been suggested that 1 TB of data can be stored in one such spot with 175 bases of DNA, assuming a density of 1.0×10^{-1} byte/base [4]. To store 1 TB of data, only 180 ng of DNA was required and successfully retrieved. Our study demonstrates that FET-based charge sensors can effectively monitor DNA mass during extreme dehydration within the same range of DNA mass as discussed in [4].

Our study also shows the potential of FET sensor integration with a physical DNA storage system to monitor DNA dehydration and track DNA's existence on one spot before moving a droplet to retrieve the mass of DNA for sequencing. We have designed a new back-gate ID-OGJFET and the dedicated electronic circuit and microfluidics cartridge for this application. These additional parts provide a wide range of sensing sites for accommodating large droplets from a few nL to > 5 uL that can hold and monitor large amounts of DNA on a scale practical for data storage applications. The ID-OGJFET’s unique characteristics allow direct-on-channel charge sensing without needing a reference solution and thus enable direct integration with digital microfluidics designs.

As with all practical data retention schemes, DNA-based data storage needs a reliable spatial reference for the data content. During data search, such localized spots of DNA must be frequently accessed to verify the presence of desired information. The integration of sensitive FET sensors helps to evaluate the existence of DNA and its amount, accelerating the random access and subsequent retrieval processes.

To further understand the experimental observations, MD simulations were conducted to explain the possible sensing mechanism involved in detecting DNA in extreme dehydration conditions. The MD simulation of DNA dehydration was simplified and implicitly modeled by reducing the assumed volume of the droplet from 14 nm to 1 nm to approximate a reduction in water. The simulations revealed that as a droplet of DNA loses water, there is an increase in surface potential and, consequently, an increase in charge. Water loss compels DNA to enhance its adsorption sites on SiO_2 and come closer to the surface. Our results demonstrate that the contour of surface potential elevates during the dehydration of DNA on SiO_2. This heightened electrostatic potential promotes increased interaction between the negatively charged phosphorus atoms on DNA and the channel containing positively charged holes (assuming a p-type channel in ID-OGJFET). Notably, MD simulations reveal that when approximately 93% of water is lost due to evaporation, DNA generates a negative electrostatic potential, a novel finding not explored previously. This negative potential, compared to bare silica, is the primary physical basis for detecting DNA in extreme dehydration.

7.7. Conclusion

Comprehending dehydrated DNA adoption on a silica surface is paramount in designing a physical storage medium for the emerging DNA-based data storage application. This work is dedicated to enhancing the understanding of the sensing mechanism of a novel field-effect transistor sensor called ID-OGJFET, aiming to measure DNA adsorption on native SiO_2 through experimental investigation and in-silico classical MD. For the first time, we modeled the structure of double-stranded dsDNA on silica in states of extreme dehydration, a topic of high interest in developing FET sensors for DNA mass monitoring in emerging DNA data storage applications. Simulations suggest a disruption in the helical structure of dsDNA when it loses water, leading to an enhanced coverage area on silica of more than ~ 26.25×10^{-6} μm^2 for a 7 nm long DNA. The denaturation of dsDNA into two single strands in the proximity of silica is also noteworthy, widening the dsDNA

over the surface. MD simulations indicate a change in surface electrostatic potential, confirming a potential shift upon the adsorption of dsDNA in extreme dehydration conditions. This shift is a highly probable reason for detecting dsDNA with ID-OGJFET in the extreme dehydration phase.

The ID-OGJFET design offers a large sensing area of ~ 16.54 mm^2 with a novel configuration of interdigital fingers on OG-JFET working with only two pads. The sensor is accompanied by a new electro-fluidic packaging scheme enabled by 3D printing and a dedicated portable readout circuit. This configuration of a dedicated electronic FET, electro-fluidic packaging, and portable readout system resembles a physical DNA storage and monitoring system for the future adoption of FET sensors in this emerging data storage technology.

Acknowledgment

The authors would like to thank Mitacs for their financial support. Also, they would like to thank CMC Microsystems for the provision of services that facilitated this research.

7.8. References

[1] A. Doricchi et al., "Emerging Approaches to DNA Data Storage: Challenges and Prospects," ACS Nano, vol. 16, no. 11. American Chemical Society, pp. 17552–17571, Nov. 22, 2022. doi: 10.1021/acsnano.2c06748.

[2] Y. Cevallos et al., "A brief review on DNA storage, compression, and digitalization," Nano Communication Networks, vol. 31. Elsevier B.V., Mar. 01, 2022. doi: 10.1016/j.nancom.2021.100391.

[3] P. Y. De Silva and G. U. Ganegoda, "New Trends of Digital Data Storage in DNA," Biomed Res Int, vol. 2016, 2016, doi: 10.1155/2016/8072463.

[4] S. Newman et al., "High density DNA data storage library via dehydration with digital microfluidic retrieval," Nat Commun, vol. 10, no. 1, Dec. 2019, doi: 10.1038/s41467-019-09517-y.

[5] J. Wu, H. Wang, A. Zhu, and F. Long, "Adsorption Kinetics of Single-Stranded DNA on Functional Silica Surfaces and Its Influence Factors: An Evanescent-Wave Biosensor Study," ACS Omega, vol. 3, no. 5, pp. 5605–5614, May 2018, doi: 10.1021/acsomega.7b02063.

[6] P. E. Vandeventer, J. Mejia, A. Nadim, M. S. Johal, and A. Niemz, "DNA adsorption to and elution from silica surfaces: Influence of amino acid buffers," Journal of Physical Chemistry B, vol. 117, no. 37, pp. 10742–10749, Sep. 2013, doi: 10.1021/jp405753m.

[7] A. Panahi, M. Ghafar-Zadeh, A. Scime, S. Magierowski, and E. Ghafar-Zadeh, "Novel Field-Effect Transistor Sensor for DNA Storage Monitoring," IEEE Trans Instrum Meas, vol. 71, 2022, doi: 10.1109/TIM.2021.3135531.

[8] A. M. García-Alegría, I. Anduro-Corona, C. J. Pérez-Martínez, M. A. G. Corella-Madueño, M. L. Rascón-Durán, and H. Astiazaran-Garcia, "Quantification of DNA through the nanodrop spectrophotometer: Methodological validation using standard reference material and sprague dawley rat and human DNA," Int J Anal Chem, vol. 2020, 2020, doi: 10.1155/2020/8896738.

[9] A. Liu, L. Wu, Z. He, and J. Zhou, “Development of highly fluorescent silica nanoparticles chemically doped with organic dye for sensitive DNA microarray detection,” Anal Bioanal Chem, vol. 401, no. 6, pp. 2003–2011, Oct. 2011, doi: 10.1007/s00216-011-5258-y.

[10] A. Ligasová and K. Koberna, “DNA replication: From radioisotopes to click chemistry,” Molecules, vol. 23, no. 11. MDPI AG, Nov. 17, 2018. doi: 10.3390/molecules23113007.

[11] J. Li et al., “Attenuated Total Reflection Surface-Enhanced Infrared Absorption Spectroscopy: a Powerful Technique for Bioanalysis,” Journal of Analysis and Testing, vol. 1, no. 1. Nonferrous Metals Society of China, Jan. 01, 2017. doi: 10.1007/s41664-017-0009-5.

[12] D. Y. Petrovykh, H. Kimura-Suda, L. J. Whitman, and M. J. Tarlov, “Quantitative analysis and characterization of DNA immobilized on gold,” J Am Chem Soc, vol. 125, no. 17, pp. 5219–5226, Apr. 2003, doi: 10.1021/ja029450c.

[13] K. Muzyka, F. Rico, G. Xu, and I. Casuso, “DNA at conductive interfaces: What can atomic force microscopy offer?,” Journal of Electroanalytical Chemistry, vol. 938, Jun. 2023, doi: 10.1016/j.jelechem.2023.117448.

[14] A. Nabok, A. Tsargorodskaya, F. Davis, and S. P. J. Higson, “The study of genomic DNA adsorption and subsequent interactions using total internal reflection ellipsometry,” Biosens Bioelectron, vol. 23, no. 3, pp. 377–383, Oct. 2007, doi: 10.1016/j.bios.2007.04.020.

[15] R. Kurrat, M. Textor, J. J. Ramsden, P. Boni, and N. D. Spencer, “Instrumental improvements in optical waveguide light mode spectroscopy for the study of biomolecule adsorption,” Review of Scientific Instruments, vol. 68, no. 5, pp. 2172–2176, 1997, doi: 10.1063/1.1148069.

[16] D. J. Niedzwiecki, J. Grazul, and L. Movileanu, “Single-molecule observation of protein adsorption onto an inorganic surface,” J Am Chem Soc, vol. 132, no. 31, pp. 10816–10822, Aug. 2010, doi: 10.1021/ja1026858.

[17] D. Capelli, V. Scognamiglio, and R. Montanari, “Surface plasmon resonance technology: Recent advances, applications and experimental cases,” TrAC - Trends in Analytical Chemistry, vol. 163. Elsevier B.V., Jun. 01, 2023. doi: 10.1016/j.trac.2023.117079.

[18] X. Chun Zhou, L. Qun Huang, and S. Fong Yau Li, “Microgravimetric DNA sensor based on quartz crystal microbalance: comparison of oligonucleotide immobilization methods and the application in genetic diagnosis,” 2001. [Online]. Available: www.elsevier.com/locate/bios

[19] T. Goda and Y. Miyahara, “Interpretation of protein adsorption through its intrinsic electric charges: A comparative study using a field-effect transistor, surface plasmon resonance, and quartz crystal microbalance,” Langmuir, vol. 28, no. 41, pp. 14730–14738, Oct. 2012, doi: 10.1021/la302977s.

[20] H. Y. Lau and J. R. Botella, “Advanced DNA-based point-of-care diagnostic methods for plant diseases detection,” Front Plant Sci, vol. 8, p. 302813, Dec. 2017, doi: 10.3389/FPLS.2017.02016/BIBTEX.

[21] P. L. Antkowiak et al., “Integrating DNA Encapsulates and Digital Microfluidics for Automated Data Storage in DNA,” Small, vol. 18, no. 15, Apr. 2022, doi: 10.1002/smll.202107381.

[22] D. Sadighbayan, M. Hasanzadeh, and E. Ghafar-Zadeh, “Biosensing based on field-effect transistors (FET): Recent progress and challenges,” TrAC - Trends in Analytical Chemistry, vol. 133, p. 116067, 2020, doi: 10.1016/j.trac.2020.116067.

[23] A. Panahi, D. Sadighbayan, S. Forouhi, and E. Ghafar-Zadeh, “Recent advances of field-effect transistor technology for infectious diseases,” Biosensors (Basel), vol. 11, no. 4, 2021, doi: 10.3390/bios11040103.

[24] M. Kaisti, “Detection principles of biological and chemical FET sensors,” Biosensors and Bioelectronics, vol. 98. Elsevier Ltd, pp. 437–448, Dec. 15, 2017. doi: 10.1016/j.bios.2017.07.010.

[25] C. F. Chang and M. S. C. Lu, “CMOS Ion Sensitive Field Effect Transistors for Highly Sensitive Detection of DNA Hybridization,” IEEE Sens J, vol. 20, no. 16, pp. 8930–8937, 2020, doi: 10.1109/JSEN.2020.2986461.

[26] T. Sakata and Y. Miyahara, “DNA sequencing based on intrinsic molecular charges,” Angewandte Chemie - International Edition, vol. 45, no. 14, pp. 2225–2228, 2006, doi: 10.1002/anie.200503154.

[27] C. C. Huang, Y. H. Kuo, Y. S. Chen, P. C. Huang, and G. Bin Lee, “A miniaturized, DNA-FET biosensor-based microfluidic system for quantification of two breast cancer biomarkers,” Microfluid Nanofluidics, vol. 25, no. 4, pp. 1–12, 2021, doi: 10.1007/s10404-021-02437-8.

[28] P. Sun, Y. Cong, M. Xu, H. Si, D. Zhao, and D. Wu, “An isfet microarray sensor system for detecting the dna base pairing,” Micromachines (Basel), vol. 12, no. 7, 2021, doi: 10.3390/mi12070731.

[29] P. Stoliar et al., “DNA adsorption measured with ultra-thin film organic field effect transistors,” Biosens Bioelectron, vol. 24, no. 9, pp. 2935–2938, May 2009, doi: 10.1016/j.bios.2009.02.003.

[30] P. Beyazkilic, A. Saateh, M. Bayindir, and C. Elbuken, “Evaporation-Induced Biomolecule Detection on Versatile Superhydrophilic Patterned Surfaces: Glucose and DNA Assay,” ACS Omega, vol. 3, no. 10, pp. 13503–13509, Oct. 2018, doi: 10.1021/acsomega.8b00389.

[31] A. Ebrahimi et al., “Nanotextured superhydrophobic electrodes enable detection of attomolar-scale DNA concentration within a droplet by non-faradaic impedance spectroscopy,” Lab Chip, vol. 13, no. 21, pp. 4248–4256, Nov. 2013, doi: 10.1039/c3lc50517k.

[32] M. Chopra, L. Li, H. Hu, M. A. Burns, and R. G. Larson, “DNA molecular configurations in an evaporating droplet near a glass surface,” J Rheol (N Y N Y), vol. 47, no. 5, pp. 1111–1132, Sep. 2003, doi: 10.1122/1.1595097.

[33] X. L. Du, D. M. Duan, R. Cao, G. Jin, and J. Li, “Enhancing DNA detection sensitivity through a two-step enrichment method with magnetic beads and droplet evaporation,” Anal Lett, vol. 43, no. 9, pp. 1525–1533, Jun. 2010, doi: 10.1080/00032710903502140.

[34] L. P. Xu et al., “Ultratrace DNA Detection Based on the Condensing-Enrichment Effect of Superwettable Microchips,” Advanced Materials, vol. 27, no. 43, pp. 6878–6884, Nov. 2015, doi: 10.1002/adma.201502982.

[35] K. Fukada, N. Kawamura, and S. Shiratori, “Trace Material Capture by Controlled Liquid Droplets on a Superhydrophobic/Hydrophilic Surface,” Anal Chem, vol. 89, no. 19, pp. 10391–10396, Oct. 2017, doi: 10.1021/acs.analchem.7b02369.

[36] B. Shi, Y. K. Shin, A. A. Hassanali, and S. J. Singer, “DNA Binding to the Silica Surface,” Journal of Physical Chemistry B, vol. 119, no. 34, pp. 11030–11040, Aug. 2015, doi: 10.1021/acs.jpcb.5b01983.

[37] S. Bag, S. Rauwolf, S. P. Schwaminger, W. Wenzel, and S. Berensmeier, “DNA Binding to the Silica: Cooperative Adsorption in Action,” Langmuir, vol. 37, no. 19, pp. 5902–5908, May 2021, doi: 10.1021/acs.langmuir.1c00381.

[38] B. M. Lowe, C. K. Skylaris, N. G. Green, Y. Shibuta, and T. Sakata, “Molecular dynamics simulation of potentiometric sensor response: the effect of biomolecules, surface morphology and surface charge,” Nanoscale, vol. 10, no. 18, pp. 8650–8666, May 2018, doi: 10.1039/C8NR00776D.

[39] B. M. Lowe, Y. Maekawa, Y. Shibuta, T. Sakata, C. K. Skylaris, and N. G. Green, “Dynamic behaviour of the silica-water-bio electrical double layer in the presence of a divalent electrolyte,” Physical Chemistry Chemical Physics, vol. 19, no. 4, pp. 2687–2701, 2017, doi: 10.1039/c6cp04101a.

[40] M. T. Hwang et al., “Ultrasensitive detection of nucleic acids using deformed graphene channel field effect biosensors,” Nat Commun, vol. 11, no. 1, Dec. 2020, doi: 10.1038/s41467-020-15330-9.

[41] F. Liu et al., “Study on the adsorption orientation of DNA on two-dimensional MoS2 surface via molecular dynamics simulation: A vertical orientation phenomenon,” Chem Phys, vol. 529, p. 110546, Jan. 2020, doi: 10.1016/J.CHEMPHYS.2019.110546.

[42] M. Morita, T. Ohmi, E. Hasegawa, M. Kawakami, and M. Ohwada, “Growth of native oxide on a silicon surface,” J Appl Phys, vol. 68, no. 3, pp. 1272–1281, 1990, doi: 10.1063/1.347181.

[43] P. Mercier and R. Savoie, “Interaction of DNA with Silica Particles: A Vibrational Spectroscopic Study,” Biospectroscopy, vol. 3, pp. 299–306, 1997, doi: 10.1002/(SICI)1520-6343(1997)3:4<299::AID-BSPY5>3.0.CO;2.

[44] K. D. Kwon, V. Vadillo-Rodriguez, B. E. Logan, and J. D. Kubicki, “Interactions of biopolymers with silica surfaces: Force measurements and electronic structure calculation studies,” Geochim Cosmochim Acta, vol. 70, no. 15, pp. 3803–3819, Aug. 2006, doi: 10.1016/j.gca.2006.05.016.

[45] J. C. Phillips et al., “Scalable molecular dynamics with NAMD,” J Comput Chem, vol. 26, no. 16, pp. 1781–1802, Dec. 2005, doi: 10.1002/JCC.20289.

[46] W. Humphrey, A. Dalke, and K. Schulten, “VMD: Visual molecular dynamics,” J Mol Graph, vol. 14, no. 1, pp. 33–38, Feb. 1996, doi: 10.1016/0263-7855(96)00018-5.

[47] S. Jo, T. Kim, V. G. Iyer, and W. Im, “CHARMM-GUI: A web-based graphical user interface for CHARMM,” J Comput Chem, vol. 29, no. 11, pp. 1859–1865, Aug. 2008, doi: 10.1002/JCC.20945.

[48] K. Vanommeslaeghe et al., “CHARMM general force field: A force field for drug-like molecules compatible with the CHARMM all-atom additive biological force fields,” J Comput Chem, vol. 31, no. 4, pp. 671–690, Mar. 2010, doi: 10.1002/JCC.21367.

[49] H. Heinz, T. J. Lin, R. Kishore Mishra, and F. S. Emami, “Thermodynamically consistent force fields for the assembly of inorganic, organic, and biological nanostructures: The INTERFACE force field,” Langmuir, vol. 29, no. 6, pp. 1754–1765, Feb. 2013, doi: 10.1021/LA3038846/SUPPL_FILE/LA3038846_SI_002.ZIP.

Chapter 8 Evaporation-based Chemical Sensing Mechanism with Interdigital Open-Gate JFET (ID-OGJFET)[1]

Paper 8: Drop-FET: A Novel Thermo-FET Sensing System for Binary Chemical Solvent Monitoring Applications

Authors: Abbas Panahi, Hamed Osouli Tabrizi, Giancarlo Ayala-Charca, Ahmad Roshanfar, Morteza Ghafar-Zadeh, Sebastian Magierowski, Ebrahim Ghafar-Zadeh

Abbas Panahi's contributions: chip design and characterization, wet tests and data analysis, simulation, and modeling, writing the paper draft and submission

The technological advantages of the OG-JFET have facilitated the implementation of an interdigital design on the chip, resulting in a relatively high direct-on-channel sensing area. This design enables the monitoring of microdroplet evaporation directly on the sensor. Since the evaporation rate of a microdroplet is influenced by its chemical composition, we leveraged this novel sensing modality to quantify the polar content of a water droplet by measuring the evaporation time through the sensor's output. This chapter delves into this innovative sensing approach, the characterization system, and the new electro-fluidics packaging scheme.

[1] This chapter is based on a submitted manuscript.

Paper: Abbas Panahi, Hamed Osouli Tabrizi, Giancarlo Ayala-Charca, Ahmad Roshanfar, Morteza Ghafar-Zadeh, Sebastian Magierowski, Ebrahim Ghafar-Zadeh. "Drop-FET: A Novel Thermo-FET Sensing System for Binary Chemical Solvent Monitoring Applications," Under Review in IEEE Trans. Instrumentation and Measurement

8.1. Abstract

This paper introduces a novel field-effect transistor (FET)-based sensing system designed for real-time monitoring of charge/polarity changes during the evaporation of micro-size water droplets containing polar substances like ethanol and methanol. The system utilizes a high transconductance interdigital open gate junction FET (ID-OGJFET) with a sizeable direct-on-channel sensing area (>16 mm^2) in direct contact with the liquid droplet. A new electro-fluidic package has also been developed to facilitate sample access on the FET chip, prevent leakage, and connect the sensor to readout systems. An experimental procedure is designed to demonstrate the functionality and applicability of this FET platform sensing system for chemical analysis, such as measuring the percentage of ethanol or methanol in water using the novel evaporation-based sensing mechanism enabled by the ID-OGJFET. Real-time video capture is employed for meticulous monitoring and control. The sensor measures ethanol and methanol concentrations ranging from 0-100 % with accuracy as low as 10 % EtOH/MetOH in water, utilizing the evaporation-based sensing mechanism and current output of the ID-OGJFET sensor. Based on these results, the proposed droplet on the ID-OGJFET (Drop-FET) sensor exhibits promise for various industrial applications, including process monitoring, quality control, and chemical analysis.

8.2. Introduction

The measurement of chemicals such as ethanol and methanol in water, or water content in ethanol/methanol, holds immense significance across various industrial domains. Analyzing two-component solutions, such as ethanol or methanol in water, is paramount in industrial settings across multiple sectors [1], [2]. These solutions serve as critical raw materials, solvents, and additives in food and beverage, pharmaceuticals, chemical manufacturing, automotive, and biofuel production [3]. Precise and real-time analysis of two-component water solutions (e.g., ethanol and methanol concentrations) ensures product quality, safety, and regulatory compliance. Industries rely on this analysis to optimize processes, maintain product integrity, and meet stringent standards [4]. Accurate water content measurement in ethanol and methanol mixtures is vital in biofuel production, as excessive water can significantly impact combustion efficiency and environmental emissions [5]. The rapid and reliable assessment of specific chemicals in solutions through online

monitoring is crucial in empowering industries to enhance process control, improve efficiency, and uphold environmental stewardship.

Various laboratory techniques, including chromatography [6], [7], and spectrophotometry [8], are recognized for detecting single and binary droplets, such as alcohol in water. While offering high sensitivity and accuracy, they primarily serve as off-line analytical measurements, impeding rapid on-site analysis needs. Optical image processing-based techniques are emerging for binary droplet analysis, correlating contact angle and surface energy with chemical components [9], [10]. However, these methods require expensive equipment, specialized training, and time-consuming setup, limiting their practical on-site application efficiency.

Novel droplet analysis technologies have emerged, including optical fiber-based sensors for ethanol concentration quantification [11] and MEMS/NEM'S resonator-based sensors tailored for droplet analysis. A dual-resonator mass sensor provides a simultaneous time of evaporation and droplet mass sensing at a picoliter scale [12]. In contrast, a microcantilever MEMS sensor measures droplets as small as 5 μm in radius, correlating evaporation time and droplet mass with alcohol content [13]. A CMOS-integrated NEMS resonator sensor analyzes single-component droplet volumes ranging from 150 aL to 15 fL [14]. Furthermore, an optomechanical device combines optical droplet measurement with resonator mechanical response for zeptoliter-scale droplet analysis [15]. Quartz resonators have been used for biochemical content analysis during droplet drying, which is promising in diagnostics [16]. Despite these advancements, the reliance on moving components and dual sensing modalities may limit on-site droplet analysis efficiency, particularly for industrial monitoring where vibration noise is prevalent. Electrochemical sensors offer potential for real-time and portable alcohol detection but often lack competency for two-component droplet analysis [17].

This paper proposes a novel thermo-FET sensing method for portable and process monitoring, detailed in Sections II[1] and III, with results and conclusions in Sections IV and V[2].

[1] Section 8.4
[2] Section 8.6 and 8.7

8.3. Related Works

Due to their highly sensitive charge detection, FET chemical sensors have recently garnered significant attention in liquid analysis. These FET-based sensors operate by measuring the variation of surface charge on an oxide layer (e.g., SiO_2) or a dielectric layer (e.g., Si_3N_4) as a charge sensing layer, using a semiconductor channel [18], [19]. This variation in surface charge is then reflected in the output drain-source current by manipulating the space charge in the conducting channel. The FET structures require a reference electrode inside the solution for sensor operation, typically based on Ag/AgCl electrodes. This reference electrode is used to measure the surface potential change on the oxide or dielectric layer of the channel [19].

FET-based chemical sensors are well-known for their ultra-high sensitivity to the charge captured at a particular distance from their gate. This includes ions, biomolecules (e.g., DNA), or chemical reactions that change the solution's positive or negative charge on the surface. FET-based droplet sensors include a silicon-FET sensor, developed and integrated with digital microfluidics for droplet analysis, including ions and proteins [20]. This integrated platform demonstrated highly sensitive droplet content analysis [20]. Another example is a droplet-gated organic FET sensor designed for single-component or ionic-included droplets [21]. The organic FET sensor exhibited promising results in droplet analysis and had good stability. A solution-gated graphene FET sensor was developed, demonstrating ultra-sensitivity towards ionic droplets [22]. This sensor was integrated with microfluidics, and a reference electrode was designed on a chip [22]. Several other FET-based chemical or biological sensors are discussed in the following review papers, offering insights into their state-of-the-art capabilities and superiority in chemical/biological target analysis [19], [23], [24].

Upon reviewing FET structures and their applications, they are clearly limited in analyzing droplets with polar solutions like ethanol-water without surface modification and a reference electrode. FET sensors typically need a reference electrode in the solution, making analyzing droplet evaporation for trace amounts of polar liquids difficult. Additionally, their ultra-small sensing sites limit their ability to support such applications and provide sensing capabilities for various droplet sizes.

Our solution involves enabling large direct-on-channel sensing areas with the ID-OGFET sensor. Our custom design addresses these challenges by introducing a back-gated FET with a significant

sensing area. This enhancement allows for tracking droplet evaporation, facilitating the measurement of evaporation time.

8.4. Portable Electrochemical Sensing Platform

8.4.1. Proposed Thermo-FET Sensing Mechanism

The ID-OGJFET sensor, fabricated through a standard microfabrication process from CMC Microsystem, features two pads connecting the source and drain fingers, forming the ID-OGJFET structure. Optical microscopy images (Fig. 8-1) reveal the sensing area with a water droplet, highlighting the grey silicon channel and the black SiO_2-Si_3N_4 encapsulation layer. The green area indicates silicon, comprising both the p-type and n-type channels. With a total die area of 100 mm^2, the developed sensing area (~16.52 mm^2) allocates ~2.36 mm^2 for each channel. A thick layer of Al/Ti is applied on the back-gate side, establishing contact with the metal on the backside. At the same time, the design reduces pad number, enhances sensing area, and creates a functional high surface area OG-JFET configuration. The interdigital layout allows a larger sensing region to accommodate droplets up to ~5-6 mm in diameter.

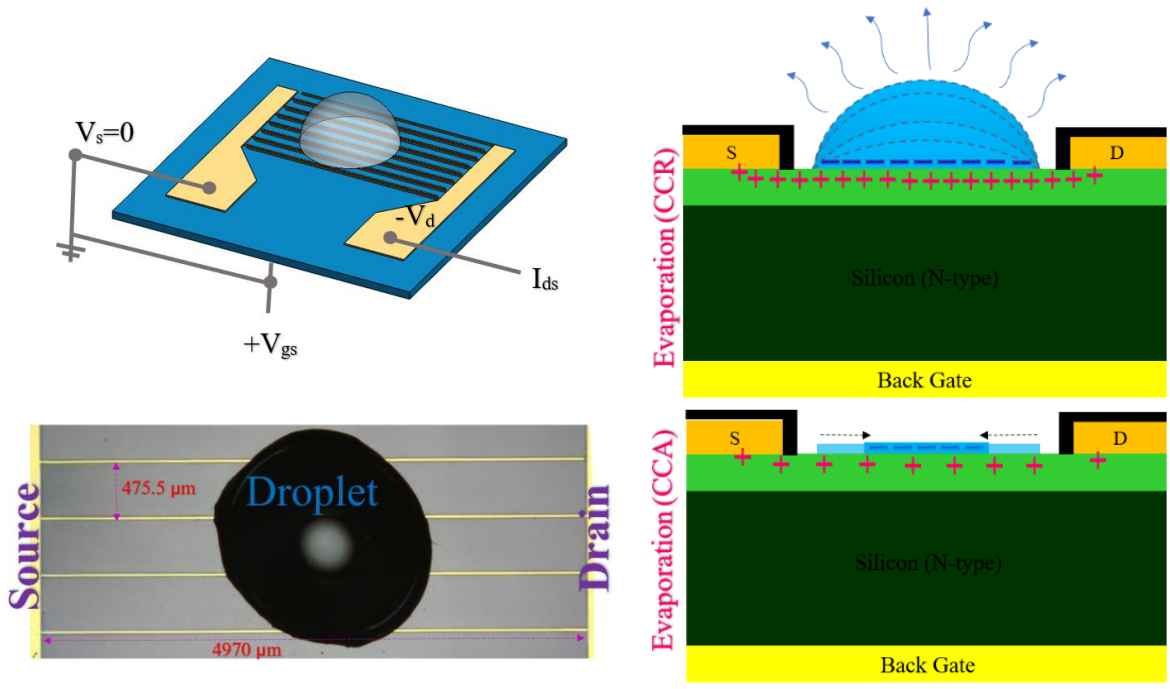


Figure 8-1. The FET sensor configuration is used to show the droplet evaporation. (a) 3D schematic of sensor holding a droplet. The droplet spreads across the sensing region and establishes chemical bonding with the sensor's surface. The droplet in the actual experiment is shown in (b). As the sensor is interdigital, it ensures the sensing of all the areas of droplets in the sensing region. The cross-sectional structure of the sensor and the sensing mechanism is shown schematically in (c).

When a liquid droplet meets the silicon dioxide (SiO_2) layer atop the ID-OGJFET, interactions like hydrogen bonding and van der Waals forces alter the surface potential, forming a double layer on the oxide layer [19]. This generates a surface charge transmitted to the semiconductor channel (p-type) of the ID-OGJFET, enhancing hole concentration and altering the drain-source current (Ids). The back gate of the ID-OGJFET controls channel conduction. In evaporation-based sensing, the open-gate design allows direct liquid-channel interaction, eliminating the need for a reference electrode [20]. This enables precise tracking of droplet edges until complete evaporation, facilitating novel chemical analysis and droplet assessment by measuring evaporation time [20].

8.4.2. Embedded Interface System

The custom-made electronic interface system generates the required voltages dropped on the drain, source, and gate to measure the drain current Ids as a function of voltage drain-source Vds and Vgs. The Ids-Vds for various Vgs values and Ids-Vgs for various Vds values are shown in Fig. 8-2. This system includes electronic digital and analog circuits incorporated with software acting as a graphical user interface (GUI).

8.4.3. Hardware interface system

This system consists of a digital microcontroller-based board incorporated with an electronic analog interface system, as illustrated in Fig. 8-2. The board has been customized to characterize the OG-JFET chip. This figure shows the main building blocks, including three high-power digital to analog converters (DACs) (AD5761R) generating DC voltage ranging from -10 to 10 V volts with the resolution of ±1.5 mV dropped on drain (D), source (S), and gate (G) of each one of eight FETs. Eight switches (ADG1401B) are used to connect one of the drains or one of the sources to the related DACs. Additionally, one ADC records ID using an IC current shunt monitor (INA282A) that plays the role of a multivariable current measurement system ranging from 0 to about 20 mA. All electronic ICs are connected to the microcontroller board through SPI serial ports assembled on the printed circuit board (PCB) (Fig. 8-2 (b)) and packaged along with the microcontroller board on a three-printed package (see Fig. 8-2 (b)). This figure shows that a packaged chip (Fig. 8-2 (b-i)) is connected to this package from the top.

8.4.3.1. Graphical User Interface

This GUI has been custom-developed using QT5, as shown in Fig. 8-2 (c). This figure demonstrates that the user can characterize the OG-JFET exposed to the droplet by specifying the drain, source, and gate voltage range. For instance, Fig. 8-2 (c) illustrates Ids-Vds curves associated with the proposed OG-JFET when there is no sample, the range of Vds is from -10 to 50 V, and the back gate is swept from 0 to 0.5 V with steps of 0.1 Volt.

8.4.3.2. Electro-Microfluidics Packaging Compartments

The electro-fluidics packaging of the device comprises an ID-OGJFET sensor integrated with a microfluidics chamber and spring-loaded connectors that can be used to probe the sensor. The sensor's transfer characteristics, including Ids-Vds, Ids-Vgs, and Ids-time, have been characterized using a probe station and semiconductor analyzer. The sensor has been connected to the semiconductor analyzer using SMU cables that connect the sensor pads using the spring-loaded connectors in the electro-fluidic fixture, as illustrated in Fig. 8-2 (b-iv). To connect the sensor to the readout system, a 3D printed electro-fluidics fixture has been employed, as shown in Fig. 8-2 (b). The fluidics compartment features a hydrophilic layer (indicated by the blue layer in Fig. 8-2 (b-iv) to ensure accurate droplet placement in the sensing area. The sensor is sandwiched between a small PCB and a hydrophobic TPU. The microfluidics layer is tightly held with an intermediate PLA—resin layer. Within the electro-fluidics compartment, spring-loaded connectors are positioned to direct electrical connections from the top layer to the sensor through the TPU layer (blue) and access the sensor's source and drain pads. The TPU layer helps prevent contact between the droplet and the pads, ensuring no short circuits occur. The PLA layer has an opening that matches the sensing area, facilitating the placement of the sample on the sensor. The ID-OGJFET sensor is situated on a conductive metal (made of Al) on the small PCB, elevated by a pin on the side of the PCB to apply a voltage to the back gate. The packaged sensor is depicted in Fig. 8-2 (b-ii). The packaging approach is reproducible and scalable, leveraging 3D printing technology to significantly reduce complexity in high-volume production for on-site industrial applications. The electro-fluidics component is compact and easily connectable to the readout system, as shown in Fig. 8-2 (b-i).

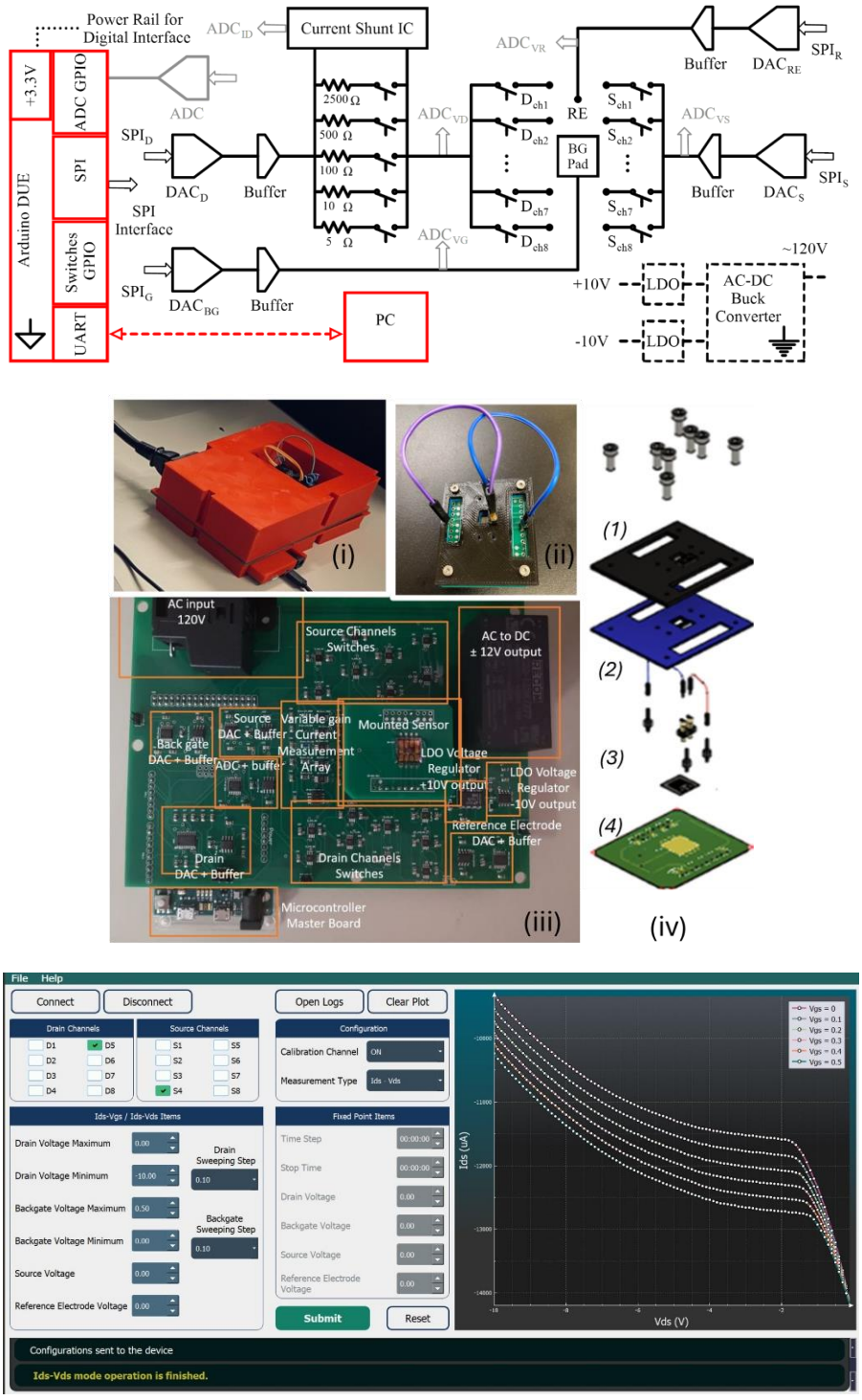


Figure 8-2. (a) The electronic readout system comprises a central block diagram of DAC, ADC, IC shunt, and DC power supply. (b): fabricated devices, (i) a photograph of a packaged readout system (i) that is connected to a computer, (ii) a photograph of a packaged electro-fluidic device, (iii) a fabricated PCB and circuit, and (iv) structure of ii consisting of (1) support layer, (2) fluidic layer, (3) probing, ID-OGJFET and small PCB for electro fluidic structure; and (c): image of GUI for setting the readout system.

8.4.4. ID-OGJFET Sensor Fabrication

The sensor's microfabrication was based on a standard foundry process offered by CMC Microsystem. The microfabrication process is detailed in [33]. The sensor's layout has been designed using L-Edit software, and DRC was checked based on the PDK provided by the manufacturer and submitted for fabrication. As shown in Fig. 8-1, the interdigital sensor was successfully developed using the standard foundry. The interdigital design methodology presented in this work provides an alternative solution for enlarging the sensing gate. While one might consider increasing the sensing area by extending the channel, such a design would significantly compromise the transconductance in the OG-JFET structure, thereby affecting the performance of charge sensing. In the proposed design, the back gate is utilized to regulate the conduction of the p-type channel under the interdigital fingers shared along the chip area.

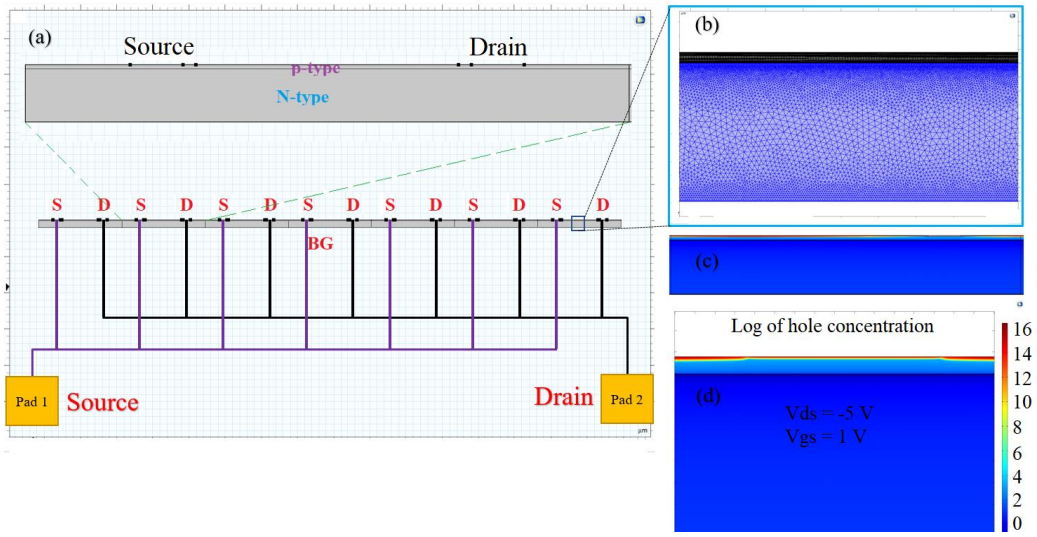


Figure 8-3. (a): The 2D CAD model of ID-OGJFET in COMSOL. (b): the meshed structure. (c): hole concentration in one channel. (d): zoomed-in concentration profile of hole in the vicinity of source and drain

8.4.5. Simulation of ID-OGJFET Sensor

Since the interdigital design of the OG-JFET represents a novel layout approach, never previously attempted with this foundry, a COMSOL simulation was established to validate the experimental behavior of ID-OGJFET in terms of the trend of I-V curves. This step was crucial for confirming the device's electronic functionality and comprehending its transfer characteristics when all the source and drain fingers are linked to two dedicated pads. The simulation model offers insights into the concentration of transport carriers (holes) along the shared channel beneath the

fingers, elucidating how carriers contribute to all source and drain fingers originating from the primary source and drain pads. The sensor's CAD model is constructed in COMSOL, as depicted in Fig. 8-3. Fig. 8-3 illustrates the concept of the interdigital OG-JFET and demonstrates how it is modeled in COMSOL, considering all the created channels between the source and drain fingers.

8.5. Results

Here, we present the results of the electronic characterization of the ID-OGJFET, along with experimental findings related to droplet evaporation analysis on the sensor. Additionally, the results of measuring the evaporation time of ethanol/methanol-water droplets are presented, which are crucial for analyzing the ethanol/methanol content of the droplet.

8.5.1. ID-OGJFET Transfer Characteristics

The ID-OGJFET's I-V characteristics were obtained as demonstrated in Fig. 8-4, which shows the Ids-Vds curves for ID-OGJFET for $0 < Vds < 10$ V and $0 < Vgs < 2.5$ V. The linear region of Ids-Vds is limited to the < 1 V. The sensor outputs increasing amounts of Ids for greater Vds voltages. Based on the sensor structure shown in Fig. 8-1 (a), the voltage polarity applied to the drain, source, and gate is essential because it changes the transfer characteristics of the sensor completely. The P-N junction can be reversed/forward-biased. A positive voltage is applied to the back gate, and a negative voltage to the drain leads to a current directly from the source to the drain. However, the opposite voltage polarity opens the P-N junction, and a considerable current is transferred from the back gate to the drain. Fig. 8-1 illustrates the reverse bias configuration utilized in the present study. In this configuration, a negative voltage is applied to the drain, while a positive voltage is applied to the gate. This bias setup turns off the P-N junction, allowing the Ids current to flow only from the source to the drain. The reversed bias condition presents more controllability over sensing the channel charging at lower voltages, where we have used this biasing for sensing chemicals. The g_m of the device has been characterized, and based on the results, the highest gm occurs in the Vgs = 0 V and Vds = -2 V, which were used for the analysis of the droplet in other experiments as the working point of the device.

8.5.2. Simulation Results

The I-V characteristics of the ID-OGJFET have been simulated using COMSOL software and are presented in Fig. 8-5. The results indicate that the simulation model captures the trend of the I-V curves concerning the back-gate's efficacy in modulating the ID-OGJFET's channel. However, the simulation does not perfectly align with experimental results due to non-idealities in fabrication and inherent limitations in the linear semiconductor models in COMSOL. The simulation, being a 2D model, contrasts with the ID-OGJFET's 3D nature, and the design parameters set in COMSOL are subject to uncertainties in the fabrication process. To address these limitations, we have calibrated the simulation model considering the back gate (Veq in COMSOL) and out-of-plane thickness as calibration parameters (see section 8.7 for more information).

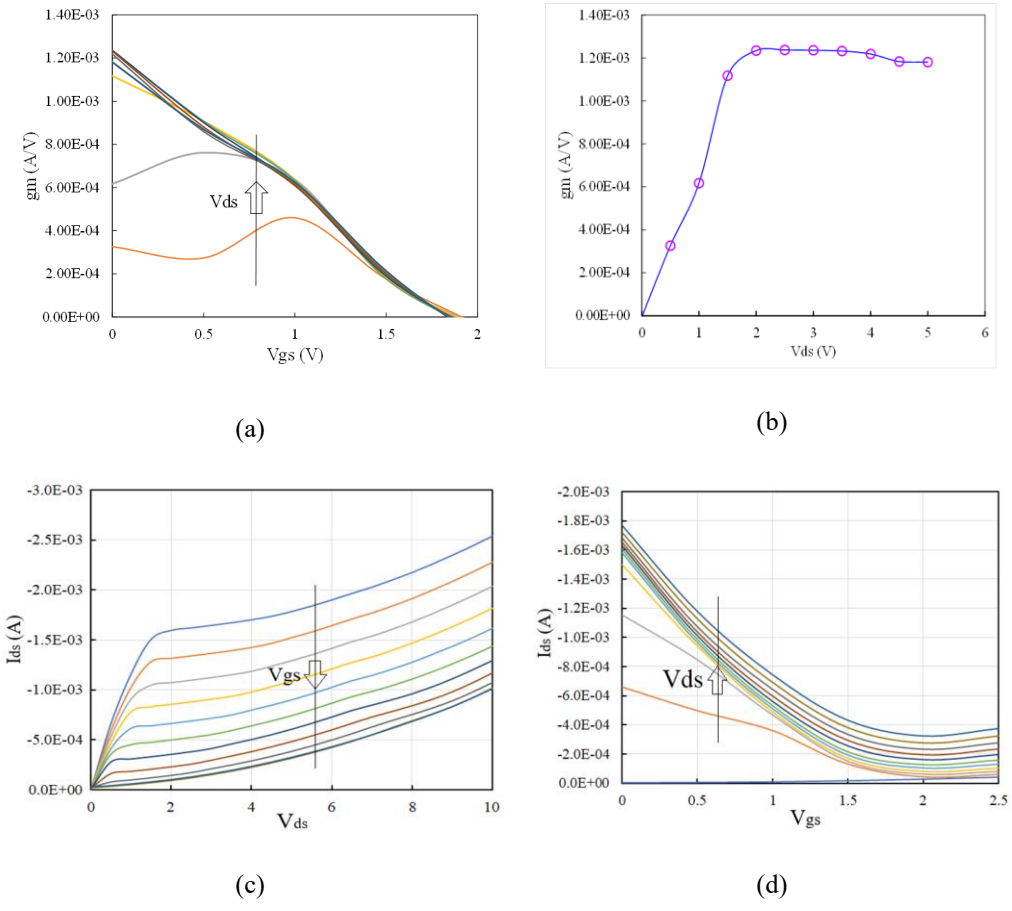
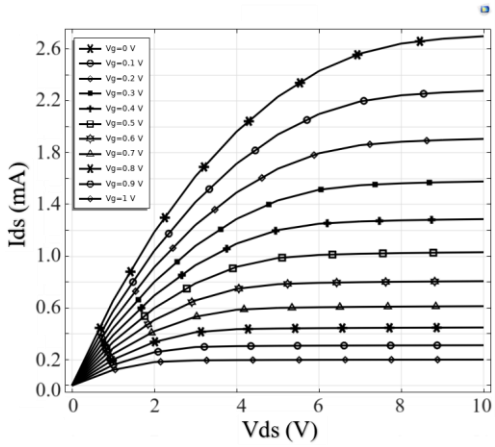
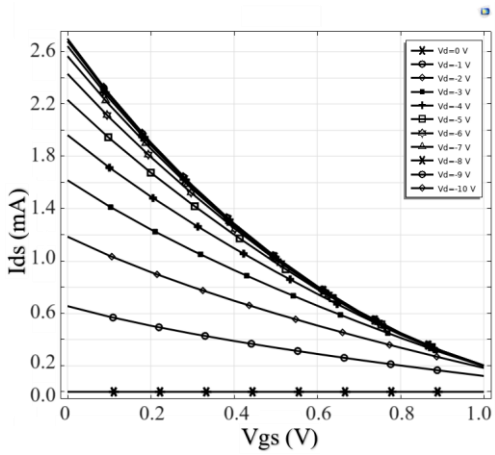


Figure 8-4. (a): gm-Vgs curve. (b): gm-Vds curve at Vgs = 0. (c): Ids-Vds curves. (d): Ids-Vgs curves of ID-OGJFET

Fig. 8-5 (b) illustrates the hole concentration profile of the ID-OGJFET sensor along the shared p-type channel, elucidating its working principle. Based on the simulation results, all fingers create a conductive channel between nearby electrodes, contributing to the output current. This model explains how the interdigital design facilitates increased sensing sites by generating multiple channels.



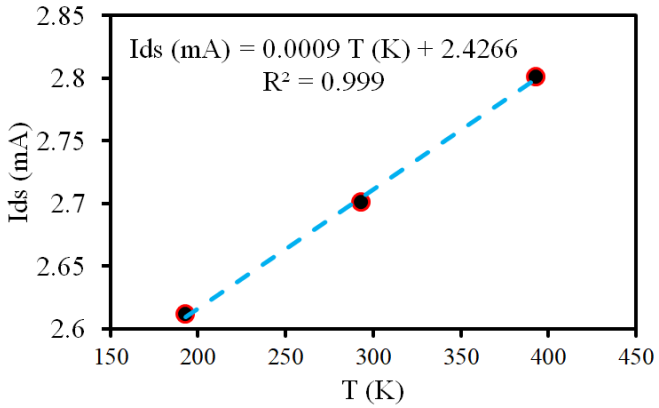
(a)



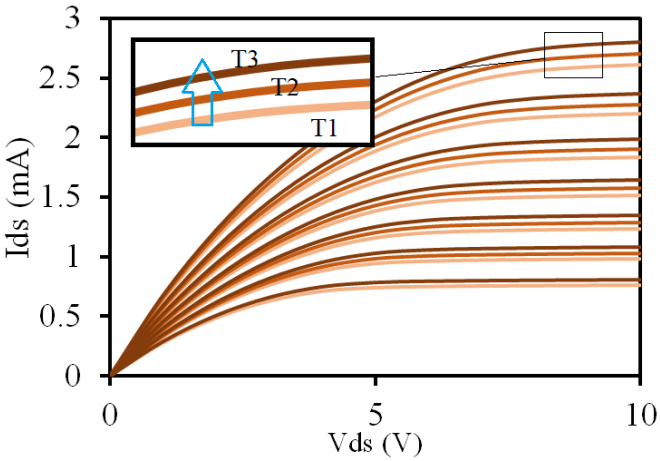
(b)

Figure 8-5. (a): COMSOL simulation result of Ids-Vds curve of an ID-OGJFET with a channel length of 100 um. (b): Ids-Vgs curves.

We have also evaluated the effect of temperature changes on the sensor's response, as shown in Fig. 8-6. The reduction in temperature leads to a decrease in current. However, the scale of temperature sensitivity might not align with experiments due to limitations in the 2D simulation approximation and the large size of the sensor. Nevertheless, the simulation does provide insights into the effect of thermal changes in the sensor and their influence on the output IDs of ID-OGJFET.



(a)



(b)

Figure 8-6. (a): the relationship between Ids and T (K). (b): Ids-Vds when Vgs is increasing for three different T (K) values

8.5.3. Droplet Evaporation Measurements with ID-OGJFET

The ID-OGJFET has been designed and customized to accommodate a wide range of droplet sizes up to ~ 7-8 µL by offering ~ 16.52 mm^2 of direct-on-channel sensing area. When the droplet evaporates under room conditions (~ 24 C) and humidity of 30-40 %, the first phase of evaporation is the pinned state, in which the droplet's primitive contact lines are pinned on the surface, and only the height of the droplet is reduced. After some minutes, the droplet starts to recede from the primitive areas, so the wet surface is reduced. The surface is the native silicon dioxide on the channel of the ID-OGJFET, and its charge changes due to interactions with water. Therefore, the sessile droplet evaporation completion can be detected when the droplet is receding, and the time-dependent monitoring of output current can distinguish evaporation phases.

When a droplet is cast on the surface of the ID-OGJFET, interactions occur between the water molecules (or other chemical components), ions, and the SiO_2-thin surface of the sensor. These interactions include van der Waals forces, electrostatic interactions, and chemical interactions such as hydrogen bonding [26]. These interactions influence the evaporation rate and overall time of evaporation (ToE). The interactions on the surface change the surface charge and potential of the p-channel in the ID-OGJFET. In its natural state, the silicon dioxide carries a negative charge without any solution. When the droplet is placed on the sensor, it becomes more negatively charged. The presence of the droplet on the wide sensing area allows for tracking the fingerprint of the surface charge of the wetted surface on the ID-OGJFET. The extent to which the droplet covers the sensing area correlates with enhancing the output current. In the design of the OGJFET, which utilizes a p-type silicon sensing channel, the sensor responds to negative surface charge by improving the current [34]. As illustrated in Fig. 8-1, the evaporation process entails the detachment of water molecules from the surface. Consequently, this water removal reduces the charge present in the double layer on the oxide layer atop the ID-OGJFET sensing site. The decrease in charge density can be detected by the charge-sensitive ID-OGJFET.

However, in the first phase of evaporation, due to the transistor self-heating, the sensor generates heat within its conductive channel [35], [36]. Conversely, when a droplet evaporates on any surface, it absorbs heat from the environment and the surface beneath, causing a decrease in surface (device body) temperature [37], [38]. This temperature decrease in the silicon-based channel reduces sensor current, as demonstrated in Fig. 8-7 after time "t_1". The current decline persists as evaporation continues until the onset of the second phase (from "t_1" to "t_5"), during which the thin layer of liquid starts to recede from the surface (see Fig. 8-7). At this point, the sensor detects the decrease in surface charge, leading to a sudden drop in the current (Ids) output ("t_6"). We have performed a temperature sensitivity test on the device, as shown in Fig. 8-6. It shows that the sensor is temperature sensitive, and in any process of cooling the sensor, it is logical to anticipate a reduction in current. The current enhancement is shown in Fig. 8-6 (a) for a Vgs = 0 V bias. Also, the same temperature gradient was studied for other values of Vgs shown in Fig. 8-6 (b), demonstrating that in all Vgs and Vds values, a temperature reduction leads to a current reduction.

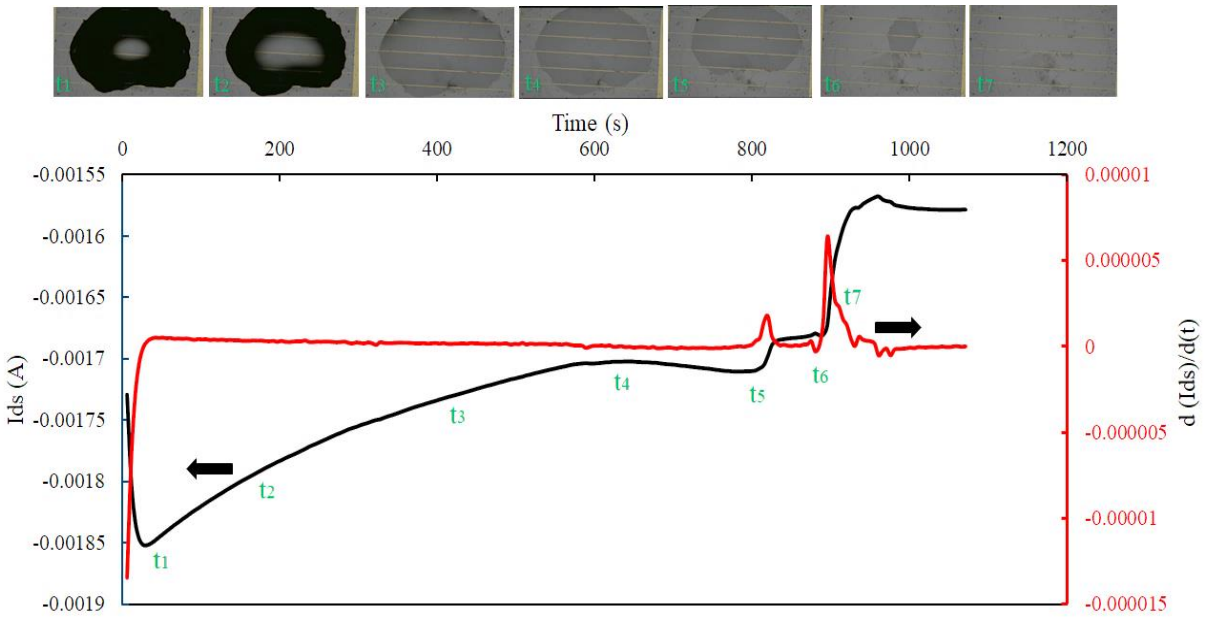


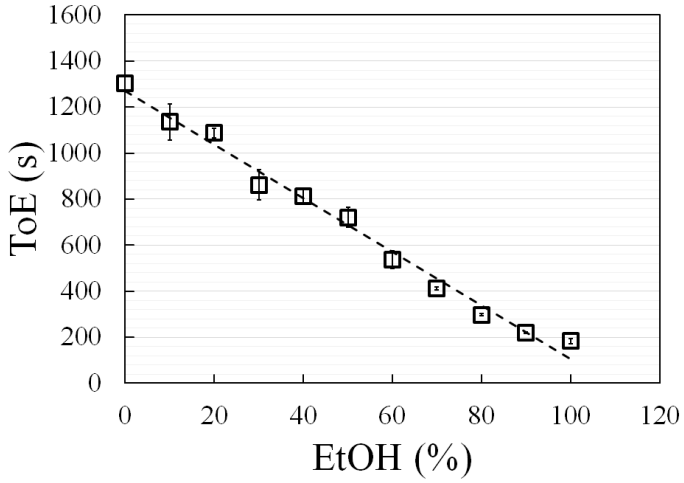
Figure 8-7. Shows the amperometric mode of ID-OGFET used to track the evaporation of a droplet until complete evaporation. The sensor is reverse biased, and the Vds is kept constant at—2 V when the Vgs = 0 and Vs = 0 V. As the droplet evaporates, optical microscopy records it during evaporation.

The curve shown in Fig. 8-7 demonstrates three distinct states when the droplet is placed on the sensor, and the sensor detects the charge of the droplet when it is spread entirely over the sensor. The current peaks because of the droplet charge induced in the channel. Due to the droplet cooling effect, the current reduces when the droplet's contact area is constant. After this phase, when the droplet becomes a thin layer of liquid, the receding phase begins, and the current sharply decreases due to a reduction in the surface charge sensed by the sensor. The derivative of Ids-time is also presented in Fig. 8-7, which clearly shows the onset of receding and, more precisely, the dynamics of droplets when only a nano-scale thin layer of liquid is spread on the sensor. Capturing such an extra thin layer of liquid during evaporation is extremely difficult with the conventional optical droplet evaporation measurement techniques due to the uncertainties in the quality of pixels of the recorded video during image analysis. However, the ID-OGJFET captures those events with excellent precision, which is leveraged by the nature of the device as a charge-sensing mechanism. According to the derivative of the Ids-time in Fig. 8-7, the first peak demonstrates the onset of the sensing droplet, and the second indicates the start of the receding phase and complete evaporation.

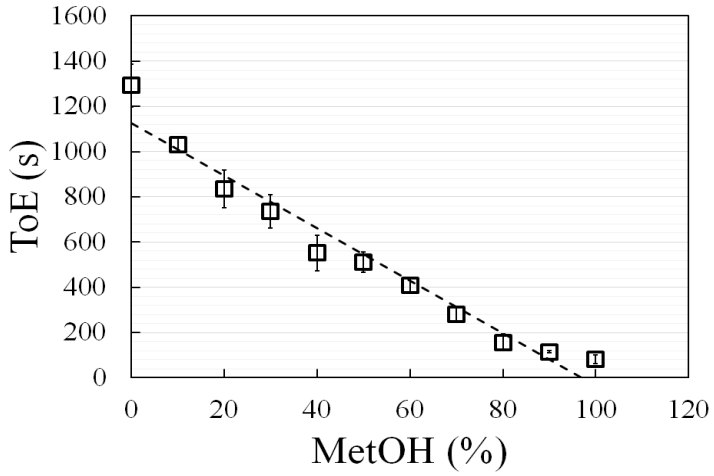
8.5.4. FET-Enabled Evaporation-based Chemical Content Measurement

To demonstrate the application of the sensing mechanism, we have designed a few examples to show how this method can be applied. Predicting alcohol concentration in water is a fundamental research question with many implications in various applications. We dissolved ethanol in water at varying concentrations to perform the experiments. Dissolving ethanol in water reduces the evaporation time since a diffusive evaporation mechanism controls the droplet evaporation. Therefore, the existence of ethanol will reduce the evaporation time and other evaporation parameters introduced in this study, such as the droplet surface energy. Our results show a steep evaporation time reduction with increased ethanol concentration that is in tune with other binary droplet evaporation dynamics. When the droplet is on the surface of the ID-OGJFET, the SiO_2 surface interacts with water and ethanol molecules, which changes the surface tension dynamics. The sensor's output current for varied concentrations of ethanol/methanol in water is measured, and the time of evaporation has been recorded as presented in Fig. 8-8. Fig. 8-8 (a) presents the resultant time of evaporation curve for ethanol in water with concentrations from 10% to 100 %. The same has been done for methanol/water droplets, as shown in Fig. 8-8 (b). The sensing mechanism introduced here provides a unique capability by which the concentration of alcohol can be measured by only determining the Ids characteristics of a droplet of solution, which gives the time of evaporation by which we can precisely measure the concentration of alcohol as presented in Fig. 8-8 (a) and (b).

Multiple experiments have revealed the detection of two evaporation phases, offering novel opportunities in droplet analysis research. The sensor's ability to correlate evaporation time with chemical content makes it valuable for various applications. Investigating direct-ethanol and methanol sensing on a bare sensor revealed its insensitivity to alcohol without surface modifications, but the evaporation sensing mechanism eliminates this need. Nonidealities in the system and sensor may impact measurement accuracy and minimum detectable alcohol concentration, necessitating further research into precise droplet delivery and surface smoothness enhancement. This study showcases a back-gated charge/thermal-sensitive FET sensor's utility for droplet analysis, paving the way for future research in droplet physics and chemical/biosensing applications leveraging FET structures.



(a)



(b)

Figure 8-8. The ToE versus alcohol concentration was measured in water using ID-OGJFET. (a): ToE versus concentrations of ethanol in water. (b): ToE versus concentrations of methanol in water

8.6. Conclusion

This paper uses a new thermo-FET sensor for binary chemical solvent monitoring. The sensor is fabricated based on a standard foundry process, which is desirable for the high-volume production of sensors for industrial applications. We have used this new sensing mechanism to correlate the ToE of two-component droplets of water-ethanol and water-methanol to the volumetric percentage of ethanol and methanol in water. The results show that the ID-OGJFET sensor, as a back-gate

FET structure, can be used for dynamic analysis of droplet evaporation and can predict the chemical components by precisely measuring ToE for industrial and laboratory applications. We have also simulated the sensor in COMSOL software to provide insights into the physics of the ID-OGJFET. We have shown that the hole carriers in the p-type channel contribute to all the drain outputs in the ID-OGJFET. The simulation predicts the trend of the ID-OGJFET's I-V curve that shows the p-type behavior of the device with a back gate. The current paper introduces ID-OGJFET integrated with a scalable electro-fluidic packaging technology and portable readout sensor, a highly desirable configuration for variegated industrial applications requiring a portable sensor.

8.7. Appendix

8.7.1. Simulation

The simulation process was performed within the semiconductor module of COMSOL Multiphysics software, aiming to estimate the sensor's electrical behavior, including its I-V curves, in the reverse bias condition of the ID-OGJFET (see Fig. 8-5). Within the COMSOL geometry builder, we construct a 2D model geometry of ID-OGJFET. However, in the model, we have used a smaller channel between fingers (100 μm) to verify only the I-V trends in the real chip, while the channel width is ~ 475 μm in the actual chip. A boundary condition was applied to the simulation in which the open-gate area and the surrounding sensor were treated as insulation. Opting for silicon as the material composition for both the p-type and n-type sections, we determine and configure the doping levels using analytic doping models 1 and 2 within the semiconductor section. For modeling the p-n junction between the p-type and n-type layers (see Fig. 8-1), we employ the continuity/heterojunction model, ensuring comprehensive representation. We implement the Shockley-Read-Hall (SRH) trapping model across the whole chip area, spanning both n-type and p-type layers to capture the intricacies of carrier trapping. Aligning with the fabrication process, metal contacts are subject to the ohmic contact model, ensuring fidelity to real-world fabrication processes. Before its application to the ID-OGJFET, the model underwent calibration using a single-channel OG-JFET, consistent with established practices in 2D simulation and semiconductor device modeling. During calibration, parameters such as Vgs and out-of-plane thickness were adjusted to ensure alignment between simulation outcomes and experimental data.

The Veq values (in the ohmic mode of back gate) within the COMSOL model encompass numerous experimental variables, necessitating calibration against the 2D model to account for multiple non-idealities inherent in fabricated chips and provide accurate estimations. This calibration process involved comparing the Ids-Vgs characteristics of a single channel chip with simulation data, from which a calibration formula for back gate voltage was derived: Vgs (exp) = Vgs (sim) × A + B. Subsequently, values for A and B were determined to be 6.2 and 0.092, respectively, and integrated into the model to refine its accuracy.

Acknowledgment

The authors would like to thank CMC Microsystems for the provision of services that facilitated this research.

8.8. References

[1] J. Martinka, P. Rantuch, and I. Wachter, "Impact of Water Content on Energy Potential and Combustion Characteristics of Methanol and Ethanol Fuels," Energies 2019, Vol. 12, Page 3491, vol. 12, no. 18, p. 3491, Sep. 2019, doi: 10.3390/EN12183491.

[2] T. Nogueira et al., "Bioethanol and Biodiesel as Vehicular Fuels in Brazil — Assessment of Atmospheric Impacts from the Long Period of Biofuels Use," Biofuels - Status and Perspective, Sep. 2015, doi: 10.5772/60944.

[3] A. Leo, A. G. Monteduro, S. Rizzato, A. Milone, and G. Maruccio, "Miniaturized Sensors for Detection of Ethanol in Water Based on Electrical Impedance Spectroscopy and Resonant Perturbation Method—A Comparative Study," Sensors, vol. 22, no. 7, 2022, doi: 10.3390/s22072742.

[4] J. A. Joseph, S. Akkermans, and J. F. M. Van Impe, "Processing Method for the Quantification of Methanol and Ethanol from Bioreactor Samples Using Gas Chromatography-Flame Ionization Detection," ACS Omega, vol. 7, no. 28, pp. 24121–24133, Jul. 2022, doi: 10.1021/ACSOMEGA.2C00055/SUPPL_FILE/AO2C00055_SI_001.PDF.

[5] T. P. Vello, R. F. De Oliveira, G. O. Silva, D. H. S. De Camargo, and C. C. B. Bufon, "A simple capacitive method to evaluate ethanol fuel samples," Scientific Reports 2017 7:1, vol. 7, no. 1, pp. 1–7, Feb. 2017, doi: 10.1038/srep43432.

[6] S. K. Tulashie, A. P. Appiah, G. D. Torku, A. Y. Darko, and A. Wiredu, "Determination of methanol and ethanol concentrations in local and foreign alcoholic drinks and food products (Banku, Ga kenkey, Fante kenkey and Hausa koko) in Ghana," Int J Food Contam, vol. 4, no. 1, pp. 1–5, Oct. 2017, doi: 10.1186/S40550-017-0059-5/TABLES/3.

[7] M. Bedner, J. A. Murray, A. A. Urbas, W. A. Maccrehan, and W. B. Wilson, "A Comparison of Measurement Methods for Alcohol-Based Hand Sanitizers," 2019, doi: 10.6028/NIST.IR.8342.

[8] P. Tipparat, S. Lapanantnoppakhun, J. Jakmunee, and K. Grudpan, "Determination of ethanol in liquor by near-infrared spectrophotometry with flow injection," Talanta, vol. 53, no. 6, pp. 1199–1204, Mar. 2001, doi: 10.1016/S0039-9140(00)00610-X.

[9] T. Ozturk and H. Y. Erbil, "Evaporation of water-ethanol binary sessile drop on fluoropolymer surfaces: Influence of relative humidity," Colloids Surf A Physicochem Eng Asp, vol. 553, pp. 327–336, Sep. 2018, doi: 10.1016/J.COLSURFA.2018.05.076.

[10] A. N. Sterlyagov, V. N. Letushko, M. I. Nizovtsev, and V. Y. Borodulin, “Experimental study of evaporation of sessile droplets of the water-ethanol solution with different concentrations,” J Phys Conf Ser, vol. 1105, no. 1, 2018, doi: 10.1088/1742-6596/1105/1/012068.

[11] E. Preter, R. A. Katims, V. Artel, C. N. Sukenik, D. Donlagic, and A. Zadok, “Monitoring and analysis of pendant droplets evaporation using bare and monolayer-coated optical fiber facets,” Opt Mater Express, vol. 4, no. 5, p. 903, 2014, doi: 10.1364/ome.4.000903.

[12] A. Prasad, -H Lin, V. R. Rao, and A. A. Seshia, “Monitoring sessile droplet evaporation on a micromechanical device †,” 2014, doi: 10.1039/c4an01389a.

[13] C. Liu and E. Bonaccurso, “Microcantilever sensors for monitoring the evaporation of microdrops of pure liquids and mixtures Microcantilever sensors for monitoring the evaporation of microdrops of pure liquids and mixtures,” 2023, doi: 10.1063/1.3276716.

[14] J. Arcamone, E. Dujardin, G. Rius, F. Pérez-Murano, and T. Ondarçuhu, “Evaporation of femtoliter sessile droplets monitored with nanomechanical mass sensors,” Journal of Physical Chemistry B, vol. 111, no. 45, pp. 13020–13027, 2007, doi: 10.1021/jp075714b.

[15] S. Sbarra, L. Waquier, S. Suffit, A. Lemaître, and I. Favero, “Optomechanical measurement of single nanodroplet evaporation with millisecond time-resolution,” Nature Communications 2022 13:1, vol. 13, no. 1, pp. 1–7, Oct. 2022, doi: 10.1038/s41467-022-34219-3.

[16] T. Yakhno, A. Pakhomov, A. Sanin, V. Kazakov, R. Ginoian, and V. Yakhno, “Drop drying on the sensor: One more way for comparative analysis of liquid media,” Sensors (Switzerland), vol. 20, no. 18, pp. 1–12, 2020, doi: 10.3390/s20185266.

[17] G. Tian, X. Q. Zhang, M. S. Zhu, Z. Zhang, Z. H. Shi, and M. Ding, “Quantification of ethanol in plasma by electrochemical detection with an unmodified screen printed carbon electrode,” Scientific Reports 2016 6:1, vol. 6, no. 1, pp. 1–6, Mar. 2016, doi: 10.1038/srep23569.

[18] A. Errachid, N. Zine, J. Samitier, and J. Bausells, “FET-Based Chemical Sensor Systems Fabricated with Standard Technologies,” Electroanalysis, vol. 16, no. 22, pp. 1843–1851, Nov. 2004, doi: 10.1002/ELAN.200403072.

[19] M. Kaisti, “Detection principles of biological and chemical FET sensors,” Biosens Bioelectron, vol. 98, pp. 437–448, Dec. 2017, doi: 10.1016/J.BIOS.2017.07.010.

[20] K. Choi, J. Y. Kim, J. H. Ahn, J. M. Choi, M. Im, and Y. K. Choi, “Integration of field effect transistor-based biosensors with a digital microfluidic device for a lab-on-a-chip application,” Lab Chip, vol. 12, no. 8, pp. 1533–1539, 2012, doi: 10.1039/c2lc21203j.

[21] L. Kergoat et al., “A water-gate organic field-effect transistor,” Advanced Materials, vol. 22, no. 23, pp. 2565–2569, 2010, doi: 10.1002/adma.200904163.

[22] R. X. He et al., “Solution-gated graphene field effect transistors integrated in microfluidic systems and used for flow velocity detection,” Nano Lett, vol. 12, no. 3, pp. 1404–1409, Mar. 2012, doi: 10.1021/NL2040805.

[23] D. Sadighbayan, M. Hasanzadeh, and E. Ghafar-Zadeh, “Biosensing based on field-effect transistors (FET): Recent progress and challenges,” TrAC - Trends in Analytical Chemistry, vol. 133. Elsevier B.V., Dec. 01, 2020. doi: 10.1016/j.trac.2020.116067.

[24] A. Panahi, D. Sadighbayan, S. Forouhi, and E. Ghafar-Zadeh, “Recent advances of field-effect transistor technology for infectious diseases,” Biosensors (Basel), vol. 11, no. 4, 2021, doi: 10.3390/bios11040103.

[25] A. Panahi and E. Ghafar-Zadeh, “A Hybrid Microfluidic Electronic Sensing Platform for Life Science Applications,” Micromachines (Basel), vol. 13, no. 3, 2022, doi: 10.3390/mi13030425.

[26] B. M. Lowe, Y. Maekawa, Y. Shibuta, T. Sakata, C. K. Skylaris, and N. G. Green, “Dynamic behaviour of the silica-water-bio electrical double layer in the presence of a divalent electrolyte,” Physical Chemistry Chemical Physics, vol. 19, no. 4, pp. 2687–2701, 2017, doi: 10.1039/c6cp04101a.

[27] A. Panahi, H. O. Tabrizi, P. Mangannavar, O. Chebotarev, A. Fung, and E. Ghafar-Zadeh, “Open-Gate Junction Field Effect Transistor (OG-JFET) for Life Science Applications: Design, Implementation and Characterization,” IEEE Sens J, vol. XX, no. XX, 2021, doi: 10.1109/JSEN.2021.3121339.

[28] B. Smaani, N. Paras, S. B. Rahi, Y. S. Song, R. Yadav, and S. Tayal, “Impact of the Self-Heating Effect on Nanosheet Field Effect Transistor Performance,” ECS Journal of Solid State Science and Technology, vol. 12, no. 2, p. 021005, Feb. 2023, doi: 10.1149/2162-8777/ACB96B.

[29] B. M. Tenbroek, M. S. L. Lee, W. Redman-White, R. John T Bunyan, and M. J. Uren, “Self-heating effects in SOI MOSFET’s and their measurement by small signal conductance techniques,” IEEE Trans Electron Devices, vol. 43, no. 12, pp. 2240–2248, 1996, doi: 10.1109/16.544417.

[30] X. Xu and L. Ma, “Analysis of the effects of evaporative cooling on the evaporation of liquid droplets using a combined field approach,” Scientific Reports 2015 5:1, vol. 5, no. 1, pp. 1–6, Feb. 2015, doi: 10.1038/srep08614.

[31] K. Zhang, L. Ma, X. Xu, J. Luo, and D. Guo, “Temperature distribution along the surface of evaporating droplets,” Phys Rev E Stat Nonlin Soft Matter Phys, vol. 89, no. 3, p. 032404, Mar. 2014, doi: 10.1103/PHYSREVE.89.032404/FIGURES/8/MEDIUM.

Chapter 9 Contributions, Future Work, and Conclusion

This thesis presents comprehensive and significant progress in enabling OG-JFET technology for biochemical sensing, transforming it from a novel concept to a viable technology. Key contributions include the design of OG-JFET sensors for chemical applications, thorough literature reviews, and simulations using COMSOL Multiphysics to explore charge-sensing physics. Additionally, the research involved implementing innovative microfluidic integration methods and developing portable characterization systems, which validated the sensor's performance and enabled its use in various applications, including pH, DNA, and neutrophil cell sensing. These advancements lay a solid foundation for future exploration of OG-JFET as a versatile biosensor.

9.1. Summary of Contributions

In this research, the main contributions are listed as follows:

1. Design of a sensor for chemical applications using OG-JFET technology for the first time: Despite a recent publication [1] showing the advantages of optical sensing with OG-JFET technology, there has yet to be research on using OG-JFET for direct-contact chemical sensing applications. In our work, we designed two chips to address this gap. The first chip design included a common source and multiple drains, facilitating multiplexing and allowing for simultaneous measurements from various sensors. This innovative design enables comprehensive analysis of the chemical environment, demonstrating the potential of OG-JFET technology for chemical/biomolecular sensing applications.
2. We conducted a comprehensive literature review to elucidate the unique benefits of OG-JFET devices compared to other FET sensors introduced thus far. This study delved into various FET sensors' structural nuances, highlighting the advantages of the OG-JFET sensor's novel design and potential for diverse applications.

3. Simulation and modeling of OG-JFET sensor Using COMSOL Multiphysics: We used COMSOL for the first time as a CAD tool to simulate the device and explore its charge-sensing physics. The simulation models were used to understand the device's DNA and pH-sensing principles. They provide insight into the sensor's charge-sensing characteristics.
4. Implementation of two OG-JFET chip designs and integration with microfluidics with customized electrofluidic packaging.
5. Collaborate with other BioSA team members to design and implement electrical fixtures: one for the standard source design of OG-JFET and another for the interdigital OG-JFET (ID-OGJFET) sensor.
6. Characterization of the OG-JFET using probe station/semiconductor analyzer and electro-fluidic fixtures developed to acquire the device's electronic properties.
7. The application of OG-JFE for pH sensing is an essential proof of concept of the H+ sensitivity capability of OG-JFET that could be used in future endeavors for DNA or RNA sensing.
8. Application of OG-JFET for Neutrophil cell sensing. Our experiments successfully demonstrated the use of OG-JFET technology for sensing the attachment of neutrophil cells through the charge-sensing mechanism of OG-JFET. This breakthrough opens new avenues for cell-related research, highlighting the potential of OG-JFET sensors in biomedical applications where cell attachment and interaction monitoring are crucial. Future research can build upon these findings to explore various cell types and their behaviors, significantly advancing the field of cellular sensing.

9. Application of OG-JFE for DNA sensing and introduction of the use of the OG-JFET as a high-potential sensing platform for integration with the emerging DNA storage on a chip

10. Molecular dynamics simulation of the interaction of DNA with the sensor’s sensing surface to understand the surface potential change when DNA exists on the surface in an extreme dehydration state. Furthermore, the atomistic simulations provide essential information about the surface potential change upon interaction with a biomolecule, which leads to surface potential change and, consequently, changes in the sensor’s conduction.

11. Integrating OG-JFET with microfluidics using two distinct innovative methods to achieve continuous flow or stationary fluidics on the chip. The novel microfluidics scheme consisted of two planar 2D parts that, when assembled, created a 3D microfluidic structure for safely delivering fluids to the sensing site. This setup facilitated the controlled delivery of solutions to the sensor, enabling the study of its charge-sensing capabilities.

12. A portable readout system was also developed, enabling the characterization of OG-JFET sensors by connecting the portable device to a laptop to obtain I-V curves. This portable device was crucial for developing portable sensing technologies using OG-JFET.

9.2. Future works

In this thesis, we demonstrate and discuss the recent progress made during this PhD study, which has significantly contributed to developing novel sensing technology. The research has examined the operational principles and charge-sensing mechanisms of a novel field-effect transistor (FET) OG-JFET device in contexts involving liquids and biomolecules. This device, previously unexplored for such purposes, demonstrates significant potential. Additionally, this research introduces innovative design strategies and microfluidic interfacing techniques, providing valuable insights for future advancements in this technology across various applications. Furthermore, this thesis presents a portable characterization system, which significantly simplifies the operation of this sensor as a portable diagnostic device and facilitates future users' adoption of this technology. The integration of OG-JFETs with novel microfluidic systems and customized electrofluidic packaging has proven effective in controlling fluid delivery to the sensing site, enhancing the accuracy and reliability of biochemical measurements. Overall, the methodologies and knowledge developed in this thesis lay a foundation for creating next-generation chemical or biological sensors based on the OG-JFET technology.

9.2.1. Specific detection of a target DNA in solution

We have shown the potential of OG-JFET for DNA sensing as a model of charged electrolytes on the sensor. The most critical next step is to work on the specific detection capability of OG-JFET by functionalizing the open gate area with surface chemistry to immobilize DNA probes on the

surface and detect DNA targets in the samples in the solution mode. For instance, silane chemistry is one of the most common surface chemistries applied to FET-based sensors. The process could be used on OG-JFET. This means that we need to keep a uniform layer of SiO_2 or Si_3N_4 in the open gate area of OG-JFET, which usually needs to be removed in the standard fabrication process offered at the time of writing this thesis. However, for any surface functionalization, we need to ensure a uniform layer of the dielectric layer. To functionalize the surface of a SiO_2 layer on a FET sensor for the detection of DNA, the first step is to clean and activate the SiO_2 surface (assuming having a uniform layer of SiO_2 as the top layer). There are well-established methods for the preparation of the surface. The surface is typically cleaned using a piranha solution, which is a mixture of sulfuric acid (H_2SO_4) and hydrogen peroxide (H_2O_2). This step removes organic contaminants and provides a hydrophilic surface rich in hydroxyl groups. After thoroughly rinsing with deionized water and drying, the surface is activated using silanization. A joint silanizing agent, such as (3-aminopropyl) triethoxysilane (APTES), introduces amino groups onto the surface. The SiO_2 layer is immersed in an APTES solution, typically in anhydrous ethanol, for a defined period, followed by rinsing with ethanol and curing at an elevated temperature to ensure strong bonding of the silane molecules to the SiO_2 surface.

The next step involves immobilizing DNA probes on the functionalized SiO_2 surface. The amino groups introduced during silanization covalently attach DNA probes via a cross-linker, such as glutaraldehyde, which reacts with the amino groups on the surface and the amine-modified DNA probes. The process begins by incubating the sensor in a glutaraldehyde solution to form aldehyde-functionalized surfaces. After rinsing to remove excess glutaraldehyde, the surface is exposed to amine-modified single-stranded DNA (ssDNA) probes. These probes hybridize specifically with target DNA sequences in the sample. The immobilization process typically occurs under controlled conditions to ensure optimal probe density and orientation. Finally, unreacted aldehyde groups are blocked using a blocking agent such as ethanolamine, and the sensor is rinsed and dried, making it ready for DNA hybridization and subsequent detection.

9.2.2. Chip design and fabrication for specific analyte detection

According to the fabrication process of OG-JFET, there is a ~ 500 nm well depth in the open gate area (developed due to processing of stacked layer of SiO_2-Si_3N_4), which needs to be considered in designing any surface chemistry and surface modification in future works. This could cause

non-uniformity and possible surface instability when a surface modification is tried on the sensor, such as graphene, graphene oxide, or modifications like silane chemistries. While we did not try functionalization of the surface and did not face this challenge practically, this huge non-uniformity should be considered, especially for short-channel OG-JFETs. One solution to this issue is to ask manufacturers to leave a particular layer of stacked SiO_2-Si_3N_4 or one of them on the open gate area for a smoother oxide surface. One of the causes of errors in the measurement could be the non-uniformity of the oxide layer on the sensor, which might cause variations in the charge sensitivity of devices.

9.2.3. Device topologies

The OG-JFET could be operated with a double gate, which requires having a solution gate on top and a back gate uniformly designed on the backside of the chip. This configuration would enable an extended gate from the solution side and introduce a new sensing modality with the solution gate. Additionally, isolating the single channel from the rest of the chip is another important future step for achieving a single isolated channel. The p-type sensing layer is uniformly shared under all devices in the current structure. However, to create a unique sensing channel, the channel could be isolated by N++ implantation or etching the p-type channel and then filling the gap with a dielectric. Furthermore, the shared back gate must be specified for each channel if the top layer is isolated. Further fabrication efforts are required to assign a separate back gate to each isolated channel on the top.

9.2.4. Microfluidics integration

We have provided two distinct methodologies to apply a microfluidics channel or well onto the OG-JFET. The first is based on 3D printing modeling and uses PDMS as the base material for microfluidic channel fabrication. The second one is entirely based on 3D printing and uses off-the-shelf electronics components such as spring-loaded connectors, which allows rapid prototyping of fluidics compartment fabrication and integration. The following steps in the microfluidics integration could be scaling down the channel microfabrication with higher precision mold fabrication techniques, such as photolithography and soft lithography, to have a channel with dimensions as low as the OG-JFET channel size (minimum viable size 5 μm) for the standard single channel OG-JFETs. Furthermore, more research is required to apply novel emerging 3D

microfluidics on the OG-JFET due to the adaptability of the sensor to 3D structures compared to the 2D ones, which causes considerable challenges in controlling the leakages to surroundings.

9.3. Conclusions

This thesis has successfully advanced the field of biochemical sensing by exploring the novel open-gate junction field-effect transistor (OG-JFET) technology. Through a comprehensive investigation that included designing innovative OG-JFET sensors, conducting extensive literature reviews, and employing multiscale and Multiphysics simulation techniques, we have demonstrated the potential of OG-JFET for various chemical and biological sensing applications. Implementing microfluidic integration methods and developing portable characterization systems have further validated the practical utility and versatility of OG-JFETs as a new multipurpose sensing platform. This research establishes a solid foundation for future OG-JFET development. It provides valuable insights that can be applied to creating next-generation biosensors, paving the way for significant advancements in sensing technologies by adopting OG-JFET.

9.4. Reference

[1] V. Adinolfi and E. H. Sargent, 'Photovoltage field-effect transistors,' Nature 2017 542:7641, vol. 542, no. 7641, pp. 324–327, Feb. 2017, doi: 10.1038/nature21050.

Appendices

In this thesis, in addition to the contributions in the form of journal papers, several publications in the form of conferences or abstracts were also contributed.

A1. Conference paper 1

A New Foundry-Based Open-Gate Junction Field-Effect Transistor (OG-JFET) as Electronic Sensing Platform (ESP) for Life Science Applications

Authors: Abbas Panahi, Hamed Osouli Tabrizi, Priyadarshini Mangannavar, Oleg Chebotarev, Andrew Fung, Ebrahim Ghafar-Zadeh

Conference: Presented at IEEE Sensors Conference, 2021 (Virtual)

This conference paper introduces the foundry OG-JFET technology, characterization, simulation, and pH test results and discusses its novelty as a new ion-sensitive FET sensor.

Abstract:

An electronic sensor platform based on ion-sensitive open-gate junction field-effect-transistors (OG-JFET) is introduced for life science applications. OG-JFET is fabricated using an established and mass-producible method. A thin layer (1.6 µm) of p-type silicon is epitaxially grown on thick (450 µm) n-type silicon to create a vertical p-n junction. The p-type layer is the main channel, with two ohmic contacts as the source and drain. OG-JFET in our design showed a 52.12 mV/pH sensitivity and 16 mV hysteresis with a 3 µA/hour drift rate. Also, a COMSOL Multiphysics model is introduced to design OG-JFET efficiently.

Keywords—Field-effect transistor (FET), biosensor, ISFET, MEMS, COMSOL, Junction Field-effect Transistor (JFET), BioFET

A1.1. Introduction

Field-effect transistors (FET) based biosensors have received significant attention over the last two decades for biomedical applications [1]. FET sensors have been proven to be low-cost, highly

sensitive, label-free, seamless miniaturization with the perfect integration capability with Lab-on-a-chip (LOC) technologies [2]. Biological FETs (BioFET) have the same structure as ion-sensitive FETs (ISFETs), but with this subtle difference, a new biorecognition element has already been covered at the gate. So far, various structures for BioFETs have been introduced [3]. Most of them are based on cleanroom microfabrication processes, which are not scalable due to the complexity of the fabrication process and the materials used, such as carbon-based 2D materials [3]. While showing extraordinary sensitivity and improving other sensing features, these sensors are not scalable in mass fabrication. Many BioFET structures are based on the well-established and almost flawless Complementary Metal Oxide Semiconductors (CMOS) technology, such as an extended gate, a floating gate, a floating-control gate, etc. The unmodified CMOS-based ISFETs (or BioFETs) are based on mass-producible CMOS technology. However, disadvantages accompany unmodified CMOS ISFET sensors [4]. The long via pads that connect the gate to the channel are the source of parasitic capacitance errors. Also, the necessity of using bulky Ag/AgCl electrodes in solution hampers further integration with Lab-on-a-Chip technologies for further personal health monitoring utilization.

In this work, we introduce a new technology for bio/chemical sensing applications that is structurally new in the ISFET sensing area. While the JFET platform already exists, the application for biosensing is new. The sensor is based on a planar JFET structure with an open gate for introducing chemical/biological samples. In this structure, an integrated back-gate avoids needing a bulky electrode in solution, such as Ag/AgCl. Chemical sensing was tested by studying the sensor's sensitivity to different [H+] concentrations in the buffer solution (PBS). Previously, the same technology was used with a quantum dot sensing layer to demonstrate photovoltage field-effect transistors, pushing the infrared detection limits in silicon [5] by taking advantage of the back-gated JFET structure for signal amplification. Porous silicon junction field-effect transistor (PSJFET) and cSi-Au-JFET sensors are another variant of JFET that has been applied for NO_2 detection [6], [7]. To the best of our knowledge, the present work using the electronic sensor platform offered by CMC Microsystems is the first reported application of the OG-JFET structure in chemical sensing.

A1.2. Proposed Method and Materials

A1.2.1. OG-JFET Sensing Mechanism

An open-gate JFET consists of a p-type layer grown on top of the n-type channel, supported by a back gate, as shown in Figure A1-1.

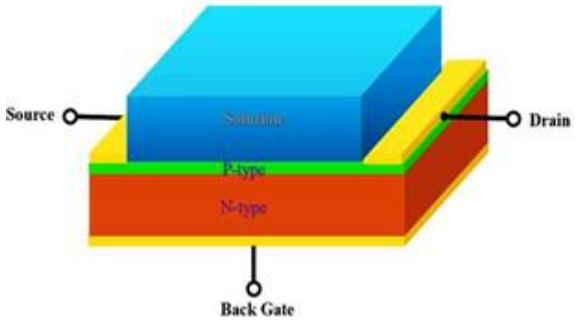


Figure A1- 1. The structure of the open gate junction field affects the transistor sensor.

As shown in Fig. A1-1, the sensor consists of a p-type layer on a very thick N-type silicon layer. The gate is on the sensor's backside, which modulates the channel conductance with voltage biases. The sensor is exposed to the chemical/biological solution/materials through the open gate area's top layer between the source and drain. Electrons/holes flow from the source to the drain (or opposite) in the p-type channel when the sensor is reversely biased. A very thin oxide layer on the outer p-type layer usually happens as the native oxide. This very thin layer of oxide interacts with solution ions and water molecules and creates a double-layer capacitance in the solution (for more detailed information, please read [3]). The double layer gives birth to a stacked layer of ions that modulate the oxide surface charge with the concentration of ions in the solution or, in other words, the potential in the electrolyte solution, which includes the biological materials and a place where chemical reactions occur. The sensor should work in reversed-biased conditions to limit the gate leakages and ensure the p-n junction diode is turned off.

A1.2.2. Design and Fabrication Processes

The fabrication of OG-JFET is based on a standard VLSI (very large-scale integration) process at Institut interdisciplinaire d'innovation technologique (3IT) at Université de Sherbrooke. In this standardized process, an epitaxial p-type (conduction channel with doping of ~ 5×10^{15}) with 1.6 µm thickness was grown on 450 µm n-type silicon substrate with estimated doping of 1×10^{18} cm^3.

Additionally, ion implantation was performed to create an ohmic source and drain contacts on the epitaxial channel, followed by lithographic aluminum patterning as a contact. The metal is passivated by a Si_3N_4. A detailed standard fabrication process for OG-JFET is shown in Figure A1-2. The fabrication begins with alignment marker patterning on a silicon wafer with an orientation of <100> and 100 mm diameter of approximately 420 µm +/- 25 µm thickness with a resistivity of 0.006 to 0.02 Ohm-cm. This step is followed by PECVD deposition of 200 nm +/- 25 of SiO_2 on the sensor top silicon later. After the deposition of SiO_2, a layer of photoresist would be deposited, which is followed by an etching process to open the space for implantation, which is required for metallization and making silicon ready for drain and source contact; before metallization is continued, a back and front annealing will be conducted, which will help to consolidate metallization. Afterward, all the front areas will be encapsulated using 500 nm thick Si_3N_4. The final fabrication stage will be opening the gate area and contact pads, as shown in Figure A1-2.

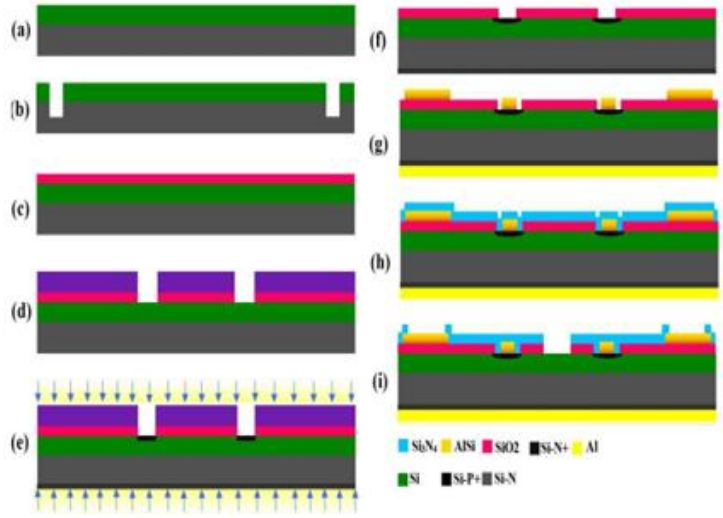


Figure A1- 2. The standard fabrication process of OG-JFET.

A1.2.3. OG-JFET Design

The sensor layout design was performed using L-Edit software (Mentor Graphics) based on the design kit provided by CMC Microsystem. Fig. A1-4 shows a schematic of the fabricated sensor.

The sensor consists of seven sensing channels (opened gate) surrounded by eight pads in the chip's primitive, with characteristics presented in Table A1-1.

A1.2.4. COMSOL Multiphysics Simulation of OG-JFET

To extract the OG-JFET's electronic transfer characteristics, a multi-physics finite element simulation was performed. In this regard, COMSOL Multiphysics 5.5 software was used to model the semiconductor device. Accordingly, a 2D sensor model was designed in COMSOL with each channel's specified size and dimensions according to the geometrical design and information provided in Table A1-1.

Table A1- 1. Design parameters values for OG-JFET

Parameters	Value
P-type length (L_{OG})	100 µm
P-type doping (NA)	5×10^{15} /cm^3
P-type channel thickness (tp)	1.6 µm
Channel depth (3D, not shown)	1000 µm
N-type length (L_{OG})	100 µm
N-type thickness (tn)	450 µm
N-type doping (N_D)	1×10^{18} /cm^3
Source / drain length and width (Ls)	20 µm and 1000 µm
Source/drain implantation doping (P++)	2×10^{16} /cm^3
N++ doping	~ 1×10^{19}
Source/Drain offset (Lo)	10 µm
Opened gate surface	silicon with native silicon oxide

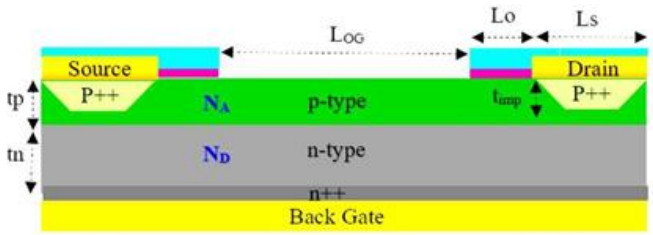


Figure A1- 3. OG-JFET design parameters that can be controlled in fabrication.

A1.2.5. Fluidic Fixture

Following the replica molding approach, a microfluidic chamber was fabricated with PDMS to test OG-JFET with fluidic samples with different pH. A PCB was designed and manufactured, then

put on top of the four-pillar 3D-printed structure to hold the PDMS microfluidics and connect the sensor to the semiconductor analyzer using spring-loaded connectors, as shown in Fig. A1-5. The PCB has a switch by which one can select the channel (see Fig. A1-4) for doing the tests.

A1.3. Results and Discussions

A1.3.1. OG-JFET Transfer Characteristics

All the measurements were conducted using a semiconductor analyzer device (Keithley 4200A-SCS Parameter Analyzer) connected to the sensor through BNC connectors on the PCB board (See Fig A1-5). The switch on the PCB was used to connect different drains (see Fig A1-4) of OG-JFETs to the BNC and semiconductor analyzer. All the tests were done by biasing the sensor in reversed bias mode by applying a negative voltage to the drains and a positive voltage to the back gate. Figure A1-6 shows the Ids-Vds curve of the dry OG-JFET and the simulation results.

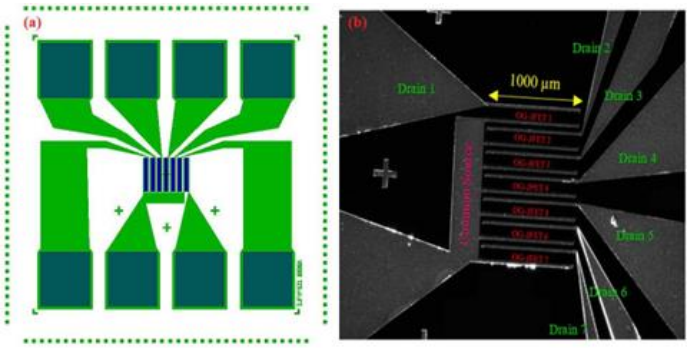


Figure A1- 4. The fabricated sensor consists of seven channels and one common source. (a) layout design, (b) the fabricated sensor

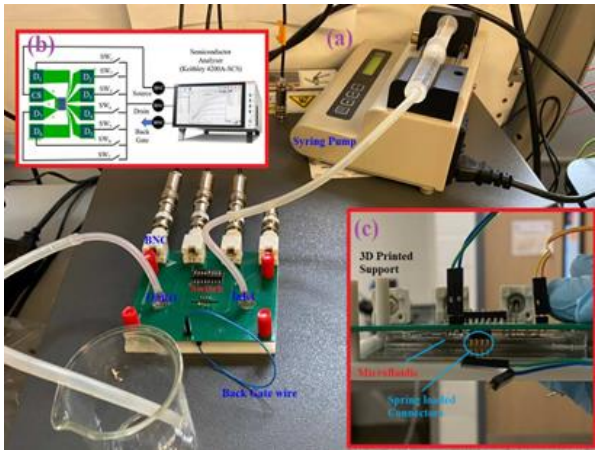


Figure A1- 5. The test setup used for pH tests on-chip. (a) connection of the syringe pump and the microfluidic channel; (b) the circuit schematic; (c) a closeup of the chip, microfluidic, 3D printed structure, and spring-loaded connectors.

Based on the Ids-Vds curve of OG-JFET for the design shown in Fig. A1-4, the sensor responded like the conventional JFET structures. However, we cannot see a perfect linear saturation region due to the long channel length (here, 100 μm). The gate bias voltage is positive, and the drain-source voltage is negative, which means increasing the gate voltage would dampen the channel conductance and decrease the current. The sensor function was also tested with the COMSOL simulation package based on the size and parameters defined in Table A1-1 and geometry in Fig. A1-4. The Ids-Vds curve we got from COMSOL is shown in Fig. A1-6. COMSOL simulation predicts the sensor response like the experiment curve trend; however, there is a specific error (11.58%, at Vds=10 V) that comes from the non-idealities of the fabrication process and likely variances of geometries and doping levels. OG-JFET sensor was tested under different pH solutions to analyze its sensitivity towards ion concentration changes in the PBS buffer solution (here [H+] concentration). Different pH solutions were prepared by adding HCL (0.1 M) and NaOH (0.1 M) solutions to the PBS and measuring the pH with a standard pH meter.

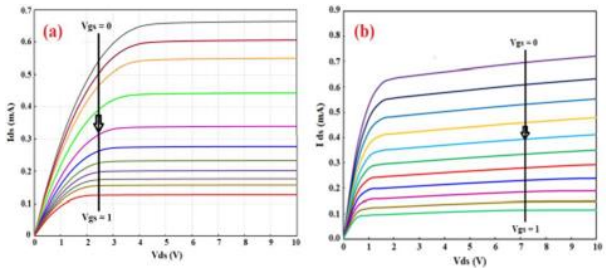


Figure A1- 6. Ids-Vds curve of OG-JFET for reversed bias condition. (a) COMSOL result; (b) experiment results

The solution was then directed onto the sensor through the PDMS microfluidic channel (shown in Fig. 5). The pH test results are shown in Figure A1-7. The sensitivity of OG-JFET is in the Nernst limit (<59 mV/pH), which shows a good sensitivity compared to the available SiO_2-gated ISFETs with sensitives between 40 to 50 mV/pH [3].

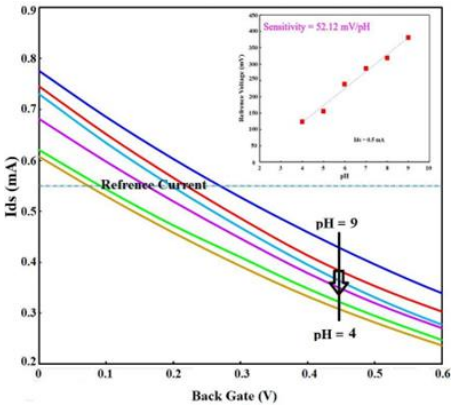


Figure A1- 7. OG-JFET response to different pH values. Inset: OG-JFET sensitivity at reference current of 0.5 mA and Vds = 5 V.

A1.4. Conclusion

OG-JFET has been introduced in this work as a new ion-sensitive field effect transistor (ISFET) based on a standard VLSI microfabrication process. OG-JFET is a mass-producible, highly sensitive, and large-sensing-area BioFET that can be tailored to different applications through layout design and microfluidic packaging design. In addition, we have performed a COMSOL simulation to model the sensor operation under various bias conditions. OG-JFET has been tested in solutions with different pH to record its response to ion concentrations (here [H+]). OG-JFET showed a sensitivity of 52.12 mV/pH, which is within the range of the standard ISFET sensing regime. However, the sensor's hysteresis in a pH load cycle was measured at 16 mV with a drift of 3 µA/hour. Based on the results and simulation studies, OG-JFET can be considered a new FET electronic sensing platform for different biosensing applications.

ACKNOWLEDGMENT

We want to acknowledge Mitacs and CMC Microsystems's support for providing products and services that facilitated this research, including Mentor Graphics, fabrication services using the Electronic Sensor Platform at 3IT, and engineering support.

A1.5. References

[1] Yu-Cheng Syu, Wei-En Hsu, Chih-Ting Lin, “Review—Field-Effect Transistor Biosensing: Devices and Clinical Applications”, ECS Journal of Solid State Science and Technology, 7 (7), 3196-3207, 2018

[2] Tanu Wadhera, Deepti Kakkar, Girish Wadhwa, Balwinder Raj. “Recent Advances and Progress in Development of the Field Effect Transistor Biosensor: A Review”. Journal of Elec Materi 48, 7635–7646 (2019). https://doi.org/10.1007/s11664-019-

07705-6

[3] Abbas Panahi, Deniz Sadighbayan, Saghi Forouhi, Ebrahim Ghafar- Zadeh, “Recent Advances of Field-Effect Transistor Technology for Infectious Diseases”, Biosensors 11, no. 4: 103, 2021, https://doi.org/10.3390/bios11040103

[4] M. Kaisti, “Detection principles of biological and chemical FET sensors,” Biosens. Bioelectron., vol. 98, no. July, pp. 437–448, 2017, doi: 10.1016/j.bios.2017.07.010.

[5] V. Adinolfi and E. H. Sargent, “Photovoltage field-effect transistors,” Nature, vol. 542, no. 7641, pp. 324–327, 2017, doi: 10.1038/nature21050.

[6] G. Barillaro, G. M. Lazzerini, and L. M. Strambini, “Modeling of porous silicon junction field effect transistor gas sensors: Insight into NO2 interaction,” Appl. Phys. Lett., vol. 96, no. 16, 2010, doi: 10.1063/1.3391620.

[7] M. Sainato, L. M. Strambini, S. Rella, E. Mazzotta, and G. Barillaro, “Sub-parts per million NO2 chemi-transistor sensors based on composite porous silicon/gold nanostructures prepared by metal- assisted etching,” ACS Appl. Mater. Interfaces, vol. 7, no. 13, pp. 7136–7145, 2015, doi: 10.1021/am5089633.

A2. Conference paper 2

A New Field-Effect Transistor-Based Sensor for Biosensing Applications

Authors: Abbas Panahi and Ebrahim Ghafar-Zadeh

Conference: Presented at 20th IEEE Interregional NEWCAS Conference (NEWCAS), 2022, Quebec, Canada

Abstract

This paper presents a new field-effect-based sensor for biosensing applications. The sensor is composed of a new structure based on the junction field effect transistor, or JFET, a well-known electronic transistor. To prepare the JFET for biosensing and solution-based sensing, the p-type JFET is opened from one side (the n-type layer is removed), allowing the application of a solution containing biochemical substances on top. The opened-gate area consists of silicon with a very thin layer of SiO2, which is naturally grown on silicon when exposed to the environment. The p-type channel length between a source and drain is about 100 µm, and its thickness is 1.6 µm with 1000 µm wideness. A standard source design is introduced, containing seven channels that further improve the sensing area (≈ 0.7 mm^2). Dried DNA demonstrates the biomolecular sensing capability of the open-gate junction field-effect transistor (OG-JFET). Experimental analysis showing a sensitivity of 30 µA/DNA- Concentration (ng/uL) for OG-JFET toward dry DNA.

Keywords—Open-Gate JFET, ISFET, Field-Effect Transistor, Biosensor, DNA Detection, MEMS, NEMS

A2.1. INTRODUCTION

Field-effect-based biosensors are becoming popular due to their unique sensing properties for biomolecular charge detection in the solution. Relying on charge sensing, field-effect transistor (FET) sensors can be utilized to detect solution charge variations due to the existence of biomolecules and their possible accompanying chemical reactions. The charge sensing in FET-based biosensors is done label-free, making it a strong candidate for detecting disease biomarkers that are extremely important for next-generation point-of-care (PoC) devices. Furthermore, Label-

free detection significantly simplifies the sensing process, which reduces the final cost of the sensor, which is cherished in PoC development. Biological field-effect transistors (BioFETs) are being used for various applications, from DNA detection to cell analysis to study the ions transport in biological cells [1], [2]. Different structures have been introduced in recent decades, showing considerable interest in these sensors [3]. The various structures developed, from the complementary metal-oxide-semiconductor (CMOS) based ion-sensitive FETs (ISFETs) that offered standard fabrication processes to FET structures based on organic and nanomaterials. However, their limited sensitivity in terms of material used and the structures led to the proposal of new physical structures and the utilization of novel materials such as carbon and nanomaterial [4], [5].

We have presented a new structure based on an open-gate junction field-effect transistor (OG-JFET) along this line. Standard microfabrication is executed to develop the sensor, enabling large-volume production. Relying on a back-gate, OG-JFET avoids the bulky top gate in solutions such as Ag/AgCl. Here, we have presented the dried-DNA results to show this sensor's efficacy for measuring surface charges without a top electrode. This characteristic is essential for alleviating packaging issues due to the necessity of using top electrodes. The OG-JFET technology has been used with a quantum dot sensing layer to validate photovoltage field-effect transistors by [6] exploiting the back-gated JFET structure. Porous silicon junction field-effect transistor (PSJFET) and cSi-Au-JFET sensors are another variant of JFET that has been used for gas detection [7], [8].

A2.1. SENSOR STRUCTURE

A2.2.1. OG-JFET Structure

The OG-JFET structure is based on conventional JFET structures in electronics, with this subtle difference in that the top gate (here, n-type) is removed to create an opened-gate area for exposing a p-type channel to the environment. As shown in Fig. A2-1, the sensor provides a back gate to control the channel's electronic transport performance. The back gate enables control over the channel conduction by applying voltages to the p-n junction in the structure. A positive voltage from the back gate and a negative from the drain with a zero-source voltage will put the sensor in reverse bias, which blocks the current from the back gate to the drain and vice versa.

A2.2.2. OG-JFET Sensing

As shown in Fig. A2-1., the sensor is made of a p-type layer on a very thick layer of support made of n-type silicon. A back gate is applied on the sensor's backside to modulate the channel's conductance with voltage bias. The chemicals and biomaterials can contact the p-type silicon in the opened top gate area. Electrons/holes flow from the source to the drain (or opposite) in the p-type channel when the sensor is reversely biased. When silicon is exposed to the environment, a specific silicon oxide layer will be created on the sensor's outermost layer, called native oxide. This thin layer of oxide interacts with the ions and molecular content of the solution, which leads to a change in the surface charge of silicon. The ion complexation on the surface of the oxide creates a double-layer capacitance that is the result of the ion layers created on the oxide surface. The double layer on the surface interacts with the bulk solution. As a result, the ions produced inside the solution due to biochemical reactions will affect the surface charge concentration, leading to a variation in the hole transport in the conduction channel. The potential levels on the sensor's surface are maximized at the surface and decrease to the potential of the bulk solution. The sensor should work in reversed-biased conditions to limit gate leakages and ensure the p-n junction diode is turned off.

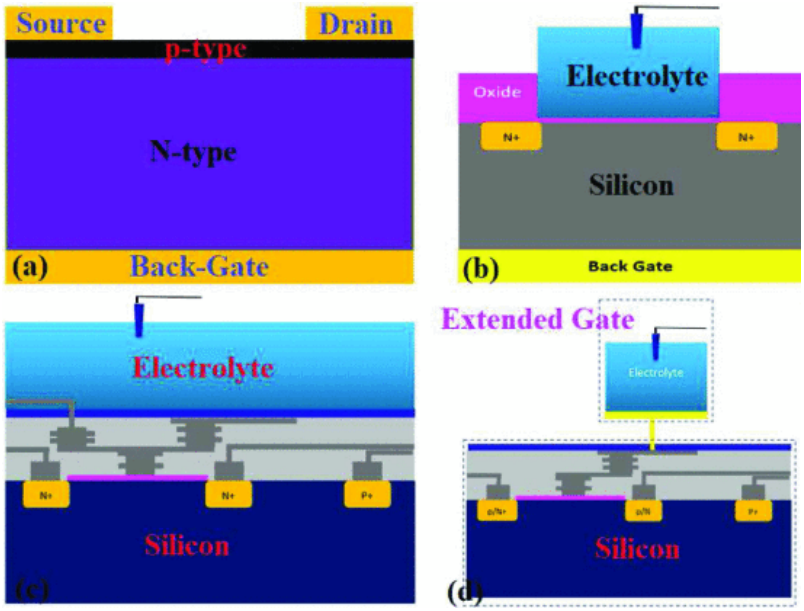


Figure A2- 1. The structure of the OG-JFET sensor in comparison to other structures. (a): OG-JFET, (b): back gate structure, (c): Modified CMOS structure, (d): CMOS extended gate

A2.2. OG-JFET DESIGN AND SIMULATION

The sensor layout was designed in L-Edit software using a standard fabrication process offered by CMC Microsystem [9]. Our previous publications [9] and [10] describe the fabrication process in detail.

A2.2.1. Sensor Desing

The sensor die dimension is about 10 mm×10 mm, creating a large design area. To make a larger sensing area, we designed a standard source structure that allows the connection of all sources while the drains are different. The structure of the sensor (See Fig. A2-1) suggests a uniform channel under the source and drain, a p-type silicon with a doping level of 5×10^{15} /cm^3. The distance between each channel on the sensor is 40 µm, and the channel 2D size on top is 100 µm × 1000 µm. The channel depth is uniform in all cross-sections, which is 1.6 µm. The geometry of the design is shown in Fig. A2-2. According to the designed geometry, a total sensing area of 0.7 mm2 is provided. The n-type layer is thick, as large as 450 µm, on which a thin layer of p-type silicon with a thickness of 1.6 µm is developed.

A2.2.2. Simulation

A finite element method (FEM) is used to simulate the sensor numerically. The COMSOL Multiphysics software models the sensor and solves the semiconductor equations. A 2D sensor model is created in the model builder of COMSOL. The boundary conditions were then applied to the sensor; however, the experimental conditions were not maintained due to software limits. For

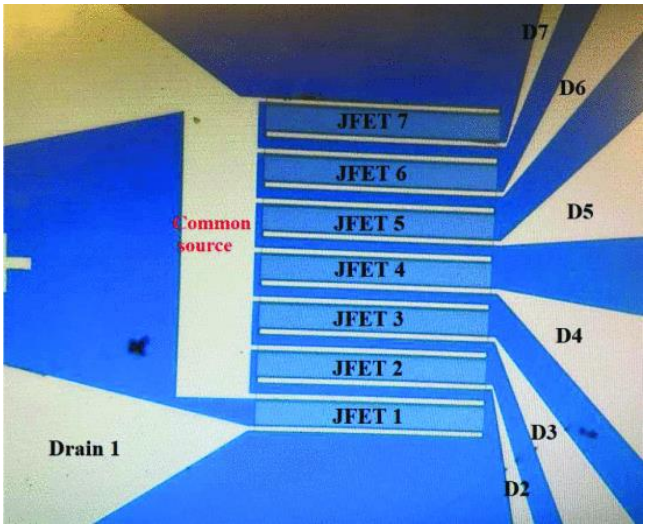


Figure A2- 2. The microscopic image of the fabricated sensor

instance, the top gate area is open to the environment; however, this was impossible to model in

COMSOL; thus, it is considered insulated. The model simplifications affect the accuracy of the simulation. However, considering the model simplifications, a linear function introduced the equivalent back gate voltage in the simulation. The sensor's geometry was meshed in COMSOL, which included the uniform meshes in the p-type area and unstructured mesh in the n-type region. The semiconductor equations, [10], were solved with finite element approximation equations, [10], were solved with finite element approximation.

A2.2.3. Biomolecular modeling

Here, single-strand DNA (ssDNA) molecules are modeled as single point charges on the sensor's surface to estimate the effect of surface charge effect. The modeling is performed based on an experiment conducted on mass monitoring of ssDNA molecules on the sensor. In the modeling, it is assumed that one charge element of the ssDNA molecule is attached to the sensor's surface and only this equivalent charge is participating in the charge effect. We have elaborated on this in [11].

A2.2.4. OG-JFET Electronic Characterization

The OG-JFET was tested with a probe station (MPI TS200-SE Probe Station) that connects the sensor to a semiconductor analyzer (Keithley 4200A-SCS Parameter Analyzer) device. To do so, the probstation was attached to the sensor. The sensor was placed on a glass slide on the conductive copper tape to create a back-gate connection. The back-gate connection was soldered. To characterize the sensor, we swept the drain voltage between 0 and 10 with a negative voltage, and then the back gate was changed from 0 to 1 in steps of 0.1 V. The back-gate voltage was positive to ensure the sensor operated in reverse bias conditions. However, in different experiments, the voltage range varied based on the condition of the experiment, but the same biasing scheme was preserved.

A2.3. Dry sensor I-V curves

The OG-JFET comprises a vertical p-n junction, creating a planar FET structure. The sensor can be operated in two modes. The first uses the p-n junction in forward bias. If such a condition is tested, the p-n junction will be opened after the voltage difference between the drain and back-gate is more than ≈ 0.67 V. After that, the drain experiences a very high drain current (> 1 mA). The I-V curves for OG-JFET operation are presented in Fig. A2-4. The figures show the I-V curve of a p-type channel for OG-JFET.

A2.3.1. COMSOL Simulation Result

The COMSOL Multiphysics software was used to simulate the OG-JFET sensor. The simulation results show that the experimental observation is correct as the results show the same trend as the experiments. According to the simulation results, the sensor response increases and then plateaus, but it is lower than the same experimental results even though the back-gate voltage is a linear approximation of the experimental results. That means the model contains errors that are inevitable due to FEM approximation.

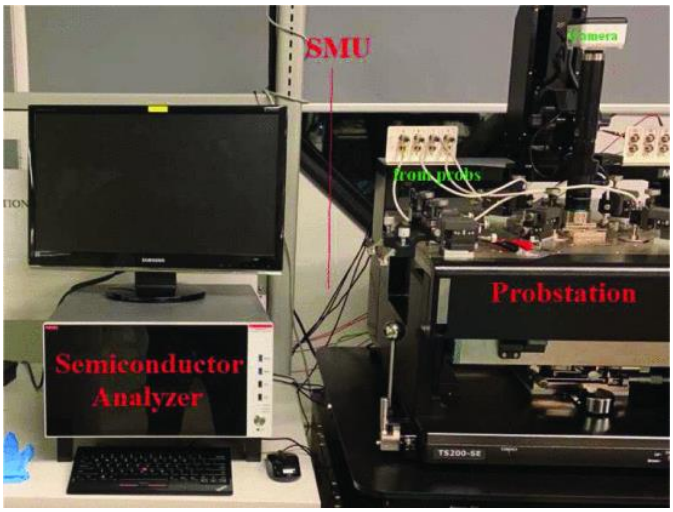


Figure A2- 3. The probstation and semiconductor analyzer are used to characterize the sensor.

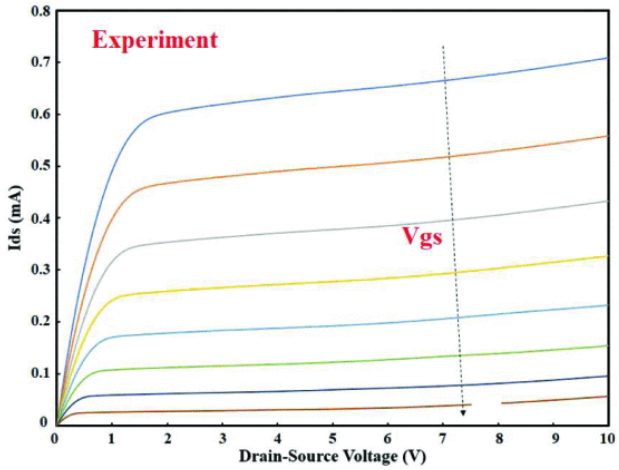


Figure A2- 4. The Ids-Vds curves of the sensor when the back gate voltage is increasing

According to Fig. A2-5, as the drain-source voltage increases, the current increases in the ohmic region, after which the current plateaus. According to the simulation, the threshold voltage at which the saturation region starts happens between ≈ 0.6 V and ≈ 1.7 V, depending on the value of the

back-gate voltage. As the simulation shows, the back-gate voltage decreases the total area available in front of charge carriers in the conduction channel. The simulation suggests the same trend as the experiment. Still, the errors are significant (10-30%) at specific drain-source voltages due to model simplifications and inconsistency between the boundary conditions and the actual sensor fabrication. To make the modeling more robust, the fabrication process's inventible errors must be controlled to meet exact values as simulation.

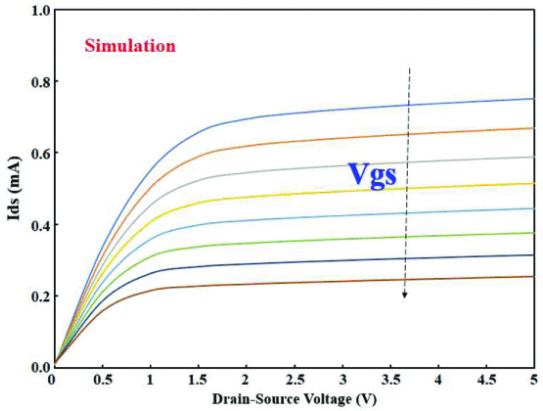


Figure A2- 5. COMSOL simulation result showing Ids-Vds of OG-JFET when back gate voltage is increasing

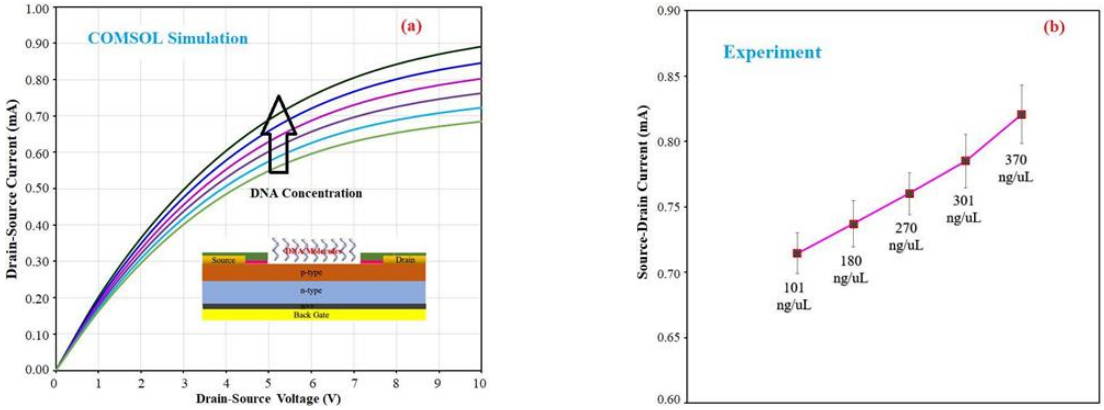


Figure A2- 6. Simulation and experimental results of dried ssDNA tests on the sensor for different concentrations (ug/nL). (a): COMSOL simulation, (b): experimental result

A2.3.2. Simulation and Experiment result of Dry DNA test

The ssDNA molecules were tested on the sensor to test the sensor's response to a surface charge variation. The results show the sensor's effectiveness in measuring dried DNA charge. The ssDNA concentration was put in ultrapure water and dropped on the sensor with a pipette. After evaporation, the sensor response was recorded. Different concentrations of DNA were used in water, which resulted in an almost linear response. Also, the existence of ssDNA molecules on the

sensor is simulated. The simulation is based on assumptions and simplifications. Nevertheless, accumulating extra negative charges on the sensor's surface increases the current.

A2.4. CONCLUSION

In this paper, a new FET biosensor is presented. The structure of the sensor is based on the OG-JFET, which is like the conventional JFET with a removed top gate. Here, an almost 0.7 mm^2 sensing area is designed on a 10 mm^2 die area by common sourcing of seven FET channels with size of 100 µm × 1000 µm. The depth of all channels is the same, which is 1.6 µm. The sensor was tested with a probstation, and the critical I-V curves were recorded. However, the results show that the sensor's response is like the conventional JFET, with different electronic characteristics. The sensor can be operated in two modes: forward and reverse bias. The reason for such a characteristic is that the sensor is made of a p-n junction that allows reverse and forward bias of the junction with the polarity of the applied voltages. It is demonstrated that the sensor I-V curves can be used to characterize sensors and evaluate biosensing performance. For example, the dried DNA with different concentrations was prepared and dropped on the sensing area. The result showed a 30 µA/DNA-concentration sensitivity for this sensor. This is an almost linear response. Also, the sensor is simulated in COMSOL multiphysics to ensure its electronic responsivity and charge sensing performance. The simulation results demonstrate the same trend as the experiment. However, there is an invertible error due to model simplifications.

ACKNOWLEDGMENT

We would like to acknowledge Mitacs and CMC Microsystems' support for providing products and services that facilitated this research. The authors also thank Morteza Ghafar-Zadeh for preparing DNA samples for experiments.

A2.5. References

[1] A. Panahi, D. Sadighbayan, S. Forouhi, and E. Ghafar-Zadeh, "Recent advances of field-effect transistor technology for infectious diseases," Biosensors, vol. 11, no. 4, 2021, doi: 10.3390/bios11040103.

[2] D. Sadighbayan, M. Hasanzadeh, and E. Ghafar-Zadeh, "Biosensing based on field-effect transistors (FET): Recent progress and challenges," TrAC - Trends Anal. Chem., vol. 133, p. 116067, 2020, doi: 10.1016/j.trac.2020.116067.

[3] A. Poghossian and M. J. Schöning, "Recent progress in silicon-based biologically sensitive field-effect devices," Curr. Opin. Electrochem., vol. 29, p. 100811, 2021, doi: 10.1016/j.coelec.2021.100811.

[4] P. Fathi-Hafshejani et al., “Two-Dimensional-Material-Based Field- Effect Transistor Biosensor for Detecting COVID-19 Virus (SARS- CoV-2),” ACS Nano, vol. 15, no. 7, pp. 11461–11469, 2021, doi:

10.1021/acsnano.1c01188.

[5] I. Novodchuk, M. Bajcsy, and M. Yavuz, “Graphene-based field effect transistor biosensors for breast cancer detection: A review on biosensing strategies,” Carbon N. Y., vol. 172, pp. 431–453, 2021, doi: 10.1016/j.carbon.2020.10.048.

[6] V. Adinolfi and E. H. Sargent, “Photovoltage field-effect transistors,” Nature, vol. 542, no. 7641, pp. 324–327, 2017, doi: 10.1038/nature21050.

[7] G. Barillaro, G. M. Lazzerini, and L. M. Strambini, “Modeling of porous silicon junction field effect transistor gas sensors: Insight into NO2 interaction,” Appl. Phys. Lett., vol. 96, no. 16, 2010, doi: 10.1063/1.3391620.

[8] M. Sainato, L. M. Strambini, S. Rella, E. Mazzotta, and G. Barillaro, “Sub-parts per million NO2 chemi-transistor sensors based on composite porous silicon/gold nanostructures prepared by metal- assisted etching,” ACS Appl. Mater. Interfaces, vol. 7, no. 13, pp. 7136–7145, 2015, doi: 10.1021/am5089633.

[9] A. Panahi, H. O. Tabrizi, P. Mangannavar, O. Chebotarev, A. Fung, and E. Ghafar-Zadeh, “Open-Gate Junction Field Effect Transistor (OG-JFET) for Life Science Applications: Design, Implementation, and Characterization,” IEEE Sens. J., vol. 21, no. 23, pp. 26503– 26514, 2021, doi: 10.1109/JSEN.2021.3121339.

[10] A. Panahi, D. Sadighbayan, E. Ghafar-Zadeh, “Electronic Sensing Platform (ESP) Based on Open-Gate Junction Field-Effect Transistor (OG-JFET) for Life Science Applications: Design, Modeling and Experimental Results” Sensors 21(22), 7491, 2021.

[11] A. Panahi, M. Ghafar-Zadeh, A. Scime, S. Magierowski, and E. Ghafar-Zadeh, “Novel Field-Effect Transistor Sensor for DNA Storage Monitoring,” IEEE Trans. Instrum. Meas., vol. 9456, no. c, 2021, doi: 10.1109/TIM.2021.3135531.

A3. Conference paper 3

Open-Gate Junction Field Effect Transistor (OG-JFET) Sensor for Life Science Applications

Authors: Abbas Panahi, Hamed Osouli Tabrizi, Priyadarshini Mangannavar, Oleg Chebotarev, Andrew Fung, Ebrahim Ghafar-Zadeh

Conference: Presented at the Canada Chemical Engineering Conference (CCEC) 2021 in the form of a presentation.

Abstract:

There have been tremendous efforts to develop biological field-effect transistors (BioFET) for different applications such as gene detection [1], cell analysis [2], enzyme reaction-based biosensors [3], and early detection of COVID-19 spike protein in human samples [4]. Owing to the superior characteristics of FET sensors in various biosensing applications, they have been recognized as a possible sensing component for point-of-care devices, which is believed to disrupt personalized medicine significantly when integrated with lab-on-a-chip technologies [5]. So far, various papers have reported FET-based sensors showing inefficient and bulky tasks through in-house microfabrication clean rooms. Nevertheless, there is still a demand for fabless microfabrication of FET sensors, which greatly influences the precision of processing and packaging for higher production yield. In this contribution, we have designed and fabricated an OG-JFET to monitor the pH of a solution, which is the basis for further development of biosensors.

A new ion-sensitive field-effect transistor named open-gate junction field-effect transistor (OG-JFET) is employed to develop the sensor for pH sensing. The sensor is proposed to be used for chemical and biological sensing applications. OG-JFET is characterized, and all the transfer characteristics required for biosensing/ion-sensing of OG-JFET have been derived. The sensor response towards H+ ion has been described by solution with different pH values. Also, we have conducted a COMSOL Multiphysics to gain a better understanding of the sensor operation and mechanism of sensing. The simulation results demonstrated good consistency with experimental results, making the simulations a reliable reference for sensor design. OG-JFET showed a

sensitivity of 55.29 mV/pH, a hysteresis of 16 mV, and a drift of 3 μA/hours. For the first time, the simulation and experimental results in this paper put forward the OG-JFET as a new ion-sensitive FET sensor for chemical and biological applications.

[1] Y. Wang, Y. Bi, R. Wang, L. Wang, H. Qu, and L. Zheng, "DNA-Gated Graphene Field-Effect Transistors for Specific Detection of Arsenic(III) in Rice," J. Agric. Food Chem., vol. 69, no. 4, pp. 1398–1404, 2021, doi: 10.1021/acs.jafc.0c07052.

[2] Y. Cho, V. A. P. Ba, J. Y. Jeong, Y. Choi, and S. Hong, "Ion-selective carbon nanotube field-effect transistors for monitoring drug effects on nicotinic acetylcholine receptor activation in live cells," Sensors (Switzerland), vol. 20, no. 13, pp. 1–13, 2020, doi: 10.3390/s20133680.

[3] H. J. Jang et al., "Electrical signaling of enzyme-linked immunosorbent assays with an ion-sensitive field-effect transistor," Biosens. Bioelectron., vol. 64, pp. 318–323, 2015, doi: 10.1016/j.bios.2014.09.020.

[4] G. Seo et al., "Rapid Detection of COVID-19 Causative Virus (SARS-CoV-2) in Human Nasopharyngeal Swab Specimens Using Field-Effect Transistor-Based Biosensor," ACS Nano, vol. 14, no. 4, pp. 5135–5142, 2020, doi: 10.1021/acsnano.0c02823.

[5] M. Kaisti, "Detection principles of biological and chemical FET sensors," Biosens. Bioelectron., vol. 98, no. July, pp. 437–448, 2017,

During his thesis, Abbas Panahi made several other contributions in the form of journal and conference papers. These contributions are listed below, along with a brief explanation of his specific roles:

B1. Collaboration Paper 1

Hamed Osouli Tabrizi, Abbas Panahi, S. Forouhi, D. Sadighbayan, F. Soheili, M.R. Haji Hosseini Khani, S. Magierowski, E. Ghafar-Zadeh. Oral Cells-On-Chip: Design, Modeling and Experimental Results. Bioengineering, 2022 (Published)

Abbas Panahi's contribution: Numerical simulation (FEM model) of the capacitive sensor and exploring the sensing mechanism of the CMOS capacitive sensor for cell detection. Writing and editing paper partially.

B2. Collaboration Paper 2

Saghi Forouhi, Hamed Osouli Tabrizi, Abbas Panahi, Ebrahim Ghafar-Zadeh, A CMOS Thermo-Capacitive Technique for Monitoring Water-Alcohol Solutions. Under Review

Abbas Panahi's contribution: Numerical simulation of the CMOS capacitive sensor and investigating the effect of different concentrations of ethanol/methanol on the sensor's output.

Conferences:

B3. Collaboration Conference Paper 1

Saghi Forouhi, Hamed Osouli Tabrizi, Abbas Panahi, Sebastian Magierowski, Ebrahim Ghafar-Zadeh. Novel CMOS Thermo-Capacitive Sensing Method for Lab-on-Chip Applications. IEEE Biomedical Circuits and Systems Conference (BioCAS), 2023, Presented

Abbas Panahi's contribution: Numerical simulation of the CMOS capacitive sensor and investigating the effect of different concentrations of ethanol/methanol on the sensor's output.